Evaluating the Effect of Decking Fasteners on the Seismic Behavior of Steel Moment Frame Plastic Hinge Regions

Bradley Wayne Toellner

Master's Thesis submitted to the faculty of the Virginia Polytechnic Institute and State University in partial fulfillment of the requirements for the degree of

Master of Science
In
Civil and Environmental Engineering

Matthew R. Eatherton

Finley A. Charney

Roberto T. Leon

April 22, 2013

Blacksburg, Virginia

Keywords: Finite Element Modeling, Low-cycle Fatigue, Seismic Behavior, Steel Moment Resisting Frames, Full-Scale Testing

Evaluating the Effect of Decking Fasteners on the Seismic Behavior of
Steel Moment Frame Plastic Hinge Regions

Bradley Wayne Toellner

ABSTRACT

A series of full-scale beam-to-column moment connection tests were completed to determine the effects of powder actuated fasteners (PAF) and puddle welds on the seismic behavior of steel moment connections. In seismic regions, PAF are currently prohibited in the connection region (referred to as the protected zone) due to the concern of low-cycle fatigue fracture. There is almost no information available in the literature regarding the seismic behavior of moment connections with PAF or puddle welds.

Full-scale connection testing is the most accurate way to investigate the behavior of different moment connections with common defects and fasteners applied in the protected zone. However, it is cost prohibitive to conduct full-scale testing programs that are sufficiently comprehensive to investigate a wide range of defect types, severity, and locations. For this reason, it is desired to develop alternative methods of investigation. A finite element (FE) model capable of simulating both the global deformation patterns and local buckling effects in a moment connection has been developed. Validated FE models will allow for further evaluation through numerical simulation of additional configurations. Furthermore, alternate, more economical, test configurations to experimentally investigate the effect of defects on steel moment connections were explored. This report discusses the full-scale test setup, results and analysis of completed experimental testing, the development of an FE connection model, and the preliminary development of alternate test configurations.

ACKNOWLEDGEMENTS

This material is based on work supported by Hilti Corporation and the American Institute of Steel Construction. In-kind funding was provided by Banker Steel Company and Applied Bolting Technology.

Valuable assistance in the preparation and conducting of tests was provided by Charles Watkins, Karim Laknejadi, Ebrahim Abbas, Ngan Dinh, and Stuart Salmon

Additional thanks are given to the members of my advisory committee Matthew Eatherton, Roberto Leon, and Finley Charney, for providing direction and recommendations regarding this research endeavor and the completion of this thesis document.

TABLE OF CONTENTS

LIST OF FIGURES

LIST OF TABLES

CHAPTER 1: INTRODUCTION

1.1 Motivation for Steel Moment Connection Testing

Widespread fractures in steel moment frames during the 1994 Northridge earthquake brought the ductile behavior of steel moment frame connections into question. Despite the expectation that steel moment connections could undergo large inelastic rotations, a disturbingly large number of these connections experienced unexpected brittle fractures without significant inelastic deformation occurring. A large number of fractures occurring in the vicinity of the welded beam-to-column connections gave rise to the need for further study of these connections. It became necessary to explore new means of preventing brittle fracture through both connection design modifications and tight restrictions on variations outside of tested conditions.

The ensuing FEMA/SAC joint research project involved testing of numerous moment connections subjected to cyclic displacement histories well into the inelastic regime. This included tests to observe the effects of composite slabs and welded shear studs on the performance of the beams. Test observations and results indicated that the length of the beam within several feet of the connection played a significant role in the performance of the connection. This region of the beam experiences large inelastic strains during cyclic earthquake type loading as plastic hinging and local buckling occurs at increased story drifts. The criticality of this region was further identified when a single test experienced a fracture at the location of a welded shear stud on the top flange near a moment connection (Ricles et al. 2002). The AISC 341 Seismic Provisions (AISC 2010a) identifies the beam ends and connection region in special moment resisting frames (SMRF) as the 'protected zone'. In the protected zone, all methods of deck attachment except for puddle spot welds are prohibited. This decision was made in part due to the single shear stud test fracture occurrence. Due to the lack of additional testing and as a precautionary decision, all other types of fasteners including welded, bolted, screwed, or shot-in attachments were prohibited in the protected zone. The lack of experimental testing into the effects of different types of fasteners, as well as other defects or defect repairs that can be common in practice indicates a vital research need. The goal of this study is to investigate the low-cycle fatigue behavior of moment connections with defects or fasteners in the protected zone of SMRF beams.

1.2 Low-Cycle Fatigue Testing Approach

An examination of previous research on low-cycle fatigue provides important context for the mechanism of steel fracture during earthquakes. In conjunction with efforts to study the effects of fasteners and other flange discontinuities due to gouges or welds, it will be critical to understand how these irregularities influence the low-cycle fatigue behavior of the protected zone. Prior research results support a relationship between low-cycle fatigue fracture and both stress triaxiality and localized cumulative plastic strain (Bao & Wierzbicki, 2004).

This paper describes a series of experimental tests and computational studies performed to improve the understanding of the behavior of the protected zone. Full-scale moment connection tests provide the means for initial study into the effect of powder actuated fasteners (PAFs) applied in the protected zone and baseline data for the validation of other methods of investigation.

The testing program included twelve tests on W24x62 beams and W36x150 beams with either extended end plate or reduced beam section (RBS) type moment connections. Half of the tests included PAFs. The general layout of these tests is provided in this document. A more in-depth explanation of the test setup is provided by Watkins (2013). The instrumentation plan was designed to capture both the global performance of the test setup and connection as well as local strain variations in the protected zone. The strain variations measured across the flanges will give information about the change in strain distribution resulting from the inclusion of PAFs. This document primarily focuses on the general results of each test specimen as well as an analysis of the performance of those specimens with regard to SMRF qualification criteria outlined in AISC 341 (2010a). General test results discussed in this document include observations of the progression of limit states as beam specimens begin undergoing plastic deformations as well as a discussion about the observed effect of PAFs and puddle welds as their inclusion and placement varied between specimens. The analysis of specimens related to qualification criteria includes a summary of their hysteretic behavior and story drift decomposition. Hysteretic profile properties include moment capacities at the qualification cycle, maximum overall moment capacities, degradation of moment capacity during various repeated cycles, and energy dissipation profiles. Story drift decomposition results include both

the absolute and relative contribution of individual system components comprising a portion of the total story drift and a discussion of differences observed between different beam types.

While these full-scale tests are designed to provide a reasonably accurate representation of the loading and boundary conditions typical in real buildings (one significant difference being the absence of a concrete slab), they prove disadvantageous for performing a large number of tests due to the costs associated with fabrication, transportation, and storage of such large beams. For this reason, it was deemed desirable to develop an economical test method that represents the same conditions of a full moment connection. This document describes the initial efforts to develop computational models and alternative testing configurations that will be continued by others in upcoming phases of the overall study.

A new coupon specimen test method is proposed to provide this economic alternative. The coupon test method would enable further utilization of the undeformed material regions of the beams used in full-scale moment connection tests. It would also provide the opportunity to expand the study beyond solely the effects of PAFs to a variety of other defect and repair techniques typical in steel beams. The general approach for coupon tests is to represent specific regions from the beam in full-scale tests. Different regions of the beam are isolated based on their location and the resulting unique stress and strain histories that they experience. A given location can be represented by a coupon specimen by subjecting it to a strain history similar to that which occurs at that location. This unique strain history will be created using axial displacement protocols which are designed to provide the same cumulative strains and peak inelastic strain magnitudes. While the present study includes the development of the coupon testing program concept, the building and performing of such tests is not within the scope of the current study.

Finite Element Method (FEM) modeling of the full moment connection is another approach for analyzing the effect of defects on protected zone behavior. This study utilizes three dimensional modeling of full-scale tests with solid brick elements to analyze localized stress and strain histories due to plastic hinging and local buckling. This stress and strain profile will be crucial for analyzing low-cycle fatigue fracture potential. FEM modeling will also be of use in transforming the behavior of the flange during full-scale connection tests into the equivalent axial displacement protocol inputs for coupon tests.

1.3 Organization of Thesis

This thesis describes several phases of the overall study of low-cycle fatigue effects in the moment connection protected zone. Phase I encompasses the full-scale testing. Phase II is the exploration of alternative testing configurations and the initial development of a suitable coupon test protocol and test setup. Phase III is the development of an FEM modeling procedure that could be used to evaluate peak strain and cumulative strain demands.

- Chapter 1 provides a motivation for investigating the effect of defects on the seismic behavior of moment connections. It also summarizes what is included in this document.

- Chapter 2 provides a discussion of the literature which is coordinated with research initiatives taken for this project. A brief discussion of general knowledge currently available in the field of low-cycle fatigue is presented. Discussion is also provided related to previous efforts to accurately model moment connections through a variety of finite element modeling techniques. Additional resources include information about stress triaxiality and the effect of strain rate on the performance of moment connection tests.

- Chapter 3 discusses the Phase I testing of full-scale moment connections including the goals of the testing, the test plan, and the instrumentation employed for data collection.

- Chapter 4 discusses the performance of all tested specimens. This includes general observations about the performance of specimens with differing variables as well as an analysis of the hysteretic behavior and story drift decomposition from each test. It describes how data from the multiple instrumentation sources can be used to decompose the imposed story drift into components for verifying adequacy of the test setup behavior, validating instrumentation accuracy, and assessing demands on the protected zone.

- Chapter 5 explains the initial development of FEM models in an effort to accurately match the physical full-scale test results. It discusses methods of validating the model as well as a discussion of discovered model sensitivities

- Chapter 6 presents the developed Phase II test setup in the form of a general description with accompanying design drawings. It also provides a description of earlier setup concepts and the brief comparison study performed on them to determine their feasibility to accurately represent full moment connections.

- Chapter 7 discusses conclusions reached within this study. These include overall observations of test performance and a summary of work intended to be carried on in future studies.

- Appendices provide instrumentation, hysteretic, and story drift decomposition plots for each test. Additionally the appendices include a discussion of general and test specific modifications performed on raw data to facilitate its use in the data analysis performed in this study.

CHAPTER 2: LITERATURE REVIEW

2.1 Cyclic Fatigue Background

Steel components are subject to two general categories of fatigue mechanisms depending on the type of loading they experience. These two types, high-cycle fatigue and low-cycle fatigue both have the potential to cause failure of the steel member. High-Cycle Fatigue (HCF) is characterized by a large number, as many as thousands or millions, of repeated loading cycles with amplitudes in the elastic range of the material. This fatigue type is common in the moving components of transportation and other mechanical systems as well as in bridges, which experience repeated loading due to passing vehicles. High-cycle fatigue has been studied significantly starting in early industrial era projects such as the lifelong performance of train wheels at a time when rail transportation emerged.

Low-Cycle Fatigue (LCF) is characterized by significantly fewer cycles, typically less than 100, with magnitudes exceeding the elastic limit of the material. Low-cycle fatigue is typical among components subjected to seismic loading as occurs during an earthquake. This mechanism of fatigue is considered to be strain-controlled as the strain range encountered, $\Delta\varepsilon$, exceeds that of the range between compressive and tensile elastic limits, ε_y. This is given by the following equation.

$$\Delta\varepsilon > 2 \times \varepsilon_y \tag{2.1}$$

Steel failure due to low-cycle fatigue is typically characterized by ductile fracture due to the high strain cycling. The mechanism of failure originates with growth and coalescence of micro-voids present in the steel. As high strain cycles continue, this void coalescence produces micro cracks that propagate through the material until material strength is reduced such that macro scale fracture occurs as the material is subjected to tension (Fell et al. 2006).

2.2 Study of Low-Cycle Fatigue

Most attempts to analytically model low-cycle fatigue are rooted in initial independent studies by Coffin (1968) and Manson (1954). The two studies attempted to uncover the relationship between inelastic cyclic loading and the occurrence of fracture for different temperatures. This work led to the development of an analytical model known as the Coffin-Manson relation which is given by the following equation.

$$\Delta\varepsilon * N^{\alpha} = C \tag{2.2}$$

The equation establishes a relationship between the applied constant strain amplitudes, $\Delta\varepsilon$, and the number of cycles to failure, N. This relationship allows a prediction of cycles to failure using material constants α and C.

Experimental studies have been performed to confirm the validity of the Coffin-Manson relation (e.g. Nip et al. 2010). In general, the relation has proved to be a reasonable predictor of material behavior in the higher cycle regime of low-cycle fatigue. However, the relation has tended to break down in cases of an exceptionally low number of cycles to failure. Materials experiencing a high amplitude cyclic strain tend to fail in fewer cycles than predicted by the Coffin-Manson relation. This is represented by a divergence of the linearity of test data at high strain values. For this reason, the region of behavior with an extremely low number of cycles to failure (approximately 10-20 cycles) has come to be known as Ultra Low-Cycle Fatigue (ULCF). Several efforts have been made to modify the Coffin-Manson relation to more accurately model experimental data falling within the ULCF regime (Xue, 2008). In one such effort, Xue proposed a two-variable (λ and m) exponential function that better models previously collected experimental data from (Coffin & Tavernelli, 1959). Figure 1 shows an example of the correlation shown by the two-variable exponential model.

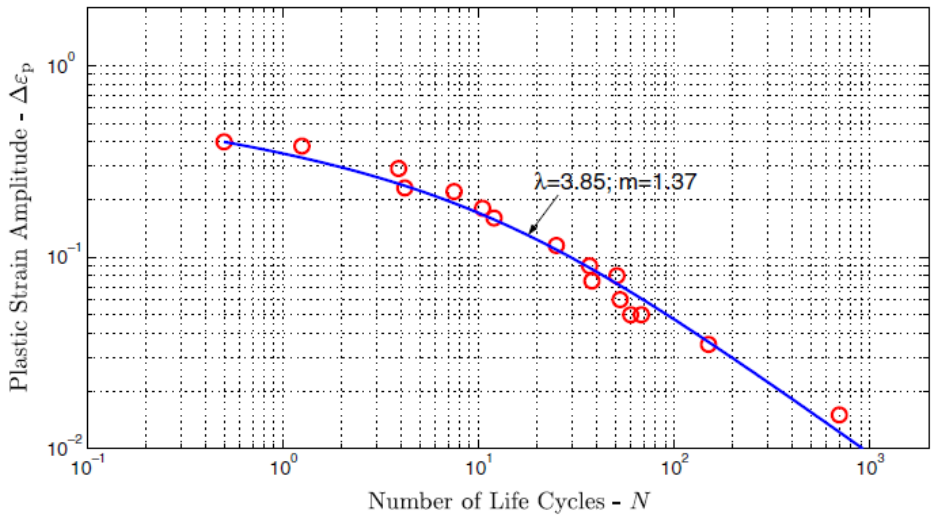

Figure 1: Overlay of Relationship Function by Xue and Experimental Data from Coffin and Tavernelli [from Xue, 2008]

While ULCF follows the same general behavior as LCF, its initiation of fracture after such a low number of cycles promotes increased consideration of it as a unique fatigue profile. In most cases, earthquakes can be considered to fall in the range of ULCF due to their low number of cycles and the potentially high strain amplitudes they exact on structures. Numerous experimental studies have been performed on the behavior of steel connections in the ULCF range. Many of them utilize repetitive cycles of the same high strain amplitudes (Fell et al. 2006)

A number of analytical models have been developed to characterize low-cycle fatigue. These models include the aforementioned Coffin-Manson relation (Manson, 1954), the Stress Modified Critical Strain (SMCS) criterion (Hancock & Mackenzie, 1976), the Cyclic Void Growth (CVG) model (Kanvinde & Deierlein, 2007), as well as several others. Among the limited studies performed on LCF and ULCF, the focus has been primarily on nominal general steel members. No prior work is available regarding the fundamentals of such fatigue types as they apply to the effect of disruptions in the homogeneity of specimens such as fasteners or defects.

2.3 Effect of Strain Rate

Most full-scale moment connection tests utilize either monotonic loading or quasi-static "slow cyclic" loading protocols. This is often preferred since test equipment for such tests is more

affordable than that of dynamic tests. It also provides for a more in-depth observation of specimen performance during the course of a test. Despite its significantly slower load rate, quasi-static testing is typically considered to be a reasonable simulation of seismic loads. A 1992 ATC-24 testing guidelines document notes that quasi-static tests are conservative due to slightly decreased specimen strengths when loaded at a slow cyclic rate rather than at a fast rate. Additionally, the rate of deterioration is slightly greater for slow cyclic loading protocols. (ATC, 1992)

A report released as part of the SAC Joint Venture partnership (2000b) identifies that weld and base metal are proven to behave in a more brittle manner when subjected to very high dynamic strain rates. It identifies true dynamic strain rates as those in the range of 10in/in/sec or greater. Acceleration records from numerous steel frame buildings indicate that strain rates during seismic events are typically on the order of 0.05 to 0.15 in/in/sec. While these strain rates are large compared to those that would be present in quasi-static loading, they are significantly smaller from the true dynamic strain rates that are shown to accompany significant changes in material ductility. For this reason, seismic events can be considered to fall into the range of intermediate strain rates in which material behavior shows no dramatic difference from that of quasi-static strain rates

SAC Joint Venture (2000b) identifies a limited number of studies that have utilized testing in the range of dynamic strain rates. A test by Uang and Bondad (1996) utilized both quasi-static and dynamic loading protocols on several pre-Northridge connection specimens in order to compare their effects. The quasi-static protocol was from ATC-24 which uses load controlled cycles until yield and then continues with displacement controlled cycles. The dynamic protocol was created based on ATC-24 to achieve similar amplitude displacements while simulating a structural response period of 1 second. Figure 2 shows an overlay of the hysteresis plots from one of each test rate type. The dynamic loaded test (red) was continued following a fracture at the beam bottom flange groove weld which occurred after a small plastic rotation. Post-fracture data is indicated by the dotted line. Results from the test program clearly show an increased possibility of brittle fracture during dynamic testing. SAC (2000b) indicates that these results are not consistent with those of other studies. SAC reports the validity of results by Uang and Bondad as inconclusive due to a lack of supporting evidence and a less than clear explanation regarding

reported test data. Among these insufficient explanations is the fact that Uang and Bondad reported an 18% increase in flange forces during a dynamic loading test despite the fact that no significant increase in moment compared to quasi-static tests was present.

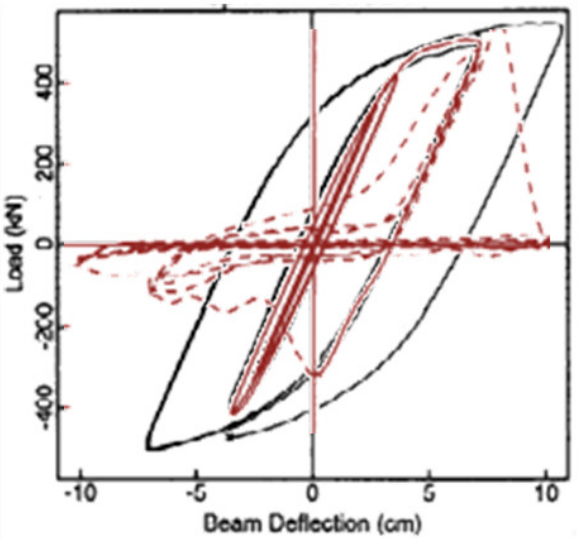

Figure 2: Hysteretic Overlay of Quasi-static (black) and Dynamic (red) Loaded Tests [individual hystereses from Uang and Bondad, 1996]

SAC Joint Venture (2000b) identifies numerous tests completed in Japan (AIJ, 1997) that sought to compare the effect of strain rate on identical high strength steel specimens with some tests including temperature as an additional variable. General conclusions from these test programs showed no adverse effects from dynamically loaded tests when temperatures were at typical levels. When considering energy dissipation and ductility behavior, it was concluded that seismic performance was actually slightly better than that of static tests. It is noted that results of dynamic tests indicate a poorer performance in low temperatures where ductility is further reduced by the combination of a high strain rate and a low temperature.

2.4 Moment Connection Finite Element Modeling

Financial and instrumentation limitations inherent in experimental studies make it impossible to conduct enough experiments or have sufficient local strain information to fully understand low-cycle fatigue. For this reason, computer modeling represents a necessary complement to experimental testing due to the low costs associated with such studies and the ability to analyze

behavior on a small scale. Increased computing ability and improvements in commercial model analysis programs in recent years has made it possible to utilize finite element methods for complex geometries, such as that of moment connections. This literature review will discuss some common modeling techniques and constraints as well as efforts that have been made to correlate simulation of steel moment connections with experimental data.

2.4.1 Shell Element Modeling

Shell element modeling exists as a simplified approach to modeling three dimensional systems with plate-like components. This is possible for basic moment connection modeling as I-shaped beams and columns can be interpreted as an assembly of plates. System geometry is modeled as a mesh of two-dimensional, typically four-node quadrilateral or three-node triangular, elements. The shell elements are usually based on thin plate theory and are assigned a thickness to account for the actual thickness of the real components they represent.

Pantelides et al. (2009) relied exclusively on shell element modeling to simulate the performance of reduced beam section moment connections. The study sought to determine critical column web stiffness for compact W14 and W18 columns in order to determine when column continuity plates are required for connection to a W30x132 beam. ANSYS (2005) software was used for modeling. The model accounted for plasticity and strain hardening in the steel constitutive model. In addition geometric nonlinearity was incorporated for large deflections. Boundary conditions were provided to represent the corresponding experimental tests. Lateral restraints were placed on the beam top flange at locations of lateral bracing. A simplified displacement history was applied to the beam in order to reduce computing time and data size. The vertical displacements applied to the free end of the beam achieved equivalent magnitudes as in experimental testing, but the model was only subjected to one cycle at each displacement magnitude. The study showed a strong correlation between simulation and experimental results as can be seen in Figure 3, taken from Pantelides et al. (2009). The correlation validated the model which allowed for additional simulation of different column geometries in the absence of any additional corresponding experimental tests.

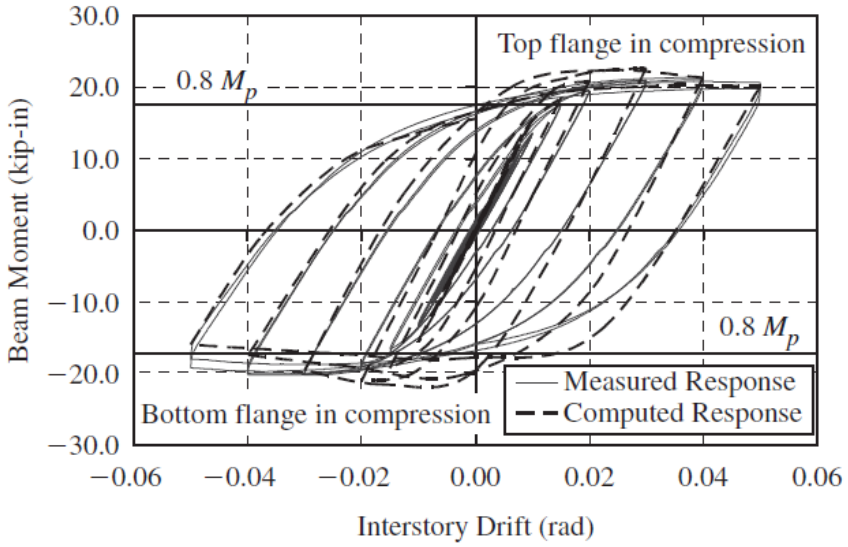

Figure 3: Hysteresis Comparison between Experimental Data and FEM Model [from Pantelides et al. 2009]

A study by Pachoumis et al. (2010) utilized similar modeling techniques. This second study utilized shell element modeling as part of a greater study to translate reduced beam section concepts to European wide flange section profiles. For this study, ABAQUS (Simulia, 2010) software was used for simulation and the model was subjected to the displacement protocol given in the AISC seismic specifications (AISC 2010a). As in (Pantelides et al. 2009), the motivation behind modeling was to correlate simulation and experimental results. Biaxial symmetry about a plane parallel to the length of the beam and column was considered as justification for modeling only half of the beam specimens as shown in Figure 4. This decision was made in order to reduce computational time. The new surface resulting from the beam and column centerline cut was laterally restrained in order to eliminate any effect due to a now asymmetric lengthwise geometry.

Pachoumis claimed a reasonable correlation of FEM simulation and experimental test data. Figure 5 shows a comparison of moment rotation results. For this particular RBS specimen geometry, the applied moment at initial yield was reported to be 80 kN-m for the FEM model and 86 kN-m for the corresponding experimental test. This would indicate that dividing the beam in half and assuming symmetrical results from the non-modeled side is a suitable simplification for the purpose of accurately predicting the applied moment necessary to achieve a prescribed displacement protocol. It should be noted that this simplification is presumably not suitable for a more in depth investigation into flange behavior as it applies to strain and local buckling patterns. Visual observation of experimental tests indicate that the typical behavior of

moment connections as a plastic hinge forms is for the web to buckle in one direction while each flange experiences an upward buckle on one side and a downward buckle on the other side. This deformation profile is not biaxial symmetric. Therefore, a study into more local effects than the global nature of Pachoumis' study would require a full model that can account for expected asymmetric behavior.

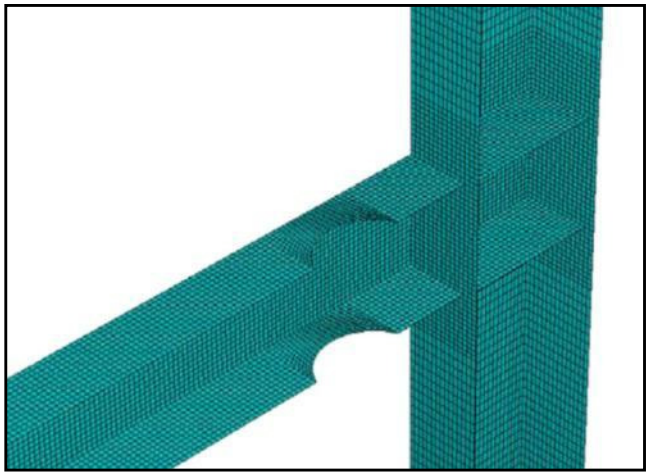

Figure 4: Shell Element Mesh for Half of an RBS Connection [from Pachoumis et al. 2010]

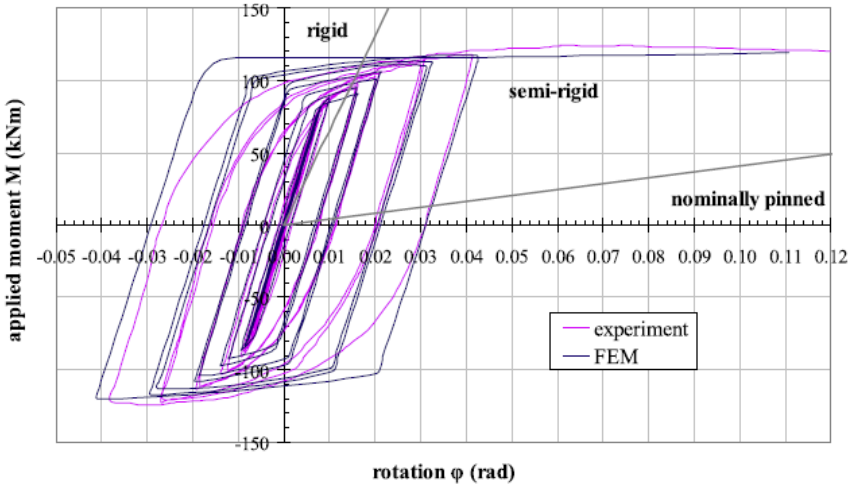

Figure 5: Hysteresis Comparison of Experimental Data and FEM Model [from Pachoumis et al. 2010]

2.4.2 Solid Element Modeling

Unlike shell element modeling, solid modeling explicitly incorporates the thickness of mesh elements in their geometry definition. This additional consideration creates three dimensional mesh elements, typically of either a four-node tetrahedral or an eight-node hexahedral (brick) shape. Solid element modeling is advantageous for problems in which analysis of stress

triaxiality is desirable. For both shell and solid elements, numerical integration is necessary to calculate the stiffness matrix for complex finite element systems. Since a fine mesh is typically required in a large portion of the moment connection region, computing time and data size become important factors. For this reason, finite element modeling programs typically recommend utilizing reduced integration, which reduces the number of points of integration in each mesh element (Simulia, 2010).

Ricles et al. in a 2000 SAC Joint Venture report (SAC Joint Venture, 2000a) reported a strong correlation between a finite element model and experimental results reported by Popov (1996) in a SAC document (SAC Joint Venture, 1996). The specimen modeled was a typical pre-Northridge moment connection. It included backing bars and supplementary beam web fillet welds. The FEM model and test specimen reported near identical elastic stiffness. The FEM model showed a maximum load of 195 kips corresponding to a total plastic rotation of 0.34 radians. Similarly, the test specimen resisted a maximum load of 192 kips to achieve a total plastic rotation of 0.35 radians. Figure 6 shows a hysteretic comparison of these results. Further model validation was achieved by the fact that at the second cycle of 2% story drift, the point at which the test specimen fractured at the conjunction of the column and beam bottom flange, the same location on the model showed the highest fracture potential. This validation provided for confidence to use the finite element model for a connection parametric study.

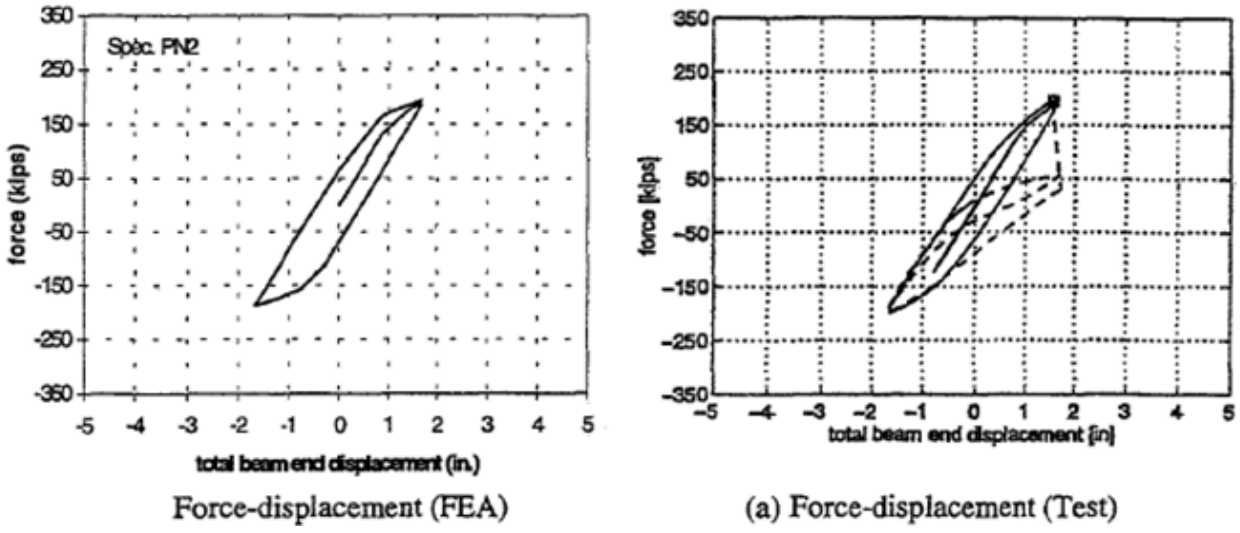

Figure 6: FEM Analysis and Test Results Comparison [From SAC Joint Venture, 2000a]

Several recent studies employed solid hexahedral elements by using the biaxial symmetry simplification discussed for shell element studies. A biaxial symmetric solid element model is shown in Figure 7. Pachoumis et al. (2010) simulated an RBS connection using solid elements under the same boundary and loading conditions applied to the shell element model previously discussed. It was found that modeling the beam flange using shell elements or solid elements gave comparable results for the applied moment necessary to achieve a relative story drift.

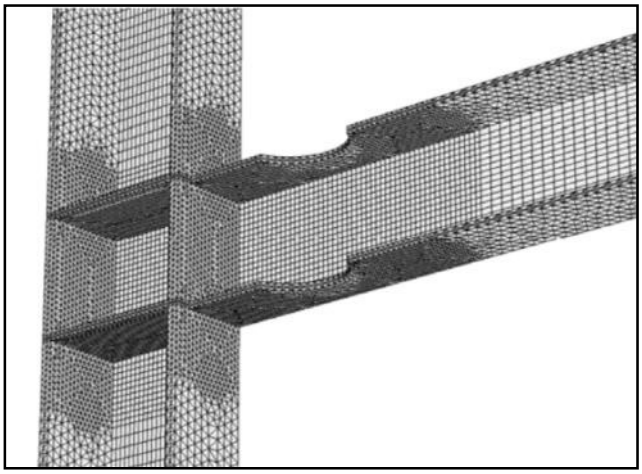

Figure 7: Solid Element Mesh for Half of an RBS Connection [from (Pachoumis et al. 2010)]

Eldermash et al. (2012) used ABAQUS solid element modeling to investigate endplate connection improvements without any experimental component. Two solid element models were developed to correspond to two reported experimental tests conducted by Sumner et al. (2000) as part of the SAC Phase 2 Steel Project. The two experimental tests included a W30x99 beam connected to a W14x193 column using sixteen 1.25 inch diameter bolts. The tests differed in the endplate thickness with the first using a 1.125 inch thickness and the second using a 1 inch thickness. Specimens were subjected to a monotonic loading protocol in order to study the strength and behavior of the connection bolts. Both models showed a strong correlation with the applied moment to rotation behavior of the test specimens. Elastic stiffness predicted by the models fell within 3% below the stiffness from experimental data. Experimental data for the maximum applied moment to rotation exceeded the simulations by up to 5%.. This validation of the FEM models allowed for an additional study into a potential connection improvement.

It was proposed that thin shims placed flush with the endplate and between the beam flanges could improve the bolt force distribution of the interior bolts passing through the added shims. One of the validated models was modified to incorporate the additional shim plates. Simulation of the new model indeed indicated an improved distribution of bolt force. This change corresponded with an apparent decrease in force in the interior bolts of up to 8%. Eldermash et al. (2012) concluded that this modification could assist in the prevention of bolt fracture during loading.

2.4.3 Stress Triaxiality

Modern low-cycle fatigue fracture models typically incorporate stress triaxiality as a contributing factor in the fracture process. While it is not a common design factor in structural engineering, it has been proposed that stress triaxiality plays a key and identifiable role in the fracture of moment frame connections (Schafer et al. 2000). Schafer sought to develop a finite element model of a single moment connection test reported by Popov (1996). Schafer's model used a quasi-static upward displacement control representative of the loading placed on the beam from the SAC test which was tested to fracture onset.

Several varying definitions of stress triaxiality exist. The most accepted definition, and that used by Schafer, defines it as the ratio of the mean stress, σ_{mean}, and the effective or von Mises stress, σ_{eff}, at a finite point. This is given by the equations below where T is the stress triaxiality and σ_i represents the stress in the corresponding "i" principal direction.

$$T = \frac{\sigma_{mean}}{\sigma_{eff}} \tag{2.3}$$

$$\sigma_{eff} = \sqrt{\frac{1}{2} * (\sigma_1 - \sigma_2)^2 * (\sigma_2 - \sigma_3)^2 * (\sigma_1 - \sigma_3)^2} \tag{2.4}$$

Scahafer's model of the moment connection test performed by Popov (1996) incorporates shear tabs as being fully connected to the column and connected to the web through constraints

representing bolts and welds. Material properties are input based on reported values from the SAC test. It is observed that the model includes simply supported connections at the column ends to represent inherent flexibility in the experimental test. The model also utilizes a biaxial symmetric plane as in aforementioned studies to improve simulation time and data size. The simulation reveals a stress state profile across the flange near the connection that is contradictory to what beam theory predicts. The shear is shown to vary from a minimum near the center of the beam to a maximum value near the flanges. Across the width and thickness of the bottom flange, the stress triaxiality follows a nonuniform profile. The triaxiality was greatest at the center below the web. This trend continued as the model reached the equivalent loading state as when fracture occurred during the test. This indicates a connection between the magnitude of the stress triaxiality and the point at which fracture occurs during increasing loading. This conclusion is supported by the fact that the location of greatest stress triaxiality from the model was consistent with the location of fracture onset in the test specimen.

CHAPTER 3: FULL-SCALE BEAM-TO-COLUMN MOMENT CONNECTION TESTS

3.1 Full-Scale Moment Connection Testing

Full-scale connection tests were performed to study the performance of steel moment connections with powder actuated fasteners (PAF) shot into the flange in the beam protected zone representing a means of decking attachment, partition connection, and other nonstructural attachments to the beam. In addition, the full-scale tests were performed to validate computational models and provide data to validate alternative test configurations.

This document provides a general layout of the test configuration, test matrix, and instrumentation plan, as well as test results. Further information regarding the test setup, reaction frame design, detailed information about the actual instrumentation locations, and PAF installation procedures can be found in Watkins (2013). This present document examines general test data including hysteretic behavior and a comparison of specimens with and without PAFs. In addition, this document decomposes story drift from each specimen to determine how much of the deformation is due to inelastic deformations of the plastic hinge and how the rest of the test setup behaves as it deforms during loading. A detailed discussion of test strain gauge data, evaluation of fractures, and the application of low-cycle fatigue models is provided by others in Eatherton et al. (2013).

The test configuration included a test column and removable cantilevered beams connected to the column using prequalified bolted endplate connections designed according to AISC 358 (AISC 2010b). In order to replicate a prescribed story drift, the test column was fixed at both ends while the beam was cycled at its free end by a vertically mounted actuator. The geometry of the test setup is intended to simulate a subassemblage of a moment frame undergoing rotation due to story drift. The 17 ft distance from the column centerline to the actuator represents the distance from the column centerline to the beam inflection point in a 34 ft long bay assuming an idealized moment distribution. Similarly, the column height of 12 ft represents the distance between column inflection points on adjacent floors assuming an idealized moment distribution, implying a building with 12 ft floor heights. Figure 8 shows a typical moment frame undergoing

lateral drift. The half span cantilever test setup is expected to accurately simulate the same rotation demands placed on a connection within a full frame. One difference could be the additional shear load placed on the test setup beam and connection due to the applied load by the actuator in order to simulate the rotation typically created by the double curvature bending of a full frame beam. This difference is assumed to be minimal and will not have a significant effect on test conclusions.

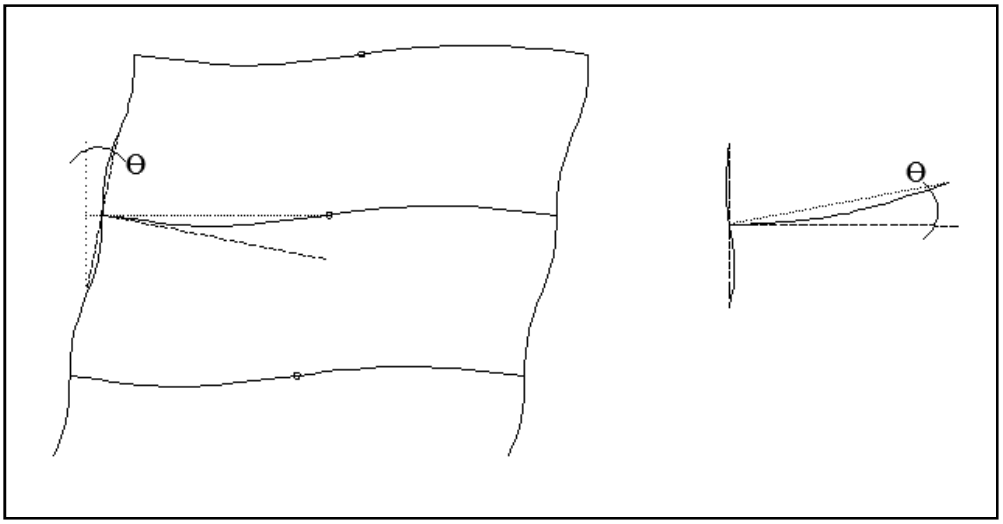

Figure 8: Full moment frame rotation (left) and Equivalent cantilever (right)

All specimens were subjected to the displacement protocol from the qualification requirements provided in AISC 341 Chapter K (AISC 2010a). The displacement protocol in AISC 341 is specified in terms of story drift. The displacement protocol of the cantilevered beam, as used in full-scale tests and presented in Figure 9, was created by multiplying the AISC 341 story drift profile by the 17 ft distance from the actuator to the column centerline. Proper attention to boundary conditions and application of required rotation values allow the test setup to behave as would be expected of a full frame.

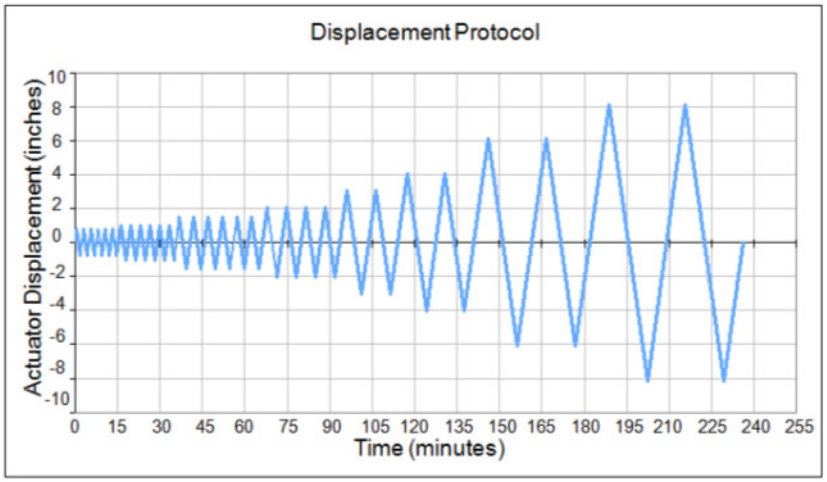

# Cycles	Story Drift (rad)	Displacement (in)
6	0.00375	0.765
6	0.005	1.02
6	0.0075	1.53
4	0.01	2.04
2	0.015	3.06
2	0.02	4.08
2	0.03	6.12
2	0.04	8.16

Figure 9: Full-Scale Moment Connection Loading Protocol (AISC 2010a)

To satisfy the qualification criteria, a specimen must undergo one complete cycle at 4% story drift while sustaining a moment resistance at the face of the column that is at least 80% of the nominal plastic moment capacity. The nominal plastic moment capacity is computed with nominal yield stress and nominal plastic section modulus.

Three individual frames form the overall reaction frame of the tests (Figure 10 and Figure 11). Watkins (2013) provides a more detailed description of the reaction frame components design and arrangement. An actuator frame provides a fixed mounting surface for a single actuator vertically above the point of loading on the beam. Diagonal members mounting on each of the frame's columns connect to the lab strong floor to provide additional global support to the frame as a whole. In addition, a single 'X' brace formed by intersecting bolted angles reduces the minor axis unbraced length of the two frame columns. This frame also provides a pair of beam lateral bracing members to restrain lateral-torsional buckling of the beam specimens.

A center reaction frame provides two additional lateral bracing locations. The location of this frame longitudinally along the test setup is dependent on the unbraced length restrictions of the various beam sections tested. A third reaction frame provides an intended fixed support for the top of the test column. It is comprised of two vertical columns with an adjoining W36x150 beam length mounted between them and to the top of the test column. The test column is a 12 ft tall W14x257 shape with sufficient drilled hole pattern to provide a mounting surface for the several bolted endplate connections. The column frame includes two diagonal members as well as an 'X' brace, as in the actuator frame, to provide stability to the frame as a whole.

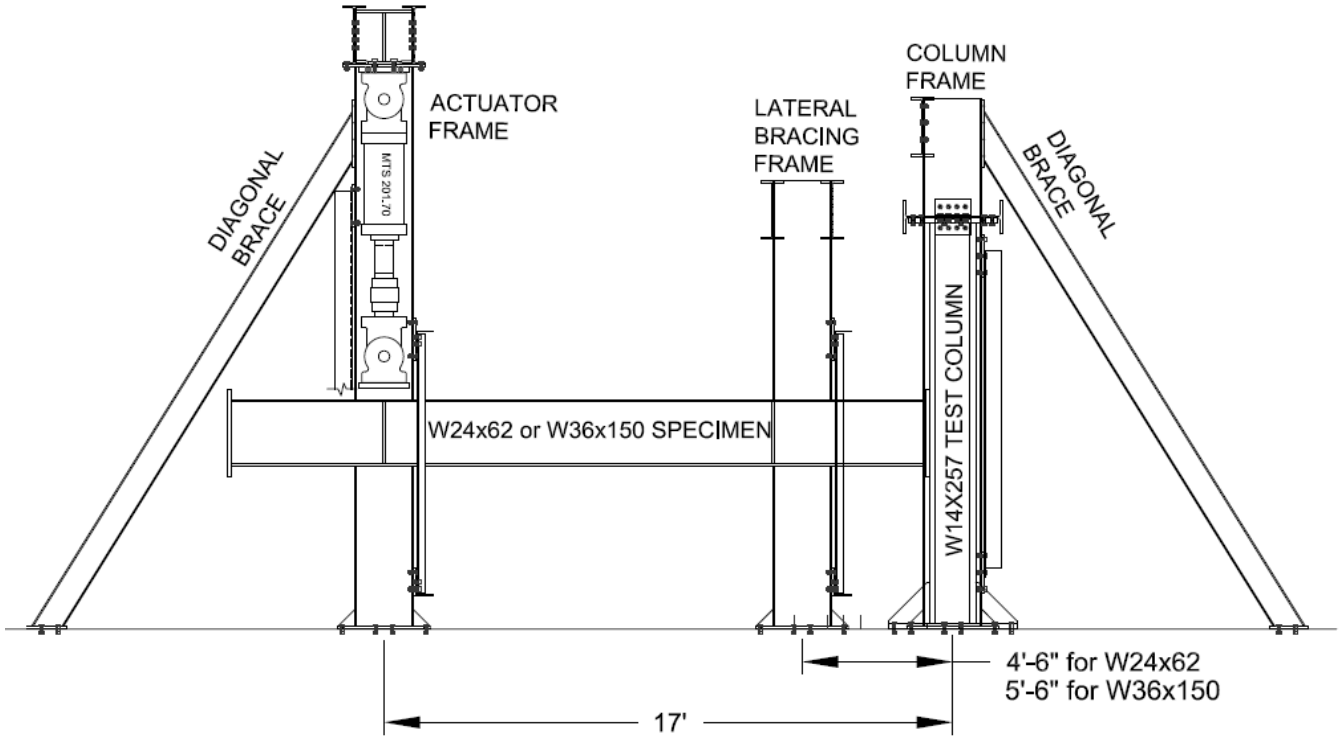

Figure 10: Full-scale Test Configuration [original drawing from (Watkins, 2013)]

Figure 11: Full-Scale Test Frame

Six 21 ft. long beams were used for testing. Three beams were W24x62 while the other three were W36x150. Since plastic hinging occurs in the localized region of the protected zone, it was possible to use both ends of a given beam for separate tests. This enabled twelve individual full-scale moment connection tests.

Table 1 shows the test matrix outlining the variable of interest of each test. The first six tests utilized the three W24x62 beams. Among these first six tests, three used specimens with bolted unstiffened extended endplate connections (BUEEP) and three used RBS connections. The final six tests utilized the three W36x150 beams. Among these six tests, three used specimens with bolted stiffened extended endplate connections (BSEEP) and three used RBS connections. The end plate design for these specimens is explained in detail in (Watkins, 2013). It is noted that while RBS specimens don't typically include endplates, they were used for these full-scale tests so that the same column could be used throughout testing. However, the use of an endplate does not significantly affect the deformations of the plastic hinge region which are the focus of this investigation.

Table 1: Test Matrix for Full-Scale Moment Connections

Test #	Specimen Name	Beam Type	Connection Type	Description	Report Figure Reference
1	RBS24	W24x62	RBS	No PAFs	Figure 13a
2	RBS24 – PAF12	W24x62	RBS	4 PAFs spaced at 12"	Figure 13b
3	W24	W24x62	BUEEP	No PAFs	Figure 13c
4	W24 – PAF12	W24x62	BUEEP	4 PAFs spaced at 12"	Figure 13d
5	RBS24 – PW12	W24x62	RBS	4 puddle welds spaced at 12"	Figure 13e
6	W24 – PAF_array	W24x62	BUEEP	PAF grid	Figure 13f
7	RBS36	W36x150	RBS	No PAFs	Figure 14a
8	RBS36 – PW12	W36x150	RBS	4 puddle welds spaced at 12"	Figure 14b
9	RBS36– PAF_array	W36x150	RBS	PAF grid	Figure 14c
10	W36	W36x150	BSEEP	No PAFs	Figure 14d
11	W36 – PAF12	W36x150	BSEEP	4 PAFs spaced at 12"	Figure 14e
12	W36 – PAF_array	W36x150	BSEEP	PAF grid	Figure 14f

The PAFs used in this study were Hilti X-ENP-19 L15 Nails (Figure 12 left). The PAFs were shot into test specimens with a 0.22 caliber Hilti DX 76-PTR tool (Figure 12 right)

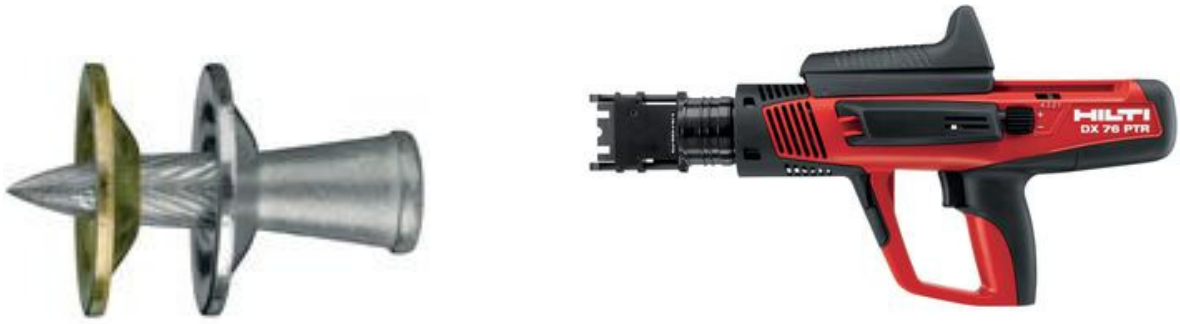

Figure 12: Hilti X-ENP-19L15 Powder Actuated Fastener (left) and Hilti DX 76-PTR (right) [from Hilti Website]

A similar variation of test variables was used for both beam types. For W24x62 beams, one RBS specimen (test 1, Figure 13a) and one BUEEP specimen (test 3, Figure 13c) were treated as control tests with no PAFs or welds. Each connection type was also tested with PAFs spaced at 12 in. along the centerline of the top flange (test 2 and test 4 - Figure 13 b and d, respectively). This is typical for deck attachments to the top flange or partition attachments to the underside of the bottom flange. The remaining RBS specimen (test 5, Figure 13e) was tested using four puddle welds spaced at 12 in. as was done with the PAFs. Currently, puddle welds are the only type of deck attachment method allowed in the protected zone. This test is performed to provide a baseline for specimen performance.

The remaining BUEEP specimen (test 6, Figure 13f) was tested using an identical grid of PAFs on both flanges. The grid on each flange included 14 rows of fasteners spaced at 2 in. with the first row occurring 2 in. from the surface of the endplate. Each row contained 3 PAFs with one occurring along the flange centerline and the others spaced 2.5 in. away from the centerline. This means the outer two fasteners in each row were centered 1 in. from the edge of the flange. PAF grid tests were intended to create a worst-case scenario. While in practice PAFs wouldn't be applied in a grid, it is possible that a PAF could be used in any of the locations present in the grid. Since local buckles may occur at slightly different locations from one test to another, the PAF grid ensured that there would be a PAF near the peak of the local buckles for a particular specimen. PAFs were spaced sufficiently far apart so as to minimize their interaction with each other. The extent of the local strain concentrations were analyzed using FEM models, although the results are not presented here. A single PAF grid test can represent a multitude of individual tests in which a PAF is present at any of the given locations. If the PAF grid specimens satisfied

qualification criteria, it would support allowing PAFs in the range of locations tested for the range of beam sizes tested.

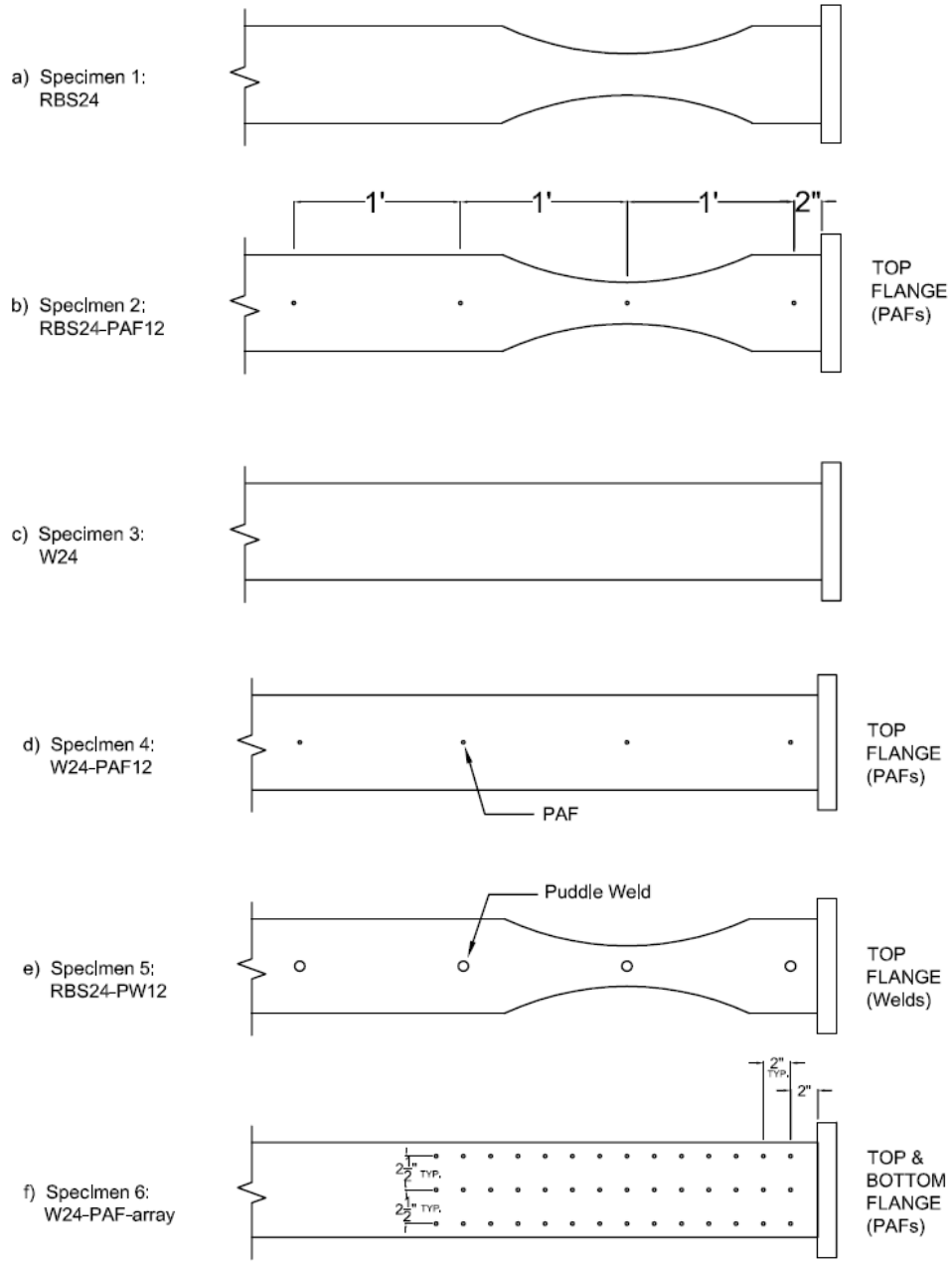

Figure 13: W24x62 Specimens

For W36x150 beams, as with the W24x62 tests, one RBS specimen (test 7, Figure 14a) and one BSEEP specimen (test 10, Figure 14d) were treated as control tests with no PAFs or welds. Another RBS specimen (test 8, Figure 14b) included puddle welds spaced at 12 in. along the top flange centerline. The final RBS specimen (test 9, Figure 14c) used a PAF grid on both flanges

as well as one side of the web. The grid geometry was unique to the RBS profile, but the test sought to provide the same means of testing PAFs in multiple locations as was discussed for the W24x62 BUEEP specimen (test 6). For test 9, the outer rows of PAFs were arranged such that they followed the curvature of the RBS cuts and were located 1 in. from the edge of the flange. This test also incorporated a grid of PAFs on one side of the web as depicted in Figure 15. A single BSEEP specimen (test 11, Figure 14e) included PAFs spaced at 12 in. along the top flange centerline. The final BSEEP specimen (test 12, Figure 14f) included a unique grid in the same fashion as the grid specimens discussed. The grid for Test 12 utilized five fasteners in a line with the PAFs in the outer rows located 1 in. from the flange edge. The test used the same web PAF grid as test 9.

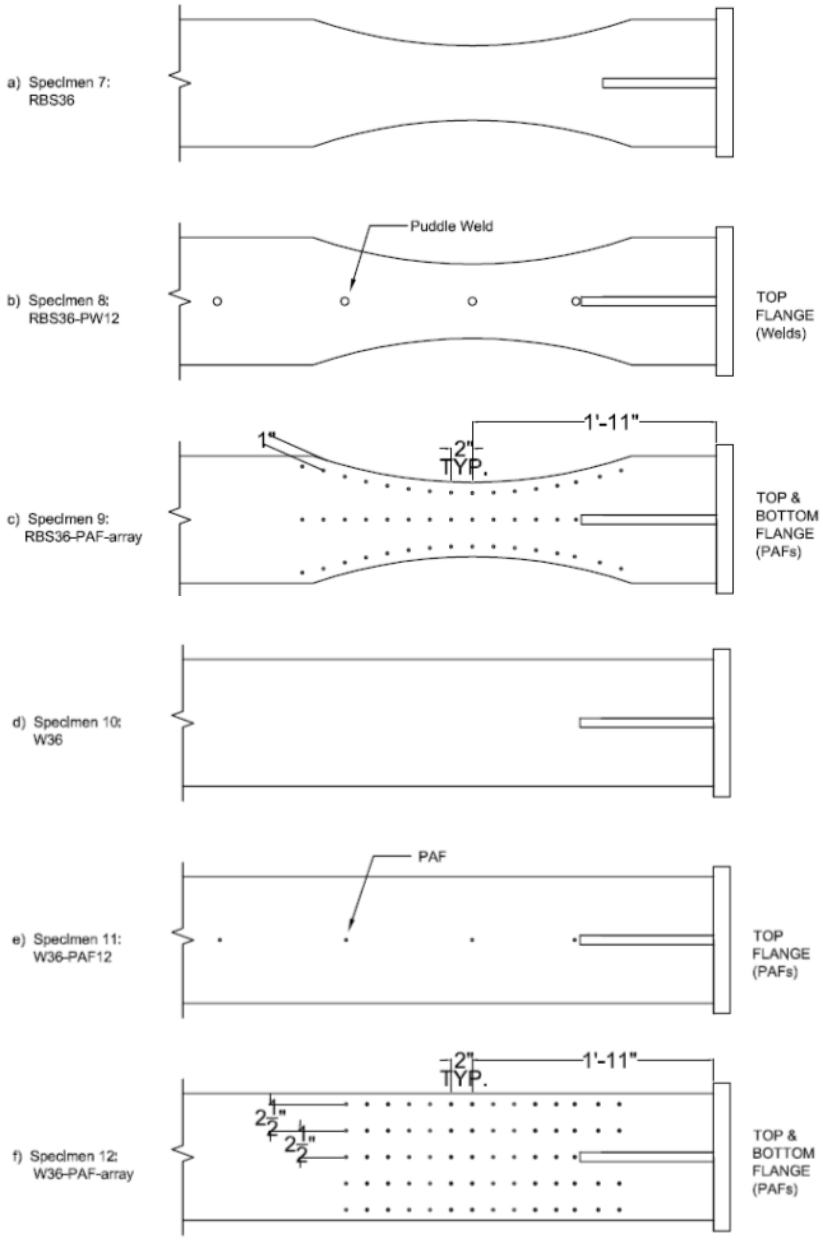

Figure 14: W36x150 Specimens

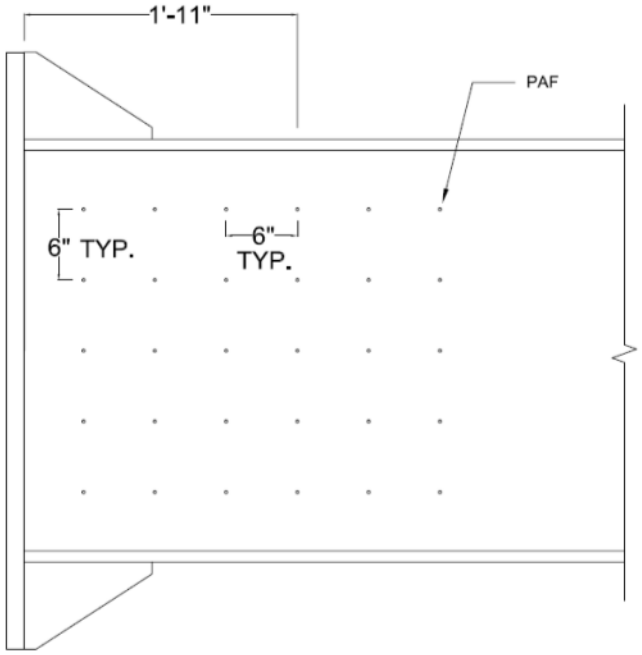

Figure 15: Web PAF Grid - Specimens 9 (RBS36-PAF-array) and 12(W36-PAF-array)

3.2 Instrumentation Plan

This section provides a general discussion about the instrumentation plan used in full-scale tests. A more thorough discussion about specific instrumentation locations is provided in Watkins (2013). A program written in the National Instruments Software LabView was used for test control and data acquisition. Instrumentation is provided to record displacements and rotation in the column, deformation in the connection region, displacements in the beam, strain distributions in the beam flanges, and the force applied to the specimen.

The loading protocol from AISC 341 (AISC 2010a) is intended to include deformation within the beam and column. The ideal boundary conditions for the column are a pinned-pinned configuration. In reality, the column was partially fixed at its bottom. Inherent flexibility of the column reaction frame resulted in the top of the column being able to move in a partially restricted manner. This type of motion is not intended in the loading protocol. For this reason, it was necessary to track any motion of the column and reaction frame for an accurate decomposition of the actual relative story drift being achieved by the connection.

Several types of instrumentation were employed in order to record the contribution of different deformation mechanisms to story drift. Nine LVDTs were utilized to track motion of the column panel zone as well as movement of the beam endplate and rotation of the beam plastic hinge. A string potentiometer extended to the top of the test column to measure motion in the top of the column. A second string potentiometer mounted to the beam beyond the plastic hinge was used in the calculation of beam deflection due to elasticity (this device was incorporated for tests 7-12). A final string potentiometer located under the beam/actuator connection was used to run the cyclic test program. Additionally, three inclinometers measured the rotation of the column and beam near the connection. Figure 16 shows a general layout of these pieces of instrumentation.

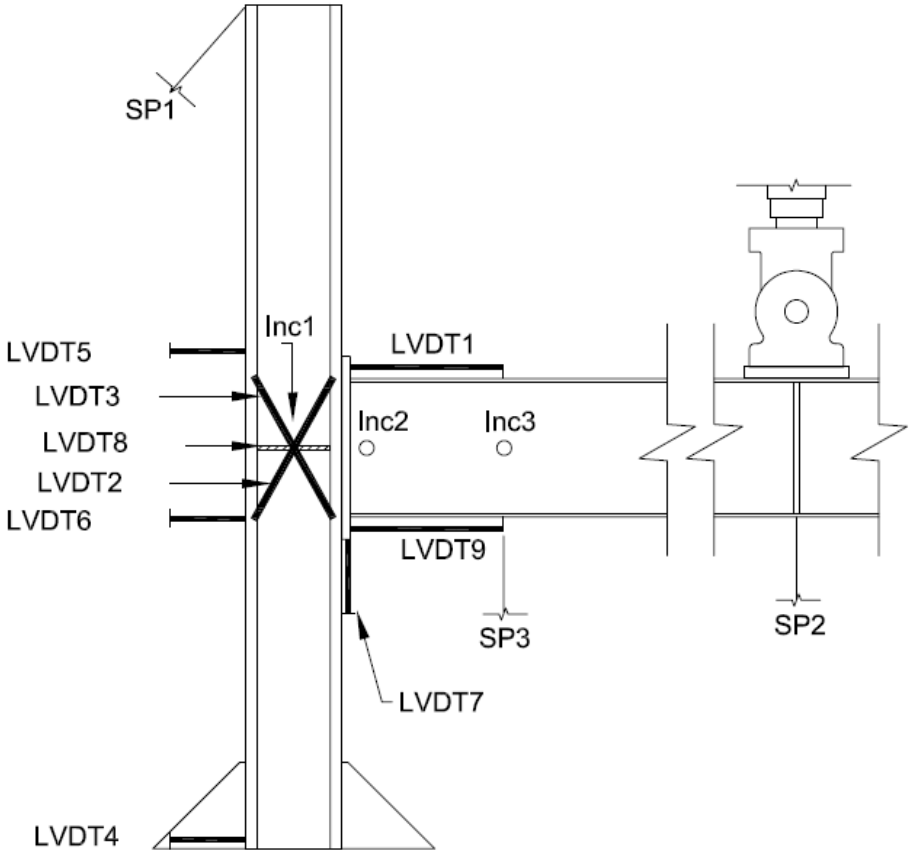

Figure 16: General LVDT and String Potentiometer Layout (Not To Scale)

High strain rated strain gauges were adhered to the top and bottom surfaces of the beam top flange in lines across the flange at the PAF locations. The strain gauge locations were held constant for specimens that had puddle welds or no fasteners and are intended to provide a comparison of strain distribution between specimens.

Figure 17 and Figure 18 show the general placement of the strain gauges for RBS and non-RBS W24x62 specimens. A similar strain gauge layout was employed for W36x150 specimens. In general, for W36 tests only two strain gauge lines were used with the first occurring approximately 13-3/8 in. from the endplate and approximately 1/4 in. beyond the end of the endplate stiffener. The second line occurred at 23 in. from the endplate. Specific strain gauge locations for each specimen are given in Watkins (2013). The motivation behind these lines of strain gauges is to provide "strain line" profiles at the defect locations. Comparison of strain line profiles between tests will be performed to assess strain concentrations that might occur due to the presence of PAFs or puddle welds.

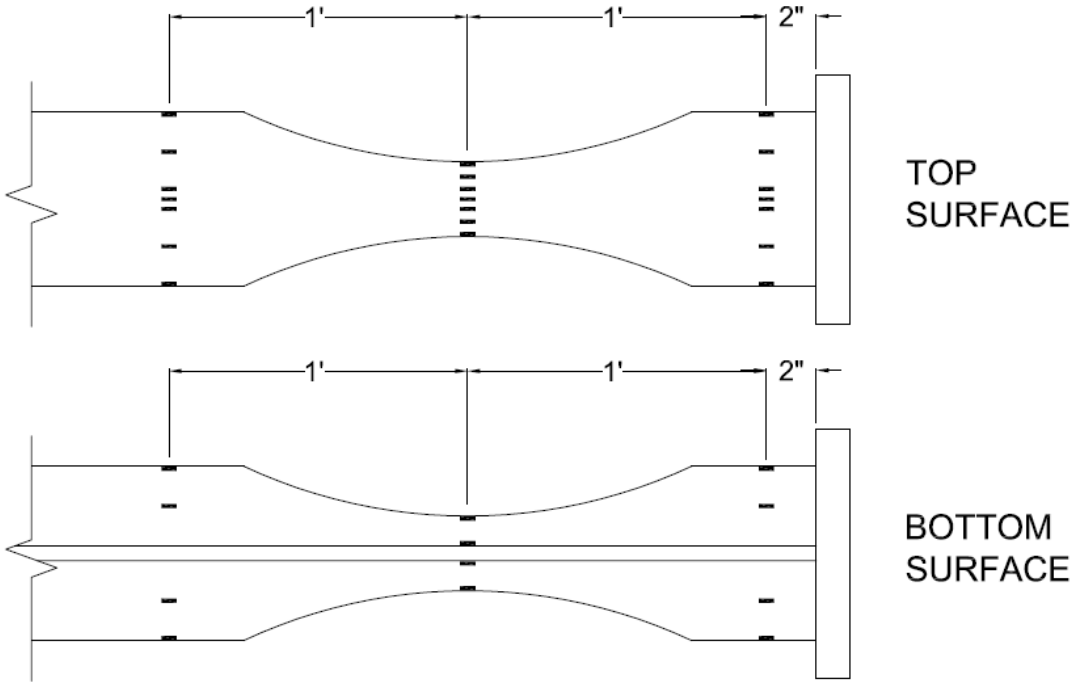

Figure 17: W24x62 RBS Specimen - Typical Strain Gauge Layout (Top and Bottom of Top Flange)

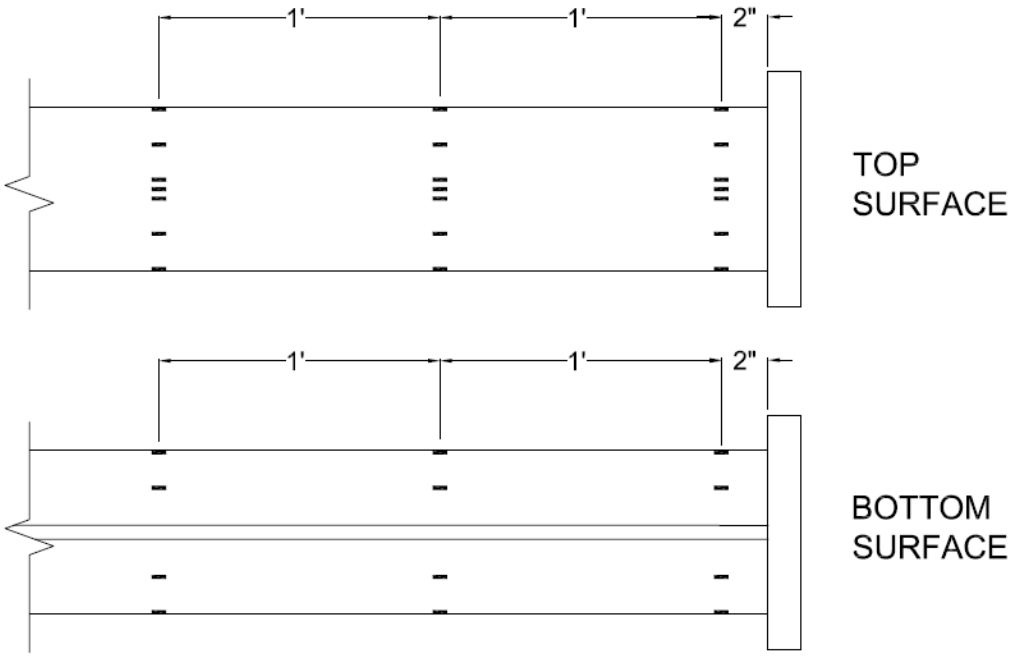

Figure 18: W24x62 non RBS Specimen - Typical Strain Gauge Layout (Top and Bottom of Top Flange)

A string potentiometer oriented vertically under the beam at the location of the actuator mount provided an accurate history of the total deflection of the beam by the actuator. This string potentiometer also served as the test program external feedback, by which the actuator was controlled to produce the required displacement protocol at the string potentiometer. The actuator is an MTS model 201.7 with force capacity of 215 kips in tension and 330 kips in compression. The actuator has a total stroke of 20". A load cell located within the actuator measured the applied force required by the actuator to achieve the displacement protocol. Typical hysteresis plots produced from moment connection tests use applied moment and story drift. The story drift is calculated as the string potentiometer displacement divided by the 17ft distance between the column centerline and the beam inflection point. Similarly, the applied moment at the face of the column is computed by multiplying the actuator force by the distance from the actuator to the face of the column.

Additional visual data collection methods include a lime and water whitewash mixture painted on the beam at the protected zone to provide a visual indication of the yielding behavior of the beam. As water evaporates out of the mixture the whitewash becomes a brittle coating over the

steel mill scale. It flakes off with the mill scale as the steel is yielded, providing a visual display of yield lines through the plastic region of the beam.

Since the low-cycle displacement protocol and its resulting beam deformations occurs over the course of several hours of testing, timelapse photography was utilized to capture visual changes in a faster format that makes the changes more obvious. Four cameras mounted around the test setup took a fixed image every 6 seconds for the duration of the test from locations providing side, top, and angled views of the protected zone as well as a fourth wide view of the entire test setup (Figure 19). The time stamped images were important for providing a visual history of the tests for any necessary correlation of significant events to corresponding data records and observations.

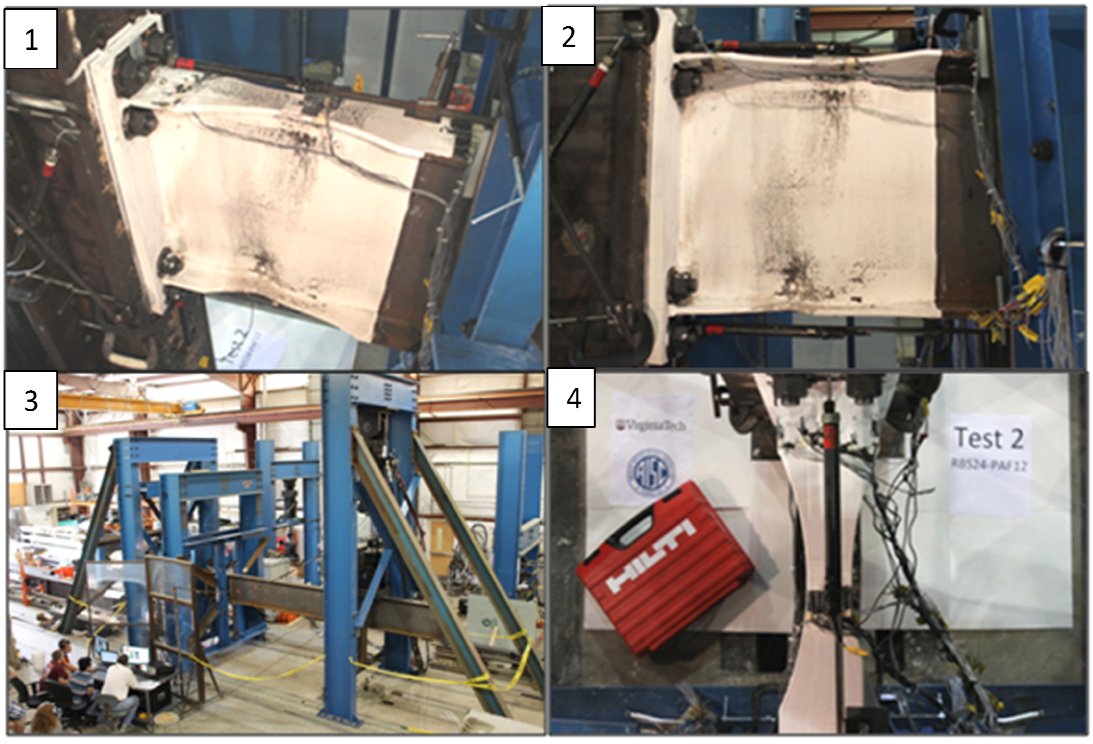

Figure 19: Timelapse Camera Views: 1) Angle, 2) Side, 3) Wide, 4) Top

3.3 Story Drift Decomposition

The test configuration used a stiffer and stronger column relative to what might typically be used with beam sizes like those used in the tests. This was expected to create more inelastic deformation in the plastic hinge region and thus will conservatively produce larger inelastic demands in the part of the beam being studied. However, it is necessary to decompose the story drift to quantify the contribution of each component (such as column deformation) to the total system story drift. This study will quantify the story drift components present in the full-scale test setup and report those contributions for the completed tests. This test data is intended for future use in predictions of connection behavior for other column geometries, but those future studies are beyond the scope of this work. The following sources account for the total system story drift of the full-scale test setup.

- Flexibility of the reaction frame
- Shear deformation of the panel zone
- Flexure of the panel zone (included in calculation for flexure of the column)
- Shear deformation of the column (included in calculation for flexure of the column)
- Flexure of the column
- Prying of the endplate connection coupled with localized deformations of the column flange and web
- Elastic flexural and shear deformation of the beam outside the plastic hinge region
- Deformation of the plastic hinge region of the beam.

Instrumentation limitations result in the story drift components of column shear and panel zone flexure being included in the calculation for flexure of the column. AISC 341 Commentary K2.3a (AISC 2010a) permits up to 25% of the total system story drift to occur in system components outside the plastic hinge region of the beam. Since this study assesses qualification requirements at a total story drift of 4%, plastic hinging of the beam at these cycles should account for at least 3% story drift. Another way to look at this requirement is that the qualification cycle should be one in which the plastic hinge deformation produces 3% story drift.

In order to quantify this distribution, it is necessary to calculate the story drift behavior of the noted system components. This is accomplished using system geometries and data from

instrumentation located in the region of the connection. The following story drift component descriptions provide a series of diagrams and accompanying equations summarizing the algorithms employed to decompose the total story drift. All diagrams represent configurations assuming an upward deflection of the beam. It should be noted that all diagrams are schematic and are, therefore, not drawn to scale.

i) Flexibility of the reaction frame

The column reaction frame is designed to be stiff and elastic during testing. The string potentiometer mounted to the top of the reaction column (Figure 16) provides a measurement of any drift of the column relative to the bottom of the column. A horizontal LVDT placed along the floor captures any motion of the base of the column. Data from this LVDT indicated a negligible amount of motion at the column base for all tests. This allows the column to be considered fixed against translation at the base and heavily restrained but still capable of motion at the top. The system story drift represented by the column reaction frame drift is shown in Figure 20.

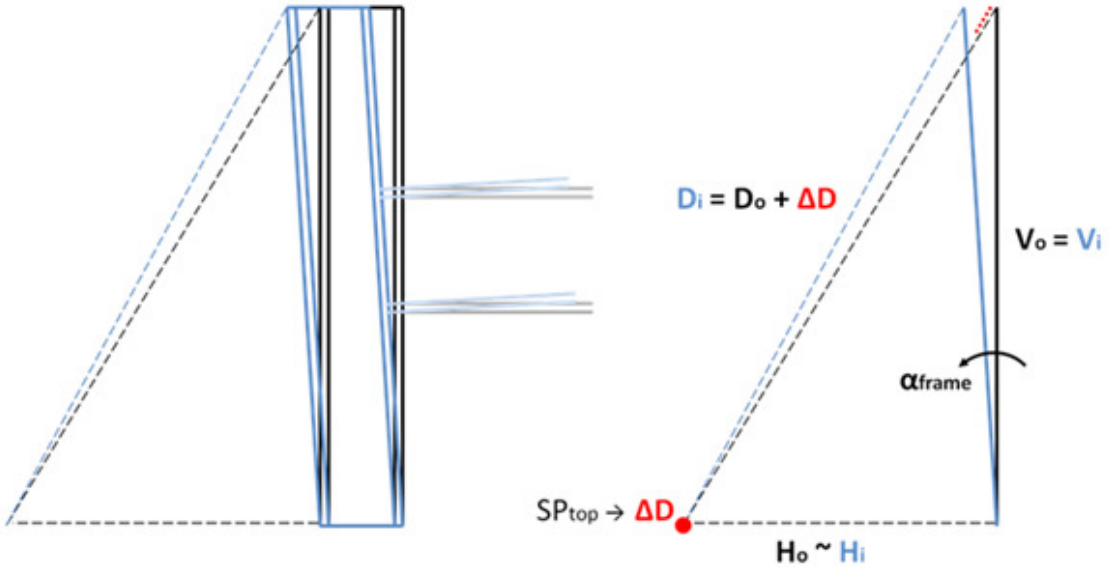

Figure 20: Frame Drift - Story Drift Component

Equation 3.1 utilizes the law of cosines to relate the angle of reaction frame drift, α_{frame}, to known system geometries and string potentiometer data of the motion of the top of the column. Equation 3.1 is written in the typical form of the law of cosines, in which α_{frame} can be solved explicitly as in Equation 3.2. H_0 and V_0 are the initial horizontal and vertical separations

between the string potentiometer base and the top of the column, respectively. D_i is the length spanned by the string potentiometer from its base to the top of the column, which varies as the column reaction frame moves. D_i deviates from the initial value of D_0, the hypotenuse of the triangle formed from H_0 and V_0, based on the time varying extension of the string potentiometer, ΔD.

$$D_i^2 = H_0^2 + V_0^2 - 2H_0V_0\cos\left(\frac{\pi}{2} - \alpha_{frame}\right) \tag{3.1}$$

$$\alpha_{frame} = \frac{\pi}{2} - \text{acos}\left(\frac{H_0^2 + V_0^2 - D_i^2}{2H_0V_0}\right) \tag{3.2}$$

ii) Shear deformation of the panel zone

Shear deformation of the column panel zone is measured using a pair of LVDTs oriented diagonally in an 'X' configuration such that they span the intersection of beam flange and column flange centerlines. The LVDTs, each mounted to one column flange, measure displacement against perpendicular reaction surfaces mounted to the opposite column flange. Shear deformation of the panel zone is assumed to behave exclusively as horizontal shearing due to beam flange forces as shown in Figure 21. Any vertical shear is accounted for by the calculation of column flexure.

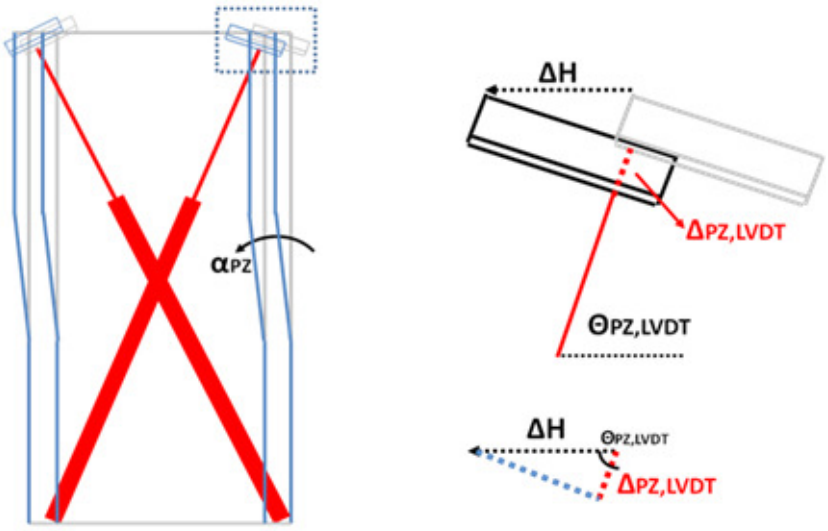

Figure 21: Panel Zone Shear - Story Drift Component

The average change in length recorded by the LVDTs, $\Delta_{PZ,AVG}$, can be converted into an equivalent horizontal component, Δ_H, by Equation 3.5 which uses the angle of the panel zone LVDTs, $\theta_{PZ,LVDT}$. The LVDTs were mounted such that they approximately spanned the opposite corners of a rectangle formed by the beam and column flange depth centerlines. While the precise angle may have varied slightly between tests, $\theta_{PZ,LVDT}$ was estimated by nominal beam and column geometries as given in Equation 3.4 where d_B and d_C are the depths of the beam and column, respectively, and tf_B and tf_C are the flange thicknesses of the beam and column, respectively. As the panel zone undergoes shear deformation, one LVDT extends and the other shortens. This difference of signs is reflected by the difference in signs in Equation 3.3 where $\Delta_{PZ,LVDT1}$ and $\Delta_{PZ,LVDT2}$ are the diagonal LVDT extensions. The resulting horizontal deflection due to shear is then related to the accompanying panel zone drift ratio, α_{PZ}, as given in Equation 3.6 by the vertical span of the LVDTs, $d_B - tf_B$.

$$\Delta_{PZ,AVG} = \frac{\Delta_{PZ,LVDT1} - \Delta_{PZ,LVDT2}}{2} \tag{3.3}$$

$$\theta_{PZ,LVDT} = atan\left(\frac{d_B - tf_B}{d_c - tf_c}\right) \tag{3.4}$$

$$\Delta_H = \frac{\Delta_{PZ,AVG}}{\cos\left(\theta_{PZ,LVDT}\right)} \tag{3.5}$$

$$\alpha_{PZ} = \frac{\Delta_H}{d_B - tf_B} \tag{3.6}$$

iii) Flexural deformation of the column

In addition to global motion of the column due to reaction frame flexibility and panel zone deformation, flexibility of the test column itself accounts for a portion of the system story drift. Figure 22 shows the general deformed shape of the column due to column flexibility. Two

methods are possible for quantifying the angular rotation of the panel zone, $\alpha_{col,rot}$. The primary method, given in Equation 3.7, uses an inclinometer, θ_{inc1}, placed at the center of the panel zone in line with the beam centerline. As an alternate method, given in Equation 3.8, two fixed, horizontal LVDTs along the back side of the column can provide this angular rotation. The LVDTs are spaced vertically at a separation approximately equal to the beam depth. The specific separation spacing, d_{sep}, is driven by clearance constraints due to the presence of cross bracing behind the column. The LVDTs measure displacements $\Delta_{COL,LVDT1}$ and $\Delta_{COL,LVDT2}$, providing the means to quantify the angle of the column. It is important to note that the column rotation angle depicted by Figure 22 and Equations 3.7 and 3.8 incorporates contributions by the reaction frame drift and panel zone shear deformations already derived. Therefore, in order to quantify the drift ratio due exclusively to column flexibility, the aforementioned reaction frame and panel zone values must be removed. This is shown in Equation 3.9. This operation also allows for the calculation of column flexure to include any deformations due to panel zone flexure and column shear

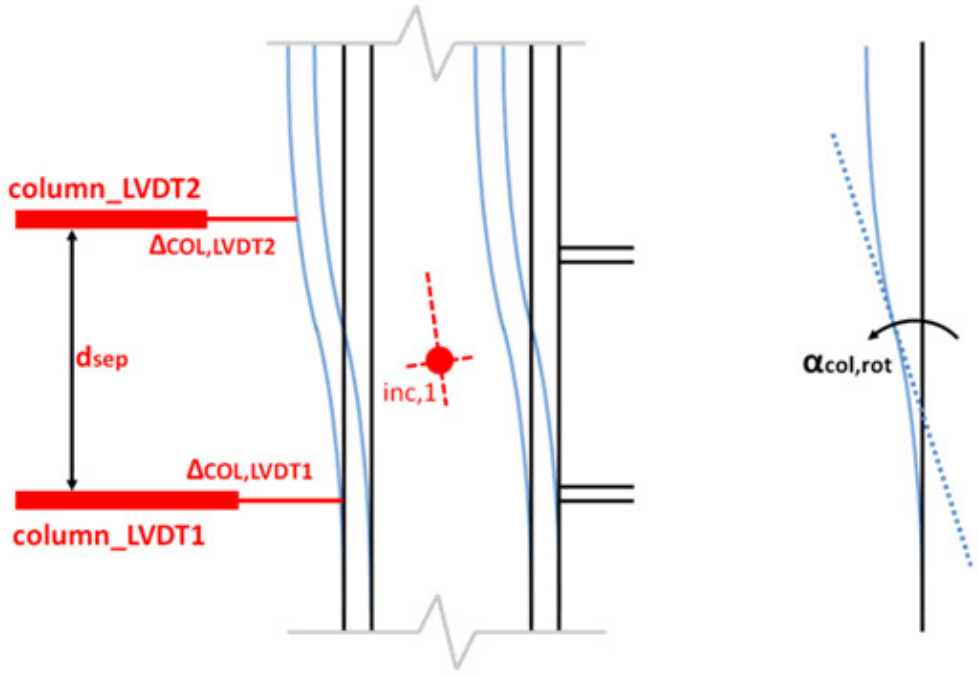

Figure 22: Column Flexure - Story Drift Component

$$\alpha_{col,rot,1} = \tan(\theta_{inc,1}) \tag{3.7}$$

$$\alpha_{col,rot,2} = \frac{\Delta_{COL,LVDT1} - \Delta_{COL,LVDT2}}{d_{sep}} \quad (3.8)$$

$$\alpha_{col,flex} = \alpha_{col,rot} - \alpha_{frame} - \alpha_{PZ} \quad (3.9)$$

While the bottom LVDT is in line with each beam type bottom flange, due to spatial restrictions of the test setup, the top LVDT was located at a consistent location above the beam top flange line. Since flexure is assumed to be greatest at the centerline of the beam, it is expected that the LVDT resulting column rotation angle will be less than the actual rotation angle. Since the column inclinometer is placed in the center of the column panel zone, it is expected that the angle recorded by the inclinometer will better represent the actual rotation of the column.

iv) Prying of the endplate connection

All bolts connecting the beam endplate to the column face were pretensioned in order to minimize relative motion between the adjoining surfaces. It is possible to estimate the relative motion due to prying, $\alpha_{endplate}$, by considering the difference in measured angle between two local inclinometers as given in Equation 3.10. One is located in the middle of the panel zone, θ_{inc1}, and one is located at the beam mid-depth and two inches from the endplate, θ_{inc2}, as shown in Figure 23.

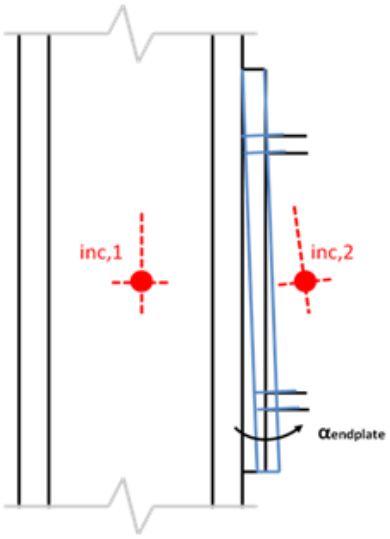

Figure 23: Endplate Prying - Story Drift Component

$$\alpha_{endplate} = \tan(\theta_{inc,1} - \theta_{inc,2}) \quad (3.10)$$

v) Elastic deformation of the beam

The applied force by the actuator causes elastic flexural and shear deformation in the beam. Although the entire length of the beam experiences elastic deformation, it is difficult to decompose the deformation of the plastic hinge region into elastic and plastic parts. An inclinometer located on the web at the beam mid-depth beyond the protected zone, however, allows the contribution of elastic beam displacement outside the plastic hinge region to be determined. Total deflection of the beam free end can be considered a summation of the vertical deflection of the beam at the inclinometer location (Equation 3.11 or 3.12), and the deflection of the remaining length of beam beyond the beam inclinometer. The rise of the beam inclinometer, $\delta_{inc,rise}$, as given by Equation 3.11 for specimens 1-6, is calculated using the recorded angular rotations of the column and beam inclinometers, $\theta_{inc,1}$ and $\theta_{inc,3}$ respectively, and the distance between them, L_1. Tests 7-12 utilized a string potentiometer to directly measure this rise of the inclinometer (Equation 3.12). From Equation 3.13, the angle reported by the beam inclinometer, $\theta_{inc,3}$, allows for a deflection calculation, δ_{rigid}, using an ideal assumption that the length of beam beyond this inclinometer, L_2, remains rigid as it deflects. Summing these two deflections results in an extrapolated deflection of the beam at the location of the actuator assuming the remaining beam length does not undergo any rotation. As given in Equation 3.14, any difference between this summed deflection and the reported input drift value of the vertical string potentiometer controlling the test, δ_{tot}, is due to elastic deflection of the length of beam beyond the inclinometer, $\delta_{el,beam,1}$. This is demonstrated in Figure 24.

The theoretical elastic deflection, $\delta_{el,beam,2}$, of the beam length, L_2, is computed using the sum of contributions due to flexure and shear from an applied actuator load, P. This is shown in Equation 3.16. Additional material properties include moment of inertia, I, modulus of elasticity, E, shear modulus of elasticity, G, section area, A, and a shape factor, α. The shape factor, α, is dependent on additional properties of web thickness, t, flange width, b, beam depth, d, and clear distance between flanges, d_1 as shown in Equation 3.15. The contribution of beam deformation

due to shear was provided by Timoshenko (1955). Calculation of the beam elastic deformation drift component, $\alpha_{elastic,beam}$, is given by Equation 3.17.

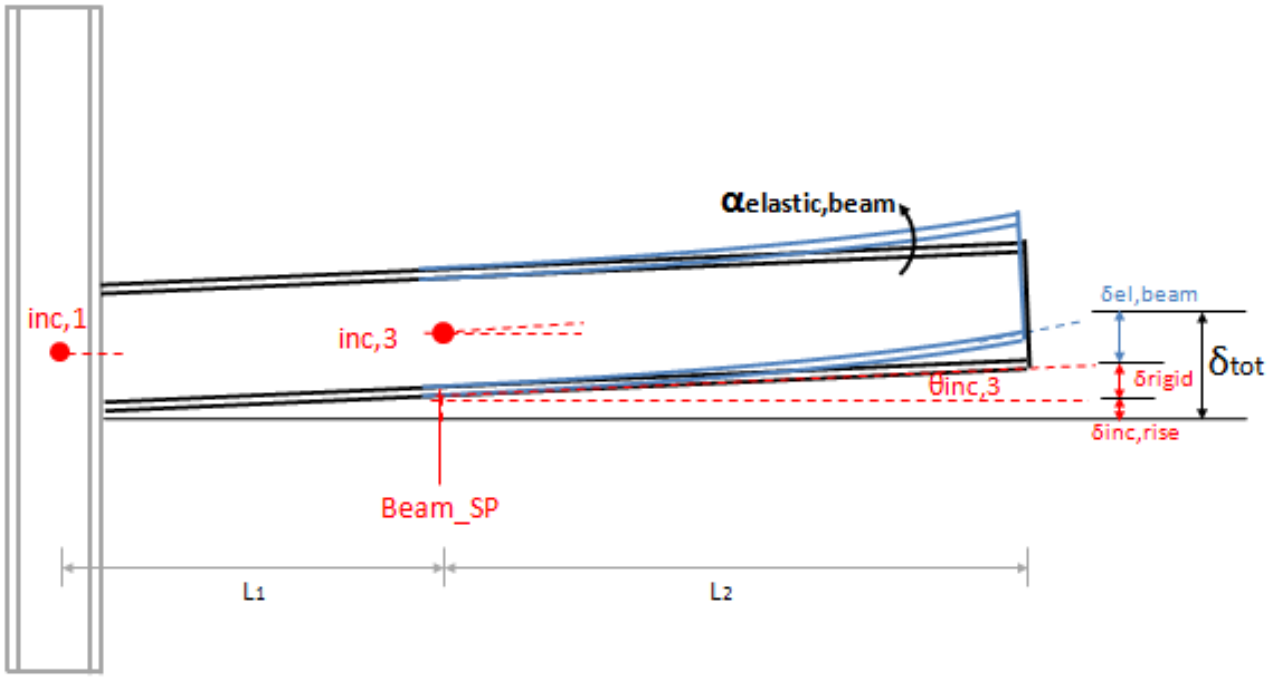

Figure 24: Beam Elasticity- Story Drift Component

$$\delta_{inc,rise} = \tan\left(\frac{\theta_{inc,1}+\theta_{inc,3}}{2}\right) \times L_1 \quad \text{(specimens 1-6)} \tag{3.11}$$

$$\delta_{inc,rise} = \Delta_{beam\_SP} \quad \text{(specimens 7-12)} \tag{3.12}$$

$$\delta_{rigid} = \tan(\theta_{inc,3}) \times L_2 \tag{3.13}$$

$$\delta_{el,beam,1} = \delta_{tot} - \delta_{inc,rise} - \delta_{rigid} \tag{3.14}$$

$$\alpha = \frac{A}{8It}(bd^2 - bd_1^2 + td_1^2) \tag{3.15}$$

$$\delta_{el,beam,2} = \frac{PL_2^3}{3EI} + \frac{PL_2\alpha}{AG} \tag{3.16}$$

$$\alpha_{elastic,beam} = \frac{\delta_{el,beam}}{17\ ft} \tag{3.17}$$

vi) Plastic deformation of the beam

Story drift due to plastic deformation of the beam is represented by the rotation occurring in the protected zone region. The hinging was highly irregular based on the particular buckling and failure mode that the beam underwent. Two methods are possible for quantifying the angular rotation of the panel zone. As in column flexure, the primary method, given as $\alpha_{plastic,beam,1}$ in Equation 3.18, is the comparison of recorded angles between two inclinometers, $\theta_{inc,2}$ and $\theta_{inc,3}$, mounted to the beam on either side of the protected zone. The alternate method used for data validation is given in Equation 3.19, based on two LVDTs (linear potentiometers for tests 4-12) located above and below the beam flange that measure the distance between the endplate and the end of the protected zone as shown in Figure 25. It is noted that this alternate method originally called for LVDTs as shown in Figure 16. Excessive out-of-plane deformation of the top flange prompted the decision to use linear potentiometers for tests 4-12. With this in mind, any further reference to the two LVDTs used to measure beam plastic hinge rotation actually corresponds to linear potentiometers for tests 4-12. The difference between LVDT deflection values, $\Delta_{BEAM,LVDT1}$ and $\Delta_{BEAM,LVDT2}$, divided by the vertical distance between LVDTs, *d'*, approximates the angular deflection of the protected zone, $\alpha_{plastic,beam,2}$. It is noted that this plastic deformation component inherently includes any beam elasticity in the protected zone. Practical instrumentation limitations make it infeasible to distinguish these two different components. Therefore, for purposes of simplification, an assumption is made that elasticity along this relatively short length of beam is small compared to the significant plastic hinging.

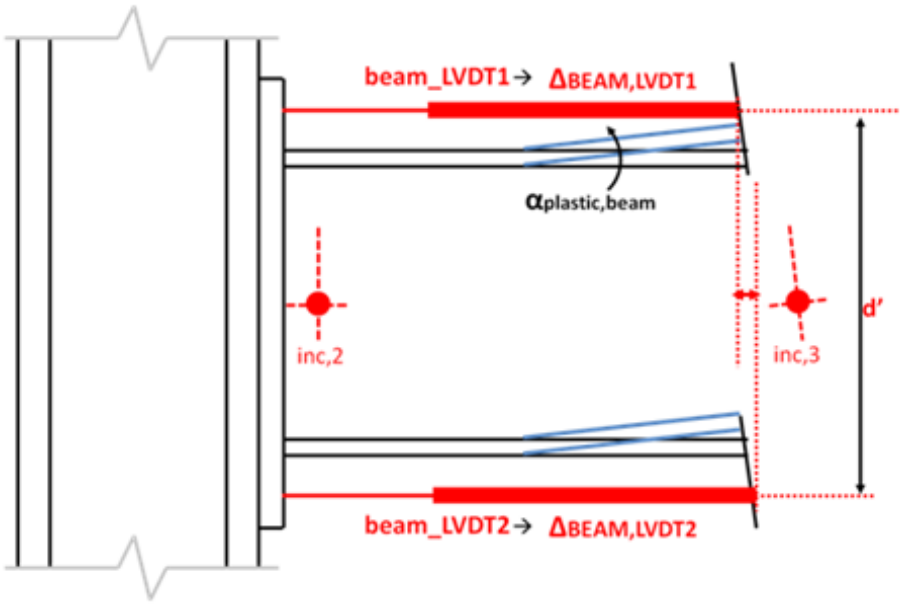

Figure 25: Beam Plasticity- Story Drift Component

$$\alpha_{plastic,beam,1} = \tan(\theta_{inc,2} - \theta_{inc,3}) \tag{3.18}$$

$$\alpha_{plastic,beam,2} = \frac{\Delta_{BEAM,LVDT1} - \Delta_{BEAM,LVDT2}}{d'} \tag{3.19}$$

vii) Total story drift

The summation of the six story drift components discussed above represents the total story drift, α_{total}, of the system. Equation 3.20 represents this summation. The actual total story drift applied to the system by the actuator is measured by the vertical string potentiometer. Comparison of the actual total story drift and the story drift component summation will provide an indication of the adequacy of the story drift algorithms in accounting for all motion of the system.

$$\alpha_{total} = \alpha_{frame} + \alpha_{PZ} + \alpha_{col,rot} + \alpha_{endplate} + \alpha_{elastic,beam} + \alpha_{plastic,beam} \tag{3.20}$$

3.4 Tension Coupon Material Testing

Tension tests were performed on six coupon specimens. Three were cut from an undeformed region of the W24x62 beam specimen used for tests 2 and 4. The other three were cut from an undeformed region of the W36x150 specimen used for tests 8 and 11. The geometry of the coupon specimens is consistent with dimensions provided in ASTM 370-07a (ASTM 2007) for tension coupons with a total length of 18 in. and a gauge length of 8 in. For both beams, the specimens were cut in a longitudinal orientation from each of the top flange, bottom flange, and web according to ASTM A6/A6M-12 (ASTM 2012). Each specimen included punch marks spaced at approximately one inch along the eight inch gauge length. This provides the means of comparing spacing before testing and after fracture. In addition, the average section area along the gauge length prior to testing was recorded in order to calculate stress from applied force.

Automatically recorded test data included displacement of the moving platform, applied force, and strain by an extensometer. Extensometer limitations only allowed direct strain readings up to 3%, at which point testing was paused and the extensometer was removed. This was done in order to prevent damage to the extensometer as increased strains occurred prior to fracture. Since strain hardening data beyond this point is desired, displacement recordings of the moving platform of the test machine can be used to calculate increased strain values.

It is observed from test data that a linear relationship exists between the recorded platform displacement and extensometer strain as the test approaches 3% strain. The change in platform displacement and the change in strain are related to yield a pseudo-gauge length for the specimen. This is given in Equation 3.21 where $\Delta\varepsilon$ is the change in strain, ΔL is the change in platform displacement, and L' is the calculated pseudo-gauge length, all of which vary for a given recording increment, i.

$$L_i' = \frac{\Delta L_i}{\Delta \varepsilon_i} \tag{3.21}$$

For each tension specimen, in each of the final twenty data recording steps before 3% strain was achieved, the pseudo-gauge length of the specimen was calculated. These twenty values were used to produce an average pseudo-gauge length. The pseudo-gauge length can then be used in

conjunction with further change in platform displacement data to produce a change in specimen strain beyond the previous 3% limit. This extrapolation method depends on an assumption that by this point in the test, no slip is occurring between the specimen and test machine platform grips. Average pseudo-length values varied between specimens. In order to maintain consistency between tests, all test data extrapolations used a pseudo-length of 11.5 in. This value was determined based on the typical value of average pseudo-length from each of the six tension tests. It is noted that utilizing this pseudo-length method as well as using an equal pseudo-length value for all tests means that extrapolated data is approximate.

Figure 26 shows the stress-strain data from all six tension coupon tests. Solid lines represent strain data reported directly from the extensometer. Dotted lines represent extrapolated data from the pseudo-length method described above. The single dashed line represents extensometer data from a test in which the W36x150 top flange coupon was reloaded after previously being loaded in a test that was halted prior to reaching significant inelastic strain. The presence of a higher first yield stress during reloading is not well understood with available data. Extrapolated data from that reloading test does align well with other tests as well as the strain hardening extrapolation from the original W36x150 top flange specimen. The six tests produced yield stresses ranging from 52 ksi to 56 ksi with an average yield stress of 54 ksi.

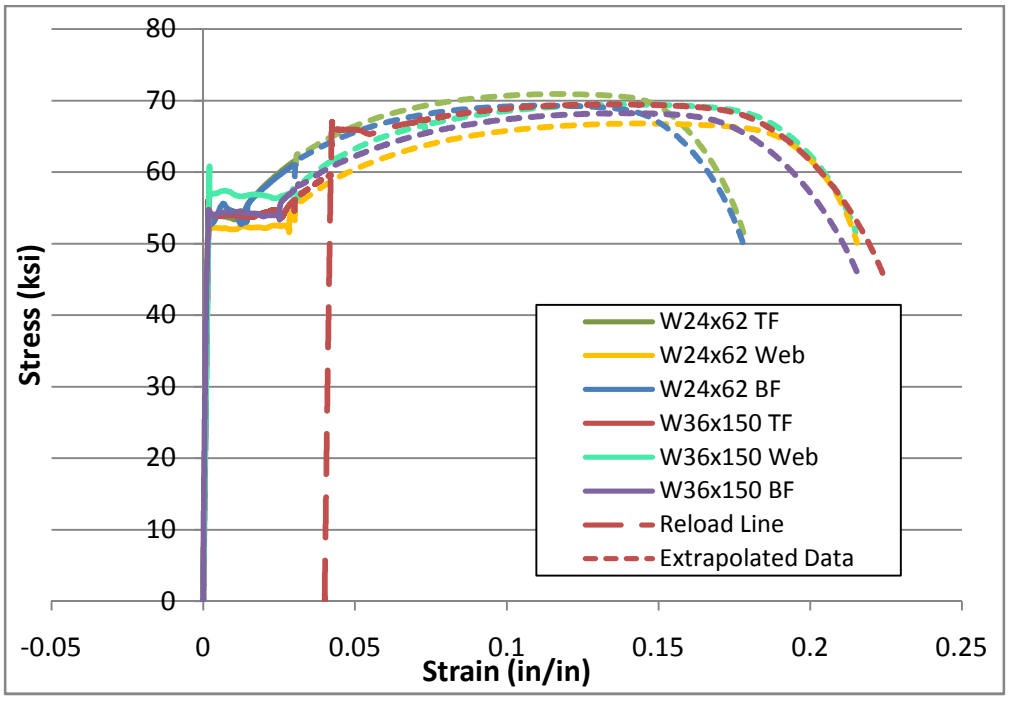

Figure 26: Tension Coupon Test Data

CHAPTER 4: TEST RESULTS

4.1 General Full-Scale Test Results

This section includes results of all twelve completed full-scale tests. The behavior of the specimens will be examined in four groups; W24x62 beams with RBS connection (specimens 1, 2, and 5), W24x62 beams with BUEEP connection (specimens 3, 4, and 6), W36x150 beams with RBS connection (specimens 7, 8, and 9), and W36x150 beams with BSEEP connection (specimens 10, 11, and 12). All hysteresis plots depict the applied moment at the face of the column as the product of the actuator applied force and a moment arm of 195.8 in. to the column face.

4.1.1 Behavior of W24x62 Specimens with RBS Connection

Test 1: W24x62 with RBS Connection and No Fasteners

Test 1 served as the control test for the W24x62 specimens with RBS connections. No PAFs or puddle welds were present on the specimen. Figure 27 shows the hysteresis behavior of from test 1. The specimen successfully completed two cycles of 4% story drift cycling while maintaining a moment greater than 80% of the nominal plastic moment capacity computed with nominal yield stress. During the subsequent cycles of 4.7% story drift, cracks formed in the bottom flange at the RBS location. Continued cycling produced a ductile tear at this location (Figure 28). Crack formation was noted in several other locations. All cracks initiated on the inside surface of local buckles where the greatest compressive strains due to local buckling occurred.

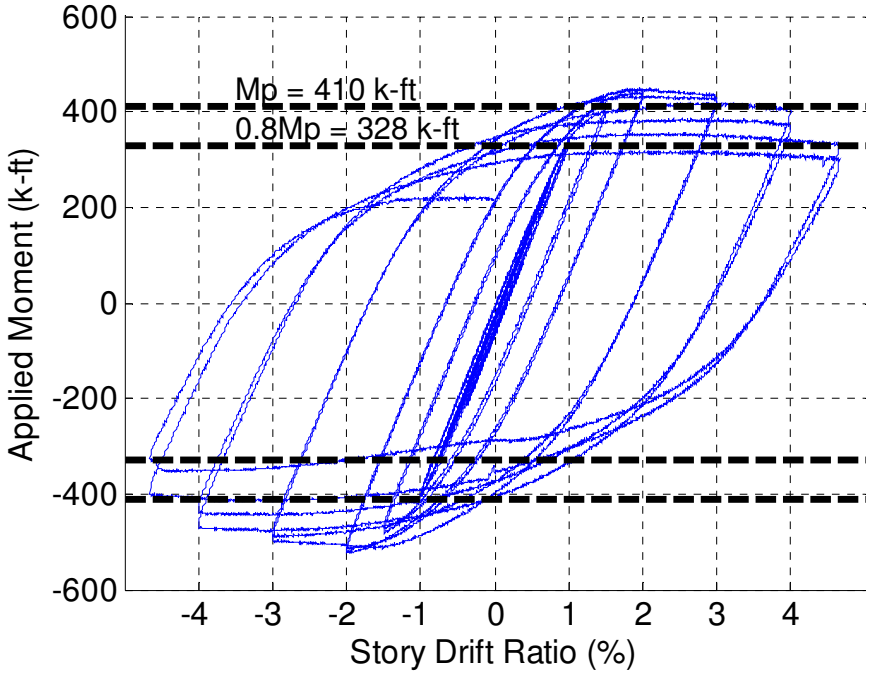

Figure 27: Specimen 1 (RBS24) Hysteresis

Figure 28: Ductile Flange Tear from Test 1

Test 2: W24x62 with RBS Connection and PAFs Spaced at 12 in.

Specimen 2 varied from specimen 1 in its inclusion of four PAFs spaced at 12 in. along the center of the top flange with the first located 2 inches from the beam endplate. Figure 29 shows the hysteresis behavior of specimen 2. As with specimen 1, specimen 2 completed the seismic qualification requirement successfully. It is noted, however, that during subsequent cycling, a

brittle fracture of the top flange and approximately 6 in. of the web occurred. This fracture occurred after one cycle of 4.7% story drift when the top flange was being pulled into tension after experiencing the shortening associated with 4.7% story drift when the beam was deflected upward. The fracture occurred at the location of the second PAF which was spaced 14 in. from the endplate, in line with the minimum flange width at the RBS cuts. Upon inspection of the fracture, it was noted that the PAF was missing after it presumably was ejected during the brittle fracture (Figure 30).

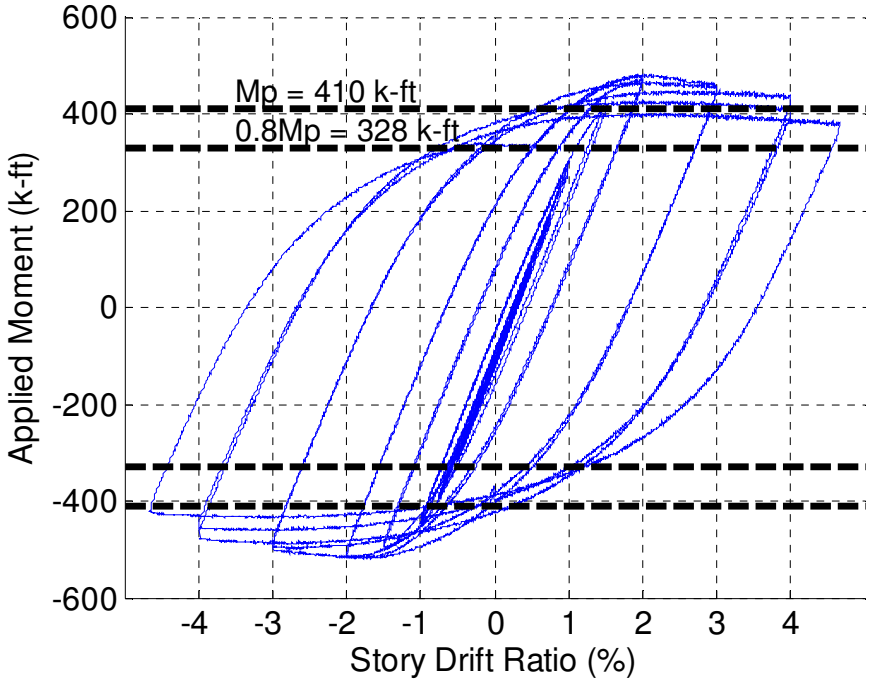

Figure 29: Specimen 2 (RBS24-PAF12) Hysteresis

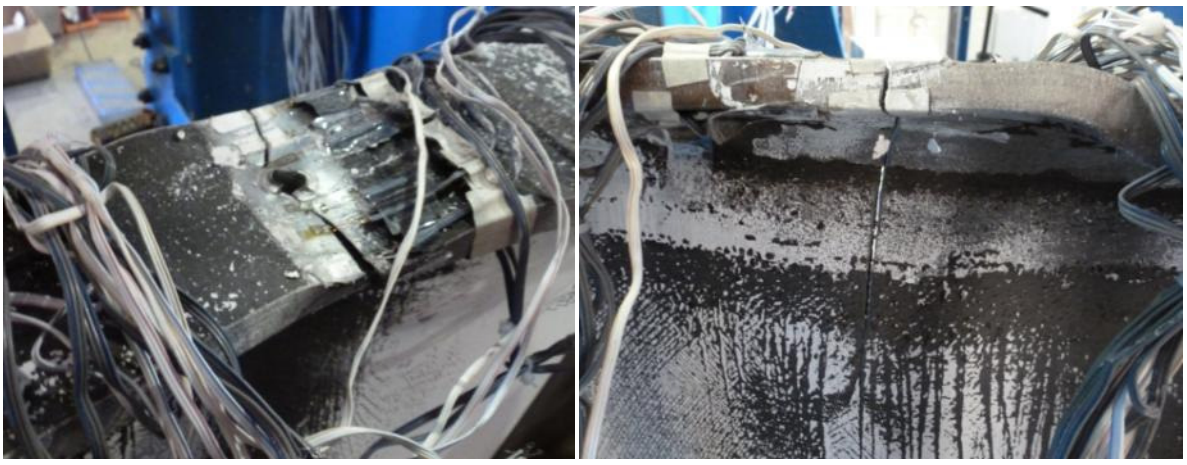

Figure 30: Brittle Flange/web Fracture from Test 2

Test 5: W24x62 with RBS Connection and Puddle Welds Spaced at 12 in.

Test 5 was a departure from PAF testing in order to assess the effects of puddle welds on seismic performance of moment connections. Puddle welds are currently the only attachment method approved for deck attachment in protected zones of SMRF connections. Four puddle welds were placed at the same 12 in. spacing as PAFs in test 2. The puddle welds were applied through pieces of galvanized 20 gauge metal decking secured to the top flange. After welding, the decking was trimmed around the welds using torching to allow strain gauges to be placed in line with the welds. Figure 31 shows one of the puddle welds with trimmed decking from the top flange.

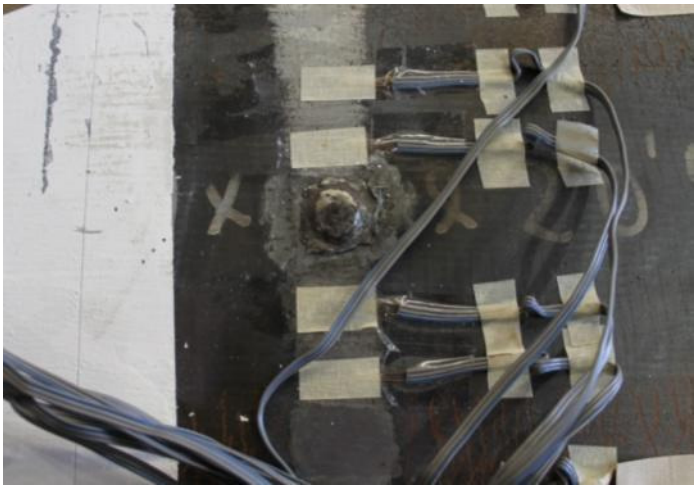

Figure 31: Typical Puddle Weld with Trimmed Decking from Test 5

Figure 32 shows the hysteresis behavior of specimen 5. During the third full cycle of 4.7% story drift, a complete fracture of the bottom flange and several inches of the adjacent web occurred. The fracture occurred in the same fashion as that of specimen 2 in which the brittle fracture occurred after the bottom flange underwent the half cycle in compression and was beginning to be pulled into tension. Apart from the fracture, cracks were observed in the flange edges at the inner surface of local buckles as occurred with specimens 1 and 2. A more thorough evaluation of the full fractures is included in Eatherton et al. (2013). It was found that for the W24x62 RBS specimens with PAFs and puddle welds, the fracture began at the flange tips and propagated toward the center of the flange. When the tear reached the center of the flange (the PAF location in test 2), the rest of the flange fractured in a brittle manner. This fracture is shown in Figure 33.

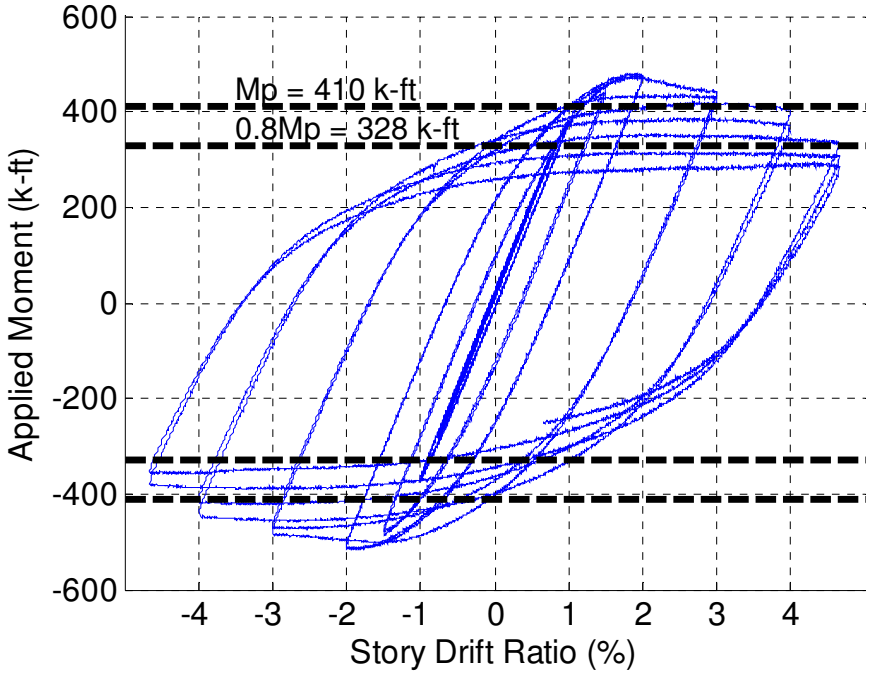

Figure 32: Specimen 5 (RBS24-PW12) Hysteresis

Figure 33: Brittle Bottom Flange Fracture from Test 5

Figure 34 shows the hysteresis overlay of all three W24x62 RBS tests. Figure 35 shows the moment envelope from the same test data.. Envelope plots show the maximum moments at each new story drift amplitude. They provide a simplified visual reference of the hysteretic behavior at peak rotations. General observations drawn from the set of three W24x62 RBS specimens are as follows;

1. All W24x62 specimens with RBS connection satisfied the qualification criteria, completing at least one full cycle of 4% story drift while maintaining at least 80% of their nominal plastic moment capacity, given by the black dotted lines in Figure 34. As can be seen from the hysteresis plot, not only did the specimens pass qualification requirements, they also maintained the 80% plastic moment strength through at least one full cycle of 4.7% story drift before experiencing additional moment capacity loss through buckling and fracture.
2. The progression of limit states was similar for all specimens in this group starting with significant yielding in the extreme fibers at the reduced section, spread of plasticity, local buckling of the flanges in association with out-of-plane buckling of the web, crack initiation typically at the flange tips on the inside face of the local buckle, and fracture propagation through on entire flange.
3. All specimens experienced some amount of fracturing at the minimum flange section. In all cases, the fractures initiated at the edge of the flange on the inside of a local buckle and propagated toward the center of the beam flange. The fracture of specimen 2 passed through a flange, but was observed as having originated at the flange edge.
4. As can be inferred from the hysteresis comparison of Figure 34, the inclusion of fasteners or puddle welds did not seem to have a significant effect on the moment-rotation behavior of the specimen as all three performed in a similar manner.

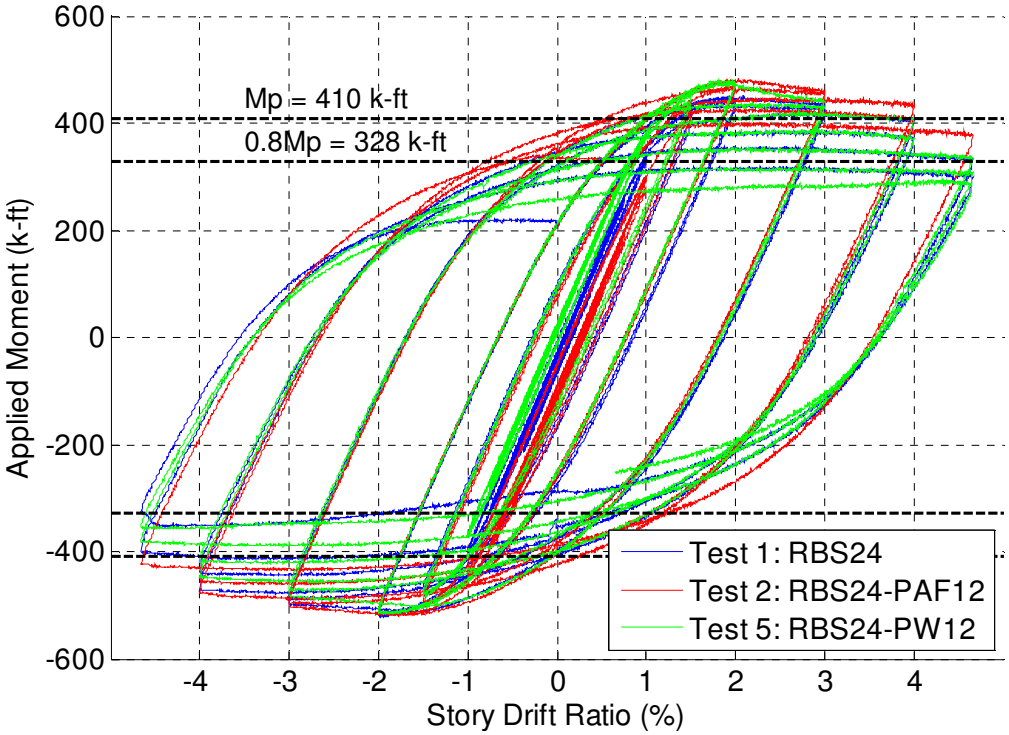

Figure 34: Hysteresis Comparison of W24x62 RBS Specimens

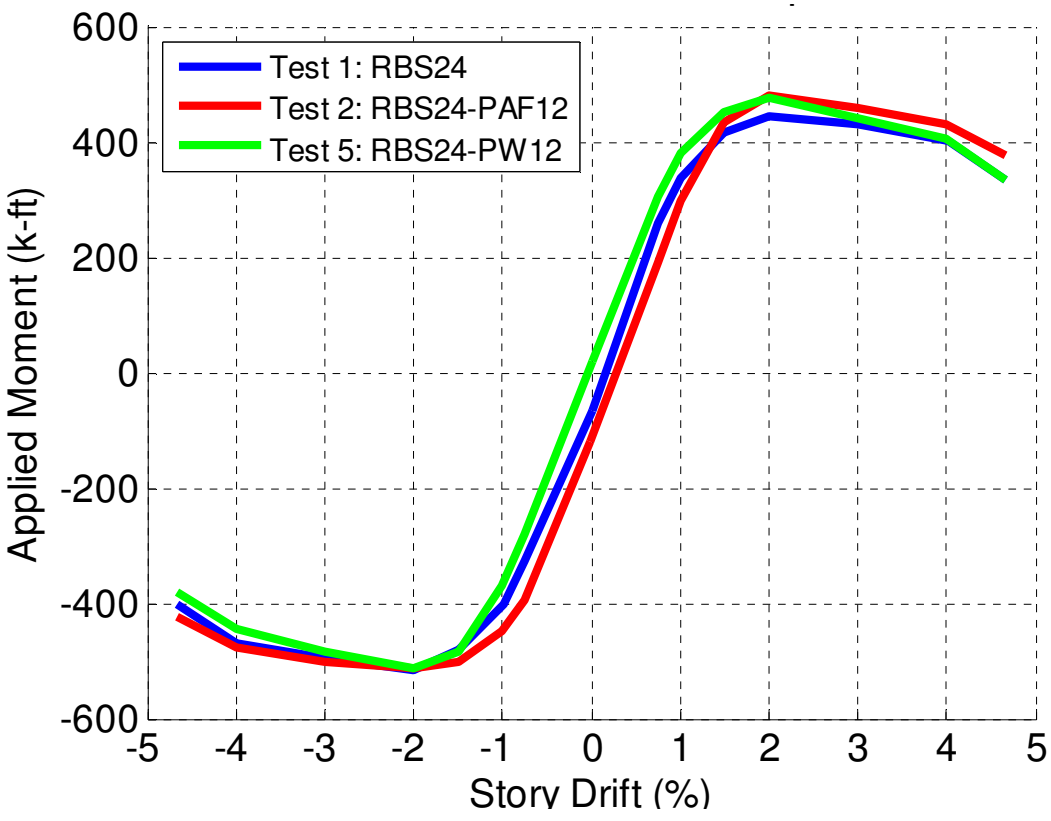

Figure 35: Envelope Comparison of W24x62 RBS Specimens

4.1.2 Behavior of W24x62 Specimens with BUEEP Connection

Test 3: W24x62 with BUEEP Connection No Fasteners

Test 3 was a control test for typical W24x62 speicmens with BUEEP connections. As with the control nature of specimen 1, no PAFs or puddle welds were present on specimen 3. The specimen provided the increased strength expected of a full flange section over that of the previous RBS specimens. Figure 36 shows the hysteresis behavior of specimen 3. Qualification requirements were met with moment capacity greater than 80% of the plastic moment capacity being maintained through a cycle of 4% story drift. The test was halted after two cycles of 4.7% story drift. Although there was some degradation in the strength, there were no signs of fracture. Subsequent test specimens were tested up to five cycles at a story drift of 4.7%. However, test 3 and test 4 were halted after two cycles in part because there were no observable signs of cracking or fracture. Figure 37 shows both specimens 3 and 4 in their deformed states at the second upward peak of 4.7% story drift. While specific local buckle locations vary slightly, both specimens showed the same general deformation behavior.

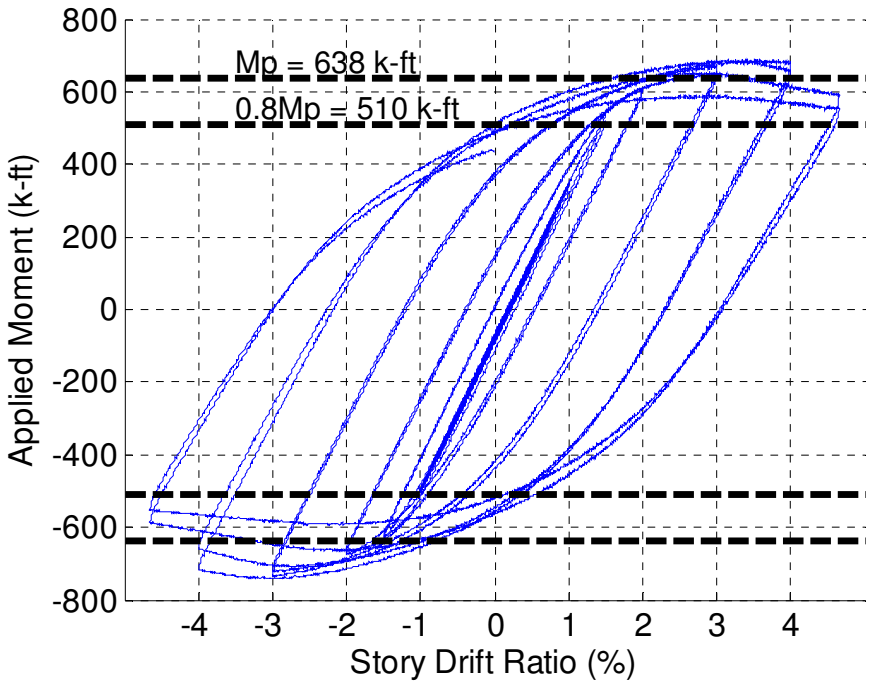

Figure 36: Specimen 3 (W24) Hysteresis

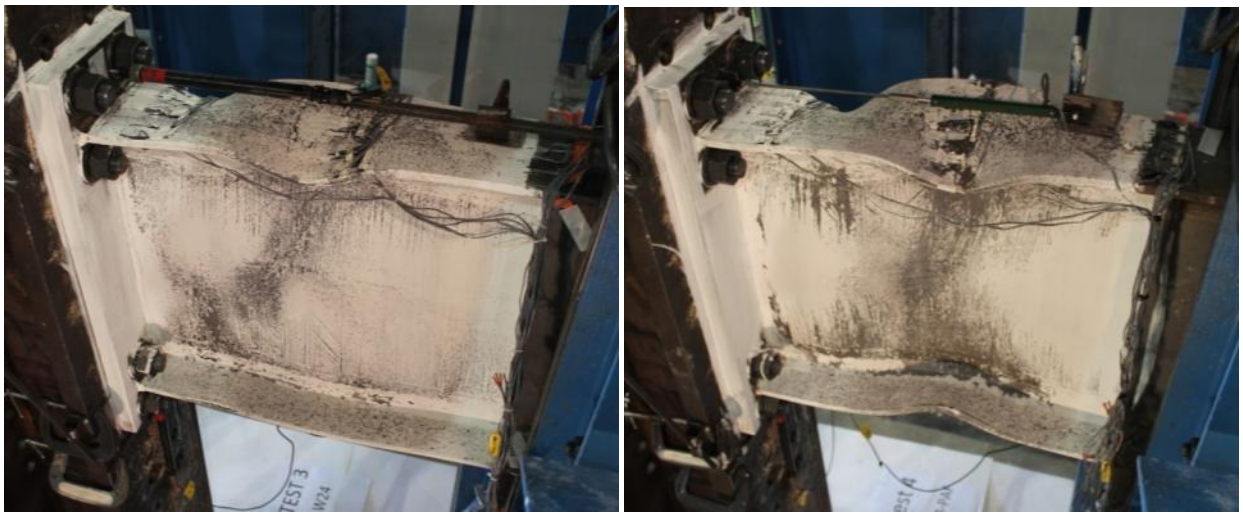

Figure 37: Deformations at 4.7% Story Drift for Test 3 (left) and Test 4 (right)

Test 4: W24x62 with BUEEP Connection and PAFs Spaced at 12 in.

Specimen 4 was a W24x62 specimen with the same linear spacing of four PAFs as used in test 2. As in test 3, all qualification and subsequent cycling was completed without any presence of crack formation or tearing. The beam also passed qualification requirements and the test was halted after two complete cycles at 4.7% story drift. Figure 38 shows the hysteresis behavior of specimen 4. Figure 37 shows the deformed state of specimen 4 during a 4.7% story drift peak in comparison to that of specimen 3.

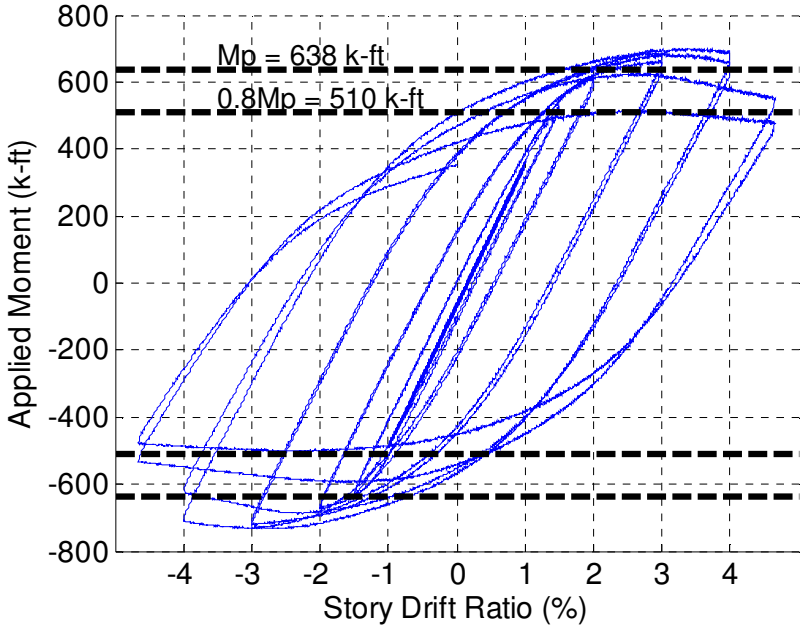

Figure 38: Specimen 4 (W24-PAF12) Hysteresis

Test 6: W24x62 with BUEEP Connection and Grid of PAFs

Specimen 6 included an array of PAFs on both the top and bottom flange. Despite the array of fasteners, the specimen maintained sufficient plastic moment capacity to pass qualification. It also proved resilient during an additional five full cycles of 4.7% story drift with no cracks or tearing observed during testing. Figure 39 shows the hysteresis behavior of specimen 6.

Further inspection of the fastener array after testing revealed the presence of cracks around several PAFs located in the center row over the specimen web. These PAFs could easily be pulled out of the flange with no resistance. Removing these fasteners revealed small tears around the holes and signs that the holes underwent stretching and elongation during cycling. These tears weren't observed in previous tests with PAFs. While the specimen didn't experience any large scale crack propagation or section fracture during the applied loading protocol including five cycles at 4.7% story drift, the presence of tearing around PAFs demonstrates that cracks can form at the PAF locations. However, compared to the fractures in the flange tips of the W24x62 RBS specimens, the fracture propagation was quite slow around the PAF. It is possible that the residual compressive stress field around the PAF affects fracture propagation, although sufficient data to support this hypothesis was not available in this testing program.

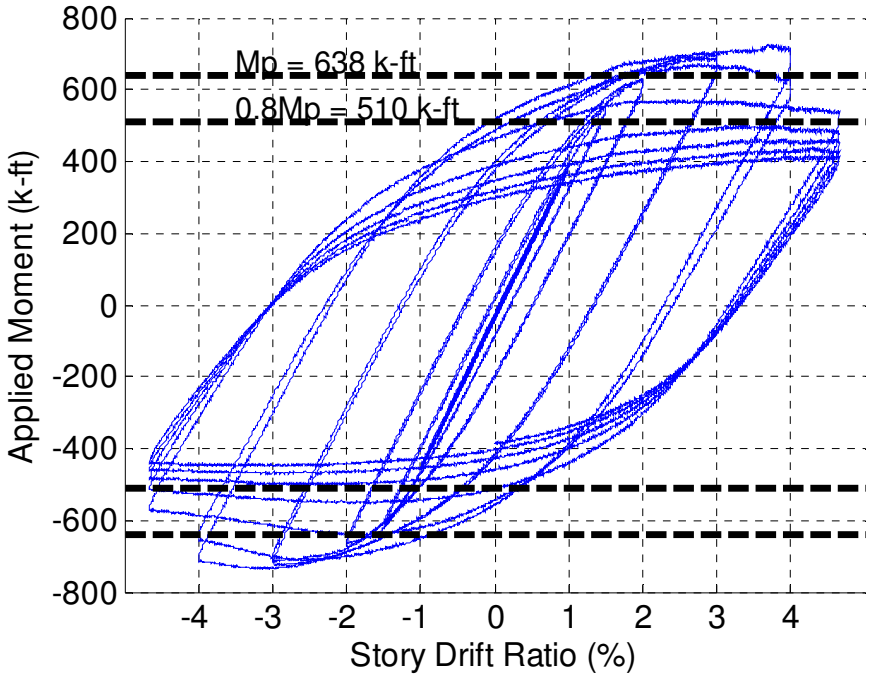

Figure 39: Specimen 6 (W24-PAF_array) Hysteresis

Figure 40 shows the hysteresis overlay of all three W24x62 BUEEP tests. Figure 41 shows the moment envelope from the same test data. General observations drawn from the set of three W24x62 BUEEP specimens are as follows;

1. All W24x62 specimens with BUEEP connections satisfied the qualification criteria.
2. The progression of limit states was similar for all specimens in this group starting with significant yielding in the extreme fibers near the endplate connection, spread of plasticity, and local buckling of the flanges in association with out-of-plane buckling of the web.
3. None of the specimens experienced significant fractures even after being subjected to multiple cycles at 4.7% story drift. It is noted that the specimen with a grid of PAFs experienced minor crack initiation around several PAFs
4. As can be inferred from the hysteresis comparison of Figure 40, the inclusion of fasteners did not seem to have a significant effect on the moment-rotation behavior of the specimen as all three performed in a similar manner.
5. Specimen 6 included an array of PAFs with a spacing selected so that the local stress fields around the fasteners were not expected to interact, but sufficiently close together to ensure fasteners would be located near the peaks of any local buckles. The specimen exhibited a moment-rotation response similar to the other BUEEP specimens and was subjected to five cycles at 4.7% story drift without fracture. During the final several cycles, tears were forming at the PAF locations but were propagating so slowly that they did not significantly affect the moment-rotation behavior.

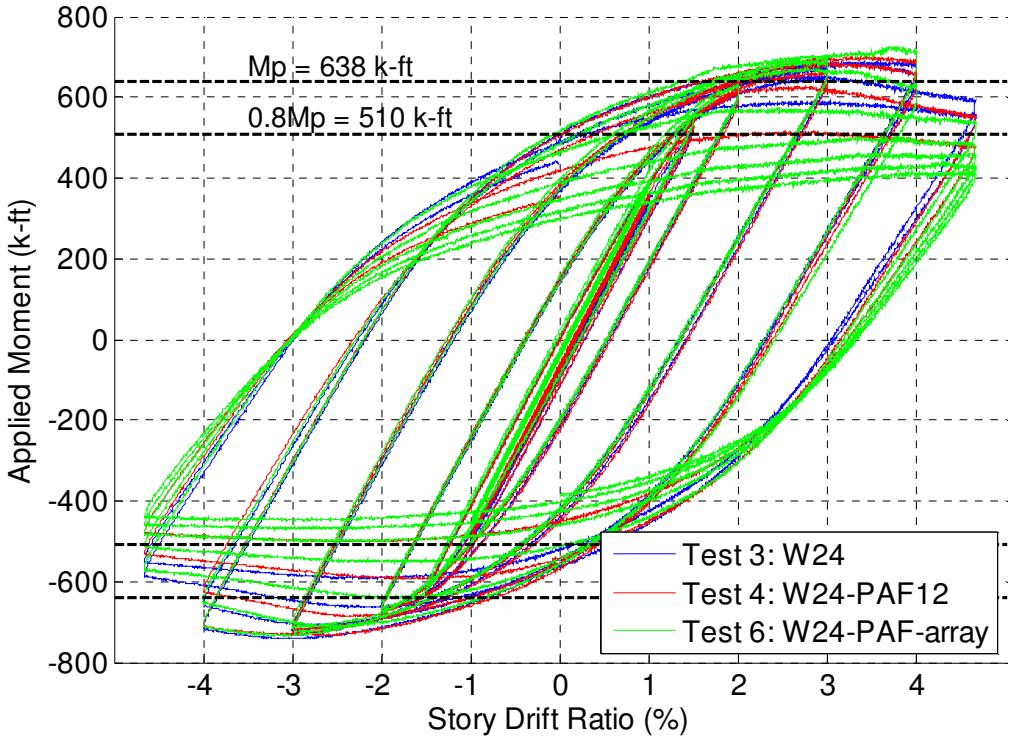

Figure 40: Hysteresis Comparison of W24x62 BUEEP Specimens

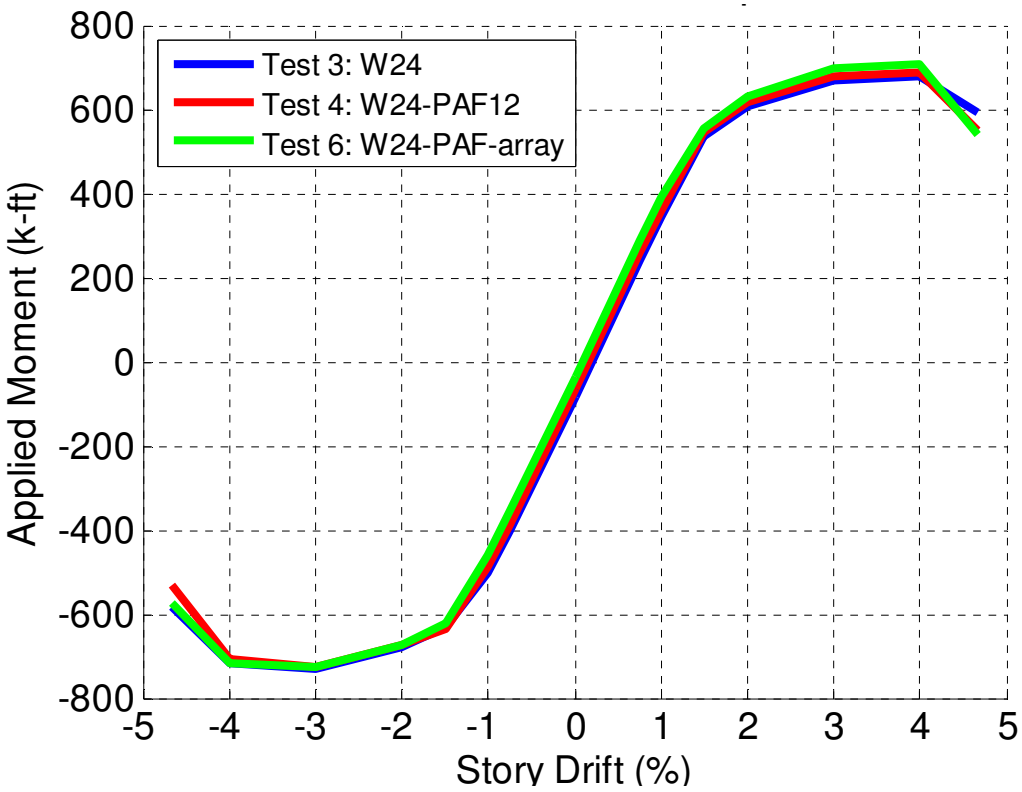

Figure 41: Envelope Comparison of W24x62 BUEEP Specimens

4.1.3 Behavior of W36x150 Specimens with RBS Connection

Test 7: W36x150 with RBS Connection and No Fasteners

Test 7 served as the control test for the W36x150 specimens with RBS connections. No PAFs or puddle welds were present on the specimen. Figure 42 shows the hysteresis behavior of specimen 7. The specimen successfully completed the 4% story drift cycles while maintaining an applied moment capacity greater than 80% of the nominal plastic moment capacity computed with nominal yield stress. After several cycles of 4.7% story drift, tearing was observed on the outer surfaces of both the top and bottom flange in the location of the interior curvature of local buckles. These tears on each flange propagated with each successive half cycle in which the flanges were pulled in tension. During the fifth cycle of 4.7% story drift, the specimen experienced a complete fracture of the top flange at the location of the RBS (Figure 43, left). By this point, the tearing on the underside of the bottom flange was significant as well (Figure 43, right). In addition, tearing was observed on both top and bottom flanges at the weld metal at the junction of the end of both top and bottom endplate stiffeners, respectively.

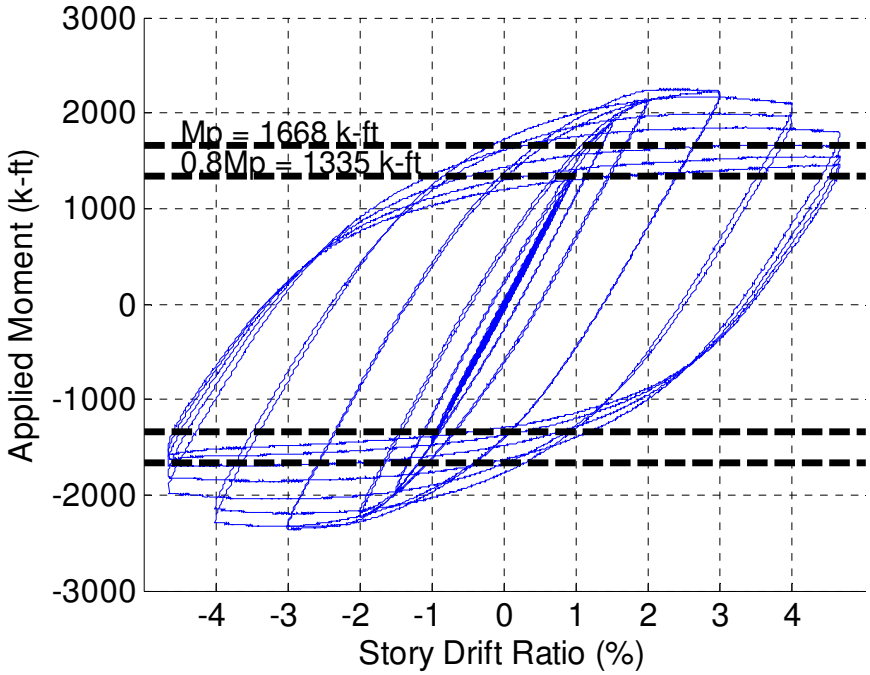

Figure 42: Specimen 7 (RBS36) Hysteresis

Figure 43: Brittle Fracture (left) and Tear Formation on the Underside of Bottom Flange Local Buckle (right) from Test 7

Test 8: W36x150 with RBS Connection and Puddle Welds Spaced at 12 in.

Specimen 8 was a W36x150 specimen with an RBS connection and puddle welds spaced at 12 in. along the top flange in the same fashion as in specimen 5. The hysteresis from test 8 is given in Figure 44. During 4% story drift cycling, tearing was observed at the same stiffener/flange junction weld metal locations as observed in specimen 7. However the specimen still passed qualifying requirements. Immediately following the first 4.7% cycling, the tearing at the bottom flange weld metal propagated sufficiently to cause a complete fracture of the bottom flange at the location of the stiffener toe. The location of the fracture indicates that its occurrence was unrelated to the puddle welds. It is noted that the location of the stiffener toe includes a large stress triaxiality in addition to large strain demands. Figure 45 shows tearing at the top flange stiffener weld metal (left) and the fracture due to tearing at the bottom flange stiffener weld metal (right).

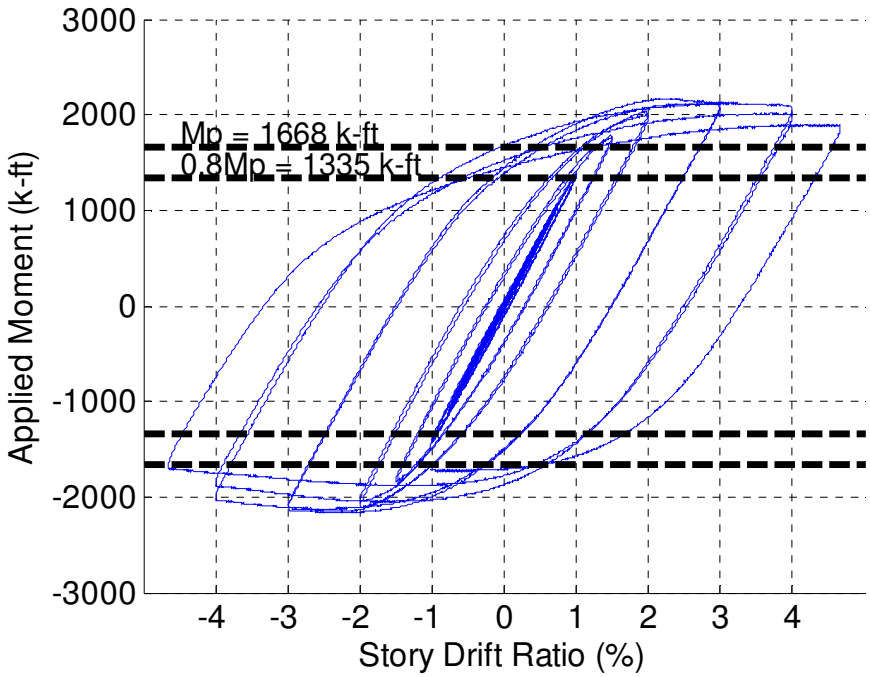

Figure 44: Specimen 8 (RBS36-PW12) Hysteresis

Figure 45: Stiffener Weld Metal Tear (left) and Bottom Flange Fracture Following Tear (right) from Test 8

Test 9: W36x150 with RBS Connection and Grid of PAFs

Specimen 9 was a W36x150 RBS specimen with a grid of PAFs. The specimen 9 hysteresis is presented in Figure 47. Specimen 9 completed qualification requirements, but did show tearing

at both flanges at the stiffener weld metal. Figure 46 shows specimen 9 during the qualification cycle when the top flange was in tension during a downward rotation of 4% story drift.

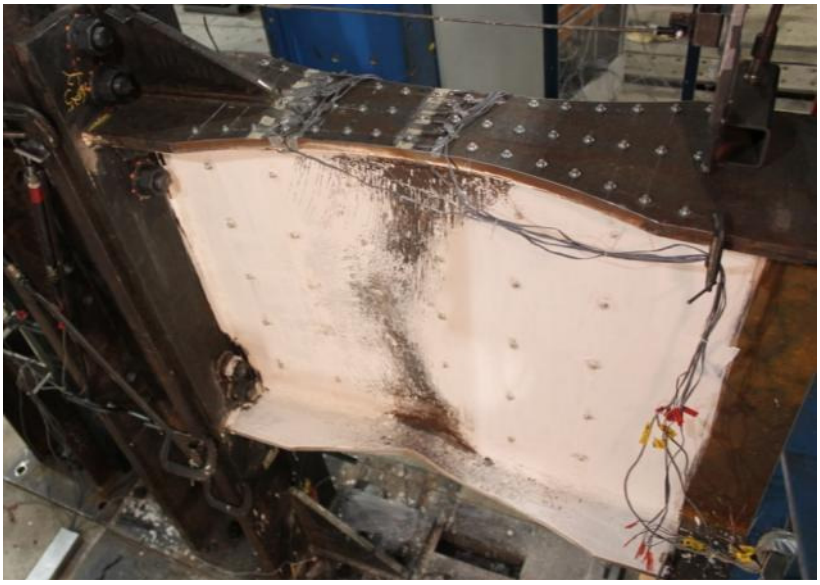

Figure 46: Deformed State during Qualification Cycle of Test 9

During the second cycle of 4% story drift, significant tearing was observed at the top flange RBS where one of the PAFs became dislodged as the hole enlarged during inelastic cycles (Figure 48 left). During the next cycle, the first at 4.7% story drift, the noted hole caused a complete fracture of the top flange at the RBS. The fracture passed through two PAF holes in line with the minimum flange width (Figure 48 right).

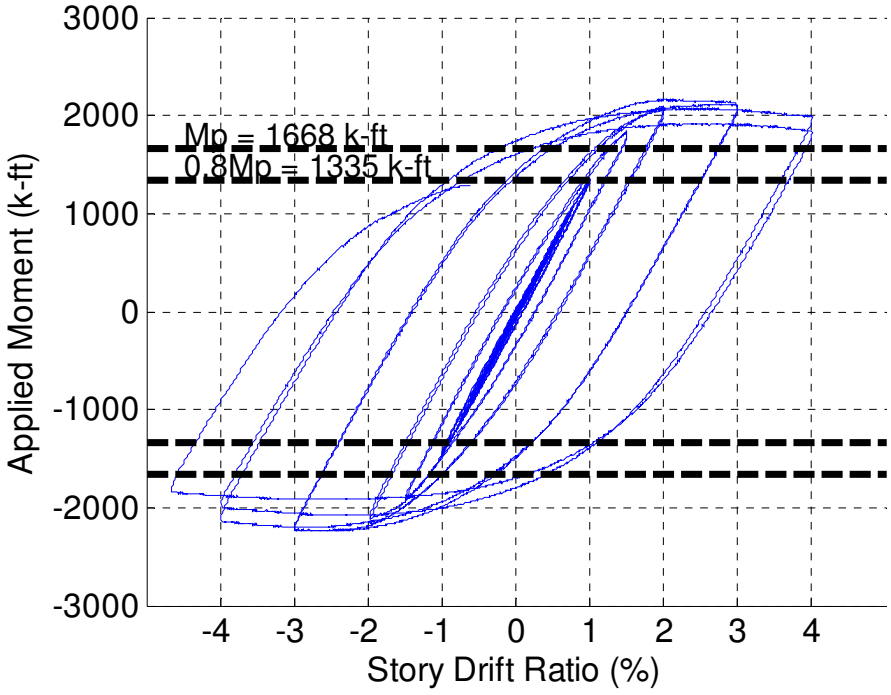

Figure 47: Specimen 9 (RBS36-PAF_array) Hysteresis

Figure 48: PAF hole during last 4% cycle (left) and full fracture during first 4.7% cycle (right) from Test 9

Figure 49 shows the hysteresis overlay of all three W36x150 RBS tests. Figure 50 shows the moment envelope from the same test data. General observations drawn from the set of three W36x150 RBS specimens are as follows;

1. All W36x150 specimens with an RBS connection satisfied the qualification criteria
2. The progression of limit states was similar for all specimens in this group. All specimens showed significant yielding in the extreme fibers at the reduced section, followed by a spread of plasticity and local buckling of the flanges in association with out-of-plane buckling of the web. Following this, crack initiation was most prominent on the inside

face of the local buckles in the region between the flange edges and flange centerlines. This trend differs from that of W24x62 RBS specimens in which crack initiation was most prominent at the flange edges.

3. All specimens experienced some amount of tearing in the region of the end weld of the endplate stiffeners to the top and bottom flanges. This tearing prompted the full bottom flange fracture of specimen 8.
4. As can be inferred from the hysteresis comparison of Figure 49, the inclusion of fasteners or puddle welds did not seem to have a significant effect on the moment-rotation behavior of the specimen as all three performed in a similar manner through the first cycle of 4.7% story drift. The strength degradation associated with local buckling was similar, but there were some variations in the development of fracture
5. Specimen 9 included an array of PAFs with a spacing selected so that the fasteners were not expected to interact, but sufficiently close together to ensure fasteners would be located near the peaks of any local buckles. The specimen exhibited a moment-rotation response similar to the other RBS specimens. A full fracture of the top flange clearly initiated at a PAF at the location of minimum flange width.

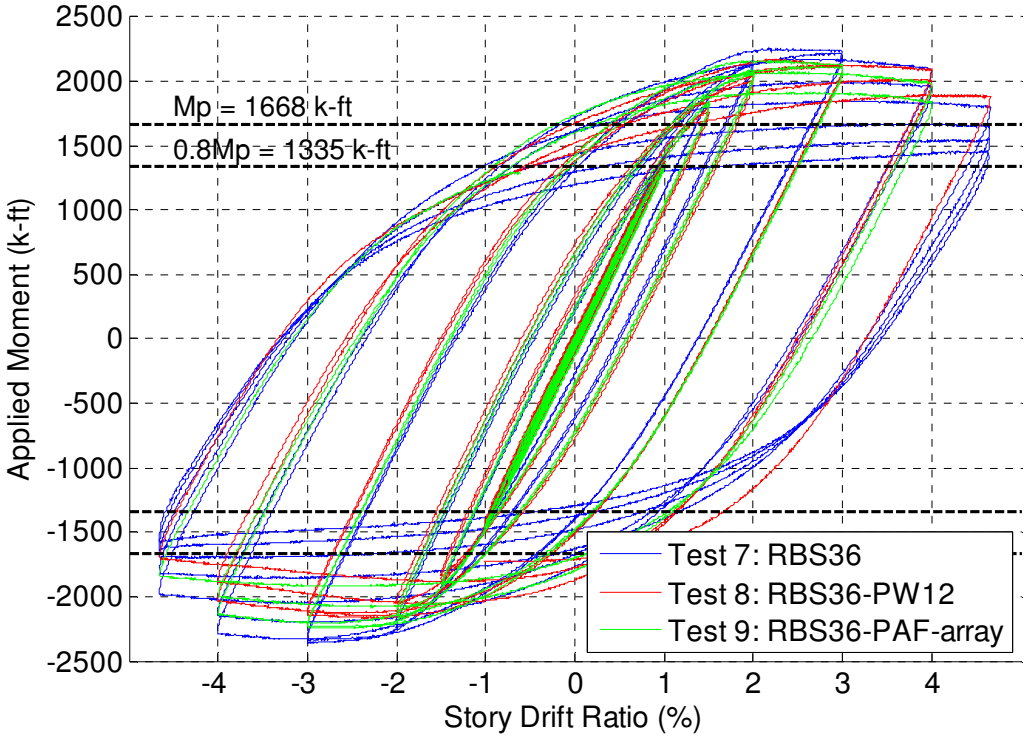

Figure 49: Hysteresis Comparison of W36x150 RBS Specimens

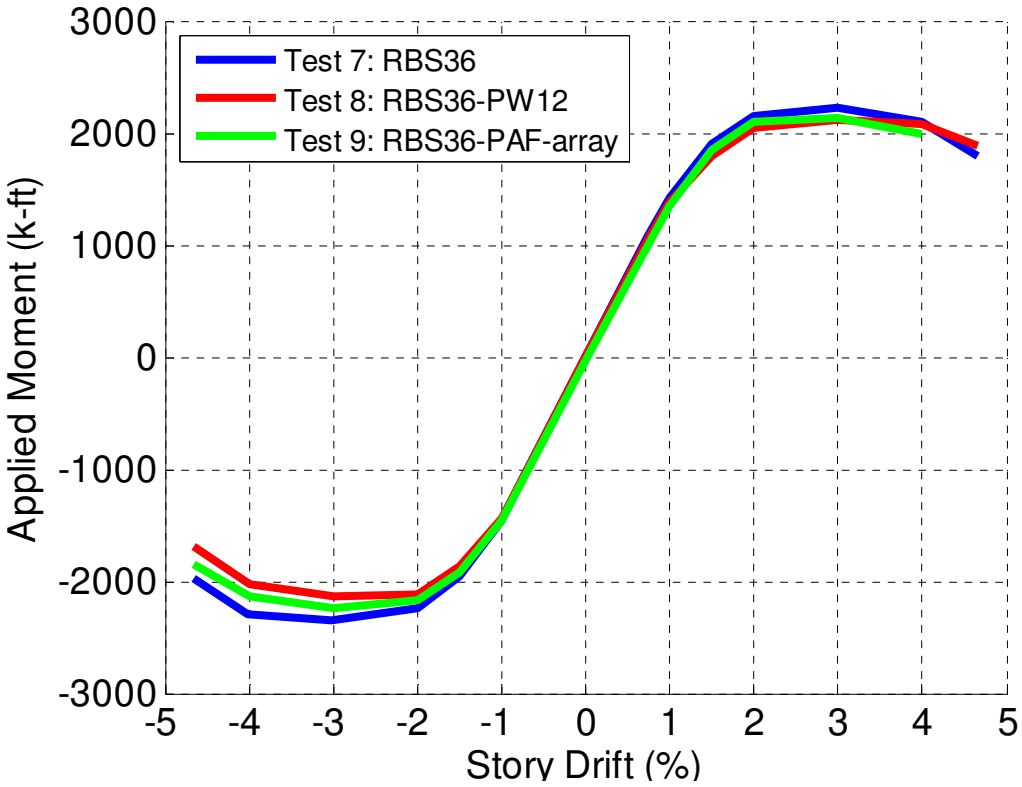

Figure 50: Envelope Comparison of W36x150 RBS Specimens

4.1.4 Behavior of W36 Specimens with BSEEP Connection

Test 10: W36x150 with BSEEP Connection and No Fasteners

Test 10 served as the control test for the W36x150 specimens with BSEEP connections. No PAFs were present in the protected zone. Qualification requirements were met and testing was ended after the specimen completed five full cycles of 4.7% story drift without failing. Figure 51 shows both specimens 10 and 11 in their deformed states at the fifth upward peak of 4.7% story drift. While specific local buckle locations vary slightly, both specimens showed the same general deformation behavior. Throughout the last amplitude cycles, tearing was observed at the endplate stiffener toe weld metal similar to the tears observed in the W36x150 specimens with RBS sections. After initially forming, the tears did not propagate significantly for the applied displacement history including five cycles at 4.7% story drift. Figure 52 shows the hysteresis behavior of specimen 10.

Figure 51: Deformations at 4.7% Story Drift for Test 10 (left) and Test 11 (right)

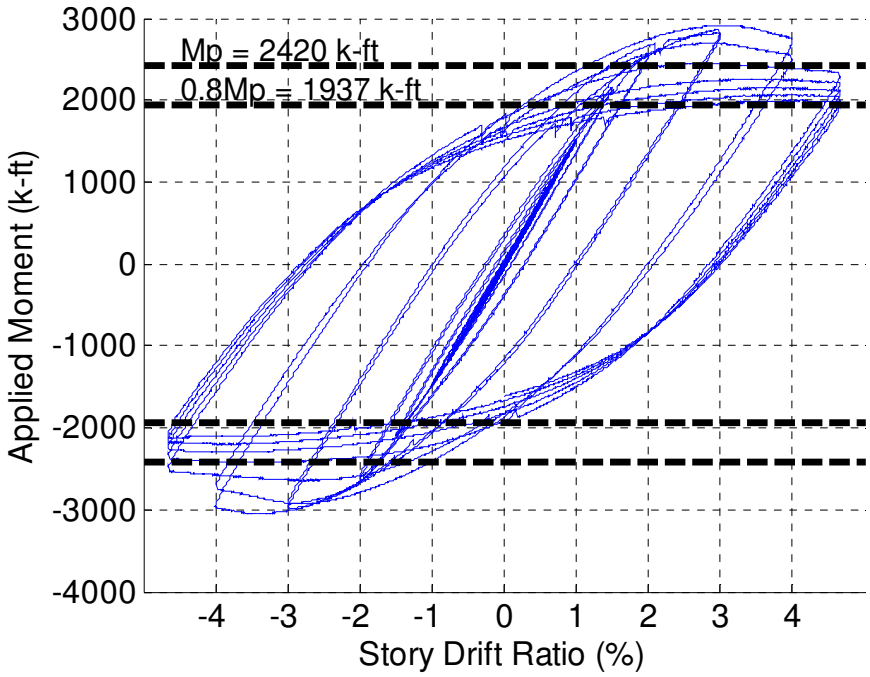

Figure 52: Specimen 10 (W36) Hysteresis

Test 11: W36x150 with BSEEP Connection and PAFs Spaced at 12 in.

Specimen 11 was a W36x150 specimen with BSEEP connection and PAFs spaced at 12 in. along the top flange in the same fashion as in specimen 4. As in the previous test, qualification requirements were met and the test was ended after five cycles of 4.7%. The same endplate stiffener weld metal tearing observations were made as in previous tests. Figure 53 shows the tearing at both the top and bottom endplate stiffener toe welds. Figure 54 shows the hysteresis behavior of specimen 11.

Figure 53: Tearing at Top Flange (left) and Bottom Flange (right) Endplate Stiffener Toe Welds from Test 11

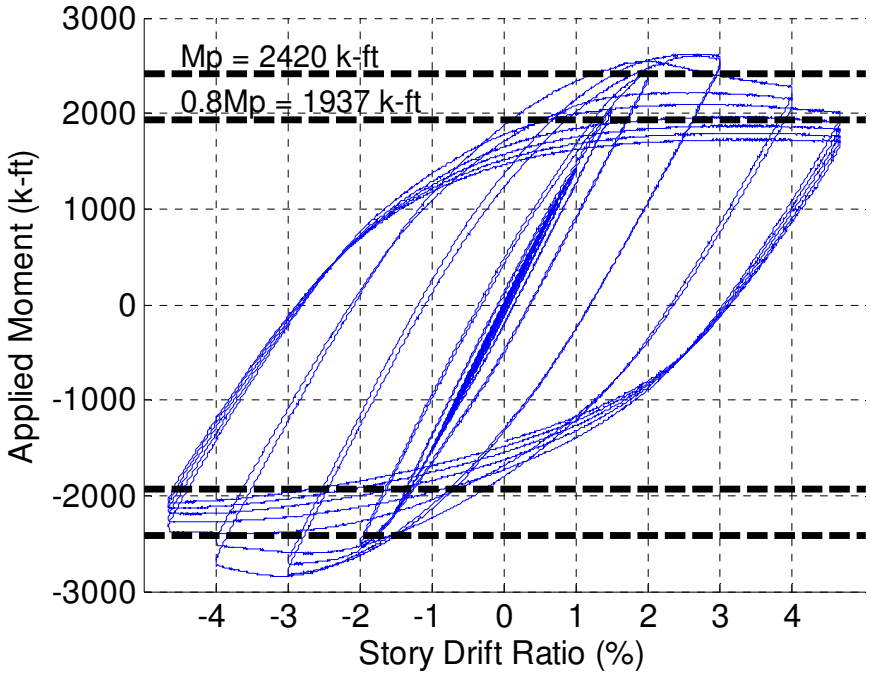

Figure 54: Specimen 11 (W36-PAF12) Hysteresis

Test 12: W36x150 with BSEEP Connection and Grid of PAFs

Specimen 12 was a W36x150 specimen with a BSEEP connection. The specimen included a grid of PAFs. Qualification requirements were met and the test hysteresis is given in Figure 55. During the second cycle of 4.7% story drift, it was observed that several PAFs fastened in the underside of the bottom flange were falling out of the beam as their holes began tearing and enlarging (Figure 56 – top left). Visual observation of the bottom flange revealed that during the

next cycle, significant tear propagation occurred, originating from a PAF hole 3.5 inches from the edge of the flange (Figure 56 – top right). During the extreme upward deflection of the fourth 4.7% cycle, the tear propagated to the flange edge. This was followed almost immediately by a full fracture of the bottom flange (Figure 56 – bottom left). The fracture extended approximately six inches up the web intersecting one of the PAFs in the web (Figure 56 – bottom right).

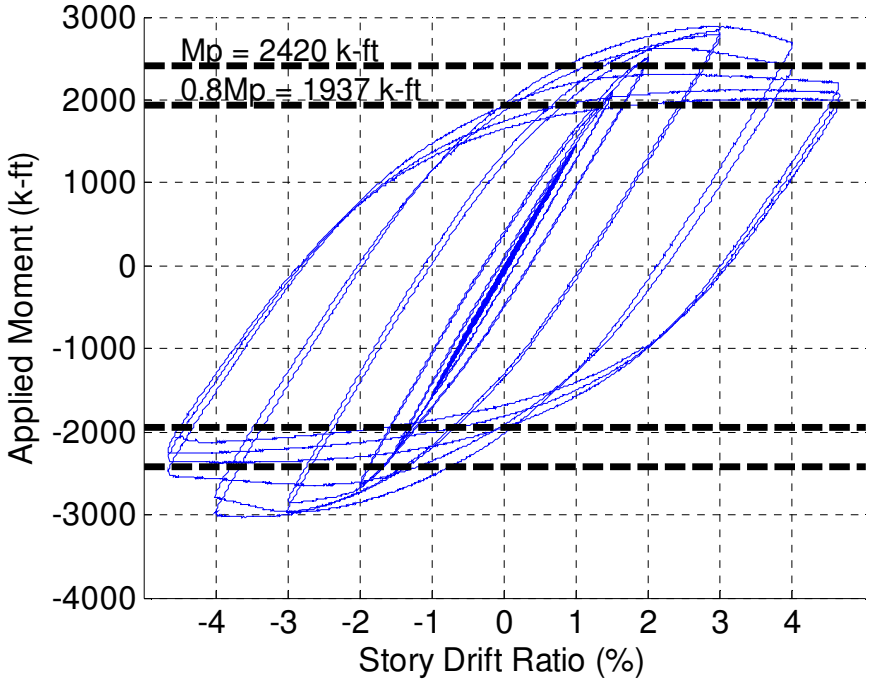

Figure 55: Specimen 12 (W36-PAF_array) Hysteresis

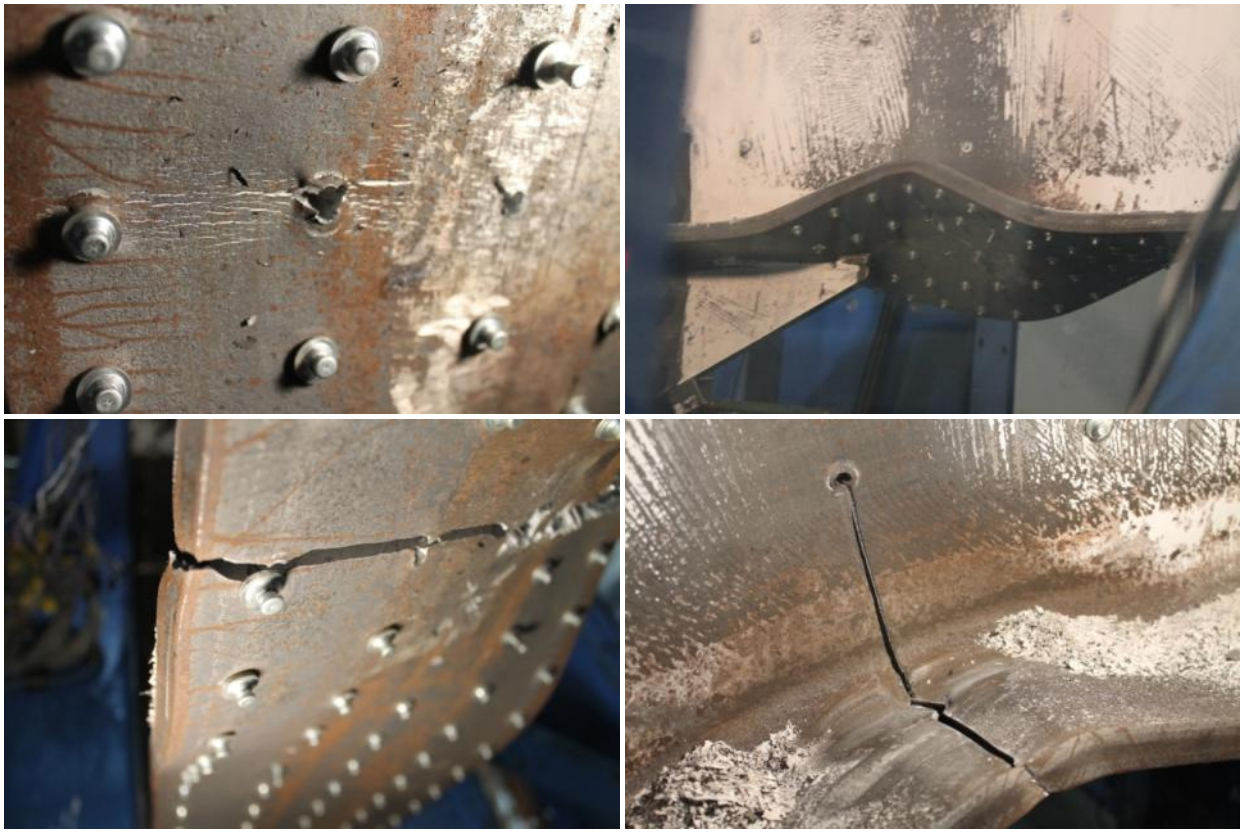

Figure 56: Test 12 - Initial PAF hole tearing (top left), Crack propagation (top right), Full flange fracture (bottom left), Fracture extension to web PAF hole (bottom right)

Figure 57 shows the hysteresis overlay of all three W36x150 BSEEP tests. Figure 58 shows the moment envelope from the same test data. General observations drawn from the set of three W36x150 BSEEP specimens are as follows;

1. All W36x150 specimens with BSEEP connections satisfied the qualification criteria
2. All specimens experienced some amount of tearing in the region of the end weld of the endplate stiffeners to the top and bottom flanges. None of these tears propagated beyond the local region of their initiation.
3. As can be inferred from the hysteresis comparison of Figure 57, the inclusion of fasteners did not seem to have a significant effect on the moment-rotation behavior of the specimen as all three showed a similar hysteresis behavior up to the point of fractures.
4. Specimen 12 included a grid of PAFs with a spacing selected so that the fasteners were not expected to interact, but sufficiently close together to ensure fasteners would be located near the peaks of any local buckles. The specimen exhibited a moment-rotation

response similar to the other BSEEP specimens. A full fracture of the bottom flange initiated at an interior PAF hole located 3.5 inches from the flange edge.

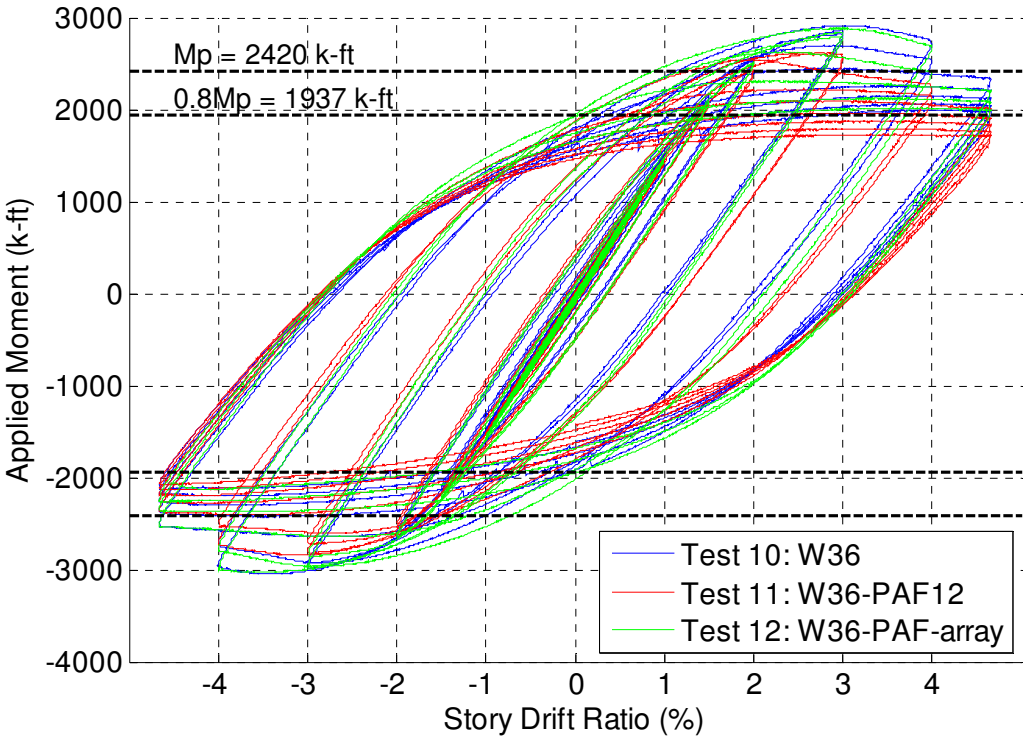

Figure 57: Hysteresis Comparison of W36x150 BSEEP Specimens

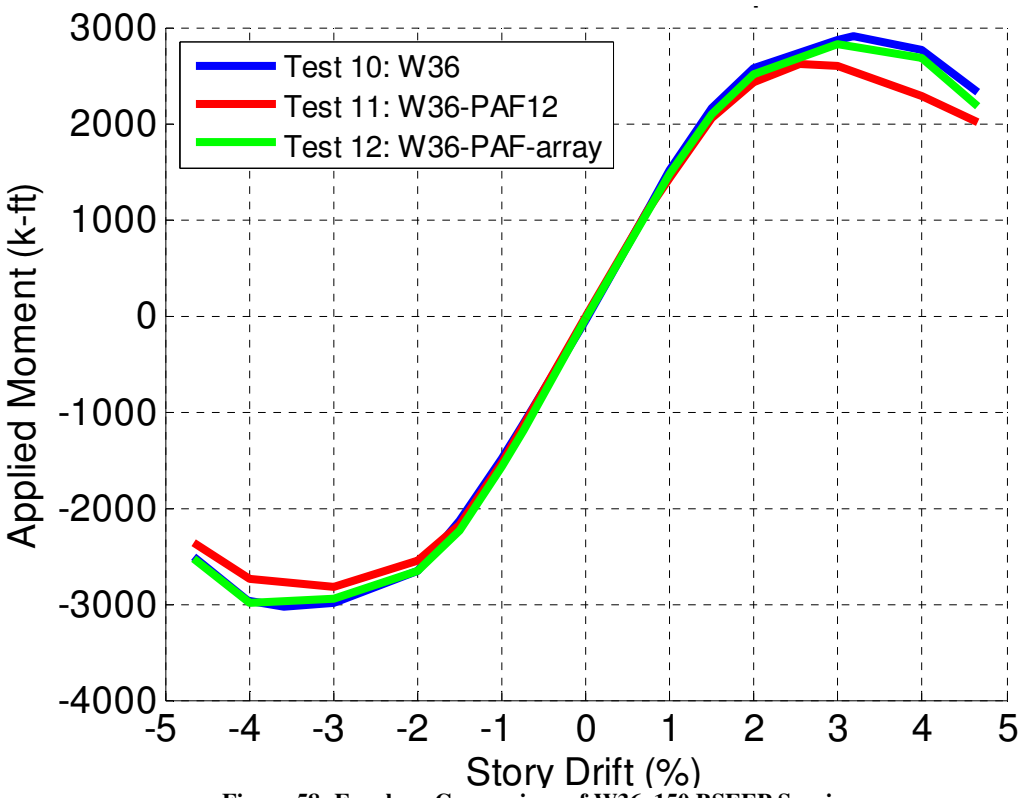

Figure 58: Envelope Comparison of W36x150 BSEEP Specimens

4.1.5 Test Results General Trends

Several general observations can be made from the completed tests. All six RBS specimens experienced some degree of fracture during 4.7% story drift cycling with test 1 producing a ductile flange tear and the other five RBS tests producing brittle fractures along an entire flange width and a portion of the web. The only non-RBS specimen to experience a fracture was specimen 12 which contained a PAF grid.

All brittle fractures occurred at the flange local buckles as the flange force transitioned from compression to tension. It is noteworthy that the fractures did not occur when the moment causing tensile stresses was at a maximum. However, the localized tensile stresses at the inside of the local buckles as they were straightening out may have been greater than the yield stress. This would indicate a general tendency for material tearing after significant compression excursions.

In addition to the tear and full fractures observed, all six RBS specimens showed a significant presence of cracks forming on the interior edge of local buckles (Figure 59). These trends indicate a tendency for crack formation and propagation in locations experiencing significant compression during cycling. Analyzing the strain history at the buckling interior curve region could provide insight into the conditions that cause the visible macro-crack formation. FEM modeling is used later in this document to briefly analyze the strain history at this region. Future FEM analysis by others will be performed to assess if the compression strains on buckle compression faces are more concentrated than tension strains on buckle tension faces.

Figure 59: Tearing of the Flange Edge from Test 5

Specimen 12 was the only non RBS specimen to experience any degree of fracture. As already noted, this fracture originated as a tear at a PAF hole on the bottom flange in the compressive region of a local buckle. The tear propagated across the flange to adjacent PAF holes before causing a full fracture of the bottom flange. Figure 56 shows visual evidence of this fracture originating at a PAF hole. The fracture of specimen 9 also originated at a PAF hole located at the compressive region of a local buckle. The fracture of specimen 12 while specimen 11 did not fracture would indicate that PAF holes along the centerline of a full flange specimen do not experience sufficient compression (as occurs near local buckles) to cause propagating tears. However, this was not the case with specimen 6 which did not fracture despite a grid of PAFs including some located in proximity to local buckles. It is noted that the flanges of the W36x150 specimens generally experience larger compressive strains than those of the W24x62 specimens undergoing the same curvature due to the greater distance from the plastic neutral axis to the flanges.

4.2 Test Specimen Strength Analysis

This section provides a summary of the moment capacity performance of all test specimens. All moment capacities in this section are reported as the applied moment at the face of the column. Figure 60 shows a reference image for the values quantified in subsequent tables. All tests satisfied qualification requirements by maintaining greater than 80% of their nominal plastic moment capacity during the first cycle of 4% story drift. Table 2 presents a summary of the moment capacities of all test specimens at both positive and negative 4% story drift during the first cycle at this displacement level. It is noted that the first five specimens (tests 1-5) were tested such that for any given cycle the beams were deflected downward (positive story drift) first. All remaining tests were reversed so that beams were deflected upward before being deflected down. The change was made after making general observations of the first five tests. It was observed that the flanges that were more likely to fracture were those that experienced compression first. The top flange included strain gauges as well as PAFs or puddle welds depending on the test specimen. For this reason, the “First Qualification Amplitude” listed in Table 2 for tests 1-5 is at 4% story drift whereas for the remaining tests it is at -4% story drift.

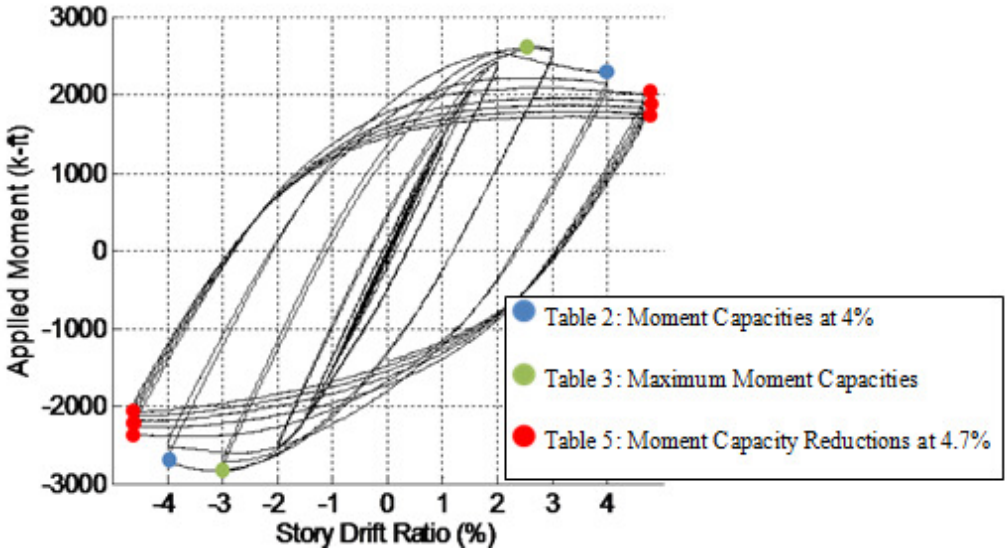

Figure 60: Moment Capacity Reference Image

Table 2: Qualification Cycle - Moment Capacity

Beam Type	.8Mp	Test	First Qualification Amplitude		Second Qualification Amplitude	
			Story Drift	Moment (k-ft)	Story Drift	Moment (k-ft)
W24x62 with RBS	328 k-ft	Test 1	4 %	402	- 4 %	-471
		Test 2	4 %	432	- 4 %	-476
		Test 5	4 %	404	- 4 %	-446
W24x62 with BUEEP	510 k-ft	Test 3	4 %	681	- 4 %	-718
		Test 4	4 %	688	- 4 %	-709
		Test 6	- 4 %	-715	4 %	709
W36x150 with RBS	1335 k-ft	Test 7	- 4 %	-2287	4 %	2091
		Test 8	- 4 %	-2033	4 %	2082
		Test 9	- 4 %	-2141	4 %	1990
W36x150 with BSEEP	1937 k-ft	Test 10	- 4 %	-2966	4 %	2754
		Test 11	- 4 %	-2733	4 %	2280
		Test 12	- 4 %	-2984	4 %	2683

It is apparent from Table 2 that during the qualification cycle, all specimens required a greater applied force by the actuator to achieve negative 4% story drift (upward deflection) than positive 4% story drift (downward deflection). This trend is consistent regardless of whether the specimen initially experienced an upward or downward deflection during the qualification cycle.

After reaching a maximum value at some point during testing, all specimens experienced a reduction in moment capacity prior to reaching the 4% qualification cycle. Table 3 indicates the

absolute maximum positive (downward deflection) and maximum negative (upward deflection) moment capacities of each specimen as well as the story drift at which the moment capacities were recorded. It also provides an average of these values for each of the four specimen types. Nominal moment capacities are listed for each beam type. A predicted moment capacity utilizes the measured yield stress of 53 ksi from tension coupon testing and nominal section properties. This value is comparable but still less than the recorded maximum moment capacities of all specimens.

Table 3: Maximum Applied Moment Capacity

Beam Type	Nominal Mp Fy=50ksi	Predicted Mp Fy=53ksi	Test	Maximum Positive Moment Capacity			Maximum Negative Moment Capacity		
				Story Drift	Moment (k-ft)	Average (k-ft)	Story Drift	Moment (k-ft)	Average (k-ft)
W24x62 with RBS	410 k-ft	435 k-ft	Test 1	2.1 %	452	471	-1.9 %	-524	-520
			Test 2	2.0 %	482		-1.8 %	-520	
			Test 5	1.8 %	480		-1.9 %	-517	
W24x62 with BUEEP	638 k-ft	676 k-ft	Test 3	3.6 %	690	706	-3.0 %	-743	-737
			Test 4	3.4 %	701		-2.5 %	-733	
			Test 6	3.8 %	726		-3.0 %	-736	
W36x150 with RBS	1668 k-ft	1768 k-ft	Test 7	2.3 %	2252	2195	-2.9 %	-2357	-2257
			Test 8	2.2 %	2171		-2.3 %	-2167	
			Test 9	2.0 %	2161		-3.0 %	-2246	
W36x150 with BSEEP	2420 k-ft	2565 k-ft	Test 10	3.0 %	2916	2809	-3.4 %	-3047	-2974
			Test 11	2.7 %	2625		-3.1 %	-2844	
			Test 12	2.9 %	2886		-3.5 %	-3030	

As seen in Table 3, the same moment at the column face imbalance is apparent as was observed in the qualification applied moments given in Table 2. All recorded moments are greater in magnitude for negative story drift than for positive story drift.

It is noted that the tendency for the beam to deflect down under its own weight as well as the weight of the shim plates under the actuator creates a resulting initial moment at the column face. It is possible to calculate this initial moment. Figure 61 shows a schematic of the contributions of several dead load components. The weight of the shim plates assumes an average 2 in. depth of the 18 in. by 18 in. stacked plates. The applied moment at the column face due to these loads is summarized by Equation 4.1

$$M = \frac{1}{2}w(21ft)^2 + P1 \times 21ft + P2 \times 16.3ft \quad (4.1)$$

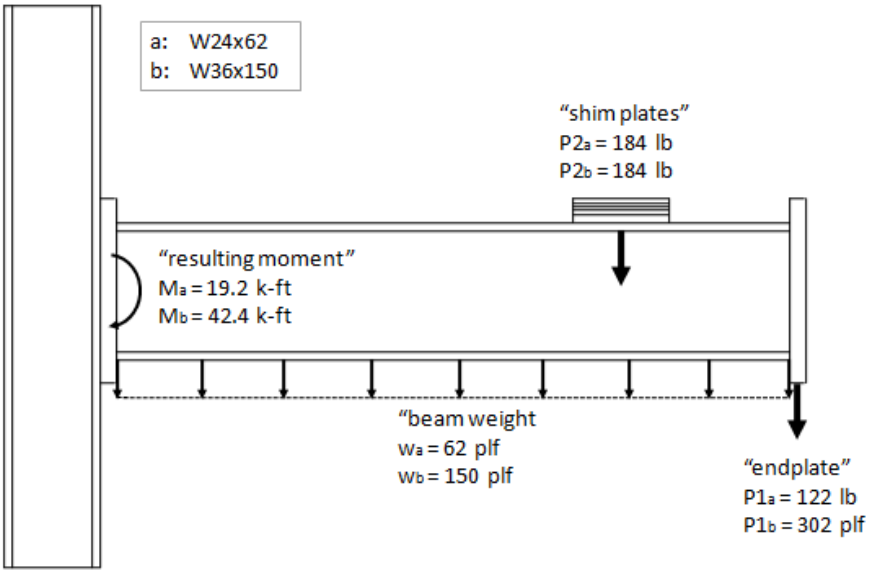

Figure 61: Initial Applied Moment Due to Self Weight (NOT TO SCALE)

This initial positive applied moment is not accounted for by the recorded actuator force during the test. This, at least in part, contributes to the apparent imbalance in moments. In reality the actual positive moment to the beam is greater than the recorded value by this initial amount already present in the beam. In the same manner, the actual negative moment is less than the recorded value by the same initial moment amount. The presence of the initial moment in the beam therefore results in a difference between positive and negative moment magnitudes equal to twice the value of the initial moment. Table 4 lists the recorded maximum and negative moments incurred by each specimen. It also lists the initial positive internal moments previously described and the adjusted positive and negative values based on the initial positive moment. The difference between these adjusted values is reported as the "Adjusted Moment Imbalance". The average value for the imbalance magnitude from all tests is 36.1 k-ft which corresponds to an actuator force of 2.2 kips. Additional asymmetry in the hysteretic behavior is also due to variable initial load placed on the beam when it was bolted to the actuator. Any gap between the sagging beam and the zero position of the actuator that could not be filled with shim plates of various thicknesses results in a deflection of the beam when bolts are tightened. This distance and the resulting initial actuator force was variable for each test depending on specimen geometries and the accuracy of endplate welds as well as the finite shim plate thicknesses available.

Table 4: Maximum Applied Moment Capacity Asymmetry

Beam Type	Test	Maximum Positive Moment (k-ft)	Maximum Negative Moment (k-ft)	Imbalance from Dead Loads (k-ft)	Adjusted Positive Moment (k-ft)	Adjusted Negative Moment (k-ft)	Adjusted Moment Imbalance (k-ft)
W24x62 with RBS	Test 1	452	-524	-19.2	471.2	-504.8	33.6
	Test 2	482	-520	-19.2	501.2	-500.8	-0.4
	Test 5	480	-517	-19.2	499.2	-497.8	-1.4
W24x62 with BUEEP	Test 3	690	-743	-19.2	709.2	-723.8	14.6
	Test 4	701	-733	-19.2	720.2	-713.8	-6.4
	Test 6	726	-736	-19.2	745.2	-716.8	-28.4
W36x150 with RBS	Test 7	2252	-2357	-42.4	2294.4	-2314.6	20.2
	Test 8	2171	-2167	-42.4	2213.4	-2124.6	-88.8
	Test 9	2161	-2246	-42.4	2203.4	-2203.6	0.2
W36x150 with BSEEP	Test 10	2916	-3047	-42.4	2958.4	-3004.6	46.2
	Test 11	2625	-2844	-42.4	2667.4	-2801.6	134.2
	Test 12	2886	-3030	-42.4	2928.4	-2987.6	59.2
						Average	**36.1**

Specimens 1-5 were tested to either fracture or the completion of two cycles of 4.7% story drift. All other specimens were tested to either fracture or the completion of five cycles at 4.7%. During these final cycles of each test, a progressive reduction in moment capacity was typical as local buckling became more severe with each subsequent cycle. Table 5 summarizes these reductions during repeated cycles of 4.7% as applicable for each test. Each test is split into positive and negative moment capacity values in order to account for the applied moment imbalance previously discussed. Numbers within parentheses represent the percent reduction of the moment capacity from the initial value calculated during the first cycle. All specimens show an expected reduction in moment capacity with each subsequent cycle prior to failure. For tests completing more than one cycle at 4.7%, the initial reduction in moment capacity reported during the second cycle varies from 4% to as much as 20%. All but one specimen experiencing fracture did so in the next half cycle following a peak in which the applied moment had reduced by 15-20% of the moment capacity from the initial 4.7% cycle. The exception to this trend is specimen 12 which fractured following a final recorded moment capacity reduction of 8.7%. As already discussed, this fracture was observed to initiate at a PAF hole. This observation implies that the presence of PAFs in the region of local buckles may have caused a fracture to develop prior to when it occurred in specimens with no fasteners.

Table 5: Moment Capacity Reduction at 4.7%

Type	Test	+/- 4.7%	Applied Moment at 4.7% Story Drift – k-ft (Percent Moment Reduction from 1st Cycle - %)				
			1st Cycle	2nd Cycle	3rd Cycle	4th Cycle	5th Cycle
W24x62 with RBS	1	+	334	299 (10.4)	Fracture	Fracture	Fracture
		-	-401	-325 (18.9)	Fracture	Fracture	Fracture
	2	+	376	Fracture	Fracture	Fracture	Fracture
		-	-422	Fracture	Fracture	Fracture	Fracture
	5	+	334	307 (7.9)	284 (14.8)	Fracture	Fracture
		-	-382	-355 (6.9)	Fracture	Fracture	Fracture
W24x62 with BUEEP	3	+	592	553 (6.5)	Test Ended	Test Ended	Test Ended
		-	-585	-550 (5.9)	Test Ended	Test Ended	Test Ended
	4	+	550	479 (13.0)	Test Ended	Test Ended	Test Ended
		-	-531	-478 (10.1)	Test Ended	Test Ended	Test Ended
	6	-	-573	-513 (10.4)	-483 (15.7)	-457 (20.2)	-440 (23.3)
		+	540	475 (12.0)	432 (20.0)	429 (20.5)	413 (23.6)
W36x150 with RBS	7	-	-1981	-1812 (8.6)	-1691 (14.6)	-1620 (18.2)	-1572 (20.7)
		+	1791	1655 (7.6)	1552 (13.4)	1458 (18.6)	Fracture
	8	-	-1695	Fracture	Fracture	Fracture	Fracture
		+	1887	Fracture	Fracture	Fracture	Fracture
	9	-	-1845	Fracture	Fracture	Fracture	Fracture
		+	Fracture	Fracture	Fracture	Fracture	Fracture
W36x150 with BSEEP	10	-	-2520	-2370 (6.0)	-2257 (10.4)	-2172 (13.8)	-2079 (17.5)
		+	2333	2216 (5.0)	2119 (9.2)	2046 (12.3)	1975 (15.4)
	11	-	-2367	-2244 (5.2)	-2177 (8.0)	-2121 (10.4)	-2071 (12.5)
		+	2003	1909 (4.7)	1826 (8.8)	1761 (12.1)	1712 (14.5)
	12	-	-2530	-2353 (7.0)	-2252 (11.0)	Fracture	Fracture
		+	2174	2078 (4.4)	1985 (8.7)	Fracture	Fracture

Figure 62 through Figure 65 shows strength degradation plots for each of the four specimen types discussed. These plots show the strength reduction ratio, η, as it varies for every new peak story drift amplitudes starting at 1%. As shown in Equation 4.2, the strength reduction ratio at any given story drift phase, i, is equal to the ratio of the moment at the second occurrence of that peak rotation, M_{cycle2}, to the moment at the first occurrence of that peak rotation, M_{cycle1}. Despite its designation as a strength reduction ratio, any value greater than 100% actually indicates an increase in moment capacity during the second instance of a peak rotation. This typically results from strain hardening of the specimen plastic hinge region.

$$\eta = \left[\frac{M_{Cycle2}}{M_{Cycle1}}\right]_i * 100\% \tag{4.2}$$

As can be seen from the comparisons, all four specimen types show similar degradation profiles. Most specimens did not experience a significant reduction in moment capacity over repeated cycles until the 4% story drift cycles. During both 4% and 4.7% cycles, most specimens showed a strength reduction of 90-95% from the first to the second peak rotation. It is noted that additional strength degradation from beyond the first two 4.7% story drift cycles, for applicable tests, are not reflected in these plots. Those values are tabulated in Table 5.

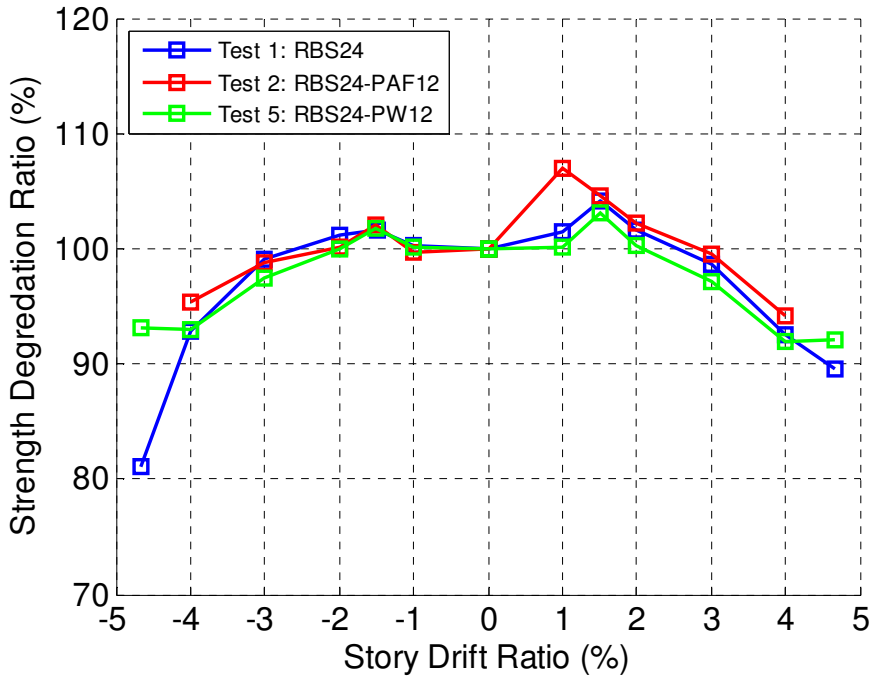

Figure 62: Strength Degradation Comparison of W24x62 RBS Specimens

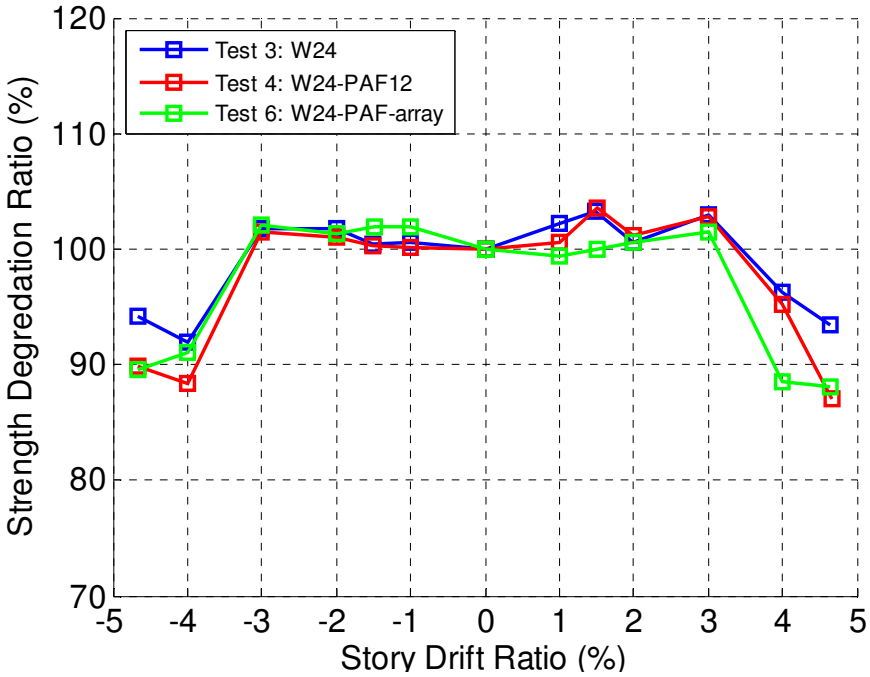

Figure 63: Strength Degradation Comparison of W24x62 BUEEP Specimens

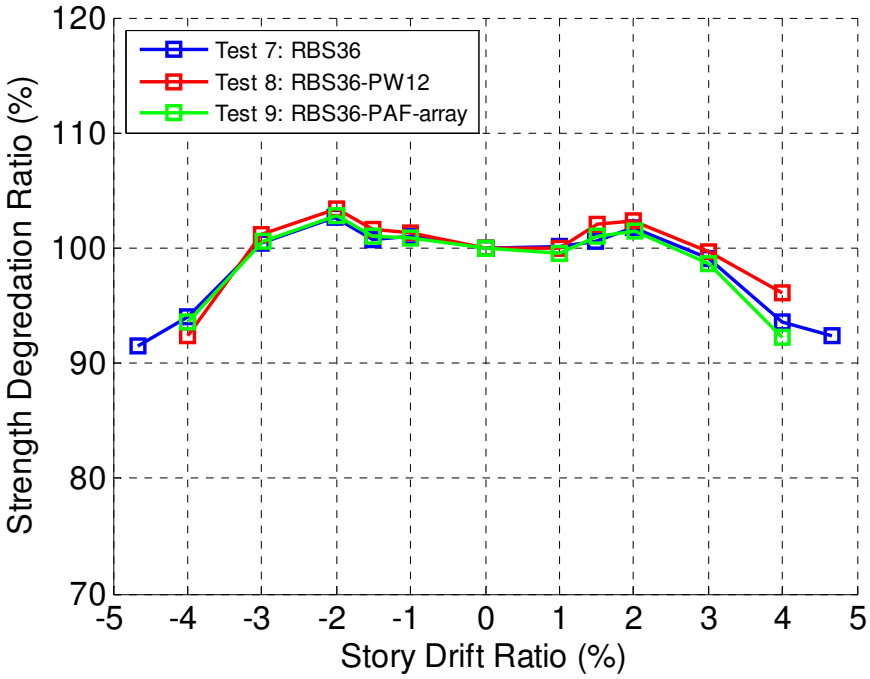

Figure 64: Strength Degradation Comparison of W36x150 RBS Specimens

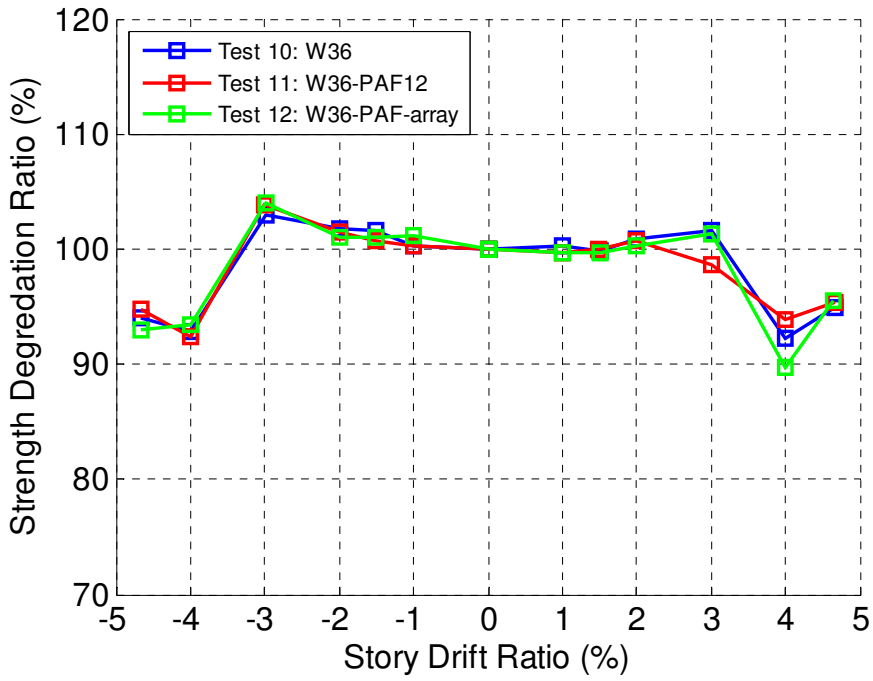

Figure 65: Strength Degradation Comparison of W36x150 BSEEP Specimens

Figure 66 through Figure 69 show the energy dissipation profiles of each of the four specimen types discussed. In full-scale moment connection tests, energy is dissipated through the inelastic deformations of the plastic hinge. As it relates to a specimen's hysteretic behavior, the energy dissipated during a single cycle of rotation translates to the area encompassed by the hysteresis curve during that cycle. Numerical integration of test data was performed to quantify the progressive energy dissipation. Line markers within the plots indicate the instances of peak rotation magnitudes (from both positive and negative peaks) starting at 1% story drift. Specific peaks prior to 1% drift cycles are not shown as line markers since any plastic deformation is negligible prior to that point.

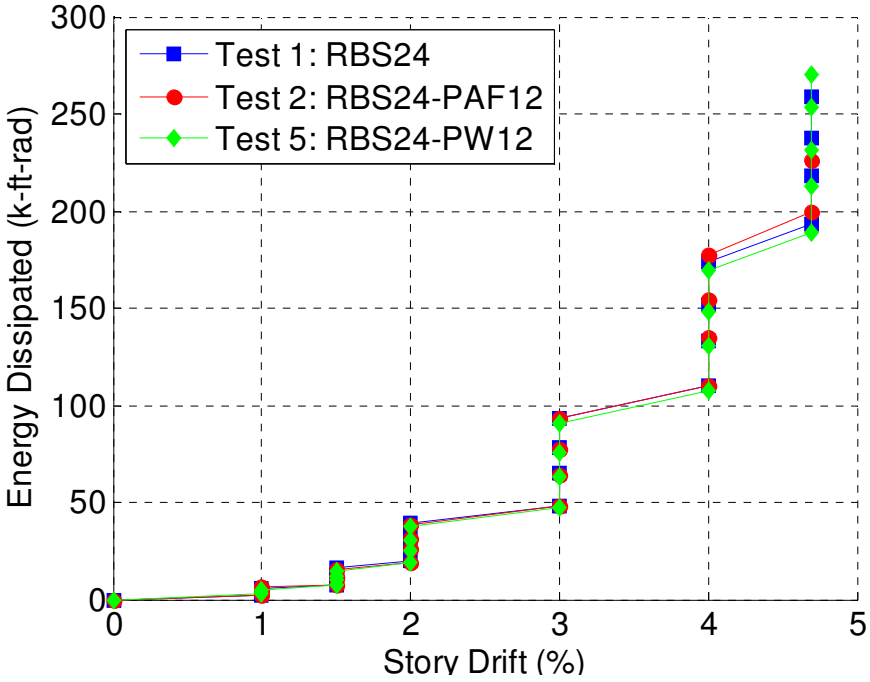

Figure 66: Energy Dissipation Comparison of W24x62 RBS Specimens

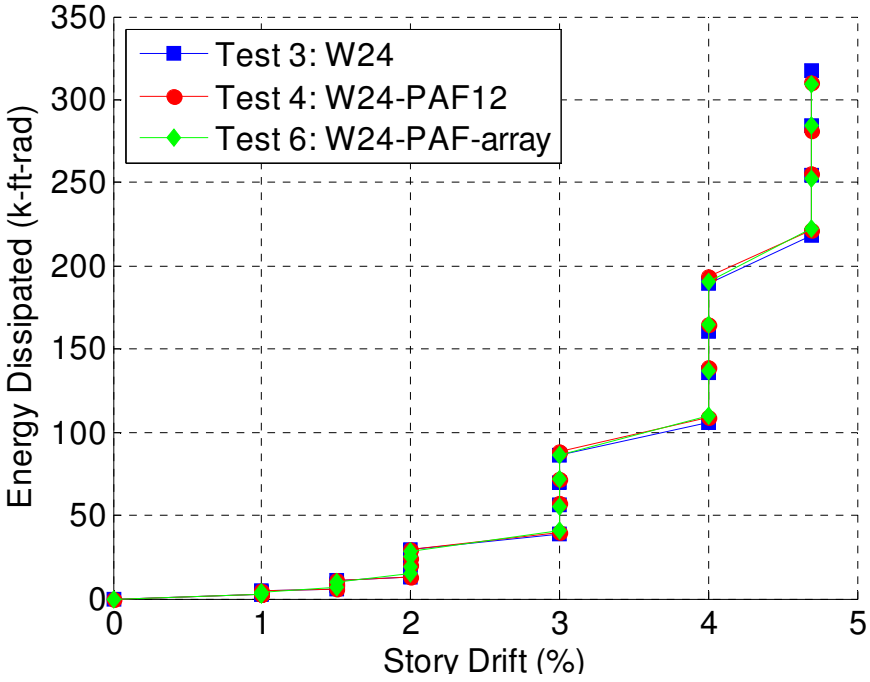

Figure 67: Energy Dissipation Comparison of W24x62 BUEEP Specimens

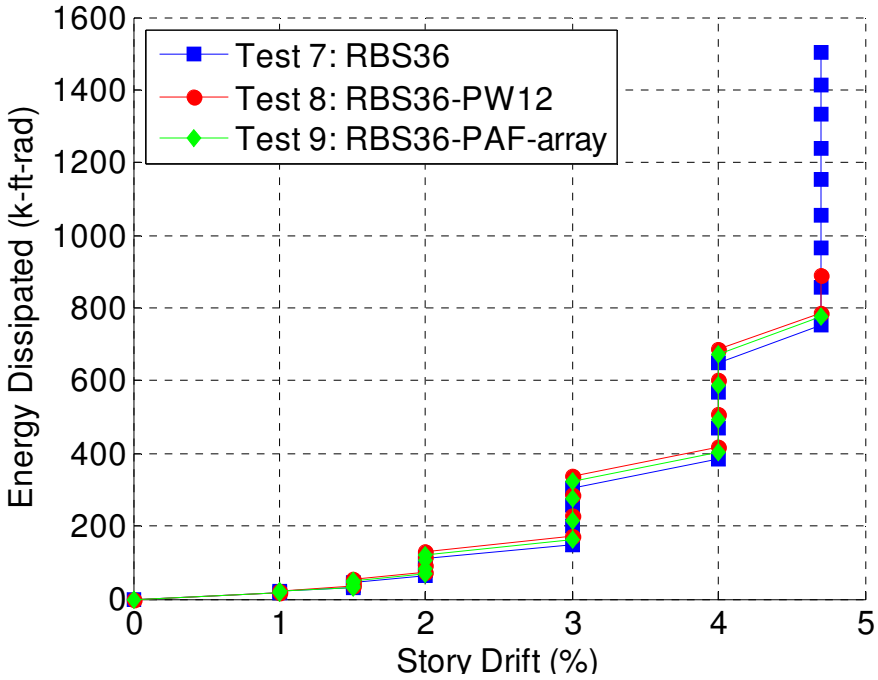

Figure 68: Energy Dissipation Comparison of W36 150 RBS Specimens

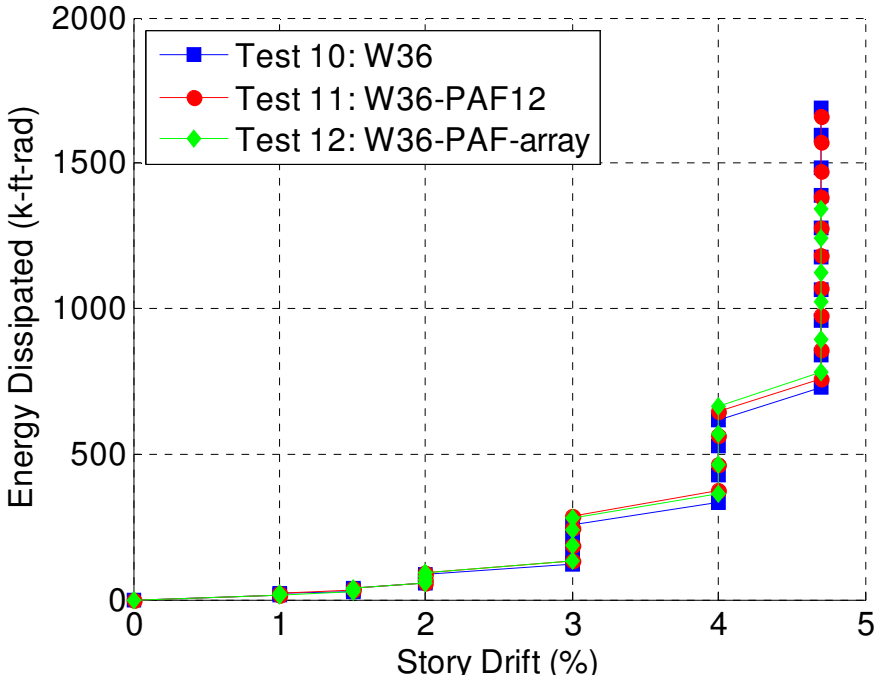

Figure 69: Energy Dissipation Comparison of W36x150 BSEEP Specimens

Energy dissipation profiles show a strong similarity between tests of each specimen type. Figure 70 shows a comparison plot of the energy dissipation behavior of each of the four specimen types. Energy dissipation values for each specimen type in the figure are created by averaging

the respective values from the three separate tests of that type at each of the story drift peaks represented by line markers. These average energy dissipation lines are plotted up until the point at which one of their three contributing test constituents failed or reached a test completion. For instance, the W36x150 RBS specimen average energy dissipation plot ends after one peak of 4.7% story drift, because that is the farthest that test 9 reached (as can be seen in Figure 68). For each of the two beam types, the inclusion of RBS appears to have no significant effect on the energy dissipation behavior of the specimens. The average energy dissipation profile of W36x150 specimens with an RBS is slightly greater than W36x150 specimens without the RBS. It is noted that this difference appears to have emerged during 2% story drift cycling. Beyond that point, both specimen types show a similar offset profile with near identical increases in total energy dissipation from one peak to another.

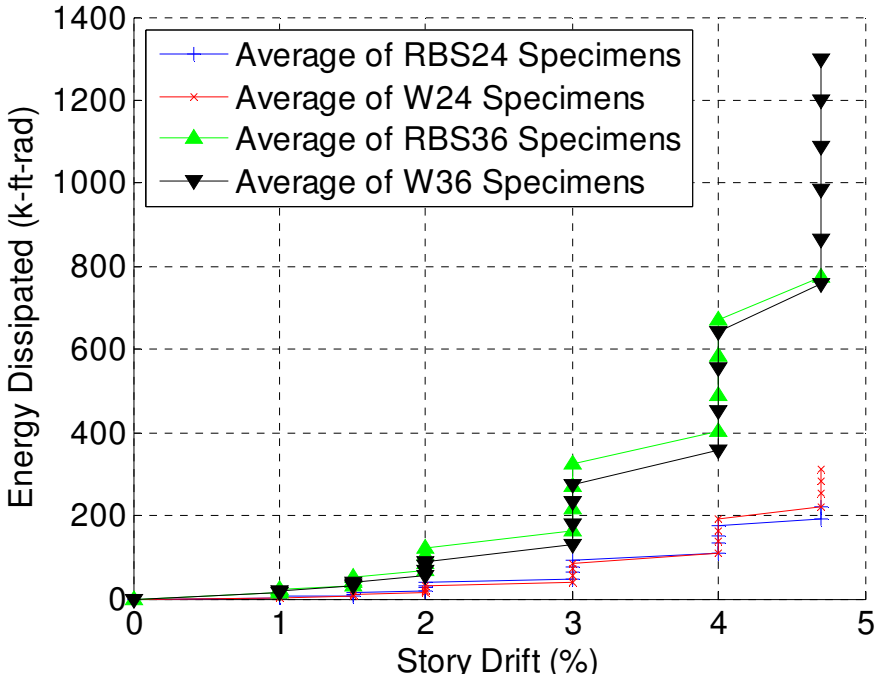

Figure 70: Energy Dissipation Comparison of All Four Specimen Types

4.3 Story Drift Decomposition of Test Data

Test data was used in conjunction with the story drift decomposition equations presented previously to separate and visualize the contributions of each component to the total story drift. Several system components used two different instrumentation methods to quantify story drift contribution. Multiple measurements for the same quantity provides the means to validate the accuracy of the data. Figure 71 shows a comparison of both instrumentation methods for

measuring the column rotation. The figure shows data from test 2 as an example of the general comparison of the two methods. The column inclinometer records a greater column rotational deformation than that of the LVDTs. This supports the supposition made in the story drift decomposition discussion section that since the LVDTs are spaced farther apart vertically than the beam depth, they will likely imply a lesser rotation angle than actually exists. Inclinometer data is plotted using Equation 3.7. LVDT data is plotted using Equation 3.8.

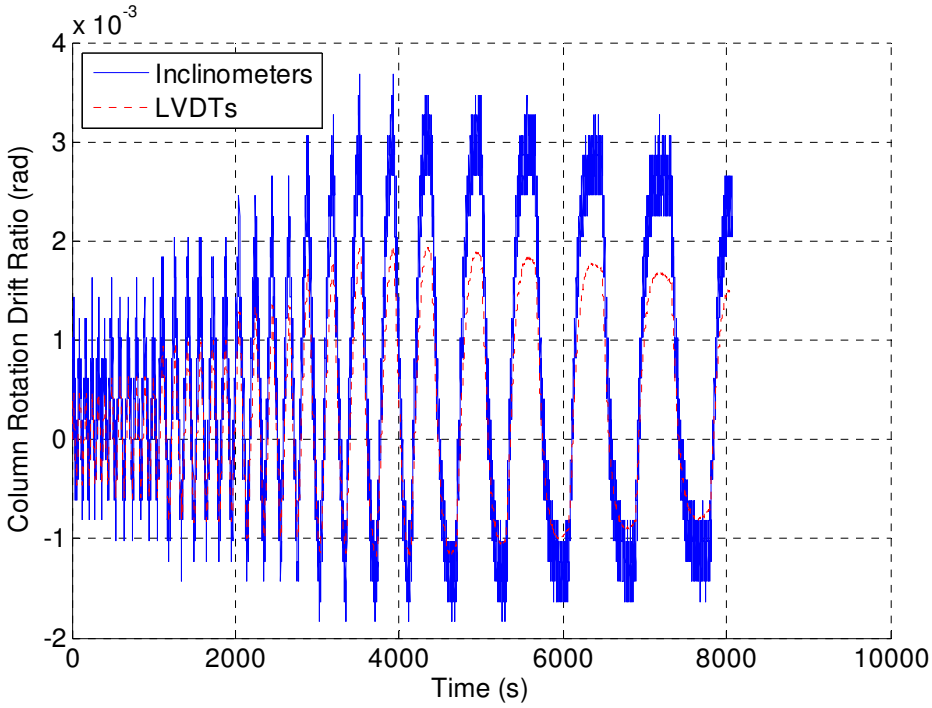

Figure 71: Column Rotation - Instrumentation Comparison from Test 2

Figure 72 shows a strong correlation between the beam plasticity story drift component calculated using inclinometer measurements and LVDT measurements. As in column flexure, the test data shown in the figure is from test 2 and represents the general trend exhibited by all tests. The last few cycles show a greater drift measurement from the inclinometers than that of the LVDTs. This trend is typical of the W24x62 specimens and can be explained by the fact that for these tests, the outer inclinometer is located several inches longitudinally beyond the point at which the LVDTs are mounted. This enables the inclinometer to account for the small degree of additional beam elasticity beyond the LVDT. Comparison data from the W36x150 tests show a near identical story drift profile between the two methods.

It is noted that the two methods are measuring slightly different motions of the plastic hinge region of the beam. Since the inclinometers are mounted to the beam web, it is possible that in some cases, their rotation measurements may be influenced slightly by out of plane motion of the beam due to buckling and local deformations near the endplate. Likewise, the LVDT deflection measurements used in the second method for calculating beam plasticity story drift are susceptible to error due to the local buckling of the flanges. Most tests that proceeded into numerous cycles at 4.7% story drift saw such significant buckling of the flanges that the LVDTs spanning the plastic hinge fell from the contact points at which they were initially adhered for most of the test. Inclinometers stayed adhered to the web better and, therefore, provided data further into the tests. For this reason, inclinometer data is used in the story drift decomposition for all tests. The inclinometer data is also preferred because of the presence of a shared inclinometer between beam plasticity calculations and the beam elasticity along the undeformed length of beam already discussed. This continuity provides for a more accurate account of elasticity along the entire length of the beam. Inclinometer data is plotted using Equation 3.16. LVDT data is plotted using Equation 3.17.

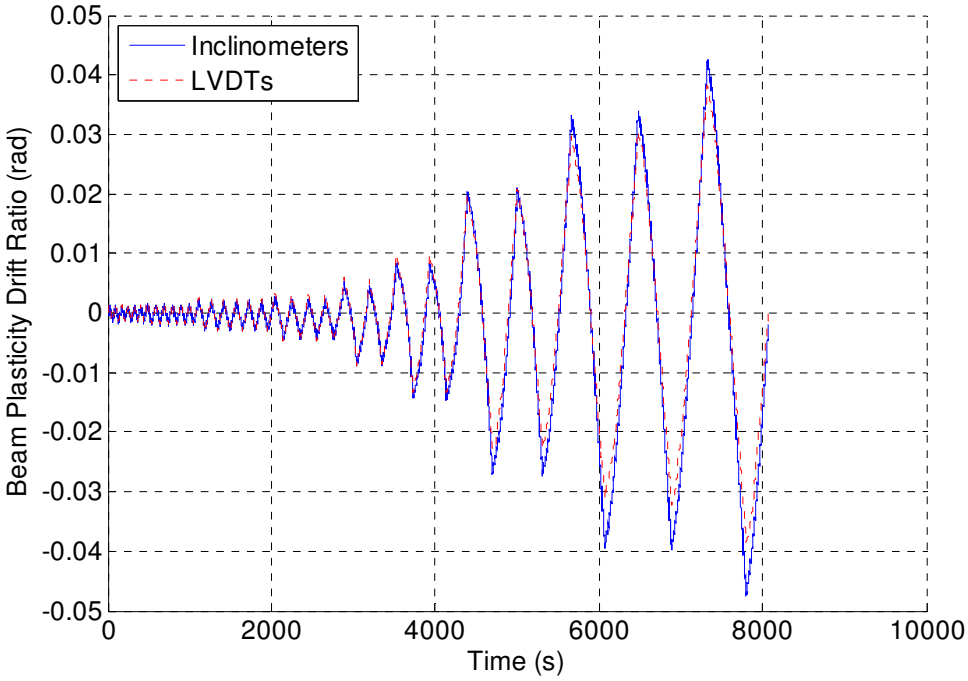

Figure 72: Beam Plasticity - Instrumentation Comparison from test 2

Figure 73 shows a typical comparison of the measured and theoretical elastic deflection of the beam using data from test 7. Measured deflection is computed using Equation 3.14. Theoretical deflection is calculated using Equation 3.16. Noise in the inclinometer data results in false data spikes seen in the early part of the test. Later cycles show a reasonable correlation between theoretical and measured beam elastic deflections.

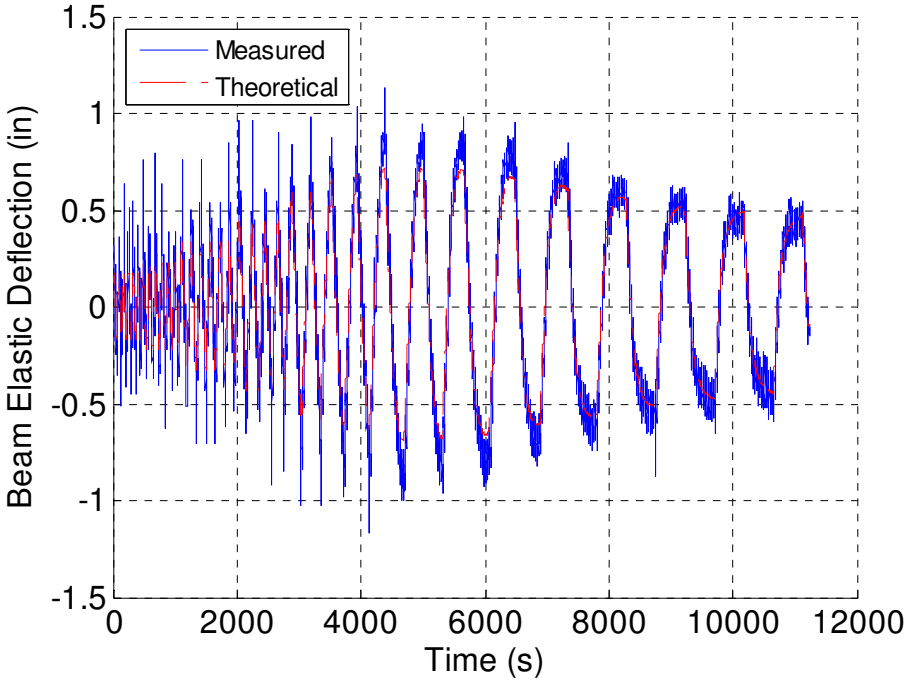

Figure 73: Beam Elasticity - Comparison of Measured and Theoretical Deflection

Story drift decomposition data is presented in three formats to best understand the degree of each component's contribution to the total system story drift. These three formats are listed below. Figures in this section utilize data from selected tests as a general reference. Appendix B provides equivalent plots for all twelve tests.

- Component Absolute Values (Line Plot)
- Stacked Component Absolute Values (Area Plot)
- Stacked Component Relative Contributions (Area Plot)

i) Component Absolute Values

Figure 74 through Figure 77 show line plots of the absolute contribution of each story drift component for one of each of the four beam types tested. As expected, during high amplitude

cycles, plastic hinge rotation is the primary contributor to story drift. Beam elasticity contributes moderately, while the other elastic components contribute less to the total story drift. It is also noted that for large amplitude cycles, each elastic component develops a plateau in its magnitude. This indicates that the elastic sources of flexibility reach limiting values of deformation associated with the plastic moment of the specimen.

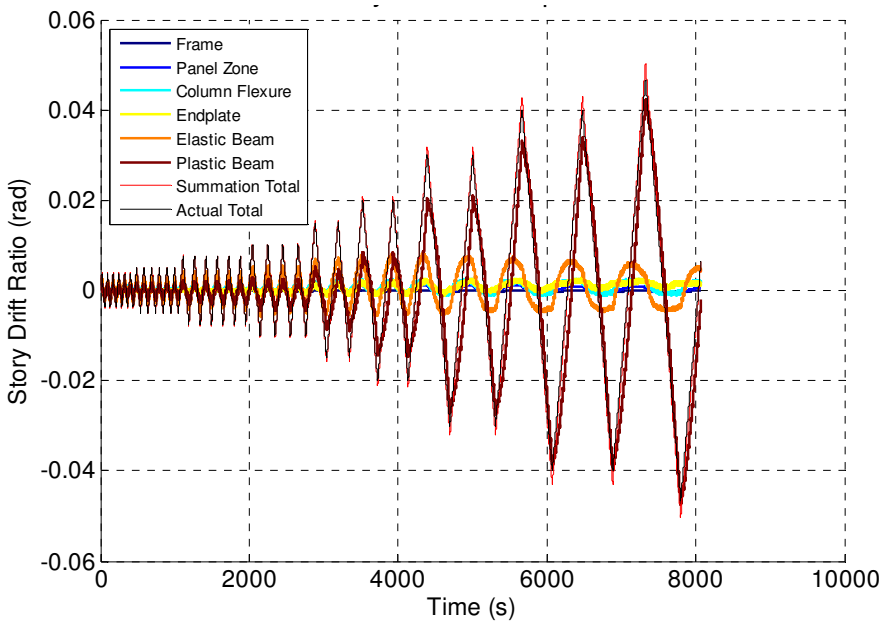

Figure 74: Story Drift Decomposition for a W24x62 Specimen with RBS (Specimen 2)

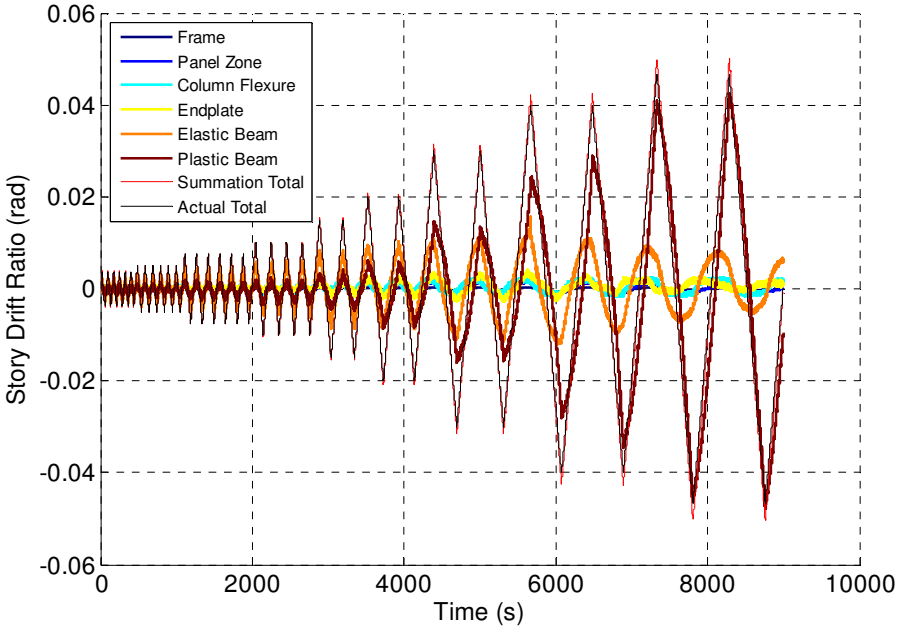

Figure 75: Story Drift Decomposition for a W24x62 without RBS (Specimen 4)

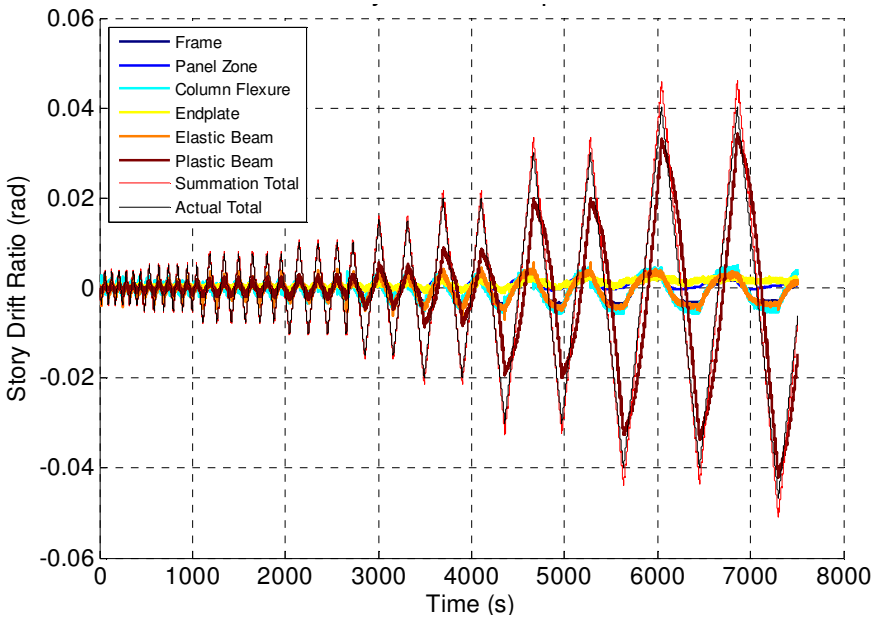

Figure 76: Story Drift Decomposition for a W36x150 with RBS (Specimen 9)

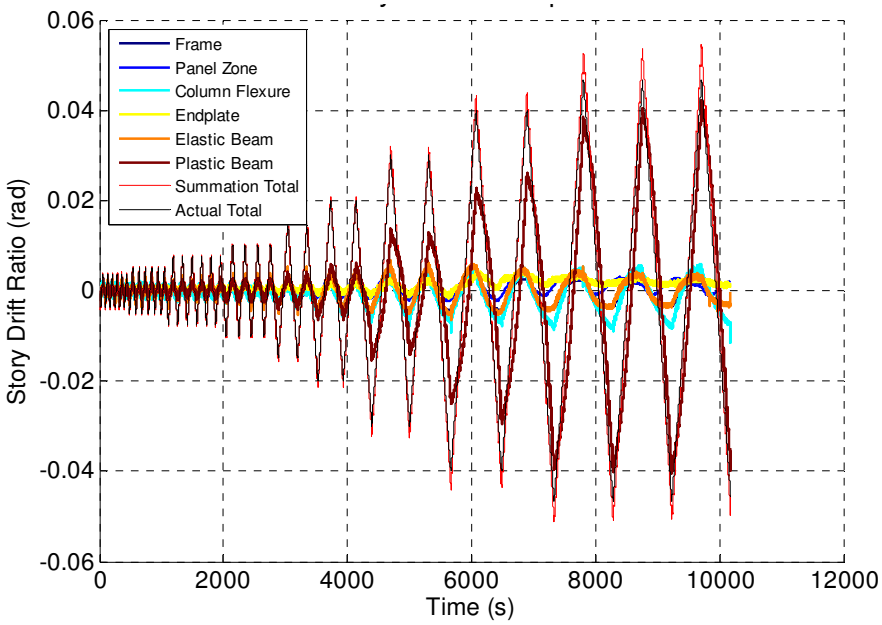

Figure 77: Story Drift Decomposition for a W36x150 without RBS (Specimen 12)

Observation of story drift plots from all tests supports a confidence that no plastic deformation of the test system occurred beyond the plastic hinge of the beam itself. Any trend toward an offset from "0" of the story drift components' cyclic behavior is attributed to unintended

instrumentation behavior or shortcomings in the equations intended to decompose the total story drift. Figure 78 presents a closer view of the story drift components during the qualification cycle of specimen 2 as an example of the general behavior observed in all tests. It is observed that not all elastic components' maximum drift magnitudes occur at the same instance. Table 6 lists the maximum positive and negative story drift magnitudes of all elastic system components. Additionally, the table lists the instantaneous maximum magnitude sum of all five elastic components. The instantaneous sum is not occurring at the time of peak story drift and therefore is not appropriate for comparison with the limits set in AISC 341 (AISC 2010a). The portion of the total story drift due to plastic hinge rotation at the peaks of the 4% qualification cycle will be presented and compared with the limit later in this section.

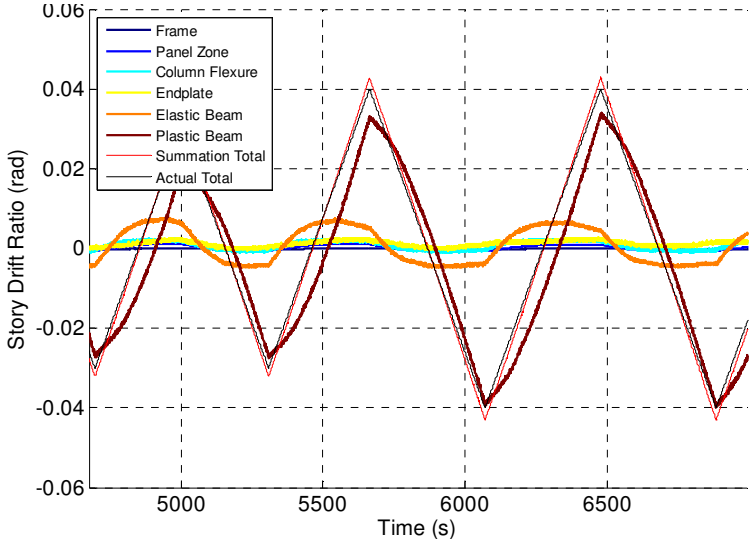

Figure 78: Test 2 - Elastic Story Drift Trends

Table 6: Maximum Story Drift Component Magnitudes

Type	Test	Sign	System Component Maximum Absolute Story Drift Excluding Beam Plasticity (%)					
			Frame Rocking	Panel Zone	Column Flexure	Endplate Prying	Beam Elasticity	Instantaneous Sum
W24x62 with RBS	1	+	0.010	0.106	0.176	0.245	0.741	1.108
		-	-0.026	-0.083	-0.181	-0.266	-0.714	-1.095
	2	+	0.010	0.124	0.253	0.286	0.846	1.354
		-	-0.030	-0.059	-0.115	-0.143	-0.578	-0.778
	5	+	0.036	0.097	0.215	0.225	0.619	1.004
		-	-0.031	-0.101	-0.161	-0.184	-0.752	-1.093
W24x62 with BUEEP	3	+	0.084	0.152	0.276	0.430	1.306	2.065
		-	-0.057	-0.130	-0.173	-0.491	-1.168	-1.839
	4	+	0.043	0.137	0.256	0.430	1.562	2.155
		-	-0.058	-0.143	-0.175	-0.286	-1.204	-1.675
	6	+	0.010	0.127	0.230	0.716	1.453	2.227
		-	-0.067	-0.176	-0.181	-0.409	-1.096	-1.766
W36x150 with RBS	7	+	0.253	0.523	0.302	0.286	0.572	1.586
		-	-0.313	-0.135	-0.762	-0.184	-0.554	-1.476
	8	+	0.212	0.256	0.494	0.245	0.631	1.399
		-	-0.303	-0.297	-0.396	-0.225	-0.552	-1.424
	9	+	0.210	0.289	0.492	0.286	0.575	1.461
		-	-0.328	-0.094	-0.576	-0.102	-0.689	-1.397
W36x150 with BSEEP	10	+	0.381	0.508	0.681	0.511	1.132	2.491
		-	-0.483	-0.381	-0.739	-0.552	-1.414	-2.434
	11	+	0.239	0.391	0.535	0.532	0.650	1.946
		-	-0.442	-0.231	-0.817	-0.225	-0.562	-1.844
	12	+	0.289	0.470	0.520	0.491	0.686	2.138
		-	-0.427	-0.238	-0.914	-0.164	-0.635	-1.944

ii) Stacked Component Absolute Values

Figure 79 shows an area plot of the system story drift contributors from test 2. Individual story drift contributions are stacked in order from frame drift through beam plasticity. This means that that the exterior of the plastic beam region represents the total summation. This calculated summation is drawn as a red line, following the profile of the test input displacement protocol

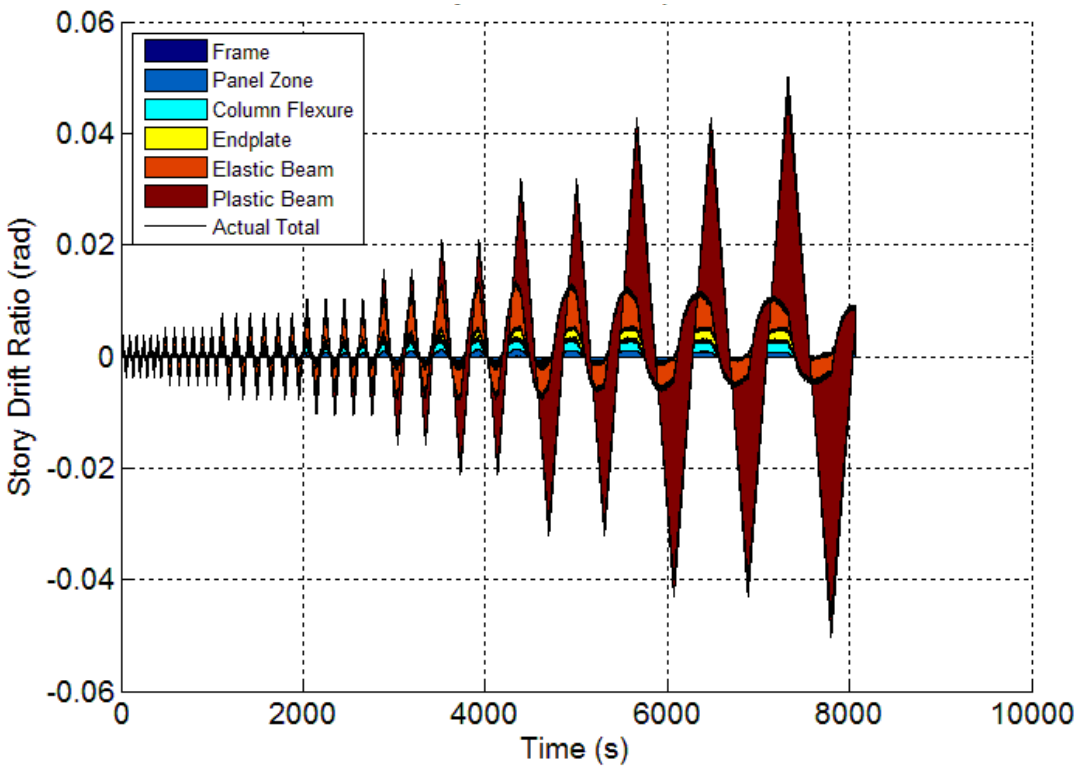

Figure 79: Stacked Story Drift Decomposition for a W24x62 with RBS (Specimen 2)

Several general observations can be made about the cyclic behavior of the story drift profile. As expected during large amplitude cycles, beam plasticity is the greatest contributor to story drift. A notable trend is apparent in that the elastic system components cycle out of phase from the more prominent beam plasticity. Elastic components occur earlier in the cycle than the plastic hinge component by approximately a quarter cycle. This can be explained by the expectation that elastic deflections are directly related to the current loading direction. The plastic hinge component behaves differently, maintaining the same sign (representing story drift orientation) beyond equilibrium regardless of whether the actuator is 'pushing' or 'pulling'. It will reverse only when plastic deformations are fully 'undone' near 0% total story drift.

Figure 80 presents the same data focused on several cycles in order to better view the cyclic behavior of the system. Section "A" represents a period of maximum positive 4% story drift in which the contribution of each constituent is apparent. Beyond this point, the actuator begins reversing its loading. As the system begins to return to a net story drift of 0% as indicated by Section "B" all components reduce in magnitude with the elastic components actually reversing orientation early in the transition back to 0%. The point at which the elastic components

transition to negative contributions is shown to the right of "A" where the still positive beam plasticity covers up the negative color bands due to area plotting limitations. The 0% total story drift at "B" indicates the current permanent plastic deformation of the beam. At this point, negative elastic contributions (hidden behind the plastic area band) are balanced by the still positive plastic deformation of the beam. If the actuator were to stop loading at this instance, presumably, the elastic deformations would correct to zero and the beam would remain deflected up by the portion of plastic story drift it had at that instant.

Section "C" is the instant at which point elastic system components have reached a maximum value and plastic deformation of the beam is finally corrected to zero. If the test were to stop at this instant, the negative elastic drift contributions would correct to zero and the beam would return to its original orientation with no lingering plastic deformation. Elastic components decrease to zero contribution at section "D" in which the system has fully reversed with maximum negative story drift composed only of beam plastic deformation. This would indicate a decrease in strength of the beam as the prior elastic deformations are able to recover to an equilibrium state while total deflection continues to increase. The loading reversal beyond "D" sees a continued reversal of the elastic components and plastic hinging.

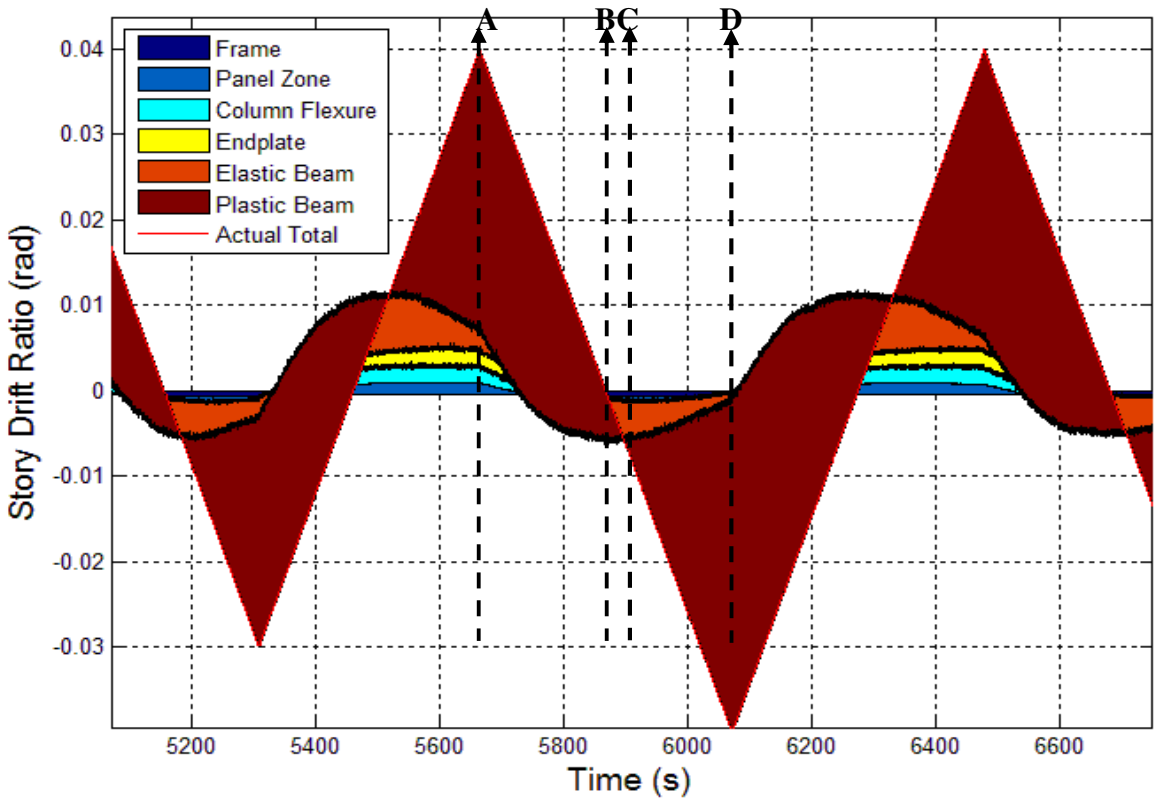

Figure 80: Stacked 4% Story Drift Decomposition for a W24x62 with RBS (Specimen 2)

iii) Stacked Component Relative Contributions

The relative contribution of each system component to the total story drift is better visualized by viewing the stacked story drift components as percentages of the summation total. In this way, the total summation of all individual story drift relative contributions always equals 100%. In order to avoid graphical shortcomings when certain contributors are of opposite signs as is shown from the overlaps in Figure 80 or a graphical singularity when the summation total approaches zero, data is only used from the positive and negative peaks of the cycles. Additionally, in order to avoid misleading cyclic profiles within relative contribution plots due to the asymmetry of the hysteretic behavior already described, these plots are separated into positive and negative story drift relative contribution plots. Figure 81 shows a graphical representation of this process of scaling peak data to a constant 100%. Figure 82 through Figure 85 show area plots of the stacked relative percent contributions of every story drift component from each of the four specimen types. Story drift labels indicate the first instance that the system

reaches a new peak amplitude, both positive and negative. Data between the component percentage breakdowns at each local peak is linearly interpolated. It is noted that the apparent presence of beam plasticity during early cycles at elastic story drifts is due to the fact that the instrumentation placed in the plastic hinge region will inherently record any elastic deformation in that region as plastic deformation (per the story drift component algorithms previously discussed). While this absolute erroneous contribution value remains comparable during subsequent cycles, the relative error is reduced significantly as plasticity becomes more significant in the plastic hinge region of the beam.

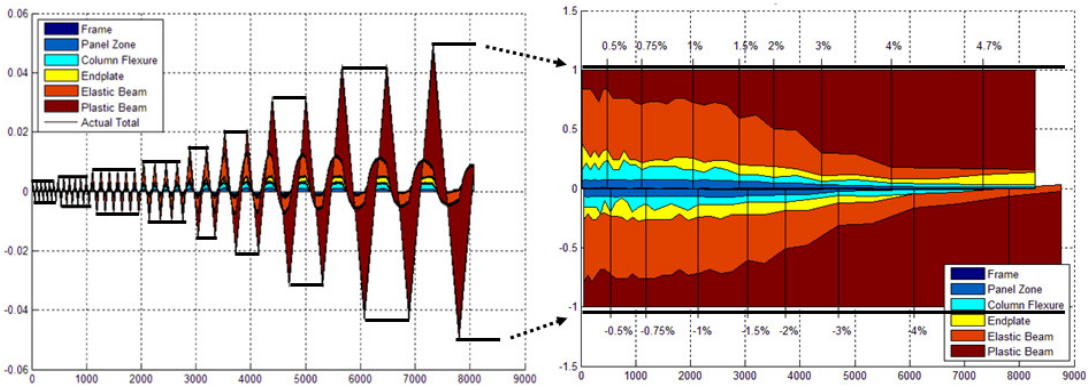

Figure 81: Translation from Absolute to Relative Story Drift Contributions

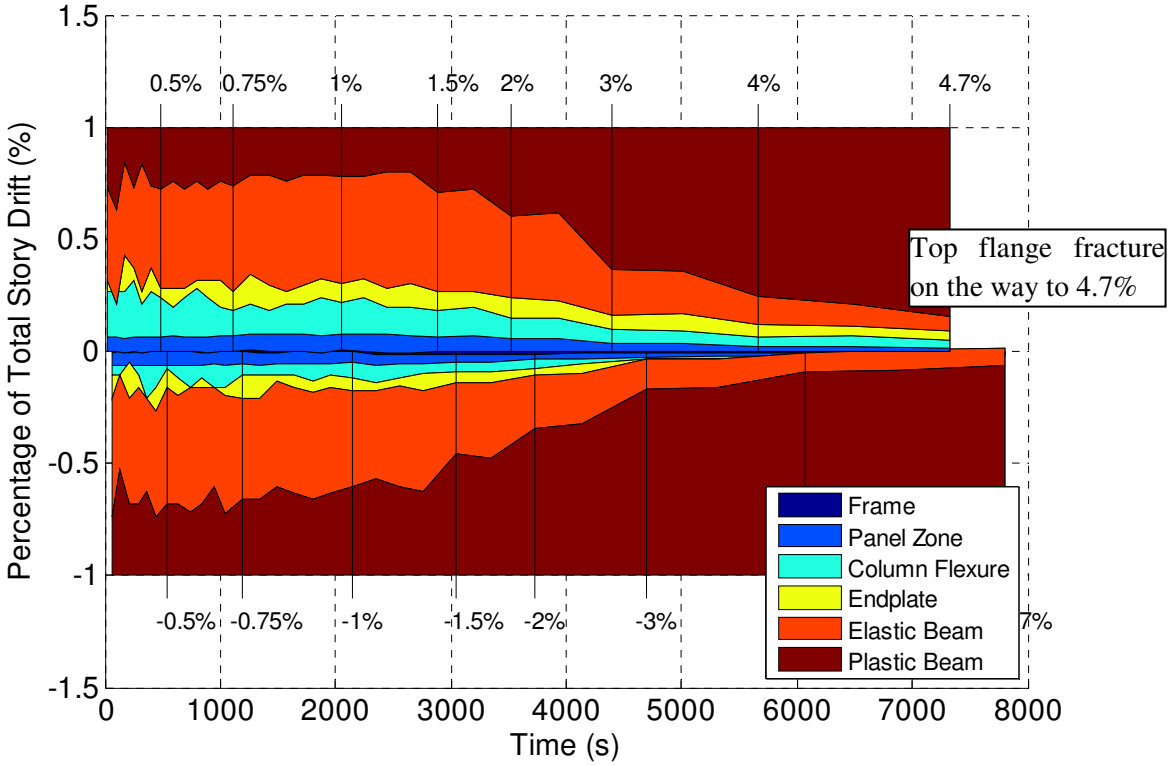

Figure 82: Relative Story Drift Decomposition for a W24x62 with RBS (Specimen 2)

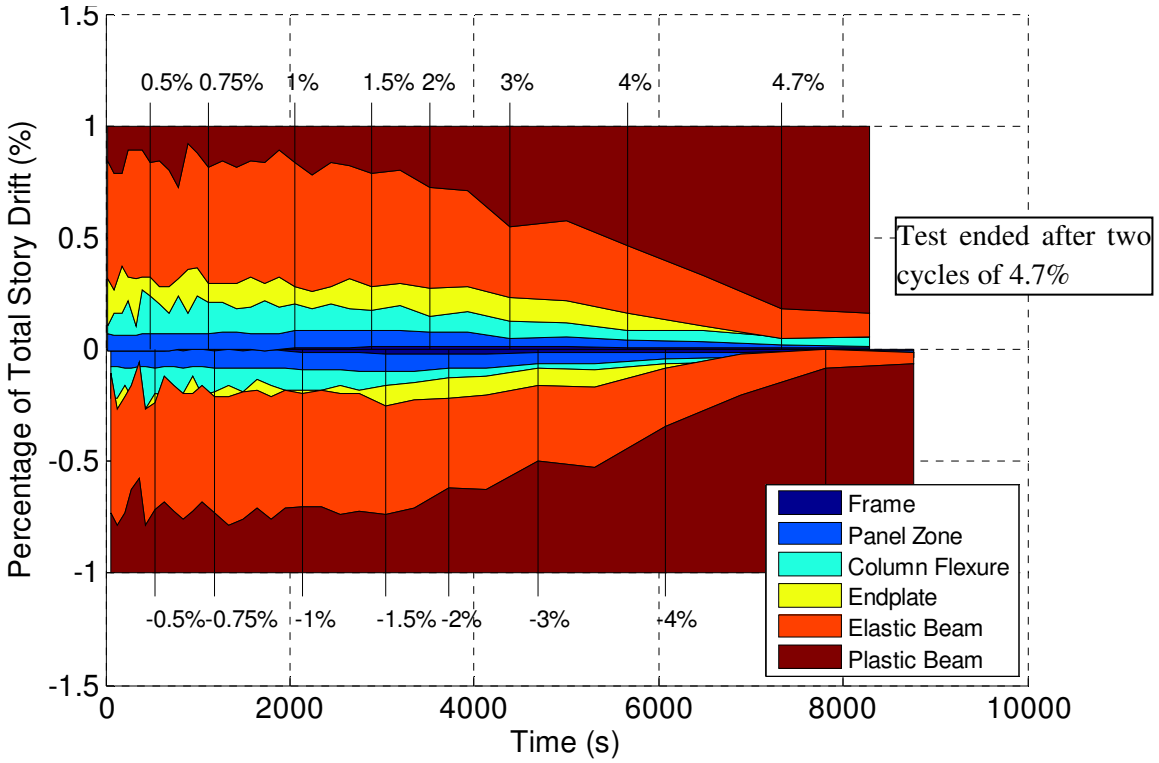

Figure 83: Relative Story Drift Decomposition for a W24x62 without RBS (Specimen 4)

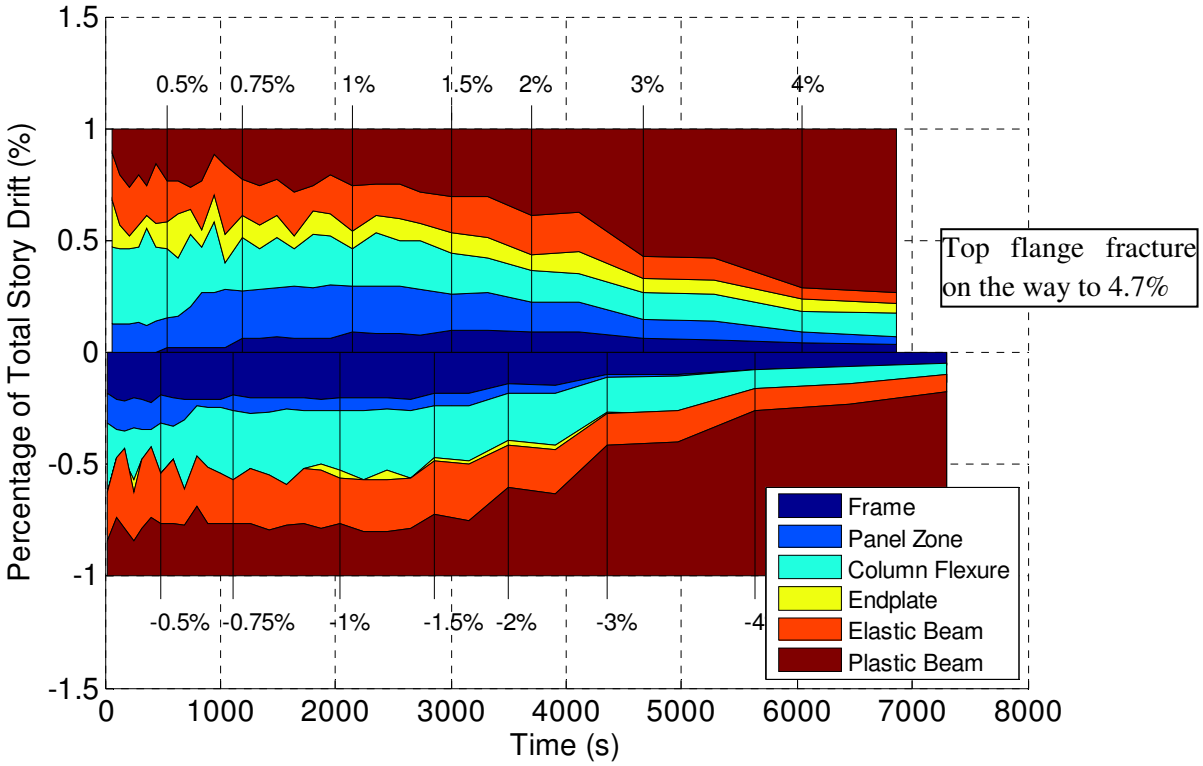

Figure 84: Relative Story Drift Decomposition for a W36x150 with RBS (Specimen 9)

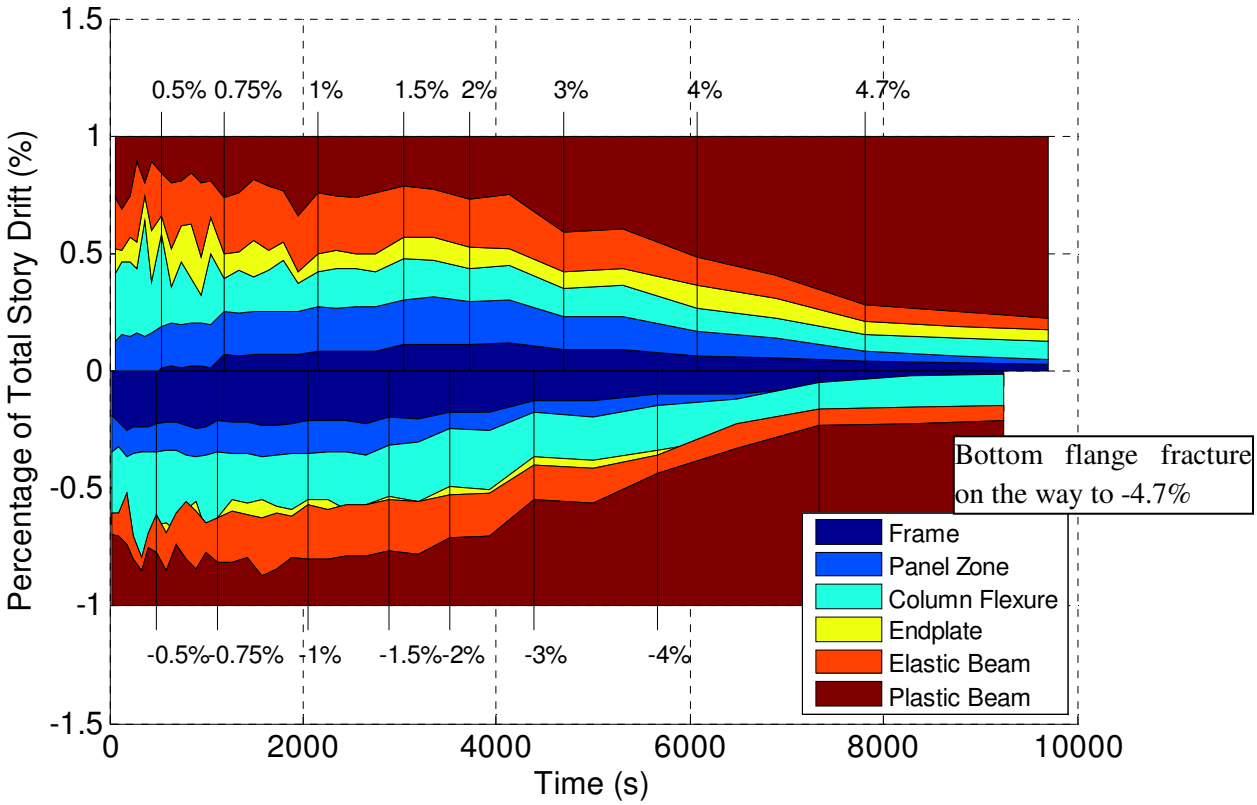

Figure 85: Relative Story Drift Decomposition for a W36x150 without RBS (Specimen 12)

Several conceptual observations can be made about the four beam types through comparison of the relative contribution percentage plots. All W24x62 specimens (1-6) showed a greater contribution from beam elasticity than the W36x150 specimens (7-12). It is also apparent from the plots that the W36x150 specimens cause larger deformations in the column components as the frame, panel zone and column flexure contributions to the total story drift are greater than for that of the W24x62 specimens. This is expected as both the W36x150 specimens have a greater moment capacity and will only begin yielding once more flexible system components have displaced or deformed due to the applied moment by the actuator.

AISC 341 Commentary K2.3a (AISC 2010a) requires no less than 75% of the total system story drift to occur in the plastic hinge region of the beam during the qualification cycle. For all tests, during the qualification cycle, the summation of the individual story drift components tends to exceed the known total (+/- 4%) by a small amount (see Figure 78). This consistent trend is likely due to imperfections in the measurements and simplifying assumptions used in the algorithms for calculation of individual story drift components. Calculation of story drift due to beam plasticity is a relatively straightforward operation, as described previously, and is therefore used for comparison here. With this in mind, it is presumed that a more accurate calculation of the percent contribution of the beam plasticity could be made by relating the calculated beam plasticity to the known actual total story drifts of +/- 4% rather than the calculated total values which exceed the actual values.

Table 7 lists the percent contribution of beam plasticity to the actual total story drift for each specimen during the second 4% drift amplitude of the qualification cycle. Table 7 lists the same ratio for each specimen during the final amplitude of 4% drift prior to the test program progressing to 4.7% drift cycles. As already noted, the testing direction was changed after test 5. This results in the story drift values of Table 7 and Table 8 being negative for specimens 1-5 and positive for specimens 6-12. Additionally, both tables provide a quantification of story drift due to beam plasticity using three different methods. The first method is the simple differential between inclinometers on either end of the beam plastic hinge. The second utilizes the difference in compression between linear potentiometers (LVDTs) both above and below the specimens' protected zone. These two methods were outlined in the discussion of story drift component algorithms (see Figure 25). The third method essentially combines beam plasticity

with the quantification of endplate prying by taking the differential between the column inclinometer and the outermost beam inclinometer (in the same manner as was used in the first method).

Table 7: Plasticity Percent of Total Story Drift for Second 4% Amplitude

Beam Type	Test	Second 4% Amplitude (End of Qualification Cycle)							
		Total Story Drift (%)		Beam Plasticity "inclinometers" (%)		Beam Plasticity "LVDTs" (%)		Beam Plasticity "with endplate" (%)	
		Calc.	Actual	Beam Plasticity	Percent of Actual Total	Beam Plasticity	Percent of Actual Total	Beam Plasticity	Percent of Actual Total
W24x62 RBS	Test 1	-4.28	-4.00	-3.58	**89.6**	-3.16	**79.1**	-3.58	**89.6**
	Test 2	-4.31	-4.00	-3.91	**97.7**	-3.11	**77.7**	-3.81	**95.1**
	Test 5	-4.29	-4.00	-3.58	**89.4**	-2.99	**74.8**	-3.60	**90.0**
W24x62 BUEEP	Test 3	-4.23	-4.00	-2.58	**64.4**	-2.51	**62.9**	-2.88	**72.1**
	Test 4	-4.23	-4.00	-2.76	**69.0**	-1.99	**49.8**	-2.84	**71.1**
	Test 6	4.21	4.00	1.98	**49.6**	2.09	**52.4**	2.56	**63.9**
W36x150 RBS	Test 7	4.42	4.00	3.13	**78.3**	3.31	**82.8**	3.25	**81.4**
	Test 8	4.49	4.00	3.19	**79.8**	3.46	**86.6**	3.33	**83.4**
	Test 9	4.58	3.99	3.25	**81.5**	3.61	**90.3**	3.50	**87.6**
W36x150 BSEEP	Test 10	4.30	4.00	1.96	**49.1**	1.70	**42.4**	2.21	**55.2**
	Test 11	4.39	4.00	2.66	**66.5**	3.26	**81.7**	3.09	**77.3**
	Test 12	4.34	4.00	2.25	**56.3**	3.19	**79.7**	2.68	**67.0**

Table 8: Plasticity Percent of Total Story Drift for Final 4% Amplitude

Beam Type	Test	Final 4% Amplitude							
		Total Story Drift (%)		Beam Plasticity "inclinometers" (%)		Beam Plasticity "LVDTs" (%)		Beam Plasticity "with endplate" (%)	
		Calc.	Actual	Beam Plasticity	Percent of Actual Total	Beam Plasticity	Percent of Actual Total	Beam Plasticity	Percent of Actual Total
W24x62 RBS	Test 1	-4.29	-4.00	-3.72	**93.1**	-3.48	**86.9**	-3.68	**92.1**
	Test 2	-4.30	-4.00	-3.95	**98.8**	-3.22	**80.7**	-3.81	**95.2**
	Test 5	-4.30	-4.00	-3.66	**91.5**	-3.03	**75.7**	-3.66	**91.5**
W24x62 BUEEP	Test 3	-4.26	-4.00	-3.17	**79.3**	-2.60	**65.0**	-3.27	**81.8**
	Test 4	-4.26	-4.00	-3.40	**84.9**	-2.21	**55.4**	-3.25	**81.3**
	Test 6	4.23	4.00	2.17	**54.3**	2.32	**58.2**	2.86	**71.7**
W36x150 RBS	Test 7	4.44	4.00	3.31	**82.9**	3.42	**85.5**	3.38	**84.5**
	Test 8	4.53	4.00	3.33	**83.3**	3.54	**88.5**	3.44	**85.9**
	Test 9	4.62	3.99	3.38	**84.5**	3.75	**93.9**	3.58	**89.6**
W36x150 BSEEP	Test 10	4.37	4.00	2.35	**58.8**	2.32	**58.1**	2.64	**66.0**
	Test 11	4.45	4.00	3.13	**78.3**	3.42	**85.5**	3.29	**82.3**
	Test 12	4.39	4.00	2.60	**65.0**	3.53	**88.3**	2.99	**74.7**

It is apparent from Table 7 and Table 8 that plastic deformation of RBS specimens contributes a significantly greater percentage of the total story drift than do non-RBS sections of the same beam type. This is expected due to the weaker moment capacity of the RBS sections. It can also be seen from the table that not all specimens satisfied the requirement for 3% story drift accounted for by plastic hinging of the beam during either the qualification cycle (Table 7) or even by the end of 4% cycling (Table 8). Another way to look at the qualification requirement is that the qualifying cycle should occur when the plastic hinge is contributing 3% story drift. For most specimens, this occurred during the 4% cycling. This was not the case for specimens 6 and 10. These specimens did not achieve 3% story drift due to plastic hinge rotation until the first 4.7% drift cycle. However, all specimens satisfied the qualification criteria of sustaining 80% of their nominal plastic moment capacity during at least on cycle in which the beam plastic hinge did contribute at least 3% story drift.

The beam plasticity percent contribution from specimen 10 is noticeably less than that of comparable specimens. This is due to the presence of recurring slip between the top of the test column and the column reaction frame. Slip first occurred at a point in the test in which the system was experiencing a greater loading than had previously been encountered. Once the slipping threshold was exceeded, the column continued to slip during each half cycle in which the load constantly reversed direction. Additional connection reinforcement was made for subsequent tests.

CHAPTER 5: FEM MODELING

5.1 FEM Modeling of the Full-Scale Moment Connection

Creation of an accurate computer model of the full-scale beam-to-column connection tests is critical for the development of further testing methods of a more general nature than full-scale connection tests. The full-scale tests use numerous forms of instrumentation in order to accurately capture strain data on the top flange as well as motion of the panel zone as a component of the story drift being simulated. However, this still presents a relative limitation for a thorough understanding of the strain behavior of the beam. An accurate computer model allows for a greater investigation into the full strain profile across the flange in the protected zone rather than the several distinct locations of strain data provided by strain gauges. It also provides the flexibility of simulating a range of moment connection variations including different beam sizes and connections with both strong and weak panel zones. This enables an investigation of numerous moment connections in the absence of actual experimental tests.

5.1.1 FEM Model Design and Techniques

A variety of moment connection geometries are possible through computer modeling, but the modeling and simulation must first be verified as providing accurate results. Initial efforts have been made to develop an accurate model of the physical tests already completed in order to validate the modeling method by comparing visual and data results between the model and tests. The current FEM model has been developed in ABAQUS version 6.10-2 (Simulia, 2010). The geometry is that of experimental test 3 which is comprised of a W24x62 beam mounted to a W14x257 column using a welded endplate connection. While several previous modeling studies utilized biaxial symmetry to simplify simulation time and data size (Pachoumis et al. 2010), this modeling effort will utilize the full connection geometry. The validated model will be used to investigate the strain patterns that develop in the regions of local buckles. For this reason, it will be necessary to model the asymmetrical buckling patterns typical of these tests.

The nominal geometry of the full test 3 setup has been used in the development of the FEM model. All assembly components are designed as individual parts in the ABAQUS CAE software. Both the column and beam were built as extruded section parts, using only nominal rectangular corners for section geometries. Meshing of these complex geometry parts requires a bottoms-up approach in which a mesh pattern is extruded along the length in the same manner that the part was built. In accordance with prior moment connection modeling endeavors discussed in the literature review, eight node hexahedral elements are used. In ABAQUS, this element type is represented by the designation, C3D8R, in which the "R" indicates reduced integration. The remaining column doubler plates, beam stiffeners, and connection endplate are all rectangular components designed using their actual geometries. Their simple geometry allows for automatic meshing of C3D8R elements. Mesh sizes varied throughout the model. Regions outside the beam protected zone were assigned a coarse mesh size to reduce computing time and resources. The protected zone was assigned a fine mesh with the beam web and flanges including three elements through their respective thicknesses.

A potential mistake in the assembly of individually meshed parts is the failure to merge mesh nodes from separate parts at locations intended to be shared edges and surfaces. In order to properly merge the mesh of separate parts, appropriate mesh seeding must be performed. As an example, the W24x62 beam was partitioned in the lengthwise location of all beam stiffener surfaces as in Figure 86. Mesh seeding values along the edges created by these partitions were duplicated in the mesh seeding of the stiffener edges. By doing this, mesh nodes are created in the exact same location along the surfaces and edges shared by the beam and stiffeners. At this point, it is possible to physically merge the geometry and mesh of the beam and stiffeners. Any duplicate nodes falling within a selected tolerance distance are automatically reduced to one node. The same partitioning and merger process was performed for the column extrusion and the doubler plates mounted in the panel zone. This method results in three final system parts, a merged beam assembly, a merged column assembly, and the rectangular endplate.

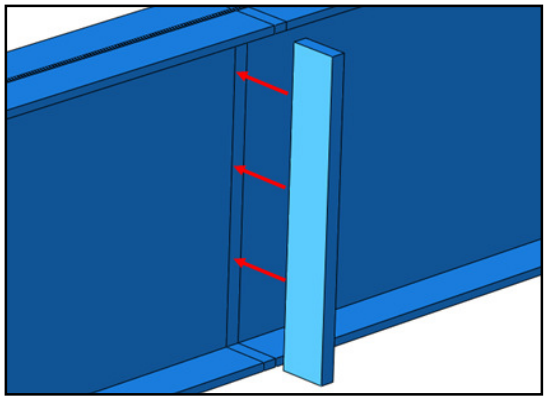

Figure 86: Merging of Individual Parts

For purposes of simplified modeling, bolted connections are not included in the model. Instead, loads are to be transmitted to the column using simple surface constraints. However, the beam, column, and endplate are not merged into one part. A fine mesh is only necessary in the protected zone while a somewhat coarser mesh is adequate in less critical regions. Within a given part, adjacent hexahedral elements must line up node to node. Therefore, modeling the assembly as one complete part would require a continuation of fine mesh sizes edges across all surfaces adjacent to the protected zone. This would result in fine mesh elements across numerous unnecessary regions. In addition this would require a significant amount of work to adequately partition all surfaces to be compatible in a full merger.

The three separate parts are linked using tie constraints. One tie constraint is between the nodal field of the endplate surface and the adjacent nodal field of the column throughout the area to be connected to the endplate. This constraint simplifies the bolted connection as a surface-to-surface fixed contact. The other tie constraint is between the opposite surface of the endplate and the surface of the beam. This constraint represents the welded beam to endplate connection. Figure 87 shows the location of these tie constraints. The three individual parts are shown separated for ease of viewing.

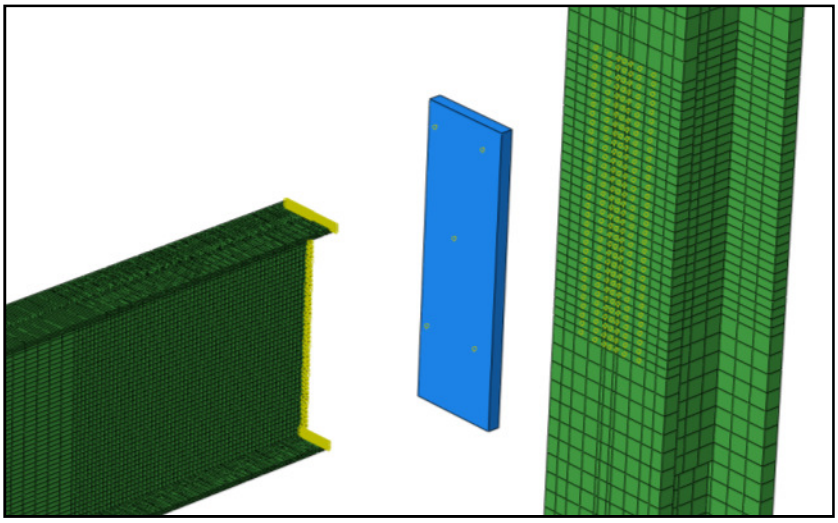

Figure 87: FEM Connection Constraints

Figure 88 shows a visual example of the boundary conditions used in the model. The lateral bracing provided by the three lateral bracing frames in the test setup are incorporated into the model as fixed out of plane constraints at distinct nodes on the top and bottom beam flange at the longitudinal location of the frames. In actuality, these lateral bracing frames have a degree of flexibility not present in the model. Any contribution of this flexibility occurs only when the out of plane web buckling of the beam causes the beam to bear on one side of the lateral bracing frame. Any effect of this flexibility on the performance of the connection is assumed to be negligible in relation to the demands placed on the beam due to forced displacements and local buckling strain concentrations.

The top and bottom surfaces of the column as well as the region of the column base stiffeners are modeled as fully fixed. In reality, this assumption is incorrect. There is a presence of a small degree of frame flexibility as quantified during the story drift decomposition study. This means that the top surface may better be modeled as a simply supported entity with a small degree of lateral flexibility. In order to model this, all top surface nodes must be linked to a single master node, at which boundary conditions and flexibility properties may be assigned. This consideration was not employed in this study.

The test displacement protocol is applied to the model using an initial displacement boundary condition. The initial displacement profile is given as a tabular input cycling through all minimum and maximum story drift displacements. The simulation assumes equal time

increments for each cycle, whereas physical testing uses a constant rate loading. This difference is assumed to cause no discrepancy in the performance of the connection.

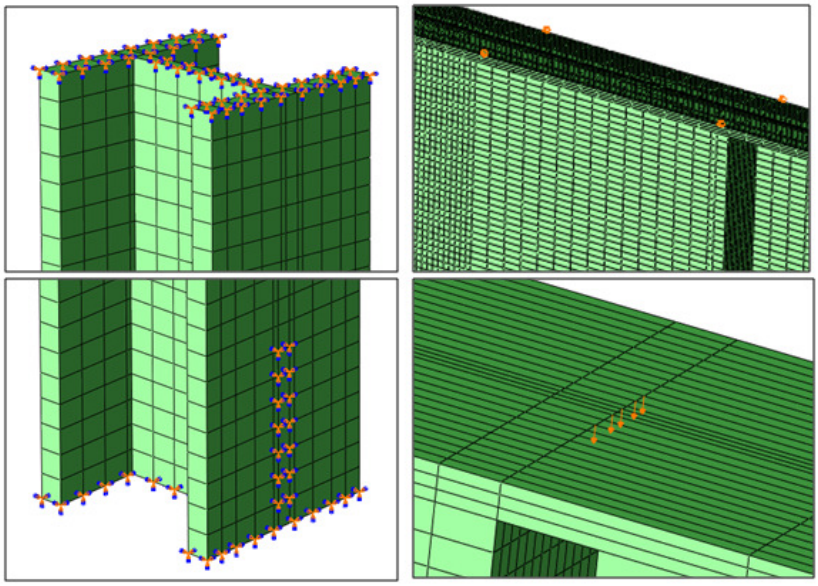

Figure 88: Boundary Constraints: Column Fixed Nodes, Beam Constrained Nodes, Beam Displacement Protocol

Plastic strain values and their respective yield stress values are necessary in order to represent the strain hardening profile of the beam material. The model utilizes isotropic hardening behavior to simulate the strain hardening effects present during continued cycles through high strain demands. These stress and strain data pairs are extracted from tension tests performed on coupon specimens cut from an undeformed region from one of the W24x62 beams. All beams are composed of A992 steel and in the absence of tension coupon tests from every beam it is assumed that all beams have the same material properties.

5.1.2 Steel Material Modeling

It was necessary to select a set of stress-strain data pairs for use in the isotropic hardening properties of the ABAQUS model. For simplicity, only the top flange specimen data is used to define finite strain hardening points, because it follows a more idealized strain hardening behavior than the bottom flange and web specimens. Figure 89 shows the strain hardening profile as described by the chosen stress-strain data points listed in Table 9.

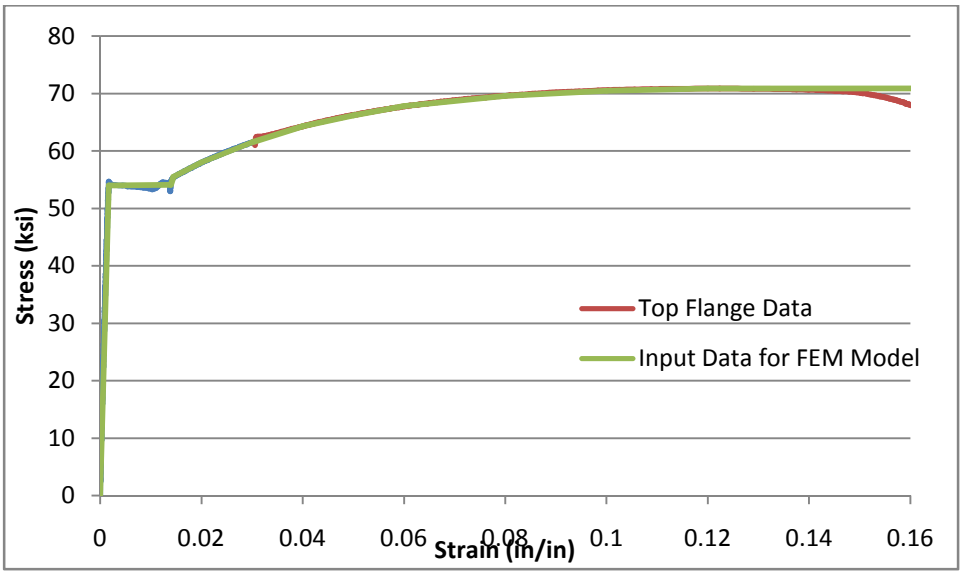

Figure 89: Isotropic Hardening Data for ABAQUS

The stress and strain values extracted from test data are translated from engineering to true values in order to account for a progressive reduction in area and elongation of the coupon over the course of the tests. Strain values are then modified to reflect only plastic strain in accordance with ABAQUS input requirements. Equations 5.1 and 5.2 show the equations used to convert engineering values to true values, where ε represents strain and σ represents stress. Elastic strain is subtracted from the resulting true strain values using an assumed modulus of elasticity of 29,000 ksi and the first true yield stress value of 54.09 ksi.

$$\varepsilon_{true} = \ln(1 + \varepsilon_{eng}) \tag{5.1}$$

$$\sigma_{true} = \sigma_{eng}(1 + \varepsilon_{eng}) \tag{5.2}$$

Table 9: Modified Isotropic Hardening Data for ABAQUS

Observed			True			Plastic	
Strain	Stress		Strain	Stress		Strain	Stress
0.000	0.00		0.000	0.00		0.000	0.00
0.002	54.00		0.002	54.09		**0.000**	**54.09**
0.014	54.10		0.014	54.86		**0.012**	**54.86**
0.015	55.50		0.014	56.30		**0.013**	**56.30**
0.020	58.00		0.020	59.16		**0.018**	**59.16**
0.030	61.50	→	0.030	63.35	→	**0.028**	**63.35**
0.040	64.30		0.039	66.87		**0.038**	**66.87**
0.050	66.20		0.049	69.51		**0.047**	**69.51**
0.060	67.80		0.058	71.87		**0.057**	**71.87**
0.080	69.60		0.077	75.17		**0.075**	**75.17**
0.100	70.50		0.095	77.55		**0.094**	**77.55**
0.120	70.90		0.113	79.41		**0.112**	**79.41**
0.300	70.91		0.262	92.18		**0.261**	**92.18**

5.1.3 FEM Preliminary Results

Simulation of the full test displacement protocol was applied to the model. This preliminary effort was analyzed to determine the validity of results in comparison with observed and measured test data. Initial imperfections were not incorporated since the strain demands being simulated would be more than sufficient to instigate plastic hinging and local buckling. The general behavior of the model is accurate. All merged components visually behave as expected with shared nodal edges and surfaces acting in congruence.

Figure 90 shows a hysteresis comparison of test 3 (W24x62 with BUEEP) results and the equivalent ABAQUS model using isotropic hardening data from the tension coupon tests previously described. It is observed that the elastic behavior of the two sources imply a difference in system stiffness. The linear elastic stiffness of the ABAQUS model exceeds that of the specimen 3 data. Presumably, this is due to the presence of the unintended sources of elastic flexibility within the test setup as discussed during story drift decomposition. Data from ABAQUS simulation indicates a greater plastic moment capacity of the beam than is observed

from test 3 data until 4% story drift. At this point, the ABAQUS model experiences a significant drop in strength to a value consistent with test 3 data.

Figure 91 shows the same test 3 data overlaid with data from the ABAQUS model using kinematic hardening. The kinematic hardening rule appears to better reflect the actual hardening occurring during test 3, because the hysteresis are more comparable than when using isotropic hardening. Using kinematic hardening, the ABAQUS model appears to underestimate the moment capacity at 4% story drift. By 4.7% story drift, the moment capacity is comparable between test and model data.

Figure 92 shows a comparison of the typical stress-strain behavior exhibited by models using the isotropic and kinematic hardening parameters. Data was taken from a specific node within the protected zone for comparative purposes. Isotropic hardening creates a stress-strain profile in which after loading to a new maximum stress in one direction, a material will behave elastically in the other direction until that same maximum stress is achieved in the other direction. Kinematic hardening creates a stress-strain profile in which after loading to a new maximum stress in one direction, the material will behave elastically in the other direction until the change in stress equals twice the initial yield magnitude. This creates the parallel strain hardening lines observed for the kinematic hardening stress-strain profile.

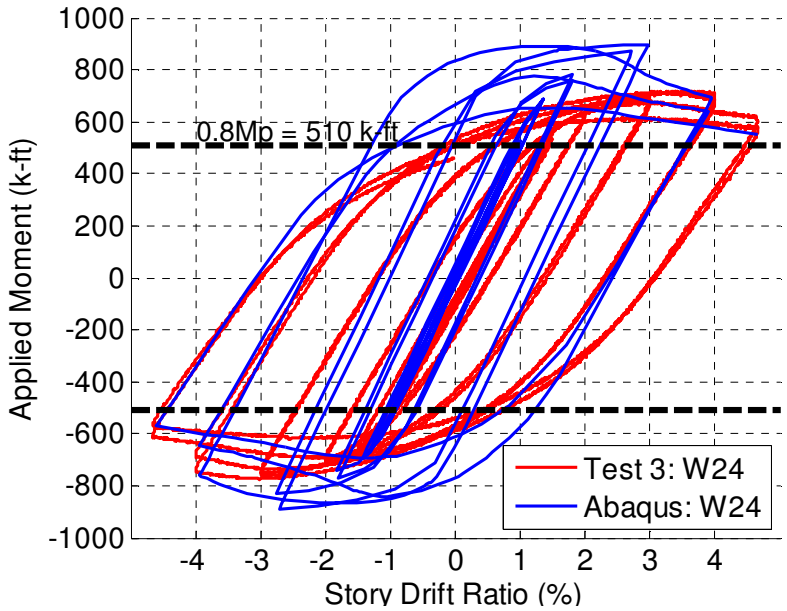

Figure 90: Hysteresis Comparison of ABAQUS Model (Isotropic Hardening) and Test 3

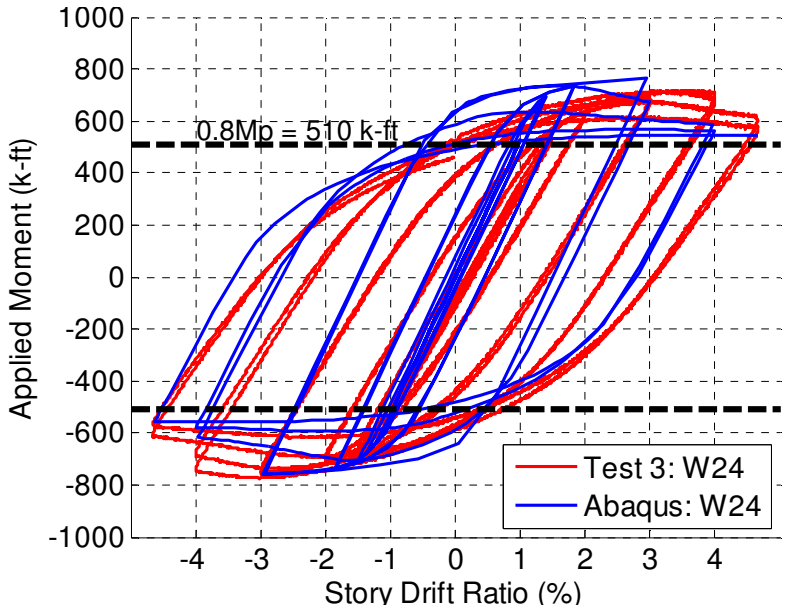

Figure 91: Hysteresis Comparison of ABAQUS Model (Kinematic Hardening) and Test 3

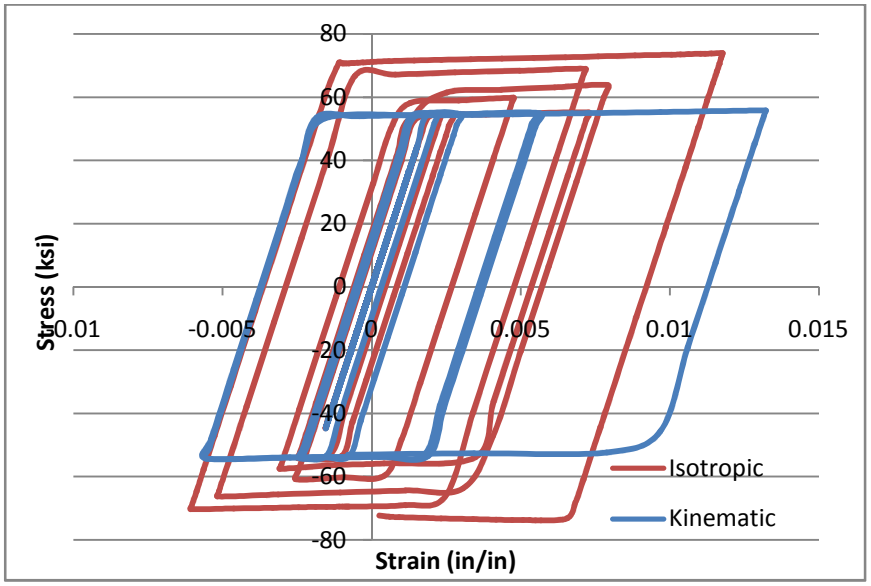

Figure 92: Comparison of Stress-strain Behavior Using Isotopic and Kinematic Hardening

Discrepancies between the FEM model and experimental results could be in part due to attributes of the test specimens not currently accounted for in the model. These include residual stresses in the specimens from differential cooling after leaving the furnace. Additional imperfections are possible within any given specimen. A combined isotropic and kinematic hardening rule will be applied to the model by others as a part of the continued study in this topic, but those results are not present in this document.

Visual ABAQUS model observations provided in this section were completed prior to running analyses with kinematic hardening. For this reason, the observations discussed are from simulations using isotropic hardening. Comparable observations using kinematic and combined hardening will be performed in future work by others and are not present in this preliminary assessment. Local buckling within the protected zone shows a general resemblance to the buckling patterns observed in the experimental tests. As seen in Figure 93 for 4% story drift, local flange buckling occurs in a double curvature manner. For a given flange, one side buckles down near the connection followed by an up buckle. The other side experiences a slight upward buckle followed by a down buckle. The pairing of these opposite buckling patterns creates a general rocking of the flange about its center while remaining relatively straight, as shown by several superimposed lines.

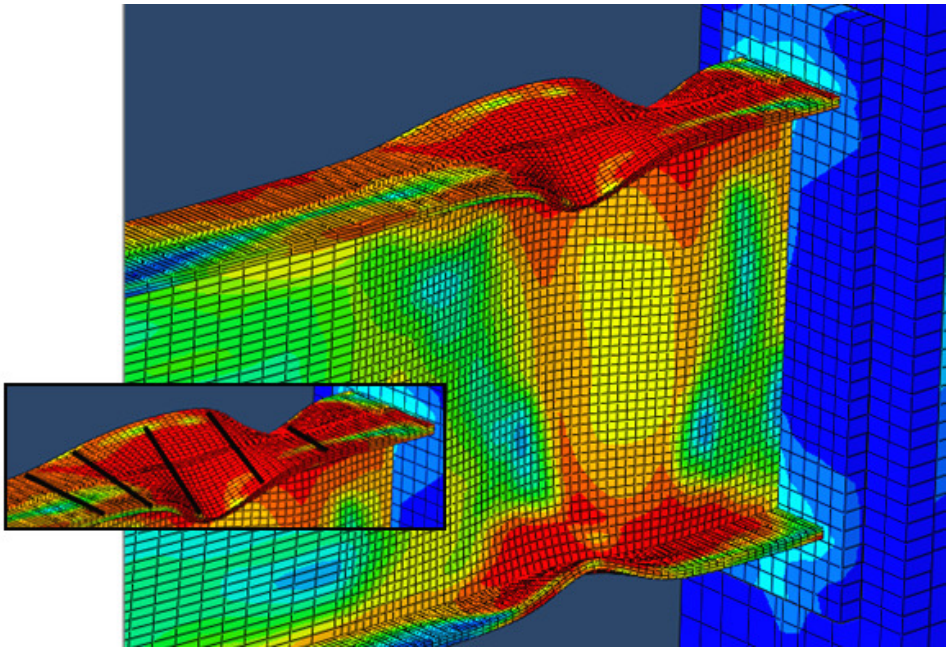

Figure 93: W24 Simulation - von Mises Stress Profile

While the general buckling pattern of the model resembles that of test observations, the amplitudes of those buckles have not shown the same resemblance. At any given instance after the onset of plastic deformation of the beam, the model tends to predict greater buckling amplitudes than are actually observed in comparable tests. Figure 94 shows an example of this observed difference. Test 4 showed a similar buckling pattern as the model, but produced a

distinctly lesser buckling amplitude than the model for the first instance of an upward deflection of the beam to 4% story drift.

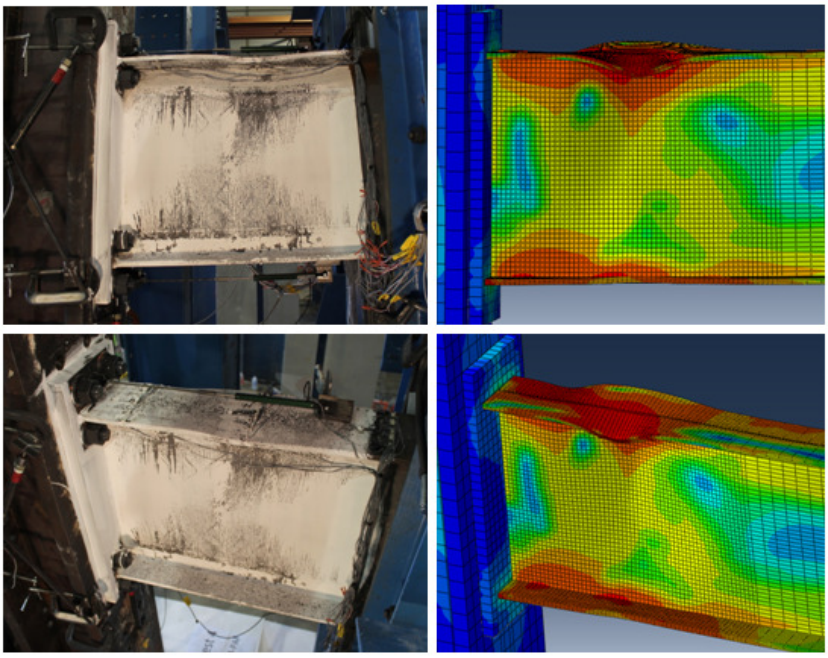

Figure 94: Buckling Comparison - Test 4 and ABAQUS

This baseline model can be used to analyze the strain history at the interior of local buckles in order to attempt to correlate the strain history behavior with the observed cracks occurring in those locations on full-scale RBS specimen tests. Results show that while the longitudinal strain at these locations vary cyclically as the buckles are 'pulled out' and 'pinched in', the strain tends to trend asymmetrically toward compression. As observed during full-scale tests, as the displacement history progresses, the compression flange will eventually buckle. As the load reverses, strain hardening of this former compression flange creates increased resistance as it is pulled in tension. Effectively, the buckle resists being fully straightened out. During the same half cycle, the opposite flange typically develops local buckling. This repeating process causes a progressive increase in flange local buckling amplitude, effectively shortening the specimen length. Figure 95 shows this progressive shortening using test 2 data. Top and bottom flange LVDTs record opposing cycles of extension and retraction, but the average of these readings, plotted as a bolder line, indicates the general shortening of the protected zone. This general compressive trend is responsible for the strain history observed at the interior of the buckles.

This compressive based strain history is shown in Figure 96 with accompanying FEM images supporting the permanent presence of buckles once they begin.

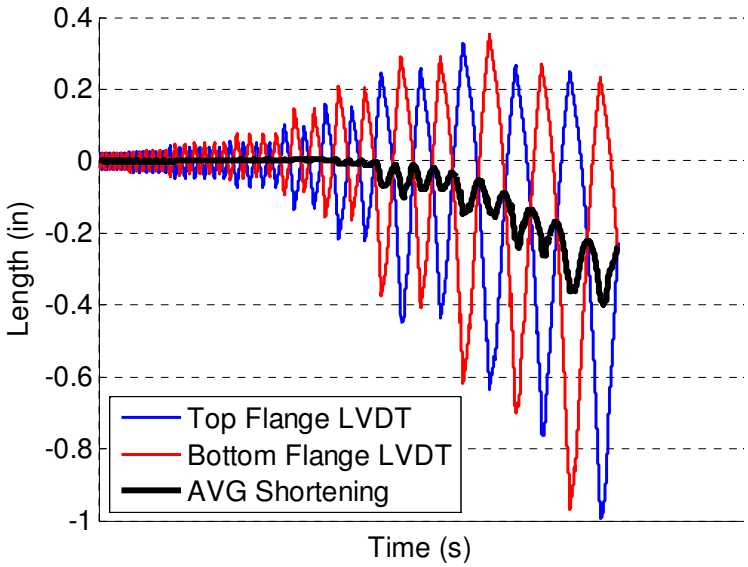

Figure 95: Shortening of the Top (red) and Bottom (blue) Length of the Protected Zone

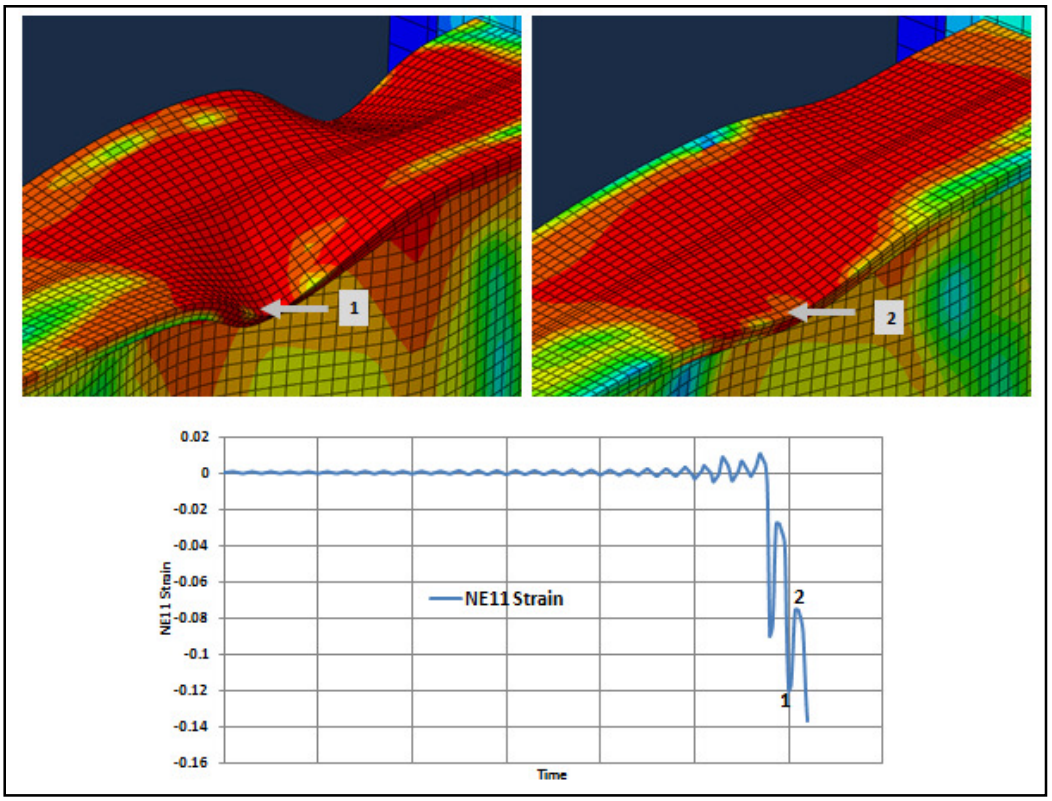

Figure 96: General Compressive Strain History at Buckle Interior Curvature

5.1.4 FEM Model Sensitivity

Of particular note is model sensitivity to material property values. It has been observed that the FEM model is proven to behave sensitively to slight changes in its inherent strain hardening data. Prior to the collection of specimen tension test data, initial isotropic strain hardening data was extracted from available literature data by Kaufmann et al. (2001) for a similar grade of steel. Figure 97 shows this published data.

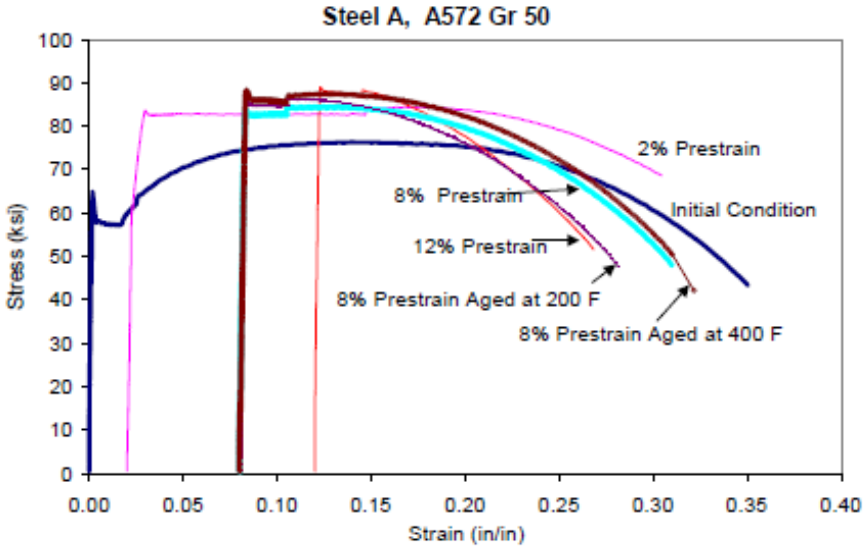

Figure 97: Strain Hardening Data (Kaufmann et al. 2001)

Since numerical data extraction from an x-y plot is subjective, numerous data values could be reasonably interpreted from the given plot line in Figure 97. Three unique sets of strain hardening data (Table 10) were interpreted from the plot. All three data sets were used as isotropic strain hardening properties for the same FEM model simulations. The effect of these unique input properties on the model was assessed visually by the longitudinal location of local buckles on the flange as it varies among the simulations (Figure 98 and Table 11).

Table 10: Strain Hardening Data Sets

Abaqus Trial 1		Abaqus Trial 2		Abaqus Trial 3	
Yield Stress	Plastic Strain	Yield Stress	Plastic Strain	Yield Stress	Plastic Strain
58.0	0	58.0	0	58.0	0
59.0	0.016	59.0	0.016	59.0	0.016
64.6	0.023	64.6	0.023	64.6	0.023
73.5	0.047	73.5	0.047	73.5	0.047
82.5	**0.093**	**82.5**	**0.093**	**83.6**	**0.093**
--	--	**86.6**	**0.129**	**88.6**	**0.138**

Figure 98 indicates a significant variation in the location of top flange local buckles as they move longitudinally from the endplate depending on the strain hardening data set input in the model. The actual visual results shown correspond to the "ABAQUS Trial 2" data set with markers indicating the location of the buckles for the other trials data sets. For purposes of this initial study, the trial 2 data set best correlates to the location of buckles seen in the equivalent experimental tests 3 and 4. While this study highlights the sensitivity of the model, the data sets explored here do not represent the final strain hardening data used in the model. That data is collected from the tension coupon tests performed.

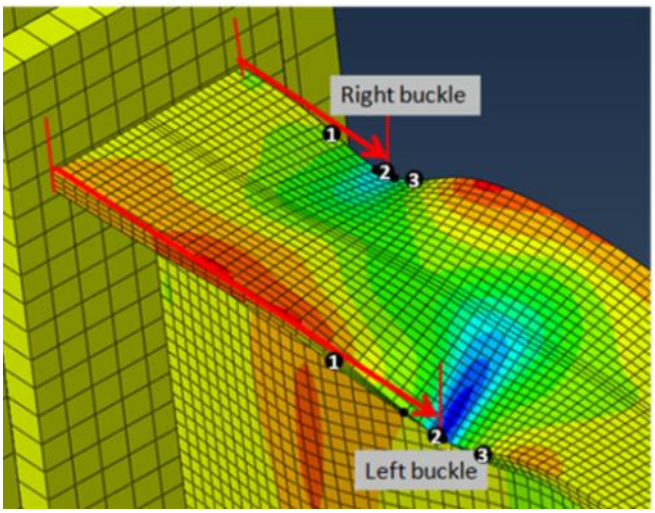

Figure 98: Strain Hardening Sensitivity Study Results

Table 11: Strain Hardening Sensitivity Study Results

	Left Buckle	Right Buckle
ABAQUS Trial 1	11.5 in	4.0 in
ABAQUS Trial 2	**15.5 in**	**6.5 in**
ABAQUS Trial 3	17.5 in	8.0 in
Test 3 (W24)	14.0 in	6.0 in
Test 4 (W24-PAF12)	15.5 in	7.0 in

CHAPTER 6: LOW-CYCLE FATIGUE FOLLOW-UP TESTING

6.1 Follow-Up Low-Cycle Fatigue Test Development

This section discusses the work performed to develop a test method that could be used by others for follow-up low-cycle fatigue testing. Continued refinement of the test method and completion of these tests is beyond the scope of this study. The general motivation behind follow-up tests is to simulate the boundary and loading conditions of a full-scale moment connection in order to continue studying the fatigue behavior of the connection. Smaller specimens than those used in full-scale testing introduce the possibility of testing both beyond the original scope and in a more economical manner. Since AISC 341 Appendix S (AISC 2010a) requires full-scale moment connection testing in order to complete approved qualification of modifications or defects of such connections, it is necessary to show that an alternative test configuration can accurately recreate the same conditions. With an acceptable test plan in place, a wide range of testing is possible.

Several early alternative test configuration concepts were explored to determine the degree to which they represent full-scale moment connection test conditions. For each concept, a unique set of boundary conditions and cyclic loading must be created so as to place the same strain demand on the specimen as experienced by the top flange of the full-scale moment connection tests. FEM models of these concepts and the full-scale moment connection tests were created on ABAQUS using shell elements for the purpose of comparing key cyclic effects including strain values and buckling amplitudes. Each model was simulated through one cycle each of the eight story drift magnitudes required in the qualification parameters of AISC 341 (AISC 2010a).

6.2 Initial Concept 1: Trapezoidal Specimen

The first concept explored is the Trapezoidal Specimen configuration (Figure 99). It utilizes a WT shape specimen representing the top half of a moment connection beam along the length of the protected zone. The specimen is bolted on both ends lengthwise to W shape beams. Both

beams are fixed symmetrically at pivot points and cycled with actuators at their free ends. This creates a double bending load on the trapezoidal shaped test specimen. A rigid strut mounted to both beams by pin connections is intended to represent the moment of inertia contribution of the missing bottom half of the beam. The strut would be reusable from test to test. All test components except the WT specimen are intended to behave elastically and can therefore be reused for all tests.

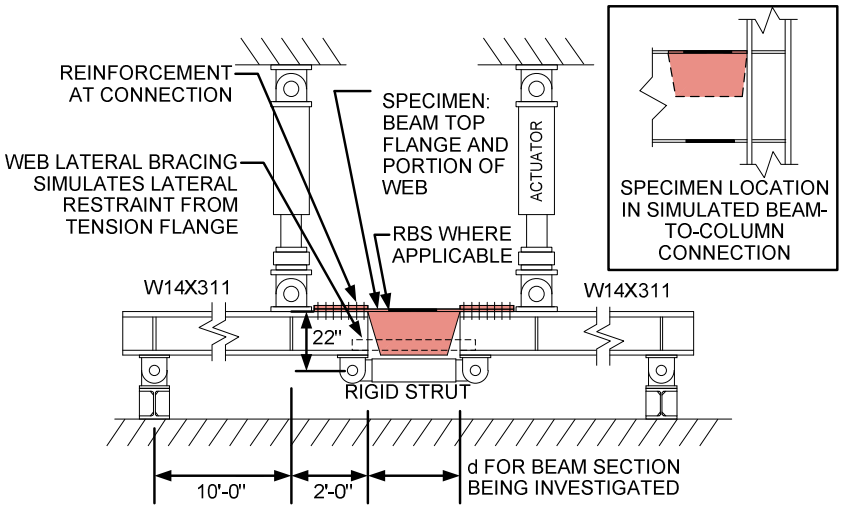

Figure 99: Trapezoidal Specimen Configuration

Observation of the trapezoidal specimen simulation (Figure 100) indicates a different global deformation mode. In this configuration, the top flange experienced no notable buckling while the mostly unrestricted web buckled significantly at higher story drifts. The obvious visual differences of this simulation with that of typical moment connections can be attributed to a significant departure from the boundary conditions present in full-scale moment connections.

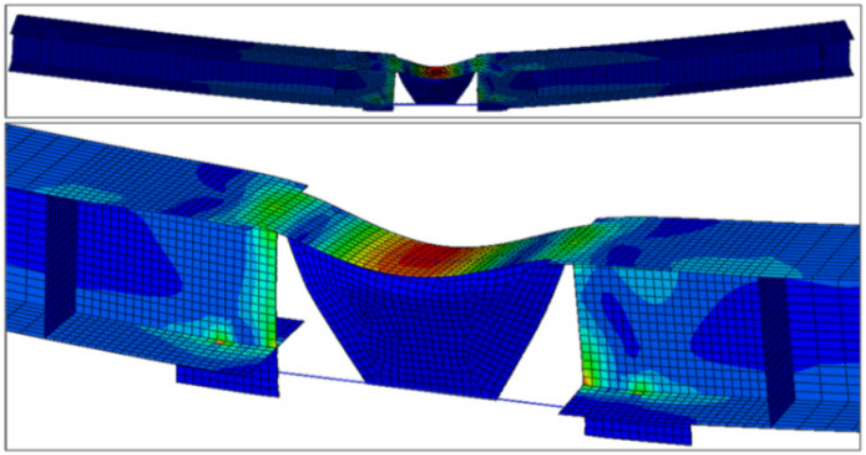

Figure 100: Trapezoid Specimen Simulation

6.3 Initial Concept 2: Half Depth Specimen

The second configuration concept is an attempt to better recreate moment connection boundary connections by designing the new tests around the existing moment connection test frame. This concept is known as the Half Depth Specimen configuration (Figure 101). As with the first concept, the setup utilizes a WT shaped specimen again representing the top half of the moment connection beam in the protected zone. The specimen would connect to the test column using its own endplate. The other end would be mounted to a reusable length of beam extending to the actuator in order to achieve the 17 ft. displacement moment arm length used in full-scale connection testing. The geometric similarity to full-scale moment connection tests would allow the half depth specimen tests to use the exact same displacement protocol. As in the previous concept, a rigid strut pinned between the column and beam would represent the missing bottom portion of the protected zone. The strut is sized and positioned to center the cyclic rotation of the system at the bottom of the WT specimen. This locating is critical to recreate the center of rotation of a typical beam at its mid-depth.

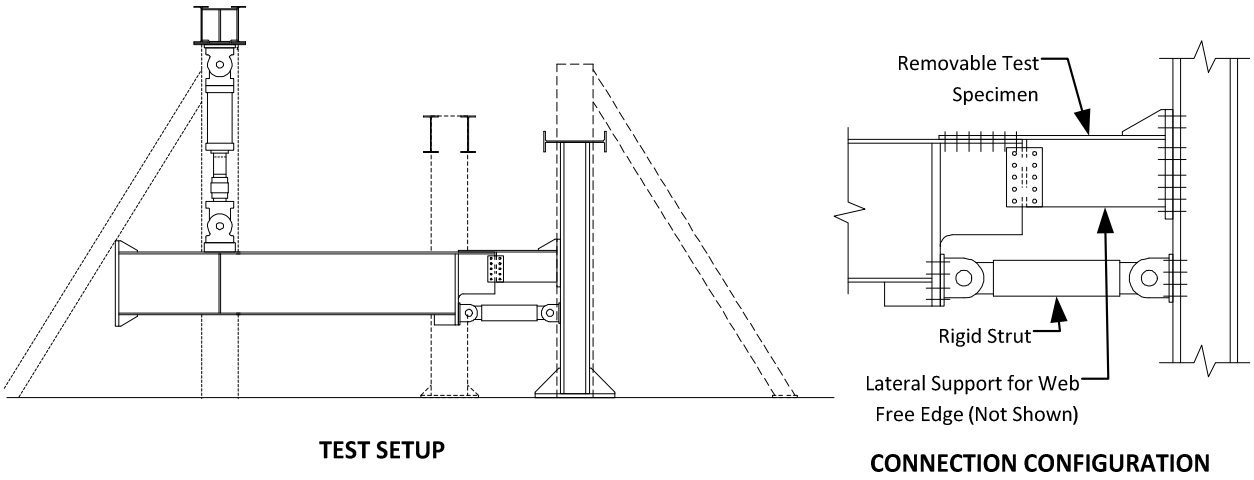

Figure 101: Half Depth Specimen Configuration

Variations in the geometry of this half depth setup were performed on ABAQUS to determine the sensitivity of the test configuration. Simulations were performed using four different strut locations. These consisted of three locations above the bottom flange line by 4, 5, and 6 inches

(centered on the three intersecting circles in Figure 102) and one location below the bottom flange line by 5 inches (not shown in Figure 102).

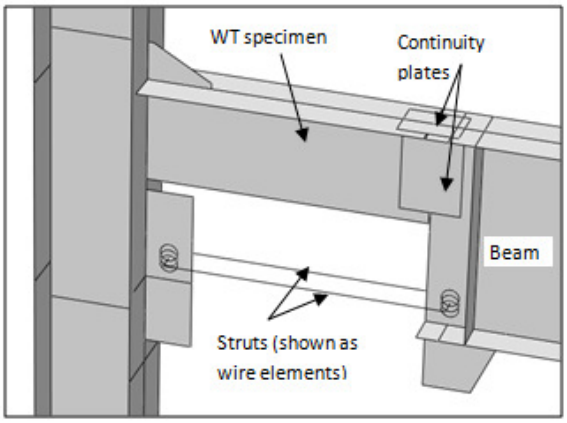

Figure 102: Half Depth Specimen Strut Variation

Upon cycling simulation, the specimen variations exhibit the same general plastic behavior and buckling profile as full-scale moment connections. Buckles along the top flange assume a double curvature on both edges. However, further analysis of these results reveals several numerical differences and model sensitivity that makes the overall concept a less than ideal option. While the general buckling profile from model variations as shown in Figure 103 is similar to that of full-scale moment connections, the accompanying strain magnitudes at these buckles and buckle amplitudes do not correlate well.

Several response properties were compared between the half depth and the full-scale connection simulations. These properties are recorded at the instant of greatest upward deflection (4%) by the beam, when the top flange is in the greatest compression it experiences. They include the upward and downward buckling amplitudes of the top flange as well as the plastic strain PE11 at the same two nodes at which the buckling amplitudes are measured. Table 12 lists a comparison of these variables.

Table 12: Half Depth Specimen Model Sensitivity

Model Type	Full-Scale	Half Depth	Half Depth	Half Depth	Half Depth	Half Depth
Displacement Scale Factor	1	1	1.2 (+20%)	1.2 (+20%)	1.2 (+20%)	1.2 (+20%)
Strut Location w.r.t. bottom flange	N/A	4 in. above	5 in. below	3 in. above	4 in. above	5 in. above
Upward Buckle Amp. (in.)	2.9	1.6	3.5	3.3	3.2	3.2
Downward Buckle Amp. (in.)	-2.9	-1.3	-2.5	-2.5	-2.5	-2.5
PE11 at Upward Buckle	0.050	0.040	0.045	0.036	0.038	0.040
PE11 at Downward Buckle	-0.020	-0.016	-0.040	-0.040	-0.034	-0.043

The cyclic displacement history of the full-scale connection configuration is based on the story drift specifications of AISC 341 Appendix S (AISC 2010a). As can be observed in the results of Table 12, the buckling amplitudes for the half depth configuration ran with the same displacements are significantly lower than that of the full-scale connection configuration. As a result, all subsequent simulations utilize a displacement profile 20% greater than used for the full-scale configuration.

Numerical results do not provide a confident assessment on the feasibility of utilizing the half depth configuration. Amplifying the displacement profile by 20% increases flange buckling amplitudes to more comparable values, but they do not deflect up and down at equal magnitudes as in the full-scale connection configuration. Furthermore, as the strut location changes, the longitudinal strain (PE11) strain values change but not with any apparent proportional relationship and the buckling amplitude values experience minimal change at best.

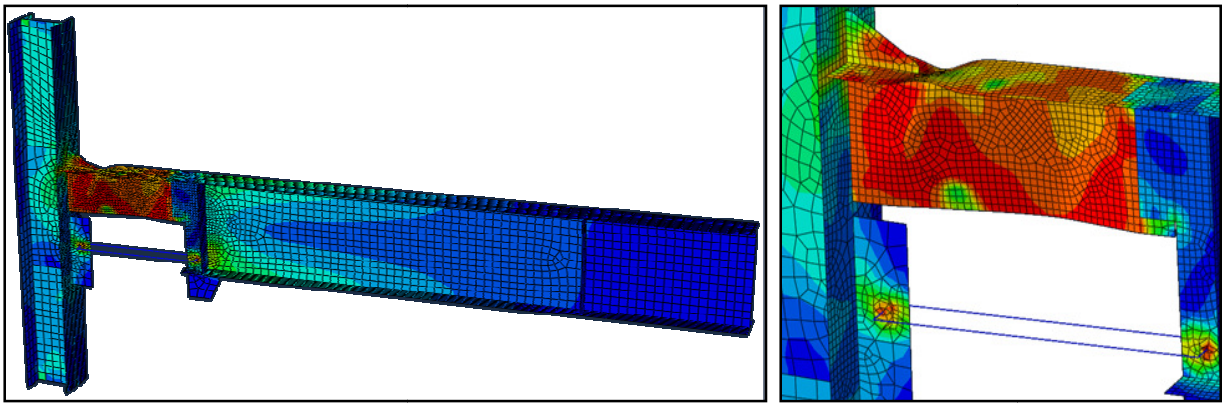

Figure 103: Half Depth Specimen Simulation – entire model (left) and specimen region (right)

One significant deviation from the deformation behavior of the full protected zone is that the half depth specimen tends to experience bending due to the rigid behavior of the pin connected strut. While the strut aims to represent the bottom half of the beam, it cannot correctly simulate the ductile nature of the web and flange. Since it is designed as a rigid, reusable member, it pushes the local plastic straining tendency to its pin connection with the beam. This creates a bending about the pin connection rather than a more natural forming plastic hinge for a typical full depth beam. In addition, the bolted connection of the WT specimen web and flange to the reusable beam attempts to simulate the continuity of a full beam but is unable to accurately represent the continuous stiffness of that beam.

6.4 Initial Concept 3: Endplate Connected Specimen

Within the option of utilizing the existing test frame for the new test configuration, it is possible to design a test that eliminates the boundary condition differences present in the half depth specimen configuration. The Endplate Connected Specimen configuration (Figure 104) represents a design one step closer to full-scale moment connection tests. The concept utilizes a full depth beam cut to the length of the protected zone. This shortened beam specimen would have bolted endplate connection on both ends, one for the moment connection to the test column and one for connection to a length of beam extending to the actuator.

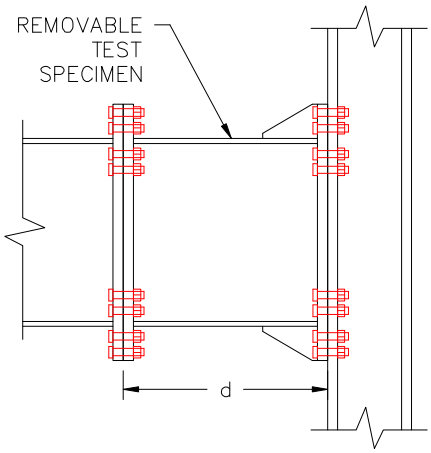

Figure 104: Endplate Connected Specimen Configuration

Within the option of utilizing the existing test frame for the new test configuration, it is possible to design a test that eliminates the boundary condition differences present in the half depth specimen configuration. The Endplate Connected Specimen configuration (Figure 104) represents a design one step closer to full-scale moment connection tests. The concept utilizes a full depth beam cut to the length of the protected zone. This shortened beam specimen would have bolted endplate connection on both ends, one for the moment connection to the test column and one for connection to a length of beam extending to the actuator. The geometric similarities of this configuration make it an adequate alternative to a full length beam. The specimen is of full depth which eliminates the need to try to precisely locate its center of rotation. A fully pretensioned endplate connection to the reusable beam at the end of the protected zone provides a suitable continuity of the beam.

As expected, cyclic simulation of this configuration provides a near identical response to that of a typical moment connection of the same beam size as seen in Figure 105. While the configuration does meet the goal of simulating a full-scale moment connection, the steps taken to reduce the boundary condition deviations from the other test concepts effectively eliminate any economical benefit of such tests. The cost associated with the fabrication and transportation of these shortened full depth specimens is an improvement from full length beams, but not enough to justify the multitude of tests intended for this phase of testing.

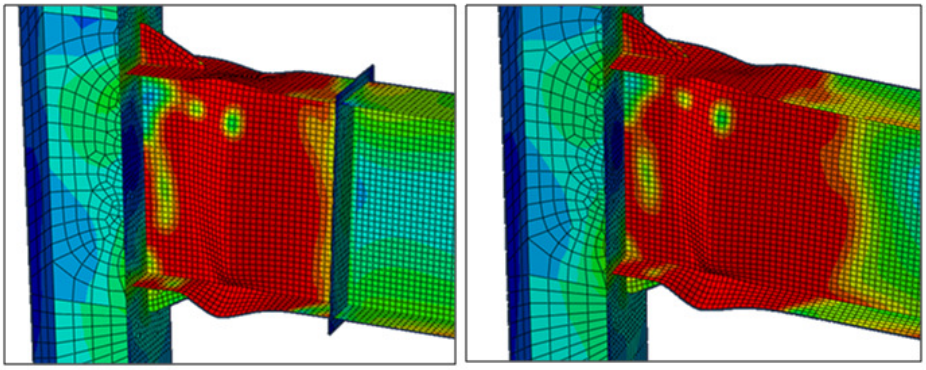

Figure 105: Endplate Connected Specimen Simulation – Comparison with Full Beam Simulation

6.5 Initial Concept 4: Coupon Specimen Configuration

Exploration of several early concepts for an alternative test setup introduces an apparent tradeoff for such attempts to represent the entire protected zone top flange. Boundary conditions prove to be a sensitive variable, and efforts taken to minimize their differences from those of full-scale moment connections tend to create larger specimens that are less economical than desired. This reality prompted a new approach to the new test plan. The final approach for further testing is the development of a coupon test program.

The stress state and strain history in the flanges of a SMRF connection undergoing large inelastic cycles is extremely complex. Figure 106 shows an SMRF connection after local buckling has occurred. In order to reproduce the same potential for low cycle fatigue existing in the full-scale connection test, the localized stress triaxiality and strain history need to be reasonably well simulated. The strain history at a given fiber in the flange is a function of the axial displacement, $\delta(t)$, and the rotation, $\theta(t)$. Creating a small scale test capable of capturing the displacement and rotation boundary conditions is difficult for the reasons listed in Figure 106.

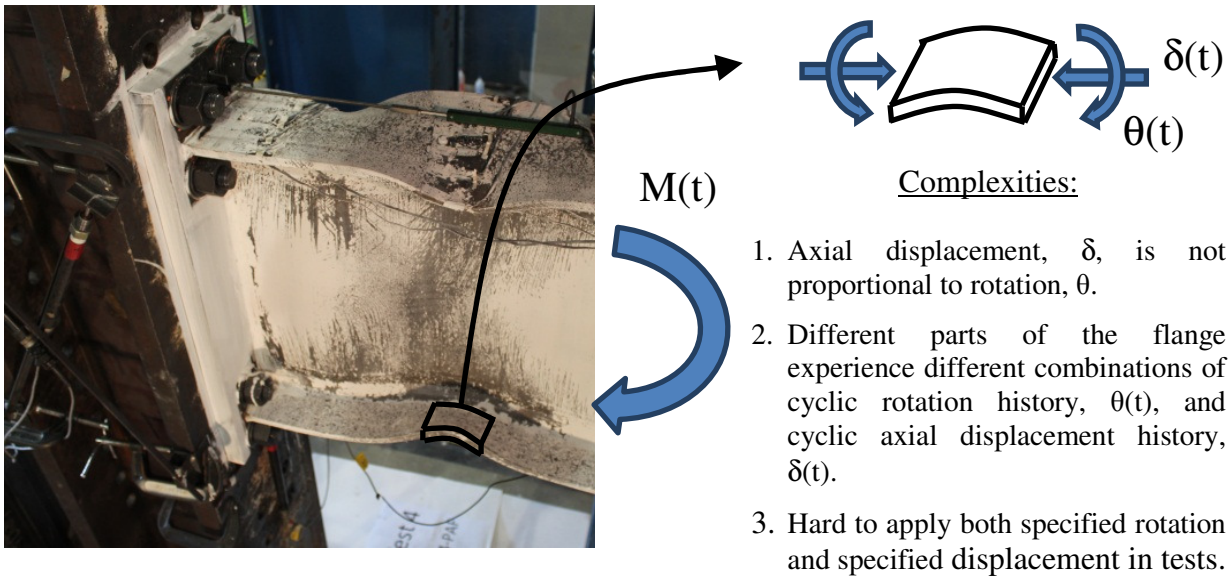

Figure 106: Complexities in Developing a Small Scale Test that Simulates the Conditions at a Local Buckle

A new test configuration will subject dogbone shaped coupon specimens through a unique cyclic displacement profile. The displacement protocol will be based on strain demands of key locations of the top flange on full-scale moment connections. Using the displacement protocol development method discussed in the following section, it will be possible to test the effect of PAFs and defect repairs in different flange locations using a single coupon test.

The proposed coupon test setup (Figure 107) is designed to provide a cyclic axial loading protocol. The setup utilizes two MTS 201.80 actuators, each with a 300 kip capacity, acting in parallel to provide a total load capacity of 600 kips. The actuators are mounted horizontally over strong floor beams spaced at 8 feet center to center and are bolted to a sliding reaction beam through which the longitudinal displacement protocol is transmitted to the center strong floor line at which location the dogbone shaped specimens are mounted in a system of bolted grips. Channel pairs running longitudinally on either side of the specimen act as gripping members through a grid of pretensioned 1-1/4" bolts. A plate is mounted to the reaction beam using a full penetration weld to provide a plane at which to bolt the rightmost channel clamps. Reaction blocks at the end of the actuators and fixed channel grips will transmit test loads into the strong floor. Support structures will be mounted into available strong floor locations to provide a surface over which the actuators and reaction beam may slide freely longitudinally on Teflon sheets while being supported vertically to maintain a horizontal test orientation.

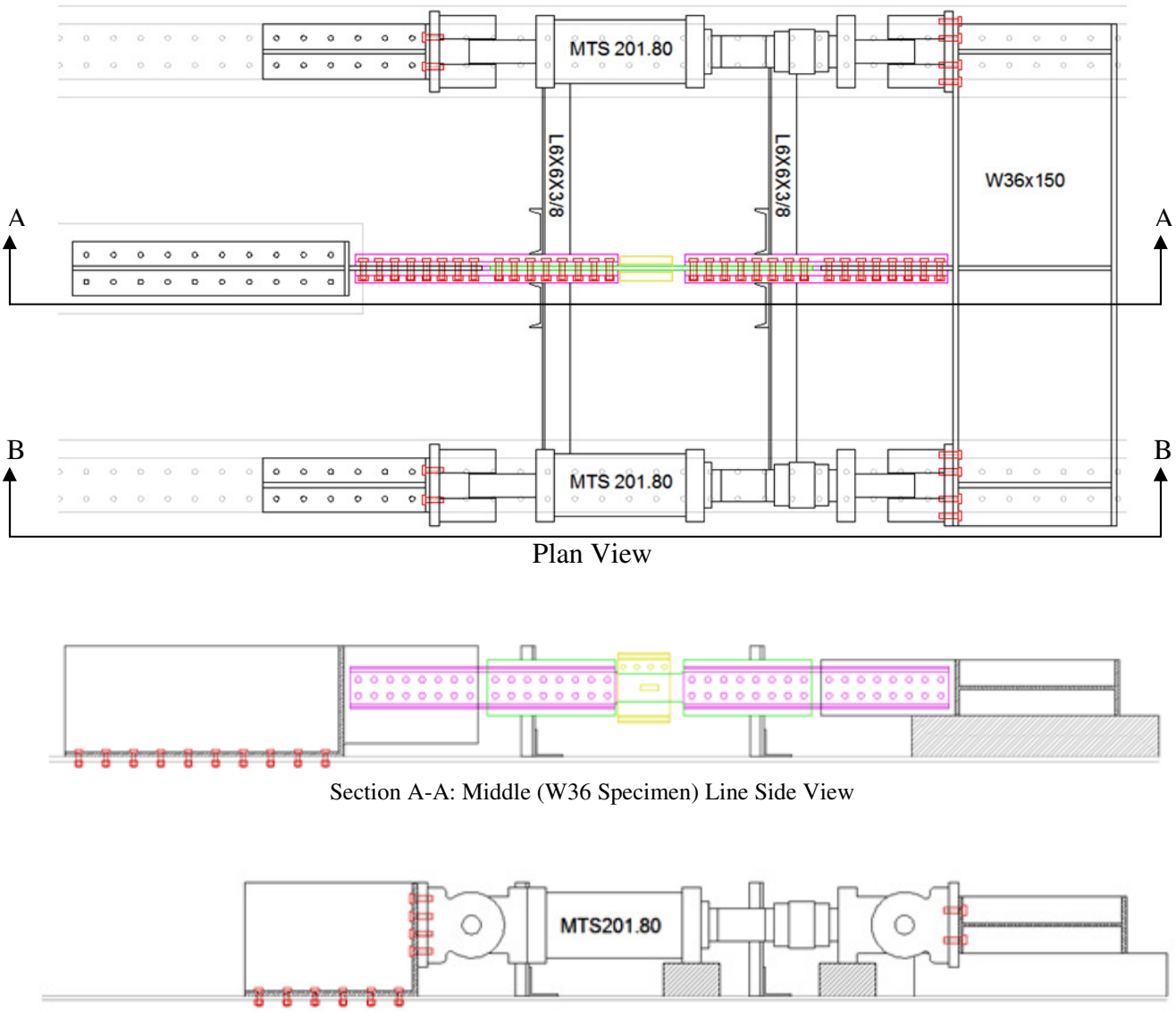

Figure 107: Coupon Test Configuration - Top and Side Views

Global buckling of the specimen and its surrounding gripping channel clamps is prevented through the use of vertical channel pairs positioned at intervals along the line of components. In addition, local buckling of the specimen will be prevented using two large channels clamped directly against the specimen itself using bolts running above and below the specimen through gap filling plates. The interface between the clamps and specimen will include either sheets of

Teflon or a suitable grease to reduce friction. A small window cut through the channels will allow for the inclusion of fasteners or welds protruding out from the surface of the specimen.

Coupon specimens will be cut from the flanges at the middle region of the W24x62 and W36x150 beams being used for full-scale moment connection testing, sufficiently far from the deformed ends. The length of the specimens is driven by the large number of bolts needed to support the loads expected during testing. Coupons will be cut such that they contain a reduced width along 15 inches at their centers. This reduced region will act as the region subjected to the input displacement protocol. It will be necessary to grind flat all portions of the beam web along the length of the coupons to ensure a proper fit within the test setup.

6.6 Test Displacement Protocol Development

Longitudinal strain along the flange of full-scale beam-to-column tests varies lengthwise depending on the location on the beam relative to the beam-to-column connection. It also varies widthwise across the flange depending on out-of-plane deformation due to local buckling from compression phases of the displacement protocol. The combination of these factors results in a varied strain history along all points on the top and bottom surfaces of the protected zone flange. Locations in the region of large out of plane buckling near the beam-to-column connection will experience greater strain magnitudes and cumulative strain over the duration of the cyclic loading protocol than other regions and are, therefore, more susceptible to possible fracture if any form of defect is present. In general, the greatest magnitude tension and compression longitudinal strains are expected along the outer and inner surfaces of buckle curvatures, respectively.

By extracting from FEM models the strain histories and cumulative strain profiles for several locations on the flange of full-scale beam-to-column connections, a new coupon displacement protocol can be developed that represents different flange regions depending on the particular test protocol used. In this way, the effect of a particular defect at various flange locations can be assessed using a single coupon test up until the point at which a possible failure of the coupon occurs. Should a failure occur, it would be an indication that the equivalent location on full-scale tests, as well as more severely strained locations, would also presumably fail during the original

full-scale connection loading protocol. Figure 108 presents a visual companion to the cyclic protocol development procedure described here:

1. FEM models of full-scale beam-to-column connection tests are simulated using the Phase I loading protocol dictated in the qualification requirements of AISC 341 Chapter K2 (AISC 2010a).
2. Specific flange locations are selected as key locations in which further low-cycle fatigue study is desired
3. Longitudinal strain data at most critical locations is extracted from the appropriate FEM model.
4. A new coupon specimen displacement protocol is created which will achieve similar peak and cumulative strains in coupon specimens. This will allow the coupon to accurately represent the original location chosen on the flange.

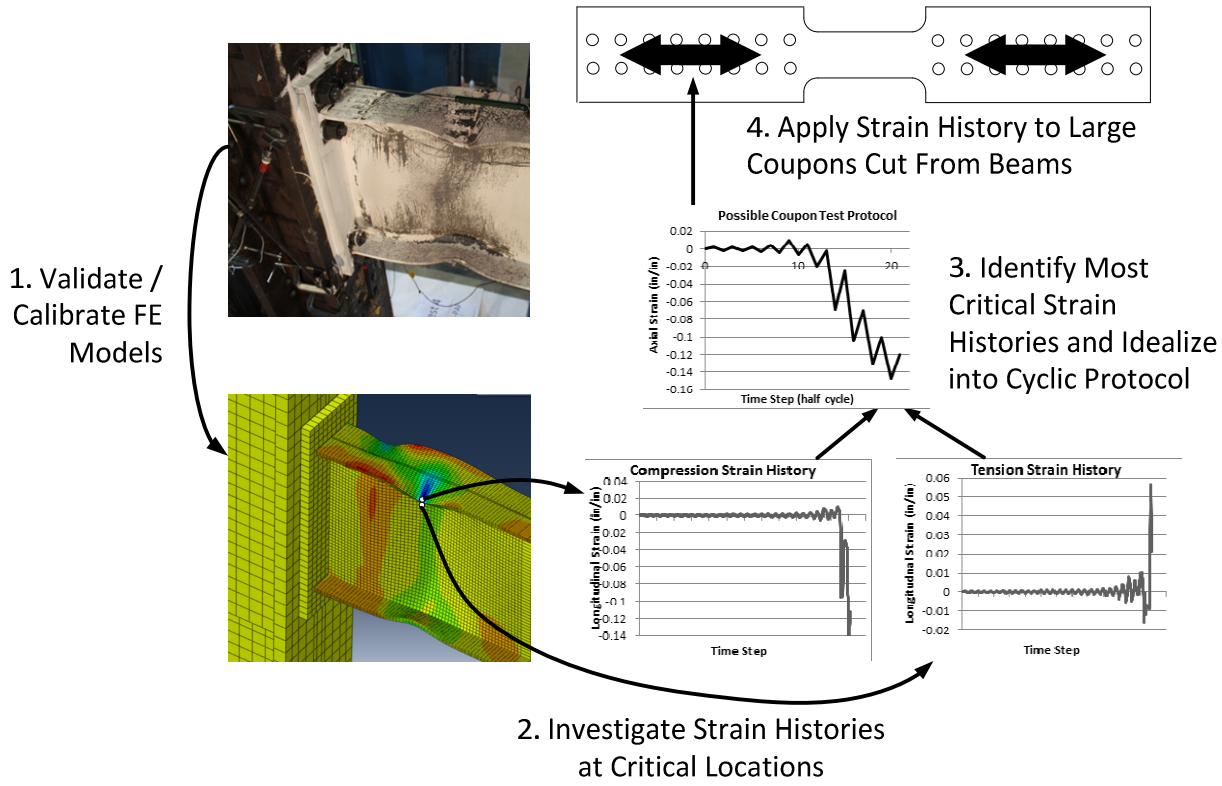

Figure 108: Schematic Drawing Demonstrating the Concept for the Coupon Test Program

6.7 Conclusions

It is difficult to recreate the deformations at a moment connection local buckle in a test setup that isolates a specific part of the flange. Attempts to do so have made it apparent that boundary conditions are extremely hard to simulate. Three initial alternative test setups that attempted to isolate the behavior of the flange at a local buckle were evaluated. None of these configurations provided both an accurate representation of the full-scale model behavior and a viable economical test method. This prompted the definition of a coupon test program and a proposed procedure for developing displacement protocols that could be capable of simulating the demands at specific flange local buckle locations. While further development of this plan and conducting of these tests is not part of this study, it is expected that the proposed methodology could be used to economically simulate the demands in moment connections.

CHAPTER 7: SUMMARY AND CONCLUSIONS

Twelve full-scale beam-to-column moment connection tests were completed using a variety of prequalified beam connection types as well as test variables including PAFs and puddle welds. All six RBS specimens experienced some degree of fracture occurring during the 4.7% story drift phase of testing. An overall conclusion can be drawn that beams comparable to those sections tested and including an RBS are more likely to fracture than beams without an RBS under the cyclic conditions simulated during testing.

For each specimen type, all tests showed a similar hysteretic behavior up to the point of fracture regardless of the inclusion of PAFs or puddle welds. This indicates that neither PAFs nor puddle welds significantly affect the load-deformation behavior prior to fracture.

Three test specimens included a grid of fasteners (W24x62 with BUEEP, W36x150 with RBS, and W36x150 with BSEEP). All three of these specimens produced hysteresis responses similar to those of the same specimen types. Both of the W36x150 fastener grid specimens experienced brittle flange fractures during 4.7% story drift cycling. Fracture of the W36x150 RBS specimen 9 did not occur significantly earlier than in earlier tests of the specimen type. The fracture of the W36x150 BSEEP specimen 12 was the only to occur for this specimen type, but it occurred late in the phase of 4.7% story drift cycling. Based on the results of the PAF grid tests, it is concluded that similar moment connections in practice that have PAFs in any of the locations present in the grid tests are expected to have similar hysteretic performance as the same connection with no PAF within the range of maximum and cumulative rotations through the AISC 341 qualification cycle.

A typical progression of limit states was observed for RBS specimens. Significant yielding first occurred in the extreme fibers at the reduced section. Plasticity then spread followed by local buckling of the flanges and out-of-plane buckling of the web. Flange local buckling was concentrated to the length of flange near the minimum flange thickness of the reduced section. For W24x62 RBS specimens, cracks typically initiated at the flange tips on the inside face of local buckles where compressive stresses and strains were the greatest. For W36x150 RBS specimens, cracks appeared to initiate several inches from the flange edge but still at the inside

face of local buckles. Fracture, originating at these cracks, propagated through the entire flange. This occurred during half cycles in which the local buckles were being pulled out.

Specimens with no RBS showed slight differences in the progression of limit states. In the absence of a reduced section, initial yielding occurred in the extreme fibers near the same location lengthwise as in RBS specimens. This was followed by a spread in plasticity. Local buckling of the flanges occurred over a slightly longer length of flange than for RBS specimens where the buckling was concentrated near the reduced section. Accompanying web buckling occurred similar to that in RBS specimens. Cracks again occurred on the inside face of local buckles, but in general they were less prominent than for RBS specimens. The only fracture for specimens without an RBS (specimen 12) occurred in a similar manner to the fractures of RBS specimens. Propagation of a tear near a PAF at a local buckle caused a full flange fracture during a half cycle in which the local buckle was being pulled out. This test is further discussed below.

The only non RBS specimens to show signs of tearing or fracture were those that included PAF grids (specimens 6 and 12). Specimen 6 did not fracture but assessment of the PAF grid after the test ended showed the early sign of tears forming at several PAF holes. This minimal tearing only occurred after five full cycles of 4.7% story drift. Specimen 12 experienced a bottom flange fracture clearly initiating at a PAF hole. This fracture occurred only after numerous cycles at 4.7% story drift. This would indicate a susceptibility of beams with PAFs located in the proximity of local buckles, where compression stresses are the greatest, to experience propagating tears that could lead to fracture prior to when this would have occurred otherwise. However, it is again noted that this increased susceptibility was only observed during numerous increased amplitude cycles beyond qualification criteria.

All tests passed the SMRF qualification requirement of maintaining 80% of their nominal plastic moment through the first cycle of 4% total system story drift. Test data reveals an imbalance between the positive and negative applied moments at a given magnitude story drift, regardless of the order of positive/negative story drift amplitudes encountered. These imbalances are likely caused by initial applied moments due self weight loads. Story drift decomposition of test data indicates that every test successfully underwent at least 3% story drift due to the plastic hinging component of the total story drift while still maintaining a moment capacity above the 80%

nominal plastic moment limit. While most tests achieved this during the qualification cycle, several tests had to enter the first cycle of 4.7% story drift before they exceeded 3% story drift due to plastic hinging.

Investigation of specimen fracture surfaces will be included elsewhere (Eatherton, 2013). That investigation will also include comparisons of strain profiles with and without fasteners as well as evaluation of low-cycle fatigue fracture potential

Initial FEM models have been developed, compared to experimental data, and are described in this document. Since validated models will continue to play a crucial role in the understanding of the behavior of the protected zone, continued improvement of the FEM model will ultimately be conducted by other project team members.

Several alternative test configuration concepts were explored. This exploration revealed the sensitivity of boundary conditions in full-scale tests. Ultimately a coupon test configuration was decided to be the most economic way to simulate the stress and strain demands placed on the protected zone. Further design of the coupon test configuration and subsequent physical coupon testing will be completed by other project team members and reported in (Eatherton, 2013)

As previously discussed in this document, up until now, there has been almost no study focused on the behavior of moment connections with defects. It is expected that the work performed in this study will provide a basis for developing alternate test methods to study the issue as well as providing key data for the effect of PAFs and puddle welds on the seismic behavior of moment connections.

REFERENCES

AIJ. (1997). *Full-Scale Test on Plastic Rotation Capacity of Steel Wide-Flange Beams Connected with Square Tube Steel Columns.* Osaka (in Japanese with attached abridged English version): Kinki Branch of the Architectural Institute of Japan, Steel Committee.

AISC (2010a). (2010). *ANSI/AISC 341-10 Seismic Provisions for Structural Steel Buildings.* Publishes by AISC.

AISC (2010b). *ANSI/AISC 358-10 Prequalified Connections for Special and Intermediate Steel Moment Frames for Seismic Applications, and supplement No. 1 (2010).* Published by AISC.

ANSYS. (2005). *User Manual Version 9.0.* ANSYS, Inc: Canonsburg, Pennsylvania.

ASTM A370-07a. (2007). *A370-07a Standard Test Methods and Definitions for Mechanical Testing of Steel Products.* ASTM.

ASTM A6/A6M-12. (2012). *A6/A6M-12 Standard Specification for General Requirements for Rolled Structural Steel Bars, Plates, Shapes, and Sheet Piling.*

ATC. (1992). *ATC-24: Guidelines for Cyclic Testing of Components of Steel Structures.* Redwood City, CA: Applied Technology Council.

Bao, Y., & Wierzbicki, T. (2004). On fracture locus in the equivalent strain and stress triaxiality space. *International Journal of Material Sciences* , 81-98.

Coffin, L. F. (1968). *Introduction to High-temperature Low-cycle Fatigue.* Ottawa, Canada: presented at 1967 SESA Spring Meeting.

Coffin, L., & Tavernelli, J. (1959). The cyclic straining and fatigue of metals. *Trans Metall Soc AIME* , 215:794-807.

Eatherton, M. R., Toellner, B. W., Watkins, C. E., & Abbas, E. (2013). *Experimental Investigation on the Effect of Powder Actuated Fasteners on Seismic Performance of Moment Connections.* Virginia TEch SEM Report Series.

Eldermash, M., Abu-Lebdeh, T., & Al Nasra, M. (2012). Finite Element Analysis of Large Capacity Endplate Steel Connections. *Journal of Computer Science* , 482-493.

Fell, B. V., Myers, A. T., Deierlein, G. G., & Kanvinde, A. M. (2006). Testing and Simulation of Ultra-Low Cycle Fatigue and Fracture in Steel Braces. *Eighth National Conference on Earthquake Engineering.* San Francisco, CA.

Hancock, J. W., & Mackenzie, A. C. (1976). On the mechanisms of ductile failure in high-strength steels subjected to multi-axial stress states. *J. Mech. Phys. Solids* , 147-160.

Hilti Products - Direct Fastening. (n.d.). Retrieved from Hilti: http://www.hilti.com/holcom/

Kanvinde, A. M., & Deierlein, G. G. (2007). Cyclic Void Growth Model to Assess Ductile Fracture Initiation in Structural Steels due to Ultra Low Cycle Fatigue. *Journal of Engineering Mechanics* , 701-712.

Kaufmann, E. J., Metrovich, B., & Pense, A. W. (2001). *ATLSS Report No. 01-13: Characterization of Cyclic Inelastic Strain Behavior On Properties of A572 Gr. 50 and A913 Gr. 50 Rolled Sections.*

Manson, S. S. (1954). *Behavior of Materials Under Conditions of Thermal Stress.* National Advisory Committee for Aeronautics.

Nip, K. H., Gardner, L., Davies, C. M., & Elghazouli, A. Y. (2010). Extremely low cycle fatigue tests on structural carbon steel and stainless steel. *Journal of Constructional Steel Research* , 96-110.

Pachoumis, D. T., Galoussis, E. G., Kalfas, C. N., & Efthimiou, I. Z. (2010). Cyclic Performance of Steel Moment-Resisting Connections with Reduced Beam Sections - Experimental Analysis and Finite Element Model Simulation. *Engineering Structures* , 2683-2692.

Pantelides, C. P., Reavely, L. D., & Adan, S. M. (2009). Analyzing Steel Moment-Resisting Connections Using Finite Element Analysis. In *Computational Structural Dynamics and Earthquake Engineering* (p. Chapter 23). London: Taylor and Francis.

Popov, E. (March 1996). *"Full-Scale Steel Beam-Column Connection Tests" in Technical Report: Experimental Investifations of Beam-Column Subassemblages (SAC 96-01, Part 2).* SAC Joint Venture Partnership.

Ricles, J. M., Fisher, J. W., Lu, L. -W., & Kaufmann, E. J. (2002). Development of Improved Welded Moment Connections for Earthquake-Resistant Design. *Journal of Constructional Steel Research, Vol. 58* , 565-604.

SAC Joint Venture. (2000a). *Development and Evaluation of Improved Details for Ductile Welded Unreinforced Flange Connections.* Bethlehem, PA: Report No. SAC/BD-00/24.

SAC Joint Venture. (2000b). *FEMA-355D: State of the Art Report on Connection Performance.*

SAC Joint Venture. (1996). *Technical Report: Experimental Investigation of Beam-Column Subassemblages.* Sacramento, CA: Rep. No. SAC 96-01.

Schafer, B. W., Ojdrovic, R. P., & Zarghamee, M. S. (2000). Triaxiality and Fracture of Steel Moment Connections. *Journal of Structural Engineering* , 1131-1139.

Simulia. (2010). *Abaqus/CAE 6.10-2, User Manual Version 6.10.* Providence, Rhode Island: Dassault Systemes Simulia, Inc.

Sumner, E. A., Mays, T. W., & Murray, T. M. (2000, May). Cyclic Testing of Bolted Moment End-Plate Connections. *Research Report No. CE/VPI-ST-00/03, SAC Report No. SAC/BD-00/21* .

Timoshenko, S. (1955). *Strength of Materials.* Huntington, New York: Robert E. Krieger Publishing Co.

Uang, C. M., & Bondad, D. M. (1996). *Dynamic Testing of Full-Scale Moment Connections.*

Watkins, C. (2013). *Effects of Powder Actuated Fasteners in the Protected Zone of Steel Moment Frames.*

Xue, L. (2008). A unified expression for low cycle fatigue and extremely low cycle fatigue and its implication for monotonic loading. *International Journal of Fatigue* , 1691-1699.

APPENDIX

Appendix A - Hysteresis Plots

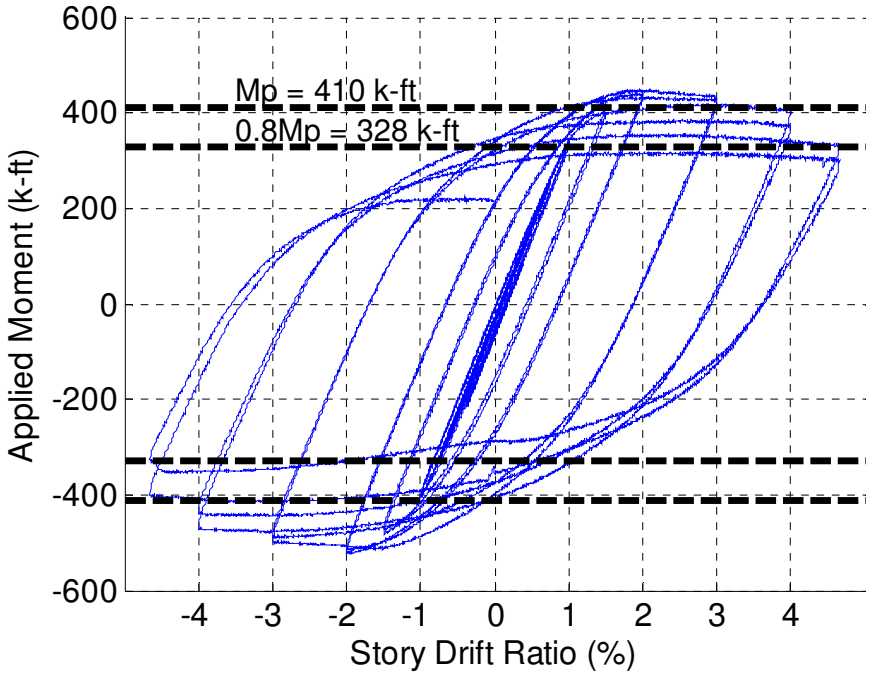

Figure 109: Specimen 1 Hysteresis

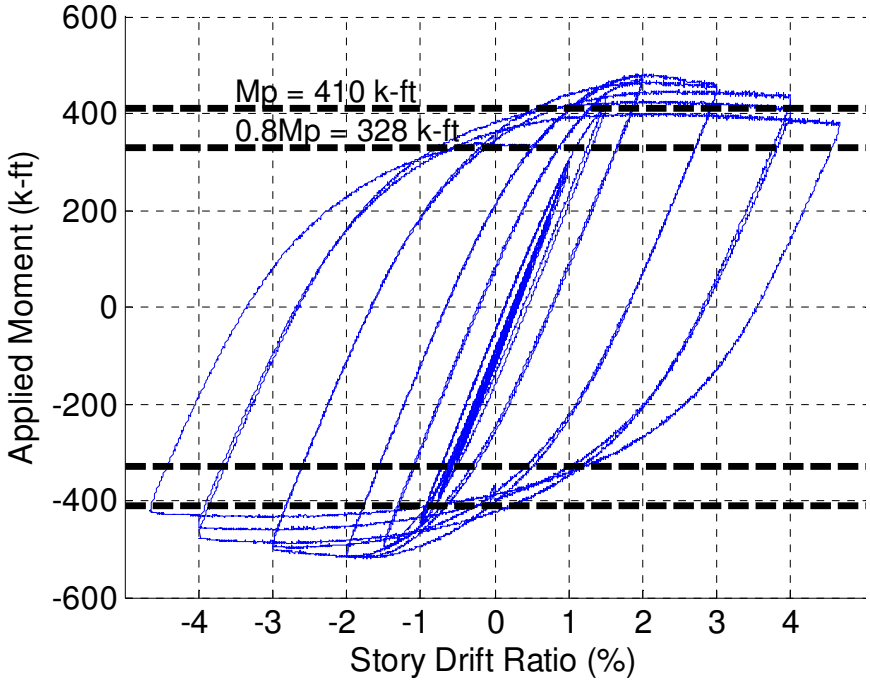

Figure 110: Specimen 2 Hysteresis

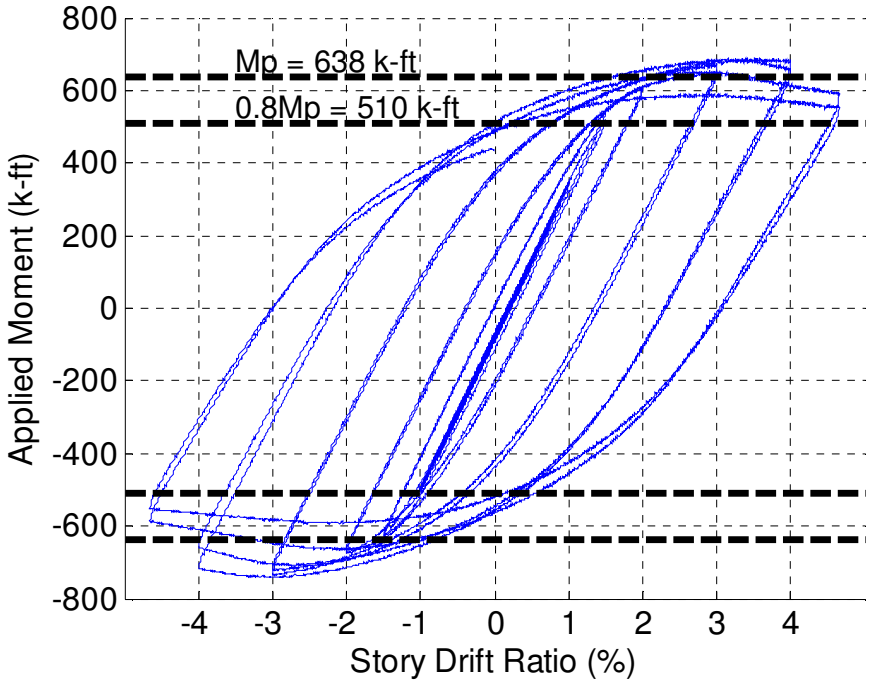

Figure 111: Specimen 3 Hysteresis

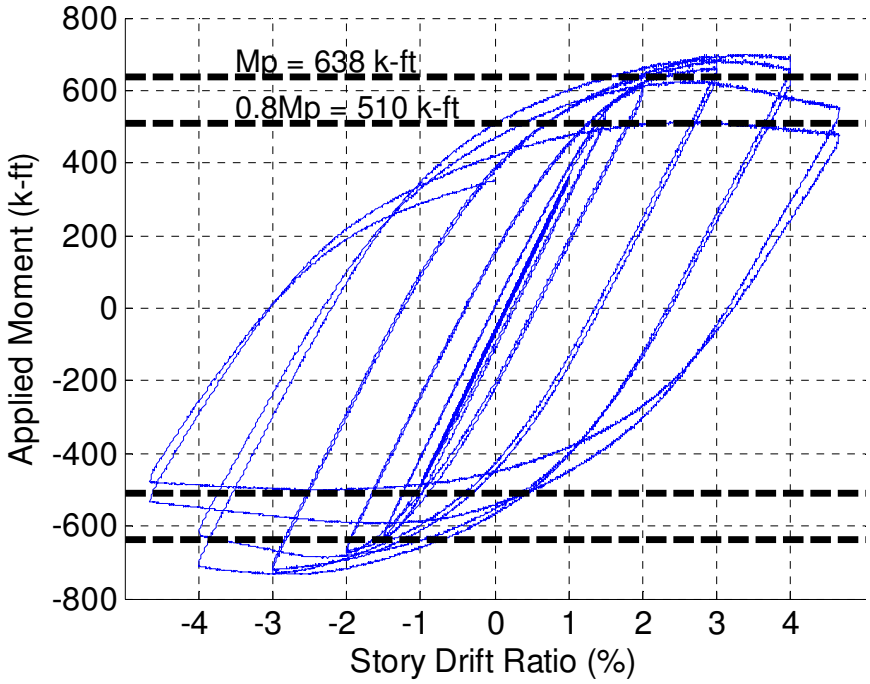

Figure 112: Specimen 4 Hysteresis

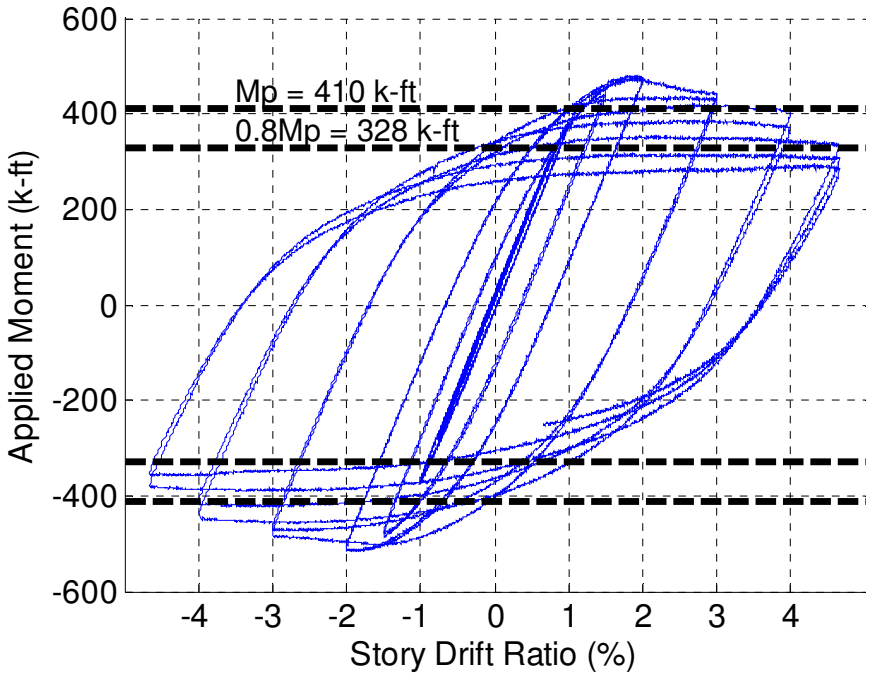

Figure 113: Specimen 5 Hysteresis

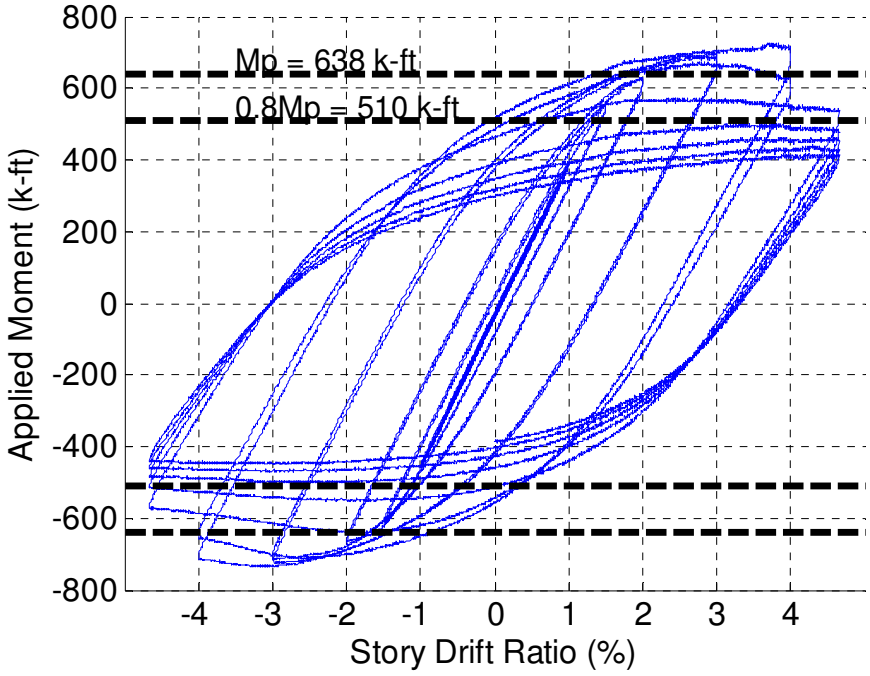

Figure 114: Specimen 6 Hysteresis

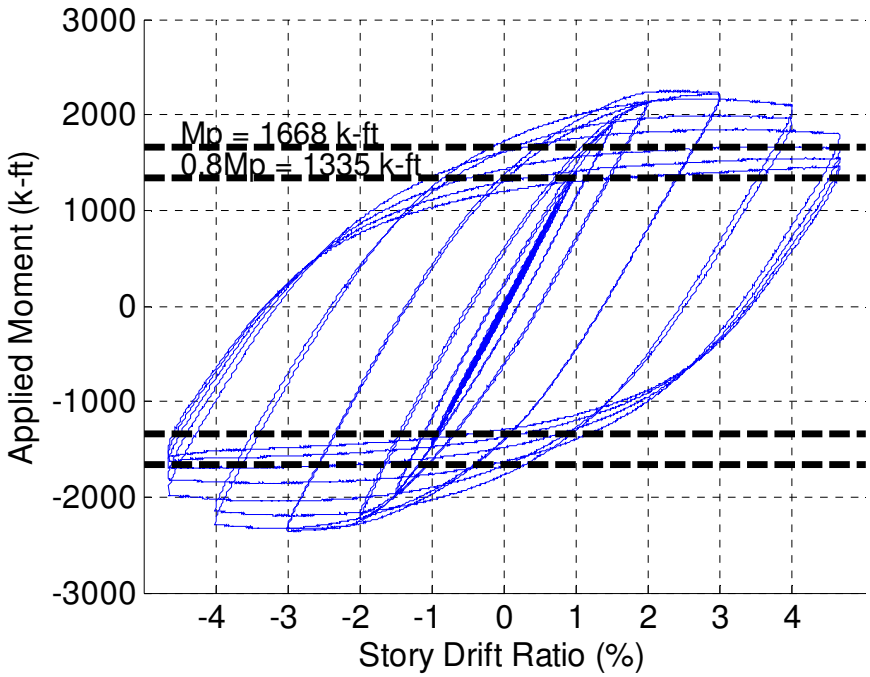

Figure 115: Specimen 7 Hysteresis

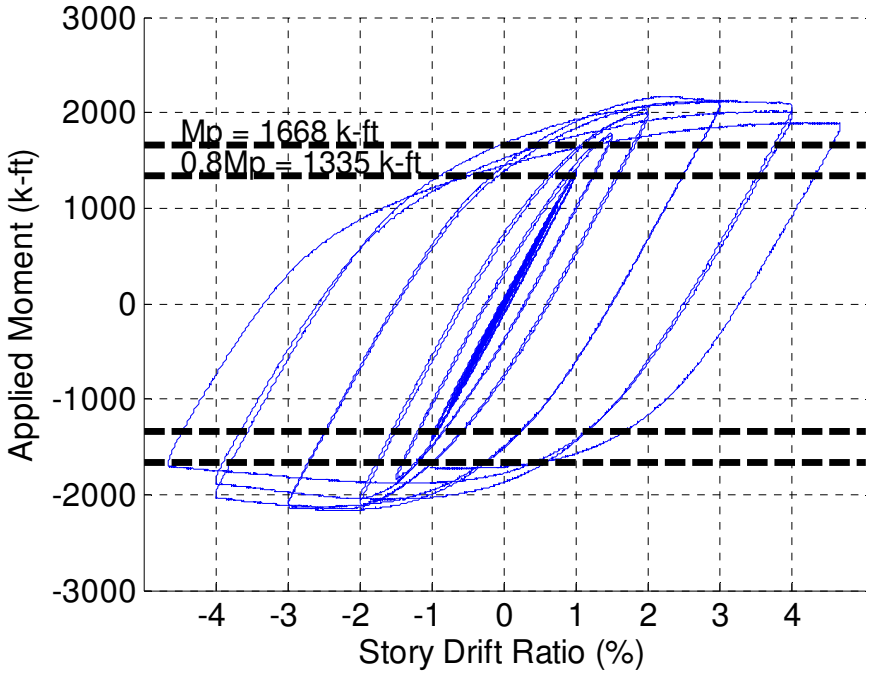

Figure 116: Specimen 8 Hysteresis

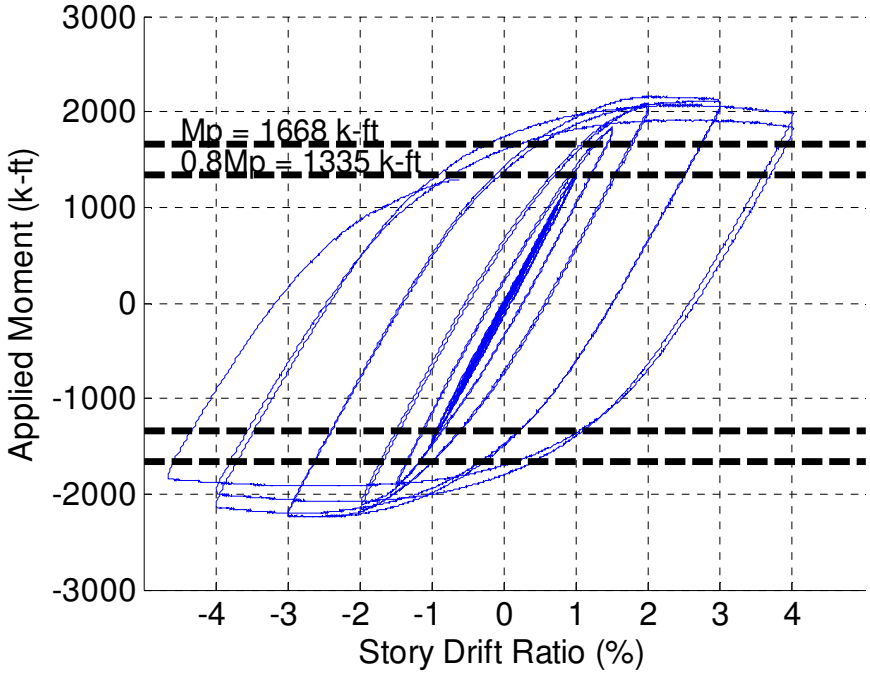

Figure 117: Specimen 9 Hysteresis

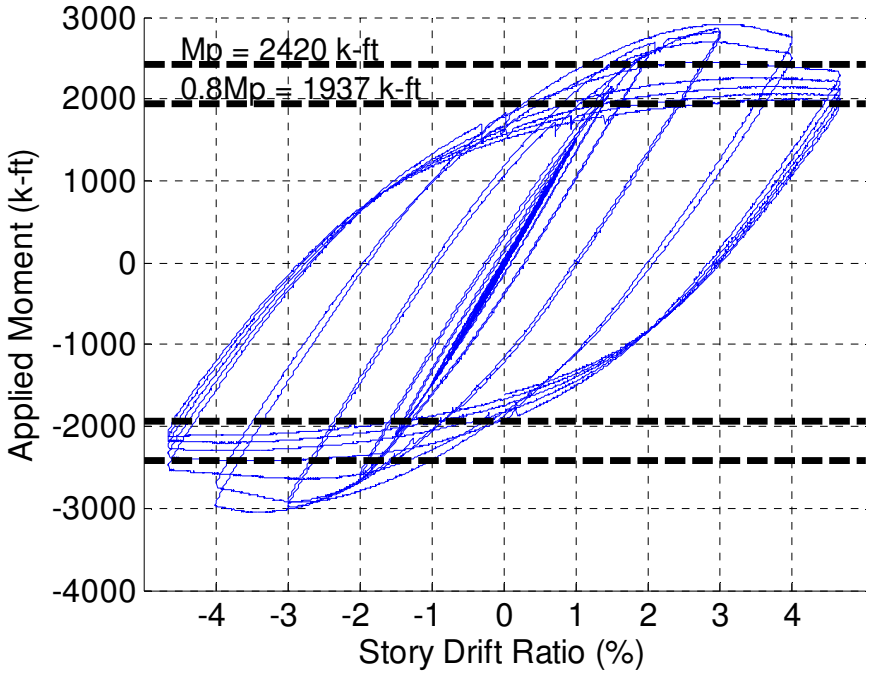

Figure 118: Specimen 10 Hysteresis

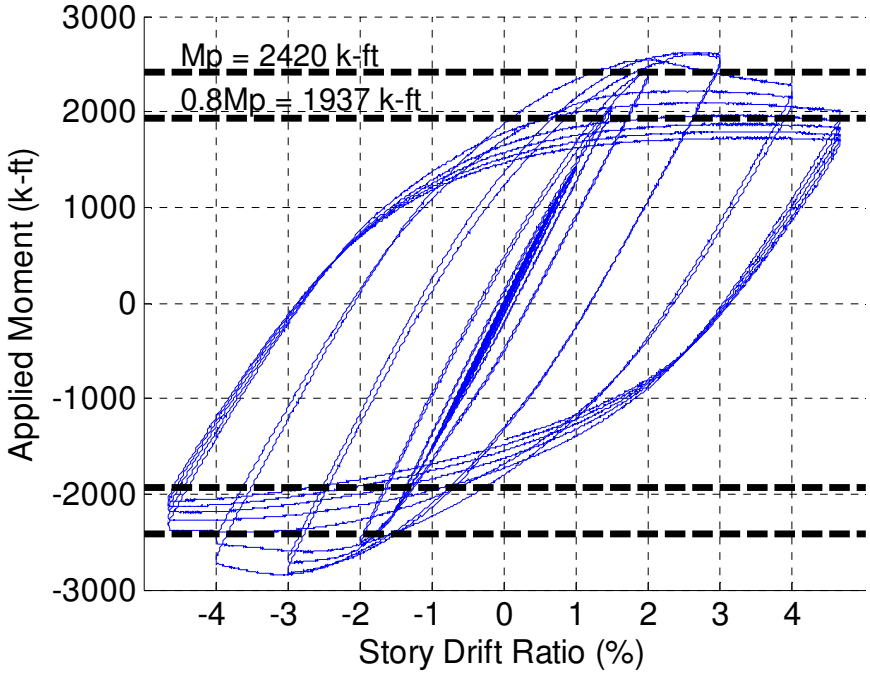

Figure 119: Specimen 11 Hysteresis

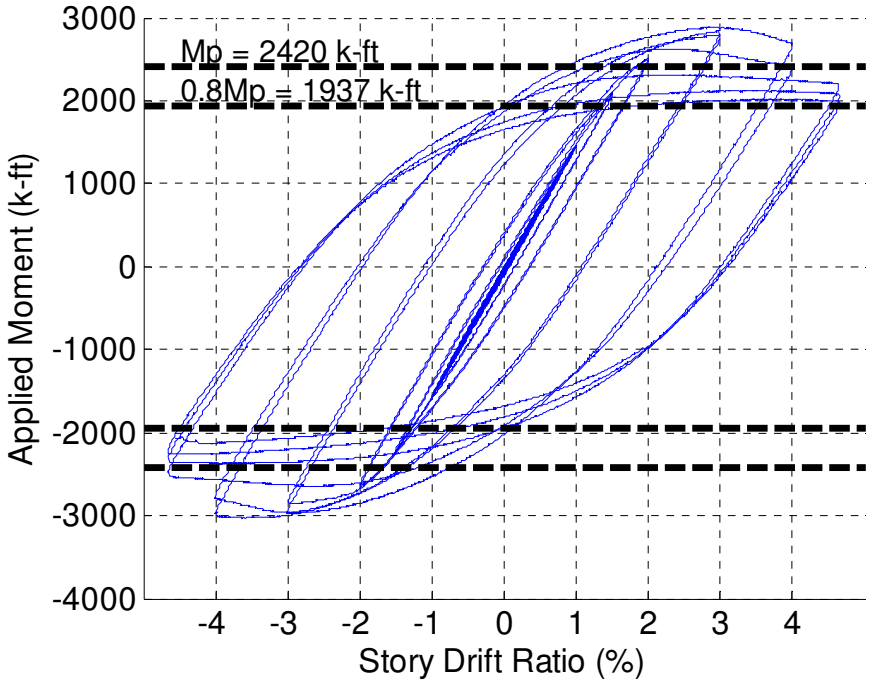

Figure 120: Specimen 12 Hysteresis

Appendix B - Story Drift Decomposition Line Plots

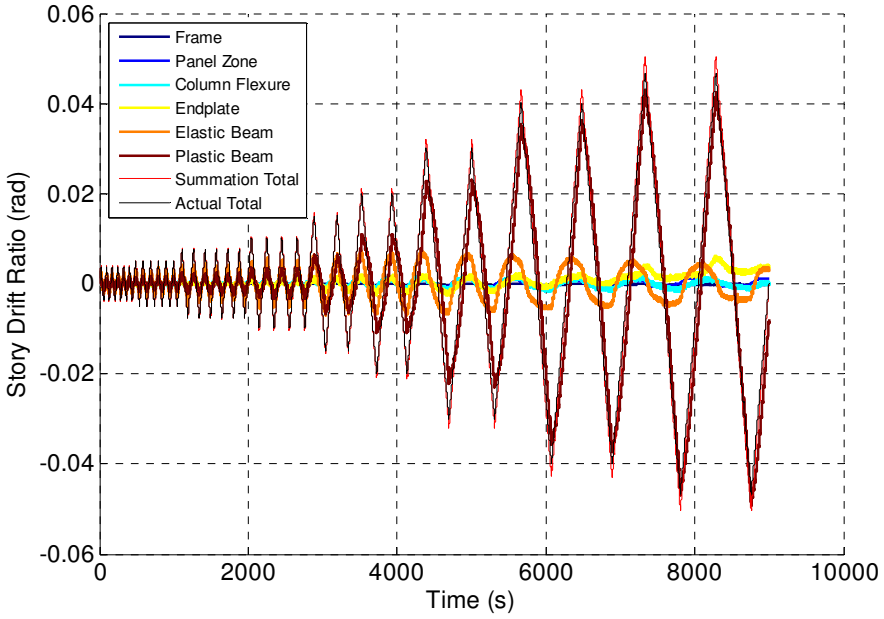

Figure 121: Specimen 1 Story Drift Decomposition Line Plot

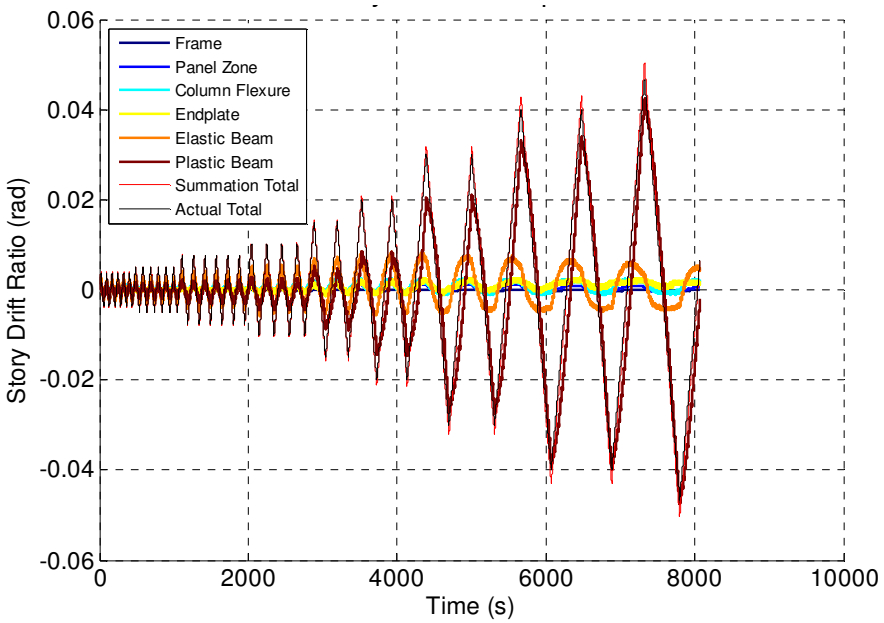

Figure 122: Specimen 2 Story Drift Decomposition Line Plot

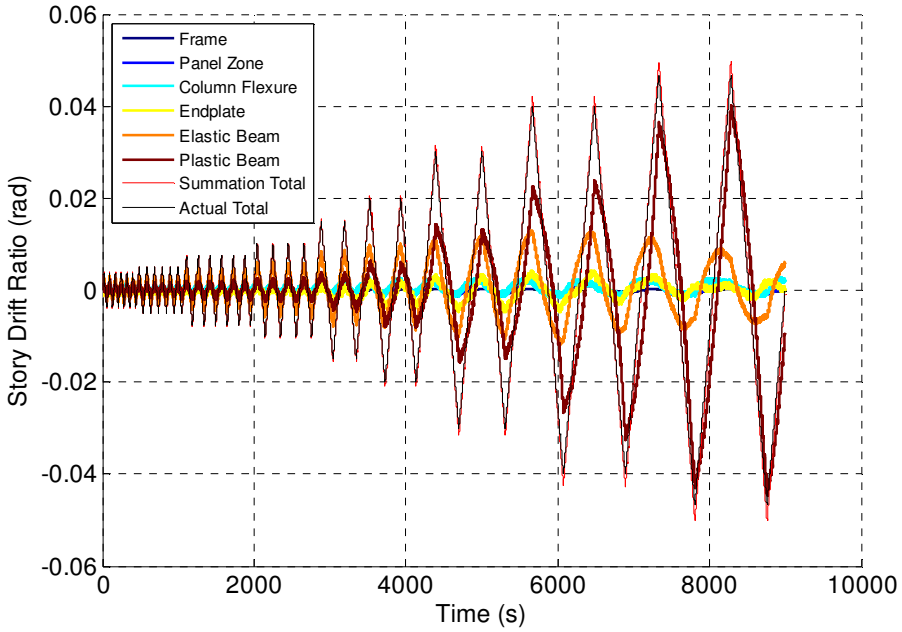

Figure 123: Specimen 3 Story Drift Decomposition Line Plot

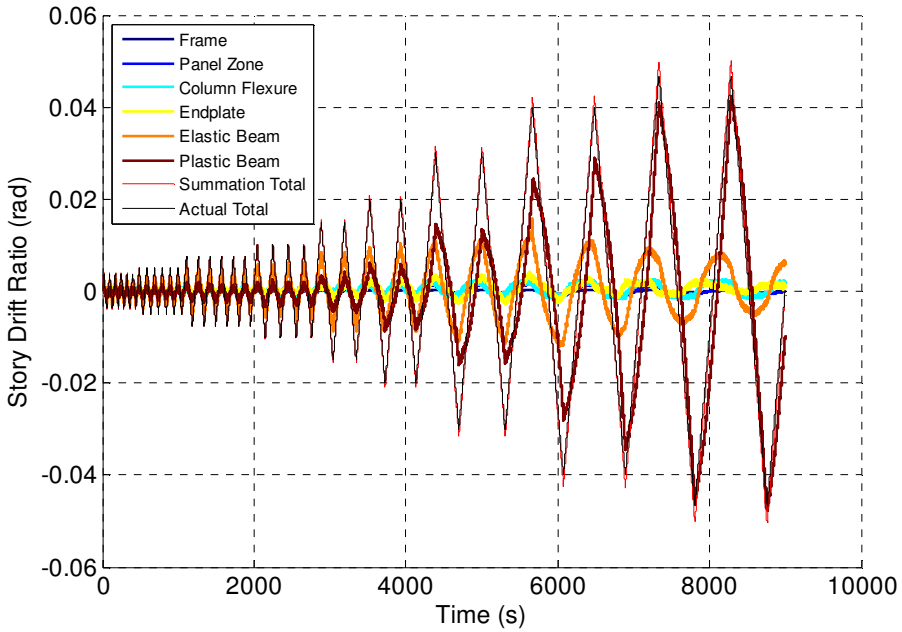

Figure 124: Specimen 4 Story Drift Decomposition Line Plot

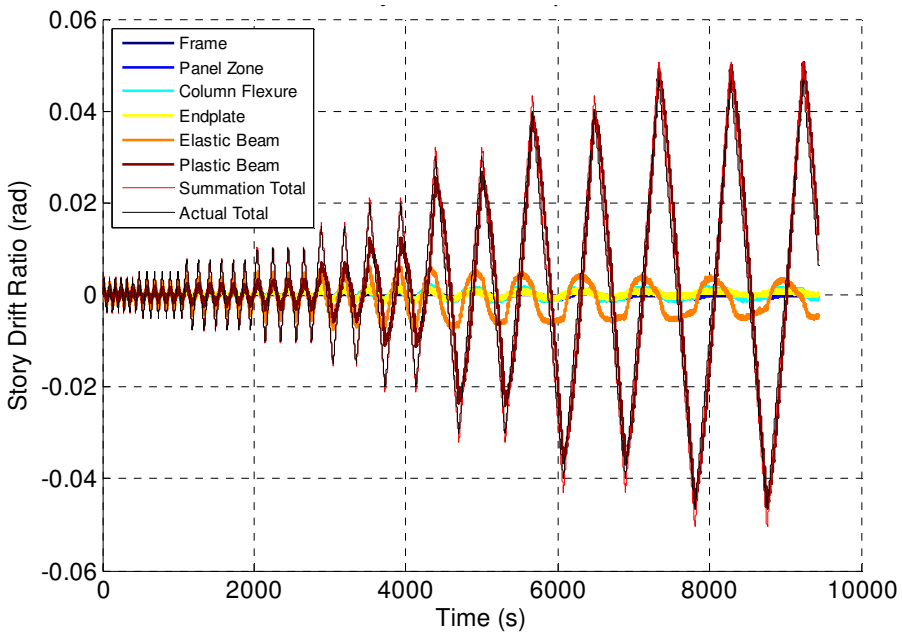

Figure 125: Specimen 5 Story Drift Decomposition Line Plot

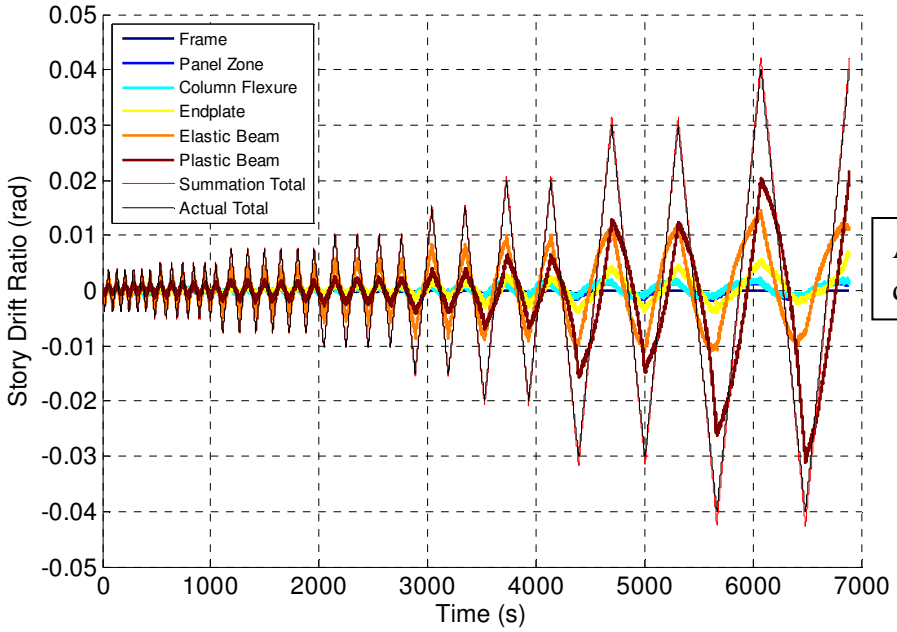

Figure 126: Specimen 6 Story Drift Decomposition Line Plot

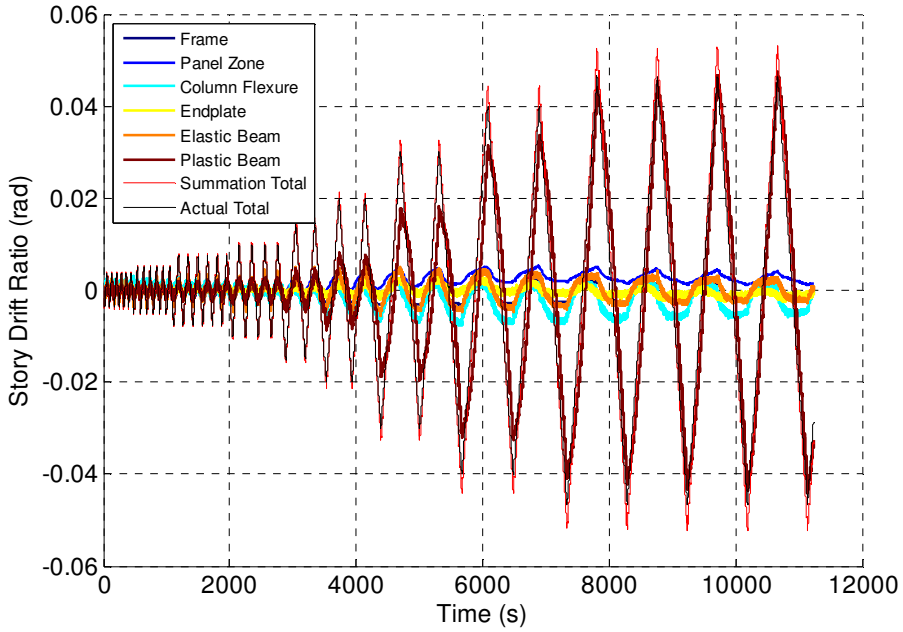

Figure 127: Specimen 7 Story Drift Decomposition Line Plot

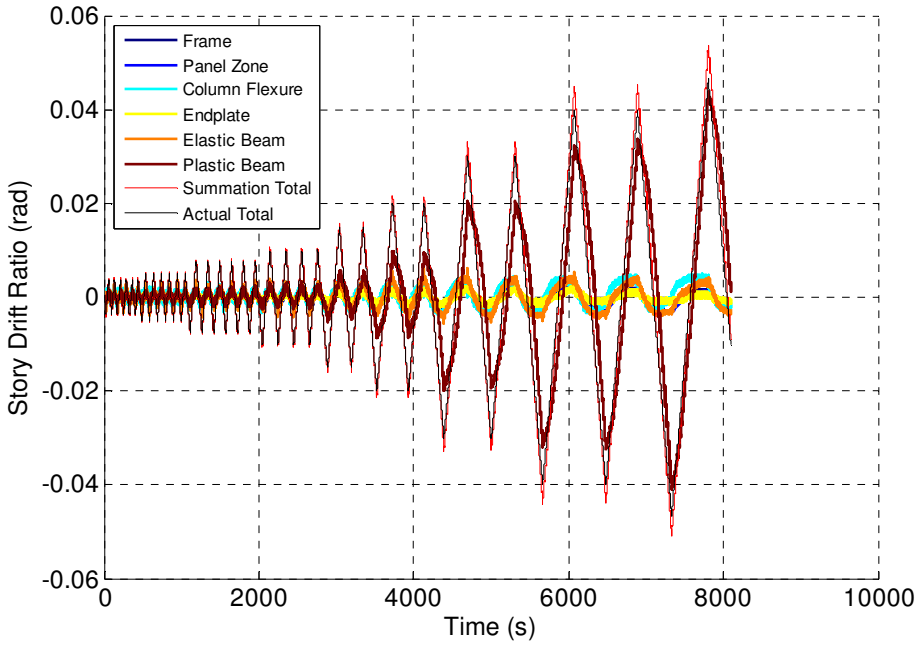

Figure 128: Specimen 8 Story Drift Decomposition Line Plot

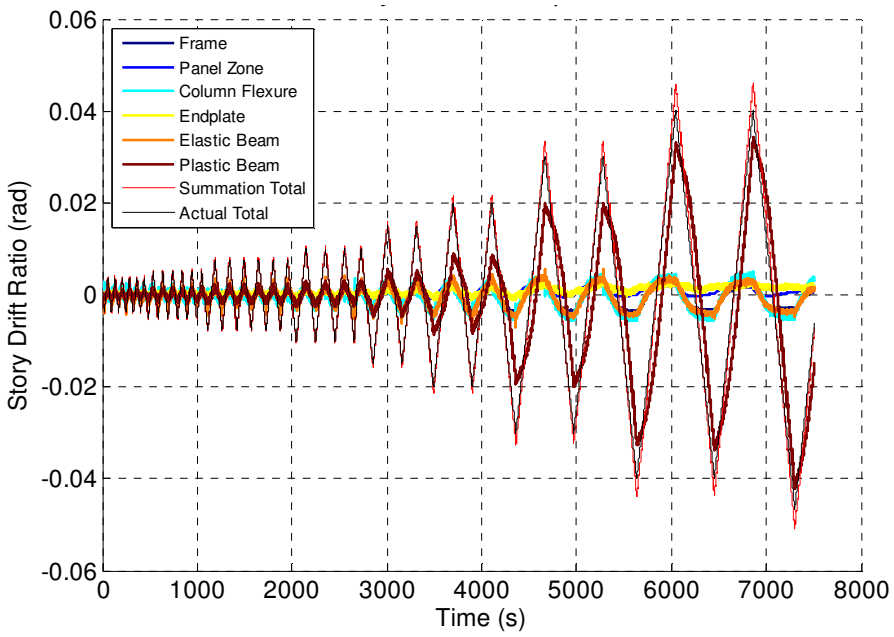

Figure 129: Specimen 9 Story Drift Decomposition Line Plot

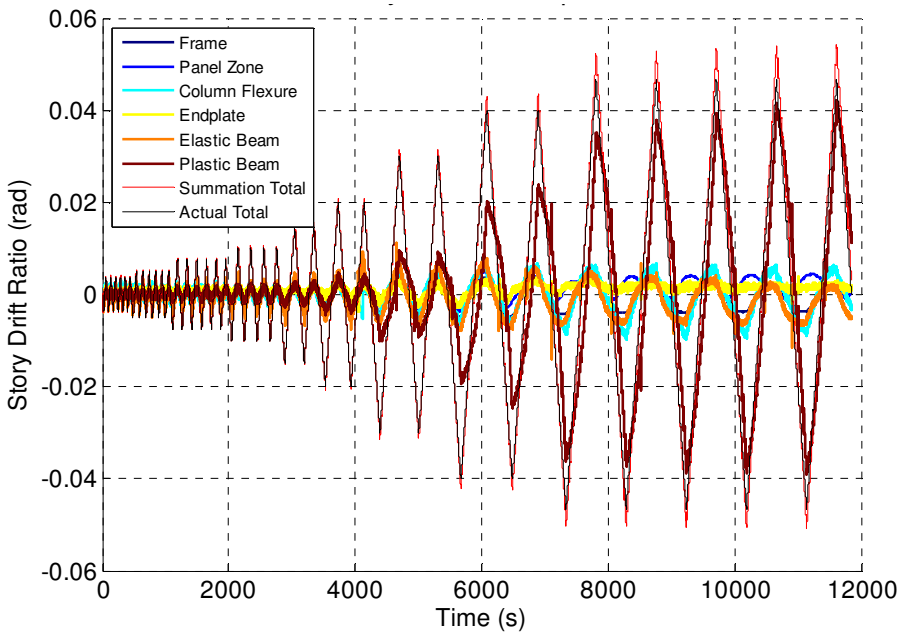

Figure 130: Specimen 10 Story Drift Decomposition Line Plot

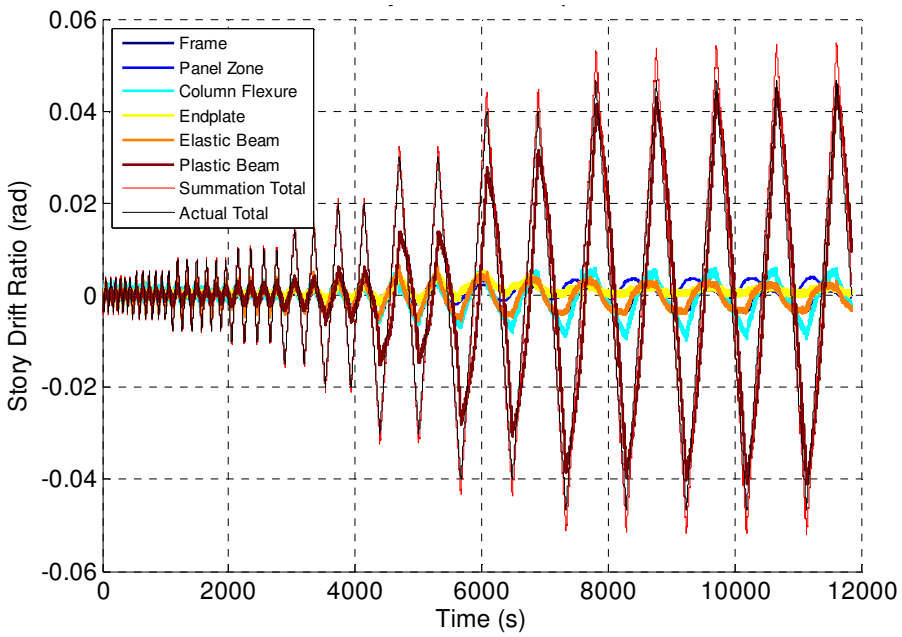

Figure 131: Specimen 11 Story Drift Decomposition Line Plot

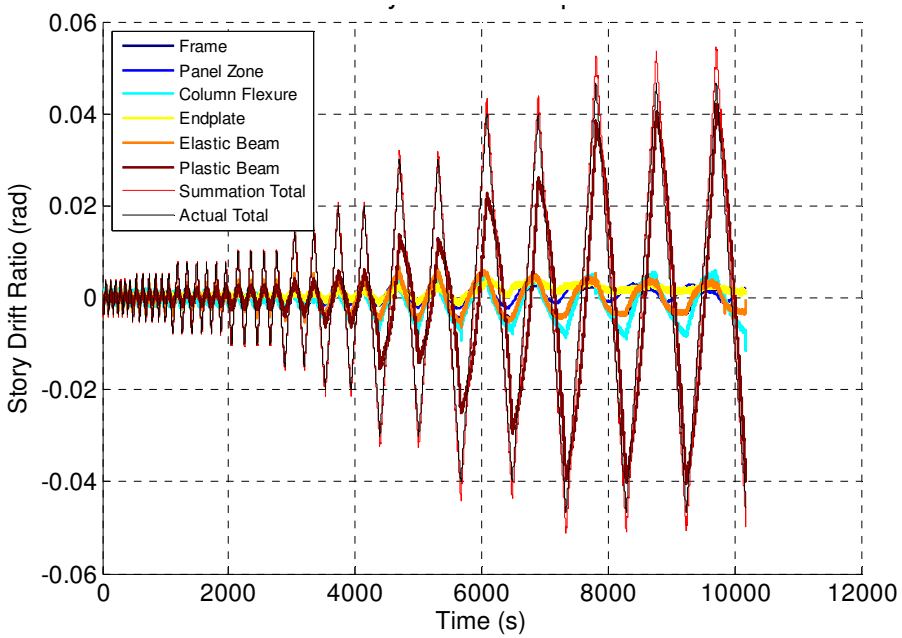

Figure 132: Specimen 12 Story Drift Decomposition Line Plot

Appendix C - Story Drift Decomposition Area Plots

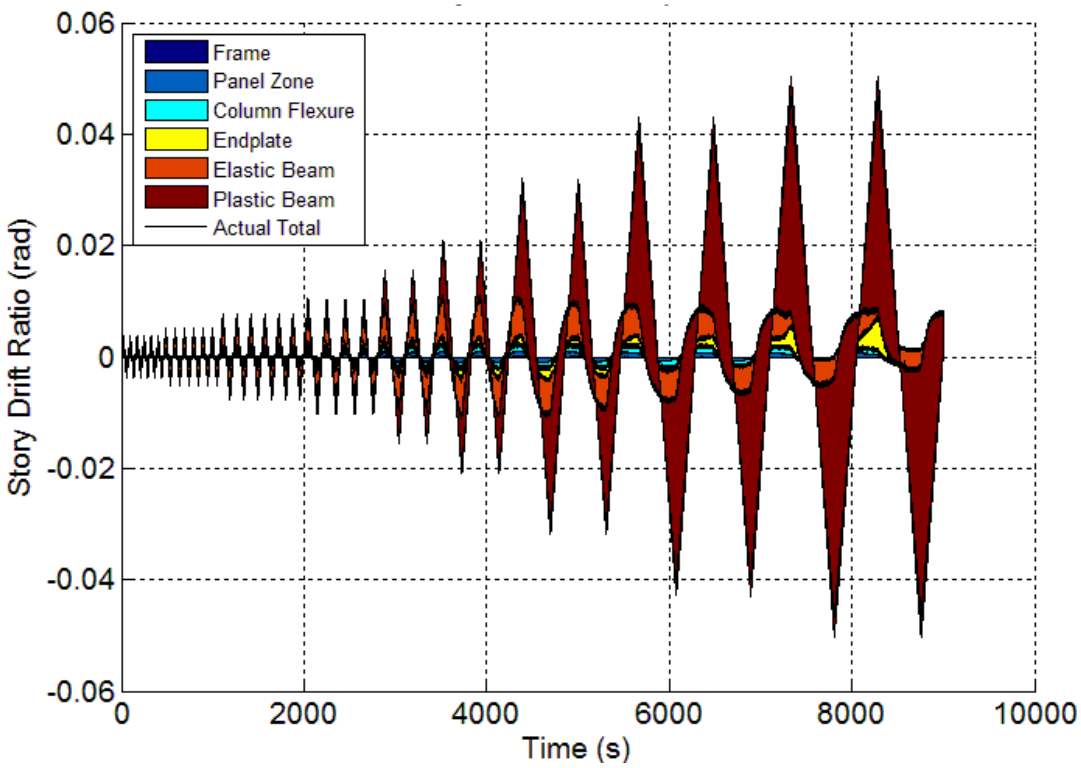

Figure 133: Specimen 1 Story Drift Decomposition Area Plot

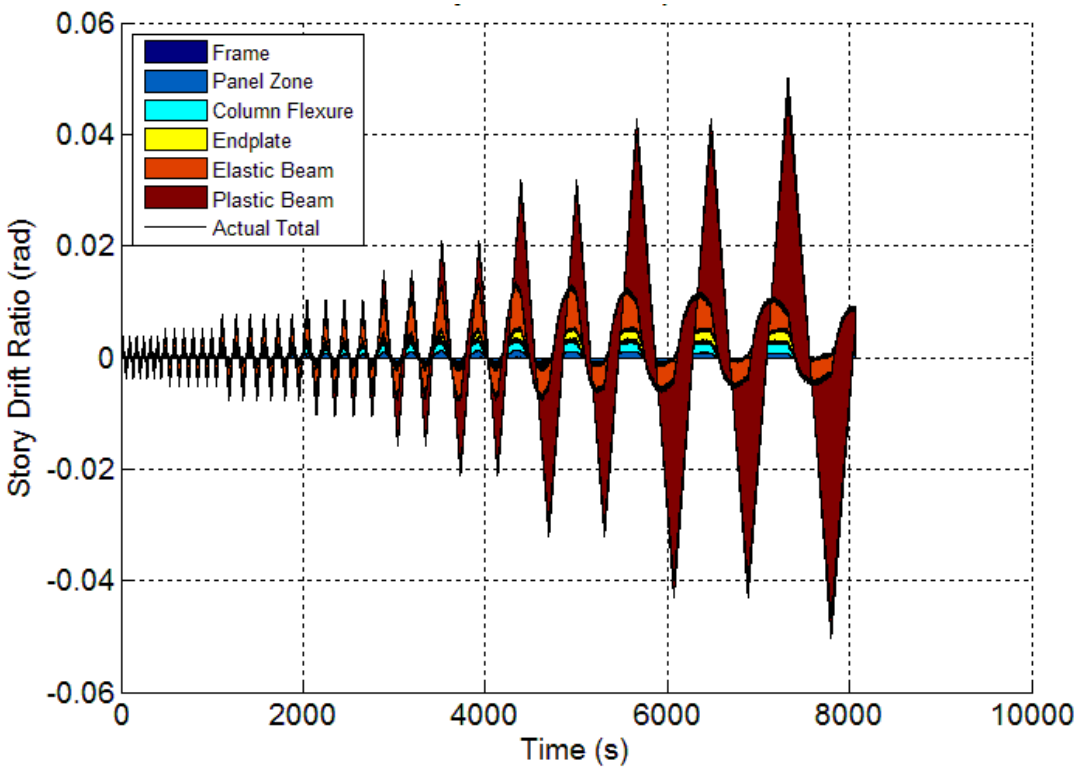

Figure 134: Specimen 2 Story Drift Decomposition Area Plot

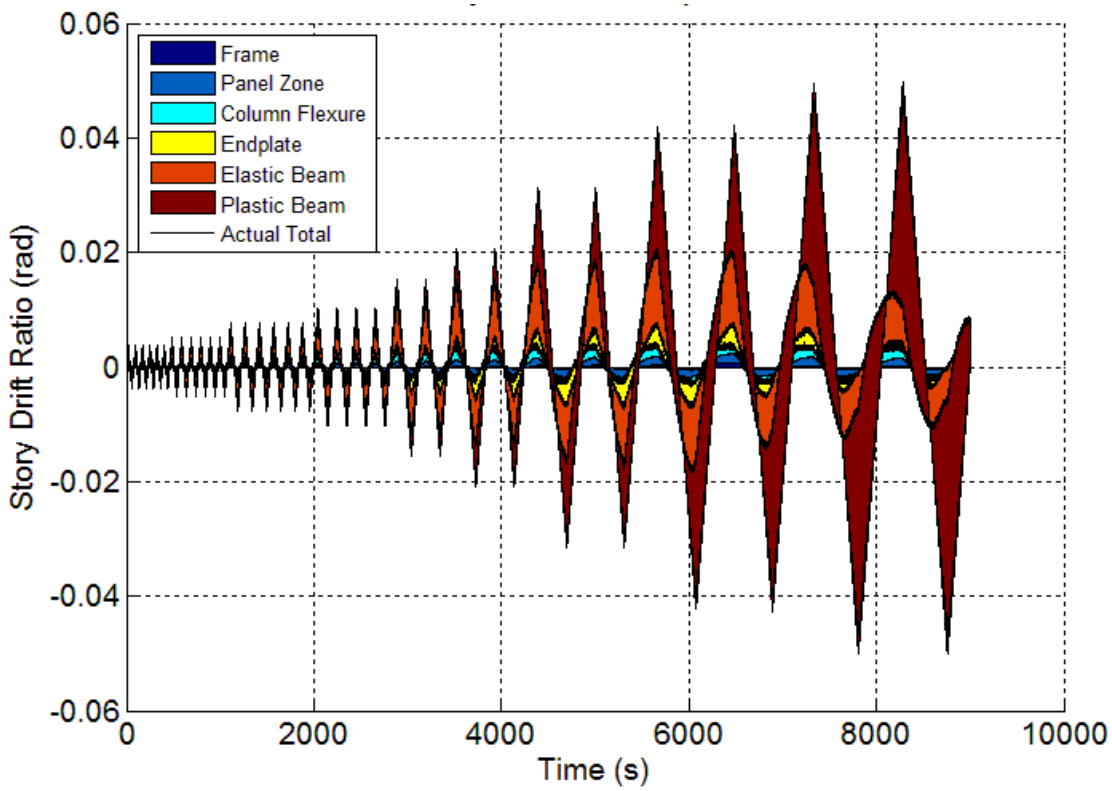

Figure 135: Specimen 3 Story Drift Decomposition Area Plot

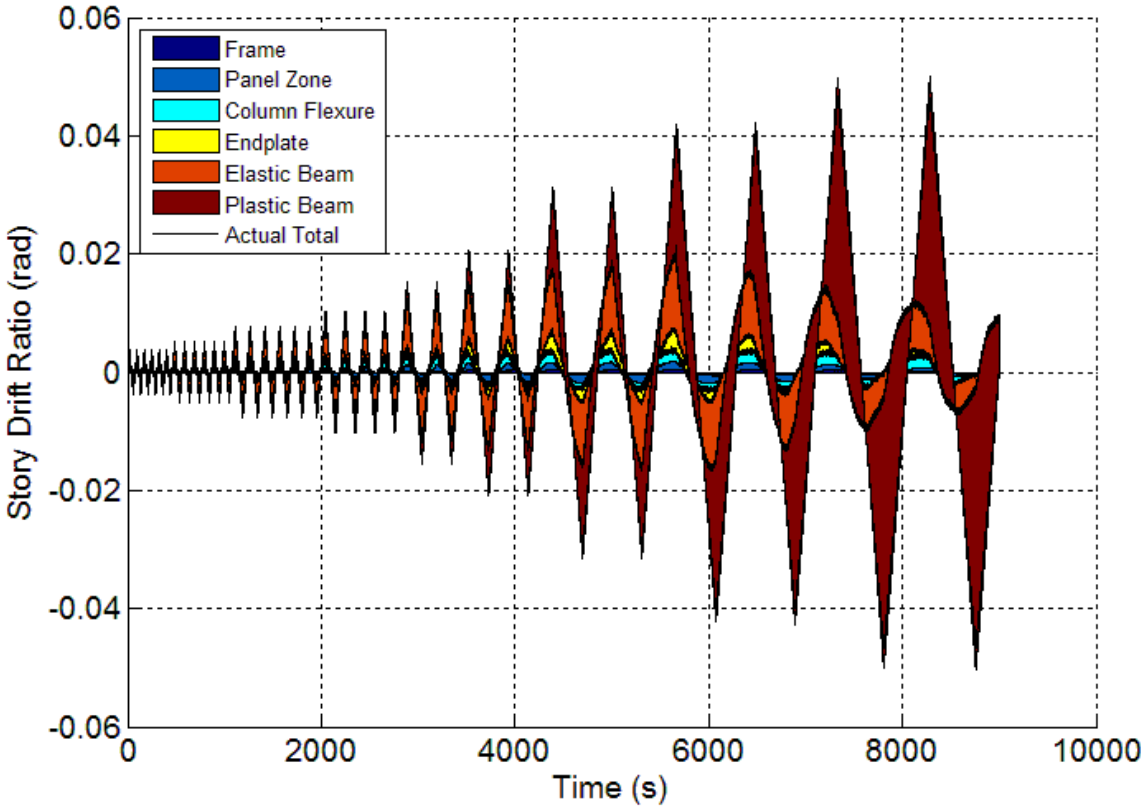

Figure 136: Specimen 4 Story Drift Decomposition Area Plot

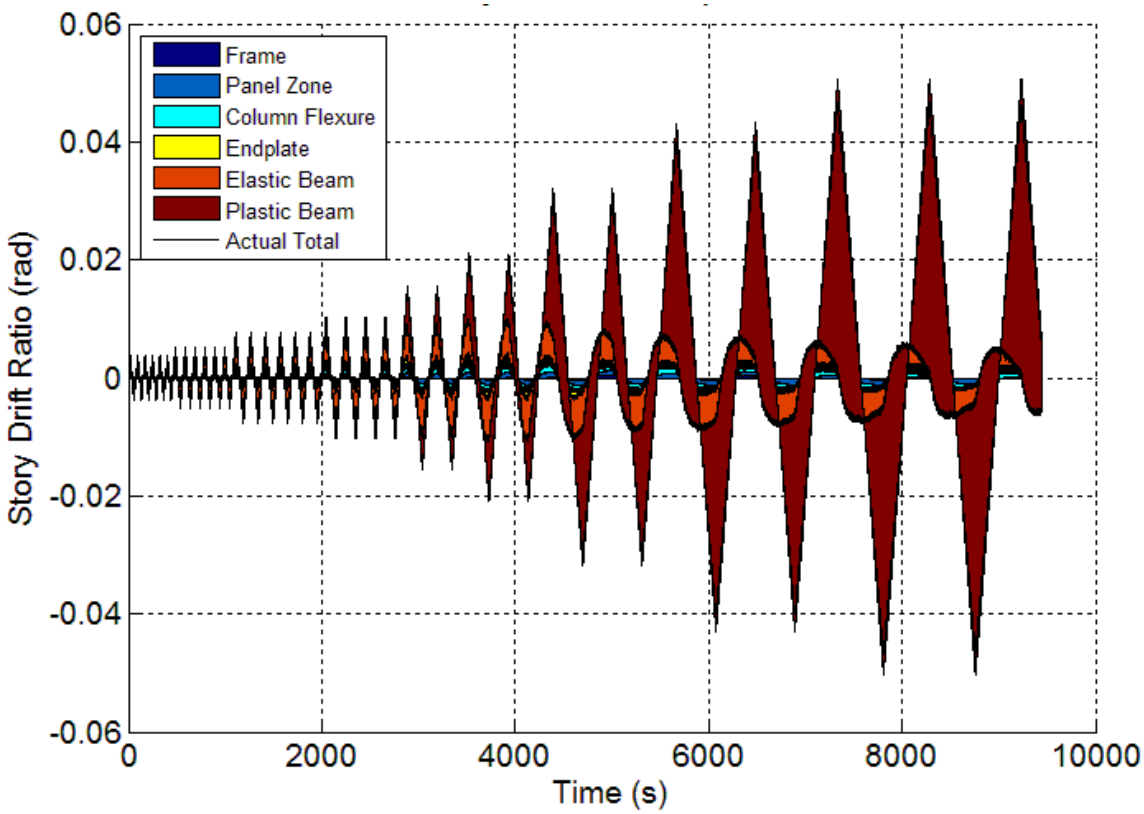

Figure 137: Specimen 5 Story Drift Decomposition Area Plot

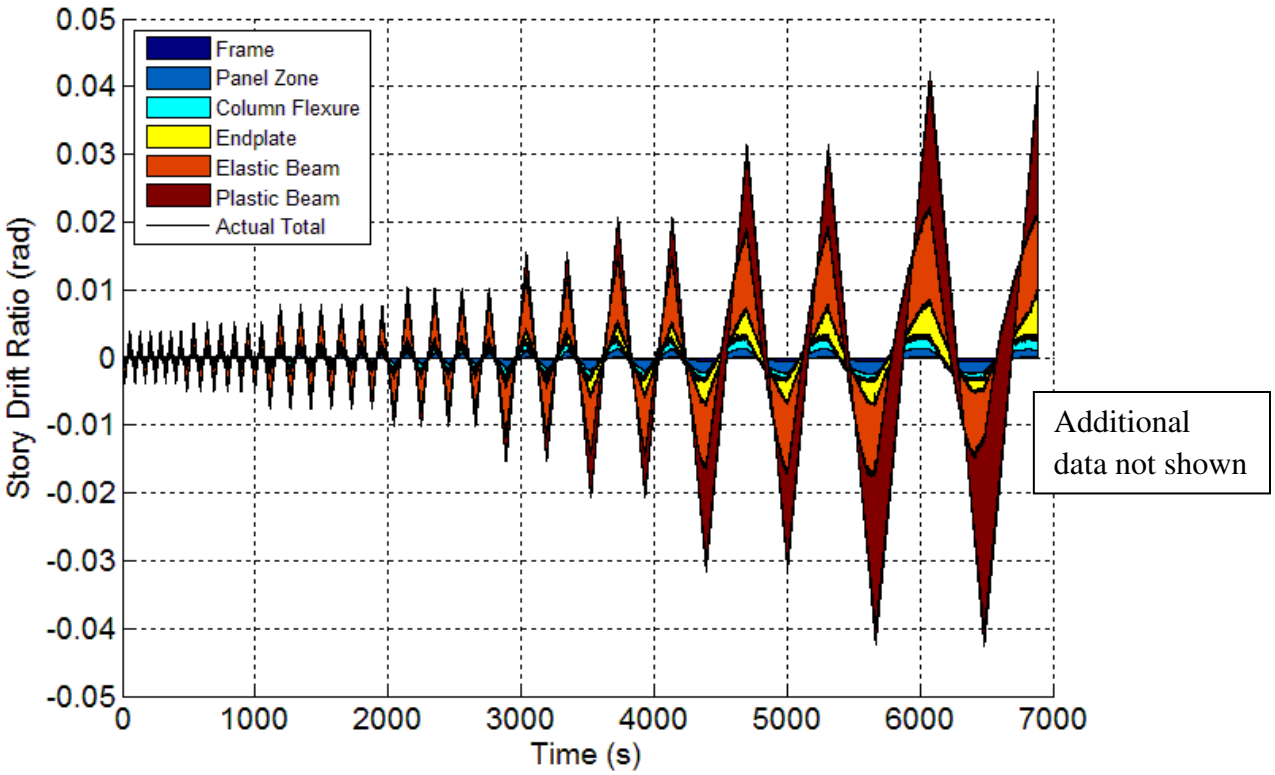

Figure 138: Specimen 6 Story Drift Decomposition Area Plot

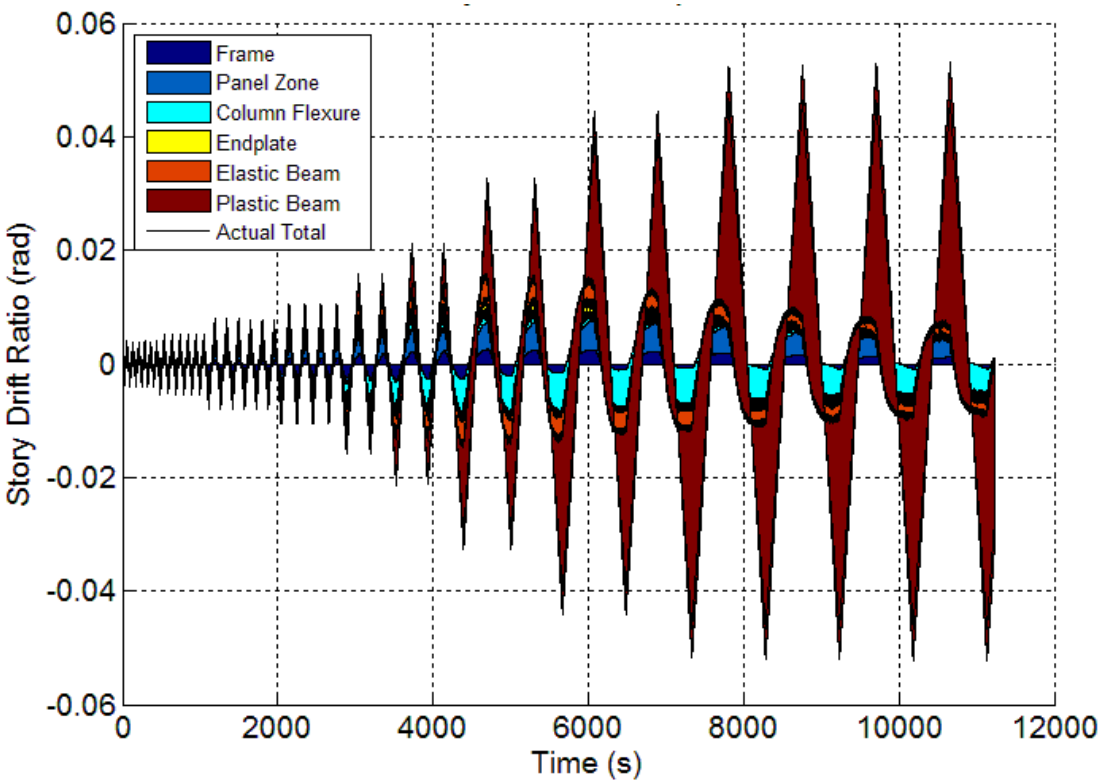

Figure 139: Specimen 7 Story Drift Decomposition Area Plot

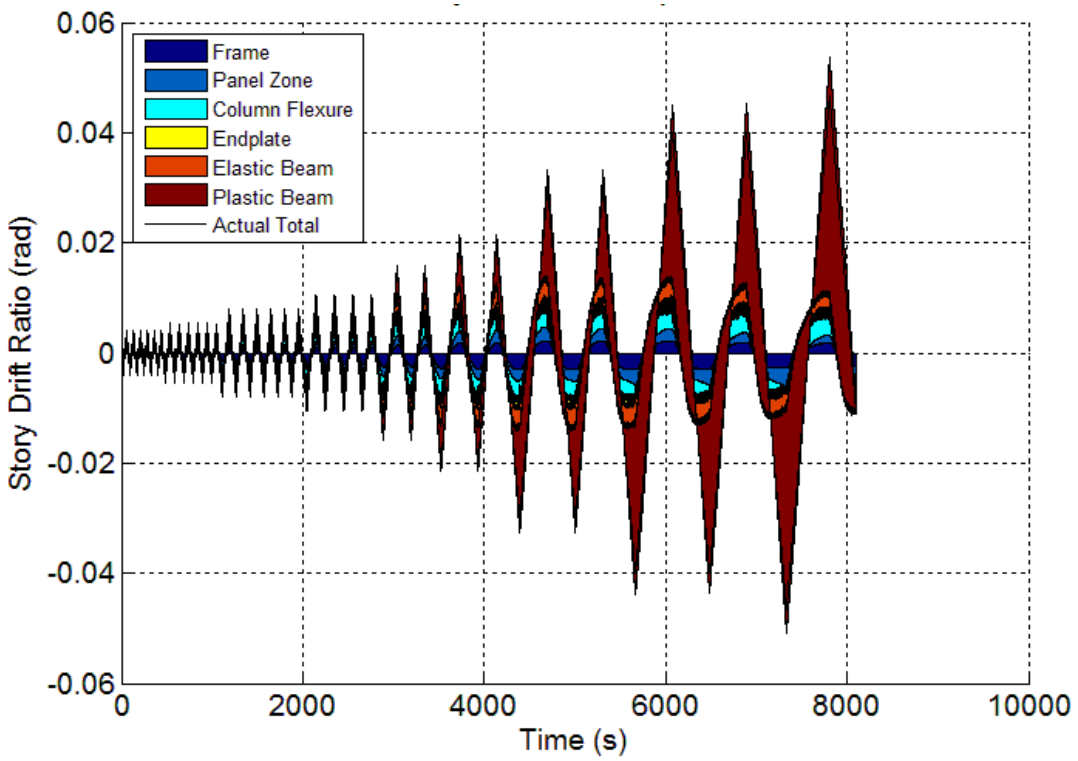

Figure 140: Specimen 8 Story Drift Decomposition Area Plot

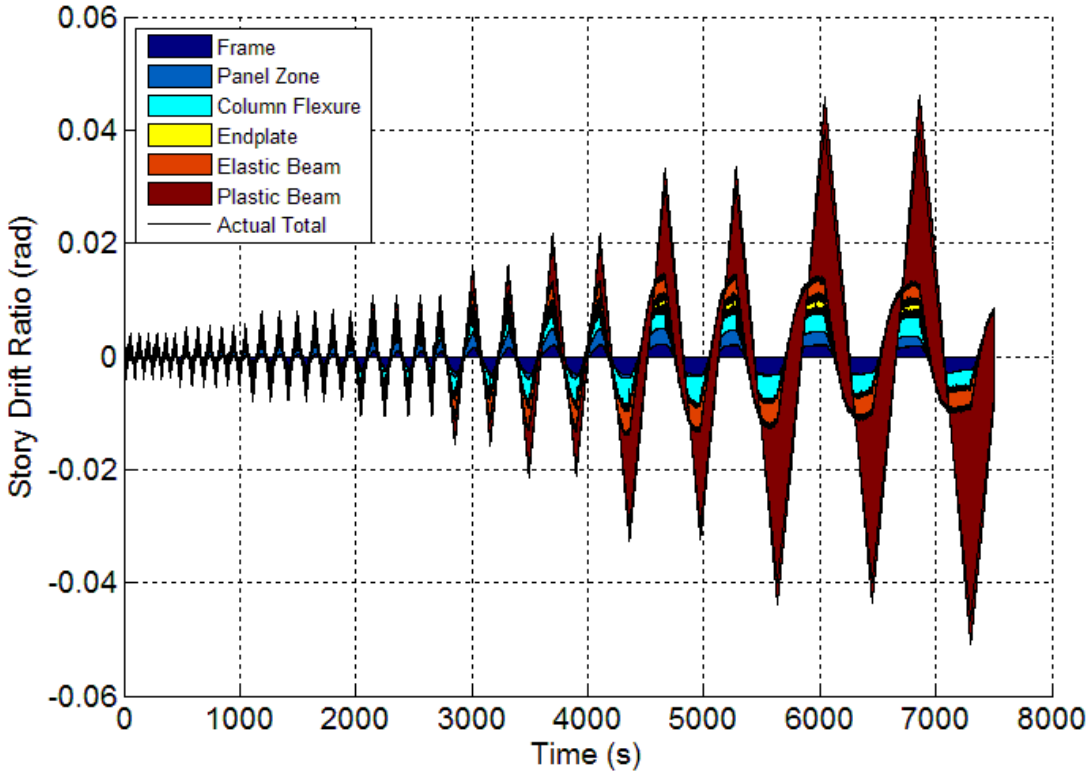

Figure 141: Specimen 9 Story Drift Decomposition Area Plot

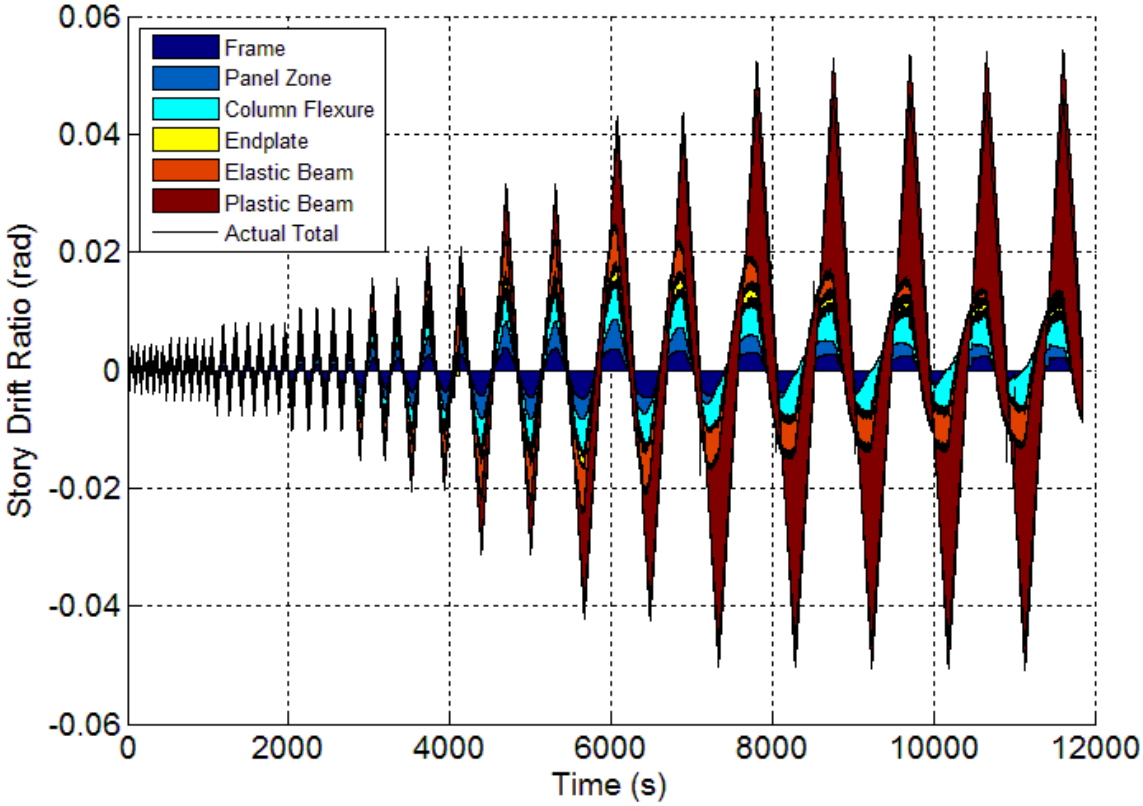

Figure 142: Specimen 10 Story Drift Decomposition Area Plot

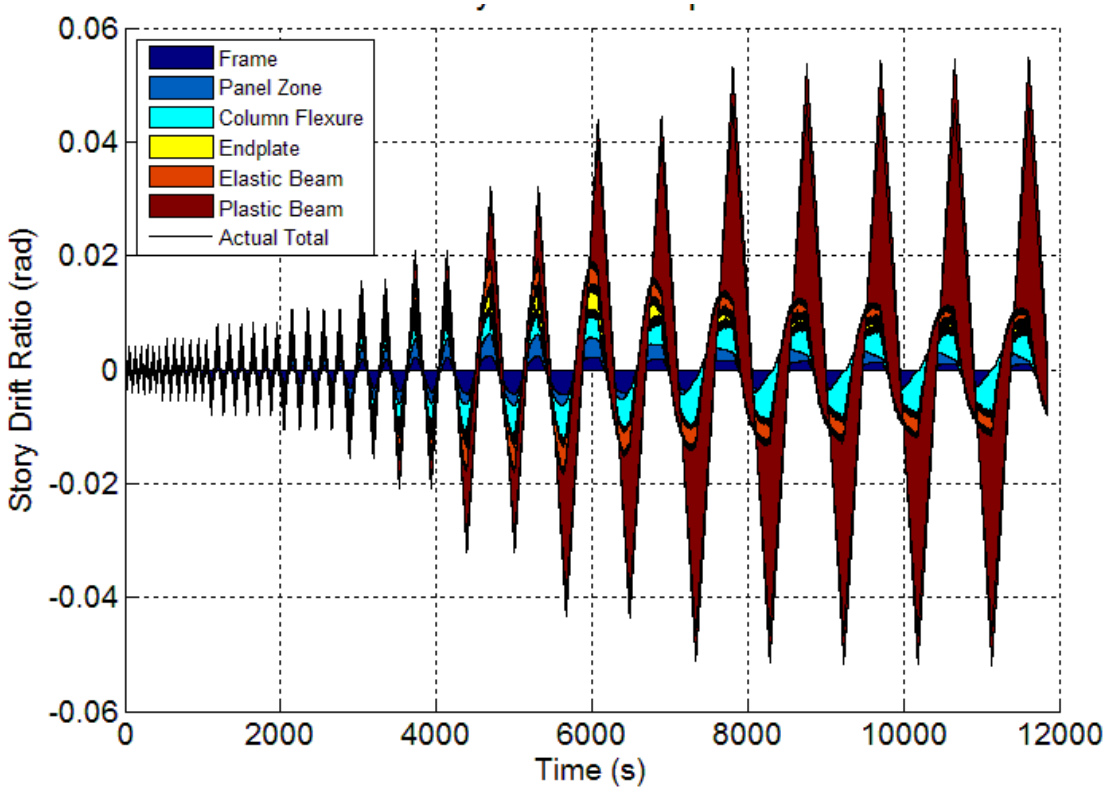

Figure 143: Specimen 11 Story Drift Decomposition Area Plot

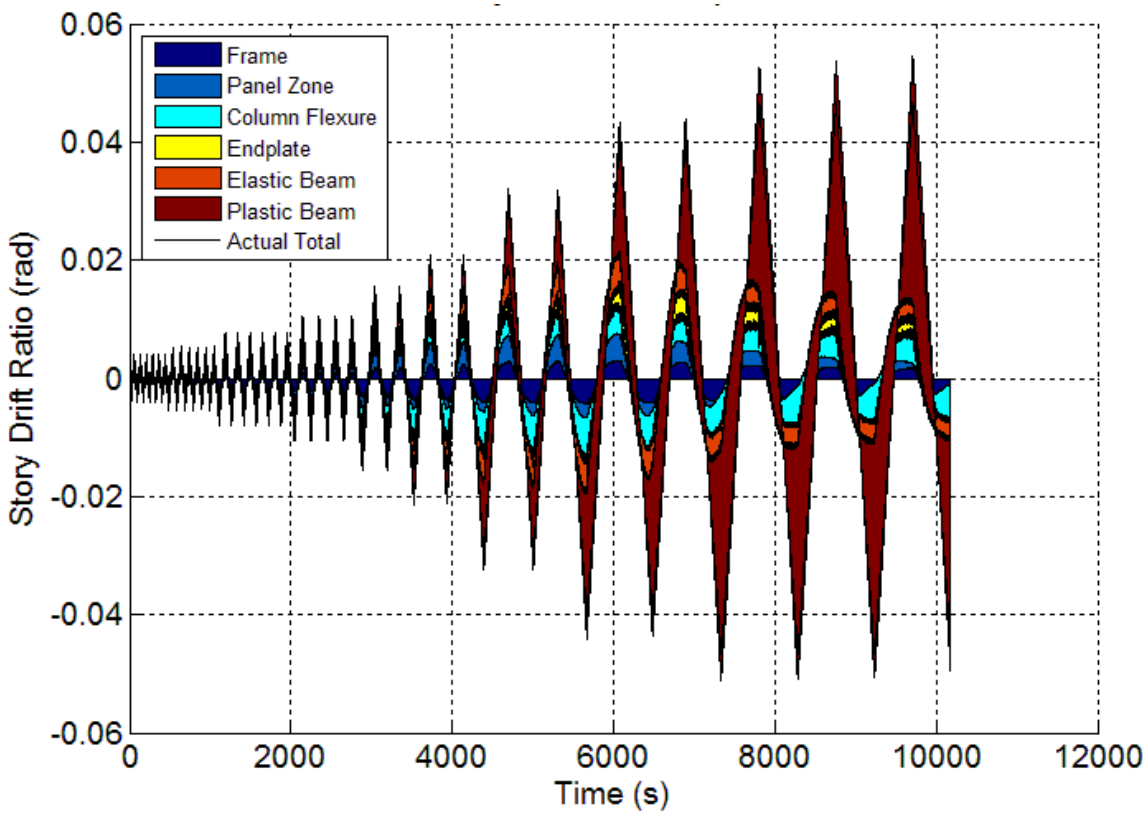

Figure 144: Specimen 12 Story Drift Decomposition Area Plot

Appendix D - Story Drift Decomposition Percentage Contribution Plots

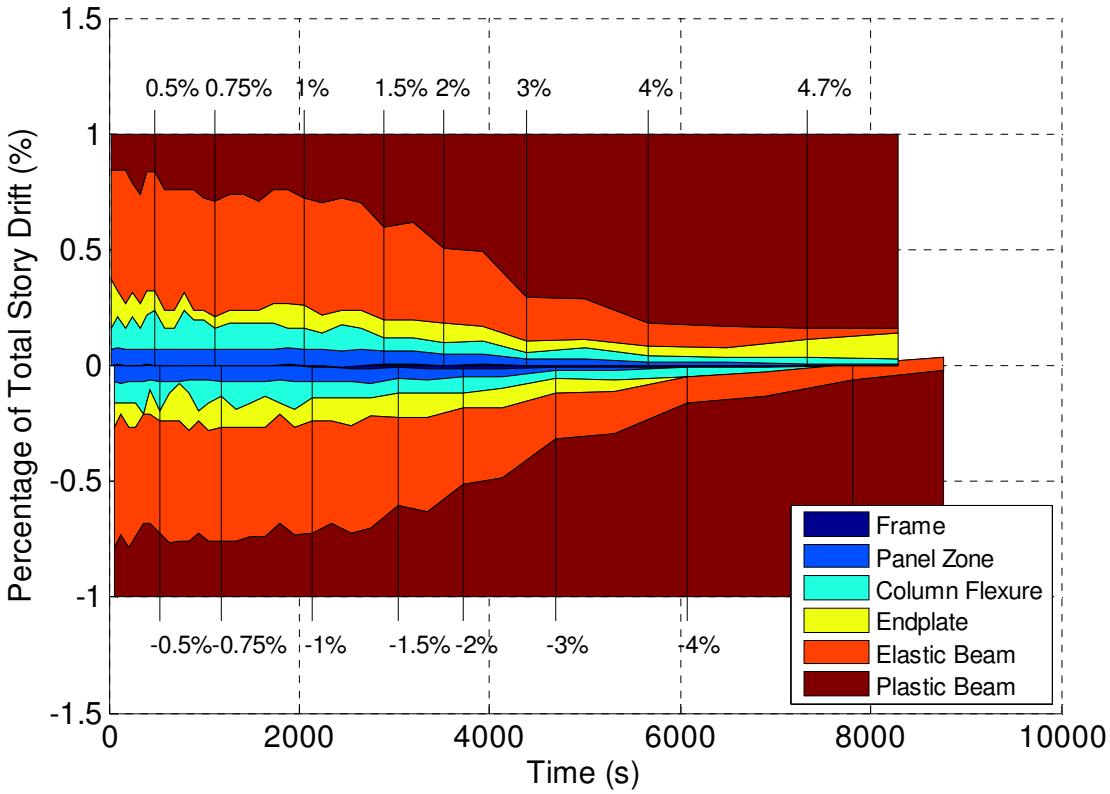

Figure 145: Specimen 1 Story Drift Percentage Contributions

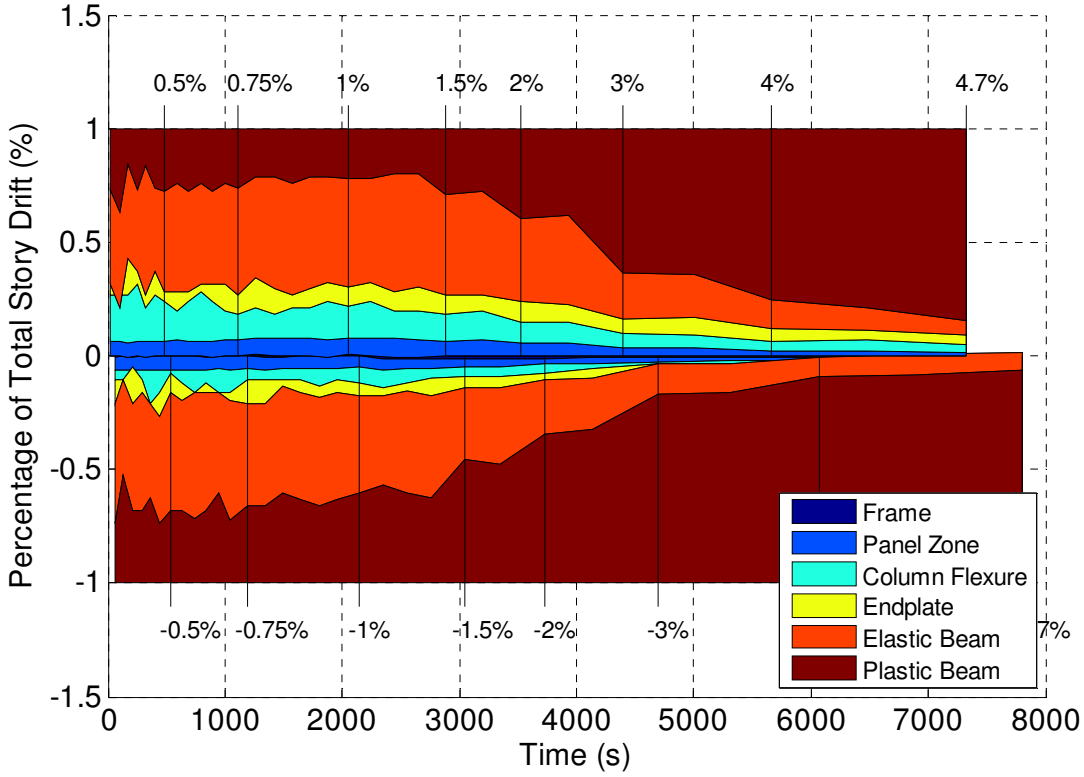

Figure 146: Specimen 2 Story Drift Percentage Contributions

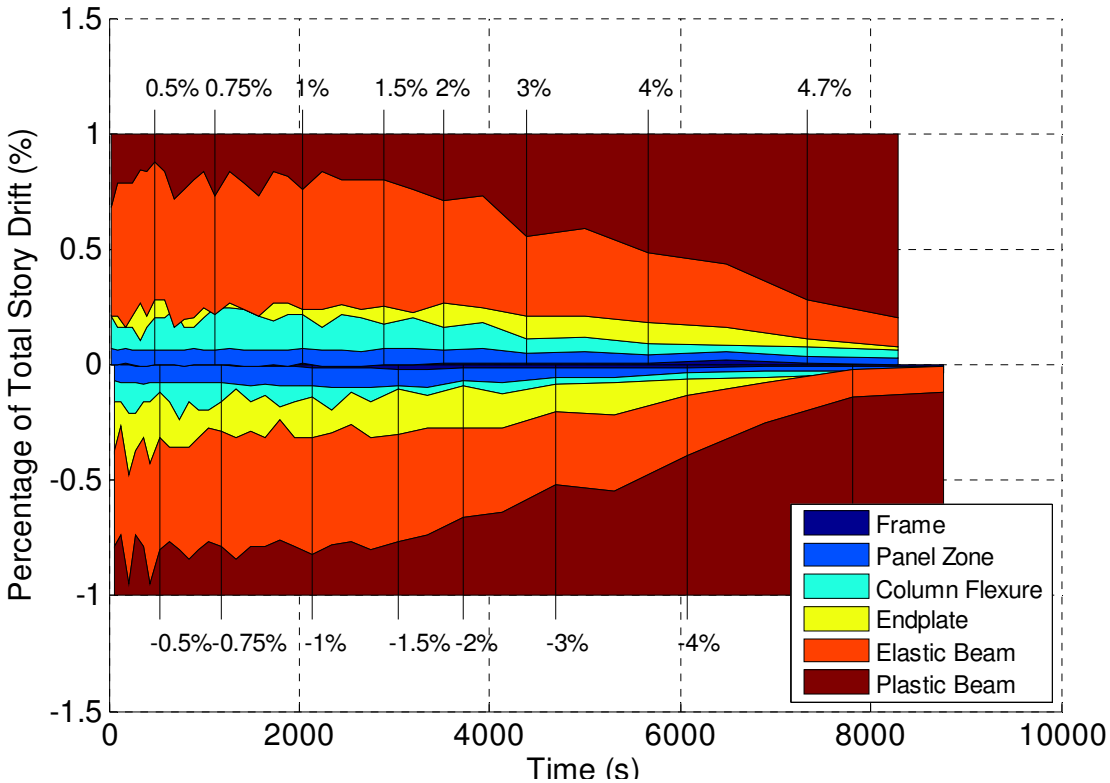

Figure 147: Specimen 3 Story Drift Percentage Contributions

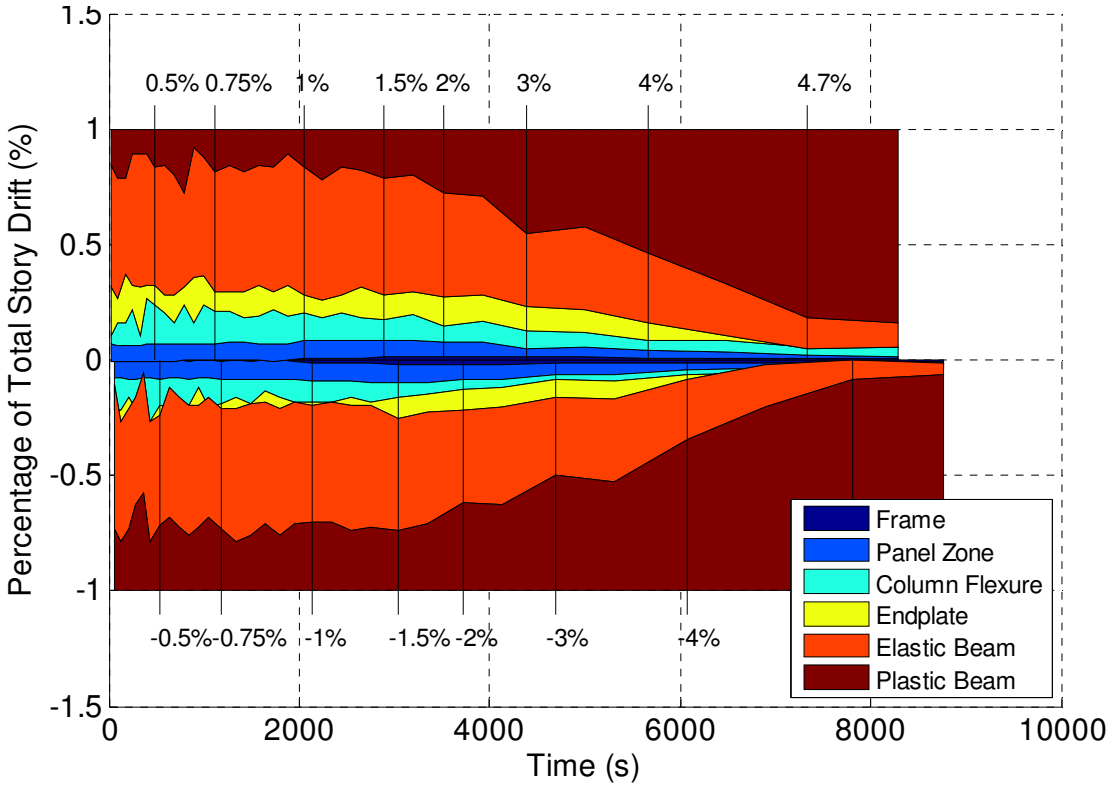

Figure 148: Specimen 4 Story Drift Percentage Contributions

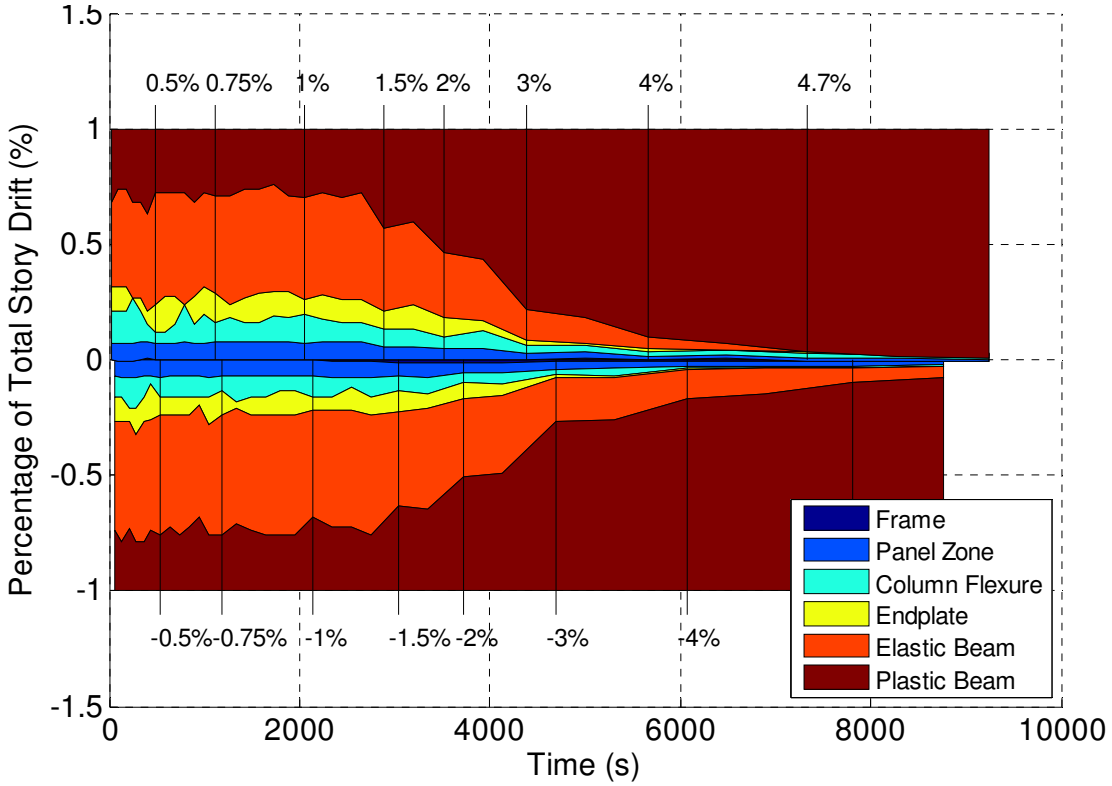

Figure 149: Specimen 5 Story Drift Percentage Contributions

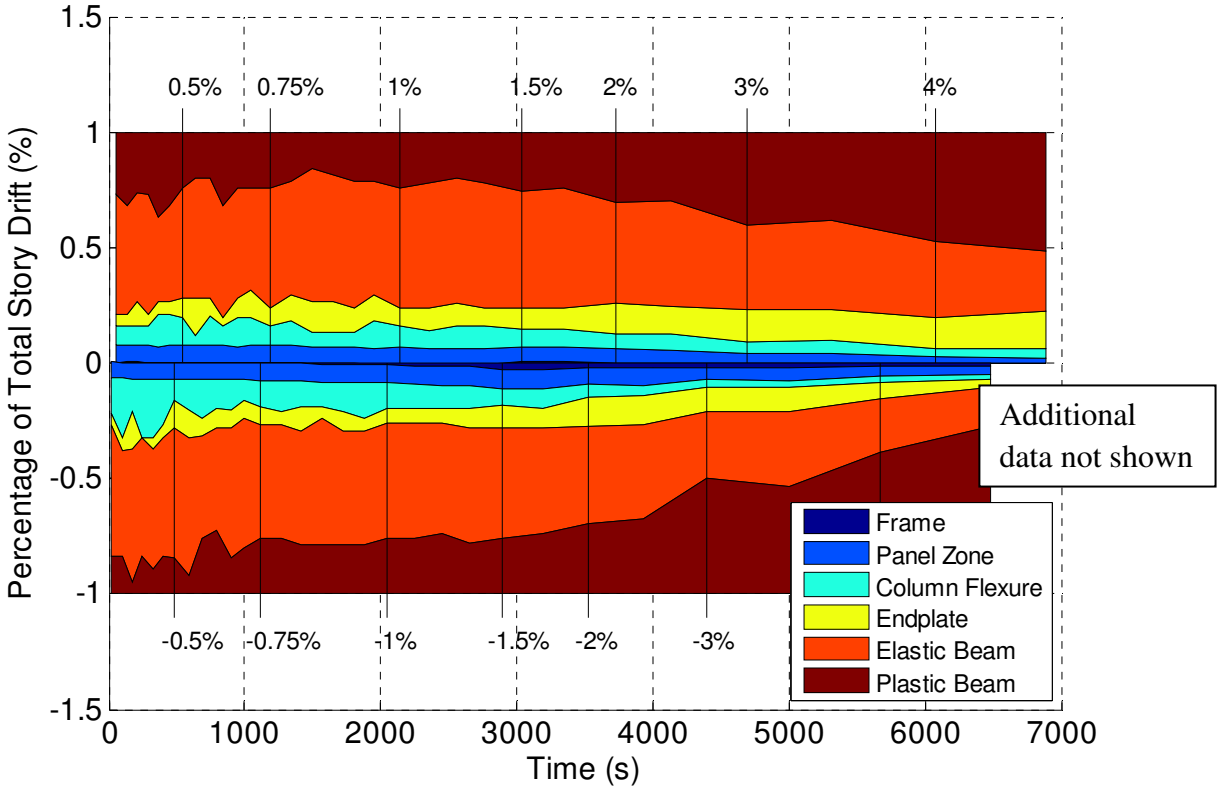

Figure 150: Specimen 6 Story Drift Percentage Contributions

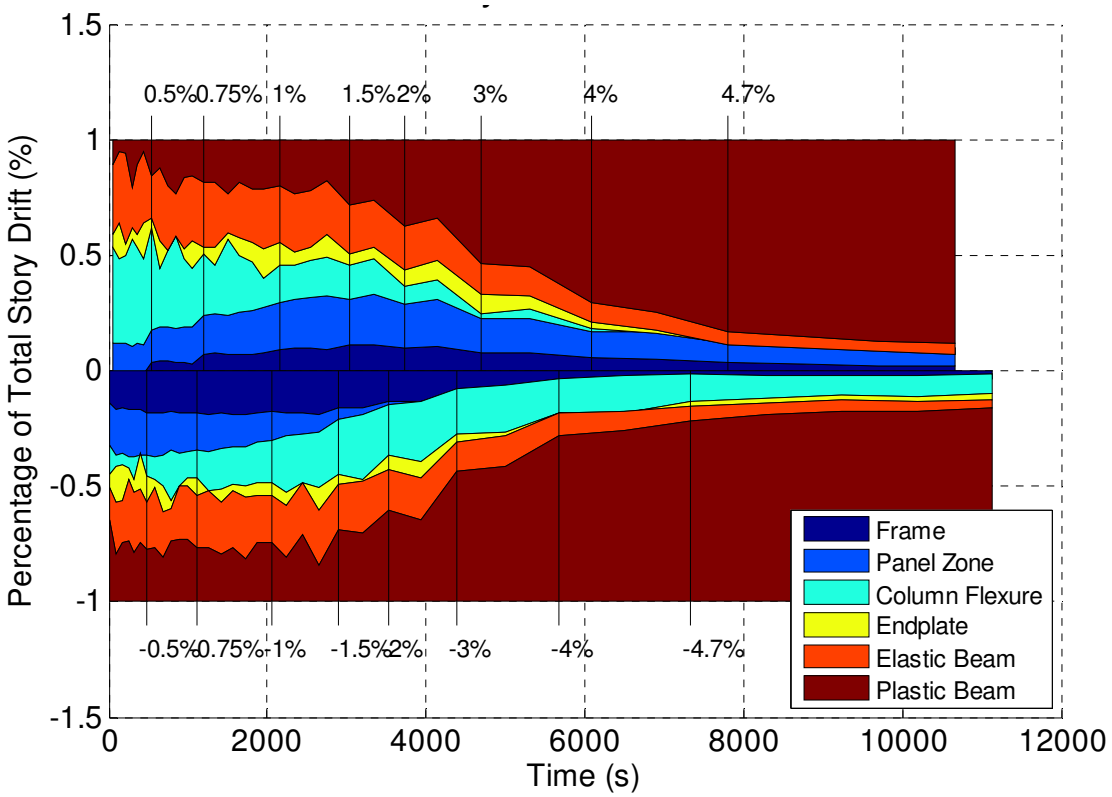

Figure 151: Specimen 7 Story Drift Percentage Contributions

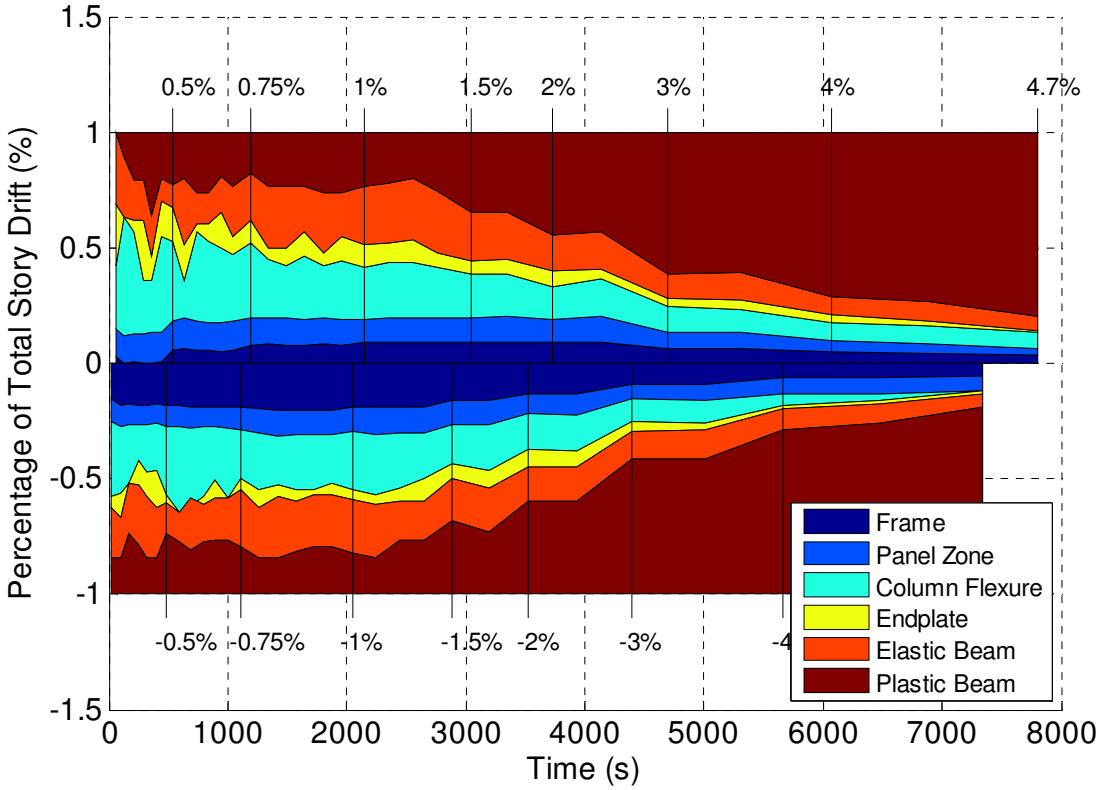

Figure 152: Specimen 8 Story Drift Percentage Contributions

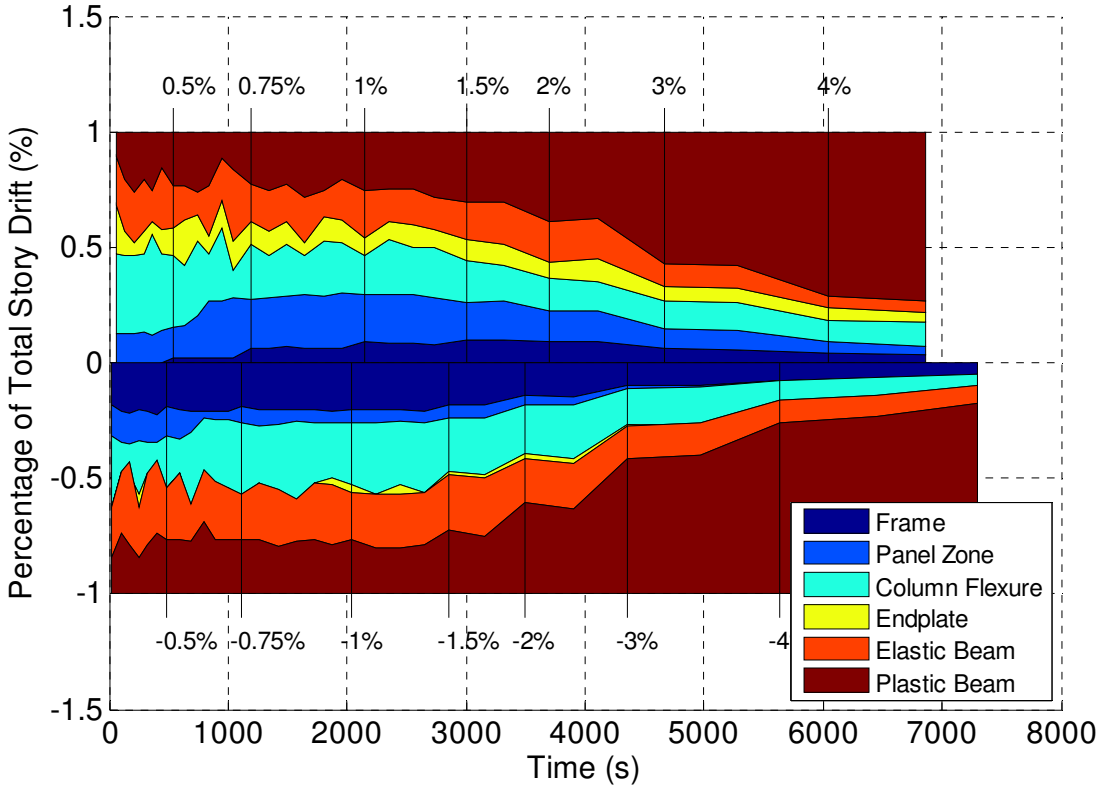

Figure 153: Specimen 9 Story Drift Percentage Contributions

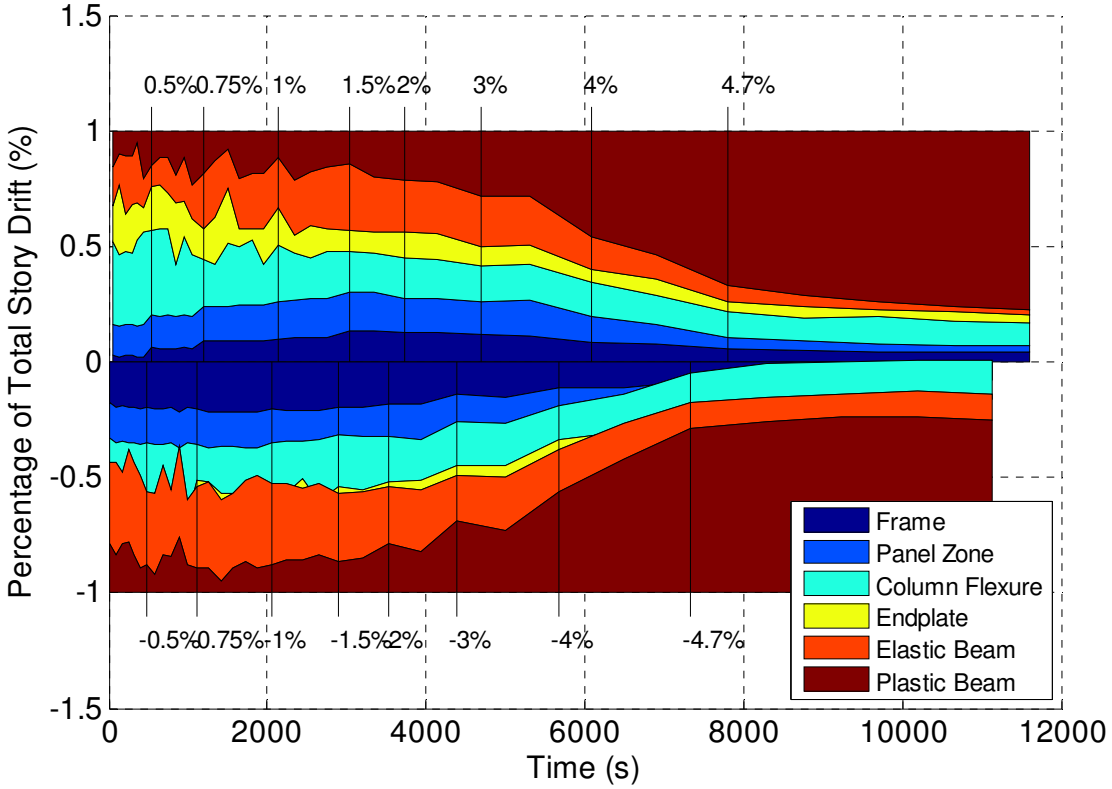

Figure 154: Specimen 10 Story Drift Percentage Contributions

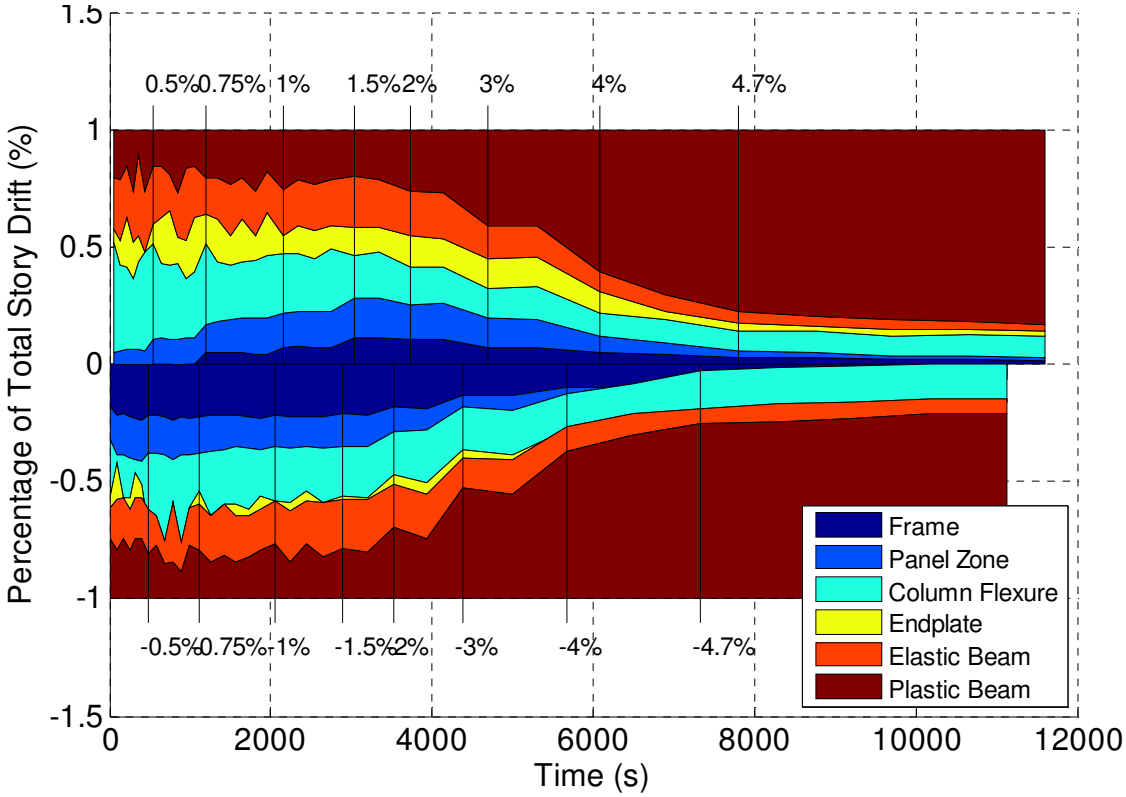

Figure 155: Specimen 11 Story Drift Percentage Contributions

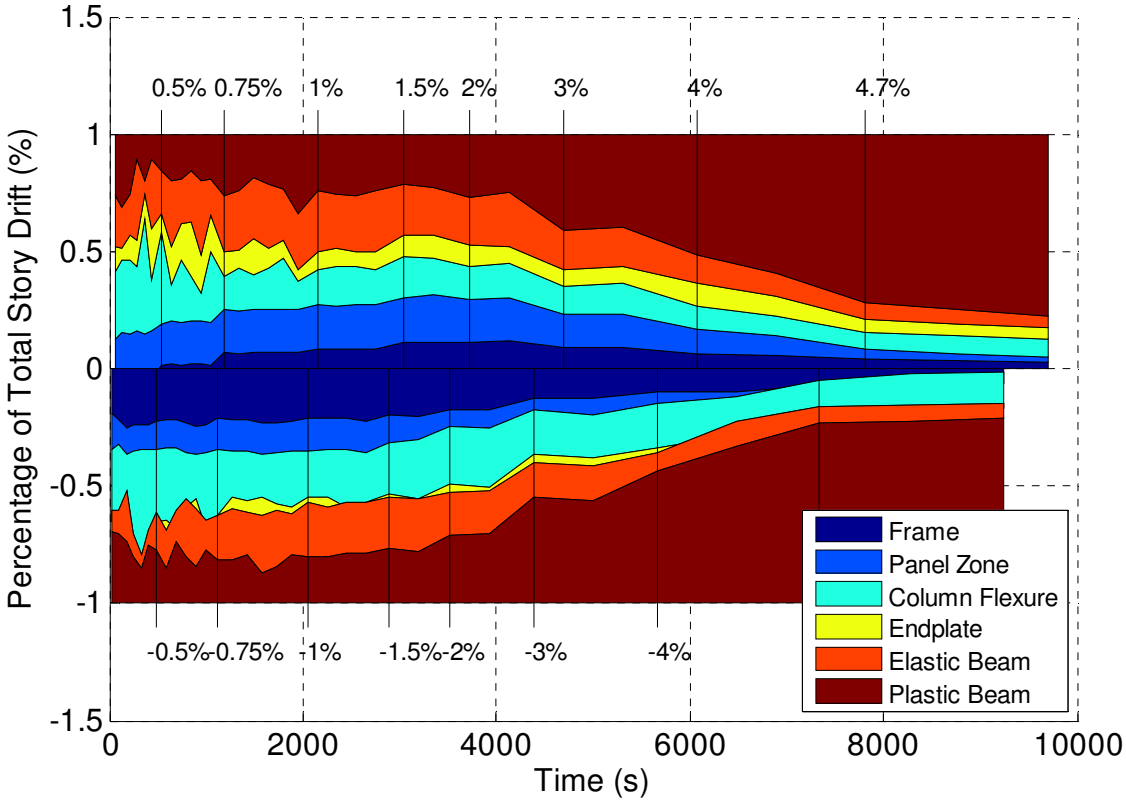

Figure 156: Specimen 12 Story Drift Percentage Contributions

Appendix E - Discussion Data File Channels for All Tests

All test data is output initially as a .dat file including 64 channels of data for tests 1-6 and 65 channels of data for tests 7-12 (inclusion of an additional string potentiometer). All data treatment was completed in Microsoft Excel, in which a .dat file can be opened as a space delimited file. This allows each data channel to occupy a column within the excel interface. The first several rows are populated with text output from Labview. These rows are to be deleted such that all remains is the array of test data. The leftmost column of data is the test elapsed time and by default occupies Excel column B (A is initially blank). Table 13 through Table 16 provide lists of the data channel (column) labels in order with the accompanying Excel column labels in which they appear. Table 13 represents tests 1-5, Table 14 represents test 6, Table 15 represents tests 7-11, and Table 16 represents test 12. Each table is followed by a short discussion about any noteworthy items for its applicable tests. In all of the tables the "Data Label" column corresponds to the order of data channels recorded and the label assigned to them in the Matlab script used to analyze all test data. These labels should only be consulted when utilizing the Matlab script. The "Actual Label" column lists the more intuitive labels for applicable channels that directly apply to labels provided in instrumentation and story drift images throughout this document.

Table 13: Data Labels - Tests 1-5

Excel Column	Data Label (Matlab)	Actual Label (Images)	Dimension
A	[BLANK]	N/A	N/A
B	Time	Elapsed Time	s
C	Timestamp	Timestamp	hhmmssss
D	Inc1	Inclinometer 3 "Outside plastic hinge"	count
E	Inc2	Inclinometer 1 "Center of Column"	count
F	Inc3	Inclinometer 2 "Beyond Endplate"	count
G	SG1	Strain Line 1 top – gauge 1	nd
H	SG2	Strain Line 1 top – gauge 2	nd
I	SG3	Strain Line 1 top – gauge 3	nd
J	SG4	Strain Line 1 top – gauge 4	nd
K	SG5	Strain Line 1 top – gauge 5	nd
L	SG6	Strain Line 1 top – gauge 6	nd
M	SG7	Strain Line 1 top – gauge 7	nd
N	SG8	Strain Line 2 top – gauge 1	nd
O	SG9	Strain Line 2 top – gauge 2	nd
P	SG10	Strain Line 2 top – gauge 3	nd
Q	SG11	Strain Line 2 top – gauge 4	nd
R	SG12	Strain Line 2 top – gauge 5	nd
S	SG13	Strain Line 2 top – gauge 6	nd
T	SG14	Strain Line 2 top – gauge 7	nd
U	SG15	Strain Line 3 top – gauge 1	nd

V	SG16	Strain Line 3 top – gauge 2	nd
W	SG17	Strain Line 3 top – gauge 3	nd
X	SG18	Strain Line 3 top – gauge 4	nd
Y	SG19	Strain Line 3 top – gauge 5	nd
Z	SG20	Strain Line 3 top – gauge 6	nd
AA	SG21	Strain Line 3 top – gauge 7	nd
AB	SG22	Strain Line 1 bottom – gauge 1	nd
AC	SG23	Strain Line 1 bottom – gauge 2	nd
AD	SG24	Strain Line 1 bottom – gauge 3	nd
AE	SG25	Strain Line 1 bottom – gauge 4	nd
AF	SG26	Strain Line 2 bottom – gauge 1	nd
AG	SG27	Strain Line 2 bottom – gauge 2	nd
AH	SG28	Strain Line 2 bottom – gauge 3	nd
AI	SG29	Strain Line 2 bottom – gauge 4	nd
AJ	SG30	Strain Line 3 bottom – gauge 1	nd
AK	SG31	Strain Line 3 bottom – gauge 2	nd
AL	SG32	Strain Line 3 bottom – gauge 3	nd
AM	SG33	Strain Line 3 bottom – gauge 4	nd
AN	SG34	Rosette 1 – gauge 1	nd
AO	SG35	Rosette 1 – gauge 2	nd
AP	SG36	Rosette 1 – gauge 3	nd
AQ	SG37	Rosette 2 – gauge 1	nd
AR	SG38	Rosette 2 – gauge 2	nd
AS	SG39	Rosette 2 – gauge 3	nd
AT	SG40	Rosette 3 – gauge 1	nd
AU	SG41	Rosette 3 – gauge 2	nd
AV	SG42	Rosette 3 – gauge 3	nd
AW	LVDT1	Beam_LVDT_1	in
AX	LVDT2	PZ_LVDT_1	in
AY	LVDT3	PZ_LVDT_2	in
AZ	LVDT4	Base_LVDT	in
BA	LVDT5	Column_LVDT_2	in
BB	LVDT6	Column_LVDT_1	in
BC	LVDT7	Endplate_LVDT	in
BD	LVDT8	Col,Web_LVDT	in
BE	LVDT9	Beam_LVDT_2	in
BF	SP1	Top_SP	in
BG	SP2	Beam_SP	in
BH	MTS_Disp	“Actuator LVDT”	in
BI	MTS_Force	“Actuator Force”	k
BJ	Voltage	“Actuator Voltage”	V
BK	Taget_Disp	“Target Displacement”	in
BL	[BLANK]	N/A	N/A

Tests 2, 4, and 5 included PAFs or puddle welds along the top flange centerline. For these tests, SG4, SG11, and SG18 are blank since a strain gauge could not be placed in the nominal center position

Table 14: Data Labels - Test 6

Excel Column	Data Label (Matlab)	Actual Label (Images)	Dimension
A	[BLANK]	N/A	N/A
B	Time	Elapsed Time	s
C	Timestamp	Timestamp	hhmmssss
D	Inc1	Inclinometer 3 "Outside plastic hinge"	count
E	Inc2	Inclinometer 1 "Center of Column"	count
F	Inc3	Inclinometer 2 "Beyond Endplate"	count
G	SG1	Strain Line 1 top – gauge 1	nd
H	SG2	Strain Line 1 top – gauge 6	nd
I	SG3	Strain Line 1 top – gauge 2	nd
J	SG4	Strain Line 1 top – gauge 3	nd
K	SG5	Strain Line 1 top – gauge 4	nd
L	SG6	Strain Line 2 top – gauge 1	nd
M	SG7	Strain Line 1 top – gauge 5	nd
N	SG8	Strain Line 3 top – gauge 4	nd
O	SG9	Strain Line 3 top – gauge 5	nd
P	SG10	Strain Line 3 top – gauge 6	nd
Q	SG11	Strain Line 4 top – gauge 1	nd
R	SG12	Strain Line 4 top – gauge 2	nd
S	SG13	Strain Line 4 top – gauge 3	nd
T	SG14	Strain Line 4 top – gauge 4	nd
U	SG15	N/A	nd
V	SG16	N/A	nd
W	SG17	N/A	nd
X	SG18	N/A	nd
Y	SG19	N/A	nd
Z	SG20	N/A	nd
AA	SG21	N/A	nd
AB	SG22	Strain Line 5 top – gauge 1	nd
AC	SG23	Strain Line 5 top – gauge 2	nd
AD	SG24	Strain Line 2 top – gauge 2	nd
AE	SG25	Strain Line 2 top – gauge 3	nd
AF	SG26	Strain Line 5 top – gauge 3	nd
AG	SG27	Strain Line 5 top – gauge 4	nd
AH	SG28	Strain Line 5 top – gauge 5	nd
AI	SG29	Strain Line 5 top – gauge 6	nd
AJ	SG30	N/A	nd
AK	SG31	N/A	nd
AL	SG32	Strain Line 4 top – gauge 5	nd
AM	SG33	Strain Line 4 top – gauge 6	nd
AN	SG34	Strain Line 2 top – gauge 5	nd
AO	SG35	Strain Line 2 top – gauge 4	nd
AP	SG36	Strain Line 2 top – gauge 6	nd
AQ	SG37	Strain Line 3 top – gauge 1	nd
AR	SG38	Strain Line 3 top – gauge 2	nd
AS	SG39	Strain Line 3 top – gauge 3	nd
AT	SG40	N/A	nd
AU	SG41	N/A	nd
AV	SG42	N/A	nd

AW	LVDT1	Beam_LVDT_1	in
AX	LVDT2	PZ_LVDT_1	in
AY	LVDT3	PZ_LVDT_2	in
AZ	LVDT4	Base_LVDT	in
BA	LVDT5	Column_LVDT_2	in
BB	LVDT6	Column_LVDT_1	in
BC	LVDT7	Endplate_LVDT	in
BD	LVDT8	Col,Web_LVDT	in
BE	LVDT9	Beam_LVDT_2	in
BF	SP1	Top_SP	in
BG	SP2	Beam_SP	in
BH	MTS_Disp	"Actuator LVDT"	in
BI	MTS_Force	"Actuator Force"	k
BJ	Voltage	"Actuator Voltage"	V
BK	Taget_Disp	"Target Displacement"	in
BL	[BLANK]	N/A	N/A

Test 6 utilized five lines of strain gauges located only on the top flange. This is indicated by the "Actual Label" column in Table 14

.

Table 15: Data Labels - Tests 7-11

Excel Column	Data Label (Matlab)	Actual Label (Images)	Dimension
A	[BLANK]	N/A	N/A
B	Time	Elapsed Time	s
C	Timestamp	Timestamp	hhmmssss
D	Inc1	Inclinometer 3 "Outside plastic hinge"	count
E	Inc2	Inclinometer 1 "Center of Column"	count
F	Inc3	Inclinometer 2 "Beyond Endplate"	count
G	SG1	Strain Line 1 top – gauge 1	nd
H	SG2	Strain Line 1 top – gauge 2	nd
I	SG3	Strain Line 1 top – gauge 3	nd
J	SG4	Strain Line 1 top – gauge 4	nd
K	SG5	Strain Line 1 top – gauge 5	nd
L	SG6	Strain Line 1 top – gauge 6	nd
M	SG7	Strain Line 1 top – gauge 7	nd
N	SG8	Strain Line 2 top – gauge 1	nd
O	SG9	Strain Line 2 top – gauge 2	nd
P	SG10	Strain Line 2 top – gauge 3	nd
Q	SG11	Strain Line 2 top – gauge 4	nd
R	SG12	Strain Line 2 top – gauge 5	nd
S	SG13	Strain Line 2 top – gauge 6	nd
T	SG14	Strain Line 2 top – gauge 7	nd
U	[BLANK]	N/A	N/A
V	[BLANK]	N/A	N/A
W	[BLANK]	N/A	N/A
X	[BLANK]	N/A	N/A
Y	[BLANK]	N/A	N/A

Z	[BLANK]	N/A	N/A
AA	[BLANK]	N/A	N/A
AB	SG22	Strain Line 1 bottom – gauge 1	nd
AC	SG23	Strain Line 1 bottom – gauge 2	nd
AD	SG24	Strain Line 1 bottom – gauge 3	nd
AE	SG25	Strain Line 1 bottom – gauge 4	nd
AF	SG26	Strain Line 2 bottom – gauge 1	nd
AG	SG27	Strain Line 2 bottom – gauge 2	nd
AH	SG28	Strain Line 2 bottom – gauge 3	nd
AI	SG29	Strain Line 2 bottom – gauge 4	nd
AJ	[BLANK]	N/A	N/A
AK	[BLANK]	N/A	N/A
AL	[BLANK]	N/A	N/A
AM	[BLANK]	N/A	N/A
AN	[BLANK]	N/A	N/A
AO	[BLANK]	N/A	N/A
AP	[BLANK]	N/A	N/A
AQ	[BLANK]	N/A	N/A
AR	[BLANK]	N/A	N/A
AS	[BLANK]	N/A	N/A
AT	[BLANK]	N/A	N/A
AU	[BLANK]	N/A	N/A
AV	[BLANK]	N/A	N/A
AW	LVDT1	Beam_LVDT_1	in
AX	LVDT2	PZ_LVDT_1	in
AY	LVDT3	PZ_LVDT_2	in
AZ	LVDT4	Base_LVDT	in
BA	LVDT5	Column_LVDT_2	in
BB	LVDT6	Column_LVDT_1	in
BC	LVDT7	Endplate_LVDT	in
BD	LVDT8	Col,Web_LVDT	in
BE	LVDT9	Beam_LVDT_2	in
BF	SP1	Top_SP	in
BG	SP2	Beam_SP	in
BH	SP3	Stringpot under Inclinometer 3	in
BI	MTS_Disp	“Actuator LVDT”	in
BJ	MTS_Force	“Actuator Force”	k
BK	Voltage	“Actuator Voltage”	V
BL	Taget_Disp	“Target Displacement”	in

Tests 7-11 eliminated the third line of strain gauges as well as the three rosettes previously used. In addition, a third string potentiometer was added to measure the rise of the inclinometer outside of the plastic hinge (Inclinometer 3). This string potentiometer data is used in the calculation of the beam elasticity story drift component. The new data channel occurs immediately after the two existing string potentiometers. This effectively shifts the last four data channels over one column as indicated in Table 15

Table 16: Data Labels - Test 12

Excel Column	Data Label (Matlab)	Actual Label (Images)	Dimension
A	[BLANK]	N/A	N/A
B	Time	Elapsed Time	s
C	Timestamp	Timestamp	hhmmssss
D	Inc1	Inclinometer 3 "Outside plastic hinge"	count
E	Inc2	Inclinometer 1 "Center of Column"	count
F	Inc3	Inclinometer 2 "Beyond Endplate"	count
G	SG1	Strain Line 1 top – gauge 1	nd
H	SG2	Strain Line 1 top – gauge 2	nd
I	SG3	Strain Line 1 top – gauge 3	nd
J	SG4	Strain Line 1 top – gauge 4	nd
K	SG5	Strain Line 1 top – gauge 5	nd
L	SG6	Strain Line 1 top – gauge 6	nd
M	SG7	Strain Line 1 top – gauge 7	nd
N	SG8	Strain Line 2 top – gauge 1	nd
O	SG9	Strain Line 2 top – gauge 2	nd
P	SG10	Strain Line 2 top – gauge 3	nd
Q	SG11	Strain Line 2 top – gauge 4	nd
R	SG12	Strain Line 2 top – gauge 5	nd
S	SG13	Strain Line 2 top – gauge 6	nd
T	SG14	Strain Line 2 top – gauge 7	nd
U	SG15	Strain Line 3 top – gauge 1	N/A
V	SG16	Strain Line 3 top – gauge 2	N/A
W	SG17	Strain Line 3 top – gauge 3	N/A
X	SG18	Strain Line 3 top – gauge 4	N/A
Y	SG19	Strain Line 3 top – gauge 5	N/A
Z	SG20	Strain Line 3 top – gauge 6	N/A
AA	SG21	Strain Line 3 top – gauge 7	N/A
AB	SG22	Strain Line 1 bottom – gauge 1	nd
AC	SG23	Strain Line 1 bottom – gauge 2	nd
AD	SG24	Strain Line 1 bottom – gauge 3	nd
AE	SG25	Strain Line 1 bottom – gauge 4	nd
AF	SG26	Strain Line 2 bottom – gauge 1	nd
AG	SG27	Strain Line 2 bottom – gauge 2	nd
AH	SG28	Strain Line 2 bottom – gauge 3	nd
AI	SG29	Strain Line 2 bottom – gauge 4	nd
AJ	SG30	Strain Line 3 bottom – gauge 1	N/A
AK	SG31	Strain Line 3 bottom – gauge 2	N/A
AL	SG32	Strain Line 3 bottom – gauge 3	N/A
AM	SG33	Strain Line 3 bottom – gauge 4	N/A
AN	[BLANK]	N/A	N/A
AO	[BLANK]	N/A	N/A
AP	[BLANK]	N/A	N/A
AQ	[BLANK]	N/A	N/A
AR	[BLANK]	N/A	N/A
AS	[BLANK]	N/A	N/A
AT	[BLANK]	N/A	N/A
AU	[BLANK]	N/A	N/A
AV	[BLANK]	N/A	N/A

AW	LVDT1	Beam_LVDT_1	in
AX	LVDT2	PZ_LVDT_1	in
AY	LVDT3	PZ_LVDT_2	in
AZ	LVDT4	Base_LVDT	in
BA	LVDT5	Column_LVDT_2	in
BB	LVDT6	Column_LVDT_1	in
BC	**[BLANK]**	**N/A**	in
BD	**LVDT8**	**Endplate_LVDT**	in
BE	LVDT9	Beam_LVDT_2	in
BF	SP1	Top_SP	in
BG	SP2	Beam_SP	in
BH	SP3	Stringpot under Inclinometer 3	in
BI	MTS_Disp	"Actuator LVDT"	in
BJ	MTS_Force	"Actuator Force"	k
BK	Voltage	"Actuator Voltage"	V
BL	Taget_Disp	"Target Displacement"	in

Test 12 reincorporated strain line 3 data. String potentiometer 3, as discussed for tests 7-11, is again present in test 12. For this test alone, the LVDT8 channel provides data corresponding to the endplate_LVDT, which previously was associated with LVDT7. As a result, this test does not have data for the column web LVDT (Col,Web_LVDT) which was formerly associated with LVDT 8. This is indicated by the bold cells in Table 16.

Appendix F - Discussion of Test Data Modifications and Treatment

The following section discusses modifications and treatment of test data in order to make it compatible with the automated data analysis script written in Matlab. These changes to the raw data files are discussed in two groups; first as general changes applied to all tests simply for purposes of formatting, second as specific changes applied individually to each test, as necessary, to account for any inadvertent disturbances of test instrumentation.

General Test Data Treatment

Note: Consult the initial paragraph of Appendix A3 prior to referencing this section. Appendix A3 discusses the initial deletion of several rows of text located at the beginning of every test output data file. Microsoft Excel was used as the interface by which these and the following modifications were made.

Delete Initial Values During Row

After deleting the initial lines of text the first row of data occurs at a time (column B) of "-1". This first row is a capture of the initial values of all instrumentation. This row is deleted for purposes of data analysis so as not to disrupt test data plotted against time which should nominally begin at "0"

Remove Test Data During Pauses

The nature of experimental tests required the occasional pausing of the test for a number of reasons including photography, test frame inspection, and instrumentation checking. These pauses were made as needed of each test and therefore occur at different times from test to test. In order to present results of the tests in a continuous manner as provided in this report, it was necessary to remove recorded test data during these pauses. The final channel of data recorded in each test is the "target displacement" of the actuator. This number constantly updates as the actuator completes the predescribed displacement protocol. During pauses, however, this number remains constant. As a result, all data rows in which this target setpoint remains constant were manually removed.

Add a new continuous time data column

The first channel of data (column B) records the test elapsed time in seconds. The deletion of test data during pauses results in a discontinuous jump in time from the beginning of the pause to the resuming of the test. In order to provide a continuous time for plotting purposes, it was necessary to add a new column of data in the previously unoccupied "Column A". This column provides an identical time up until the first region of data deletion. At this point instead of jumping to the post pause time, the next row of data is manually entered assuming a time step of 0.140008 seconds. This is the default time step of data recording used in all tests. The following rows of continuous time data (Column A) is then automatically populated in excel by adding the

previous time value to the difference of times in the adjacent "Column B" time step using excel's ability to reproduce an operation by dragging the cell to repeat. This process must be repeated at each region of removed test data from pauses due to the presence of a discontinuity in time. In this way the time in column B ultimately represents a raw data elapsed time while the new column A values represent the nominal time that will be used in all plots in which a continuous test is desired. All plots in this report utilize this continuous time data.

Test Specific Data Treatment

This section lists test specific data treatment performed

Delete any post fracture data rows (Tests 1, 2, 5, 7, 8, 9, 12)
A large number of tests experienced partial fractures of the beam prior to the completion of the test program. For all of these tests, data recording was manually stopped soon after the fracture, but until this is done, data will continue to record. The impact of a fracture tends to disrupt many pieces of instrumentation which can result in false readings that can dramatically extend the data range in plots such that data trends cannot be visualized. For this reason, it is necessary to delete the rows of data beyond the final recording prior to fracture. Fracture can easily be located in the data by referencing the final readings of the "Actuator Force" data channel. The actuator load cell will report a dramatic drop in force as soon as fracture occurs.

Inclinometer data adjustment – See implementations in list of specific test data modifications
Inclinometers report angular position in the form of counts, a unit of measurement unique to the devices. While all three inclinometers have a range of +/- 45 degrees from vertical, the transition between positive and negative angles includes an inherent discontinuity. Inclinometer angled in one direction from vertical will report counts in an intuitive manner starting at 0 counts (e.g. 0,1,2,3,etc). Rather than report negative counts in the other angular direction, the inclinometers jump from 0 to 65535 counts and then decrease in linearly (e.g. 65535, 65534, 65533). Due to the cyclic nature of the tests, this results in an undesirable jump from 0 to 65535 as the inclinometer cycles back and forth through positive and negative angles. To correct this, a conditional statement was used in Excel to locate data rows in the negative range simply by detecting the presence of a large data value (for instance, anything larger than an arbitrary value of 50000). The conditional statement replaces these numbers with an equivalent negative number using the following algorithm

{new value} = {old value} – 65536

Applying this algorithm corrects the previous discontinuity with values that cycle through positive and negative counts around the vertical value of zero. The matlab script translates these counts to the unit of degrees using the calibration factor provided in the inclinometer documentation. The calibration factor provided, 0.011721 degrees per count, was confirmed using manual calibration of one of the inclinometers. Since inclinometer data does not zero out based on an initial value as in most other instrumentation devices, the matlab script performs this action as part of its data processing routine.

Column string potentiometer adjustments – See implementations in list of specific test data modifications

The string potentiometer recording the motion of the top of the test column utilized an extension line to extend the string potentiometer all the way from the floor where it was mounted. Observation of test data from the first half of testing revealed that the knot connecting the string potentiometer line to the extension line periodically slipped during tests. This is indicated by an instantaneous drop in the data (always a decrease since the slipping knot allowed the string potentiometer line to retract. For all applicable tests, this data channel was manually changed to remove these offsets. Manual adjustment was only completed in locations where it was clear that the drop in data was due to the knot slipping. Adjustment was not performed when it was not possible to distinguish the slipping of the knot and an actual decrease in data due to motion of the column.

Test 1: RBS24

i. Inc1 (Column D) data modified using the inclinometer adjustment procedure previously described. Figure 157 provides a visual representation of this adjustment. The "before" image shows raw inclinometer data. The "after" image shows the same data after applying the adjustment of recorded count values discussed previously as well as the zeroing out of the data based on its initial value.

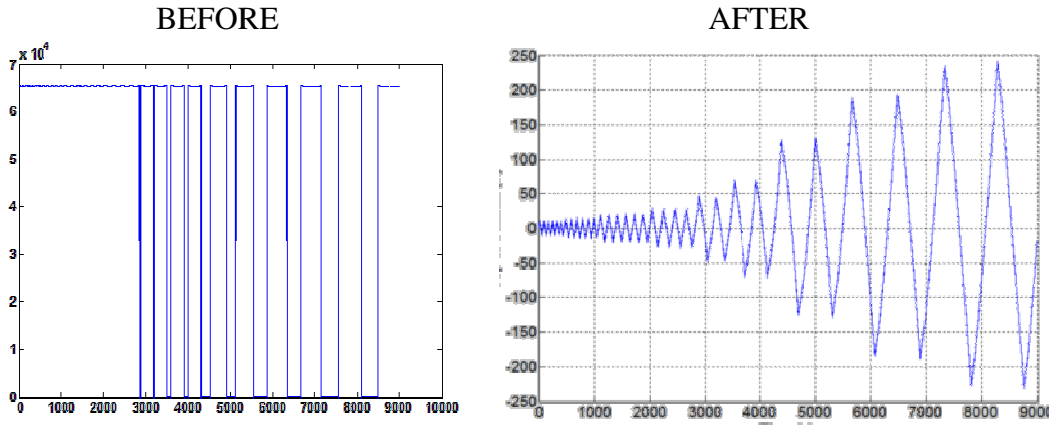

Figure 157: Test 1 - Inc1 Data Modification

ii. Column string potentiometer data was modified using the adjustment procedure previously described. Figure 158 provides a visual representation of this adjustment

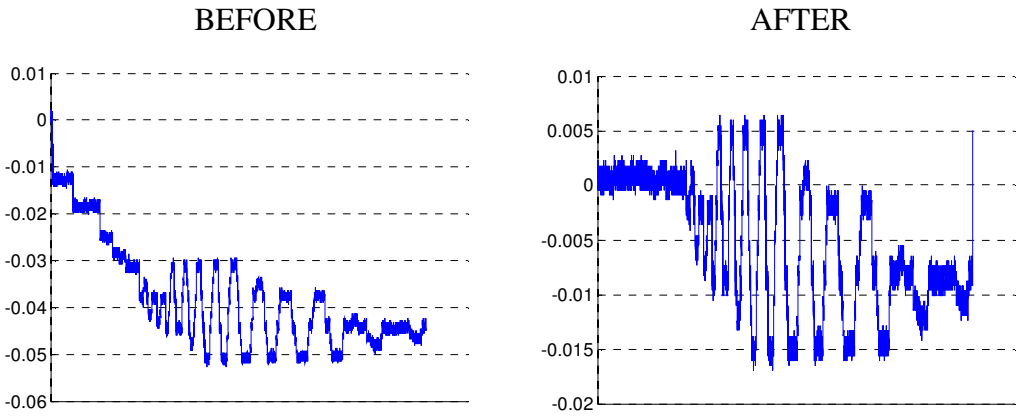

Figure 158: Test 1 - Column String Potentiometer Data Modification

Test 2: RBS24-PAF12

i. Inc1 (Column D) data modified using the inclinometer adjustment procedure previously described)

ii. Column string potentiometer data was modified using the adjustment procedure previously described.

Test 3: W24

i. Inc1 (Column D) data modified using the inclinometer adjustment procedure previously described)

ii. Column string potentiometer data was modified using the adjustment procedure previously described.

Test 4: W24-PAF12

i. LVDT3 Data was modified to account for an inadvertent bump of the LVDT which resulted in the LVDT reaction piston to reacting against a new surface after raw data time 6790 (continuous 6581) seconds. The bumping of the LVDT occurred over the course of about 2 seconds after which time it continued to operate undisturbed. In order to modify the data, recordings made during the apparent bumping of the LVDT were simply replaced with the previous undisturbed reading. The enables a continuity of data for plotting which is negligible compared to the duration of the test and the rate of change of the data values. Data after the disturbance was offset by 0.1232 in. for the remainder of the test. Figure 159 shows this modification. The

"before" image is from LVDT3 raw data. The "after" image incorporates the offset described.

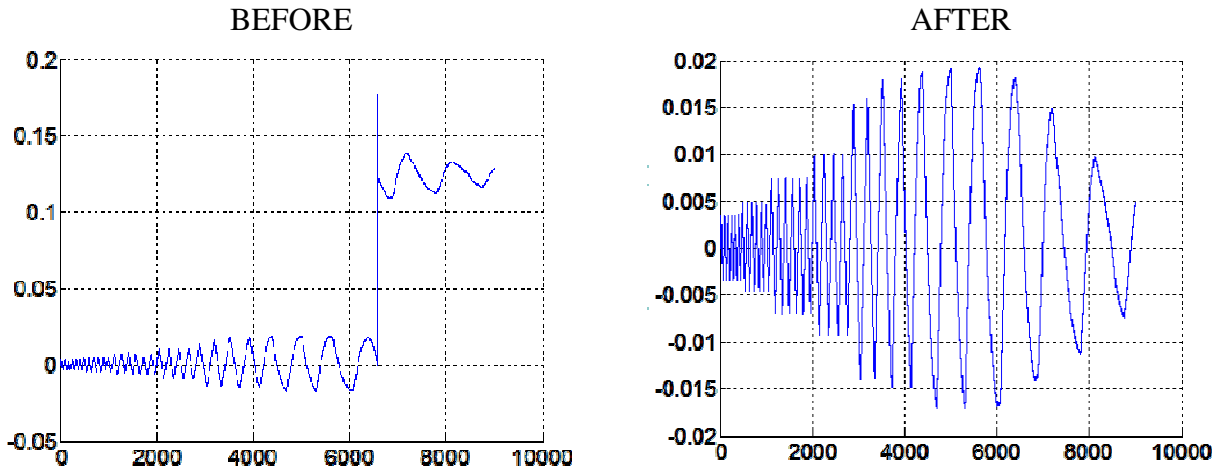

Figure 159: Test 4 - LVDT3 Data Modification

ii. Column string potentiometer data was modified using the adjustment procedure previously described.

Test 5: RBS24-PW12

i. Inc1 (Column D) data modified using the inclinometer adjustment procedure previously described)

ii. Column string potentiometer data was modified using the adjustment procedure previously described.

Test 6: W24-PAF_array

i. Inc3 (Column F) recorded a discontinuous jump in angle at raw data time 7323 (continuous time 7323) seconds. This was likely due to a partial slip of the adhesive connecting it the beam. After this time, the inclinometer continued to read cyclic data trends which appear consistent with other tests. This data was therefore offset by a value of 3376 counts to provide an apparent continuity with the data prior to the offset. After raw data time 9962 (continuous time 9962) seconds, the inclinometer begins providing a false reading for the remainder of the test. This is likely due to an inadvertent contact of wire conductors. No treatment is possible for this data range. It is simply disregarded from further data analysis.

ii. Column string potentiometer data was modified using the adjustment procedure previously described.

Test 7: RBS36

i. LVDT1 data beyond raw data time 7461 (continuous time 7334) seconds is not valid due to a failure of the adhesive fixing the LVDT in place. No treatment is possible for data beyond this point. LVDT1 provides a redundant measurement of the degree of plastic hinging. For this reason, story drift decomposition can still be computed using the primary method of inclinometer differentials discussed in the story drift decomposition section. Figure 160 shows the loss of data due to the adhesive failure.

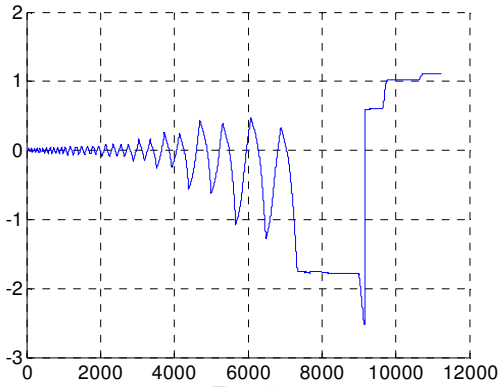

Figure 160: Test 7 - LVDT1 Data Loss

Test 8: RBS36-PW12

i. No additional data modification necessary

Test 9: RBS36-PAF_array

i. Test 9 was stopped at raw data time 2675 (continuous time 2675) due to a tripped sensor within a hydraulic pump. This occurred while the actuator was deflected 1.32 in. above the zero deflection point of the beam on its way to 0in. Before resuming testing, the actuator was manually controlled to return the beam to a deflection of 0 in. The test program was then reinitiated starting from the current point of 0 in. deflection and continuing with the displacement protocol as if it had reached 0in from the previous stop point of 1.32 in. Restarting the test program created a second data output file in which instrumentation devices were zeroed from their initial reading at 0 in. deflection. In order to merge the two data files so that the final file included the entire test, it was necessary to edit the values of numerous data channels in the second data file so that they were based on the initial data readings from the first data output file. This was done in Matlab by applying the algorithm below to all strain gauge, LVDT, and string potentiometer data channels;

{new value} = {old value} + {initial value from part 2} – {initial value from part 1}

The two files were than combined one after another and the initial data row from the second data file was deleted. This results in a discontinuity in which the deflection of

the beam jumps from 1.32 in. to 0 in. in one standard time step (.140008 seconds). The continuous time data (Column A) was modified such that the first data row from the second phase of the test occurs .140008 after the final data row from the first phase of the test. The discontinuity can be seen in Figure 161. Since the beam would nominally have continued to 0 in. deflection before continuing on with the test program, it is apparent that the manual return to 0 in. not occurring in the test data does not compromise any of the subsequent data recordings.

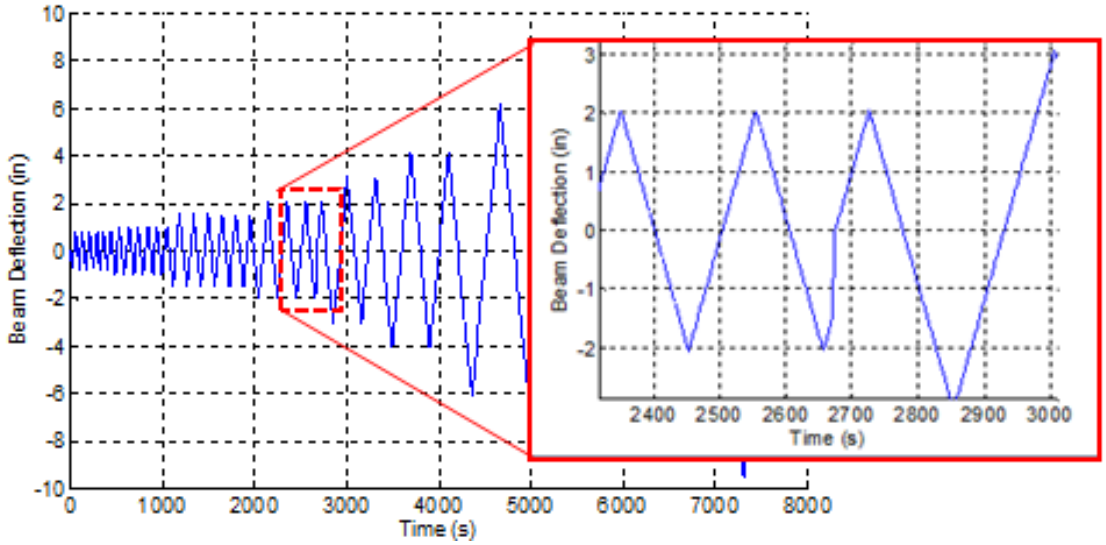

Figure 161: Test 9 - Data discontinuity due to data file merger

Test 10: W36

i. Test 10 placed increased loads on the reaction frame beyond what had previously been encountered. These increased loads led to a small degree of slip between the top of the test column and the support frame mounted to it. This slip occurred back and forth due to the cyclic nature of the test. The impulse nature of the slip resulted in numerous data spikes within all three inclinometers. The adhesive bond of the inclinometers was not compromised during these instances of slip and it was determined that the data spikes were simply a false recording due to the digital devices response to the slip. These false readings only exist for a fraction of a second each. In order to provide more graphically continuous plots for story drift decomposition, these spikes were manually replaced with the values of the data channel immediately preceding the spike. Figure 162 provides an example of this data modification of inclinometer 1.

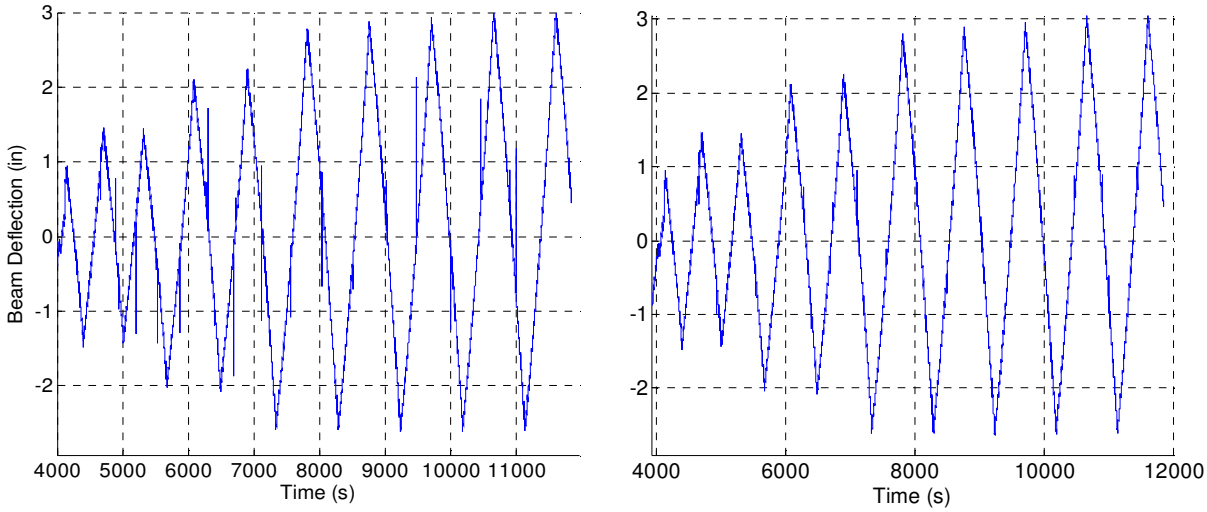

Figure 162: Test 10 - Inclinometer Data Spike Removal

ii. LVDT9 data beyond raw data time 12117 (continuous time 8280) seconds is not valid due to a failure of the adhesive fixing the LVDT in place. No treatment is possible for data beyond this point.

Test 11: W36-PAF12

i. LVDT1 data beyond raw data time 11693 (continuous time 10560) seconds is not valid due to a failure of the adhesive fixing the LVDT in place. No treatment is possible for data beyond this point.

Test 12: W36-PAF_array

i. No additional data modification necessary

Appendix G – Data Files Naming and Contents

Singular files used in test data analysis

Name: Data_Analysis_all_tests.m
Description: Matlab script used for data analysis for all tests. The file includes comments throughout its lines of code. Generally, the script loads modified data files for any test number listed near the top of the script (By default the script reads the Test_#_Data.dat files discussed below). The script parses the data channels and assigns them names as described in Appendix E. Story drift algorithms use specific instrumentation as described in the report. All plots used in the report were created from the large group of commented lines at the bottom of the script. These different plot groups can be individually uncommented as desired.

Name: Test_Geometry.dat
Description: Single file containing important measurements that varied from test to test. The file contains twelve columns, one for each test in order from 1-12. The file contains 8 rows which are assigned specific labels within the "data anaylsis" script in the 'Test Geometry' section.

Name: Extra_Code_Sections.m
Description: Matlab script in which small groups of lines of code are stored. Rather than fill the primary data analysis script with a large number of code lines that are not typically used, some line groups are cut and pasted into the "extra code sections file". Most of these groups were used in the automated collection of test data reported in the results tables of applied moment and story drift data in the report. These line groups are commented and can be copied as a group into the "data analysis" matlab script as necessary

Typical files for every test

Name: Test_[test/specimen number]_Data.dat
Example: Test_7_Raw_Data.dat
Description: Raw data files automatically written during testing. This file is kept as an original unedited source of test data

Name: Test_[test/specimen number]_Data_Bad_Data_Included.dat
Example: Test_7_Data_Bad_Data_Included.dat
Description: Data file following the **general data modifications** described in Appendix F. This data file is kept as a source of generally formatted data and does not include the manual test specific modifications made to data. In this report, the only use of these data files are as "before" images in the test specific data modification section of Appendix F

Name: Test_[test/specimen number]_Data.dat
Example: Test_7_Data.dat
Description: Data file following the **general and test specific data modifications** described in Appendix F. This file incorporates all formatting and modification procedures as necessary for each test. All hysteretic, story drift, and instrumentation plots provided in this report use this edited data in order to provide easy viewing of data as it applies to best understanding the behavior of each test specimen. For tests requiring no specific instrumentation data modifications, no 'Bad_Data_Included' file is created.

Name: Test_[test/specimen number]_Peaks.dat
Example: Test_7_Peaks.dat
Description: Data file containing two columns. Column 1 contains the row numbers from the fully formatted test data files (e.g. Test_7_Data.dat) at which peak amplitudes occur. Column 2 contains the string potentiometer 2 (under the actuator) recorded value. This data file is used in the reporting of values at specific cycles (e.g. 4% qualification cycles, 4.7% repeating cycles). It is also used in the development of the relative story drift contribution plots presented in the body of the report as well as in Appendix C since these plots only utilize peak data and interpolate between these points.

Appendix H – Specimen 1 (RBS24) Raw Instrumentation Data

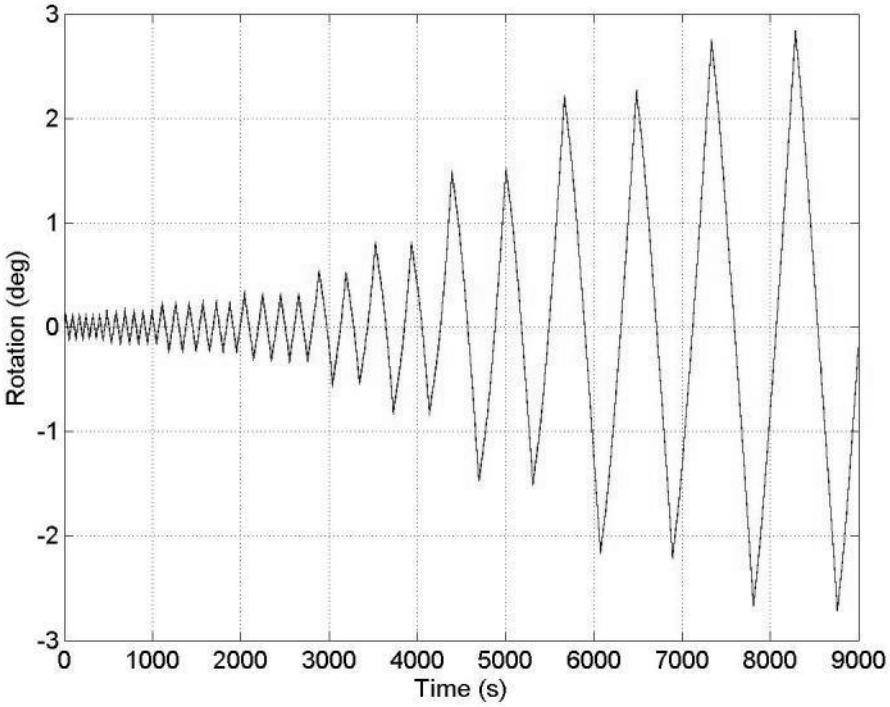

Figure 163: Specimen 1 (RBS24) - Inclinometer 3 (beam)

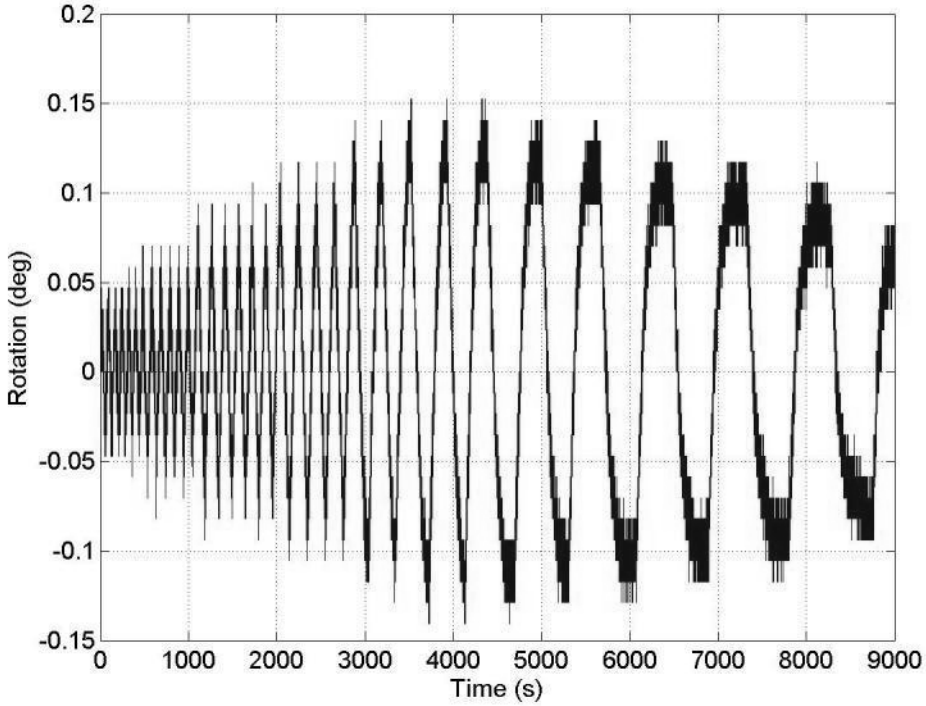

Figure 164: Specimen 1 (RBS24) - Inclinometer 1 (column)

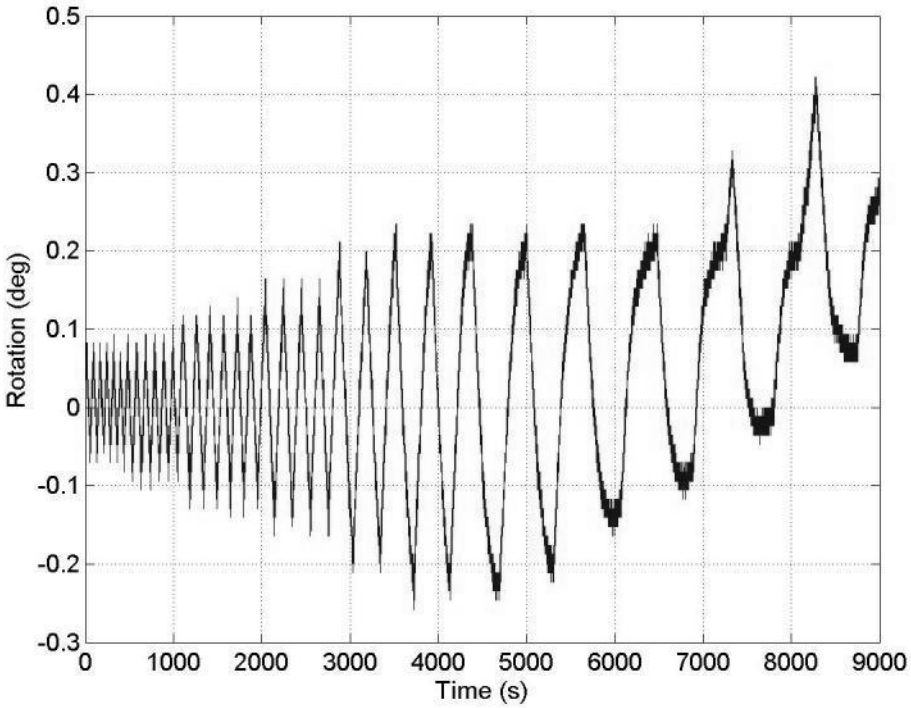

Figure 165: Specimen 1 (RBS24) - Inclinometer 2 (endplate)

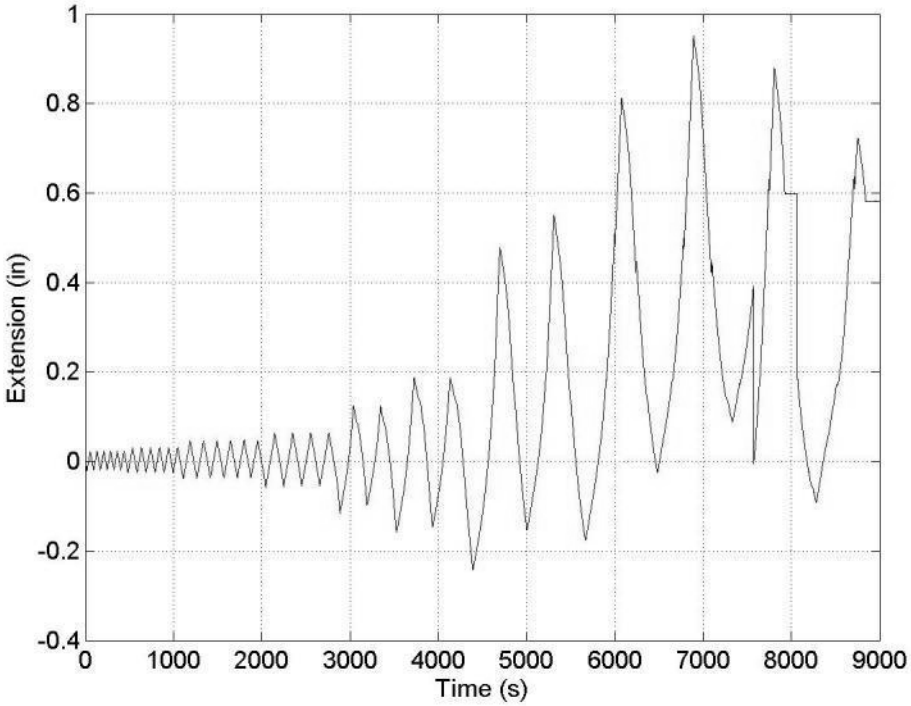

Figure 166: Specimen 1 (RBS24) - LVDT1

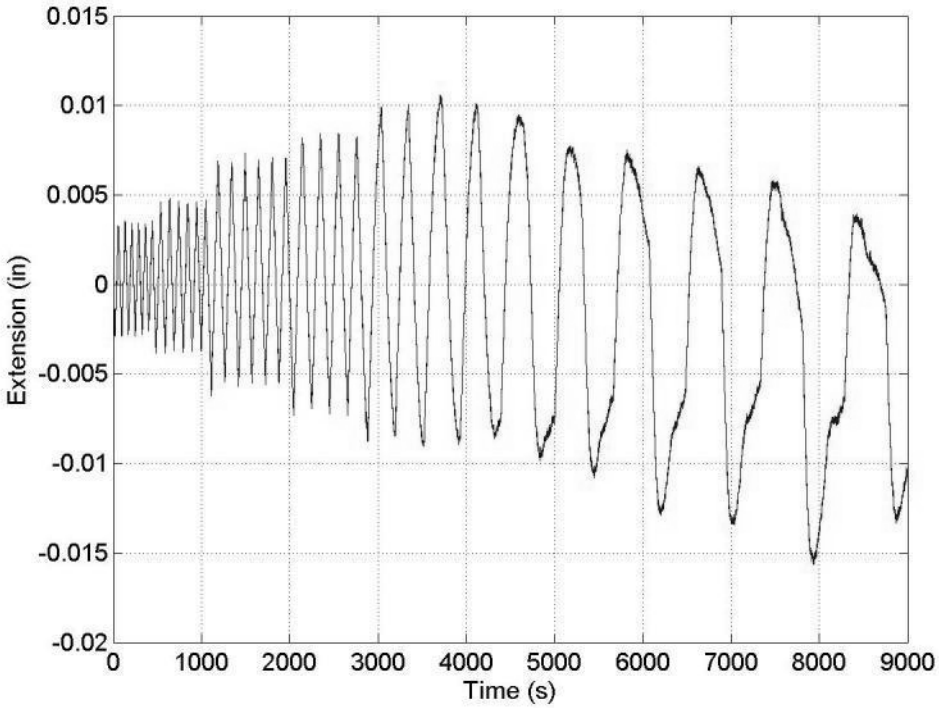

Figure 167: Specimen 1 (RBS24) - LVDT2

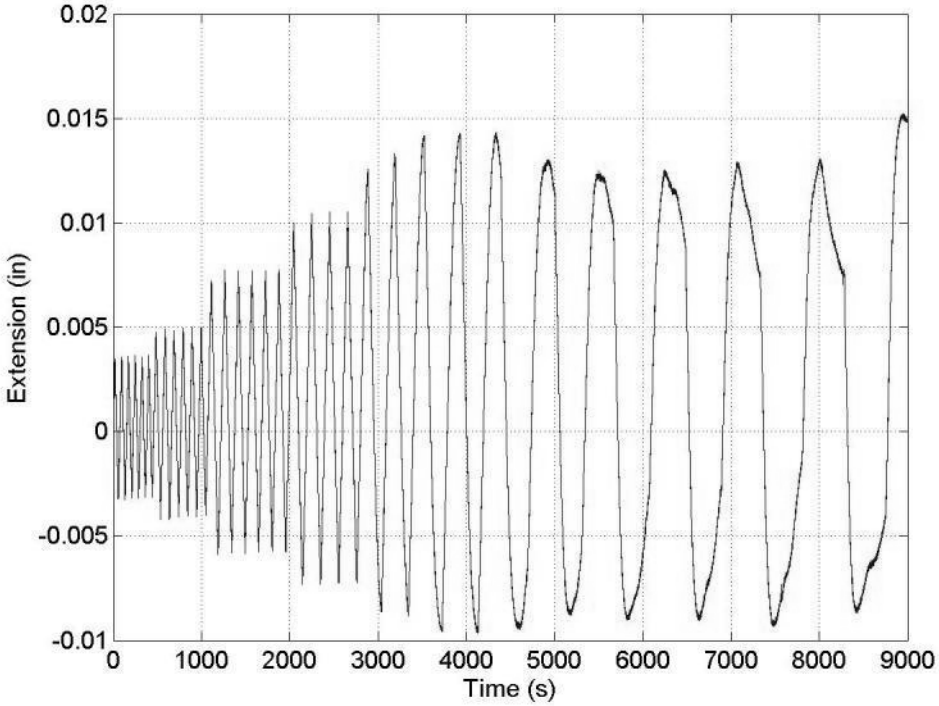

Figure 168: Specimen 1 (RBS24) - LVDT3

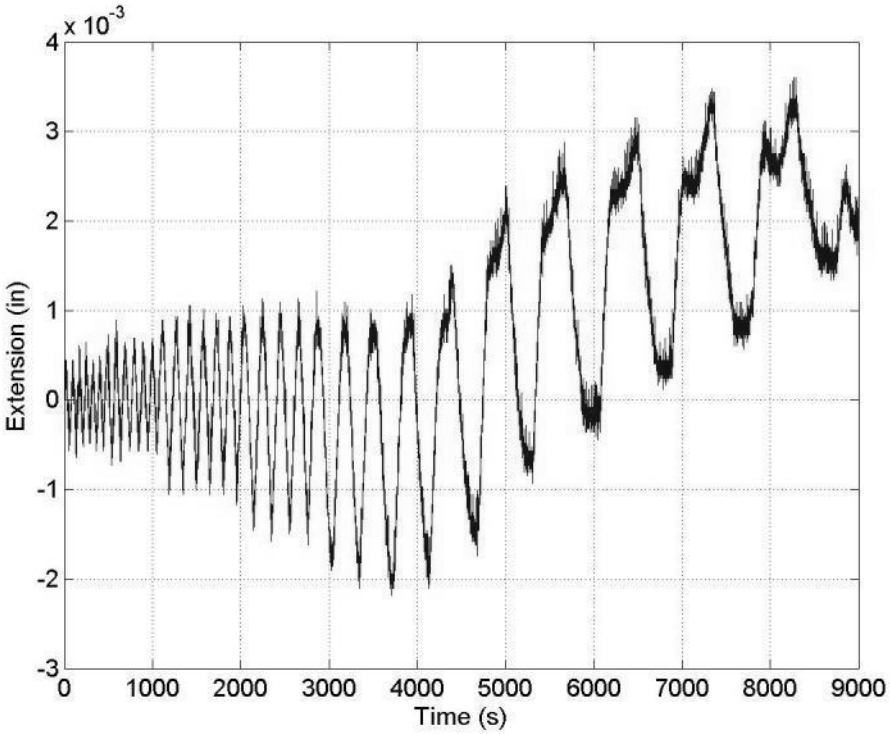

Figure 169: Specimen 1 (RBS24) - LVDT4

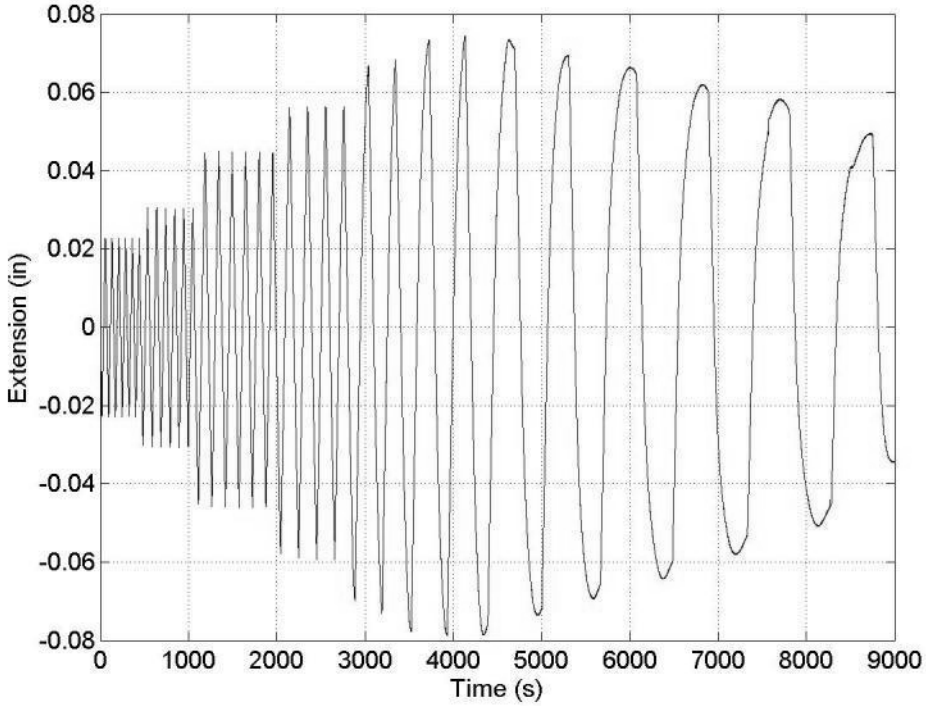

Figure 170: Specimen 1 (RBS24) - LVDT5

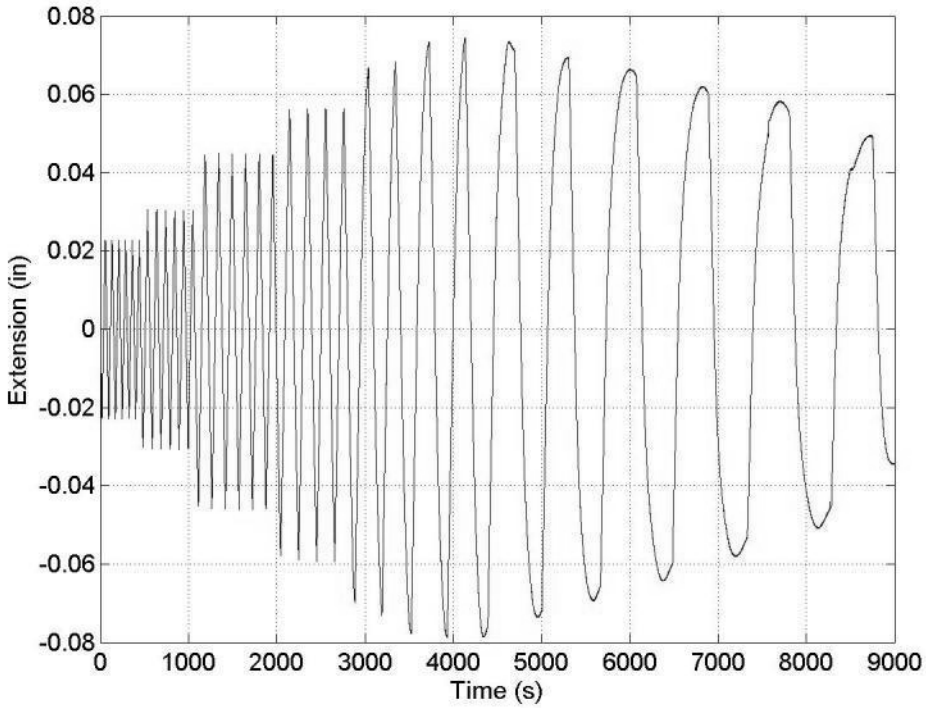

Figure 171: Specimen 1 (RBS24) - LVDT6

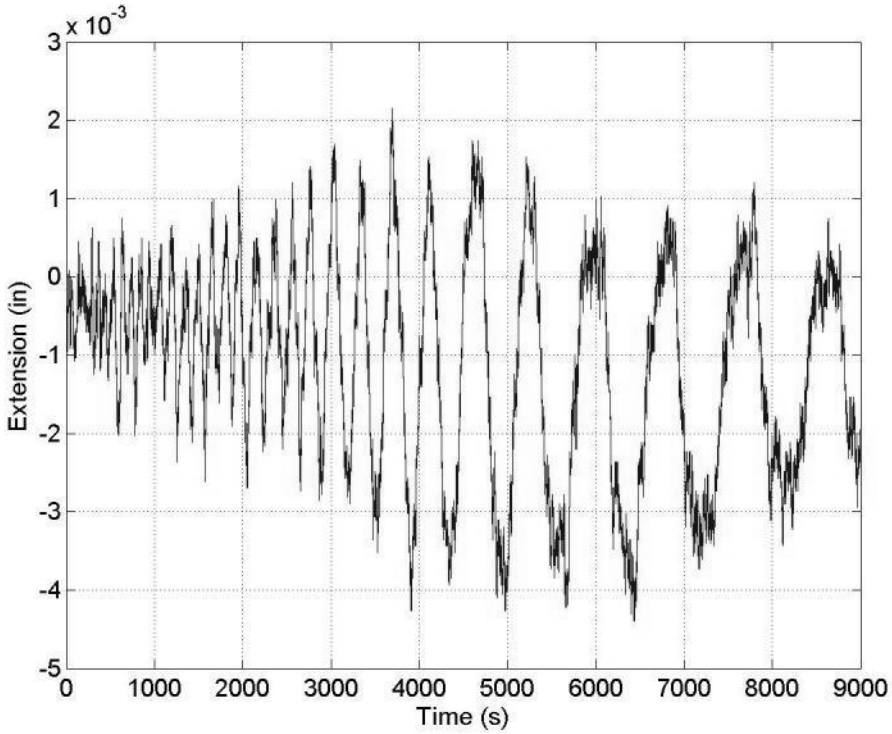

Figure 172: Specimen 1 (RBS24) - LVDT7

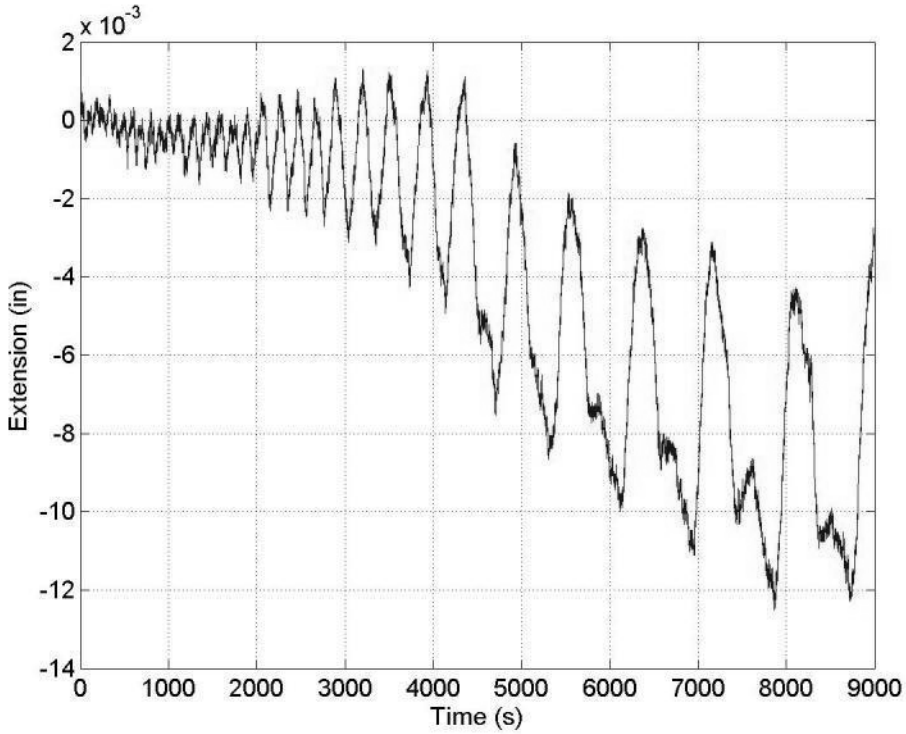

Figure 173: Specimen 1 (RBS24) - LVDT8

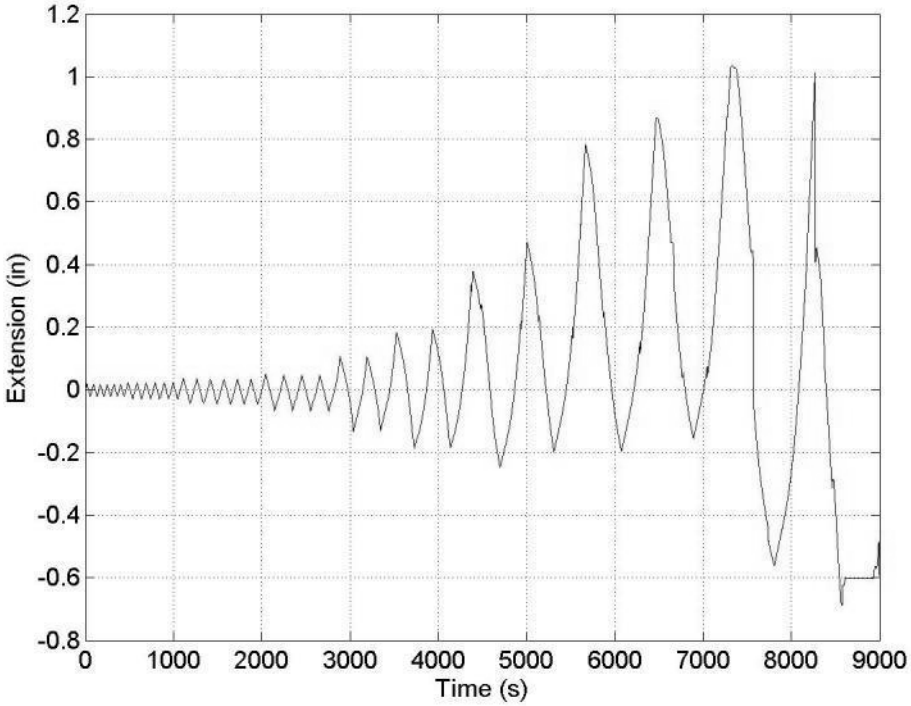

Figure 174: Specimen 1 (RBS24) - LVDT9

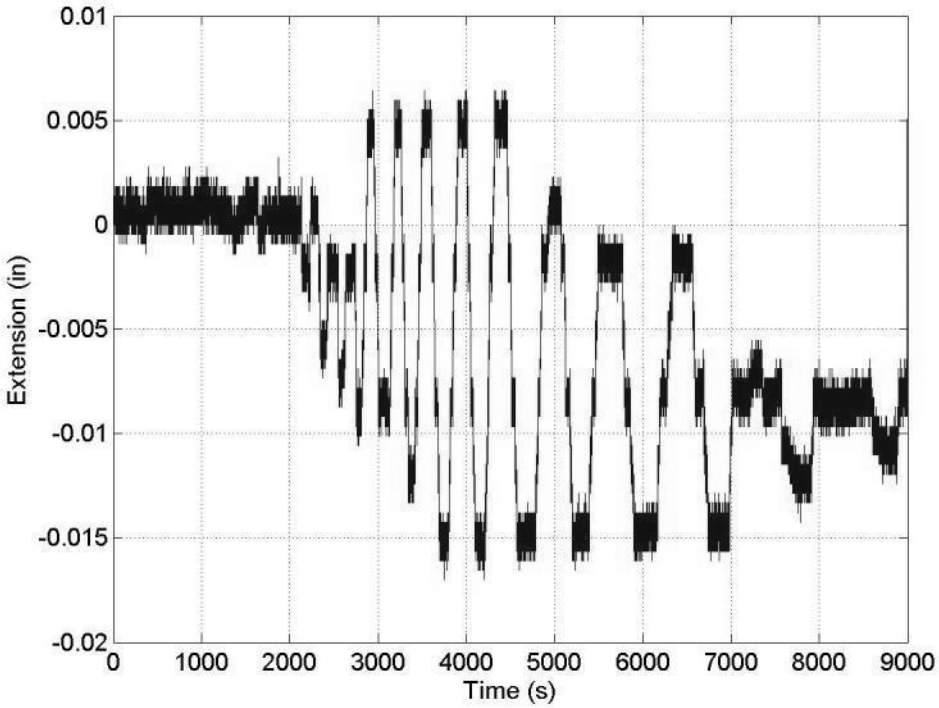

Figure 175: Specimen 1 (RBS24) - String Potentiometer 1 (column)

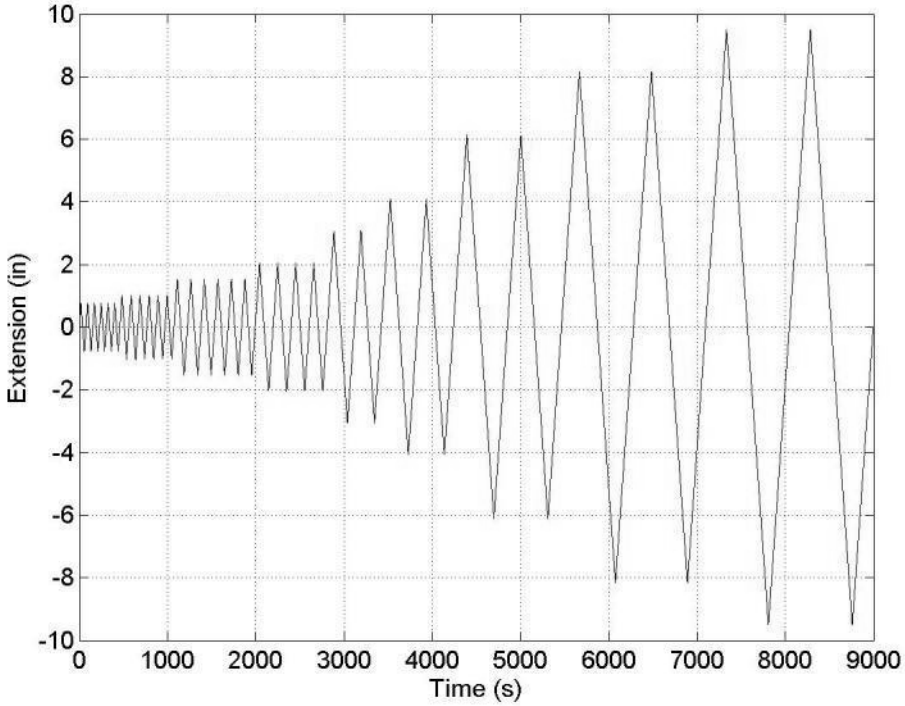

Figure 176: Specimen 1 (RBS24) - String Potentiometer 2 (actuator)

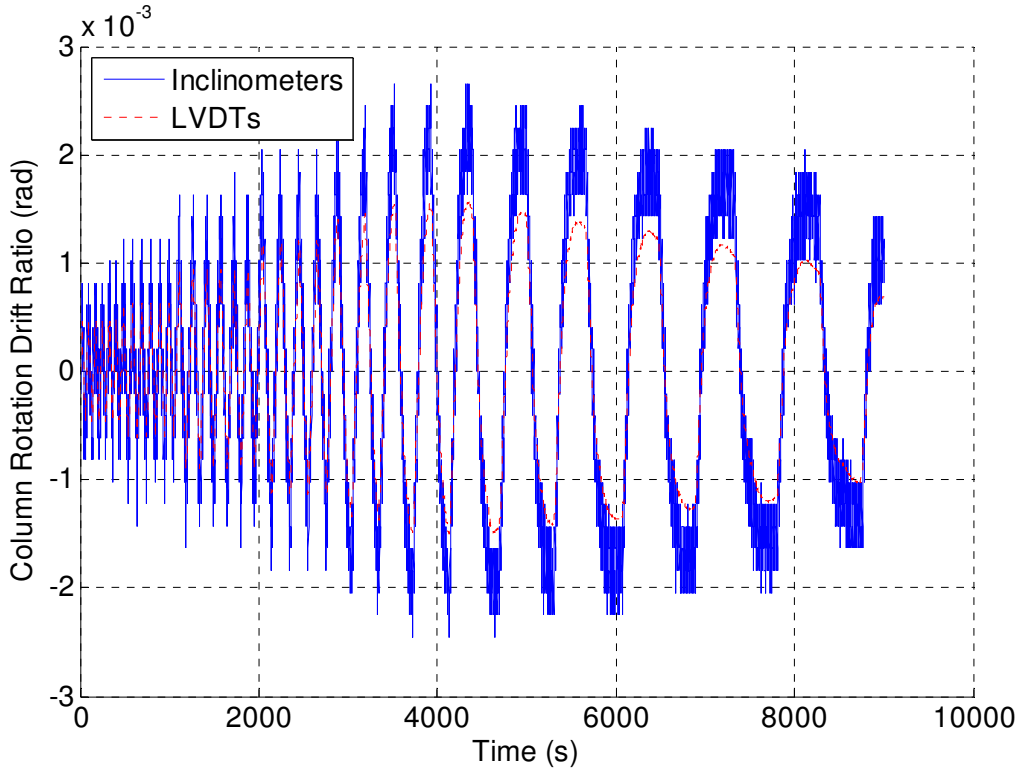

Figure 177: Specimen 1 (RBS24) - Column Rotation Comparison

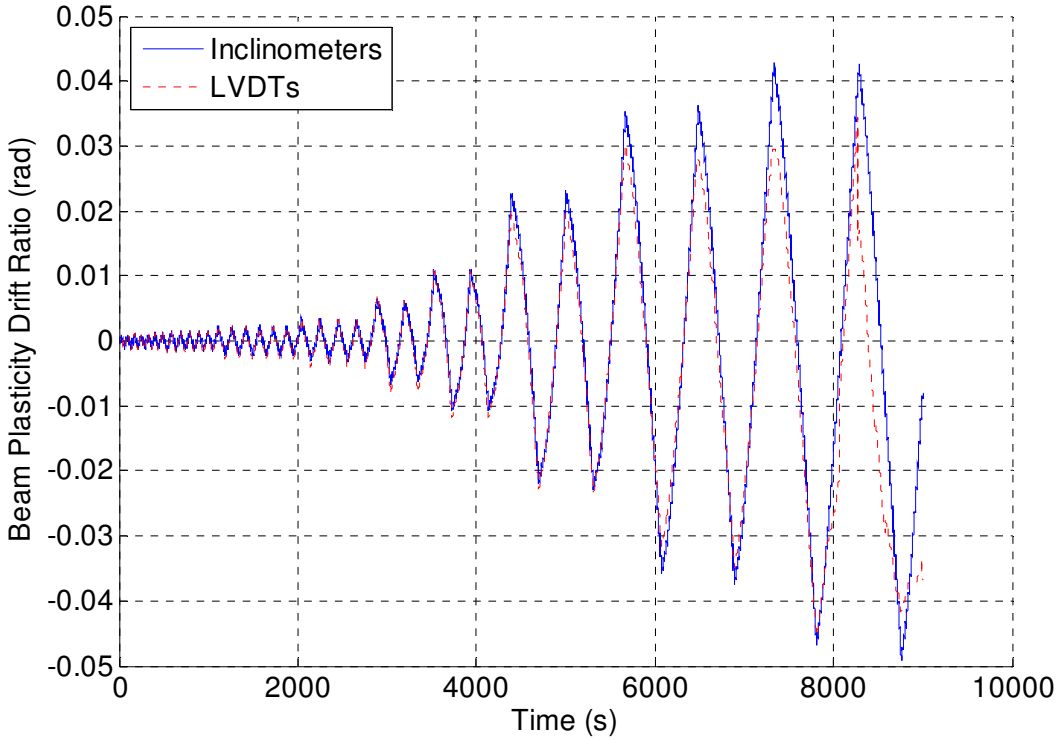

Figure 178: Specimen 1 (RBS24) - Beam Plasticity Comparison

Appendix I – Specimen 2 (RBS24-PAF12) Raw Instrumentation Data

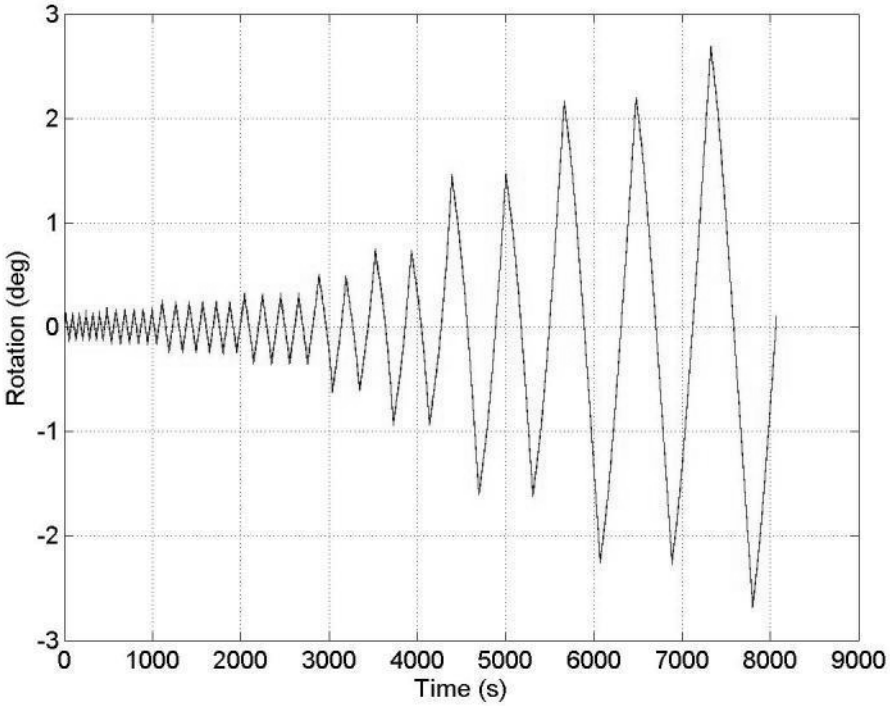

Figure 179: Specimen 2 (RBS24-PAF12) - Inclinometer 3 (beam)

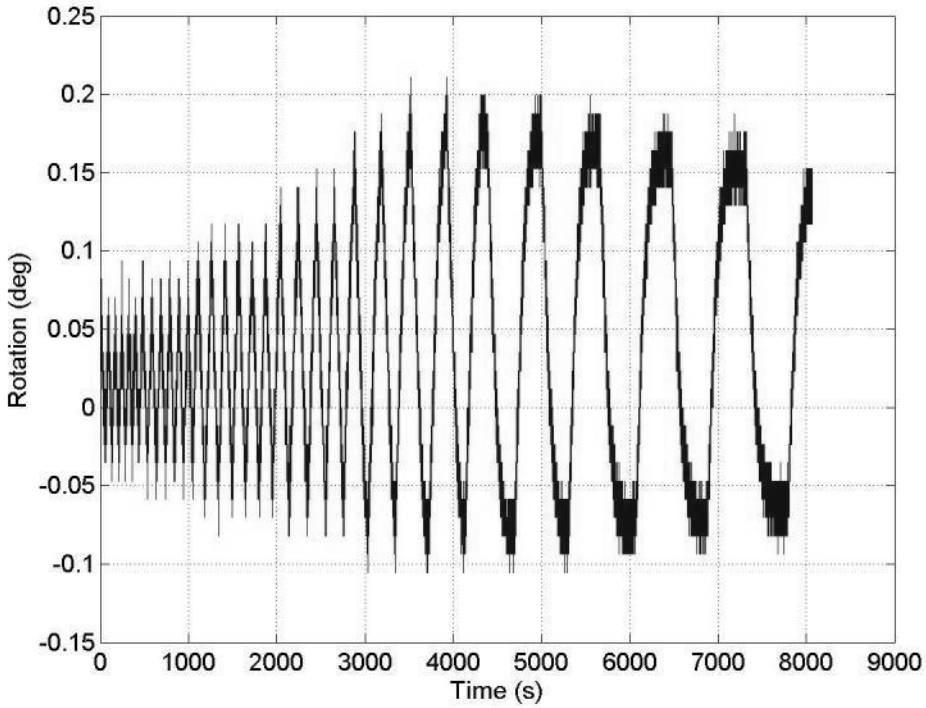

Figure 180: Specimen 2 (RBS24-PAF12) - Inclinometer 1 (column)

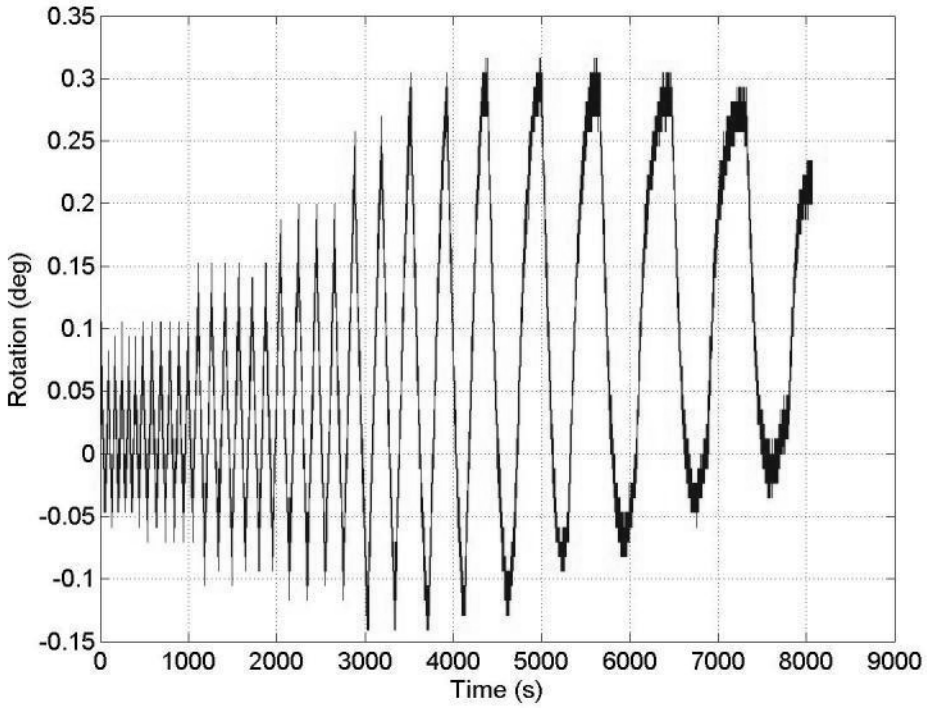

Figure 181: Specimen 2 (RBS24-PAF12) - Inclinometer 2 (endplate)

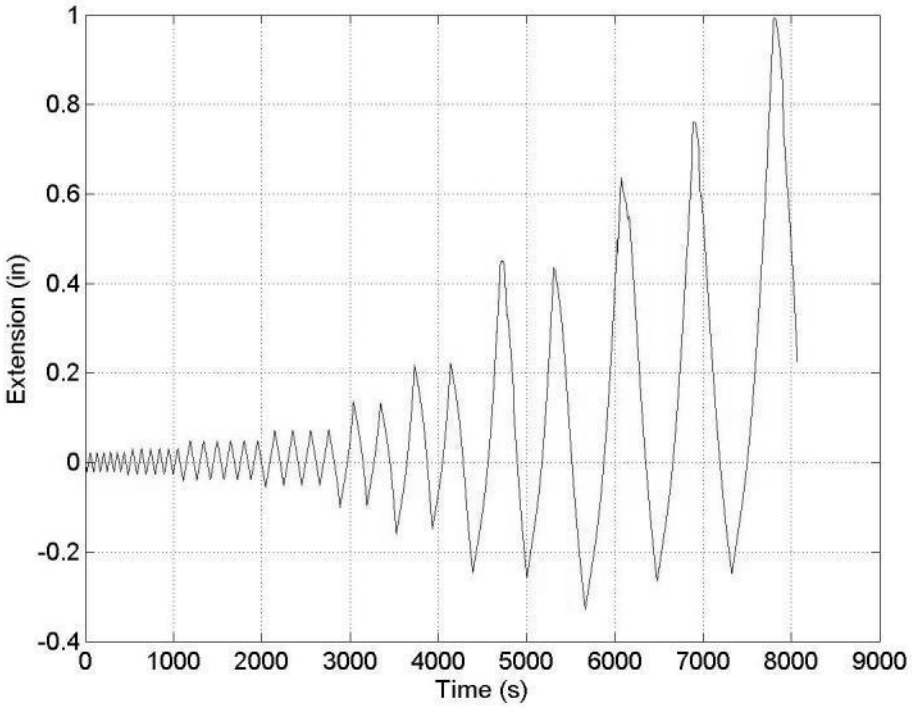

Figure 182: Specimen 2 (RBS24-PAF12) - LVDT1

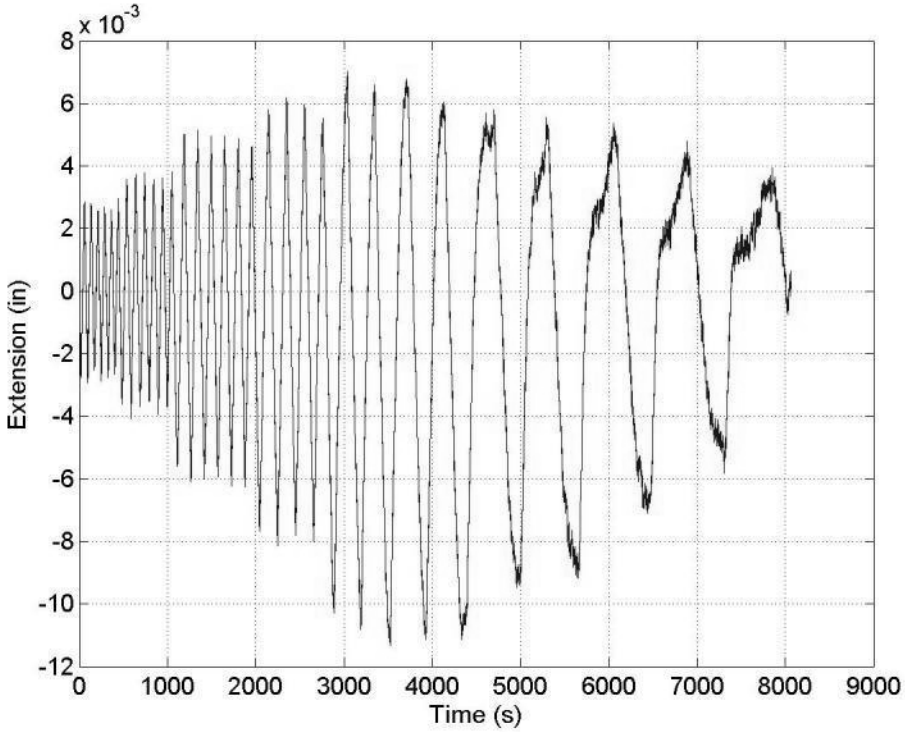

Figure 183: Specimen 2 (RBS24-PAF12) - LVDT2

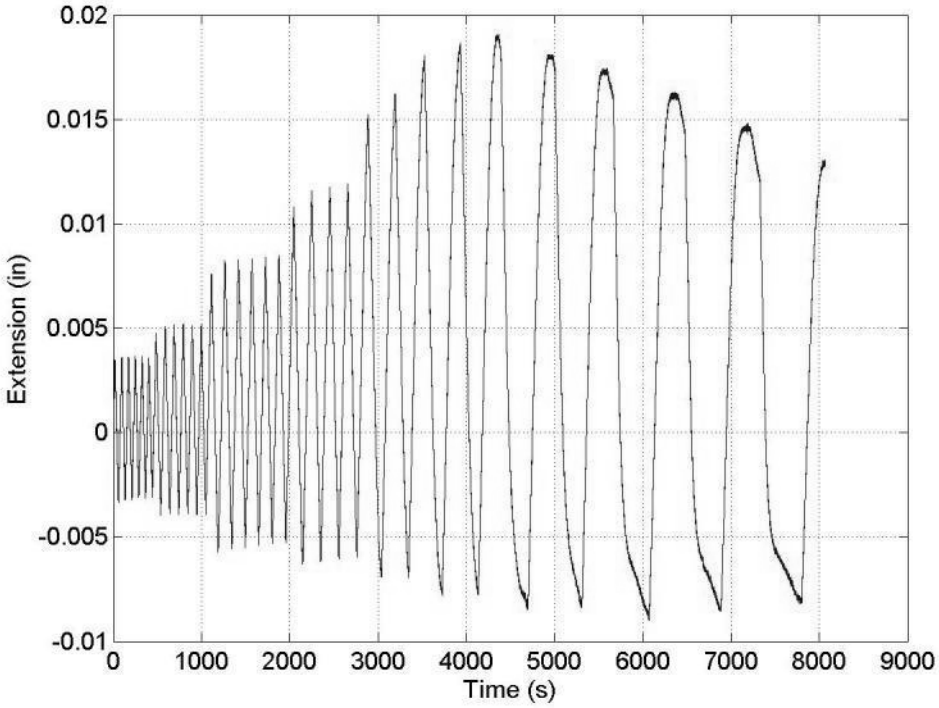

Figure 184: Specimen 2 (RBS24-PAF12) - LVDT3

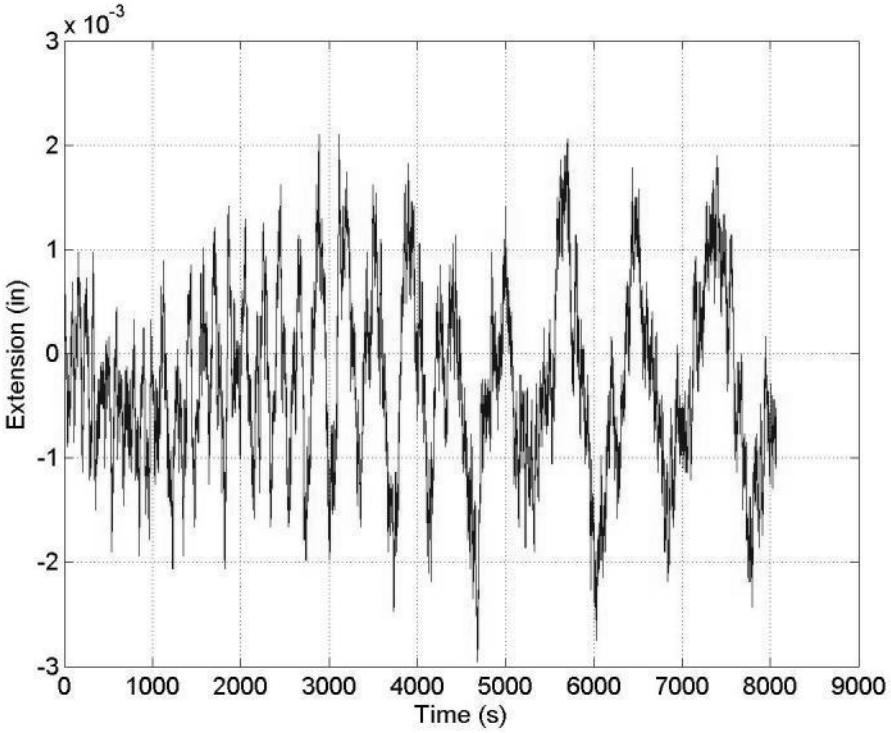

Figure 185: Specimen 2 (RBS24-PAF12) - LVDT4

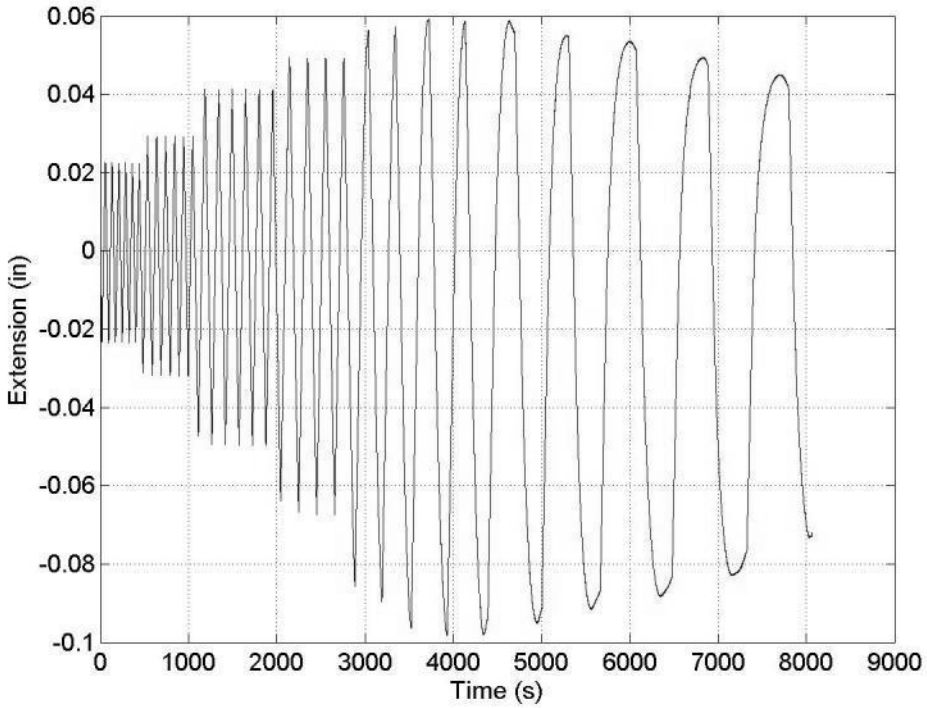

Figure 186: Specimen 2 (RBS24-PAF12) - LVDT5

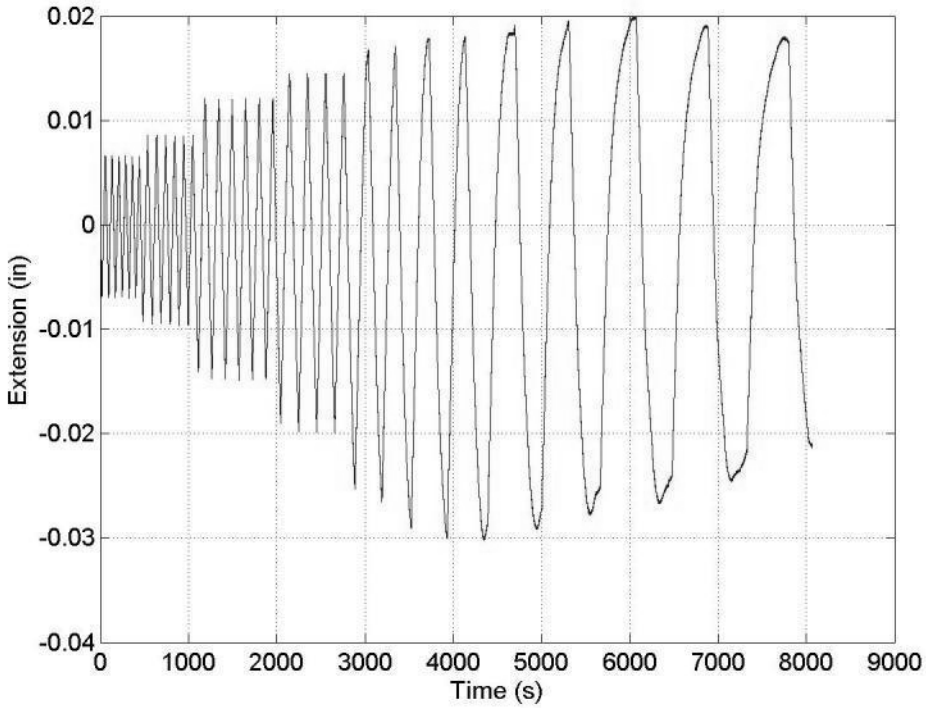

Figure 187: Specimen 2 (RBS24-PAF12) - LVDT6

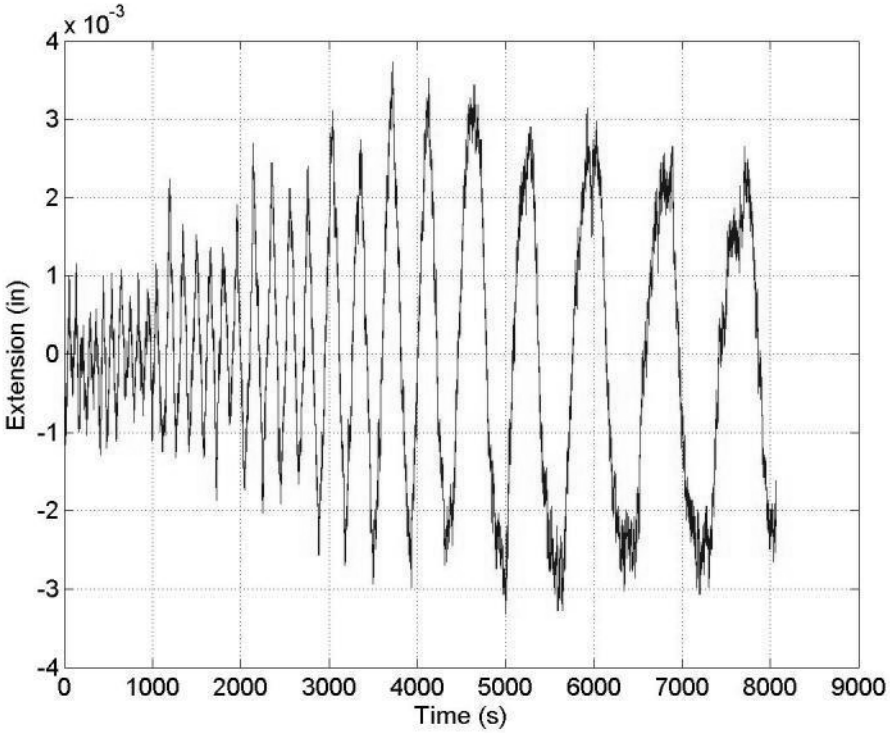

Figure 188: Specimen 2 (RBS24-PAF12) - LVDT7

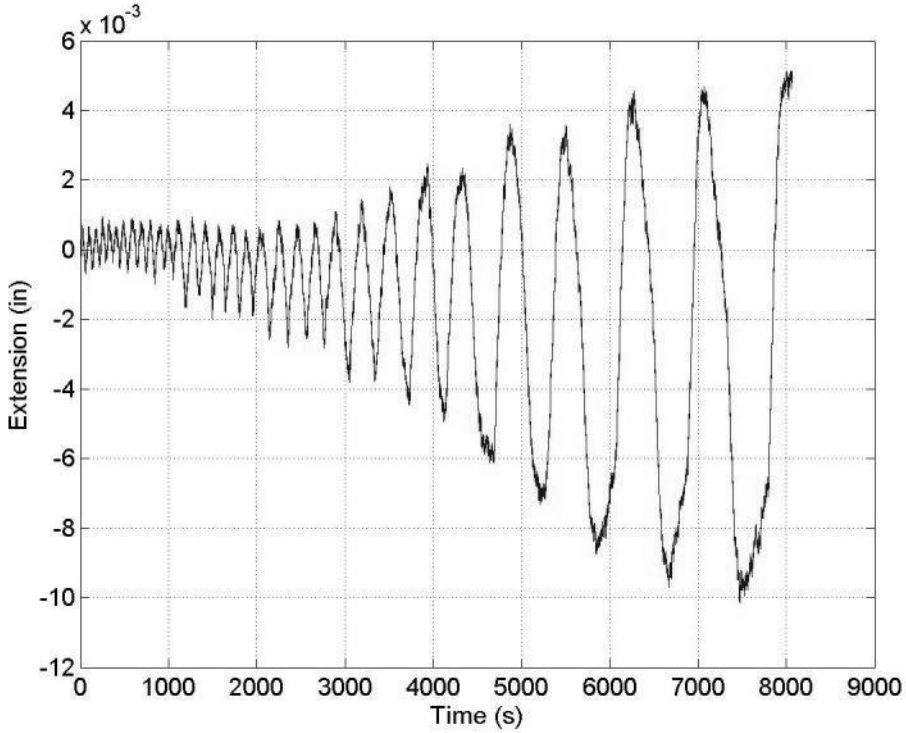

Figure 189: Specimen 2 (RBS24-PAF12) - LVDT8

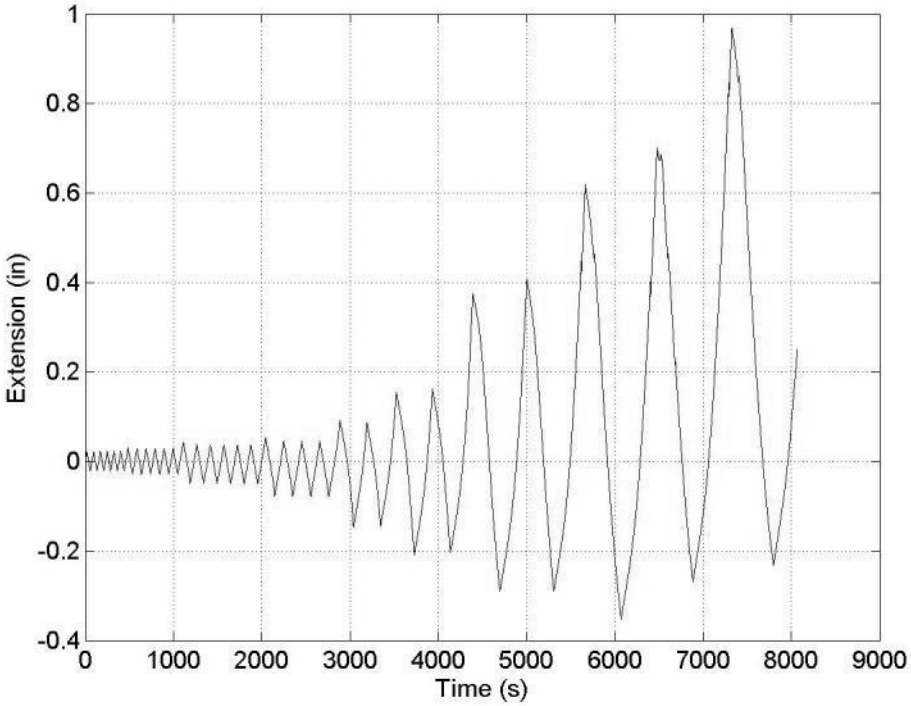

Figure 190: Specimen 2 (RBS24-PAF12) - LVDT9

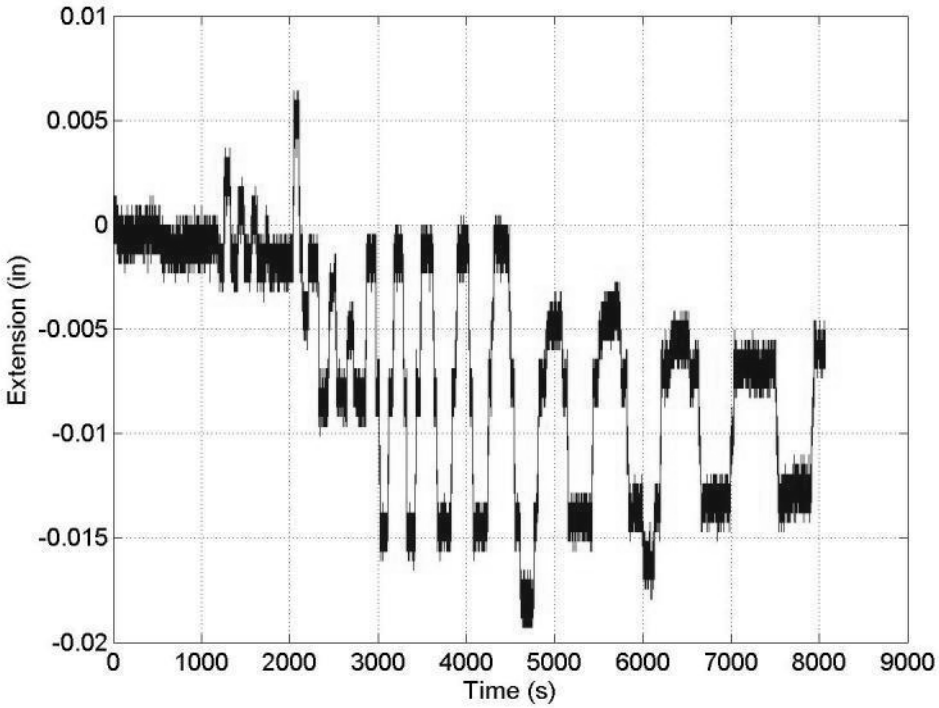

Figure 191: Specimen 2 (RBS24-PAF12) - String Potentiometer 1 (column)

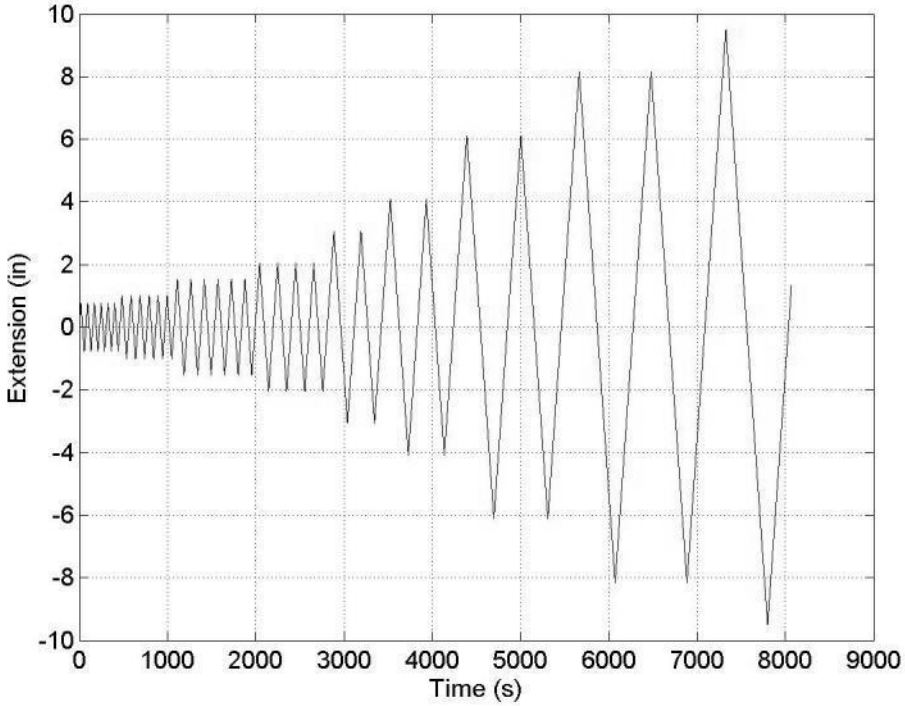

Figure 192: Specimen 2 (RBS24-PAF12) - String Potentiometer 2 (actuator)

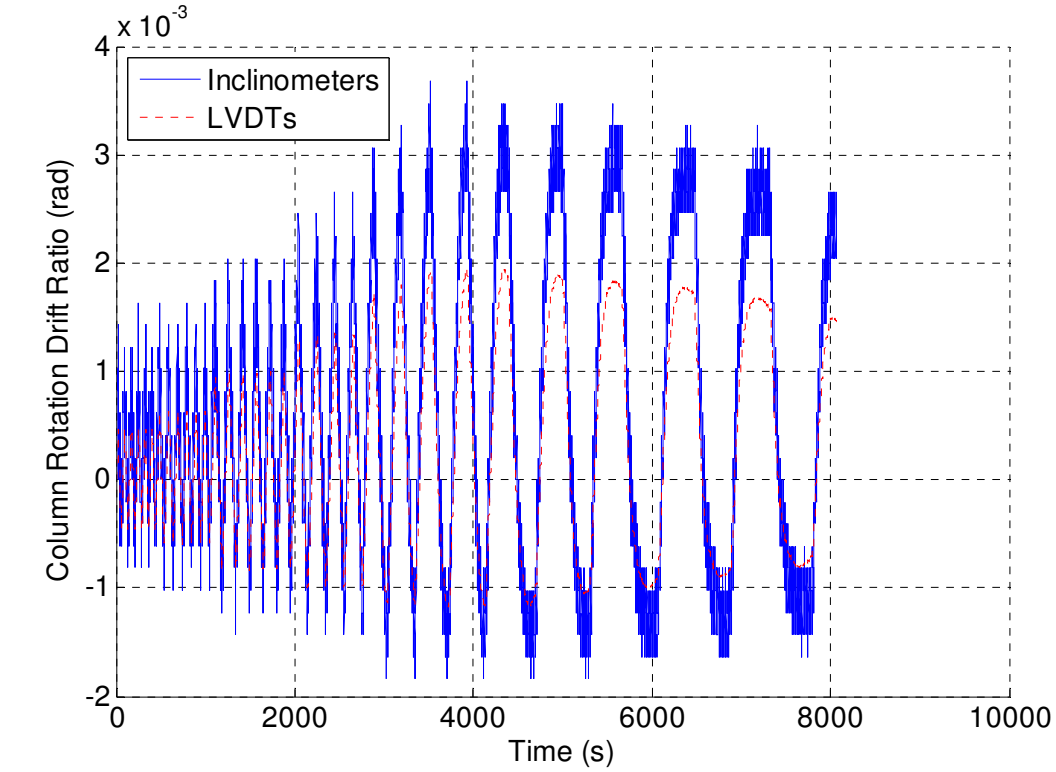

Figure 193: Specimen 2 (RBS24-PAF12) - Column Rotation Comparison

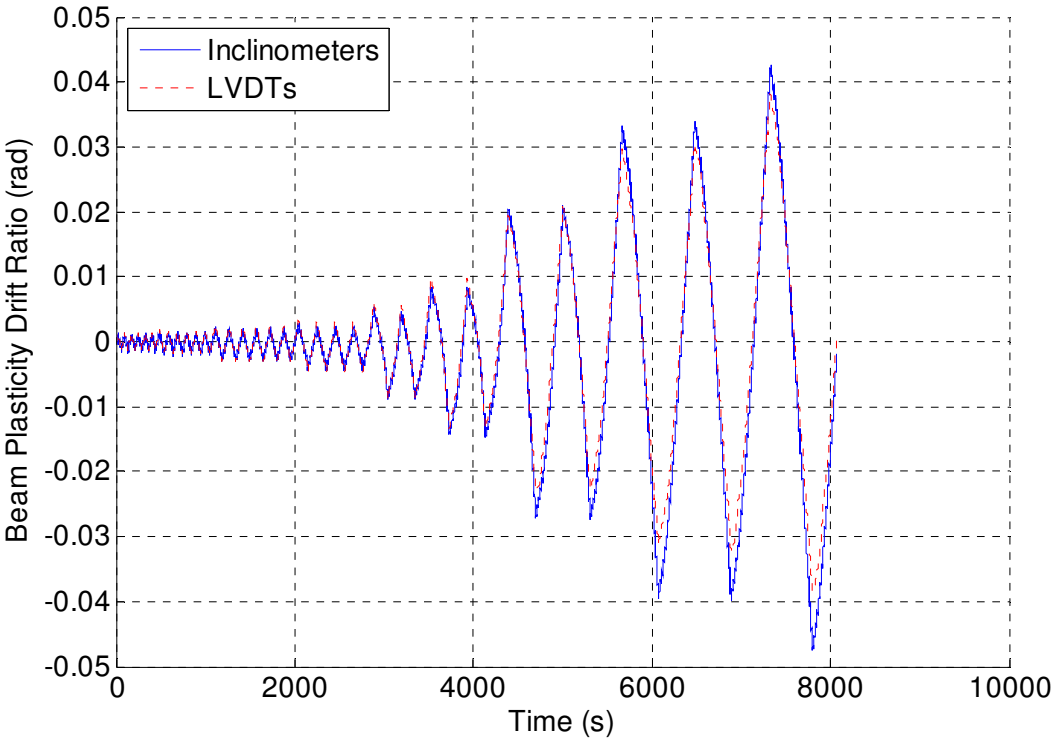

Figure 194: Specimen 2 (RBS24-PAF12) - Beam Plasticity Comparison

Appendix J – Specimen 3 (W24) Raw Instrumentation Data

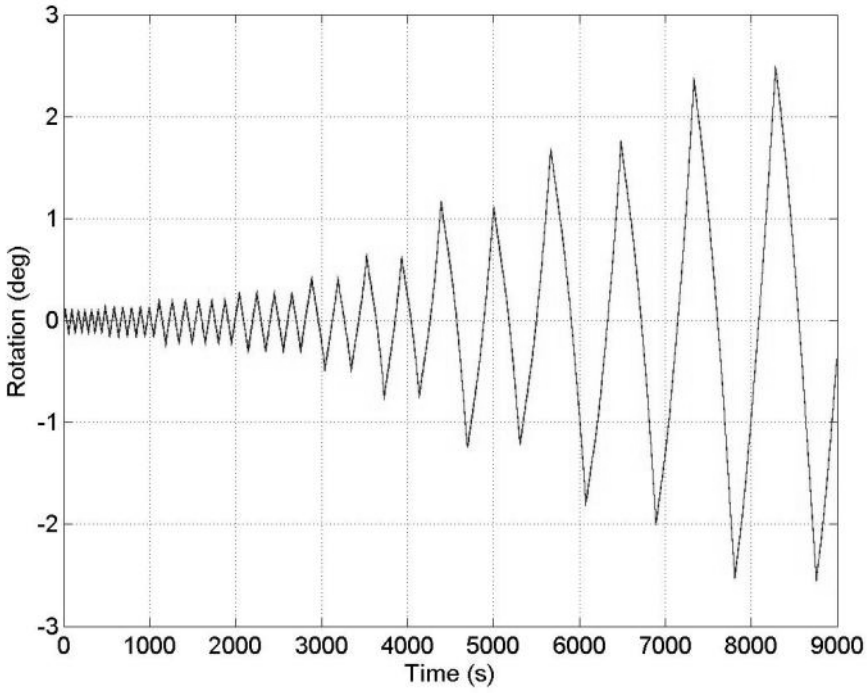

Figure 195: Specimen 3 (W24) - Inclinometer 3 (beam)

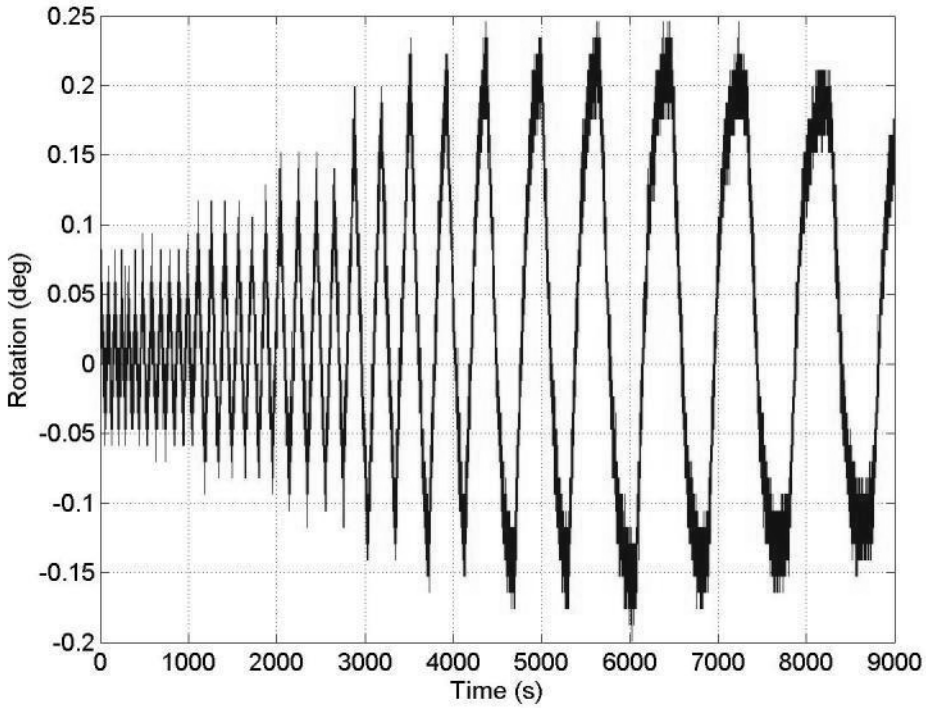

Figure 196: Specimen 3 (W24) - Inclinometer 1 (column)

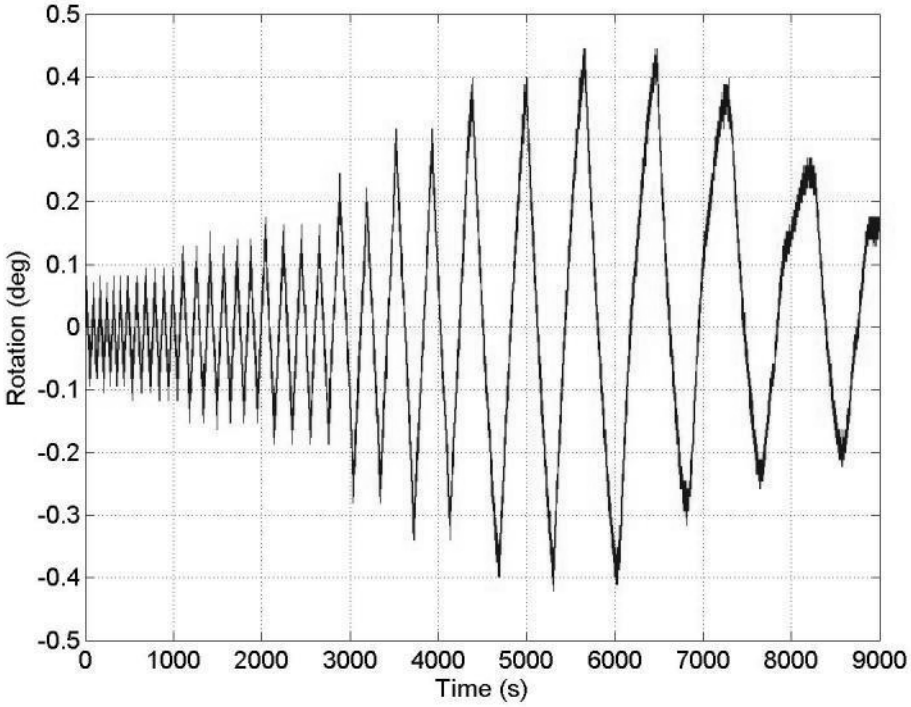

Figure 197: Specimen 3 (W24) - Inclinometer 2 (endplate)

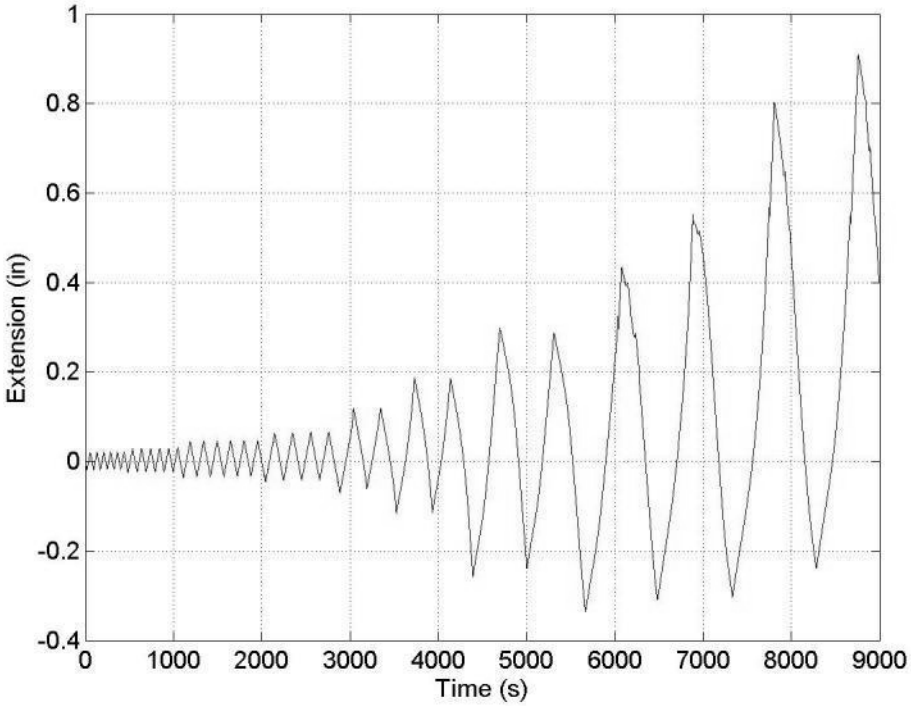

Figure 198: Specimen 3 (W24) – LVDT1

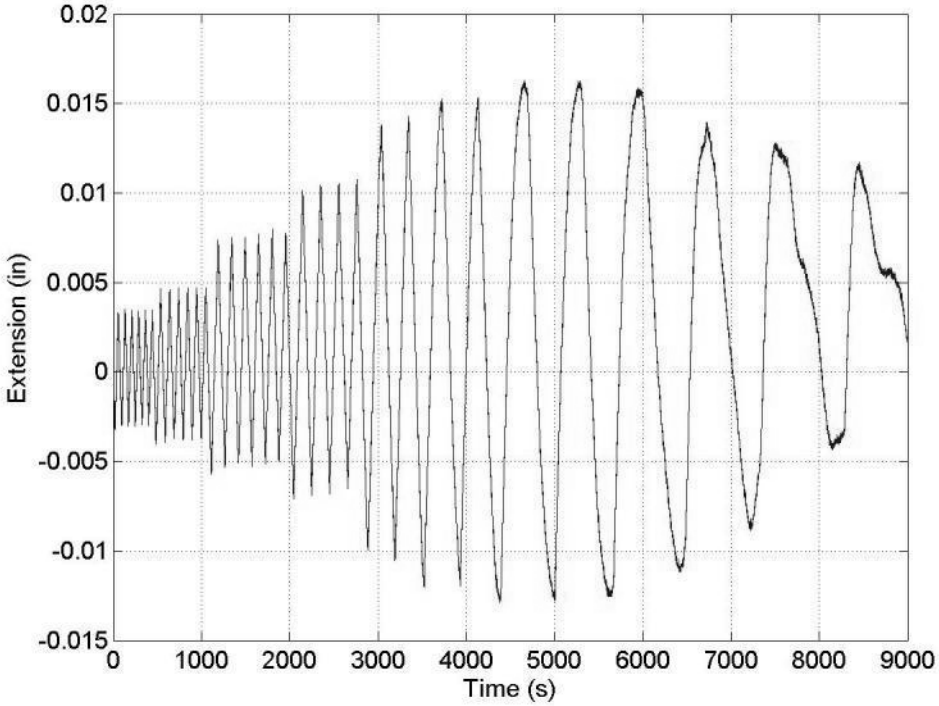

Figure 199: Specimen 3 (W24) – LVDT2

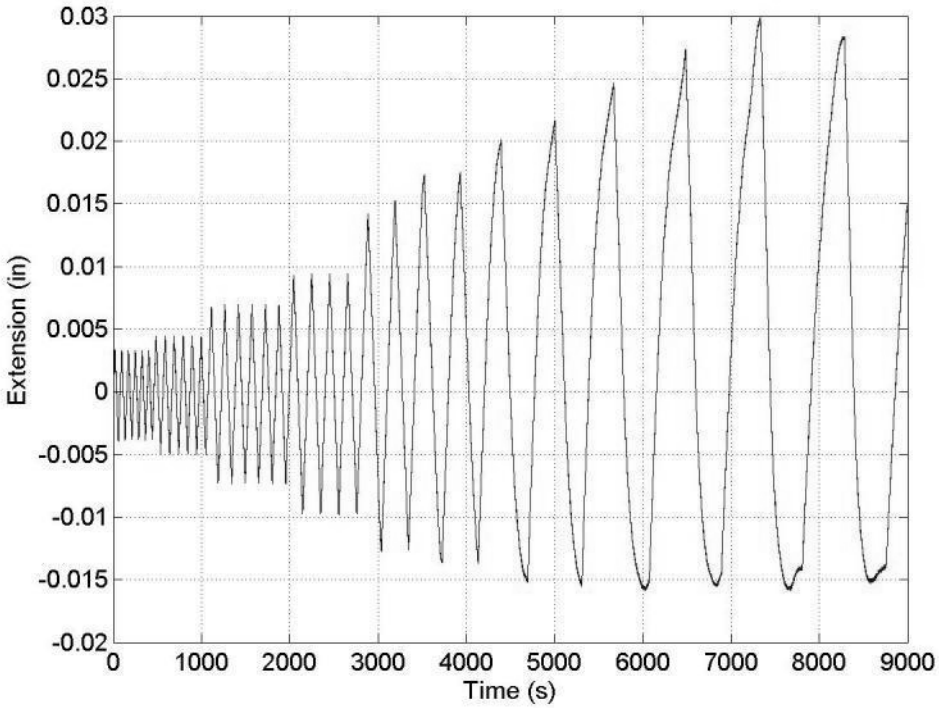

Figure 200: Specimen 3 (W24) – LVDT3

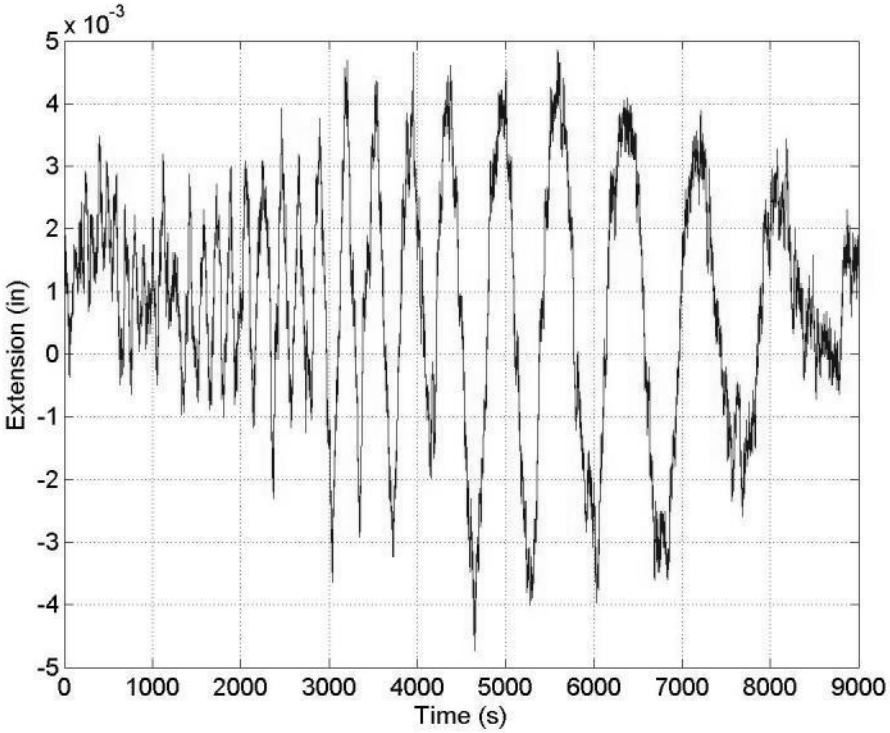

Figure 201: Specimen 3 (W24) – LVDT4

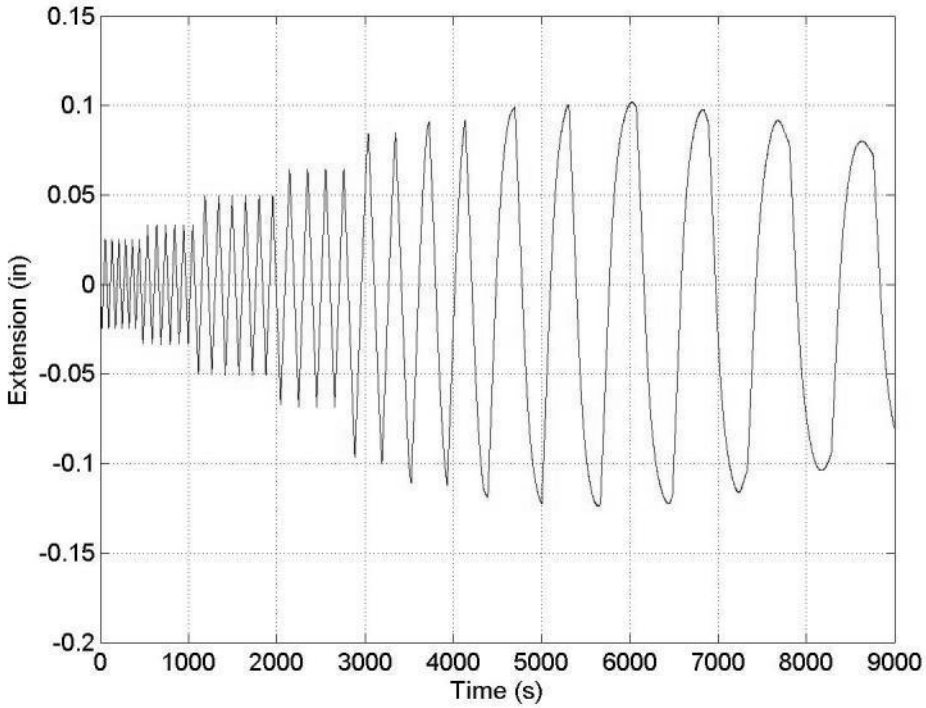

Figure 202: Specimen 3 (W24) – LVDT5

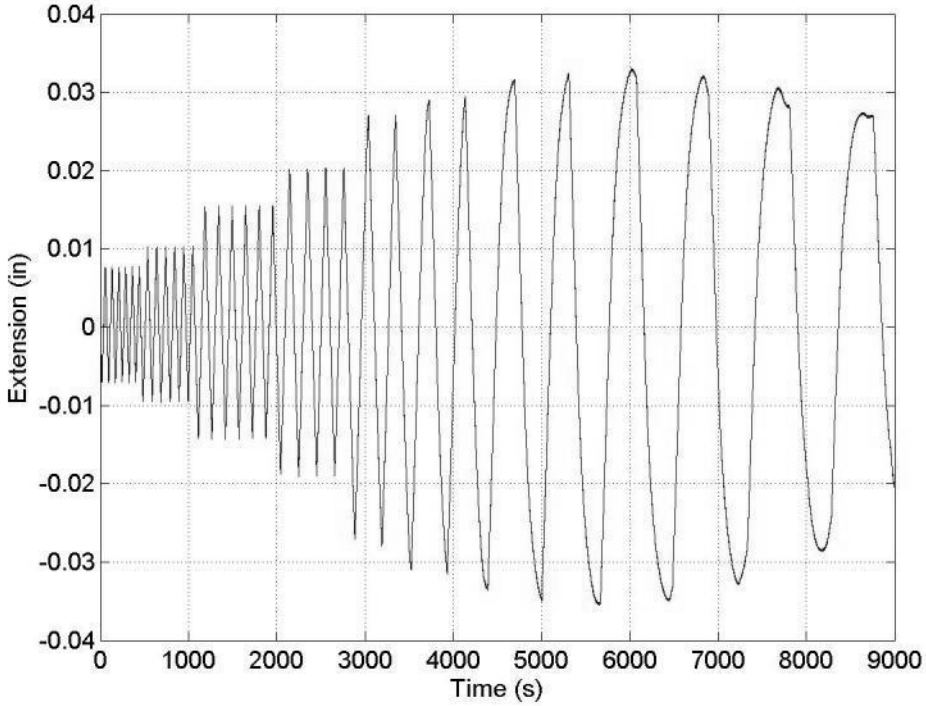

Figure 203: Specimen 3 (W24) – LVDT6

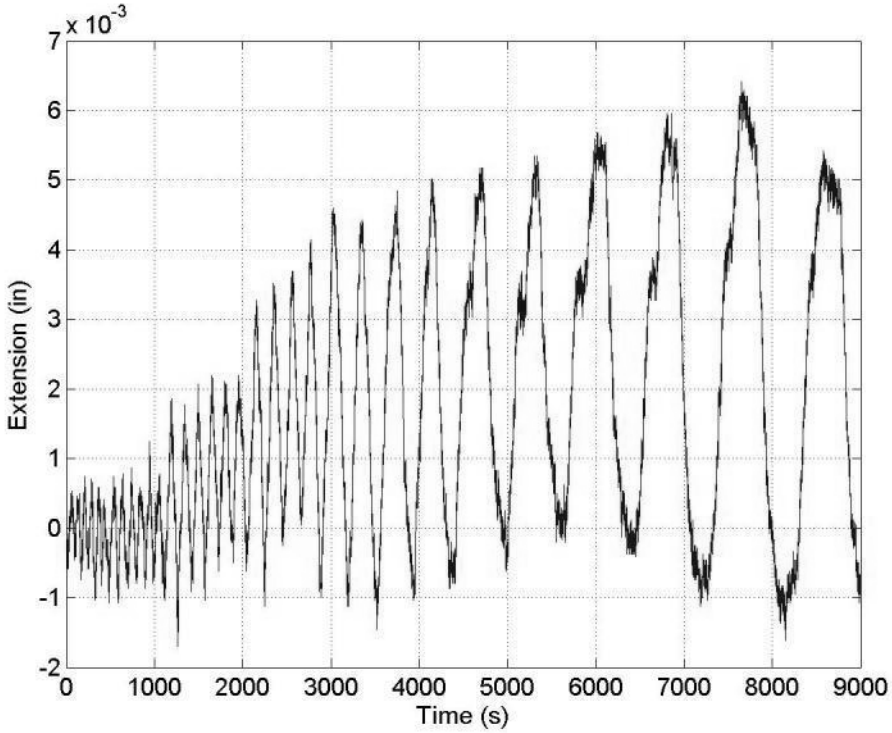

Figure 204: Specimen 3 (W24) – LVDT7

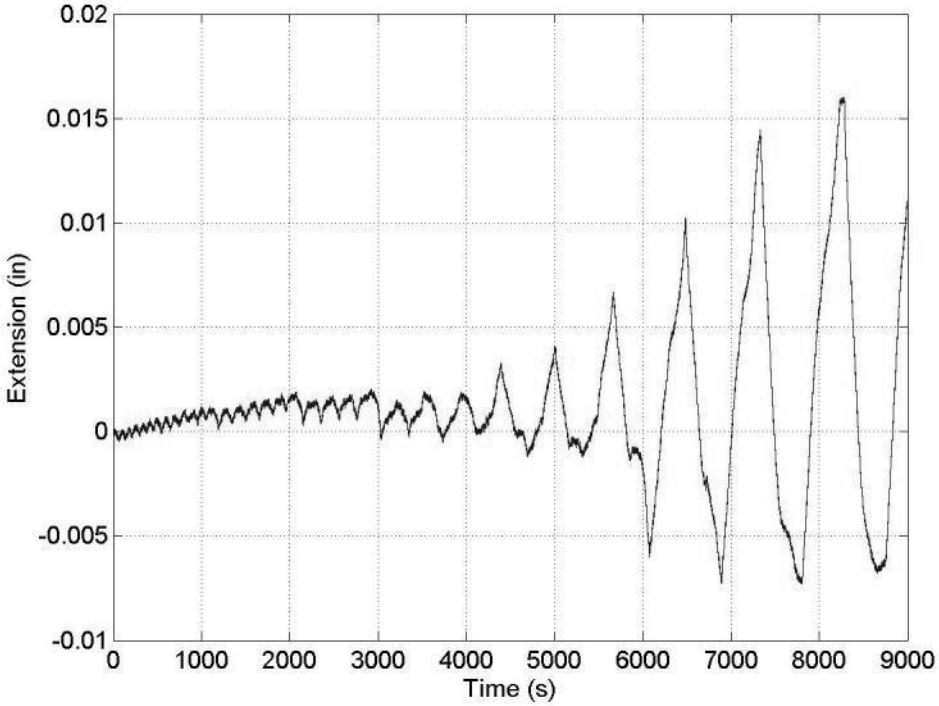

Figure 205: Specimen 3 (W24) – LVDT8

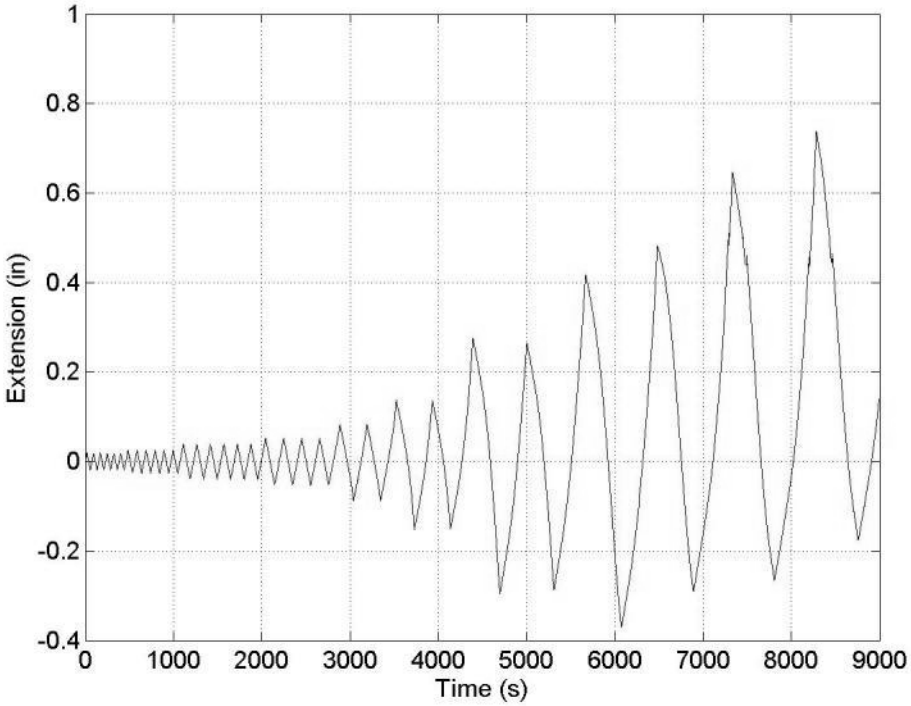

Figure 206: Specimen 3 (W24) – LVDT9

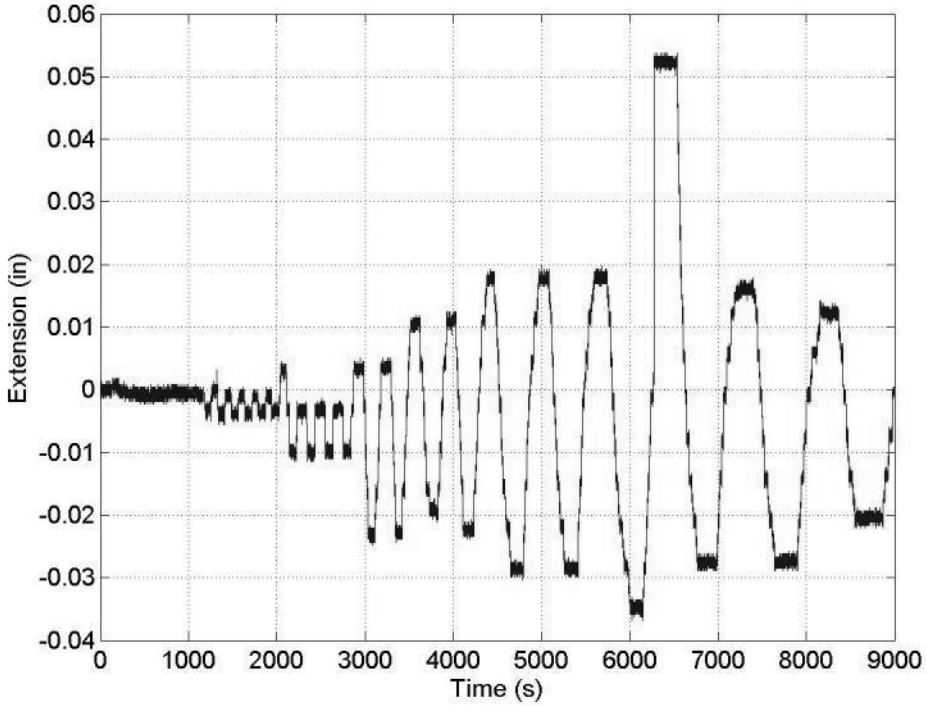

Figure 207: Specimen 3 (W24) - String Potentiometer 1 (column)

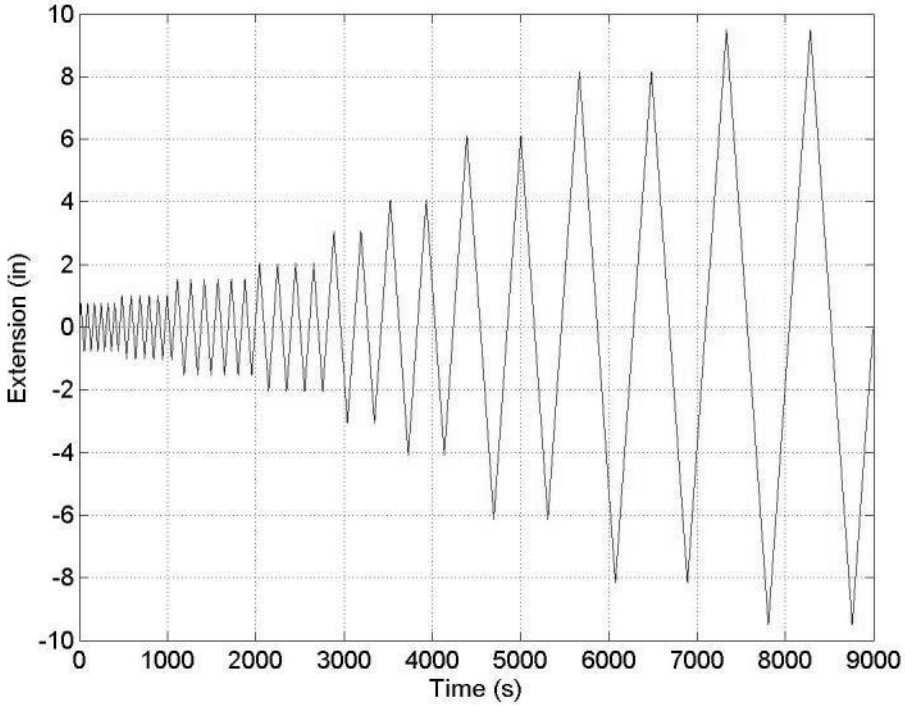

Figure 208: Specimen 3 (W24) - String Potentiometer 2 (actuator)

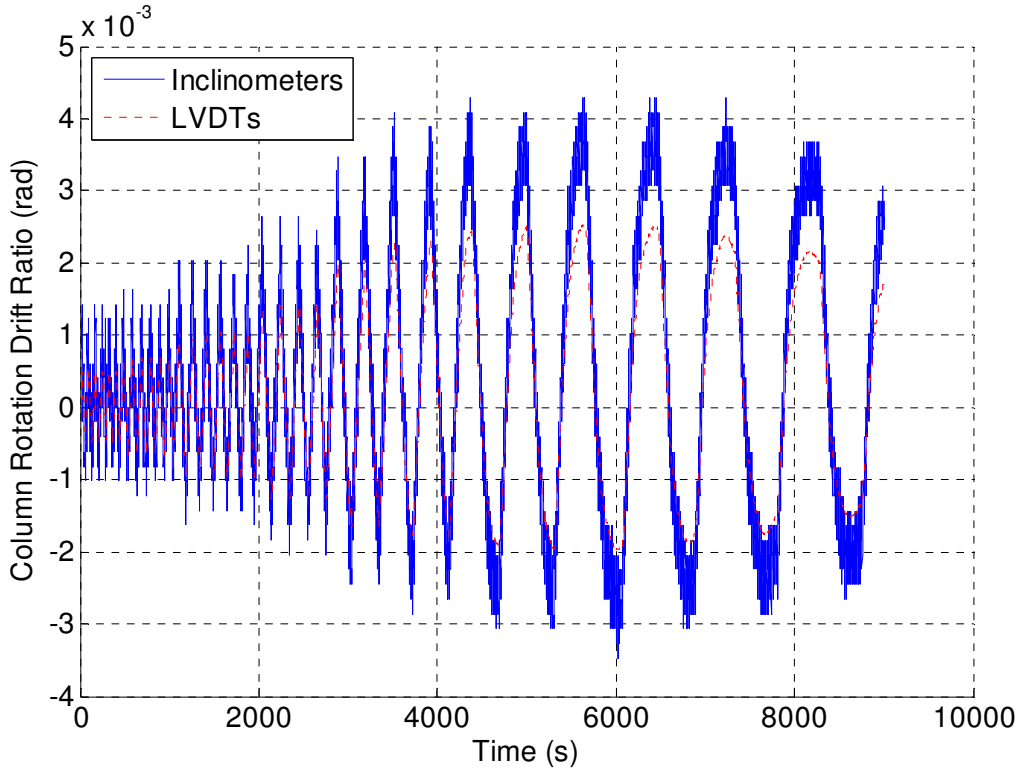

Figure 209: Specimen 3 (W24) - Column Rotation Comparison

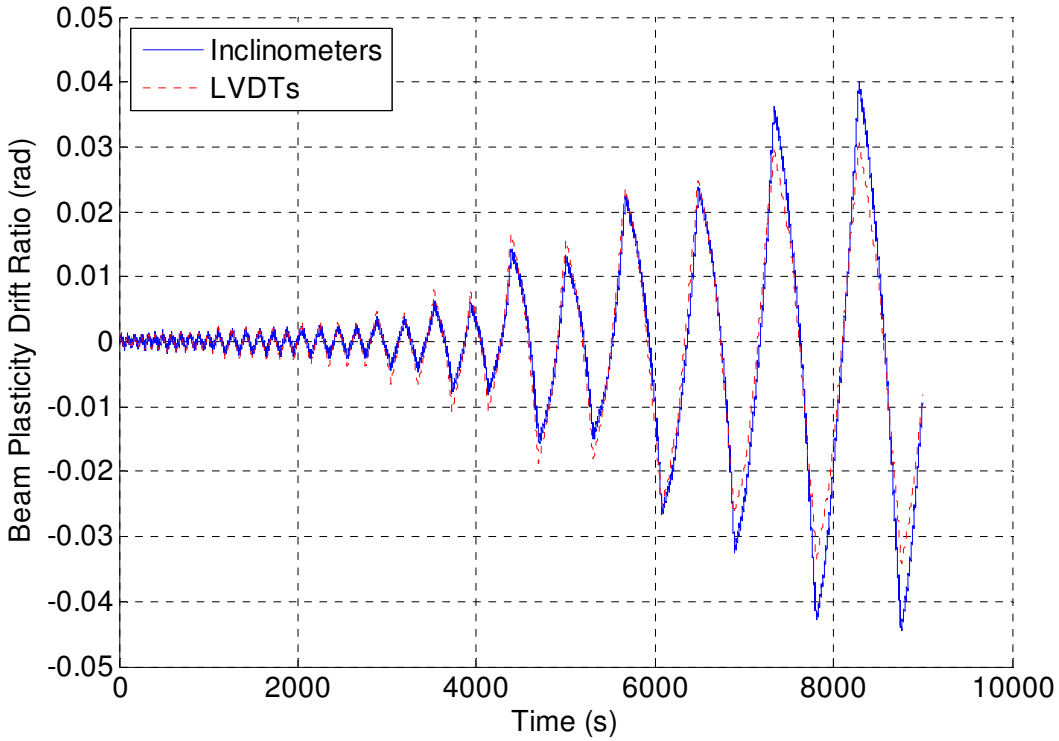

Figure 210: Specimen 3 (W24) - Beam Plasticity Comparison

Appendix K – Specimen 4 (W24-PAF12) Raw Instrumentation Data

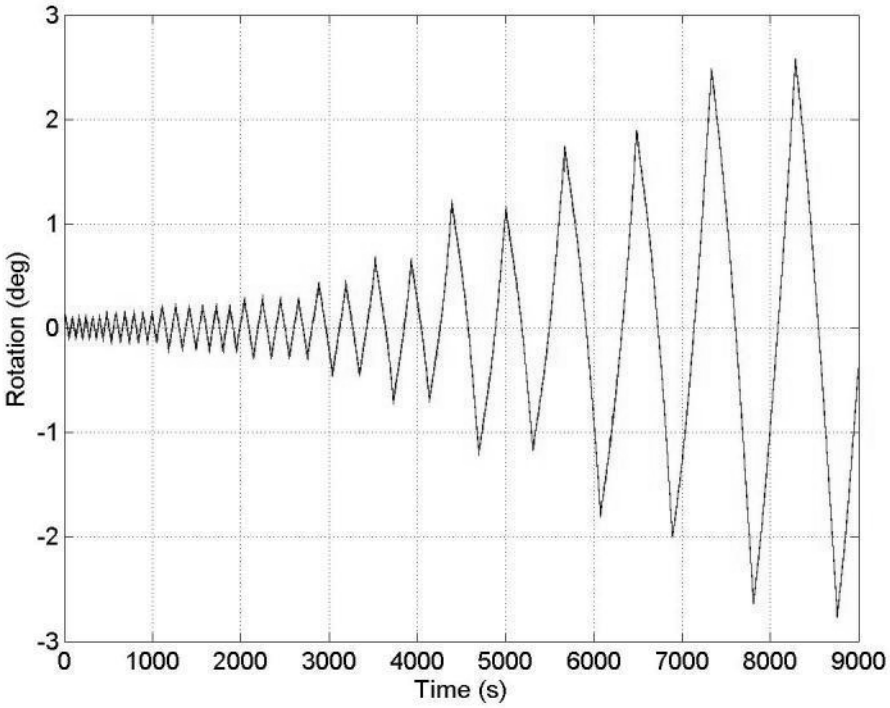

Figure 211: Specimen 4 (W24-PAF12) - Inclinometer 3 (beam)

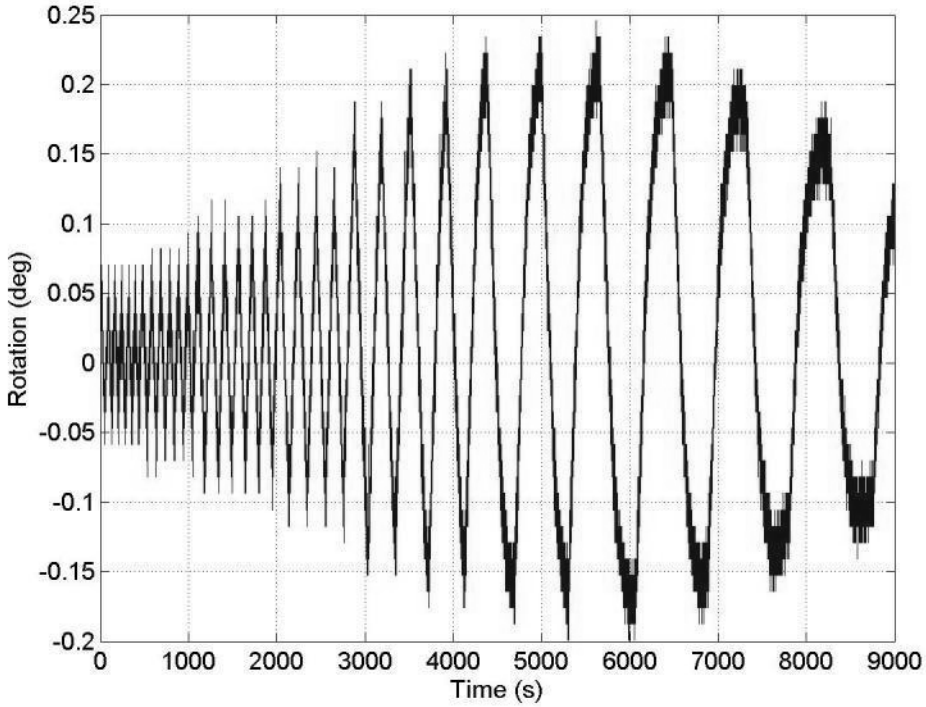

Figure 212: Specimen 4 (W24-PAF12) - Inclinometer 1 (column)

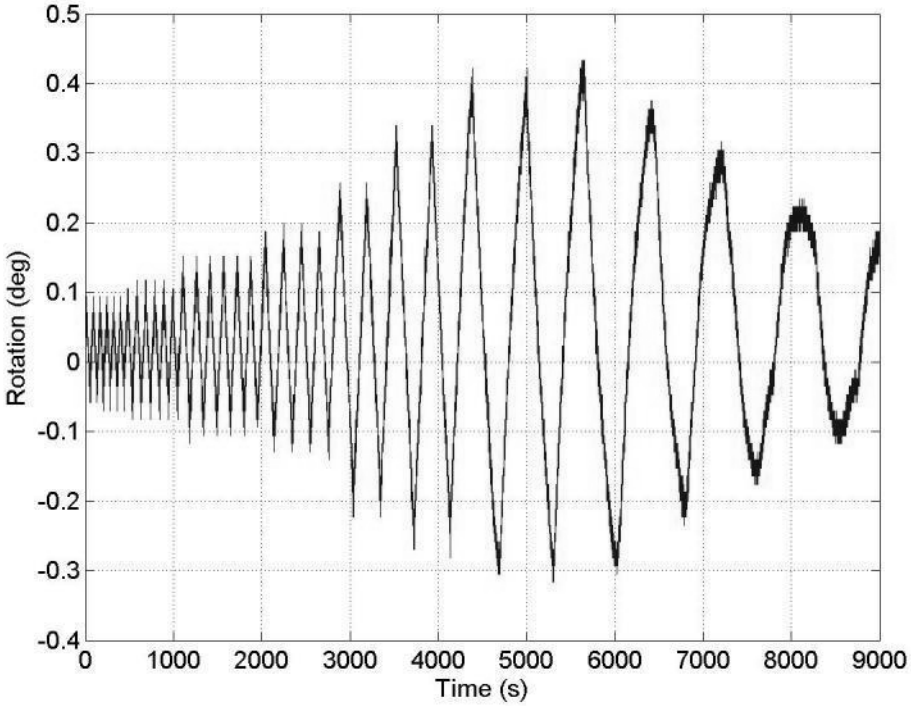

Figure 213: Specimen 4 (W24-PAF12) - Inclinometer 2 (endplate)

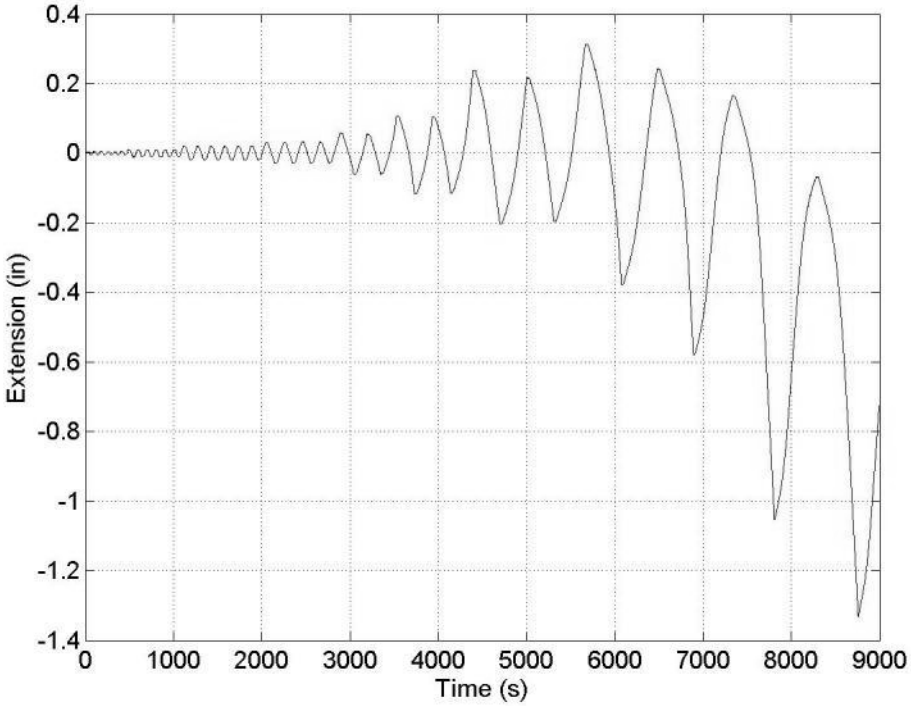

Figure 214: Specimen 4 (W24-PAF12) – LVDT1

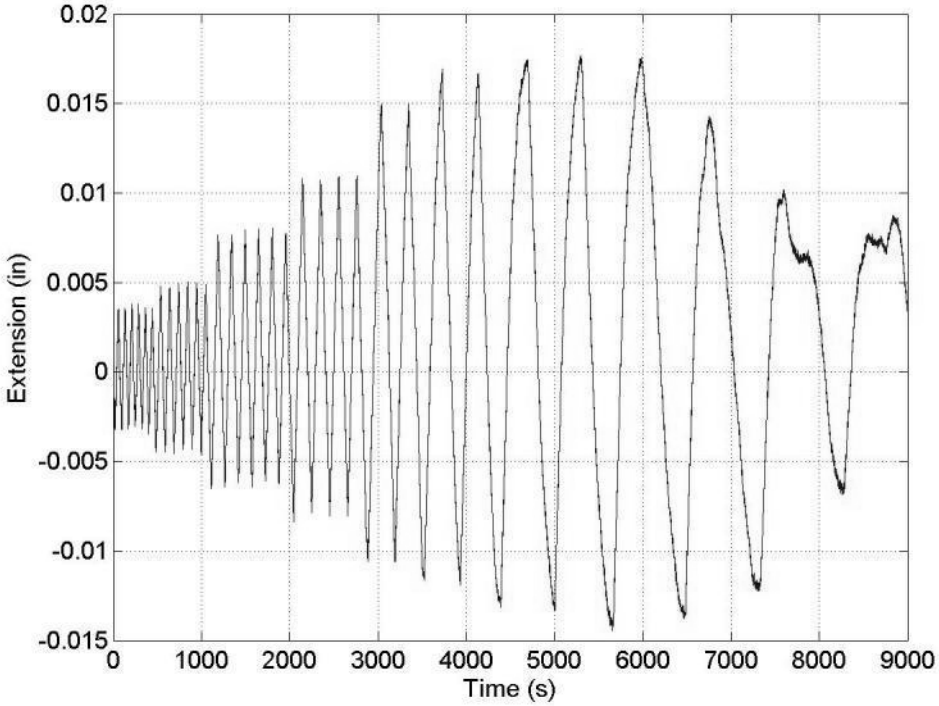

Figure 215: Specimen 4 (W24-PAF12) – LVDT2

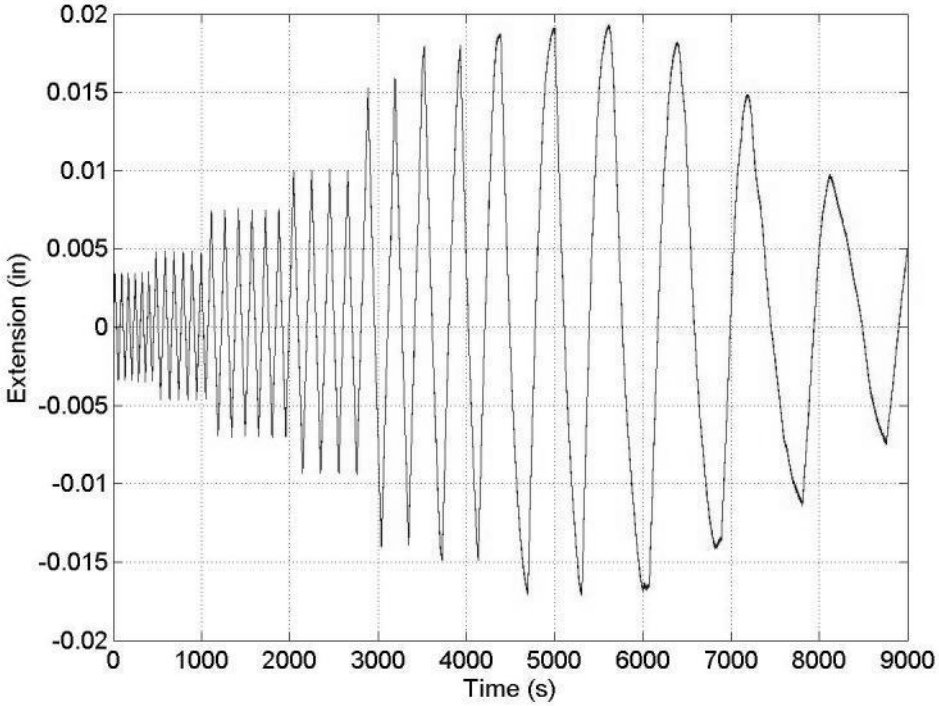

Figure 216: Specimen 4 (W24-PAF12) – LVDT3

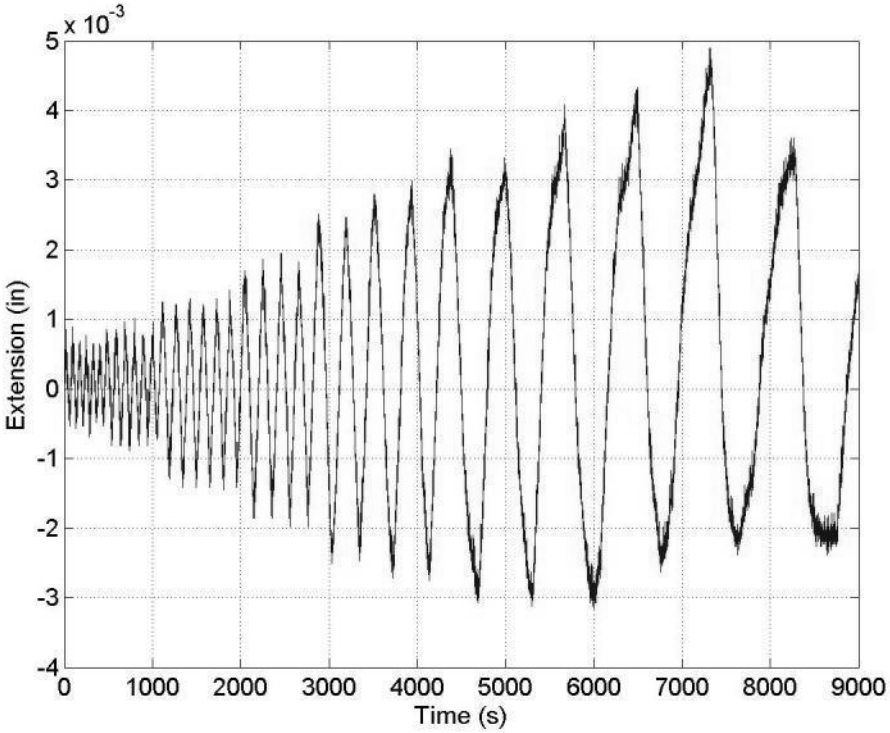

Figure 217: Specimen 4 (W24-PAF12) – LVDT4

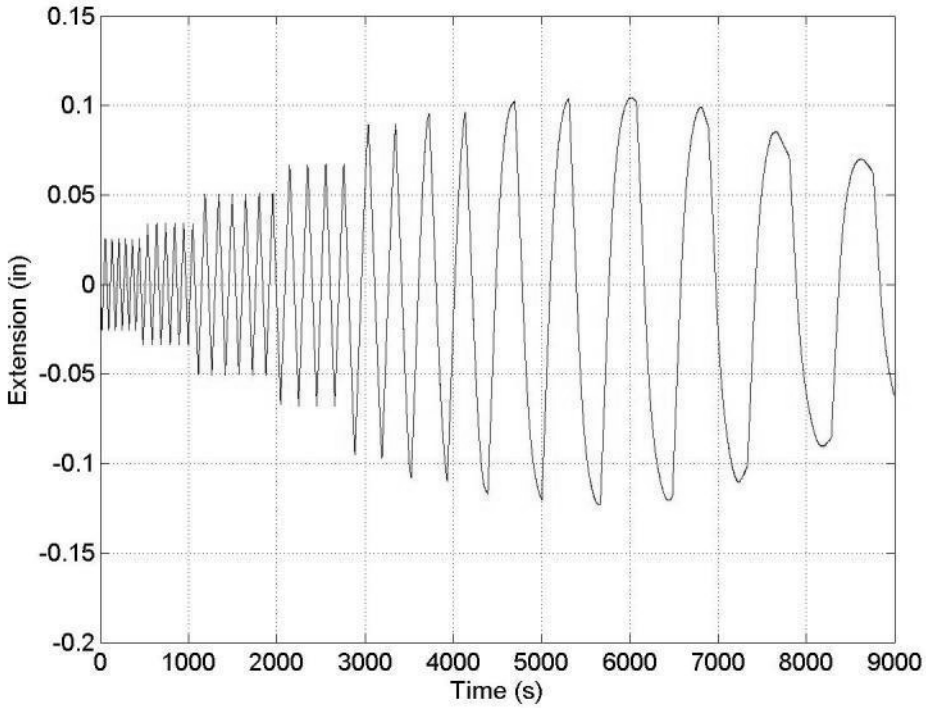

Figure 218: Specimen 4 (W24-PAF12) – LVDT5

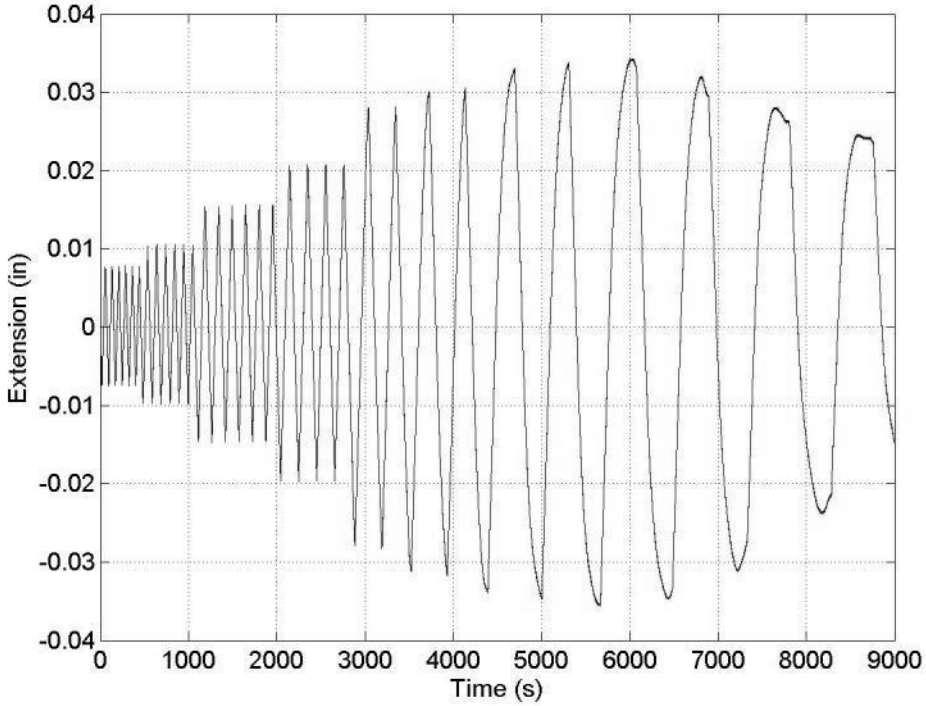

Figure 219: Specimen 4 (W24-PAF12) – LVDT6

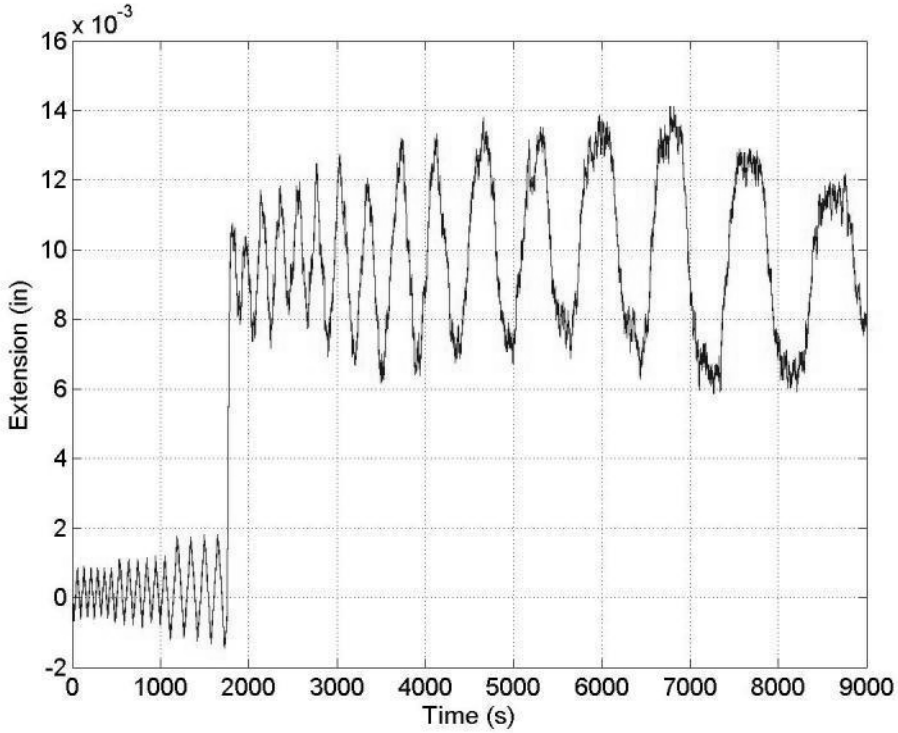

Figure 220: Specimen 4 (W24-PAF12) – LVDT7

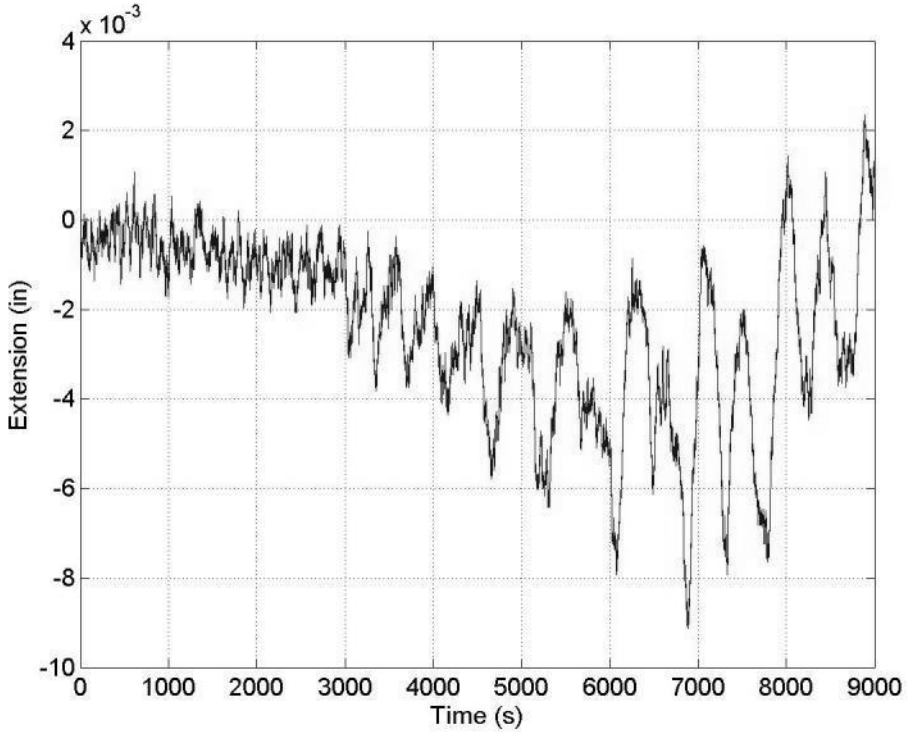

Figure 221: Specimen 4 (W24-PAF12) – LVDT8

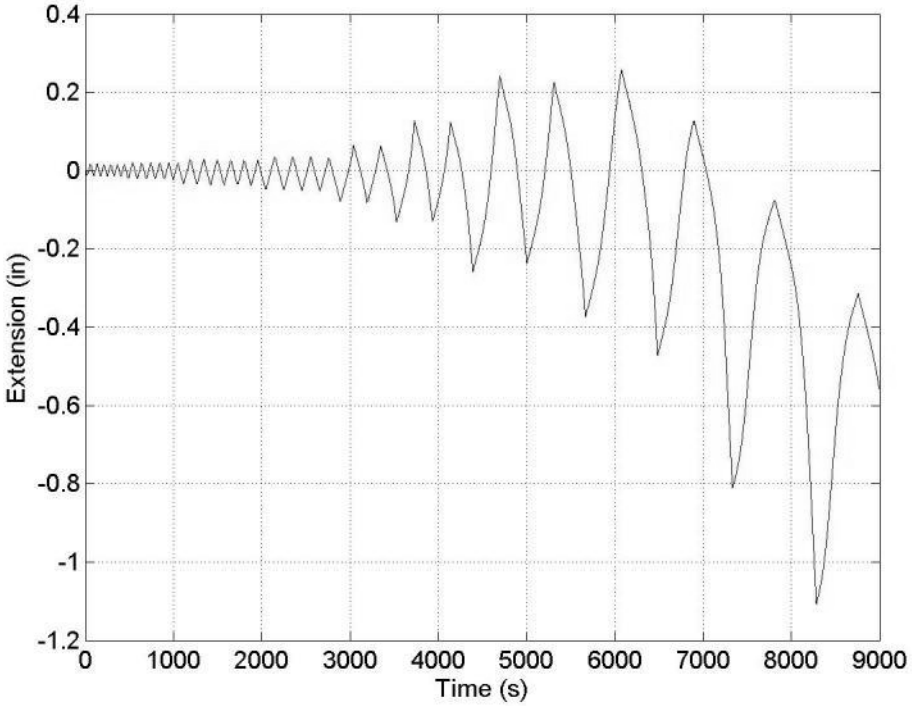

Figure 222: Specimen 4 (W24-PAF12) – LVDT9

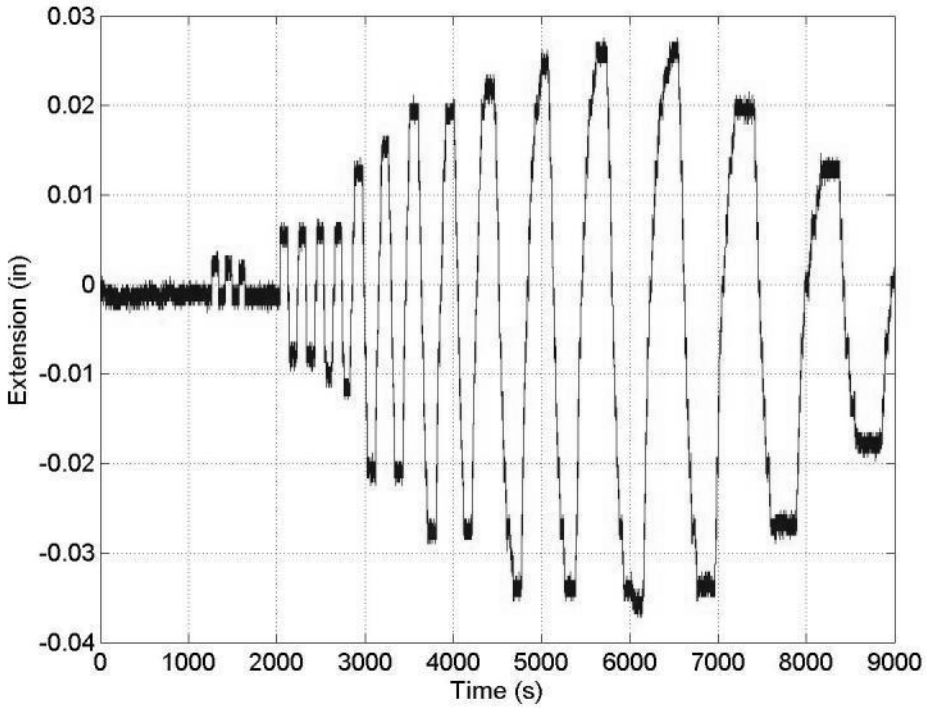

Figure 223: Specimen 4 (W24-PAF12) - String Potentiometer 1 (column)

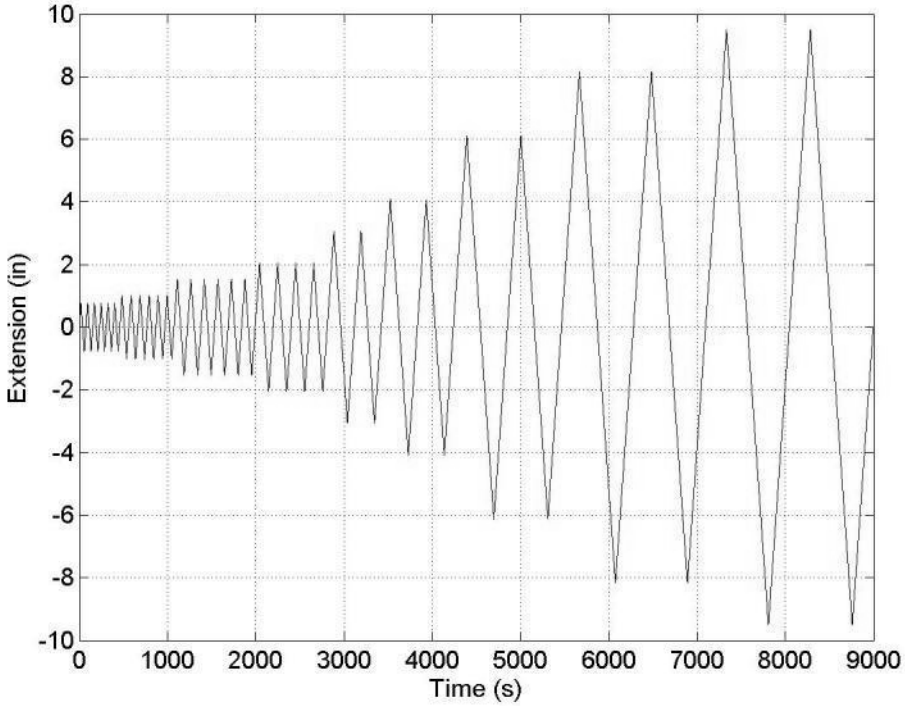

Figure 224: Specimen 4 (W24-PAF12) - String Potentiometer 2 (actuator)

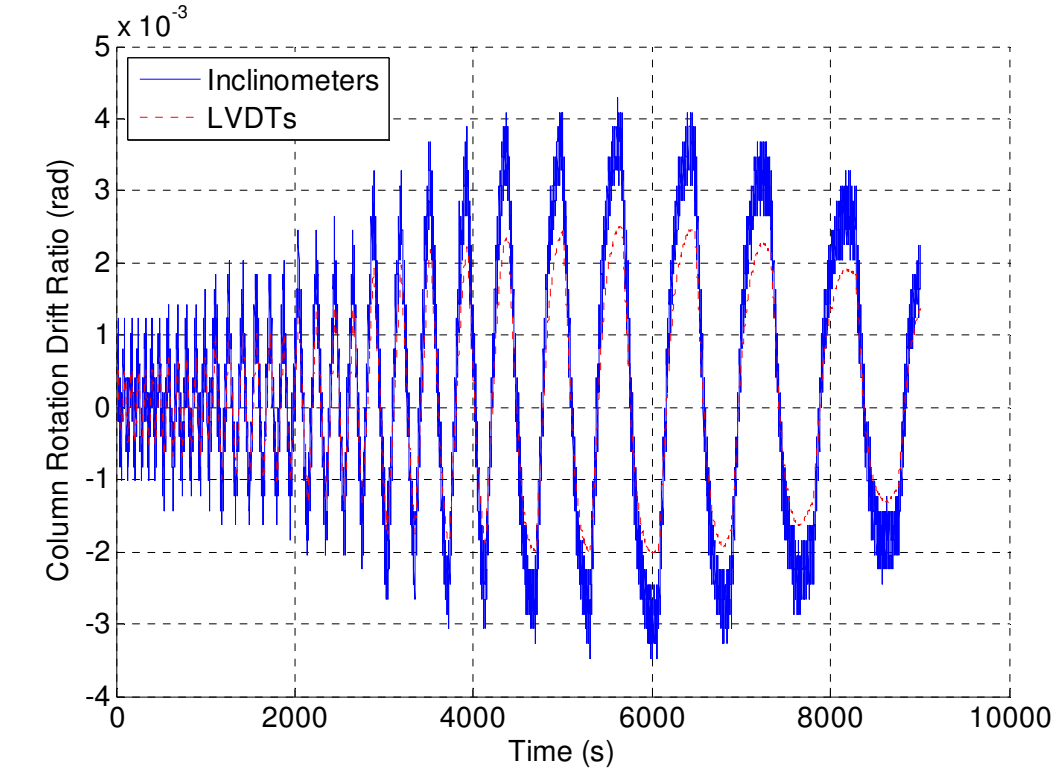

Figure 225: Specimen 4 (W24-PAF12) - Column Rotation Comparison

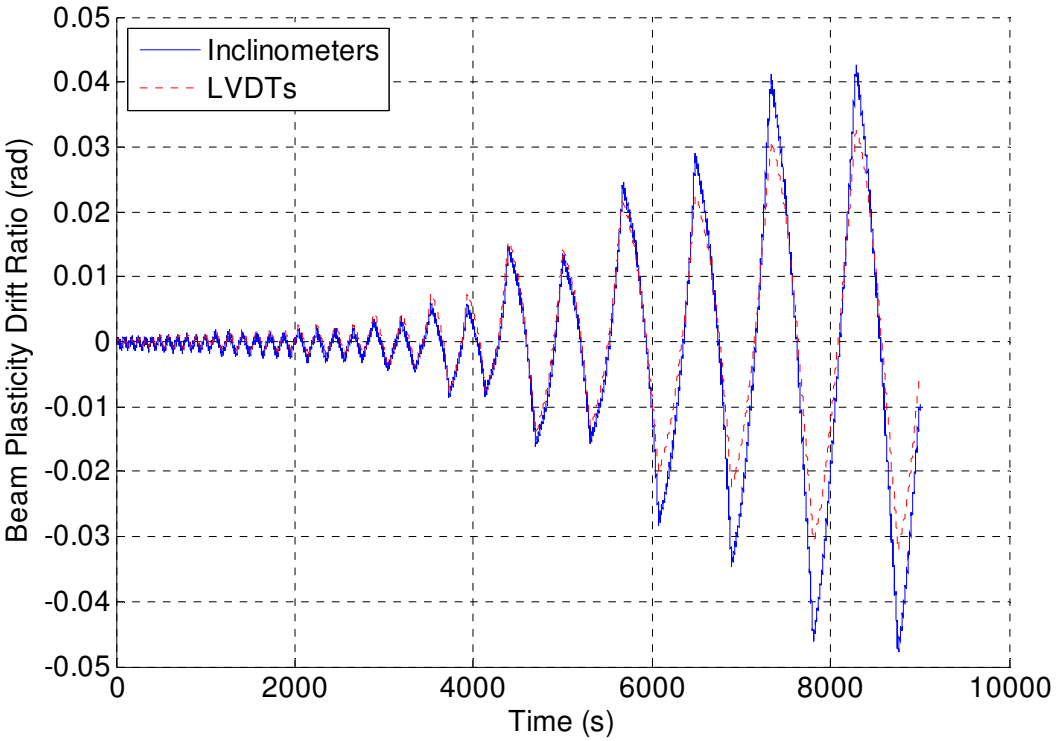

Figure 226: Specimen 4 (W24-PAF12) - Beam Plasticity Comparison

Appendix L – Specimen 5 (RBS24-PW12) Raw Instrumentation Data

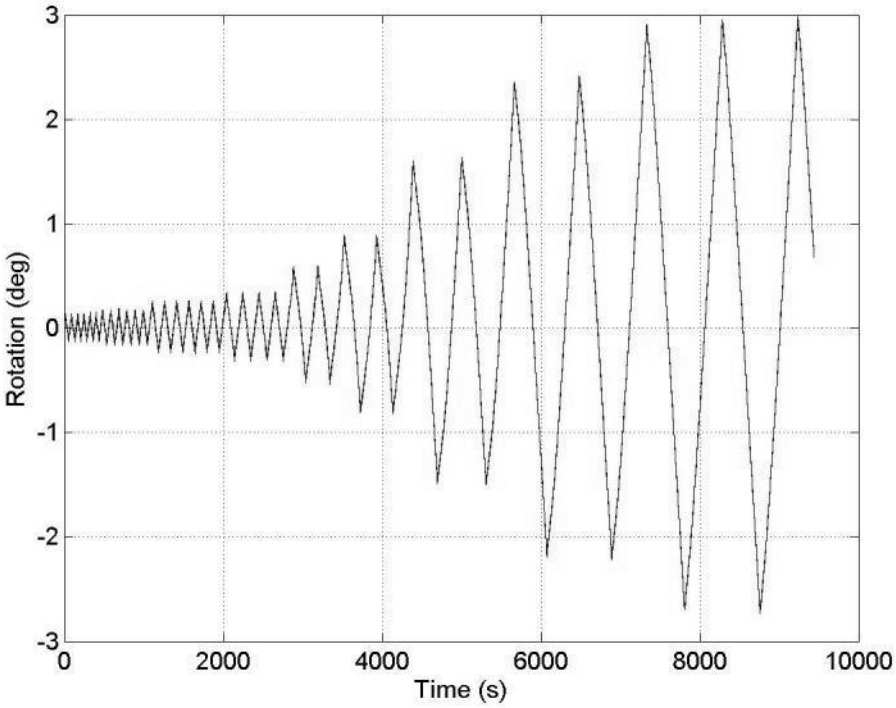

Figure 227: Specimen 5 (RBS24-PW12) - Inclinometer 3 (beam)

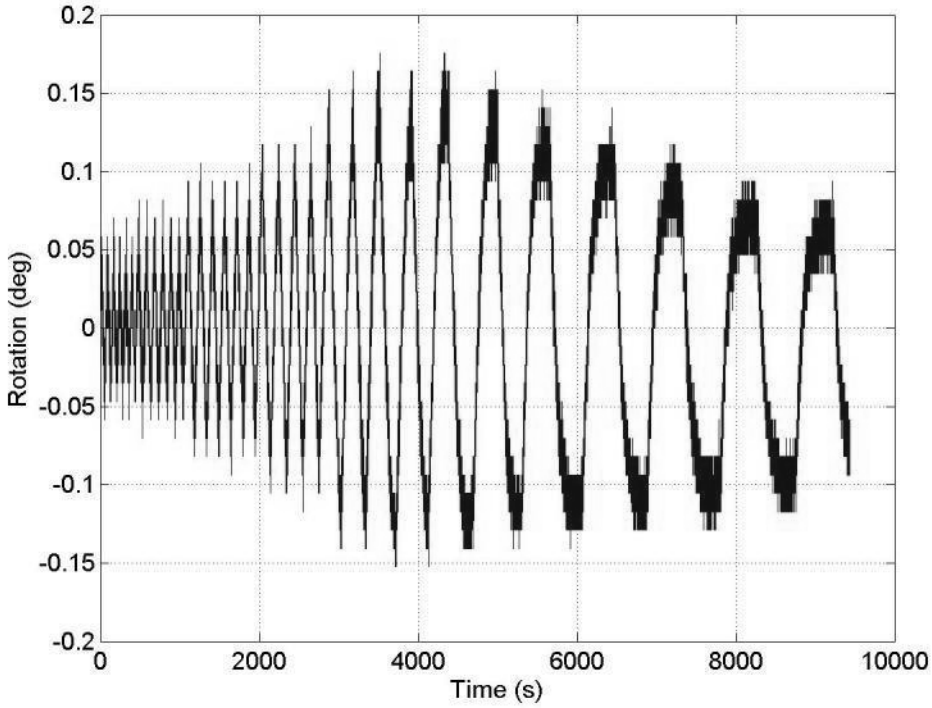

Figure 228: Specimen 5 (RBS24-PW12) - Inclinometer 1 (column)

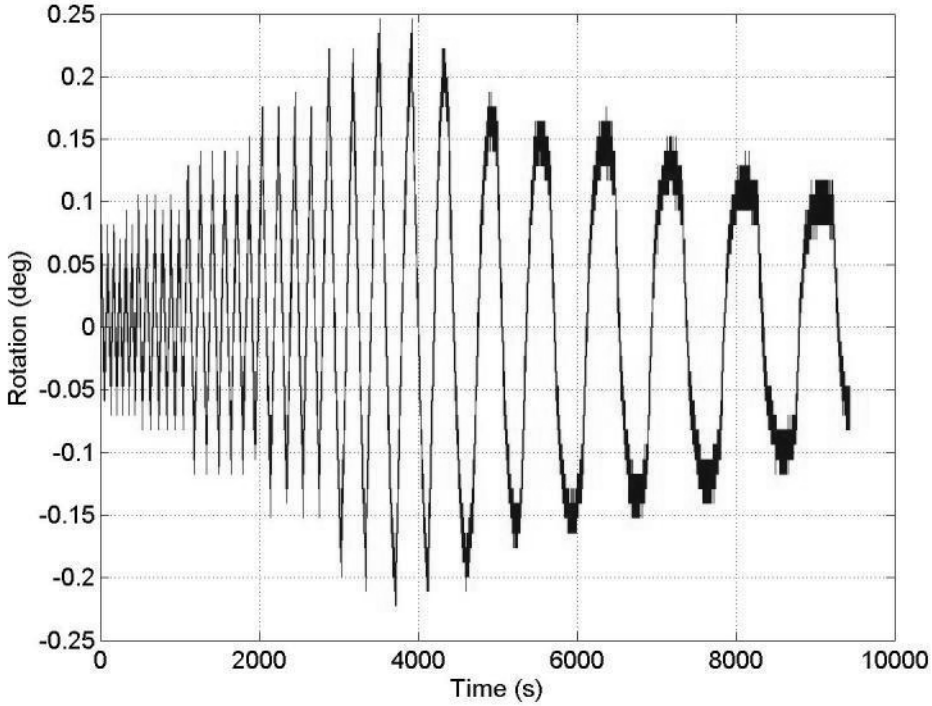

Figure 229: Specimen 5 (RBS24-PW12) - Inclinometer 2 (endplate)

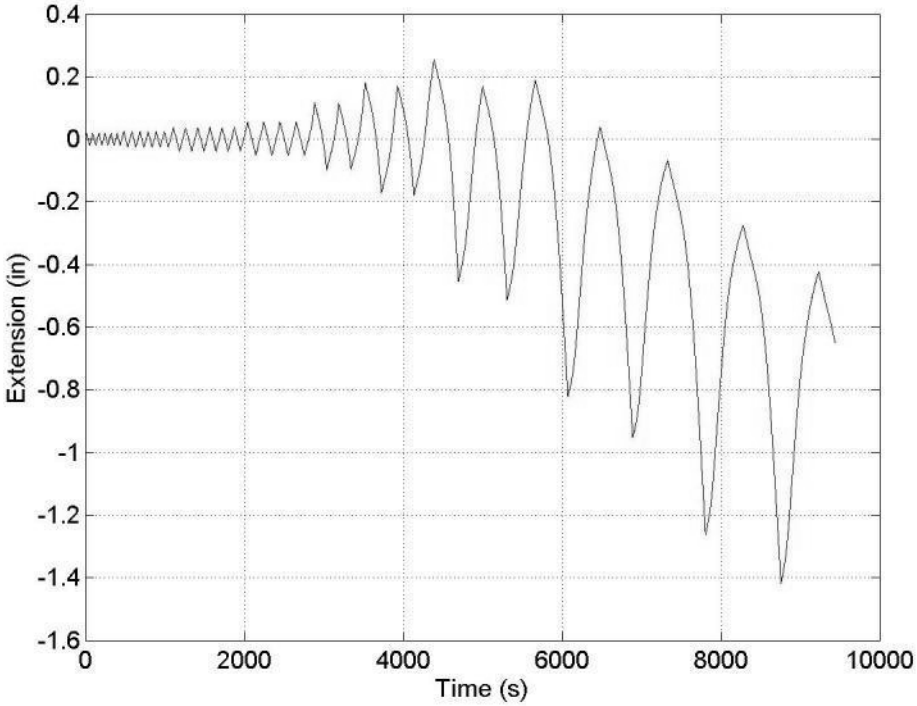

Figure 230: Specimen 5 (RBS24-PW12) – LVDT1

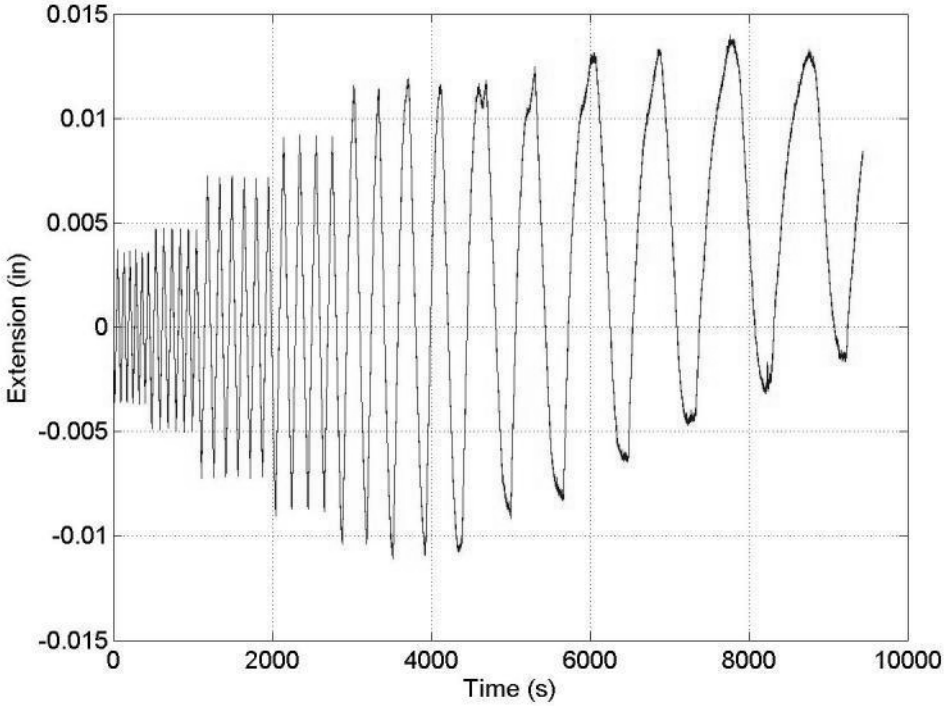

Figure 231: Specimen 5 (RBS24-PW12) – LVDT2

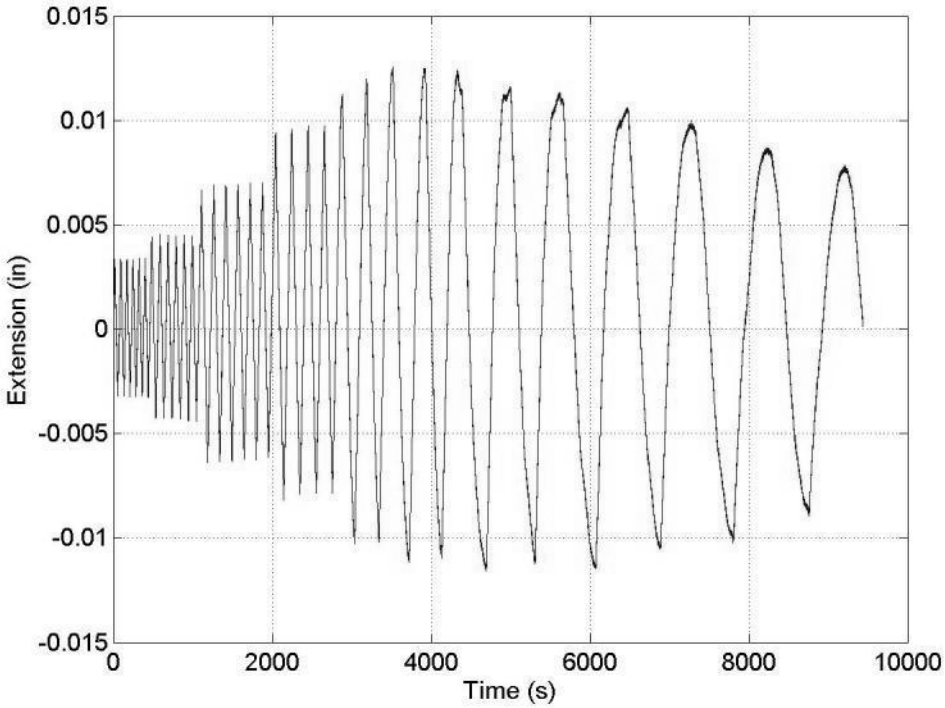

Figure 232: Specimen 5 (RBS24-PW12) – LVDT3

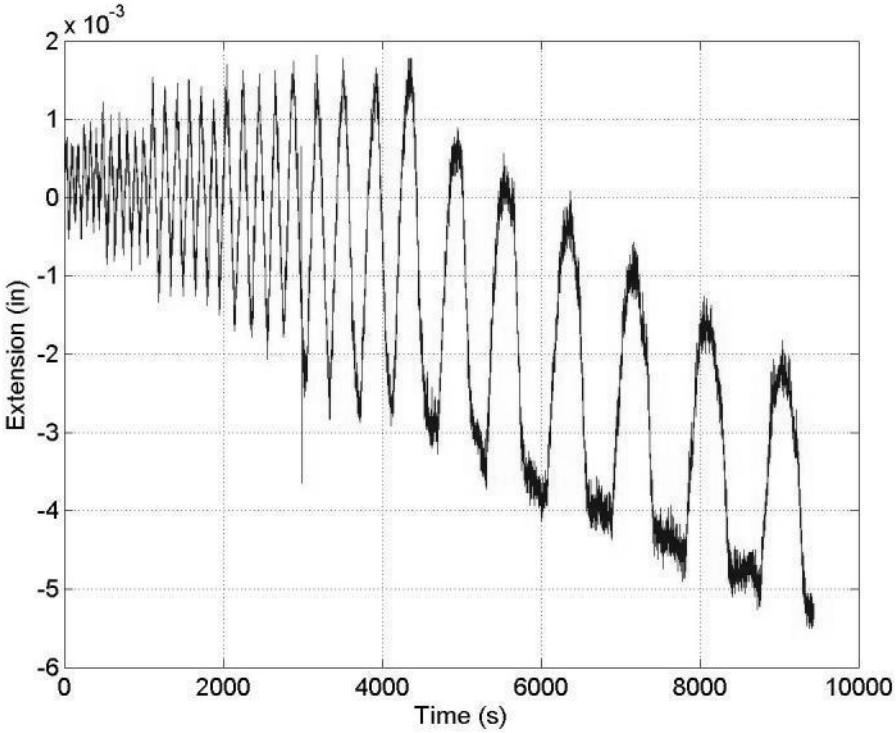

Figure 233: Specimen 5 (RBS24-PW12) – LVDT4

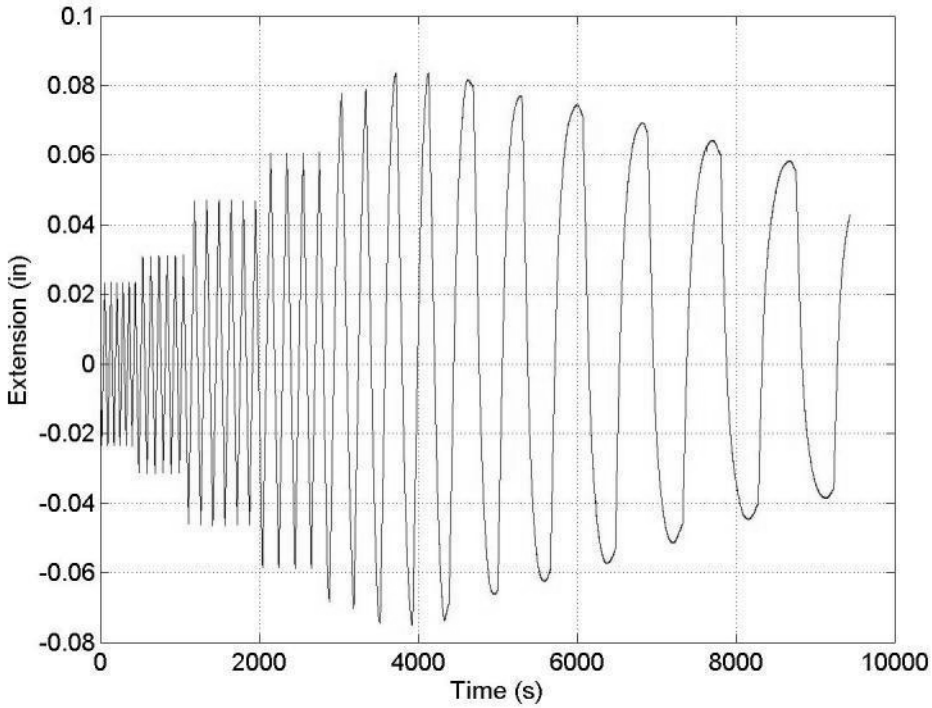

Figure 234: Specimen 5 (RBS24-PW12) – LVDT5

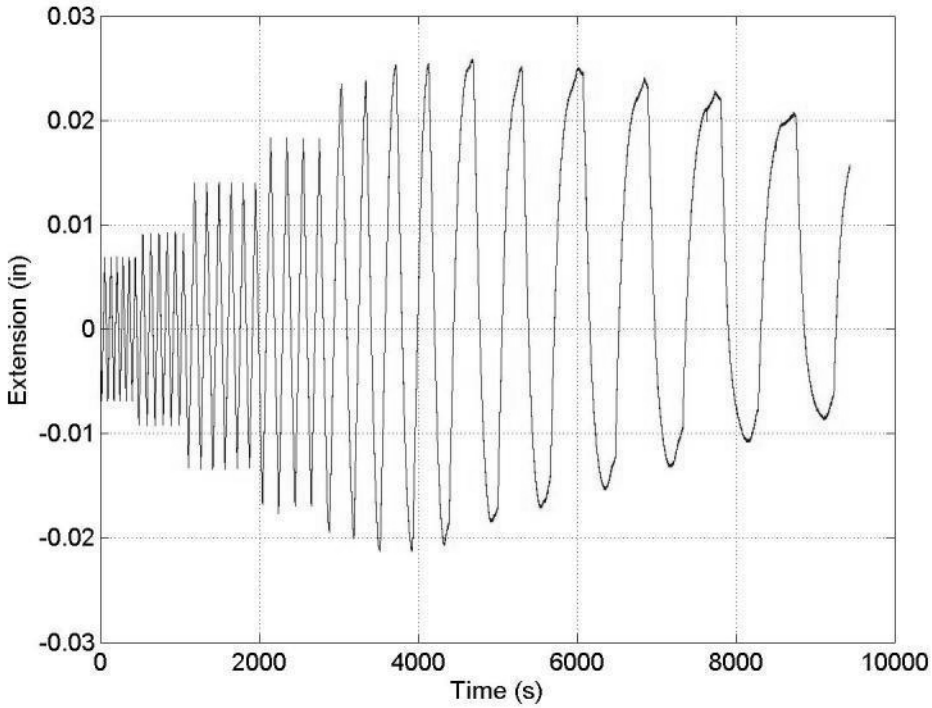

Figure 235: Specimen 5 (RBS24-PW12) – LVDT6

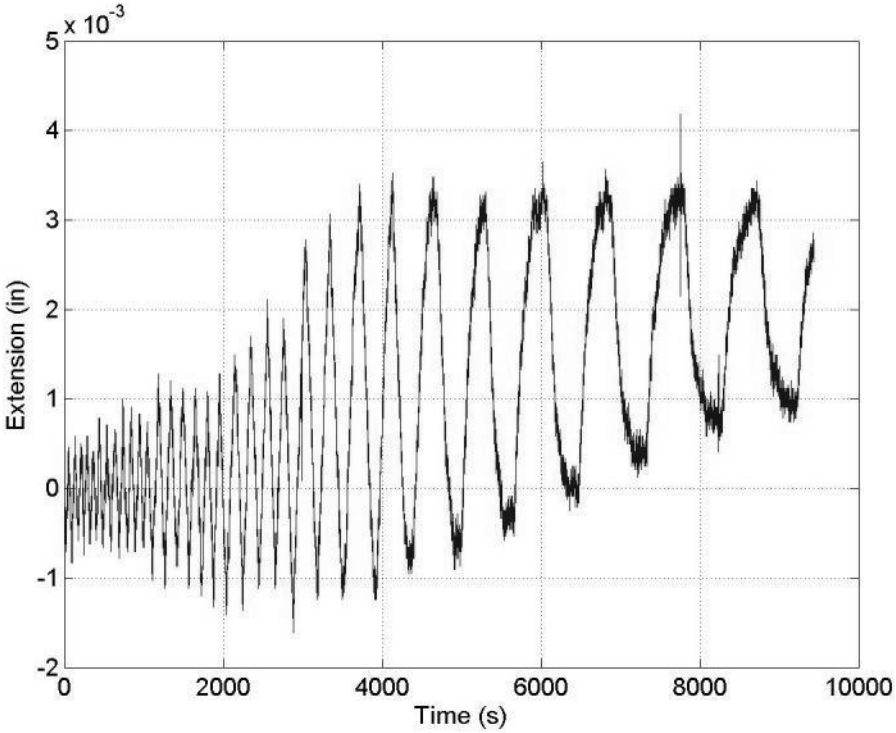

Figure 236: Specimen 5 (RBS24-PW12) – LVDT7

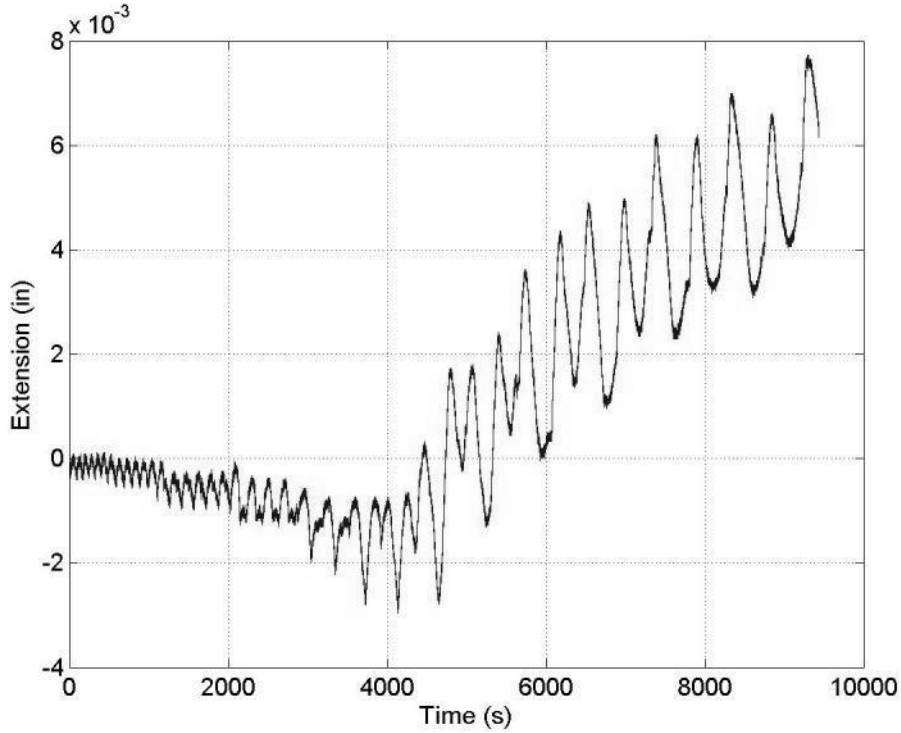

Figure 237: Specimen 5 (RBS24-PW12) – LVDT8

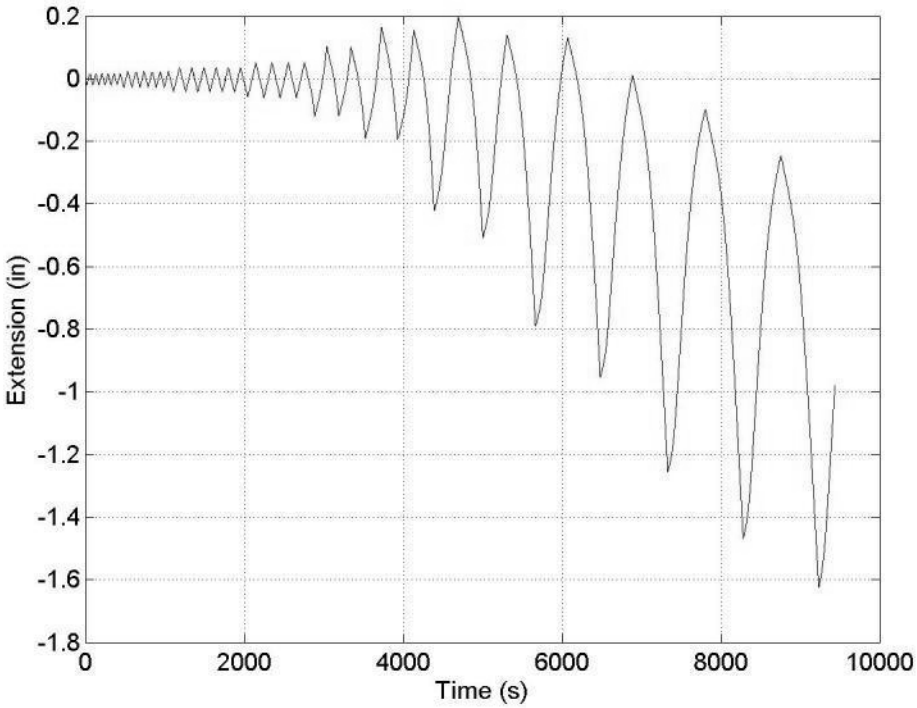

Figure 238: Specimen 5 (RBS24-PW12) – LVDT9

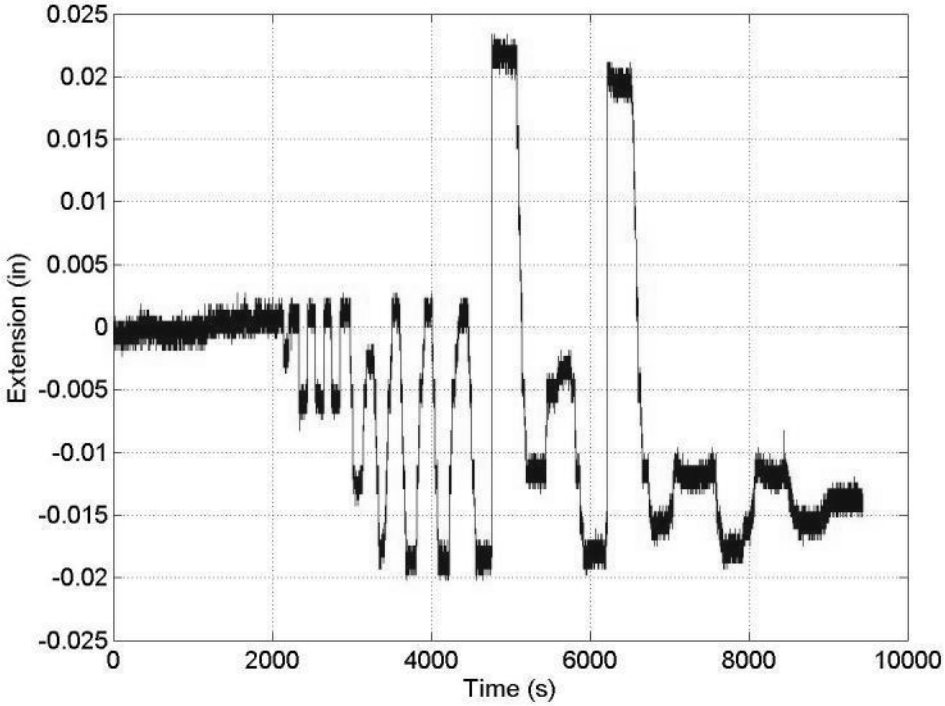

Figure 239: Specimen 5 (RBS24-PW12) - String Potentiometer 1 (column)

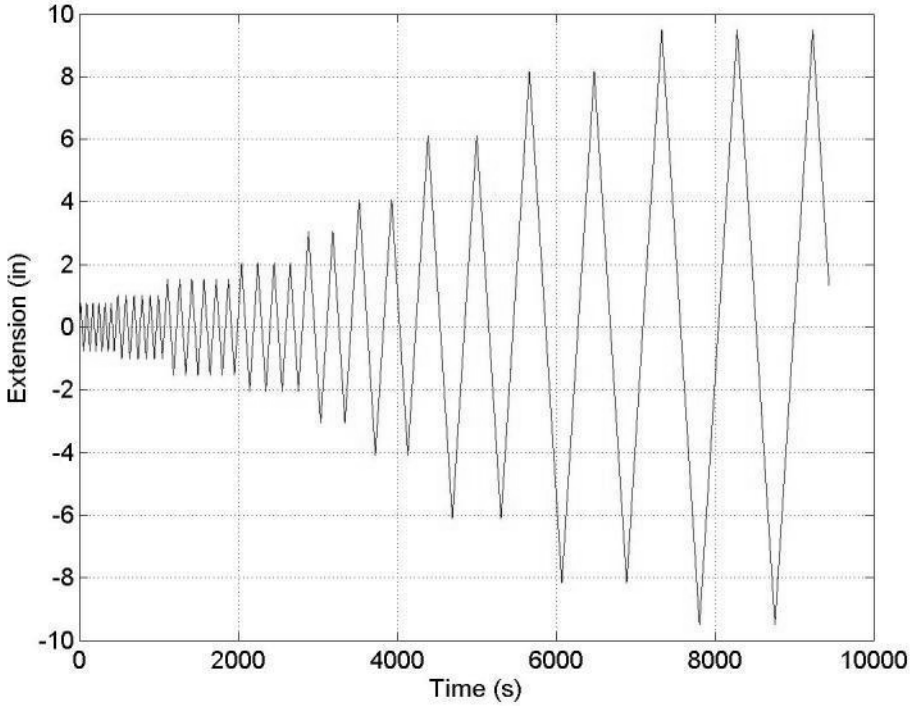

Figure 240: Specimen 5 (RBS24-PW12) - String Potentiometer 2 (actuator)

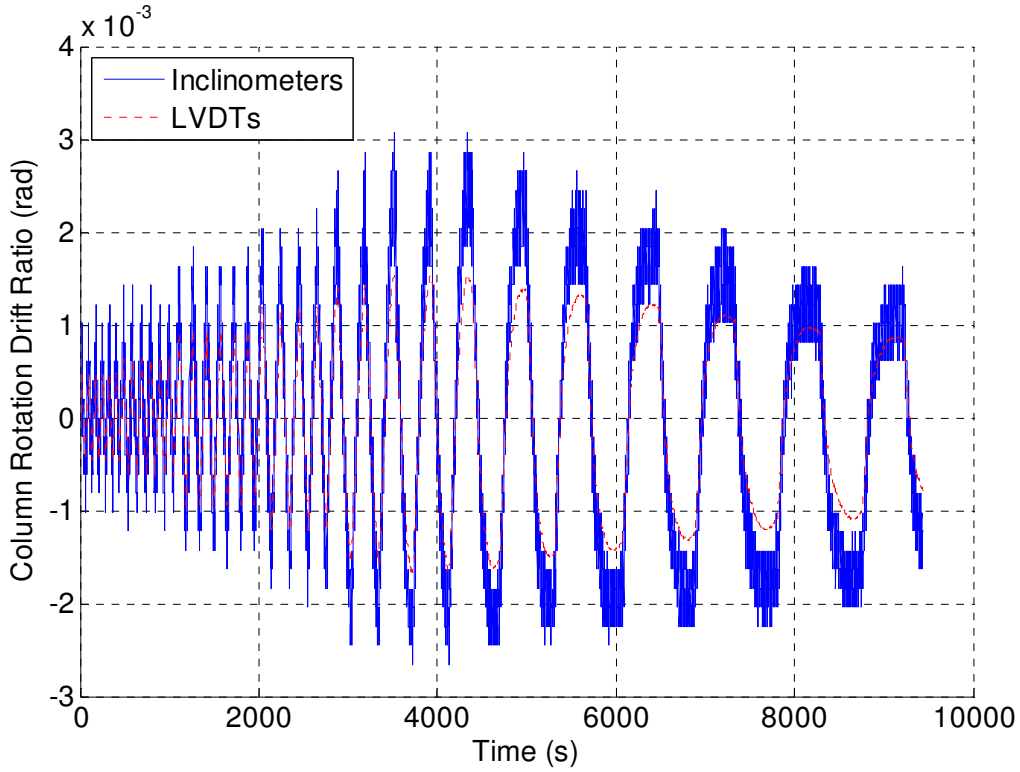

Figure 241: Specimen 5 (RBS24-PW12) - Column Rotation Comparison

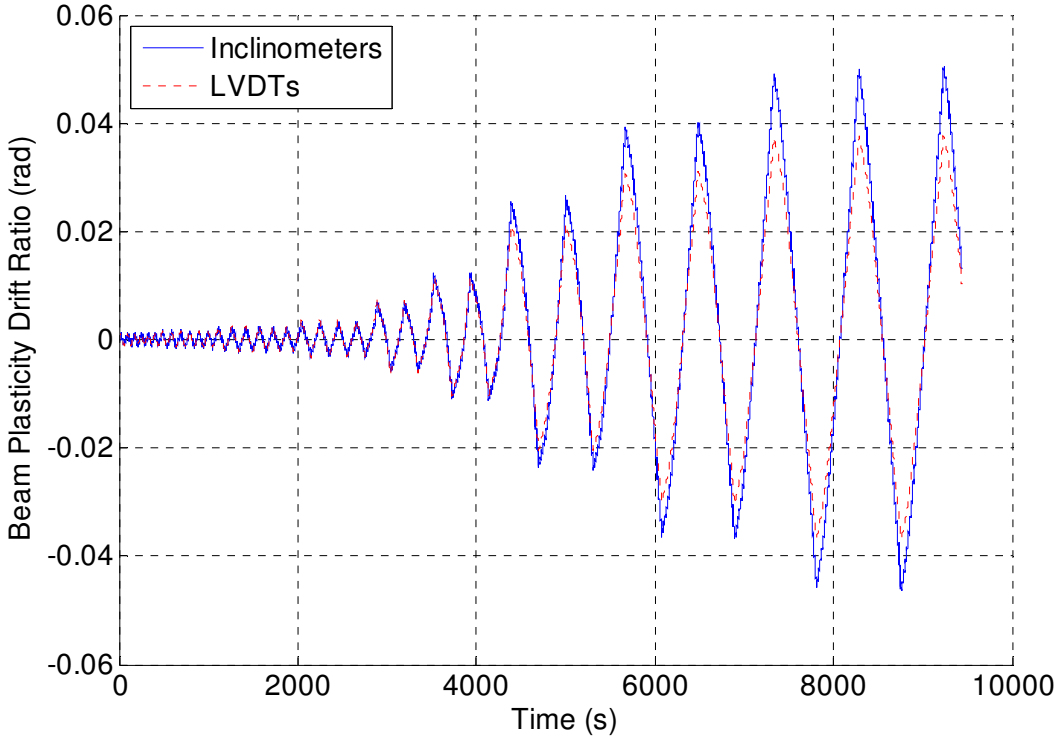

Figure 242: Specimen 5 (RBS24-PW12) - Beam Plasticity Comparison

Appendix M – Specimen 6 (W24-PAF-array) Raw Instrumentation Data

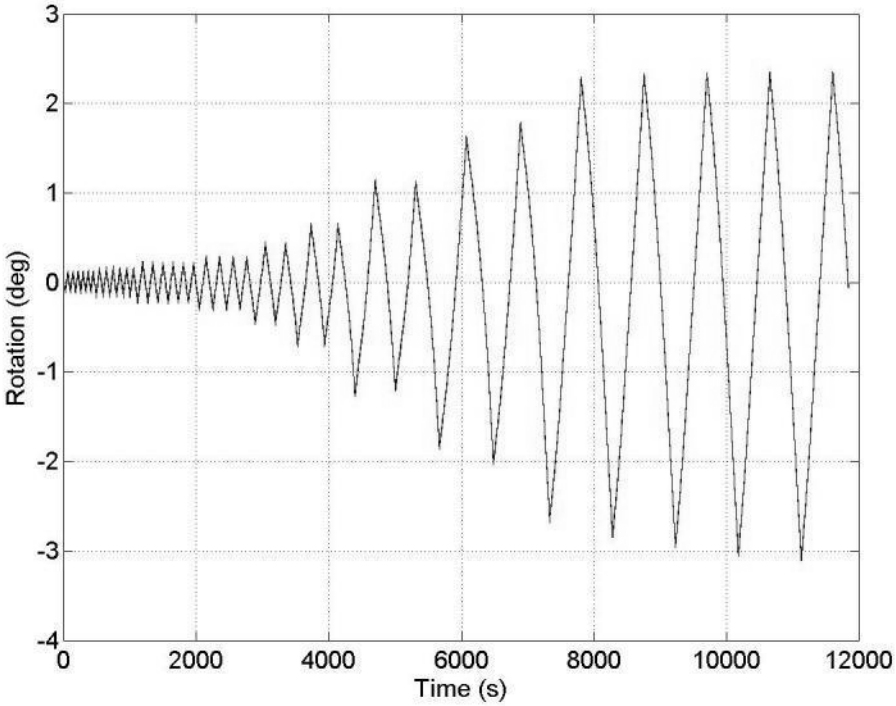

Figure 243: Specimen 6 (W24-PAF-array) - Inclinometer 3 (beam)

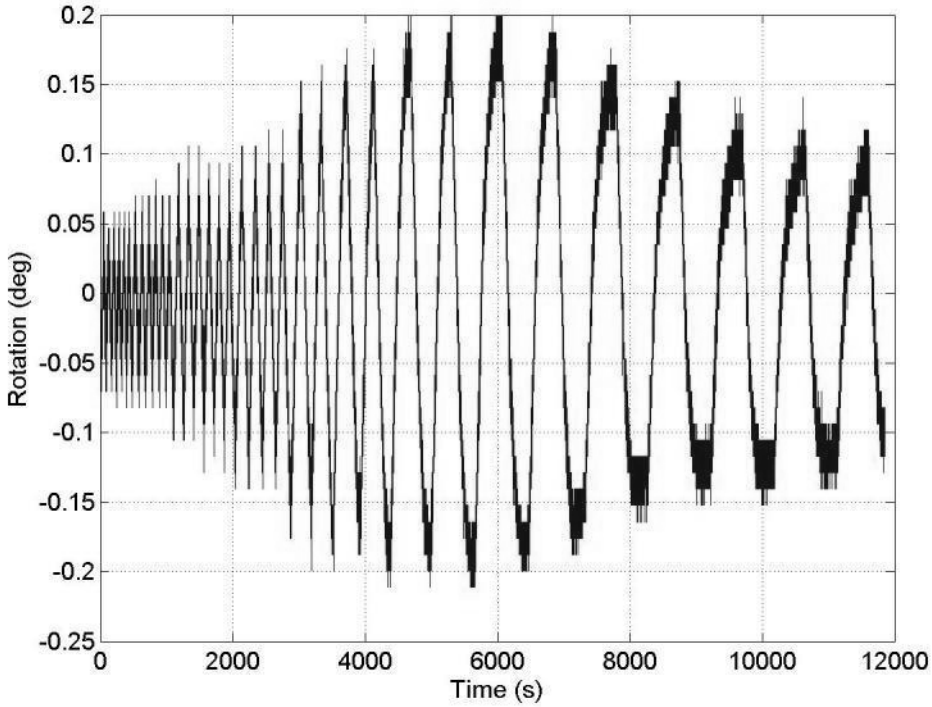

Figure 244: Specimen 6 (W24-PAF-array) - Inclinometer 1 (column)

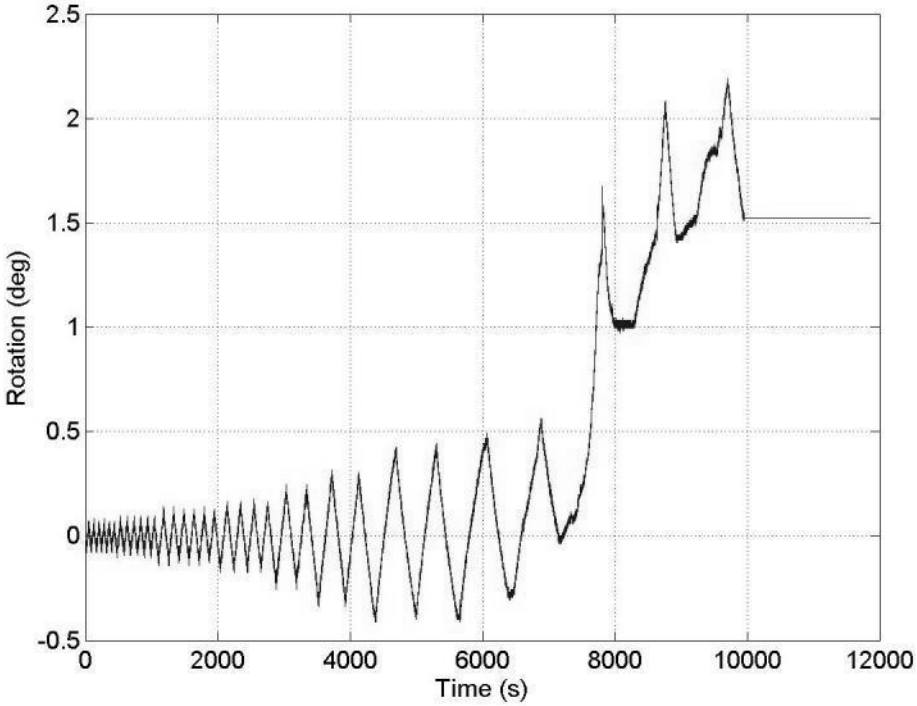

Figure 245: Specimen 6 (W24-PAF-array) - Inclinometer 2 (endplate)

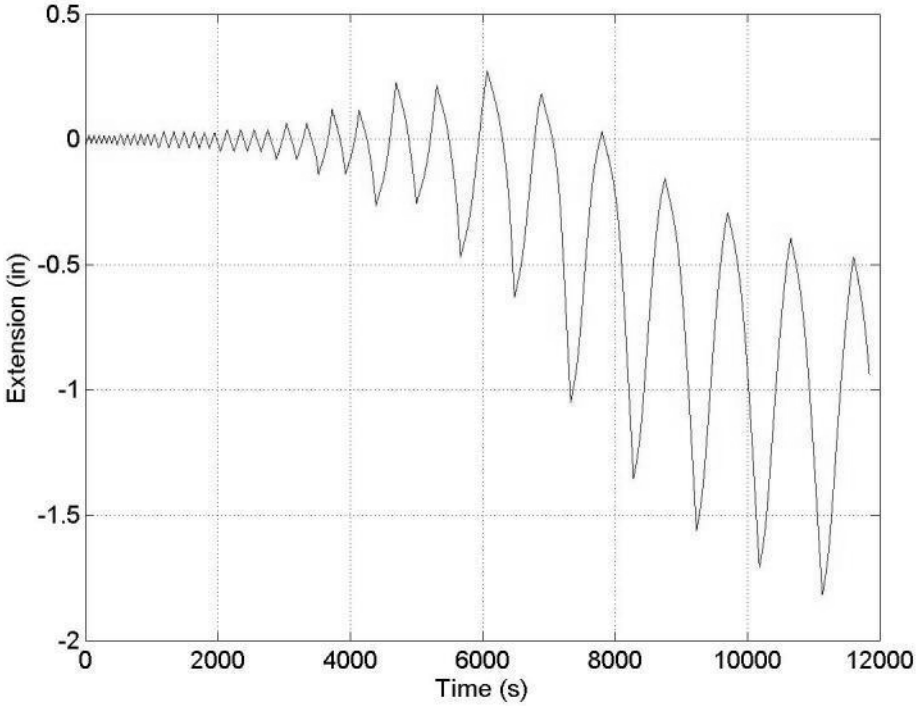

Figure 246: Specimen 6 (W24-PAF-array) – LVDT1

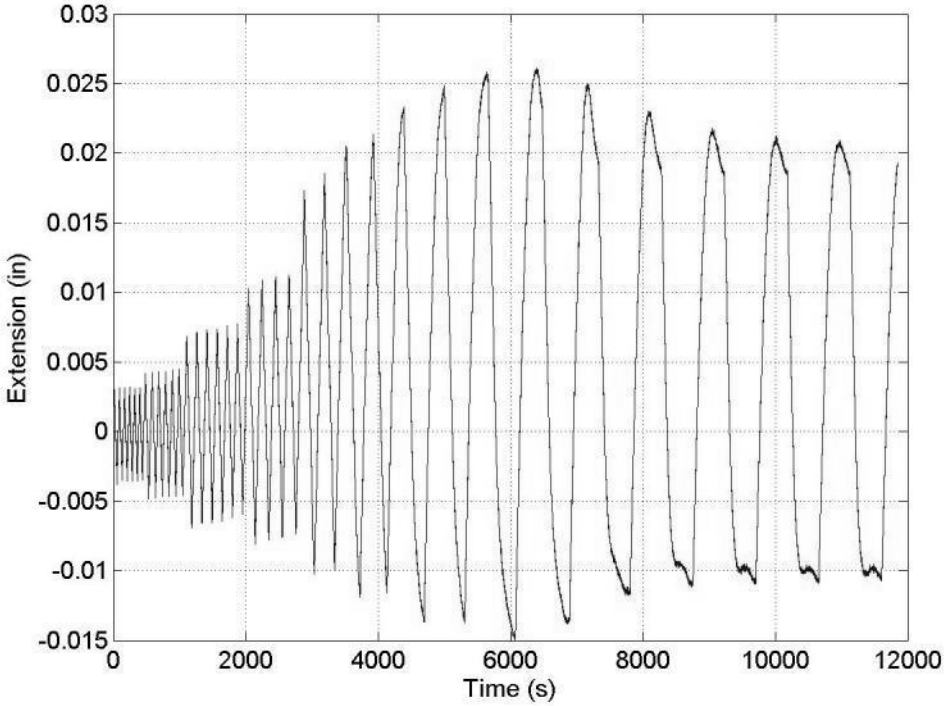

Figure 247: Specimen 6 (W24-PAF-array) – LVDT2

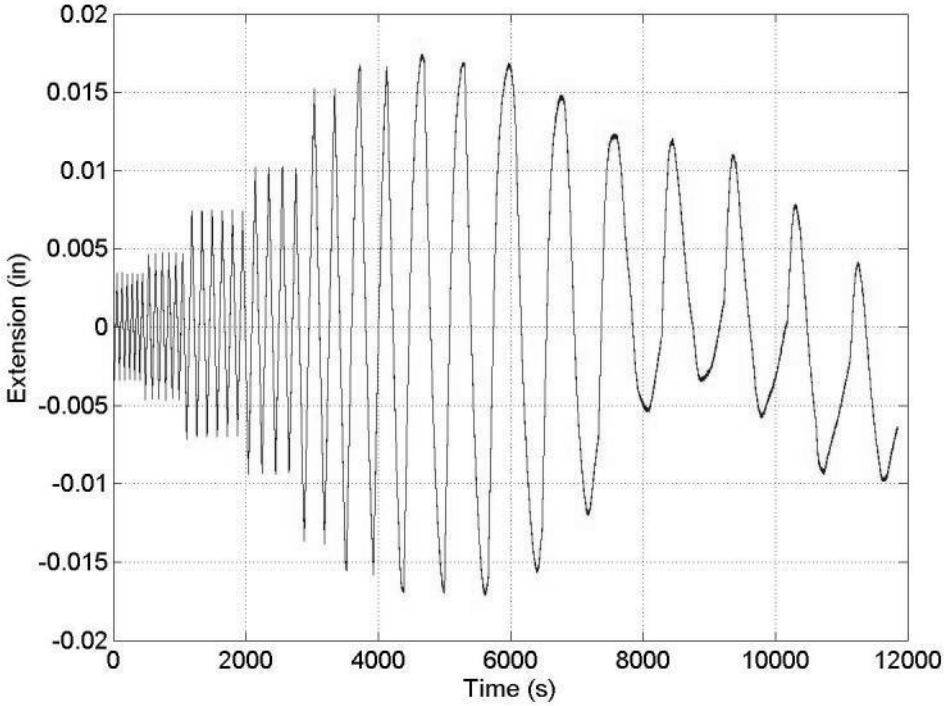

Figure 248: Specimen 6 (W24-PAF-array) – LVDT3

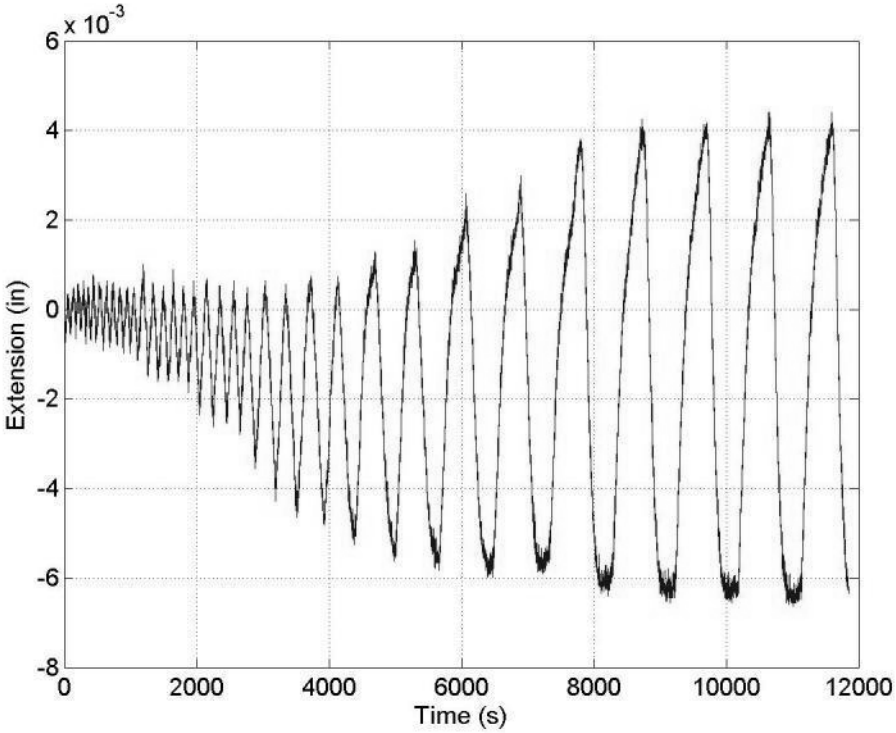

Figure 249: Specimen 6 (W24-PAF-array) – LVDT4

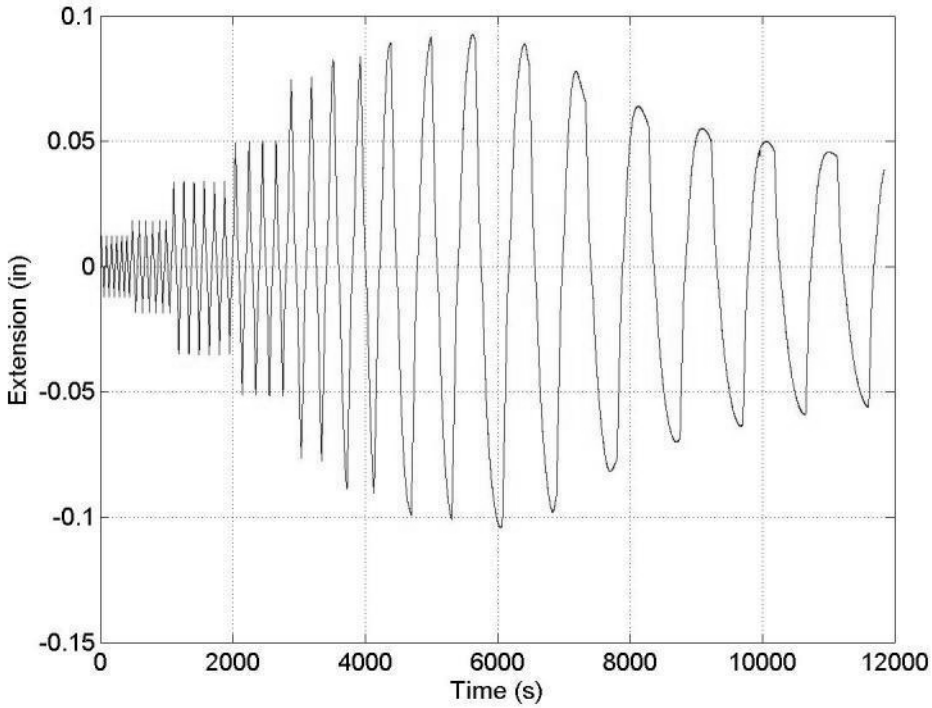

Figure 250: Specimen 6 (W24-PAF-array) – LVDT5

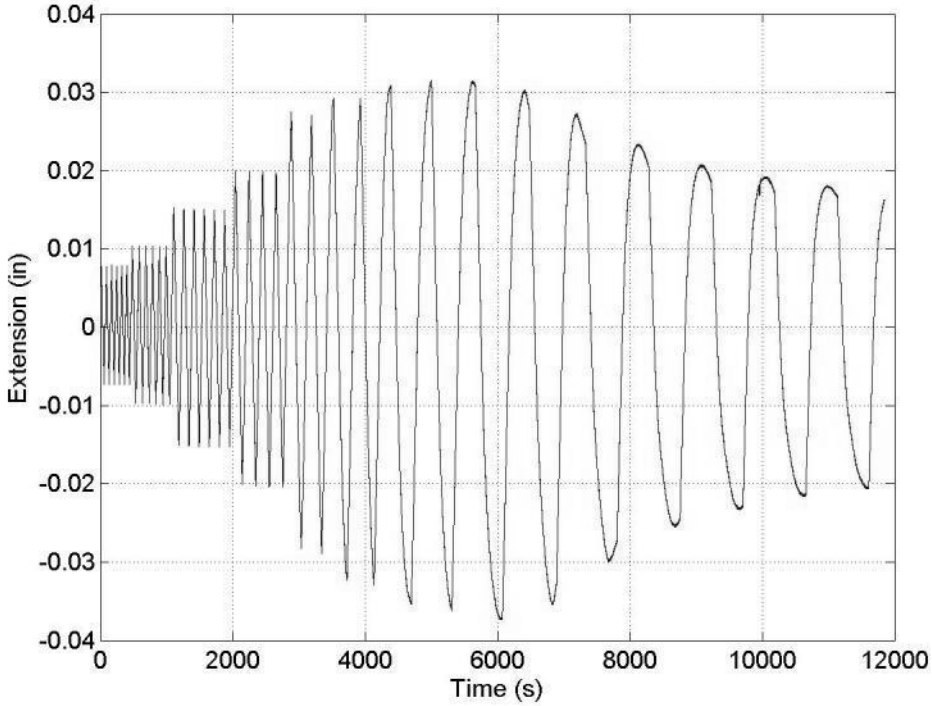

Figure 251: Specimen 6 (W24-PAF-array) – LVDT6

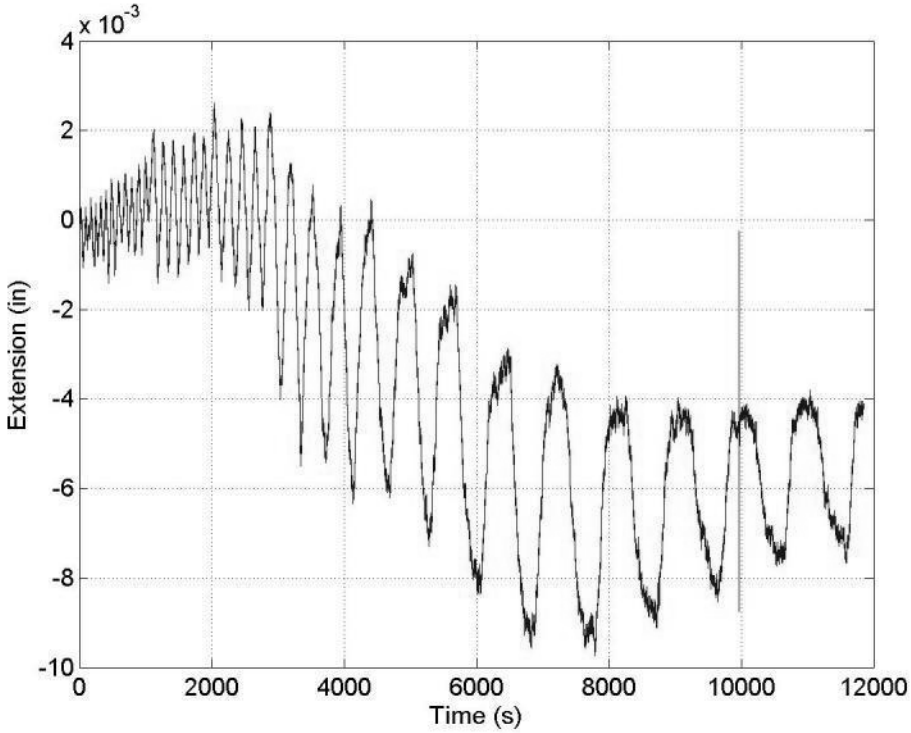

Figure 252: Specimen 6 (W24-PAF-array) – LVDT7

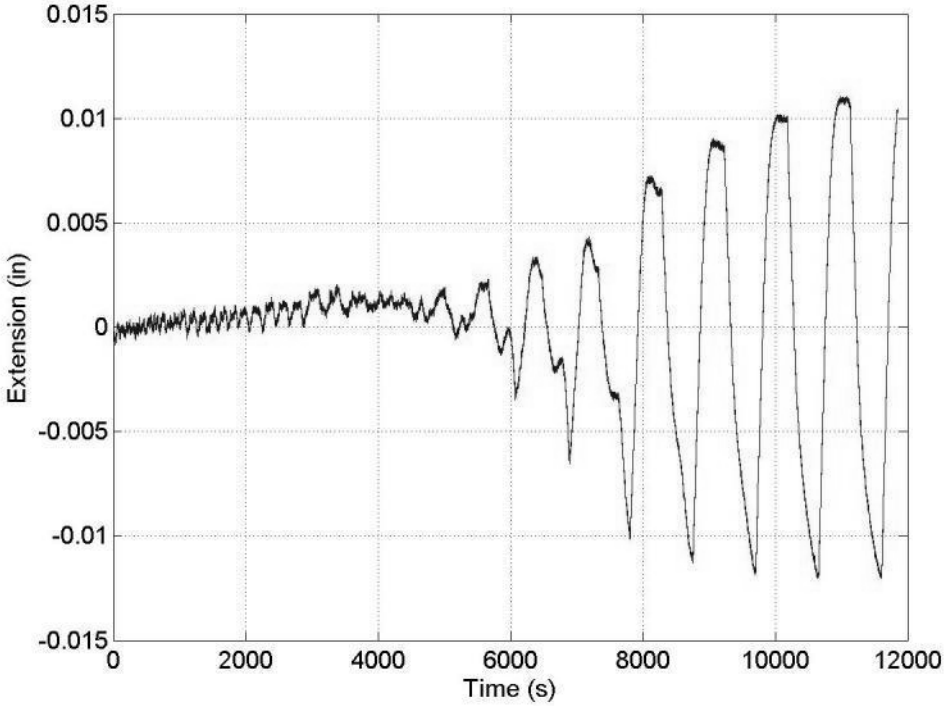

Figure 253: Specimen 6 (W24-PAF-array) – LVDT8

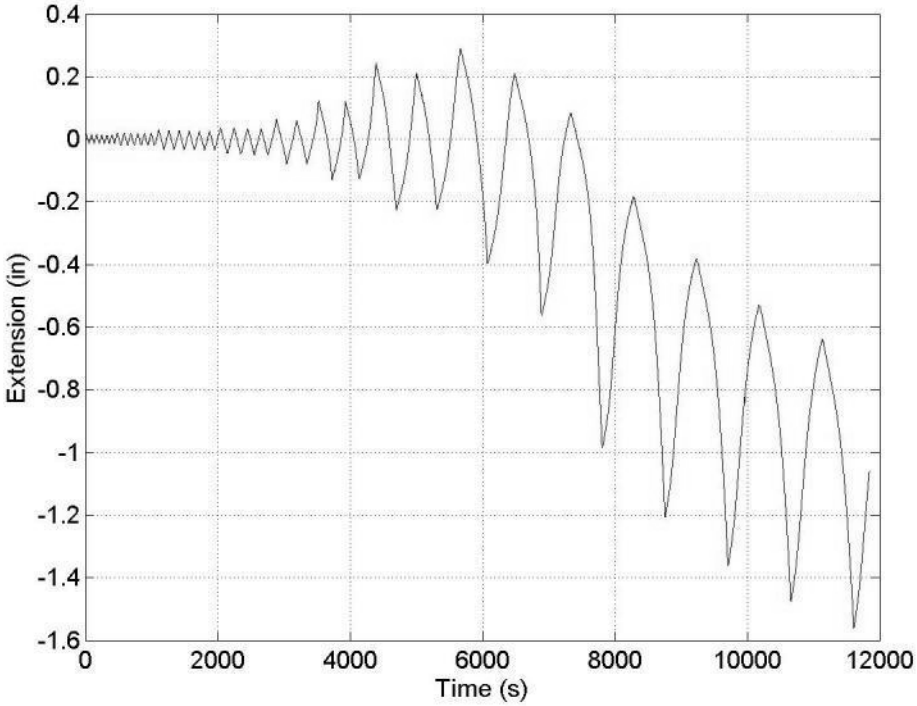

Figure 254: Specimen 6 (W24-PAF-array) – LVDT9

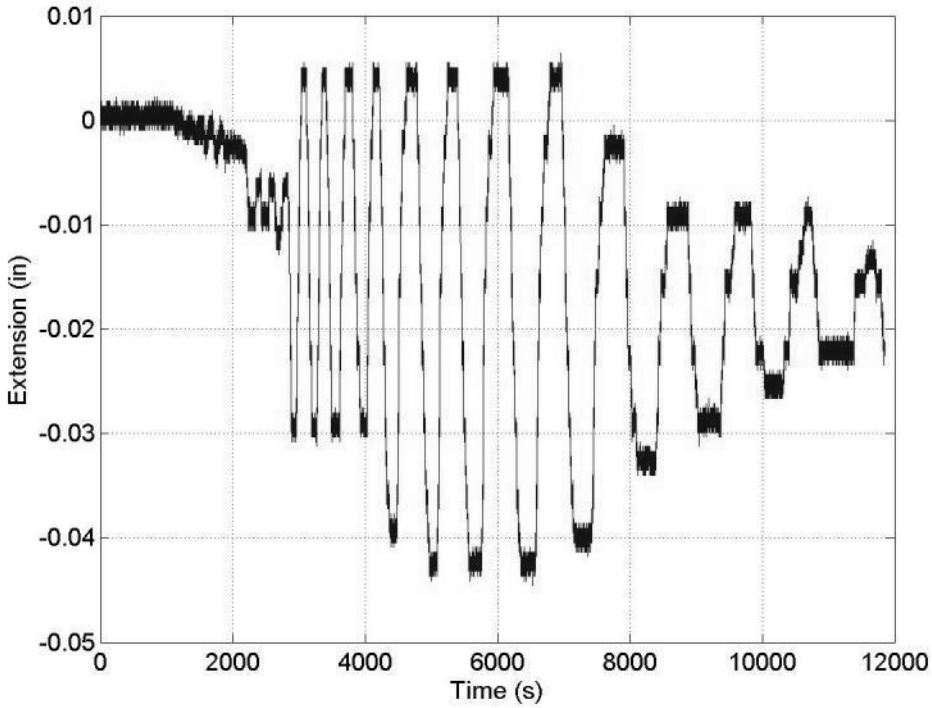

Figure 255: Specimen 6 (W24-PAF-array) - String Potentiometer 1 (column)

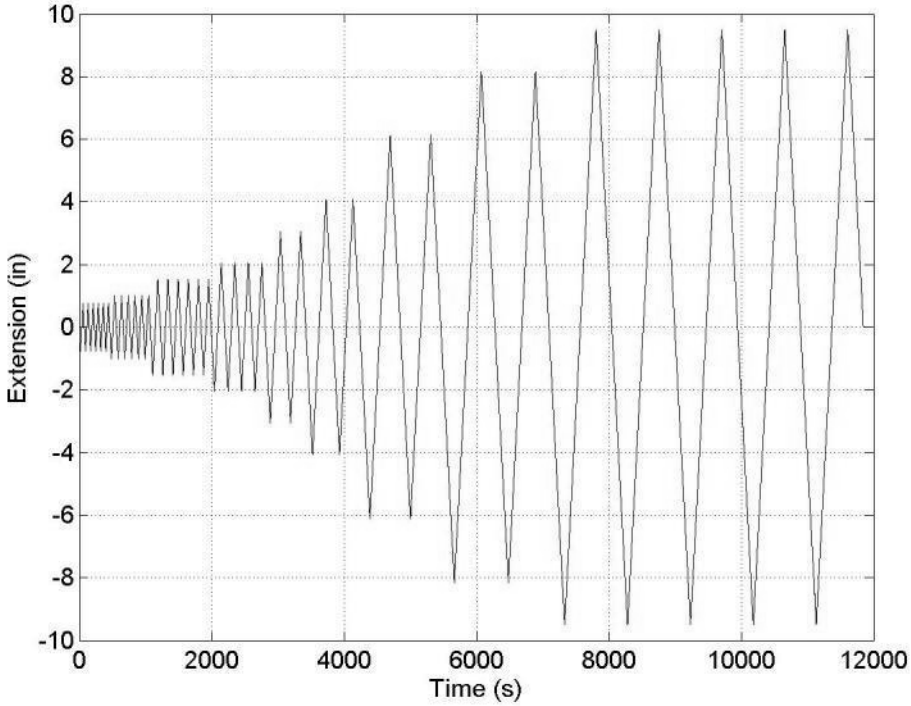

Figure 256: Specimen 6 (W24-PAF-array) - String Potentiometer 2 (actuator)

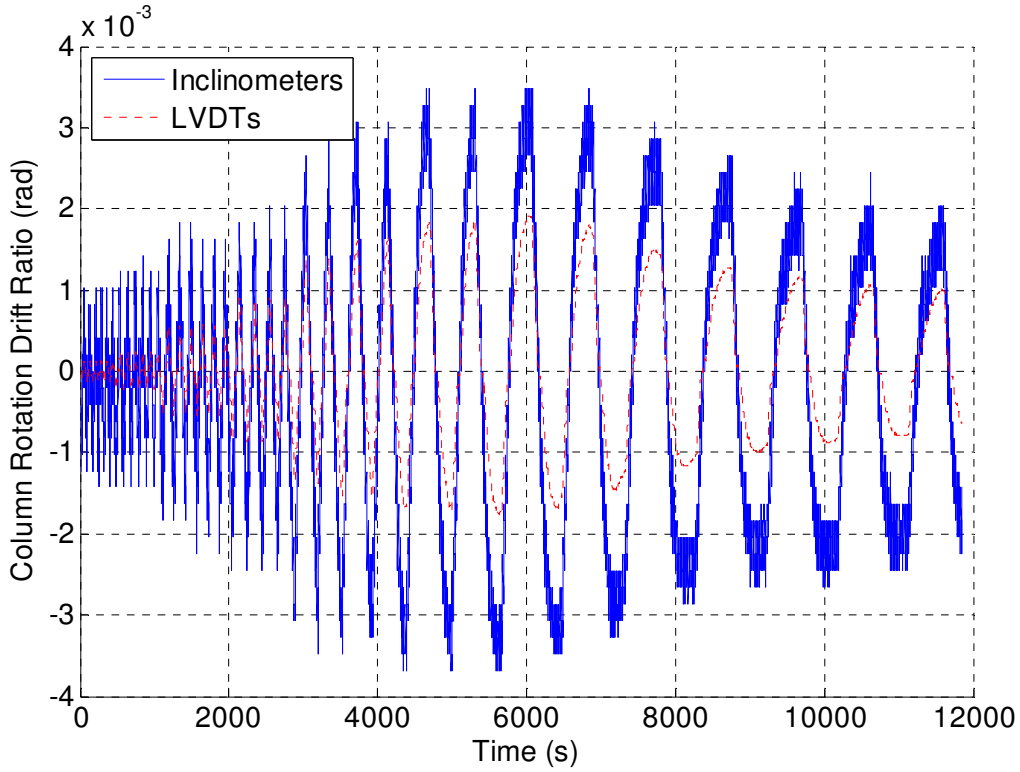

Figure 257: Specimen 6 (W24-PAF-array) - Column Rotation Comparison

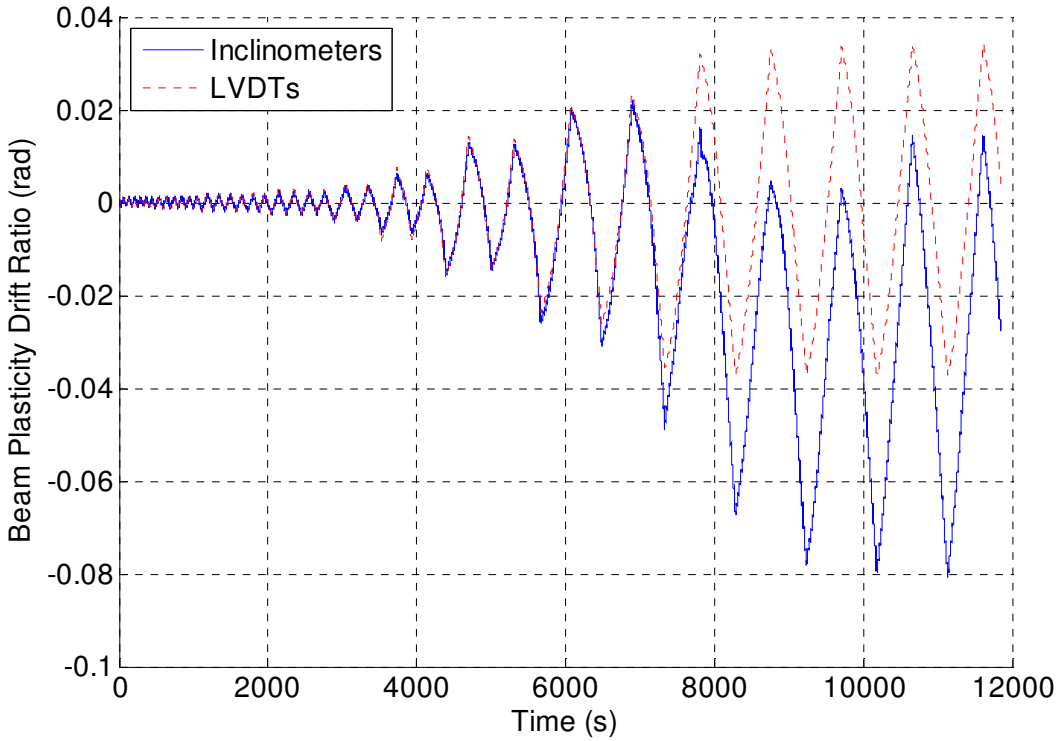

Figure 258: Specimen 6 (W24-PAF-array) - Beam Plasticity Comparison

Appendix N – Specimen 7 (RBS36) Raw Instrumentation Data

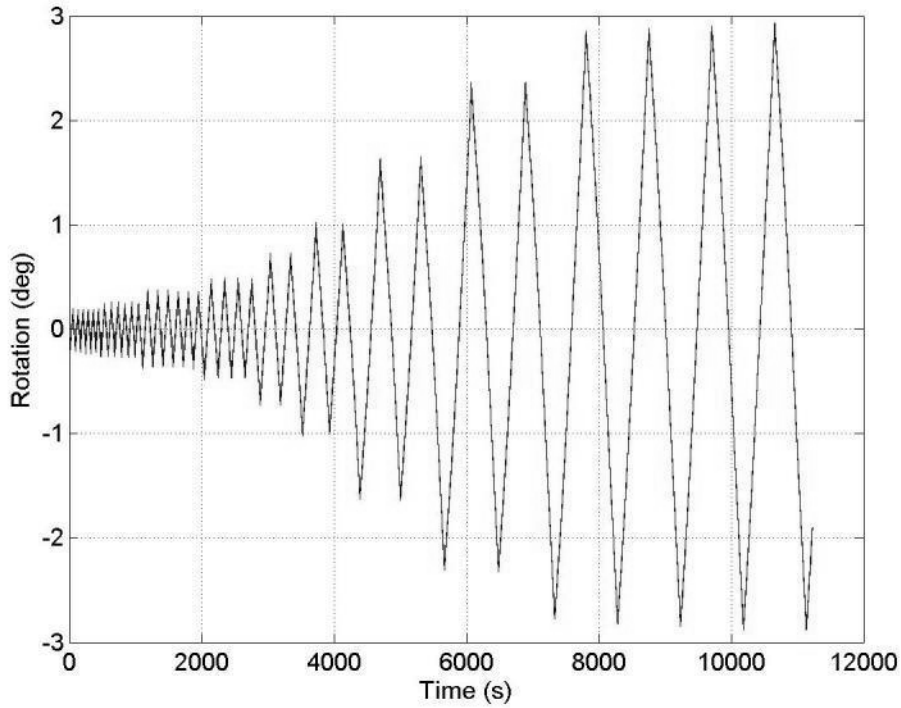

Figure 259: Specimen 7 (RBS36) - Inclinometer 3 (beam)

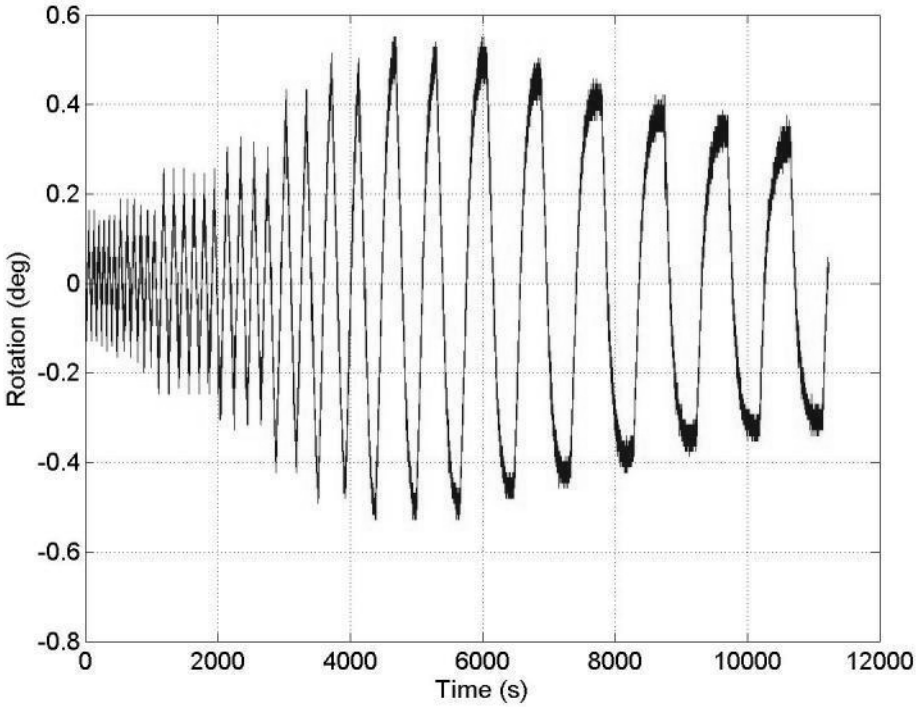

Figure 260: Specimen 7 (RBS36) - Inclinometer 1 (column)

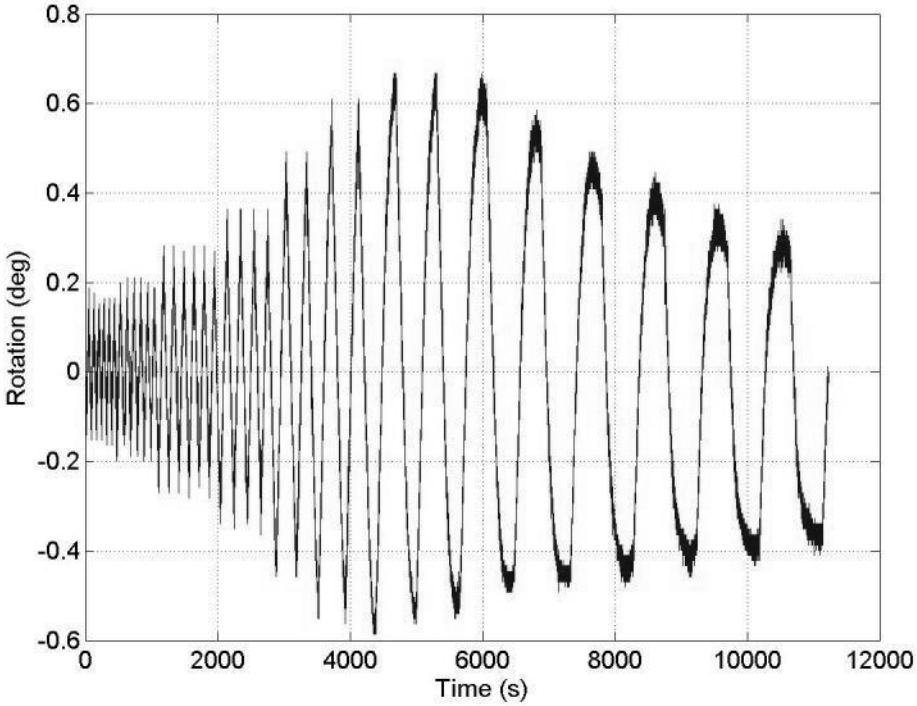

Figure 261: Specimen 7 (RBS36) - Inclinometer 2 (endplate)

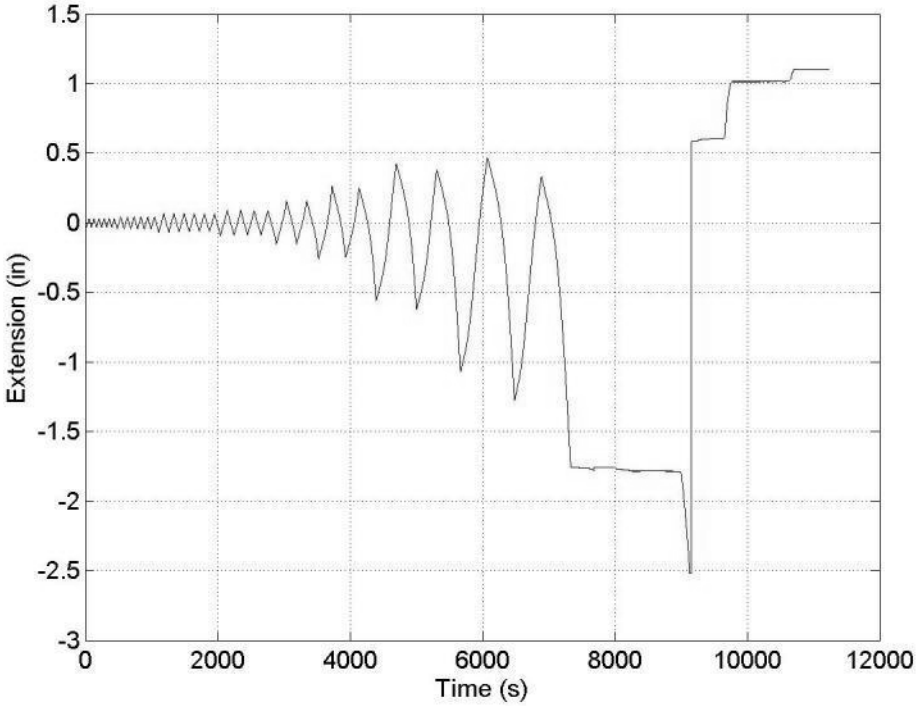

Figure 262: Specimen 7 (RBS36) – LVDT1

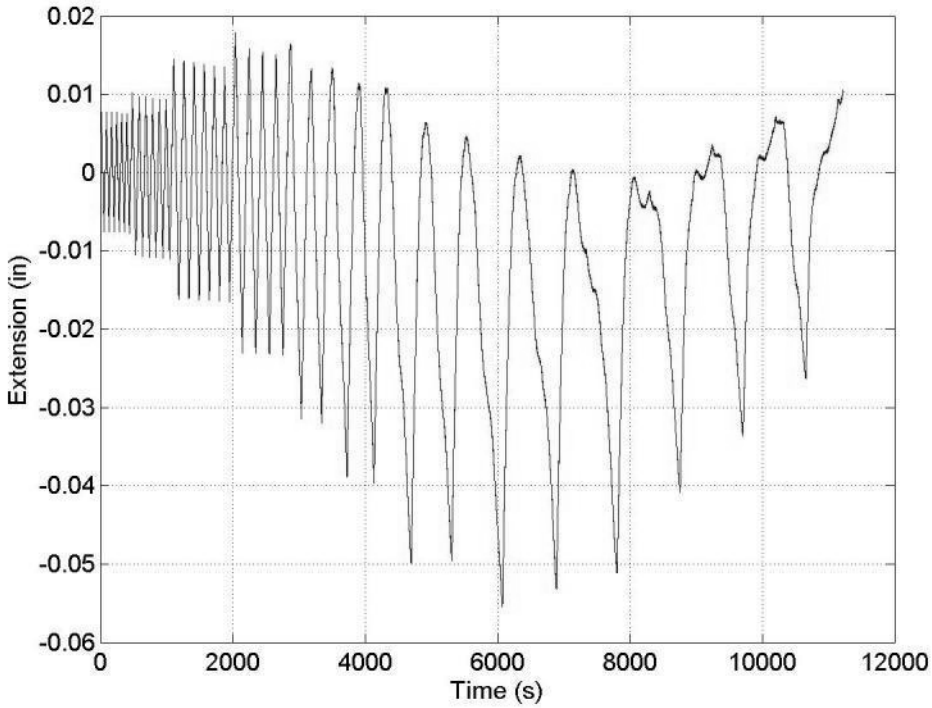

Figure 263: Specimen 7 (RBS36) – LVDT2

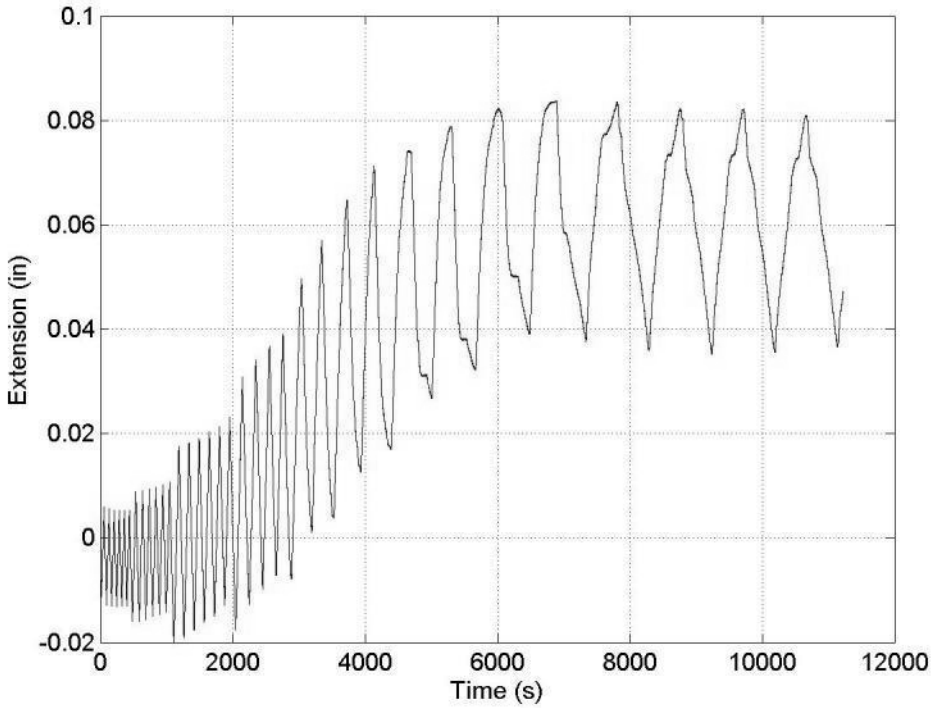

Figure 264: Specimen 7 (RBS36) – LVDT3

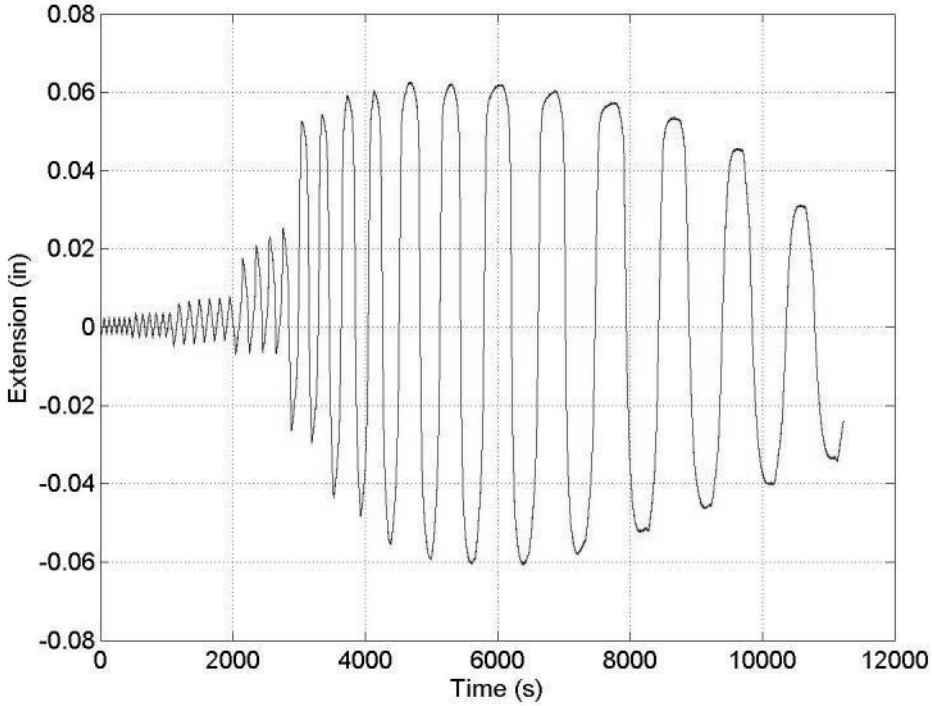

Figure 265: Specimen 7 (RBS36) – LVDT4

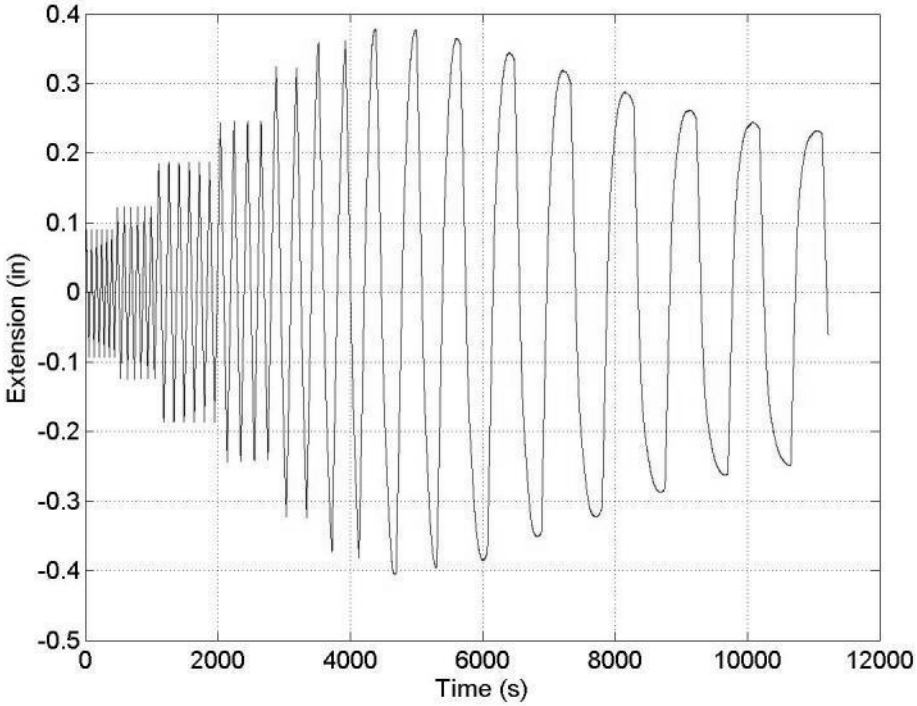

Figure 266: Specimen 7 (RBS36) – LVDT5

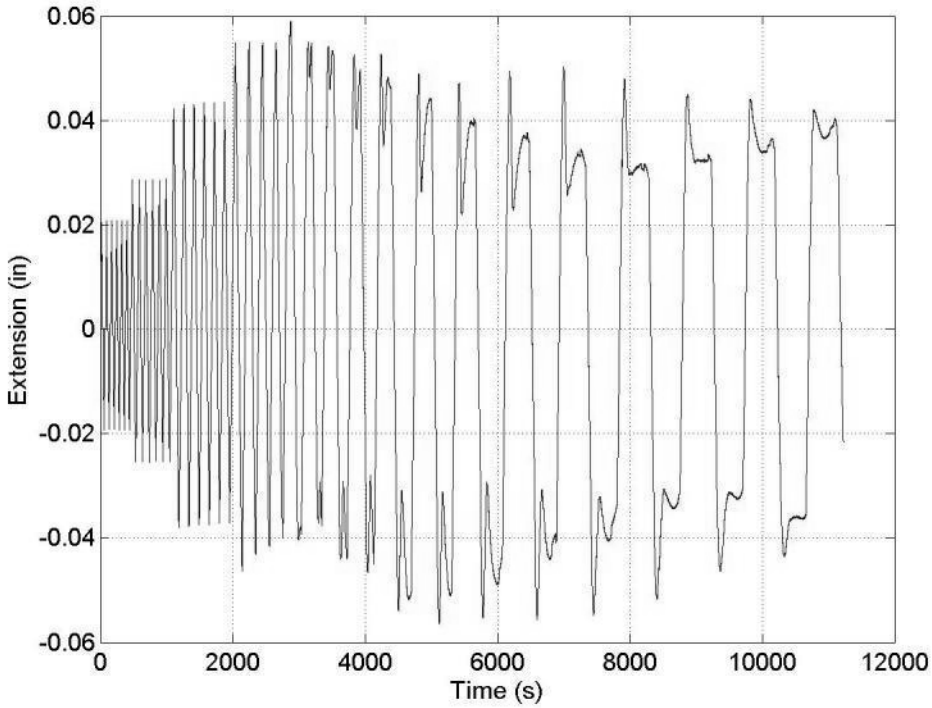

Figure 267: Specimen 7 (RBS36) – LVDT6

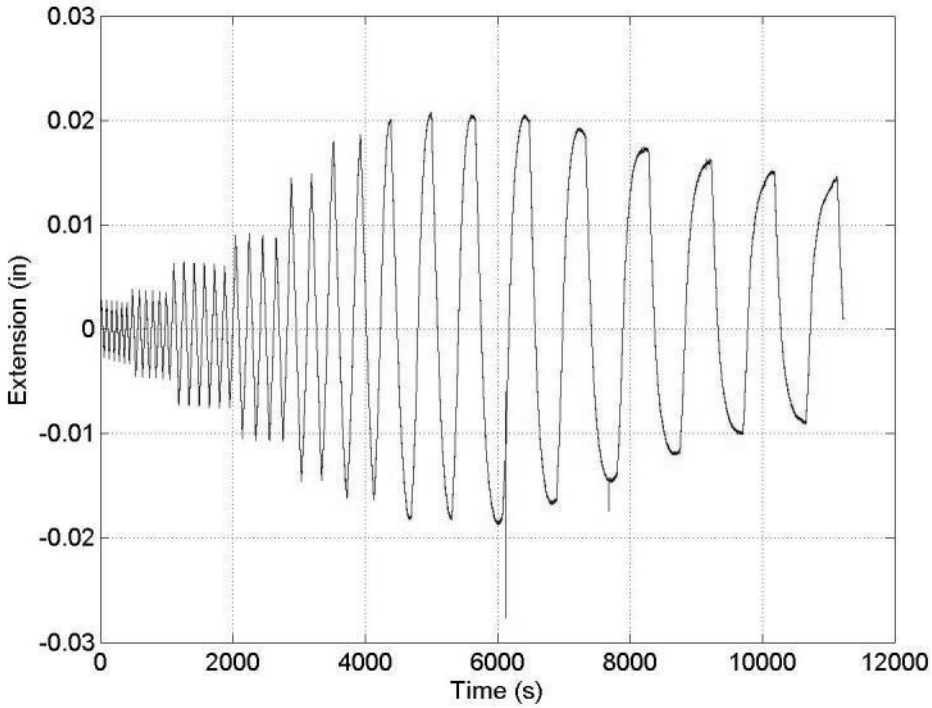

Figure 268: Specimen 7 (RBS36) – LVDT7

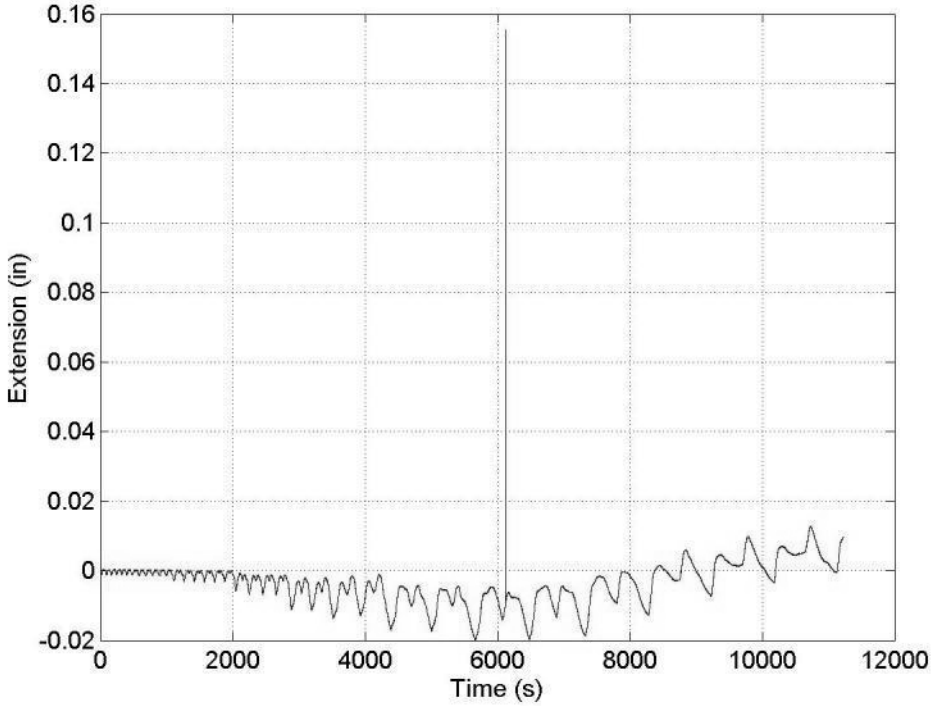

Figure 269: Specimen 7 (RBS36) – LVDT8

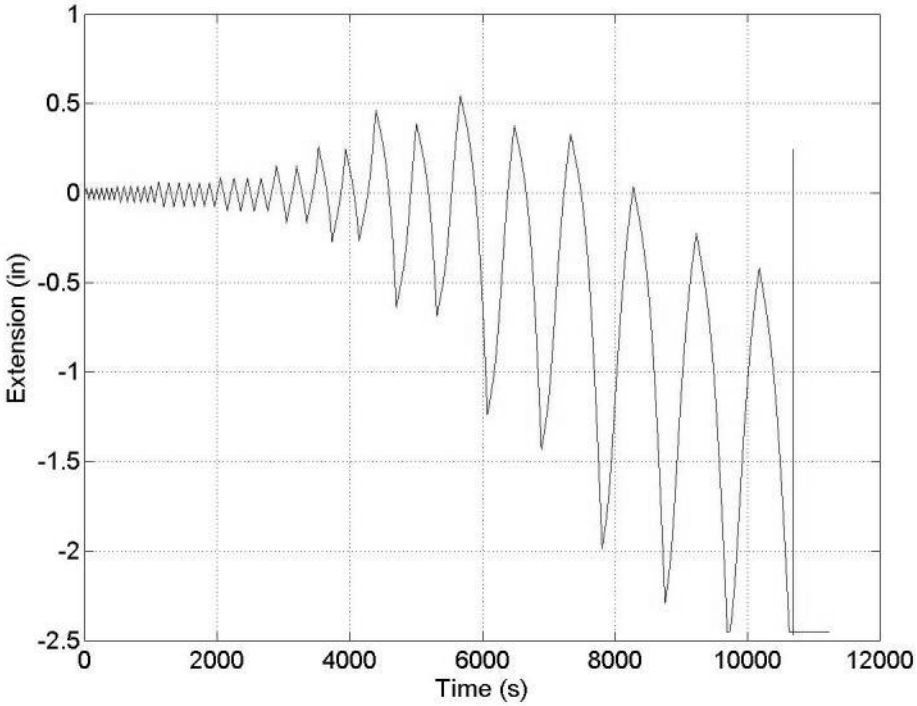

Figure 270: Specimen 7 (RBS36) – LVDT9

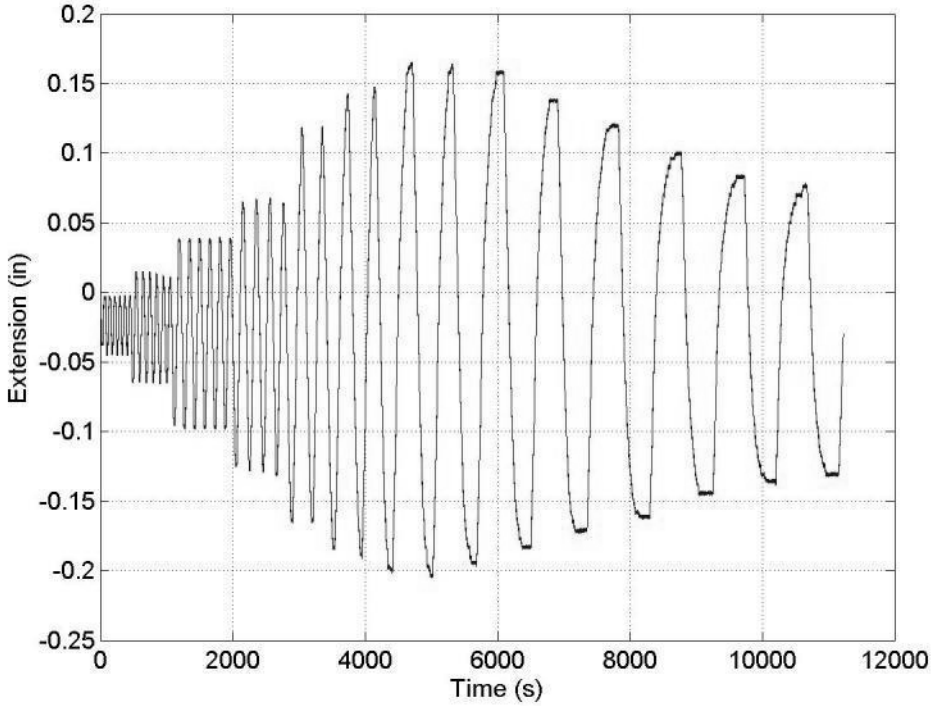

Figure 271: Specimen 7 (RBS36) - String Potentiometer 1 (column)

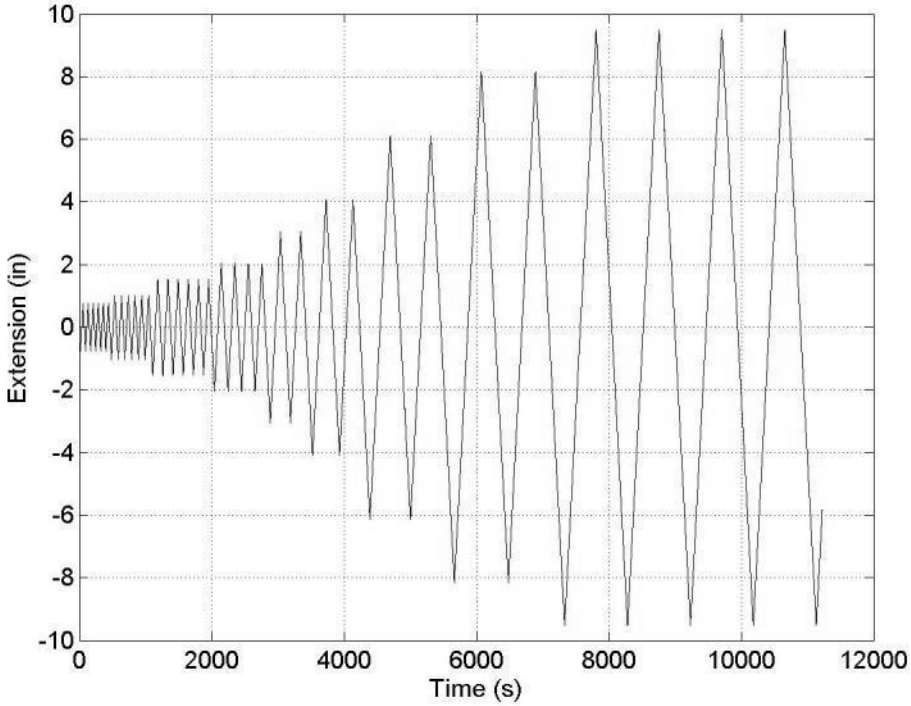

Figure 272: Specimen 7 (RBS36) - String Potentiometer 2 (actuator)

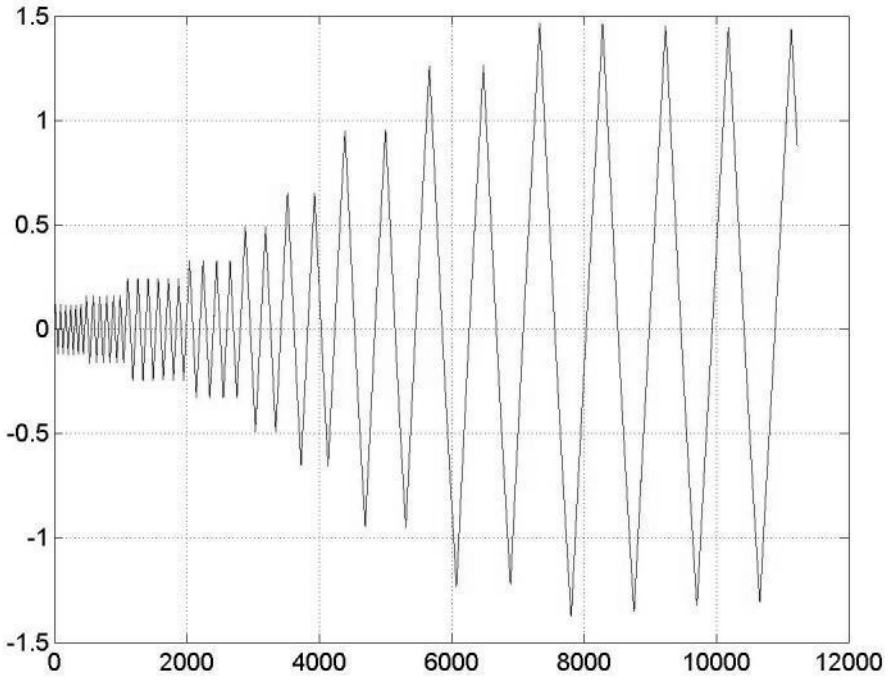

Figure 273: Specimen 7 (RBS36) - String Potentiometer 3 (beam)

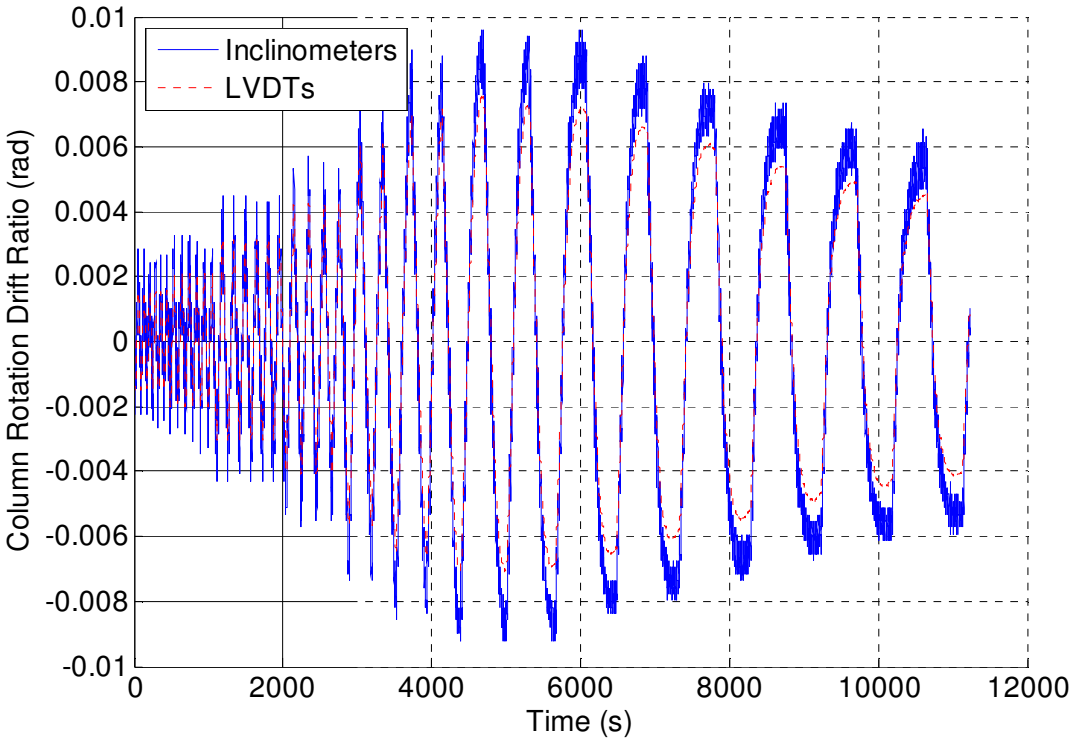

Figure 274: Specimen 7 (RBS36) - Column Rotation Comparison

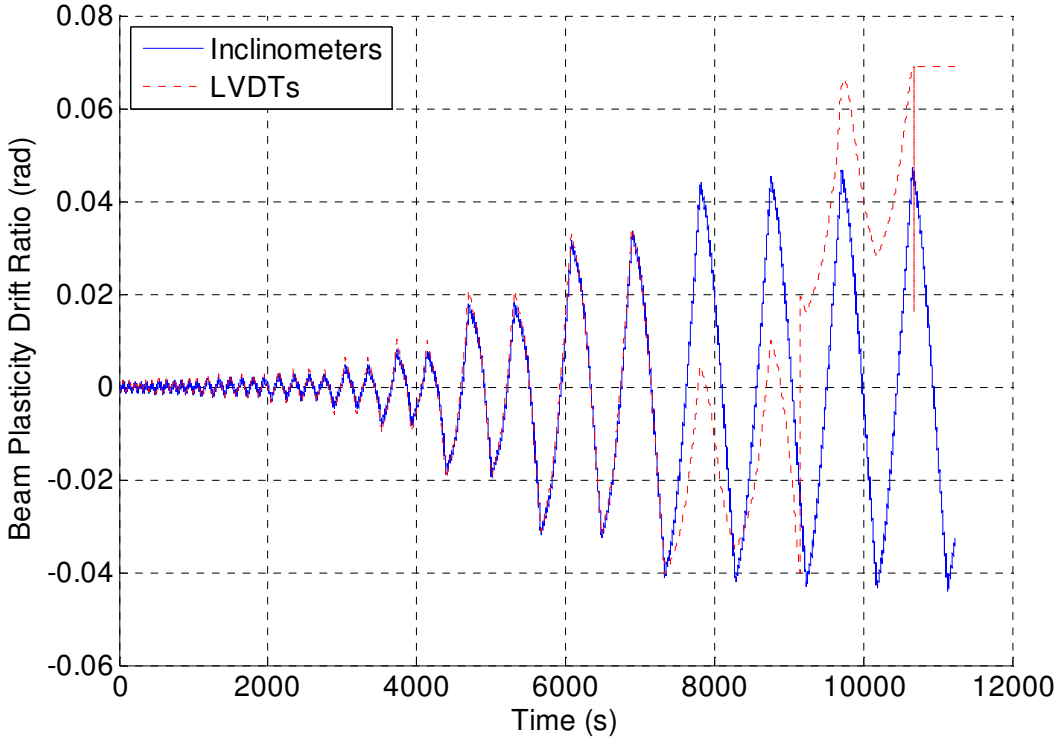

Figure 275: Specimen 7 (RBS36) - Beam Plasticity Comparison

Appendix O – Specimen 8 (RBS36-PW12) Raw Instrumentation Data

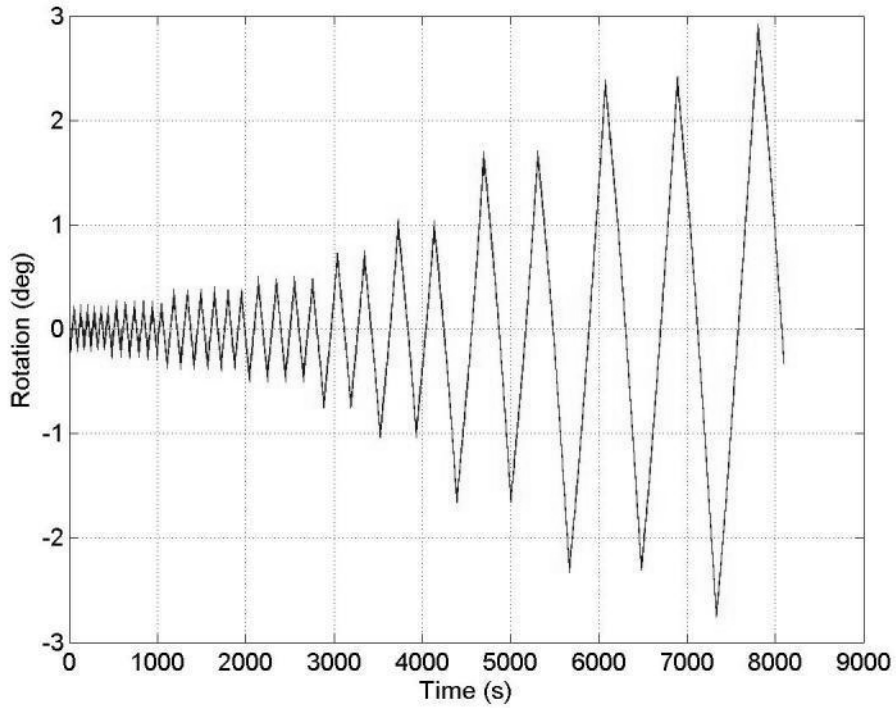

Figure 276: Specimen 8 (RBS36-PW12) - Inclinometer 3 (beam)

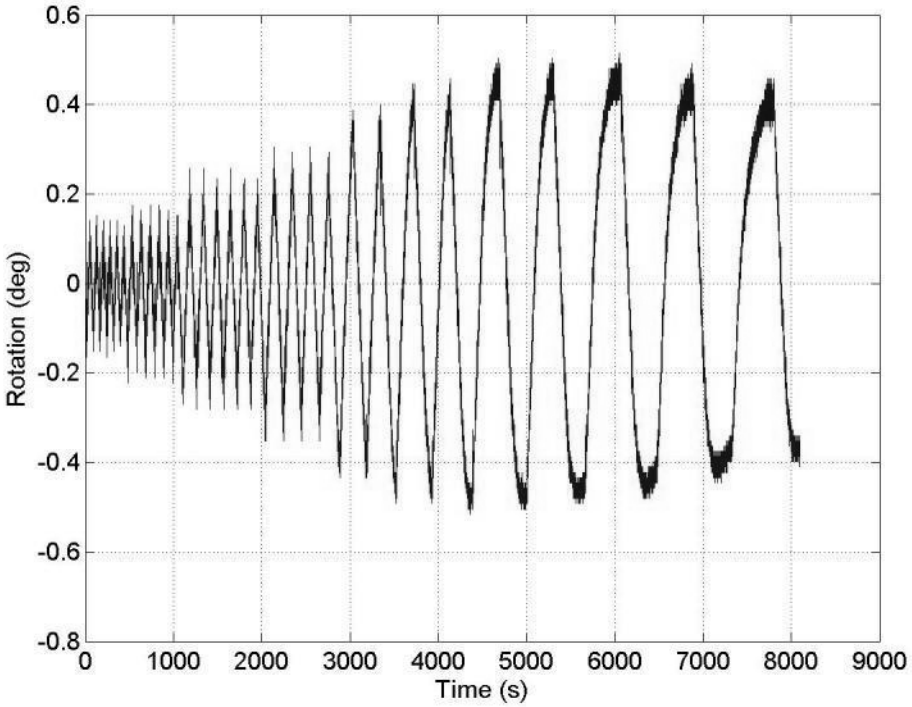

Figure 277: Specimen 8 (RBS36-PW12) - Inclinometer 1 (column)

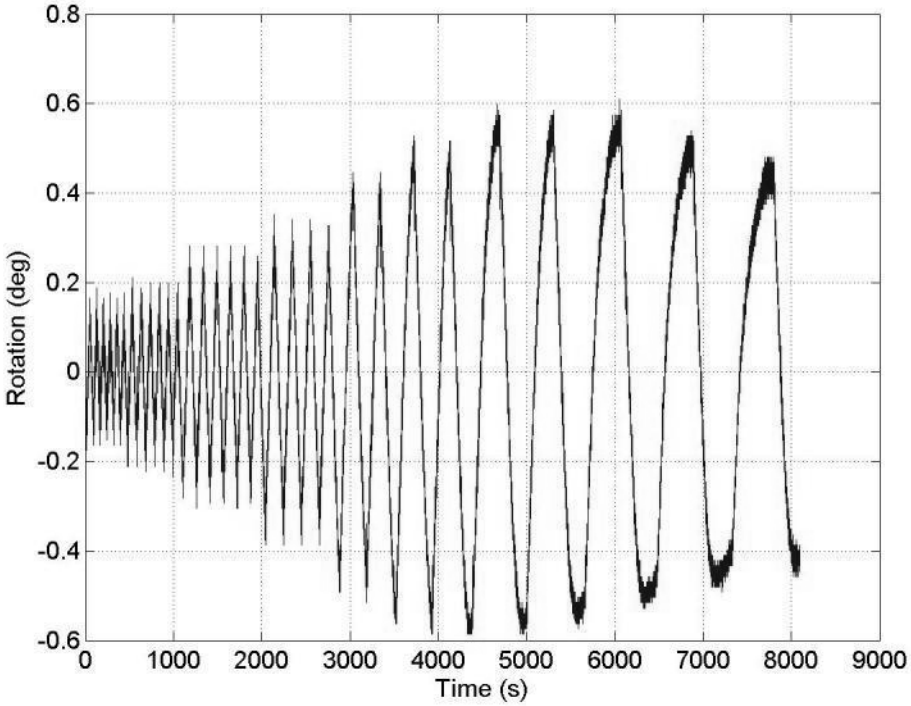

Figure 278: Specimen 8 (RBS36-PW12) - Inclinometer 2 (endplate)

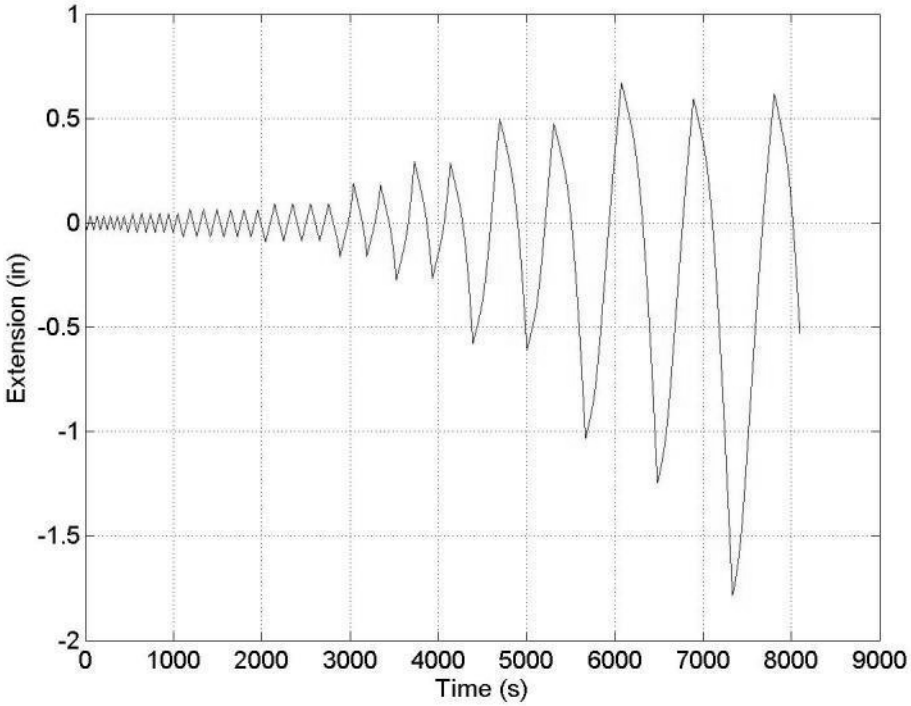

Figure 279: Specimen 8 (RBS36-PW12) - LVDT1

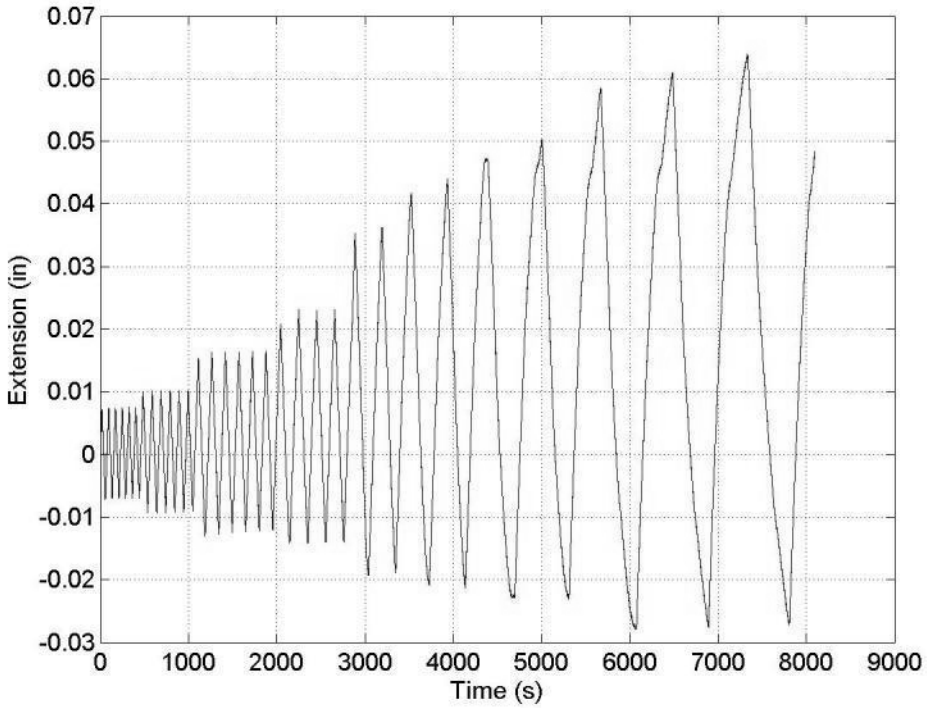

Figure 280: Specimen 8 (RBS36-PW12) – LVDT2

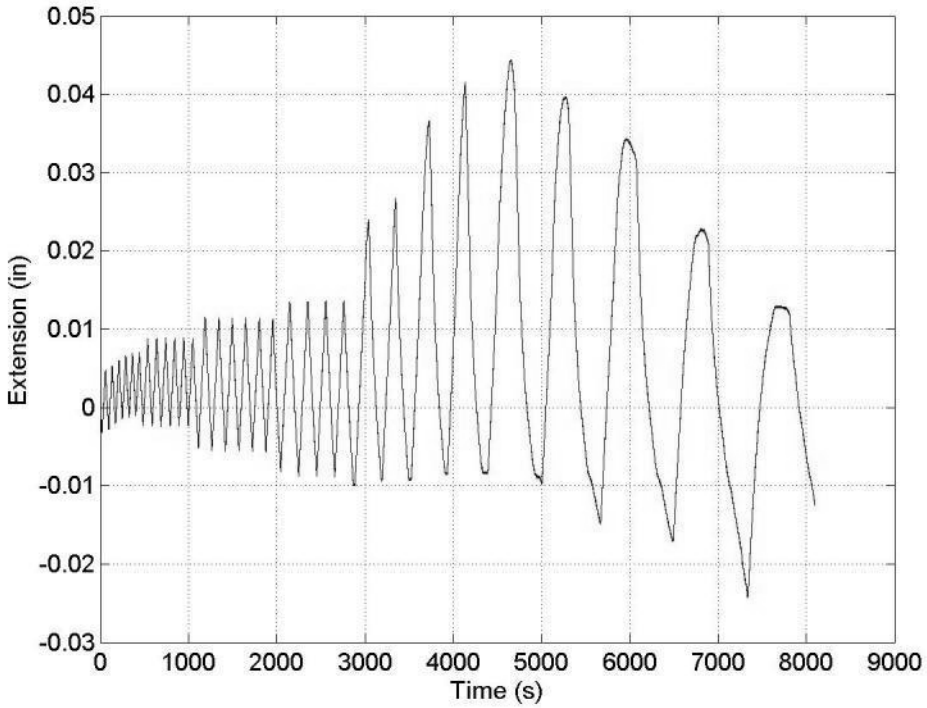

Figure 281: Specimen 8 (RBS36-PW12) – LVDT3

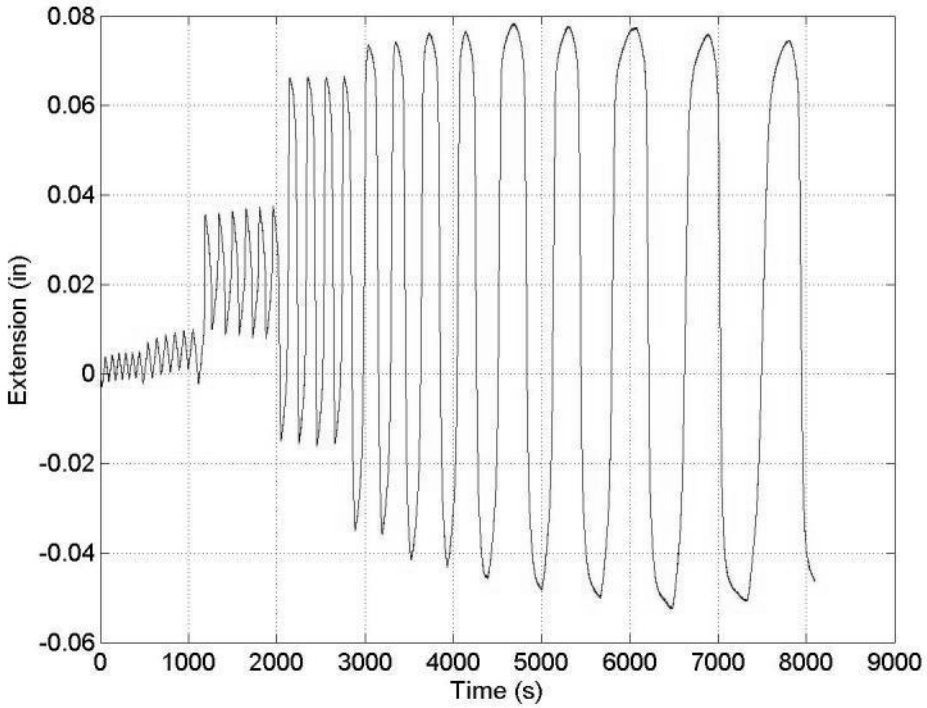

Figure 282: Specimen 8 (RBS36-PW12) – LVDT4

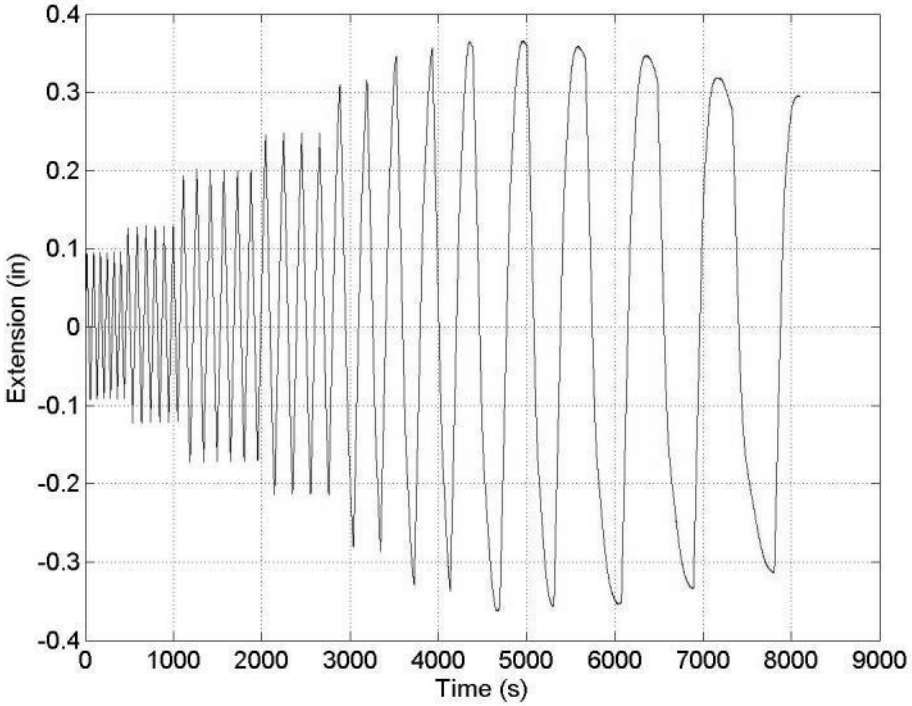

Figure 283: Specimen 8 (RBS36-PW12) – LVDT5

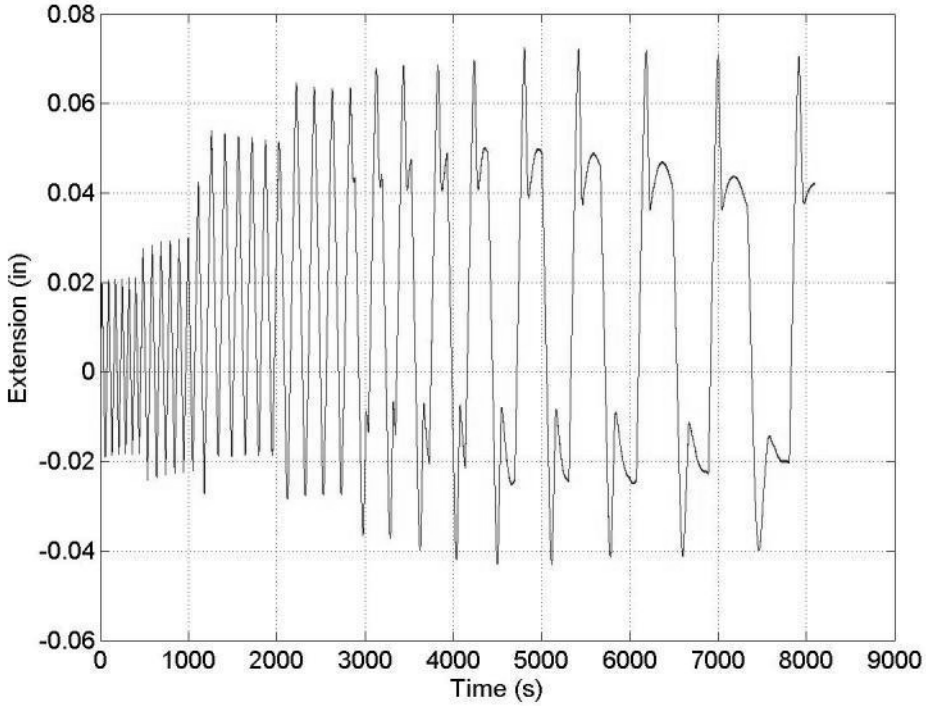

Figure 284: Specimen 8 (RBS36-PW12) – LVDT6

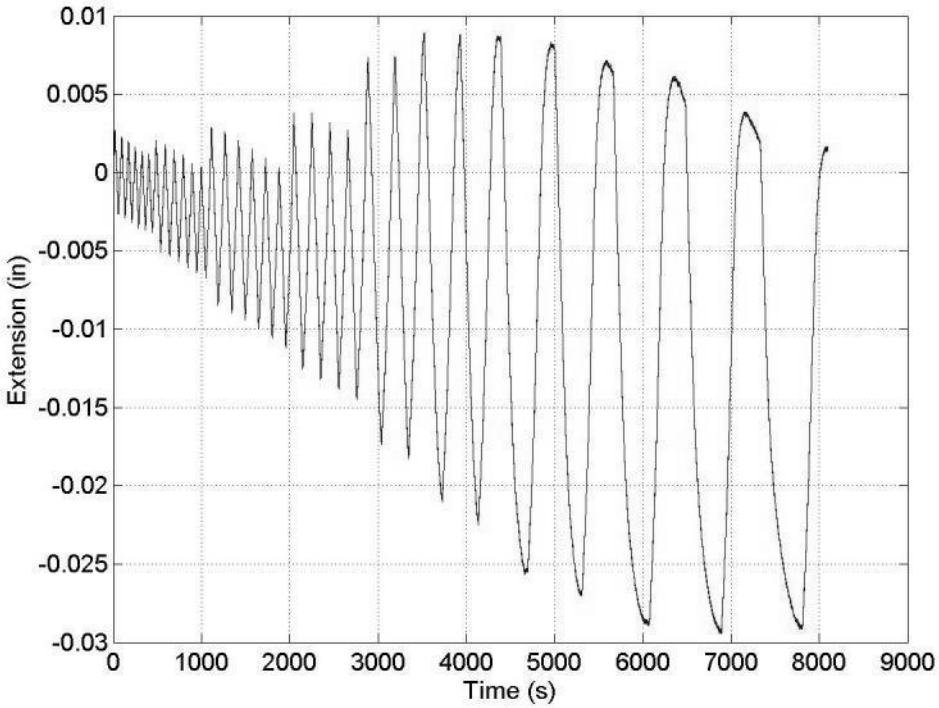

Figure 285: Specimen 8 (RBS36-PW12) – LVDT7

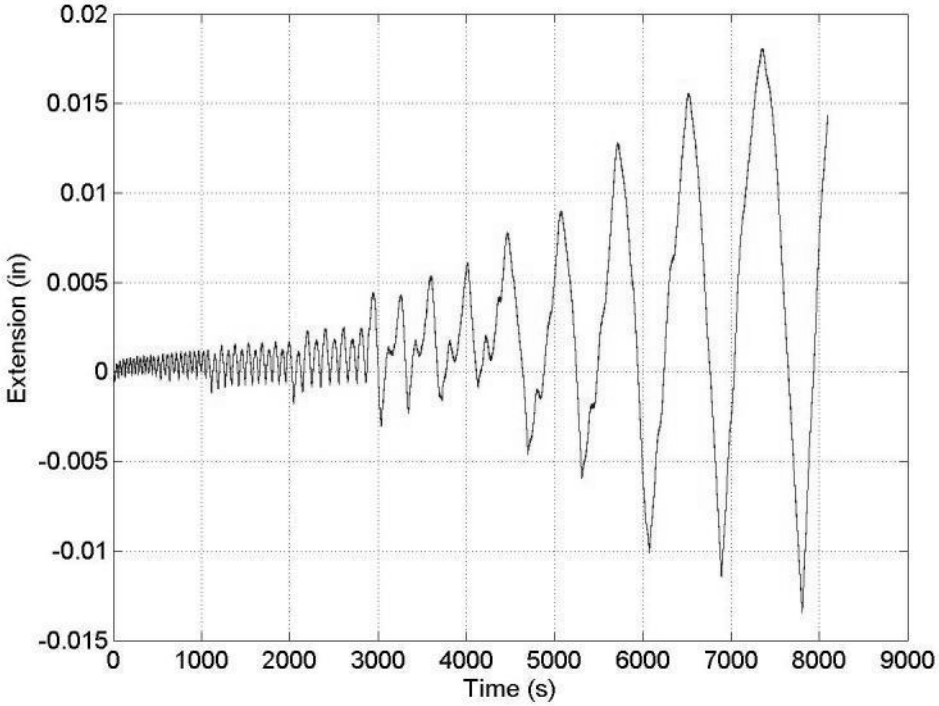

Figure 286: Specimen 8 (RBS36-PW12) – LVDT8

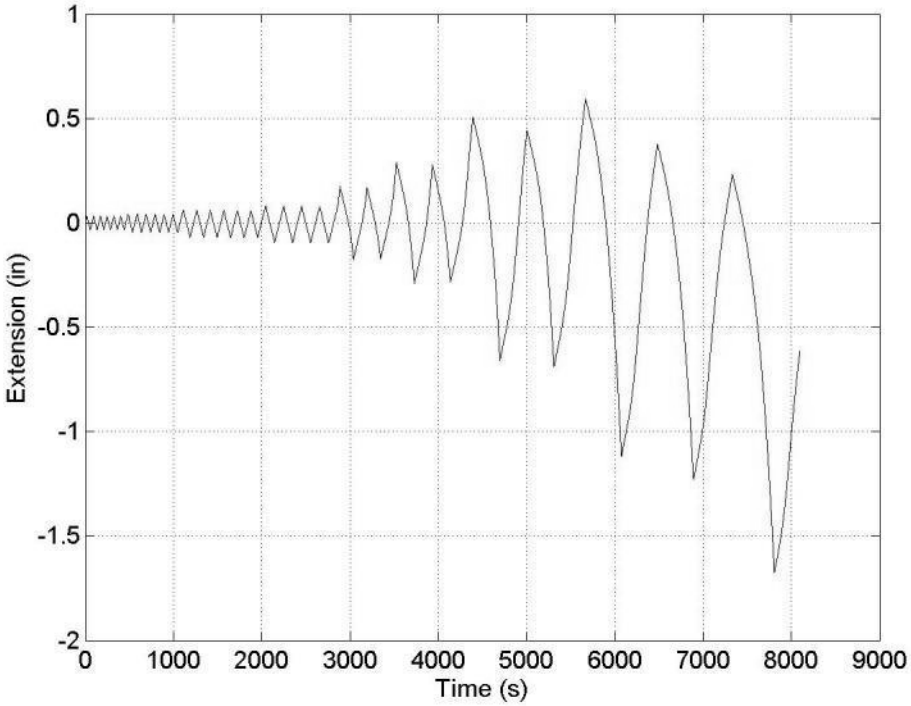

Figure 287: Specimen 8 (RBS36-PW12) – LVDT9

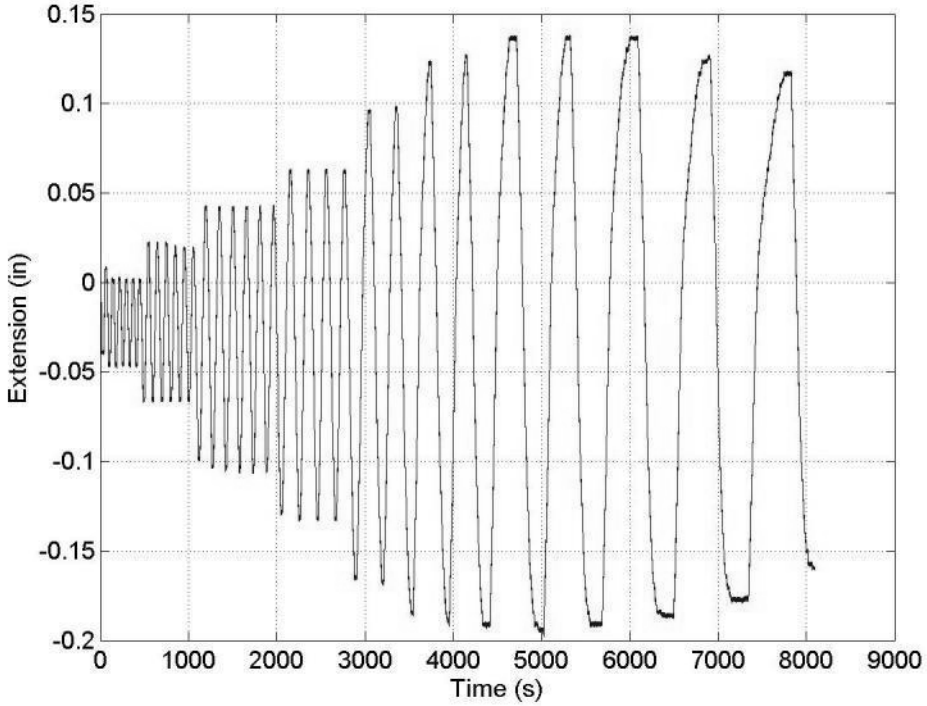

Figure 288: Specimen 8 (RBS36-PW12) - String Potentiometer 1 (column)

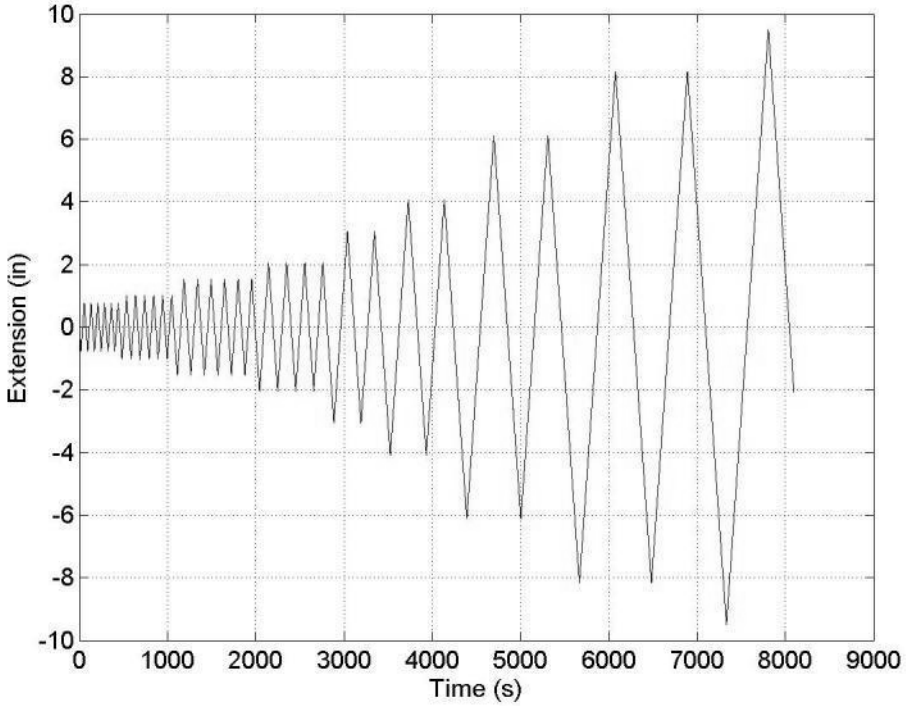

Figure 289: Specimen 8 (RBS36-PW12) - String Potentiometer 2 (actuator)

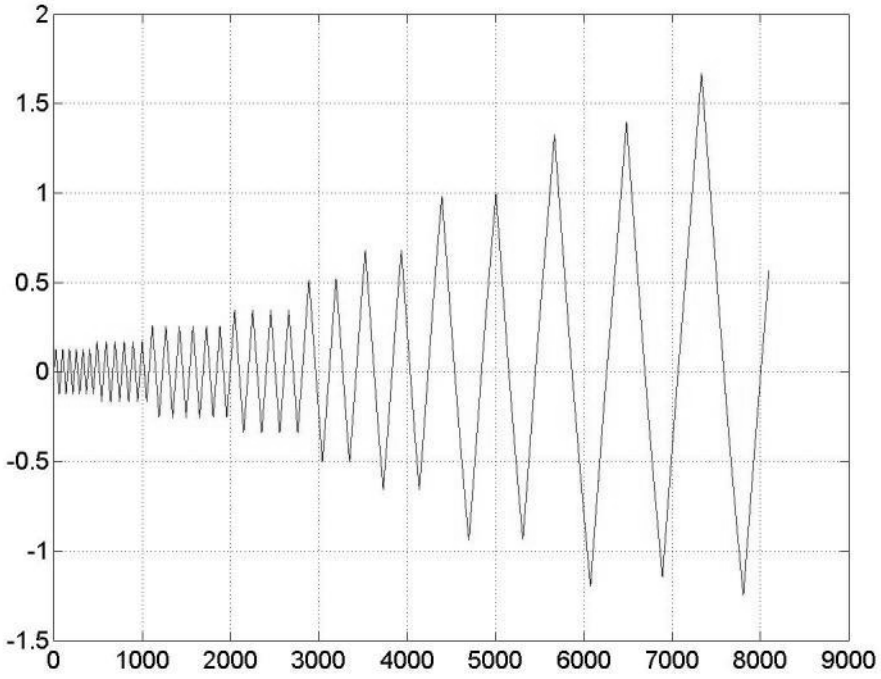

Figure 290: Specimen 8 (RBS36-PW12) - String Potentiometer 3 (beam)

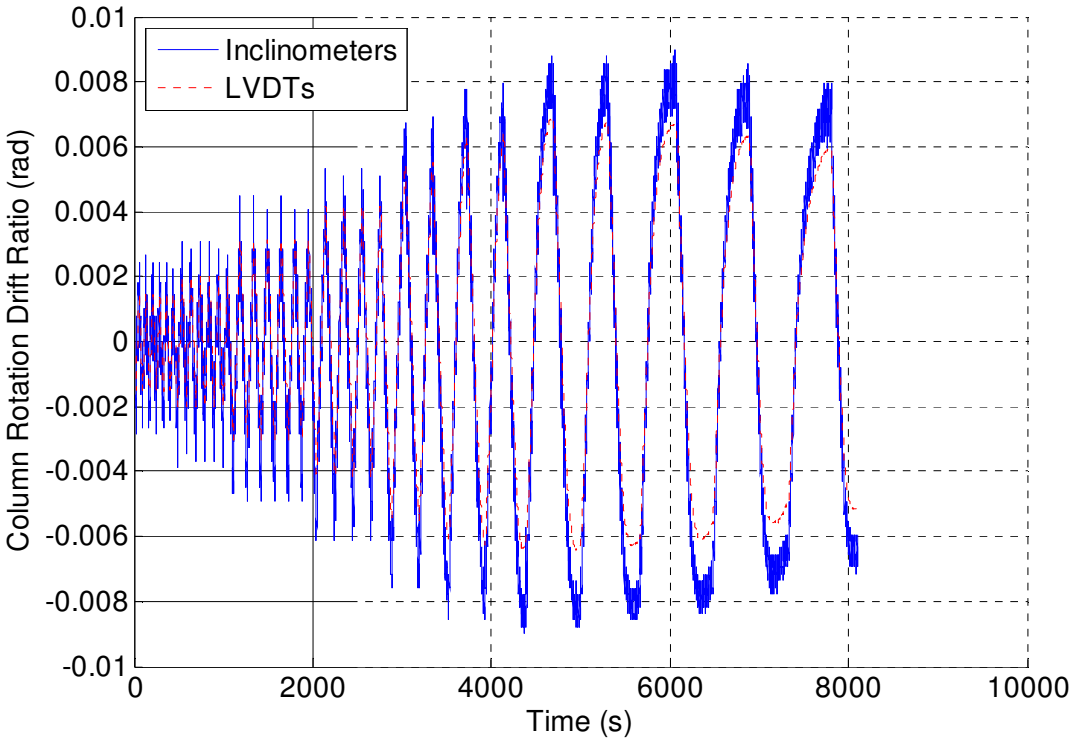

Figure 291: Specimen 8 (RBS36-PW12) - Column Rotation Comparison

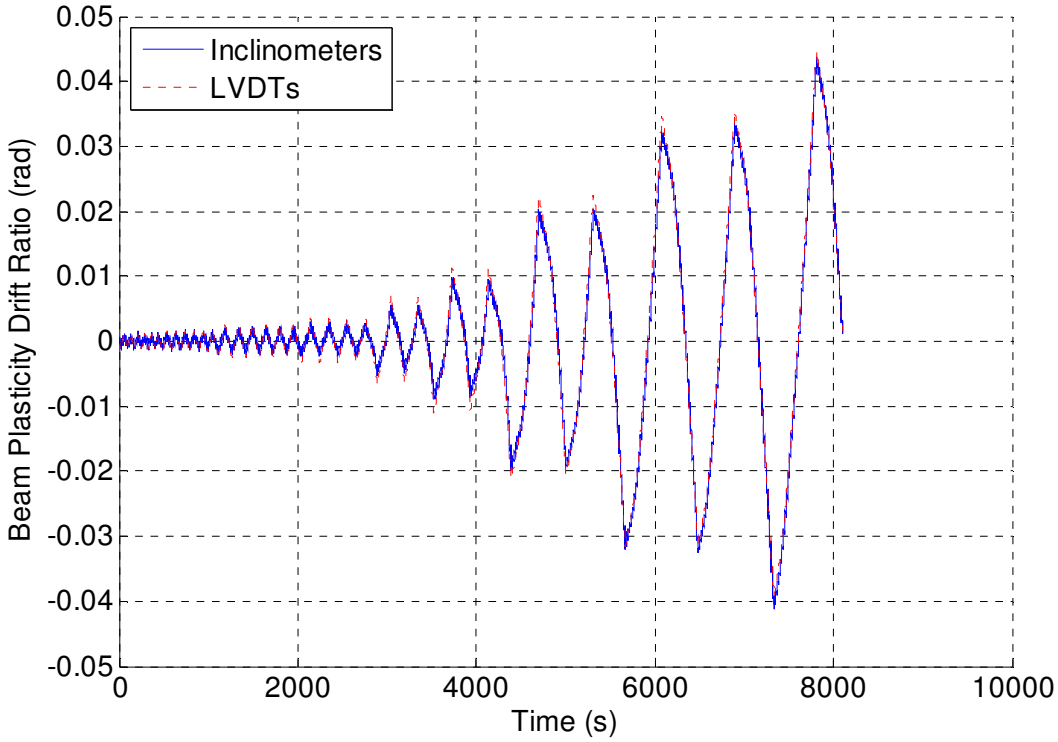

Figure 292: Specimen 8 (RBS36-PW12) - Beam Plasticity Comparison

Appendix P – Specimen 9 (RBS36-PAF-array) Raw Instrumentation Data

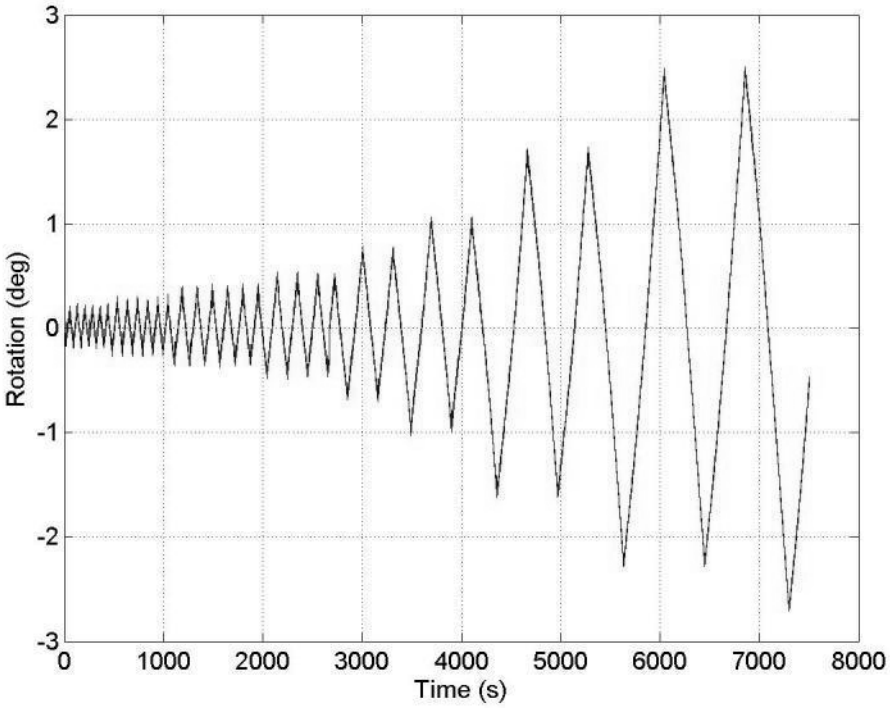

Figure 293: Specimen 9 (RBS36-PAF-array) - Inclinometer 3 (beam)

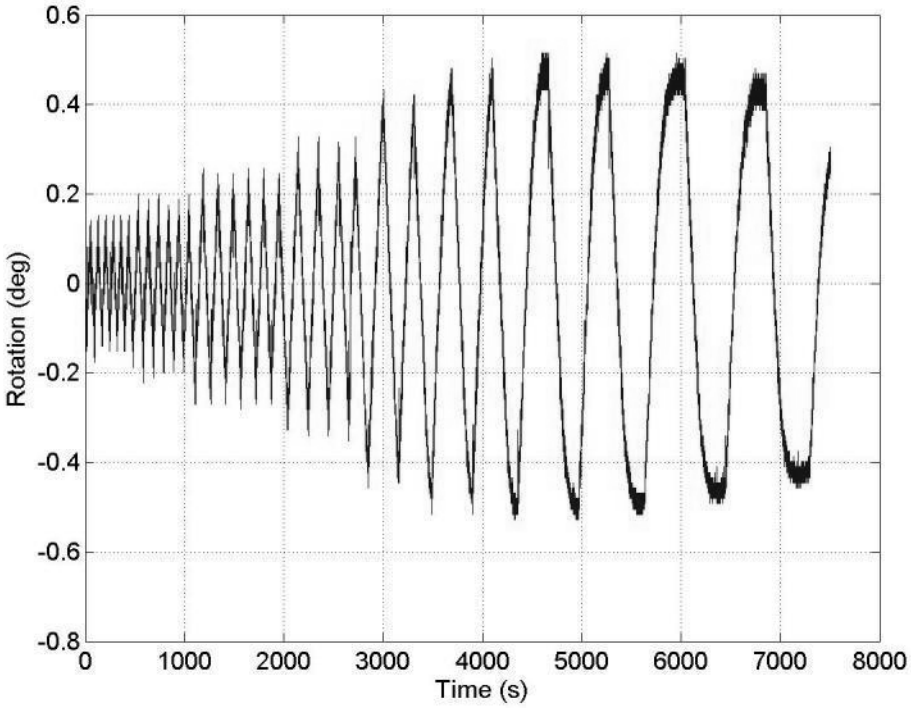

Figure 294: Specimen 9 (RBS36-PAF-array) - Inclinometer 1 (column)

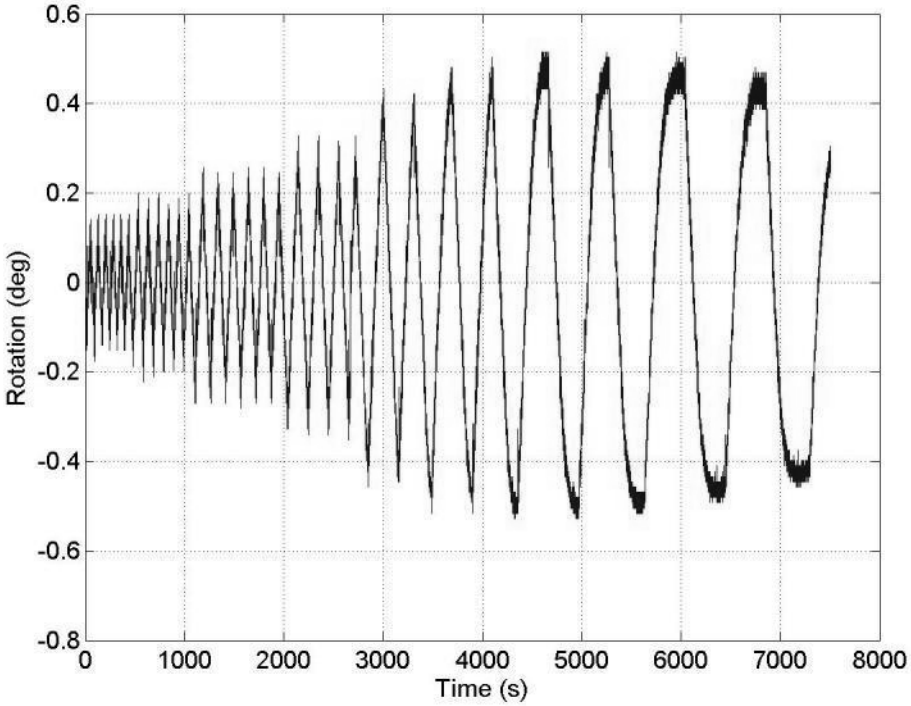

Figure 295: Specimen 9 (RBS36-PAF-array) - Inclinometer 2 (endplate)

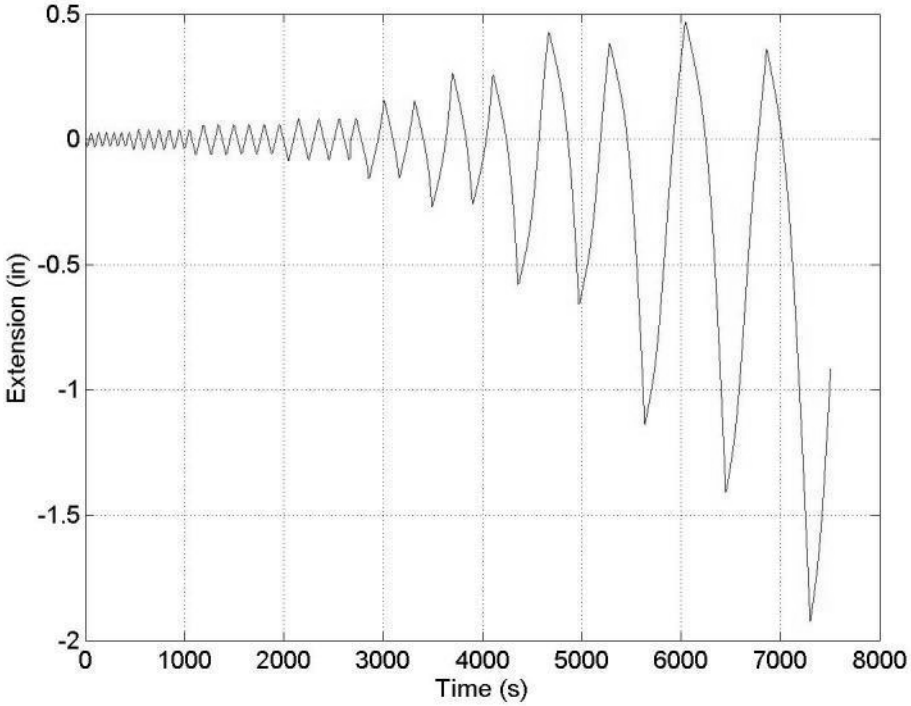

Figure 296: Specimen 9 (RBS36-PAF-array) - LVDT1

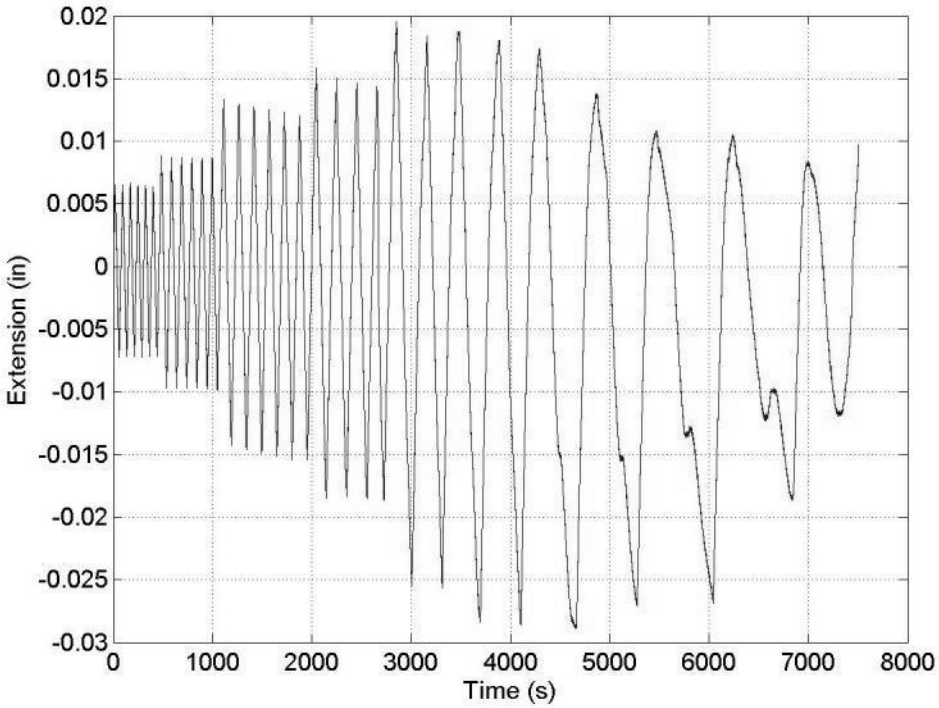

Figure 297: Specimen 9 (RBS36-PAF-array) – LVDT2

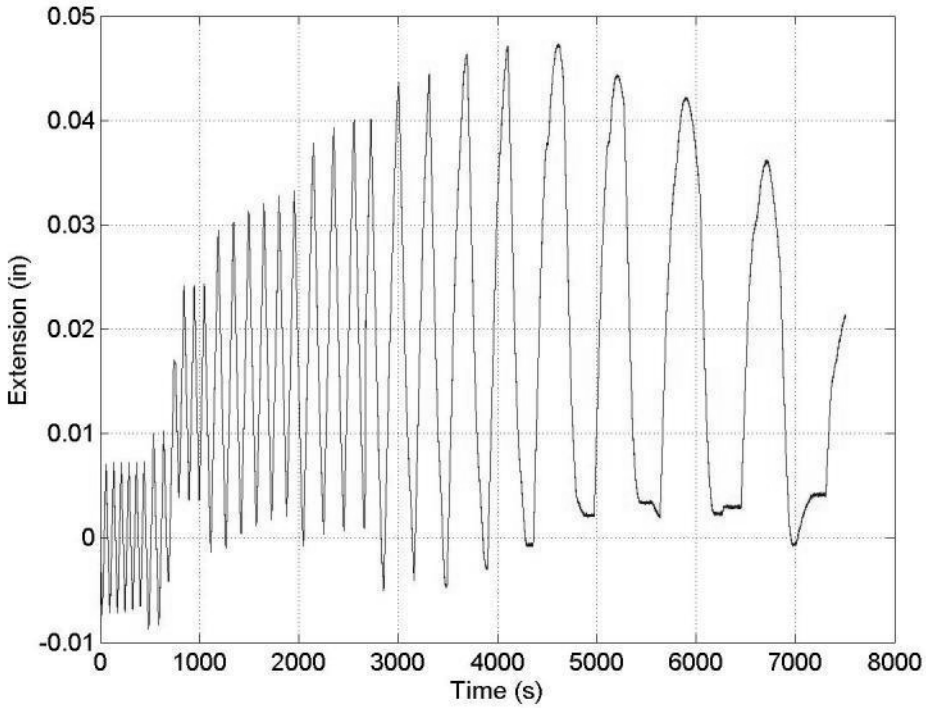

Figure 298: Specimen 9 (RBS36-PAF-array) – LVDT3

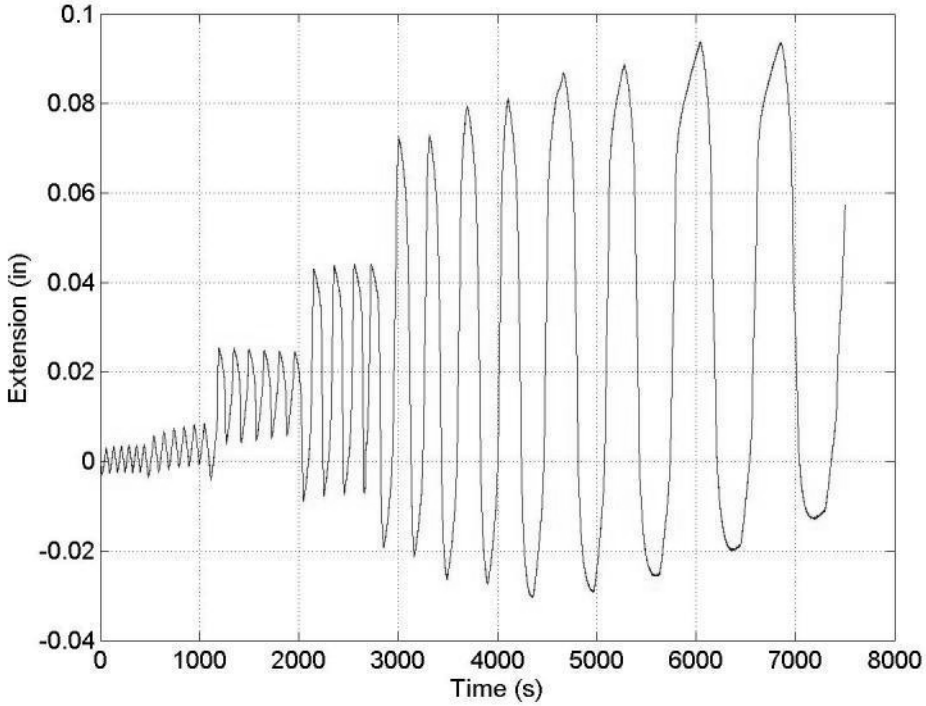

Figure 299: Specimen 9 (RBS36-PAF-array) – LVDT4

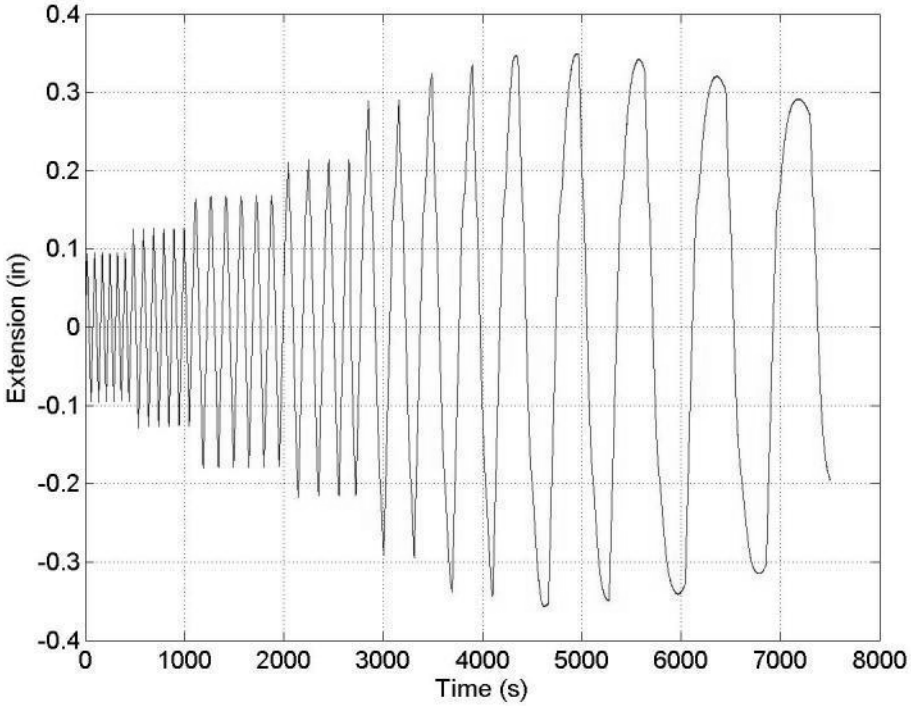

Figure 300: Specimen 9 (RBS36-PAF-array) – LVDT5

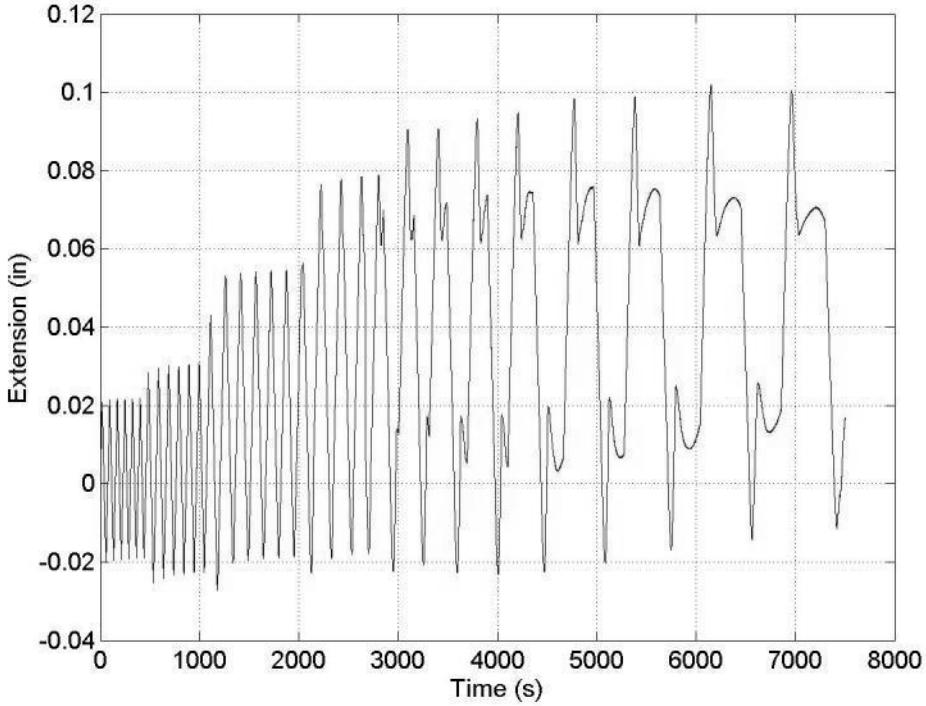

Figure 301: Specimen 9 (RBS36-PAF-array) – LVDT6

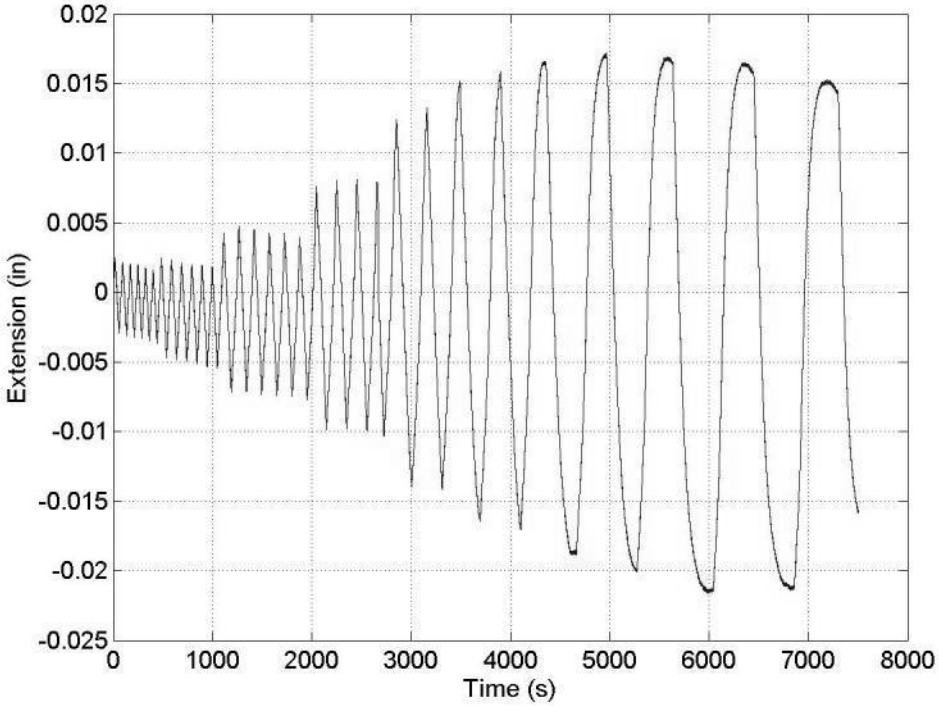

Figure 302: Specimen 9 (RBS36-PAF-array) – LVDT7

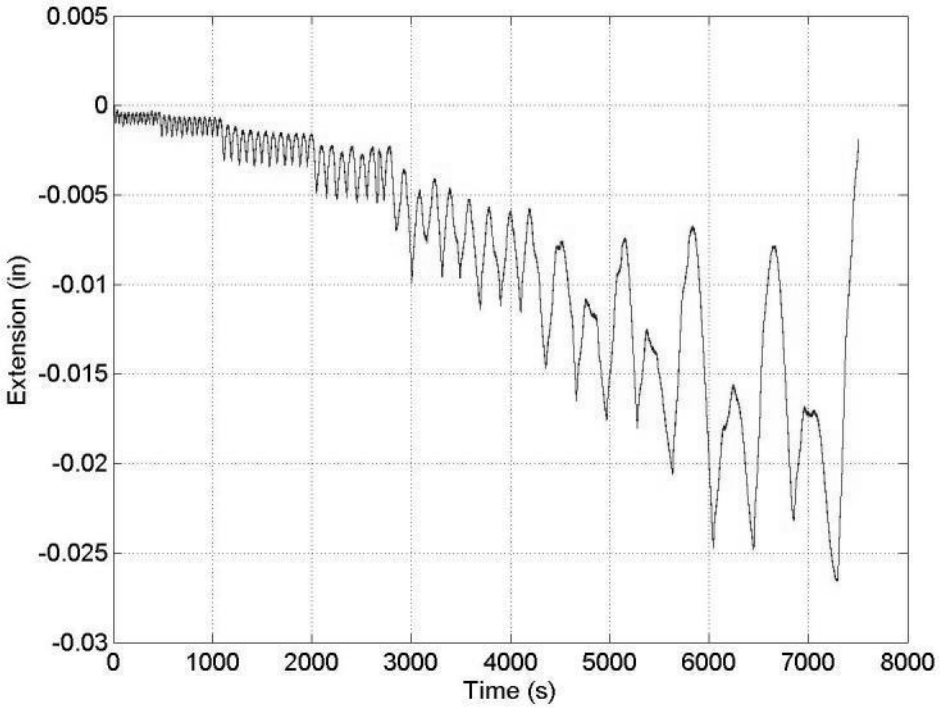

Figure 303: Specimen 9 (RBS36-PAF-array) – LVDT8

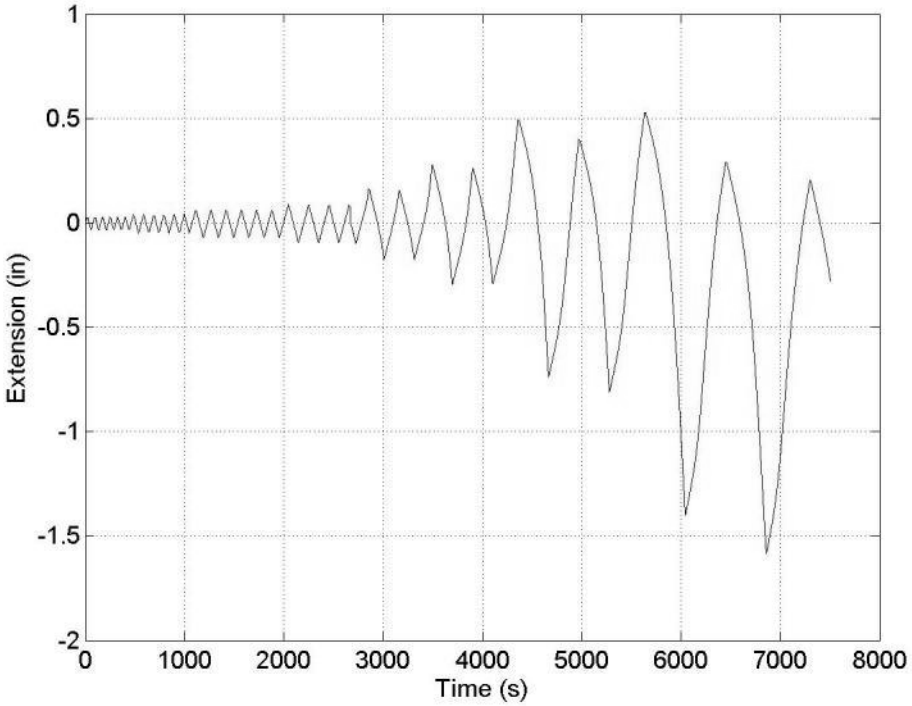

Figure 304: Specimen 9 (RBS36-PAF-array) – LVDT9

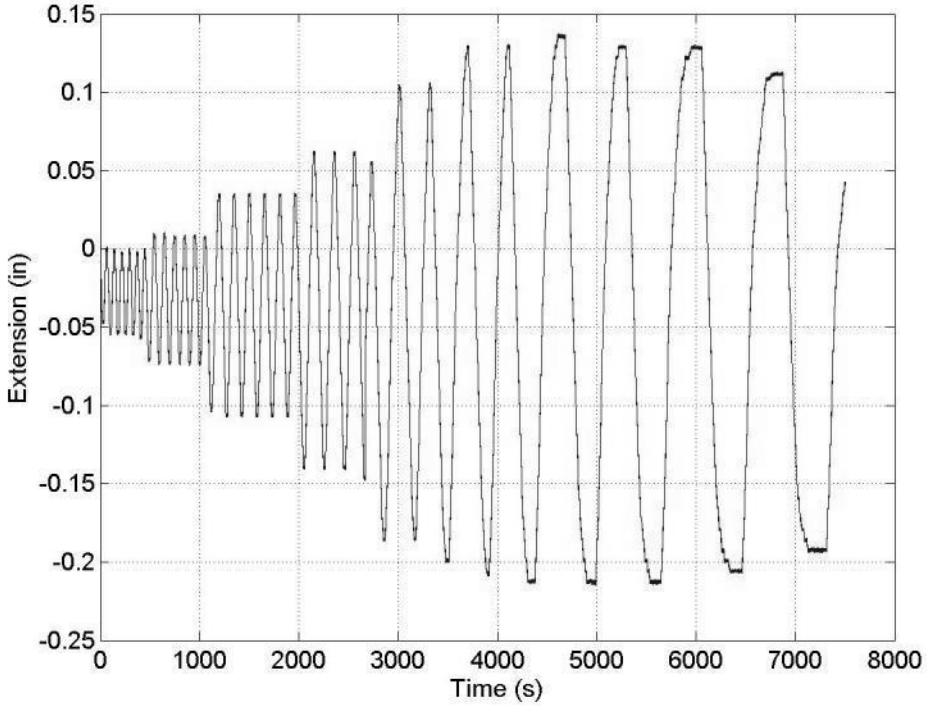

Figure 305: Specimen 9 (RBS36-PAF-array) - String Potentiometer 1 (column)

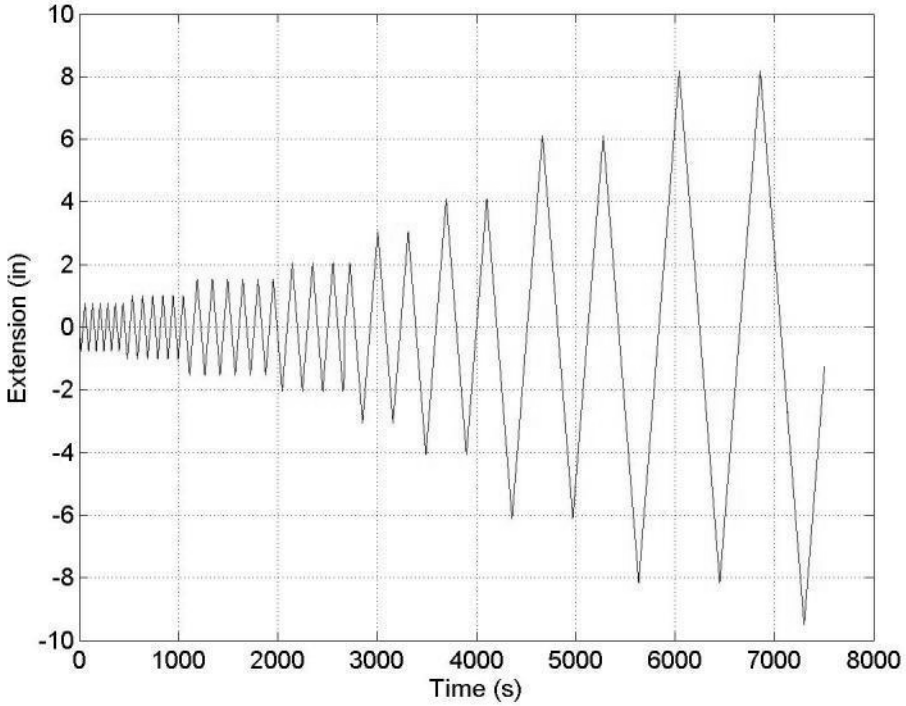

Figure 306: Specimen 9 (RBS36-PAF-array) - String Potentiometer 2 (actuator)

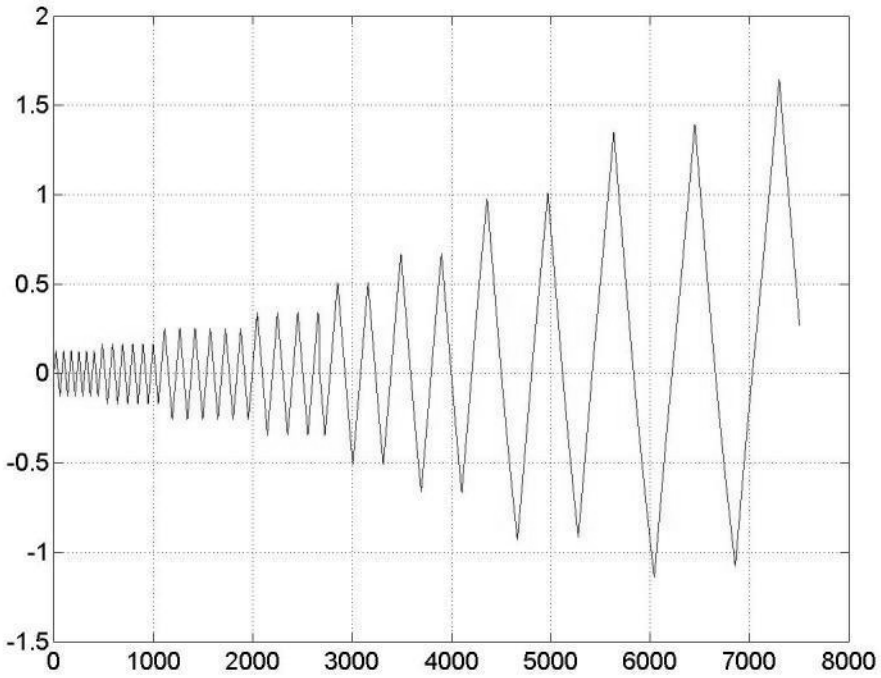

Figure 307: Specimen 9 (RBS36-PAF-array) - String Potentiometer 3 (beam)

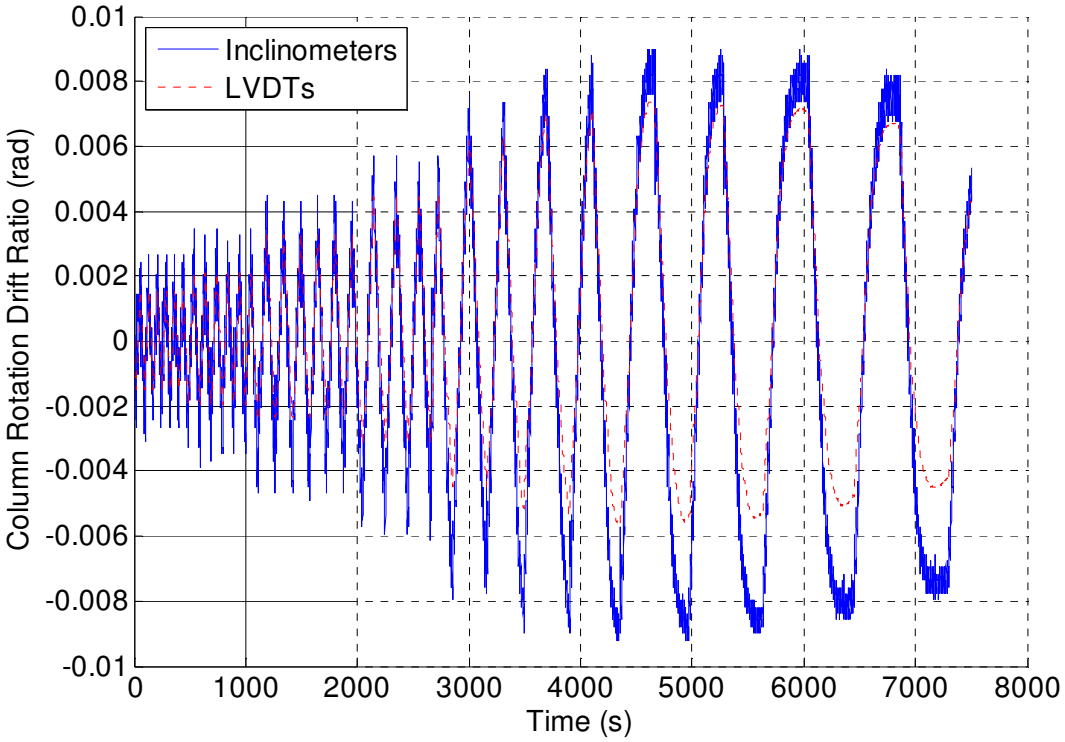

Figure 308: Specimen 9 (RBS36-PAF-array) - Column Rotation Comparison

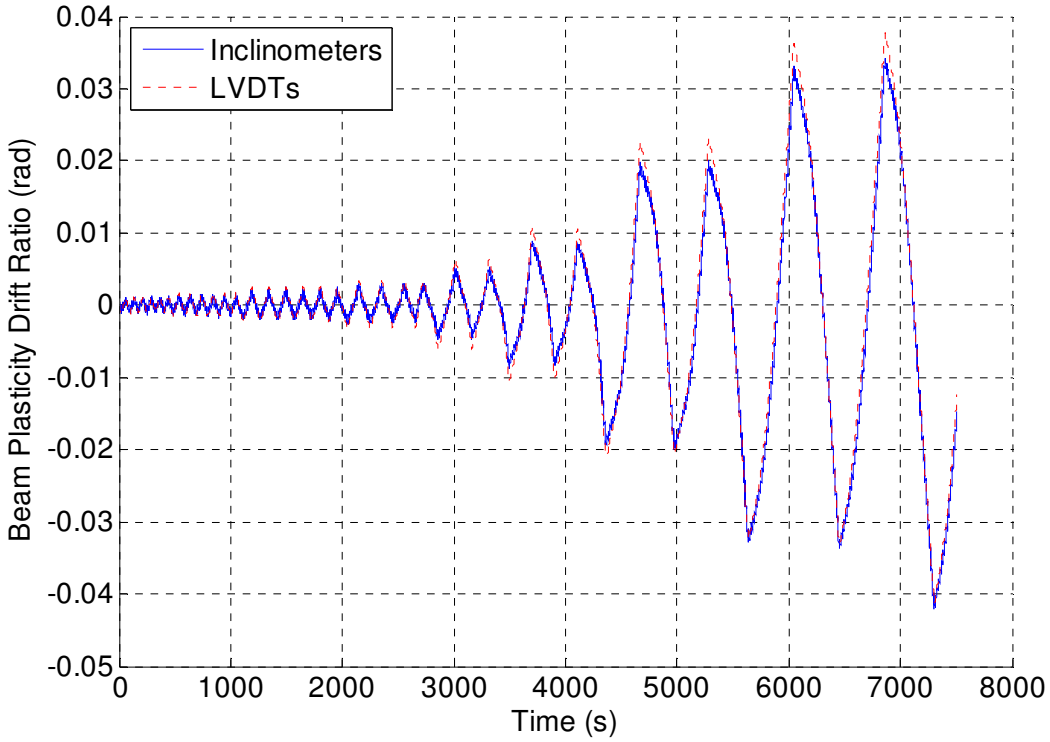

Figure 309: Specimen 9 (RBS36-PAF-array) - Beam Plasticity Comparison

Appendix Q – Specimen 10 (W36) Raw Instrumentation Data

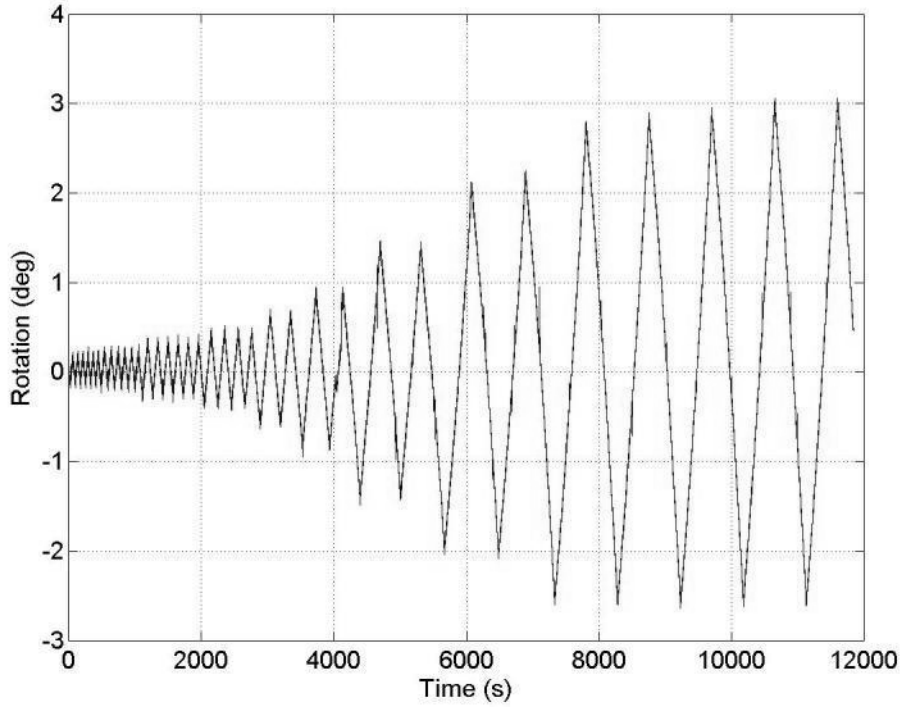

Figure 310: Specimen 10 (W36) - Inclinometer 3 (beam)

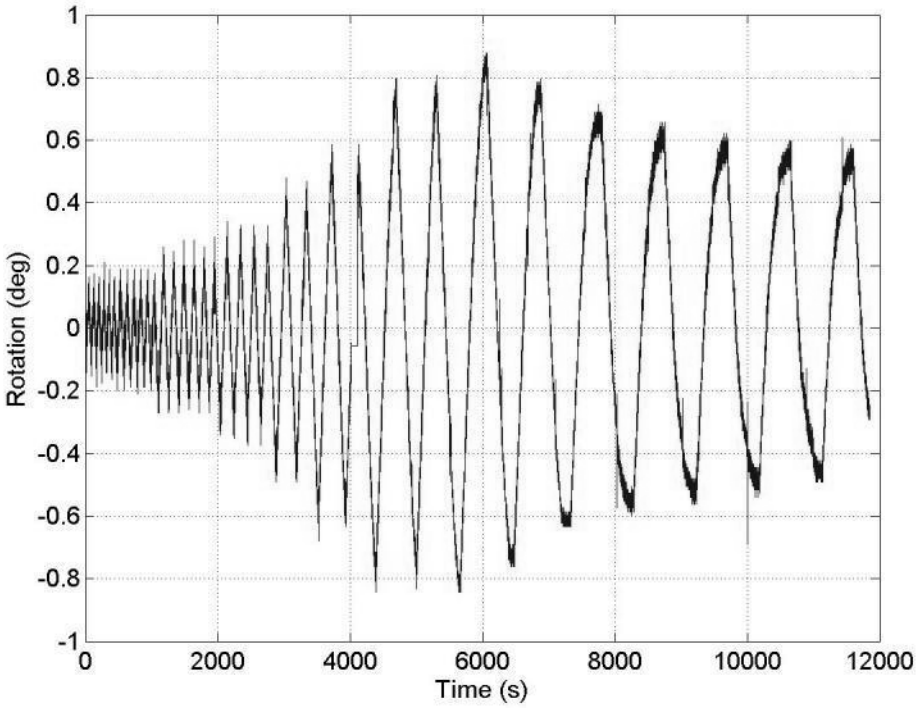

Figure 311: Specimen 10 (W36) - Inclinometer 1 (column)

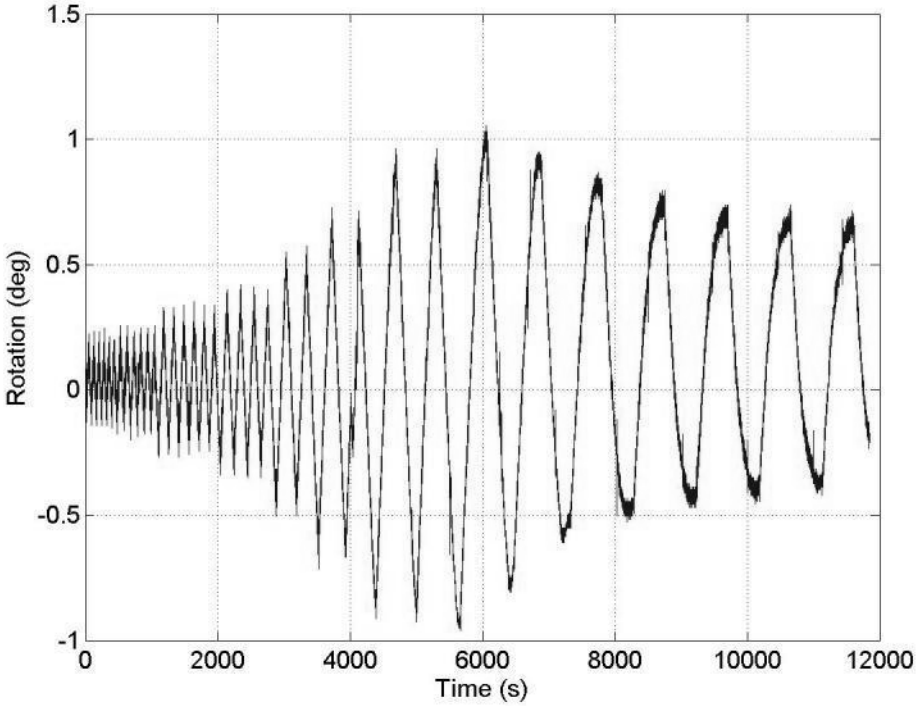

Figure 312: Specimen 10 (W36) - Inclinometer 2 (endplate)

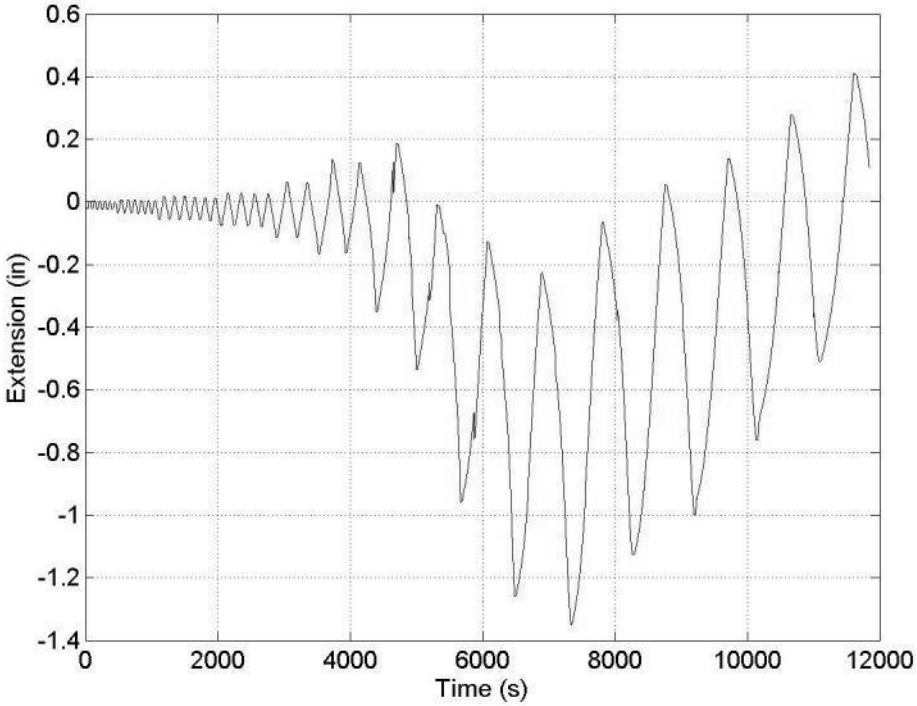

Figure 313: Specimen 10 (W36) - LVDT1

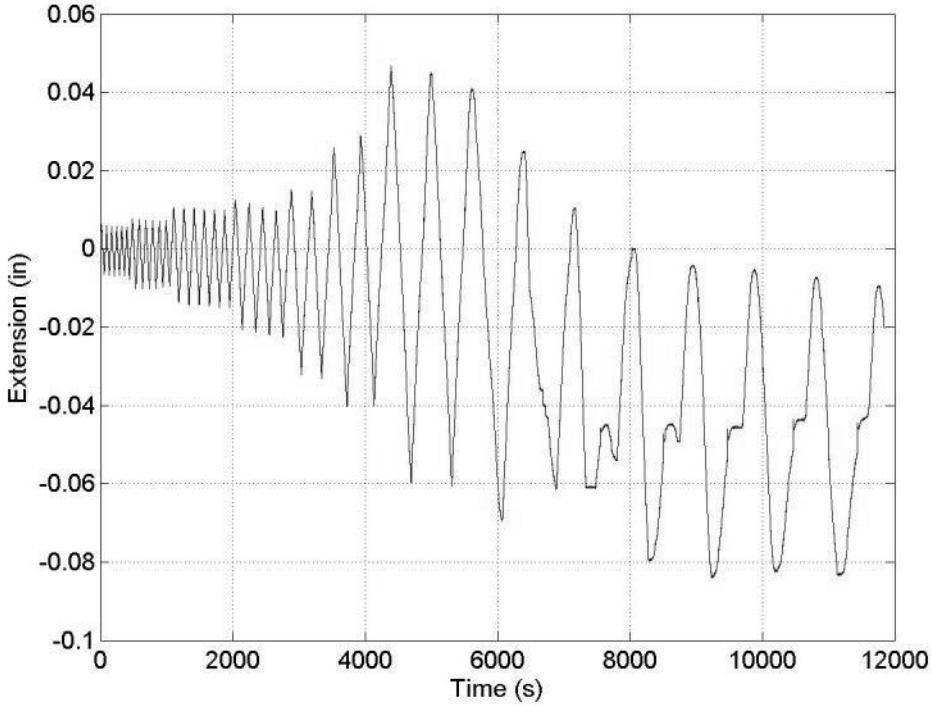

Figure 314: Specimen 10 (W36) – LVDT2

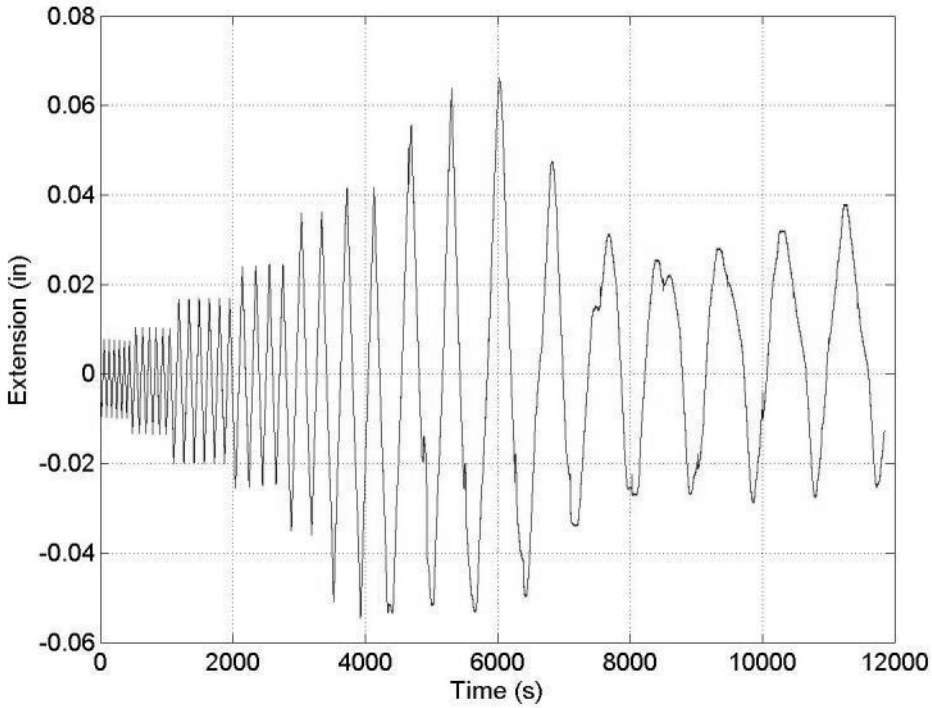

Figure 315: Specimen 10 (W36) – LVDT3

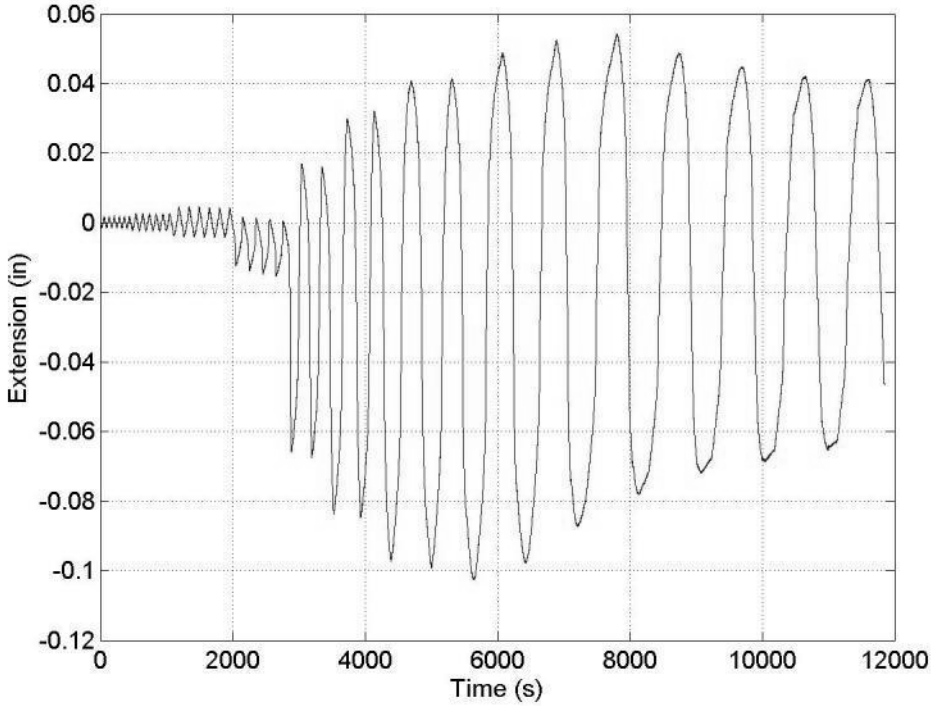

Figure 316: Specimen 10 (W36) – LVDT4

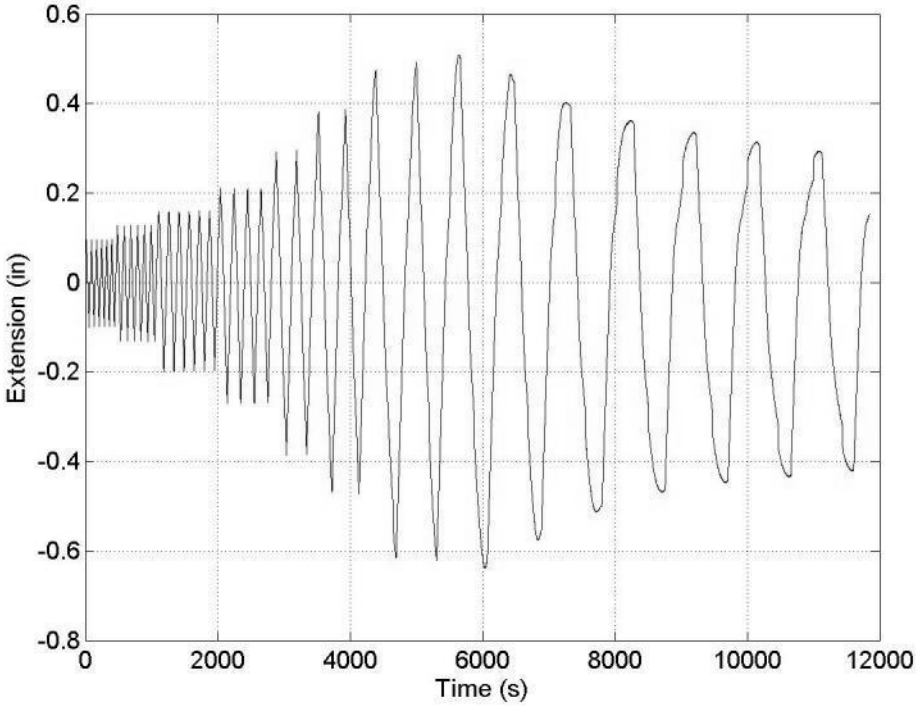

Figure 317: Specimen 10 (W36) - LVDT5

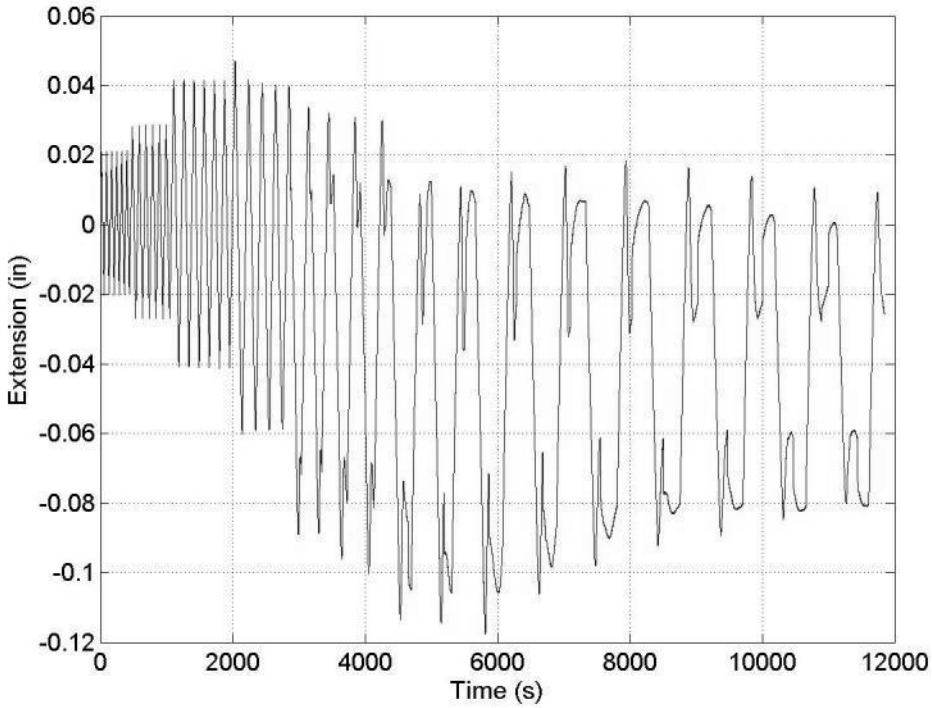

Figure 318: Specimen 10 (W36) – LVDT6

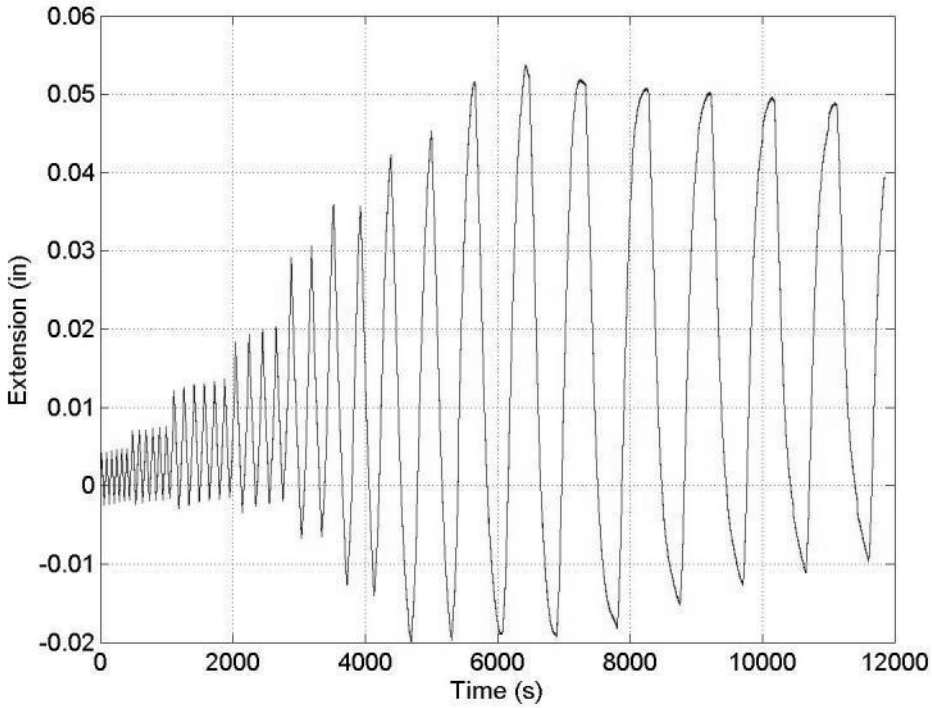

Figure 319: Specimen 10 (W36) – LVDT7

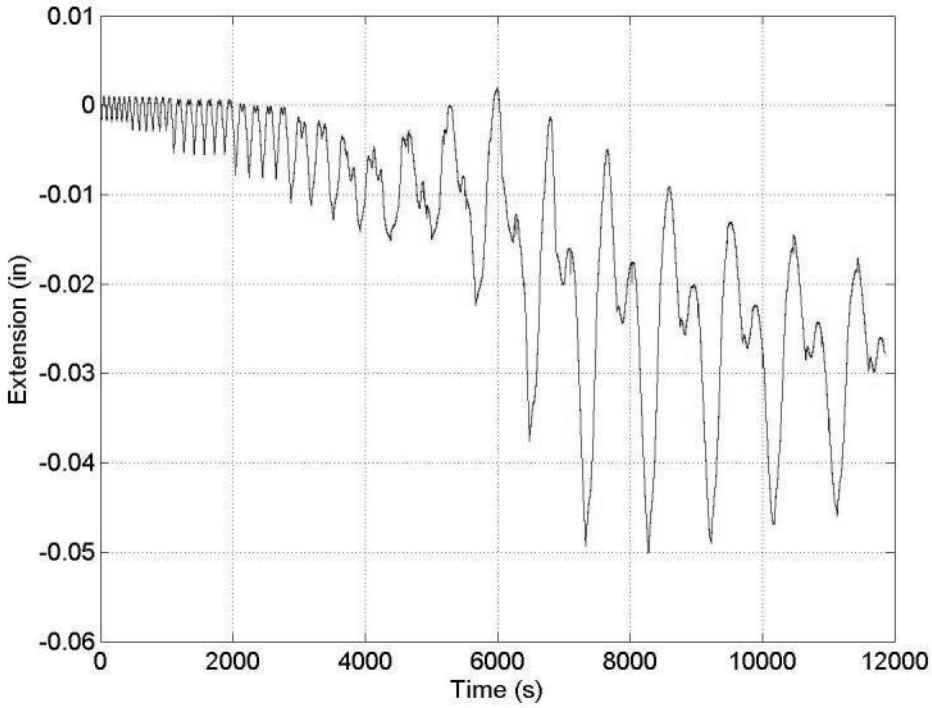

Figure 320: Specimen 10 (W36) – LVDT8

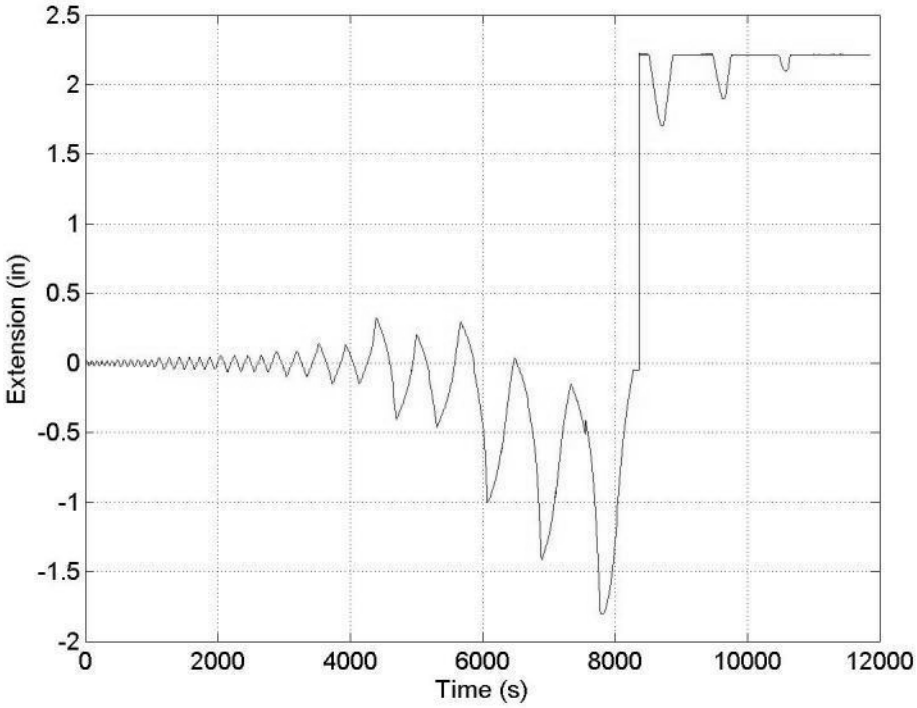

Figure 321: Specimen 10 (W36) – LVDT9

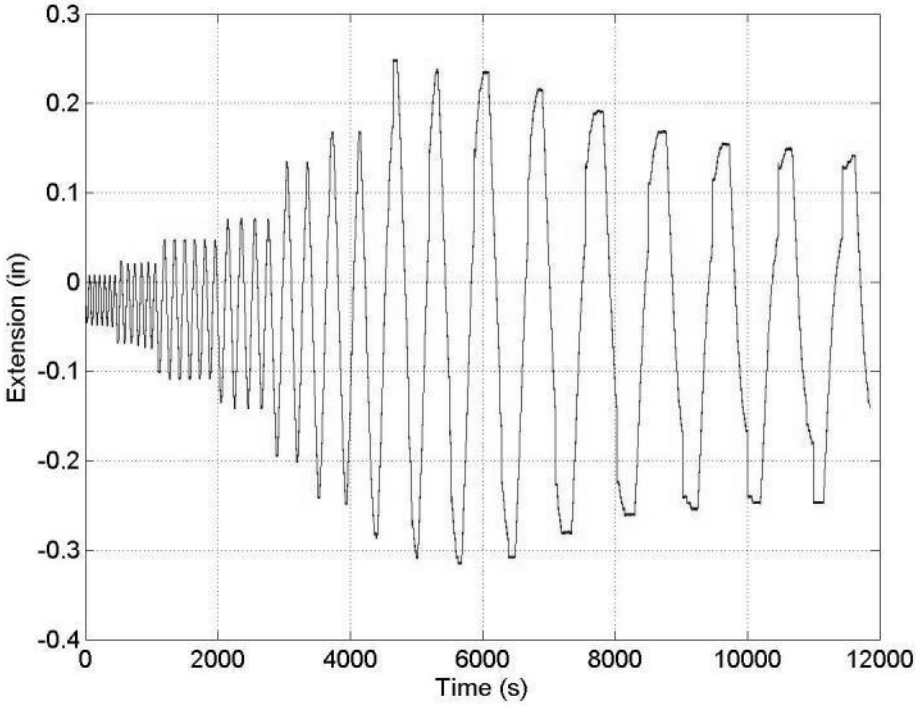

Figure 322: Specimen 10 (W36) - String Potentiometer 1 (column)

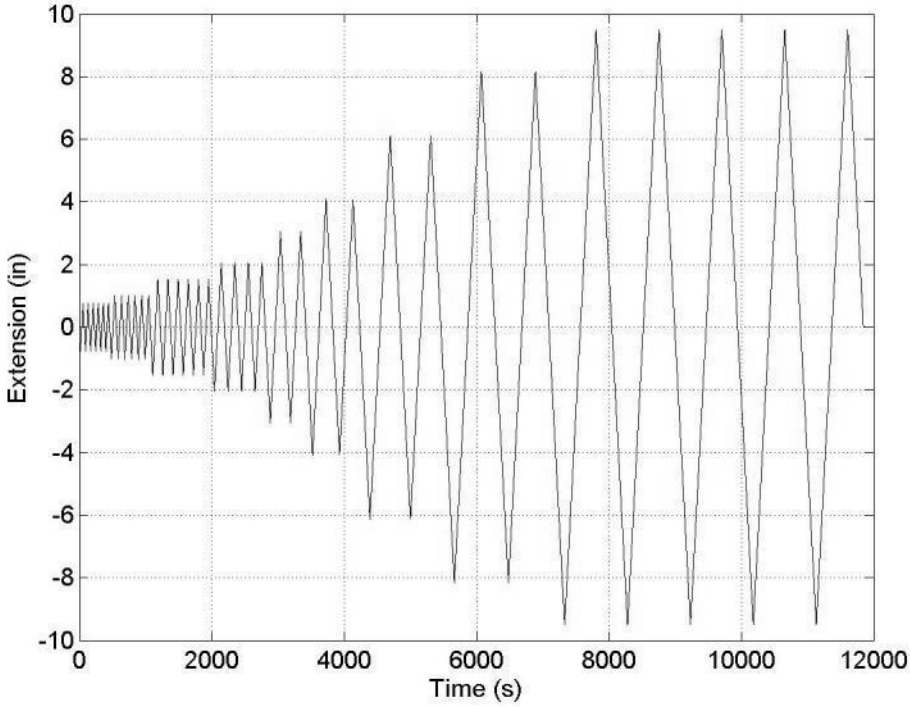

Figure 323: Specimen 10 (W36) - String Potentiometer 2 (actuator)

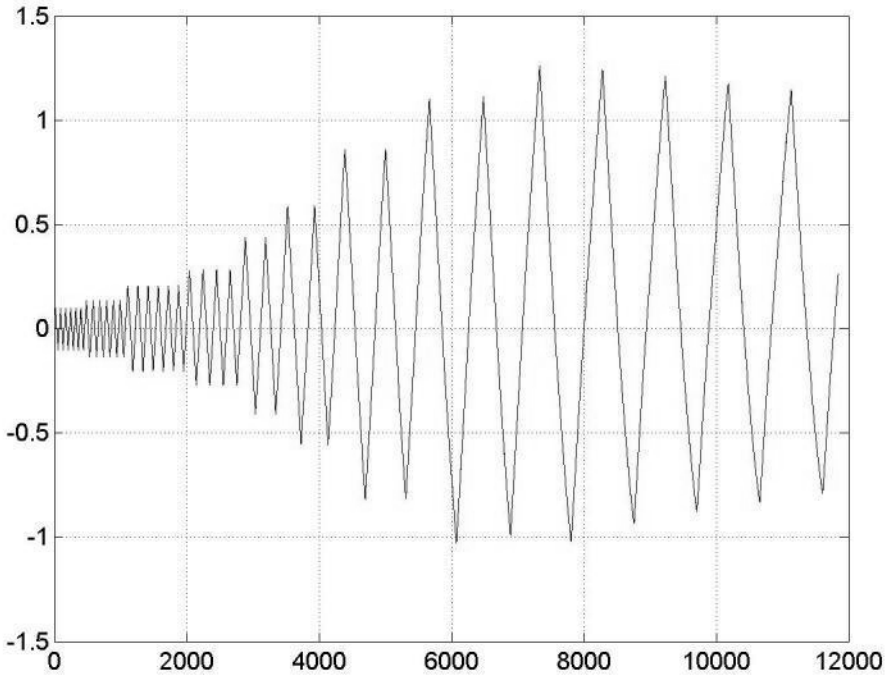

Figure 324: Specimen 10 (W36) - String Potentiometer 3 (beam)

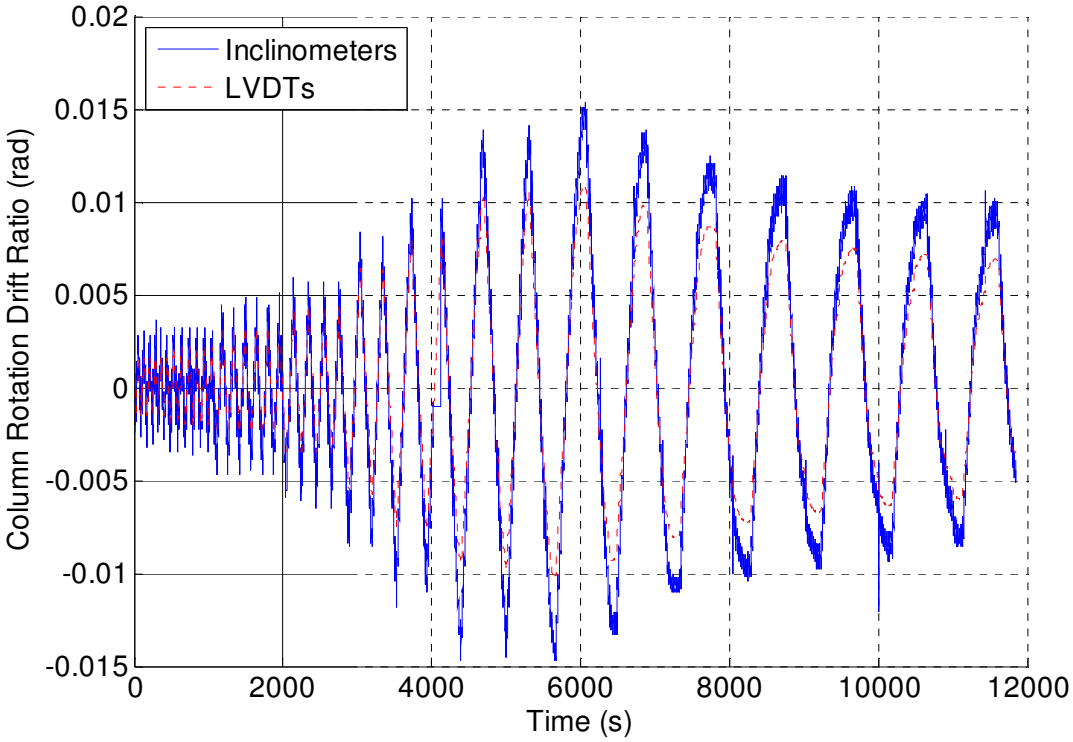

Figure 325: Specimen 10 (W36) - Column Rotation Comparison

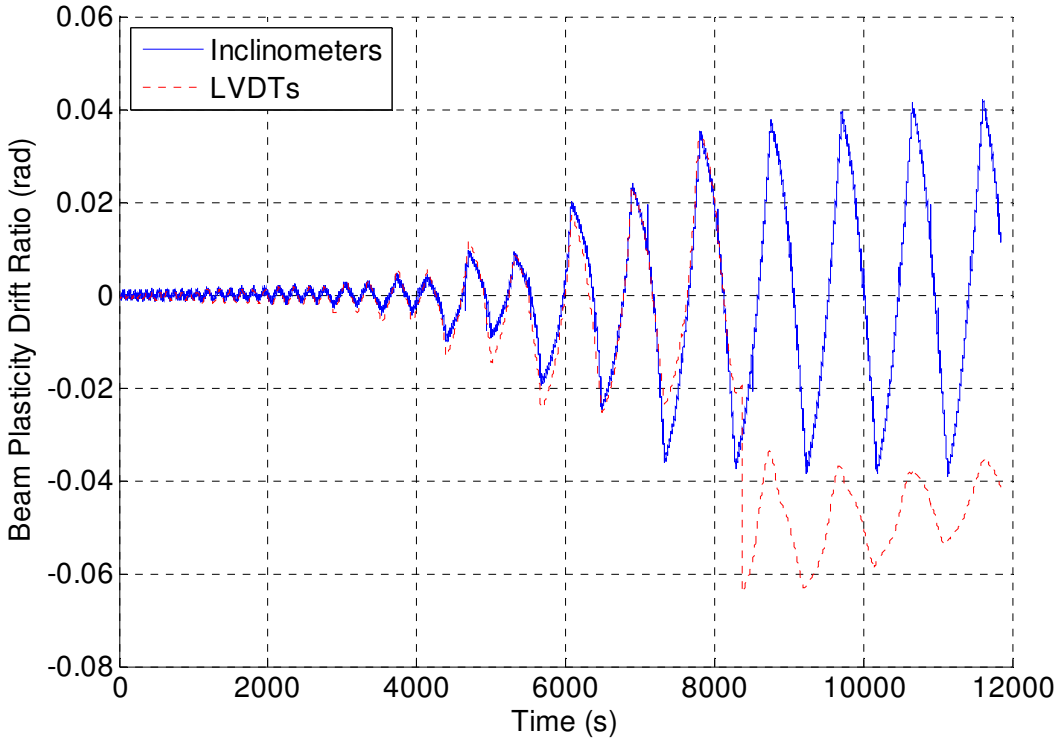

Figure 326: Specimen 10 (W36) - Beam Plasticity Comparison

Appendix R – Specimen 11 (W36-PAF12) Raw Instrumentation Data

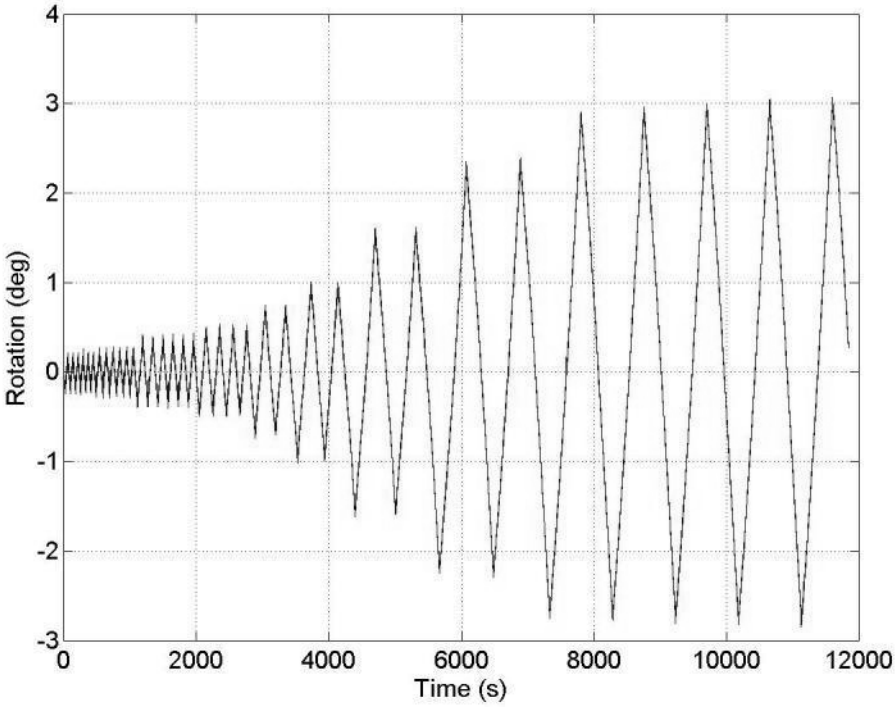

Figure 327: Specimen 11 (W36-PAF12) - Inclinometer 3 (beam)

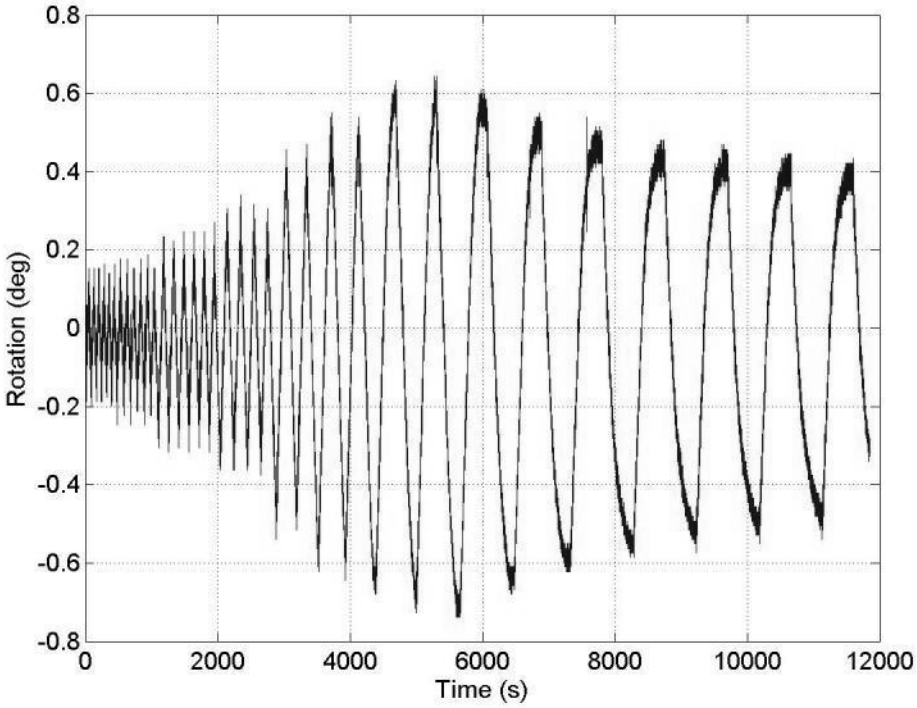

Figure 328: Specimen 11 (W36-PAF12) - Inclinometer 1 (column)

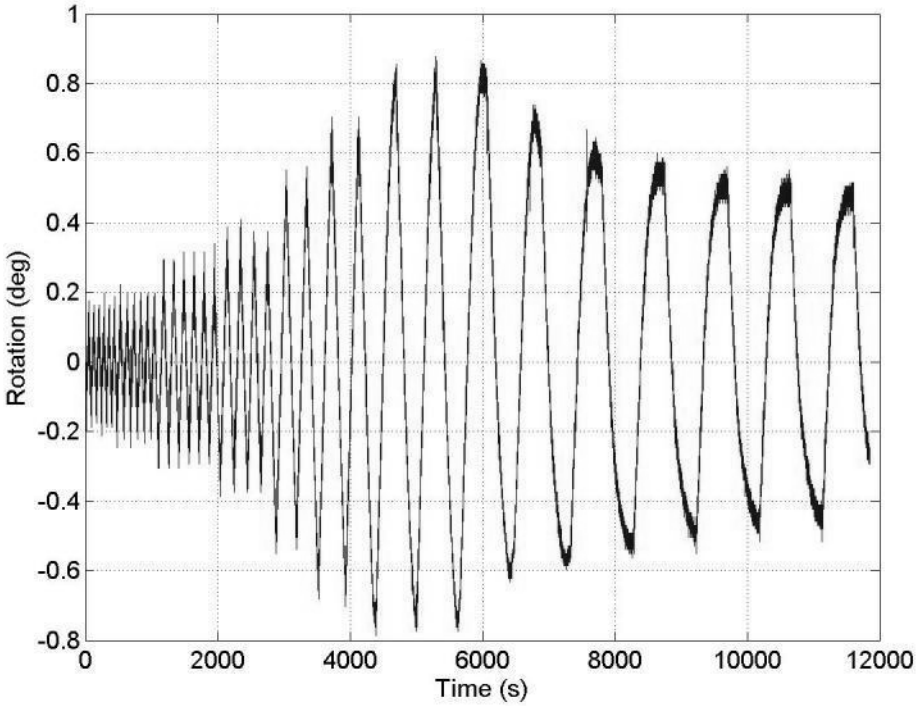

Figure 329: Specimen 11 (W36-PAF12) - Inclinometer 2 (endplate)

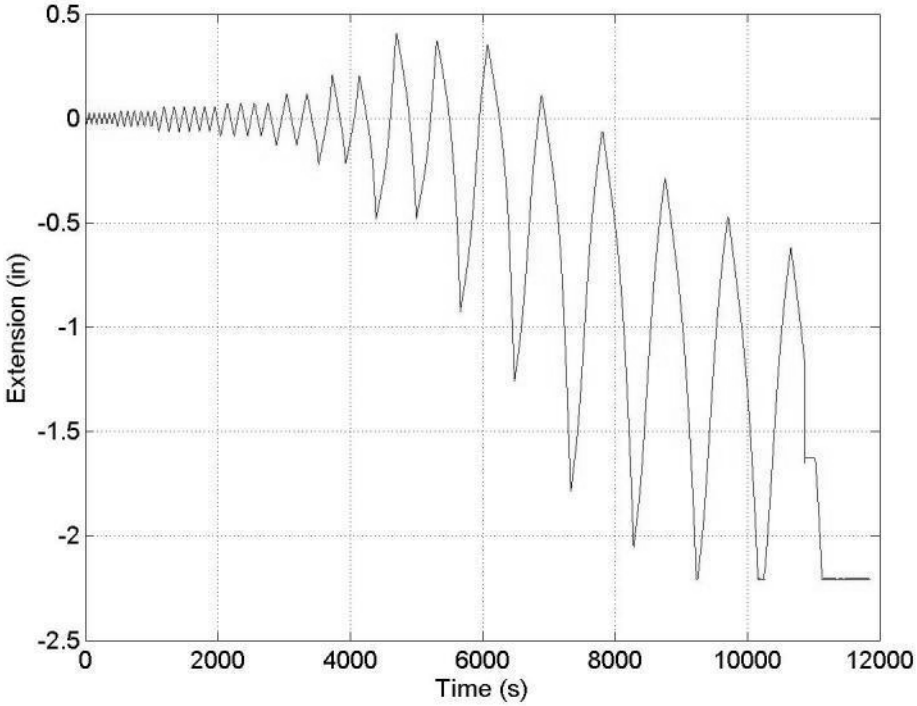

Figure 330: Specimen 11 (W36-PAF12) – LVDT1

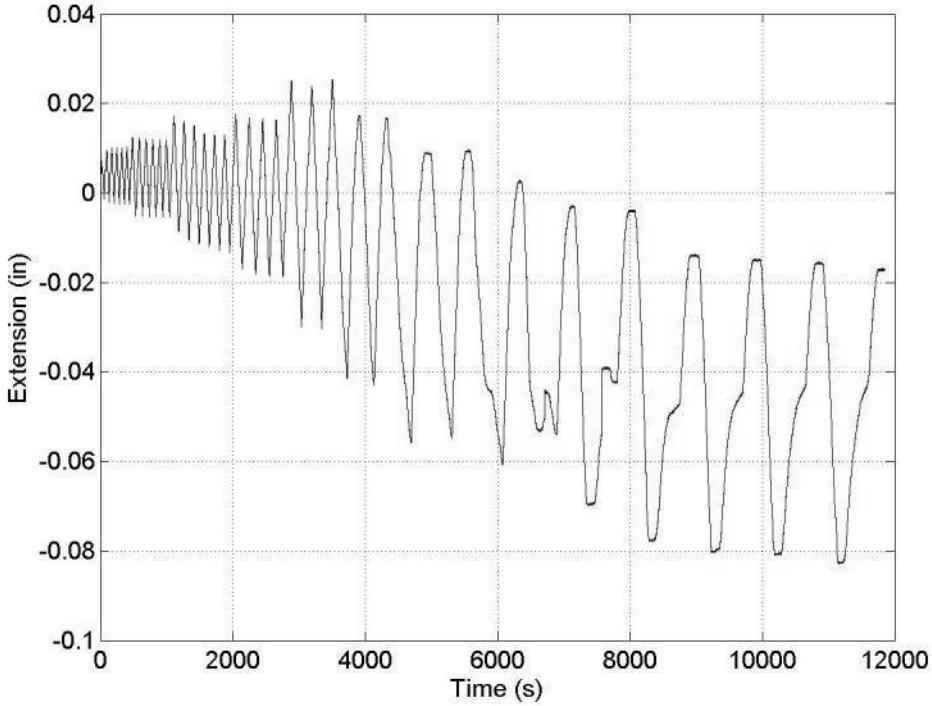

Figure 331: Specimen 11 (W36-PAF12) – LVDT2

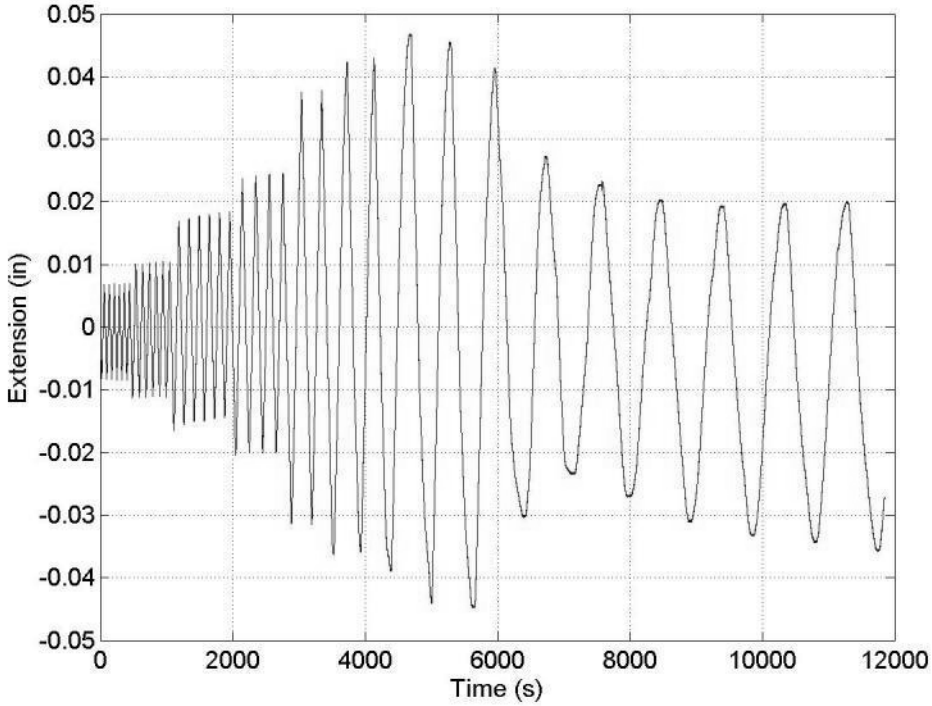

Figure 332: Specimen 11 (W36-PAF12) – LVDT3

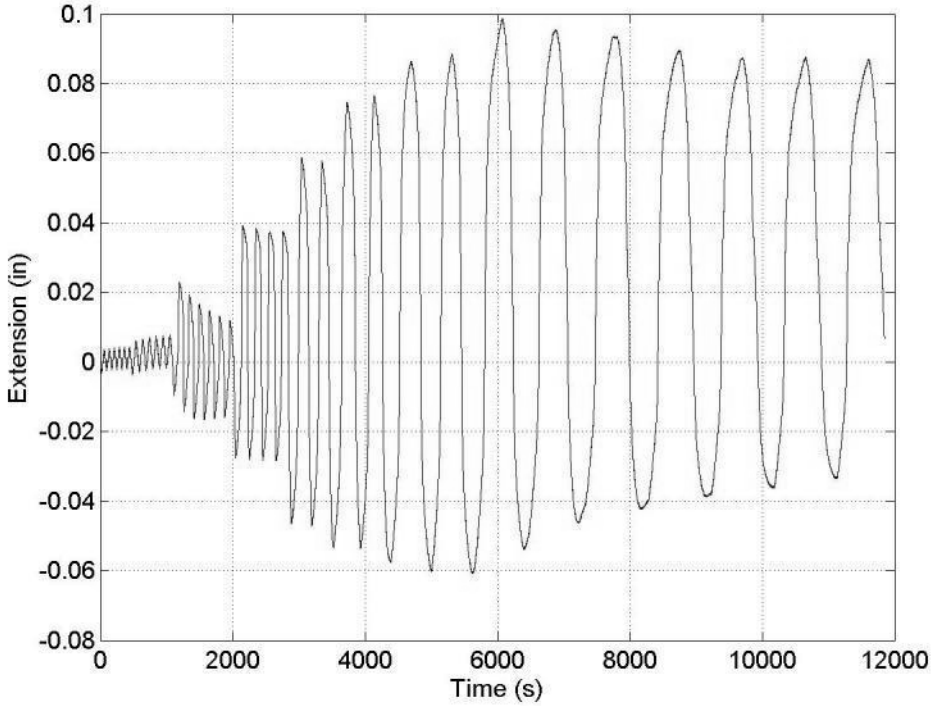

Figure 333: Specimen 11 (W36-PAF12) – LVDT4

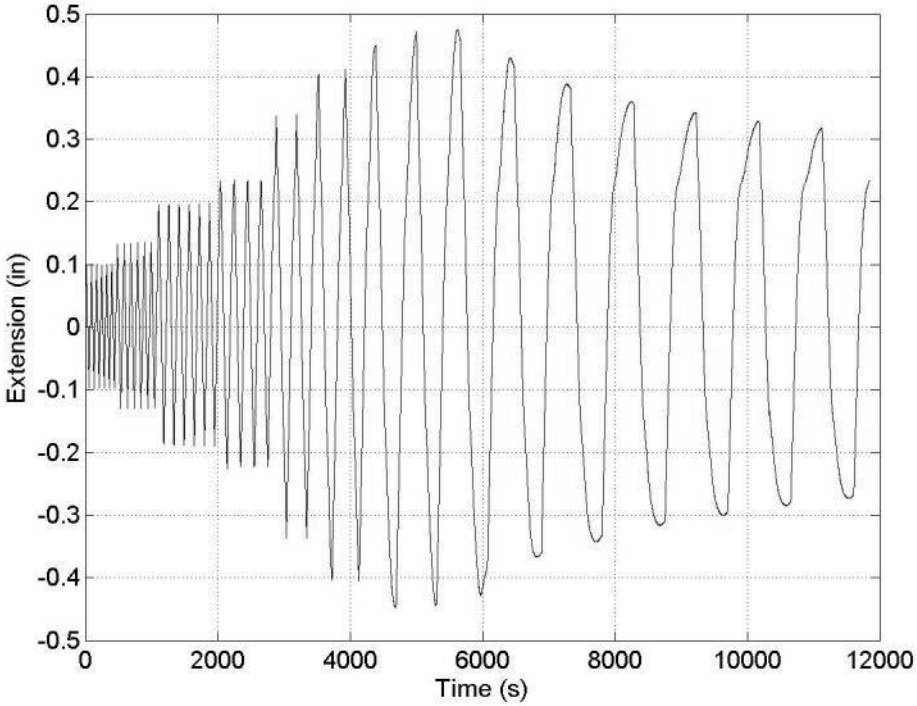

Figure 334: Specimen 11 (W36-PAF12) – LVDT5

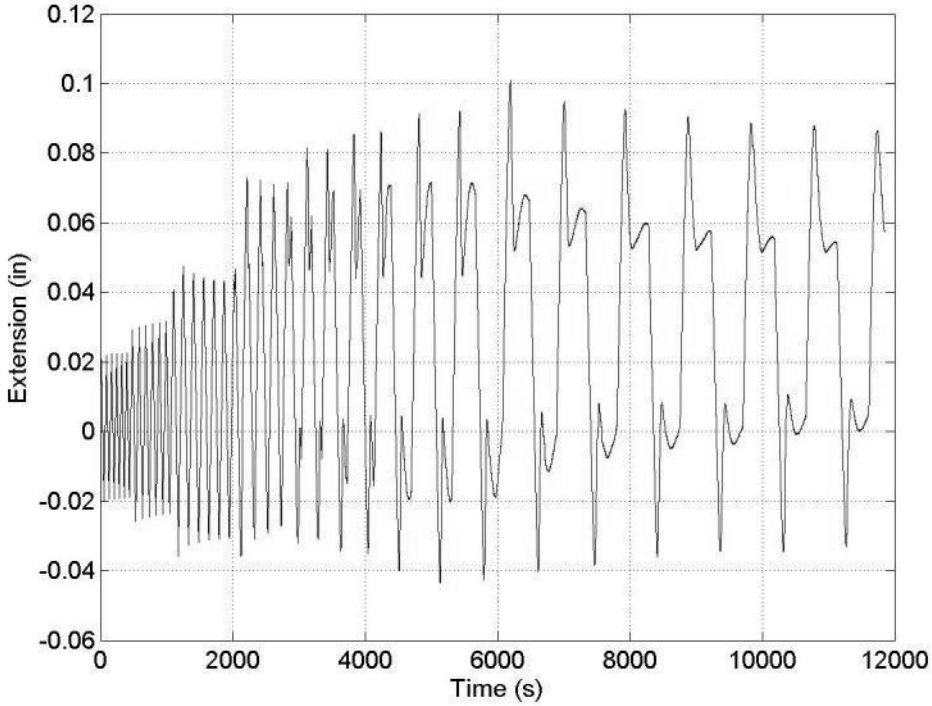

Figure 335: Specimen 11 (W36-PAF12) – LVDT6

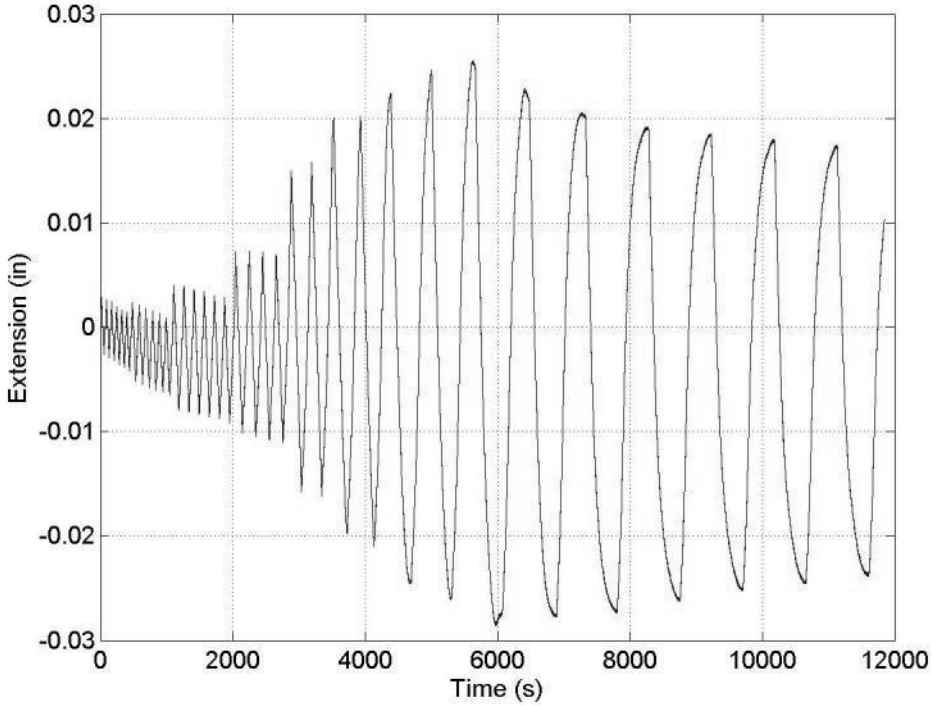

Figure 336: Specimen 11 (W36-PAF12) – LVDT7

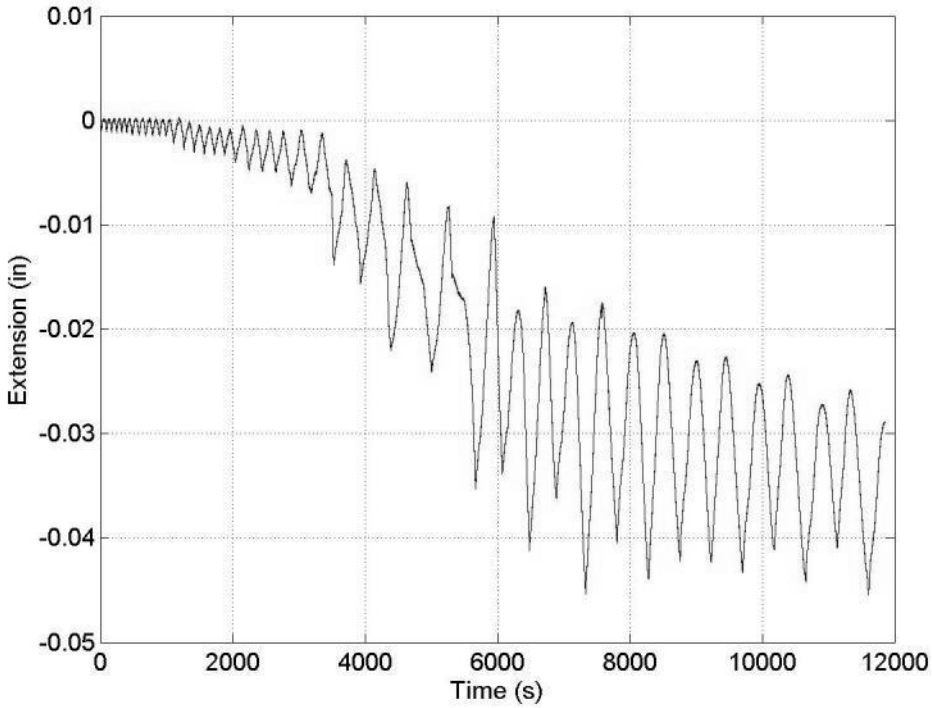

Figure 337: Specimen 11 (W36-PAF12) – LVDT8

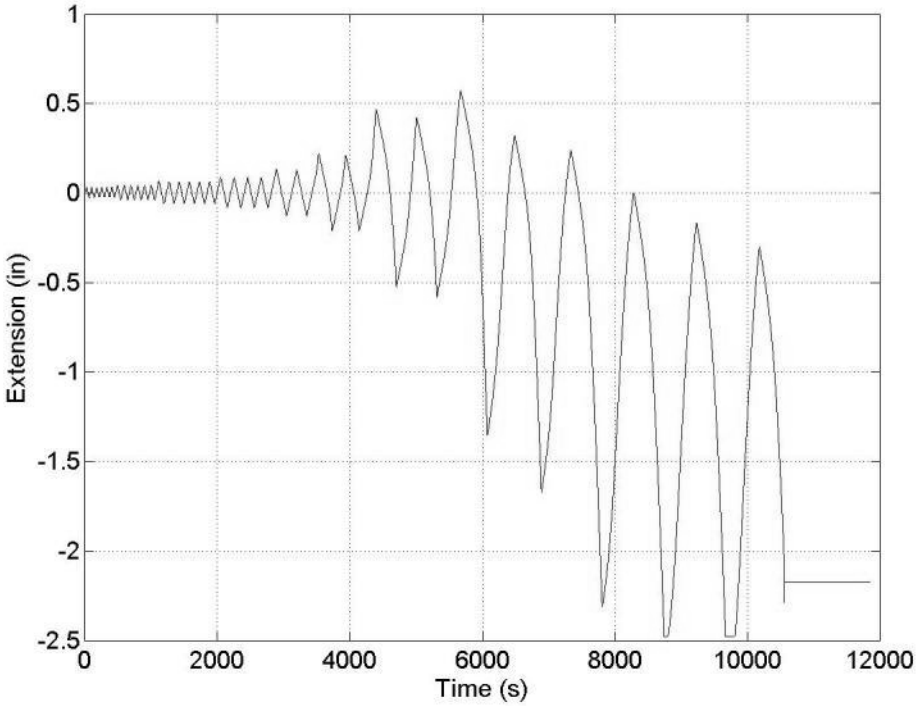

Figure 338: Specimen 11 (W36-PAF12) – LVDT9

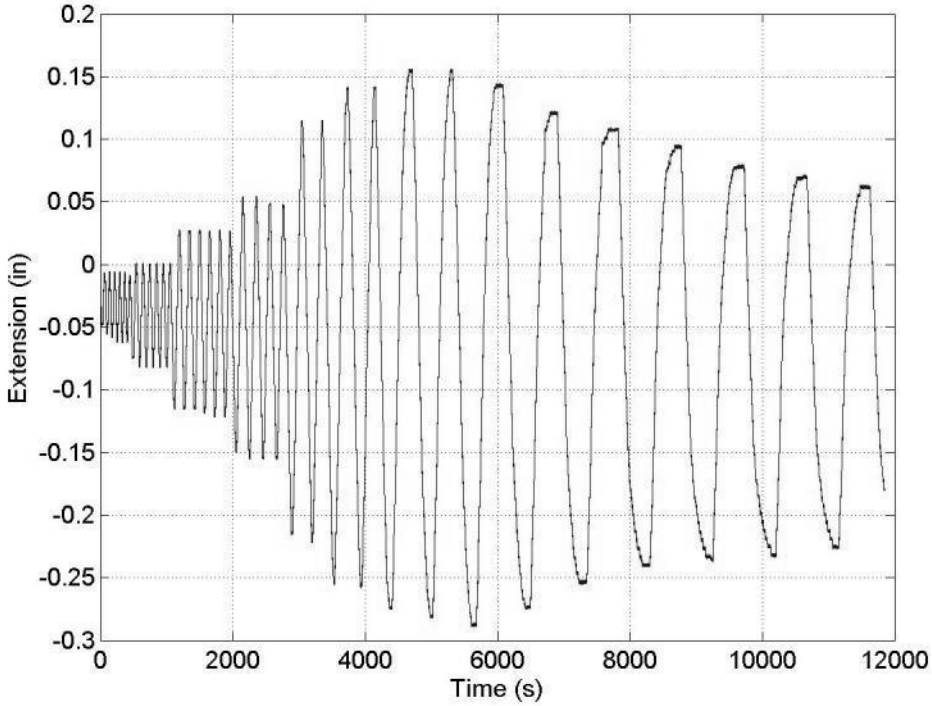

Figure 339: Specimen 11 (W36-PAF12) - String Potentiometer 1 (column)

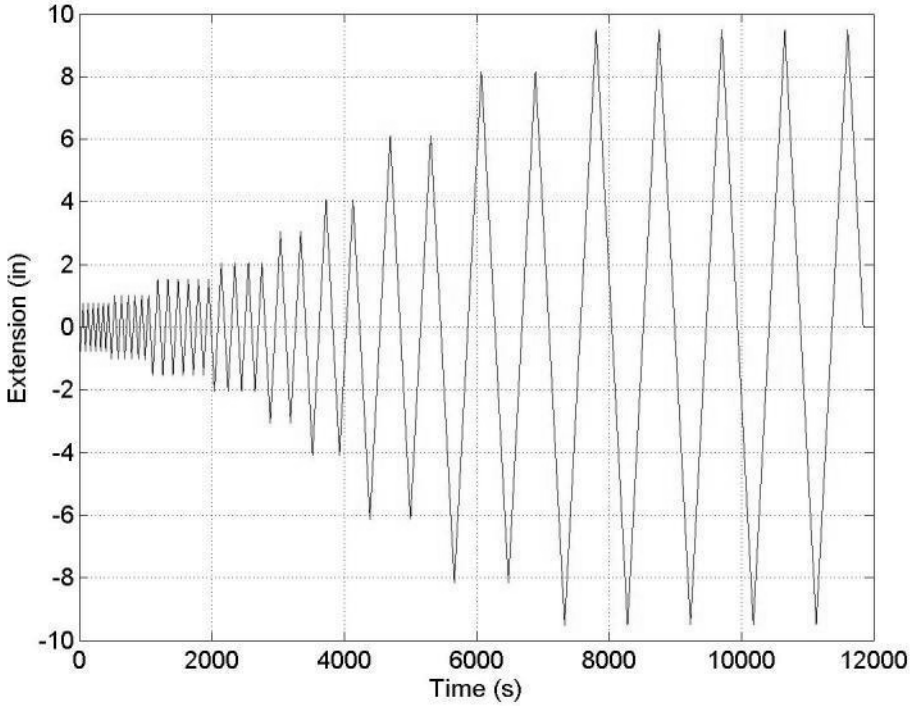

Figure 340: Specimen 11 (W36-PAF12) - String Potentiometer 2 (actuator)

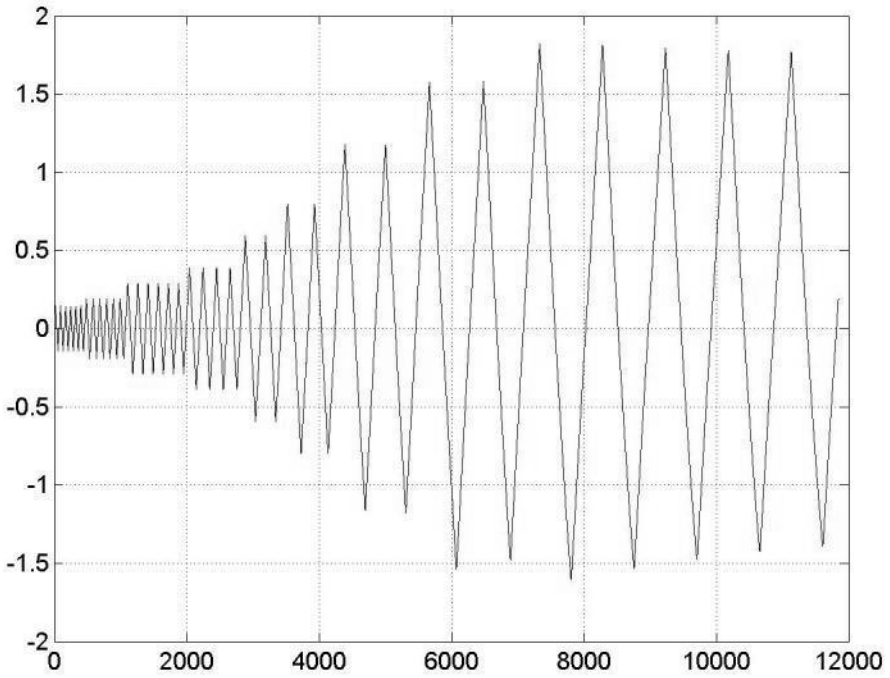

Figure 341: Specimen 11 (W36-PAF12) - String Potentiometer 3 (beam)

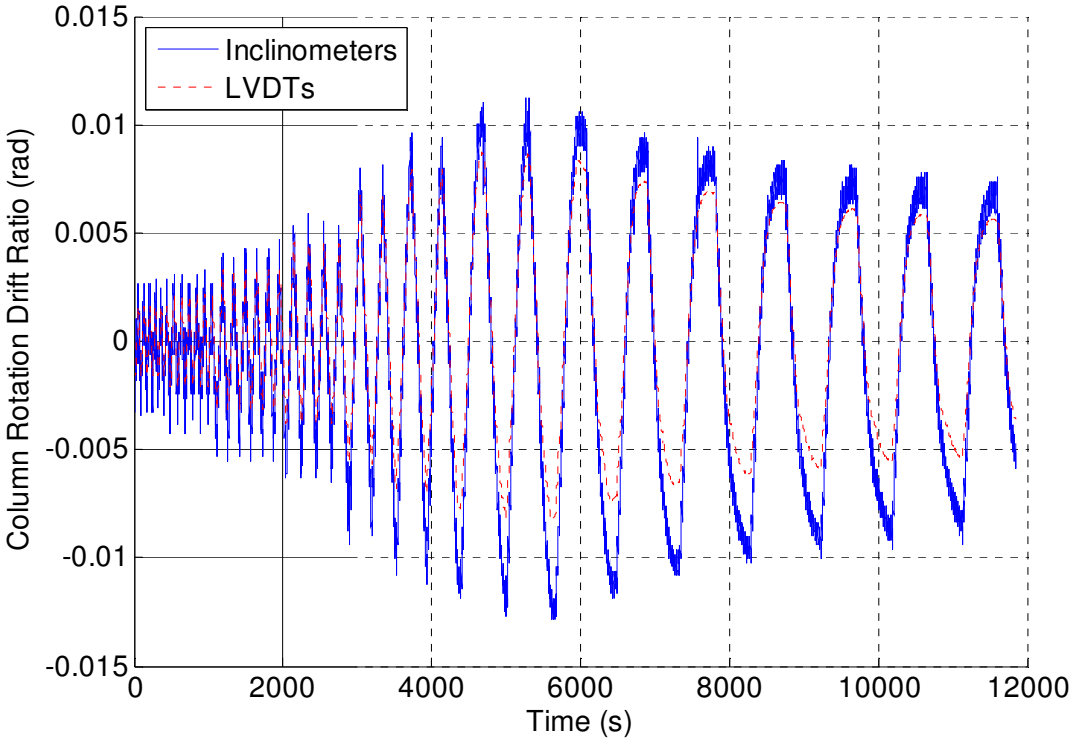

Figure 342: Specimen 11 (W36-PAF12) - Column Rotation Comparison

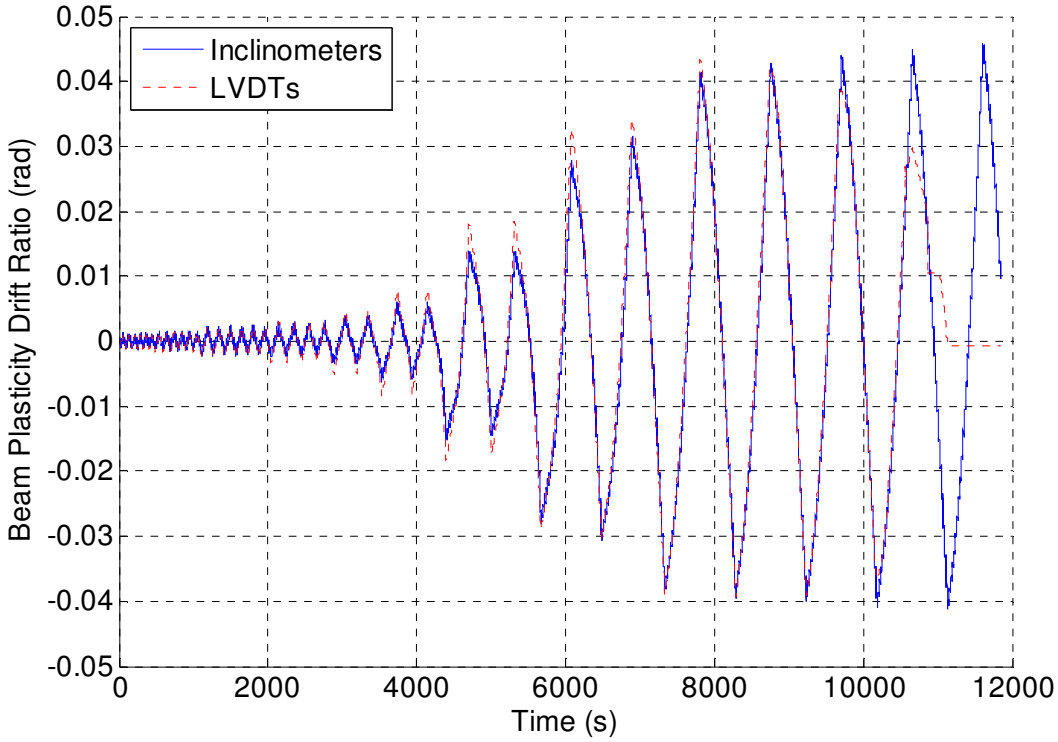

Figure 343: Specimen 11 (W36-PAF12) - Beam Plasticity Comparison

Appendix S – Specimen 12 (W36-PAF-array) Raw Instrumentation Data

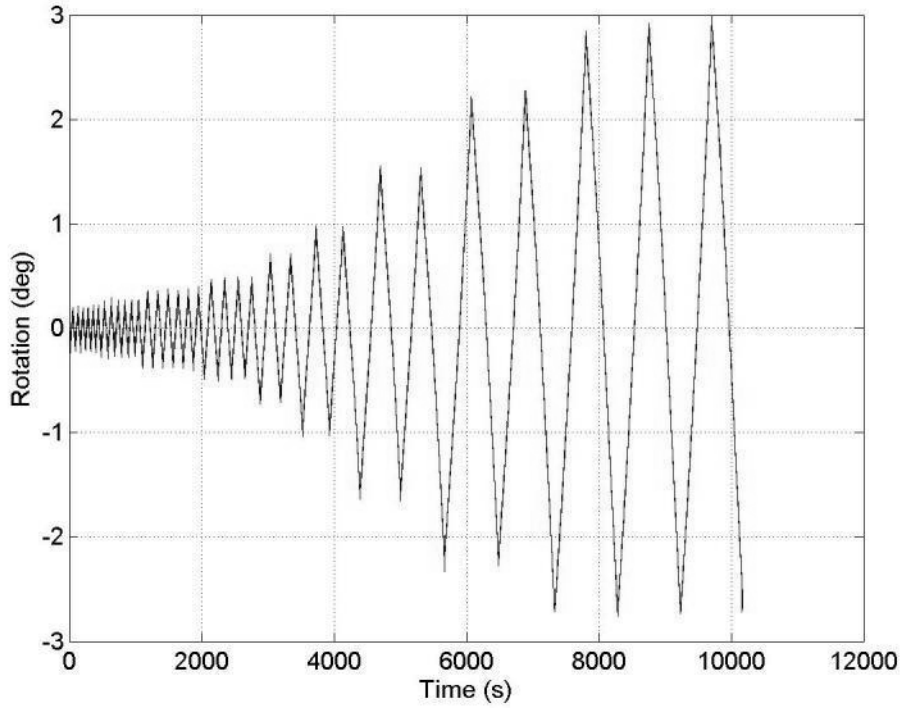

Figure 344: Specimen 12 (W36-PAF-array) - Inclinometer 3 (beam)

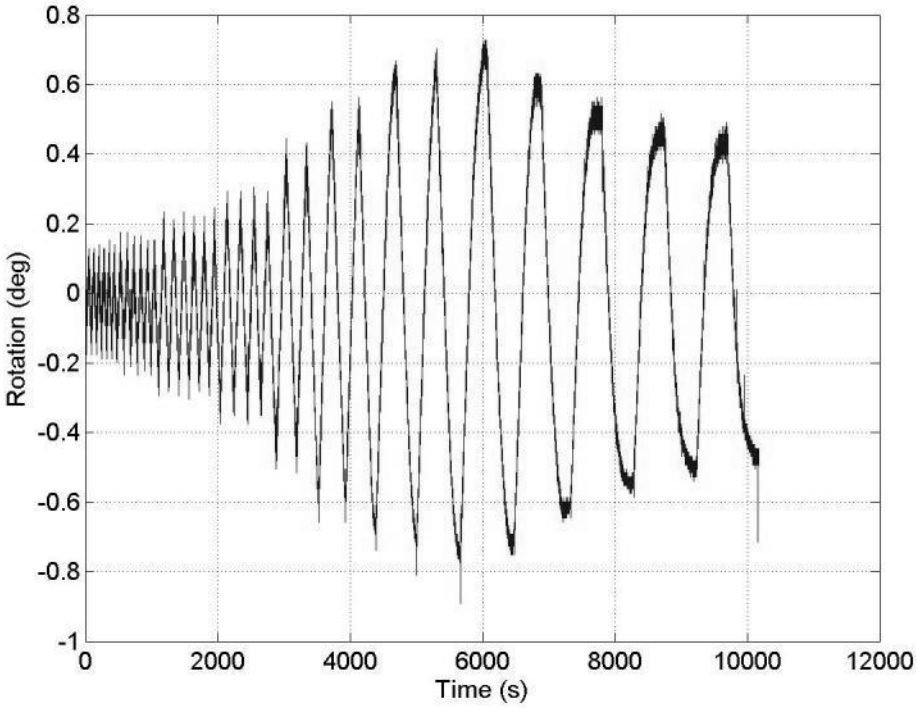

Figure 345: Specimen 12 (W36-PAF-array) - Inclinometer 1 (column)

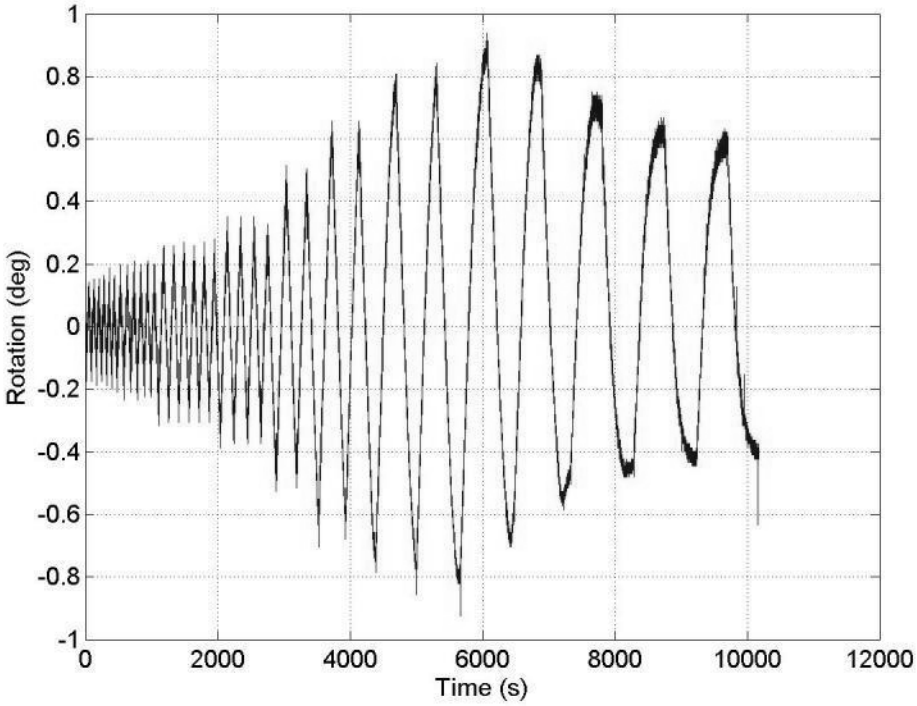

Figure 346: Specimen 12 (W36-PAF-array) - Inclinometer 2 (endplate)

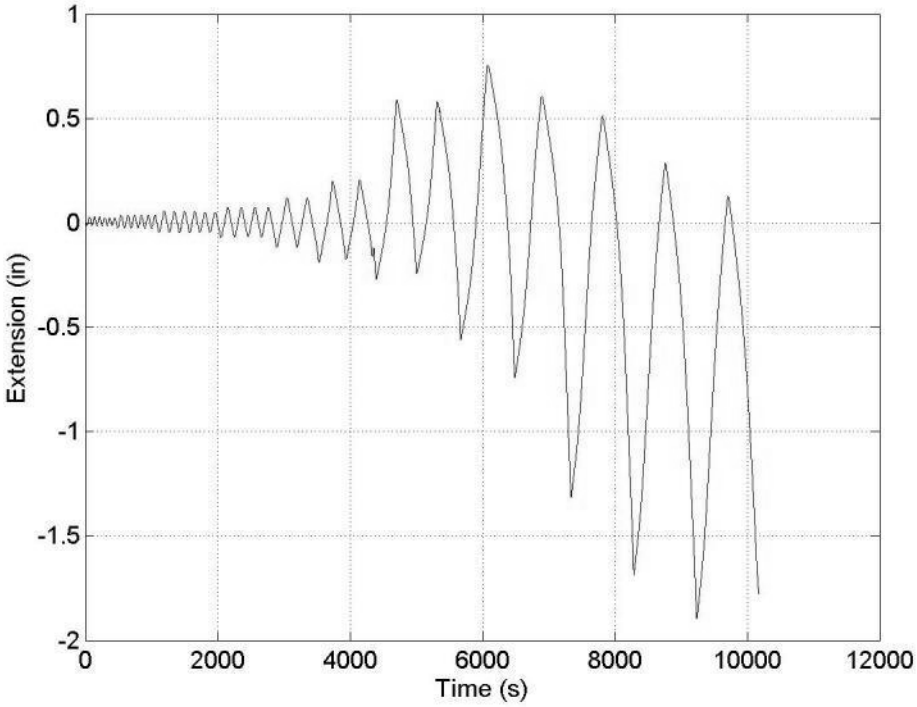

Figure 347: Specimen 12 (W36-PAF-array) - LVDT1

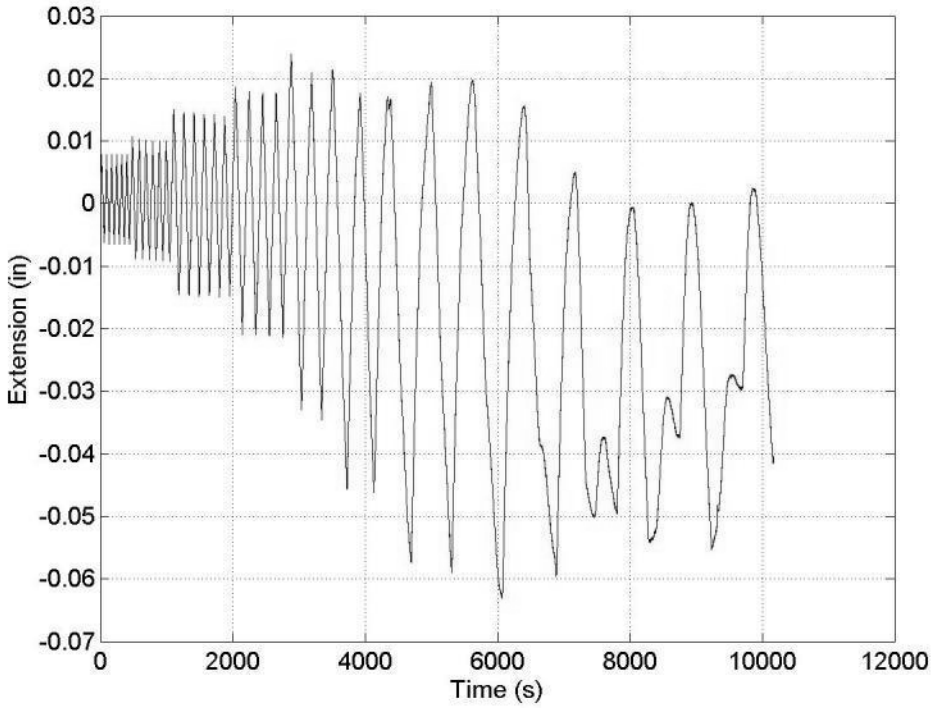

Figure 348: Specimen 12 (W36-PAF-array) – LVDT2

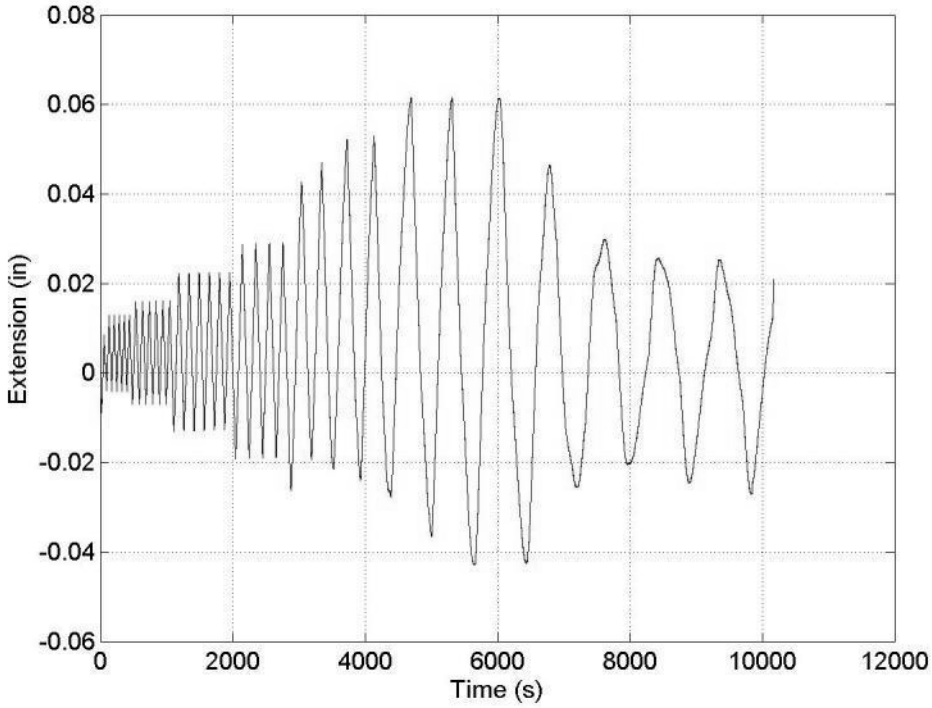

Figure 349: Specimen 12 (W36-PAF-array) – LVDT3

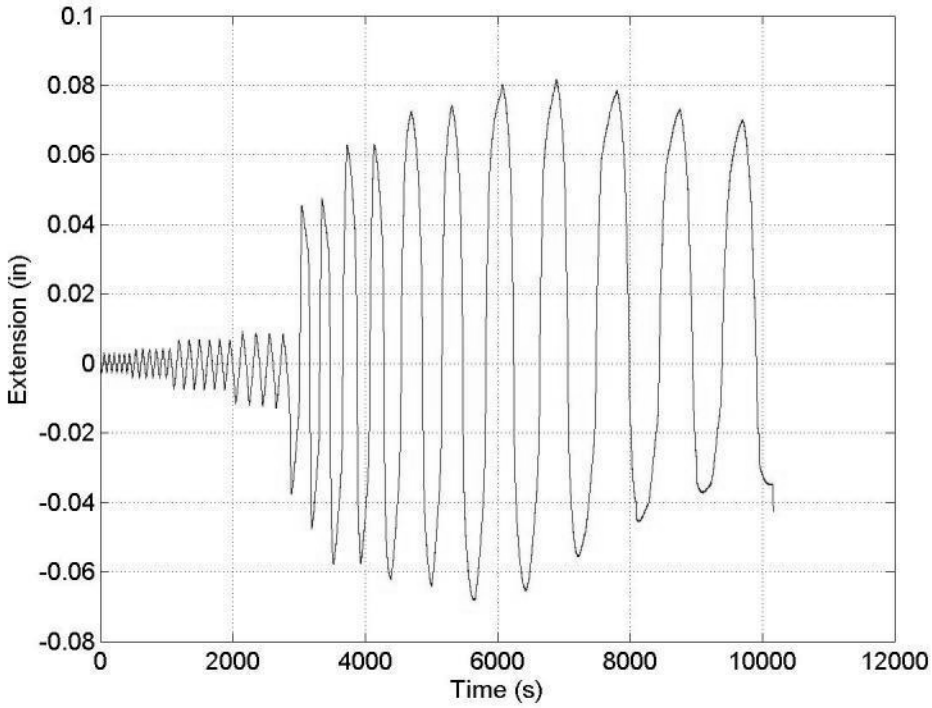

Figure 350: Specimen 12 (W36-PAF-array) – LVDT4

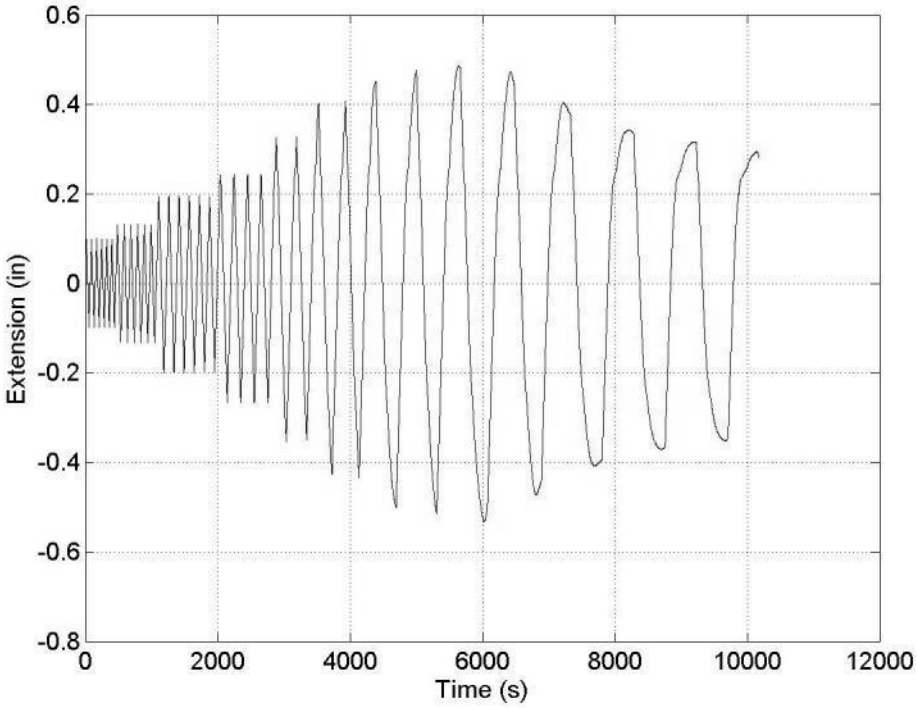

Figure 351: Specimen 12 (W36-PAF-array) – LVDT5

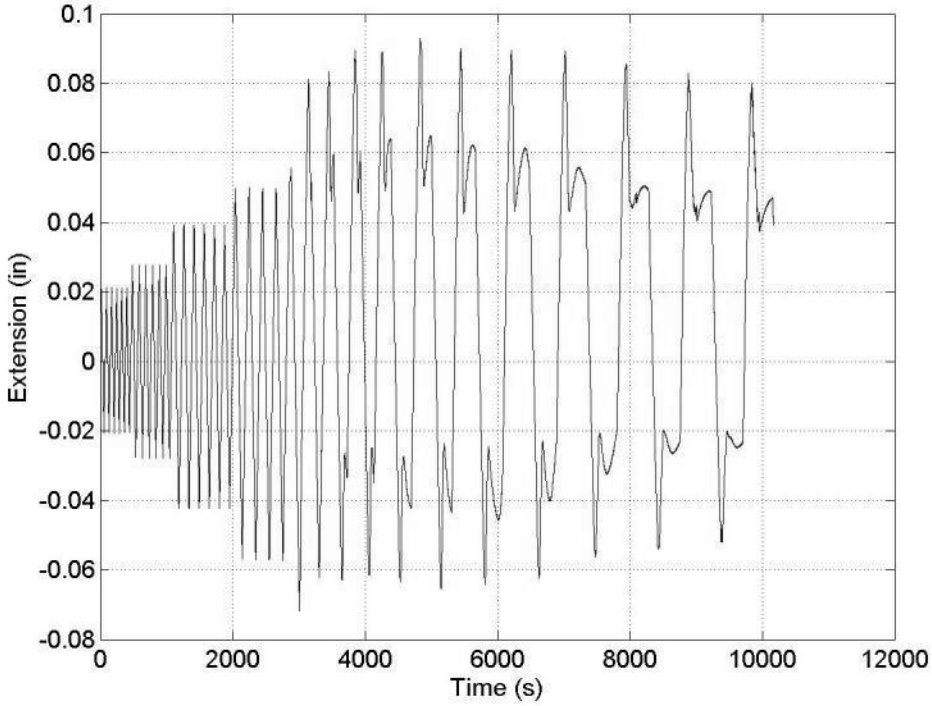

Figure 352: Specimen 12 (W36-PAF-array) – LVDT6

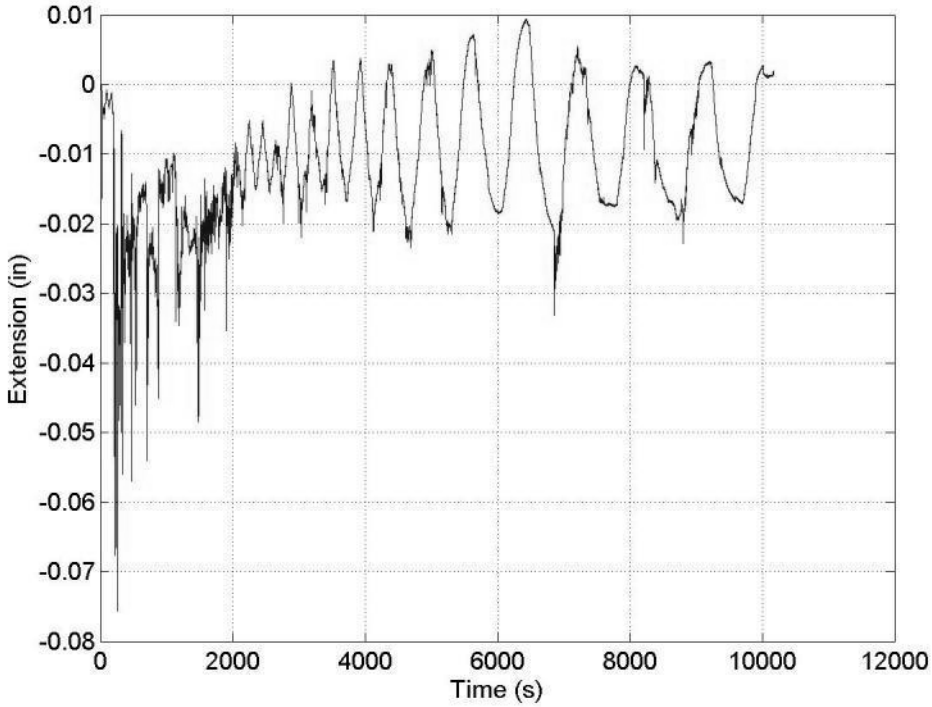

Figure 353: Specimen 12 (W36-PAF-array) – LVDT7

LVDT 8 data not collected during this test

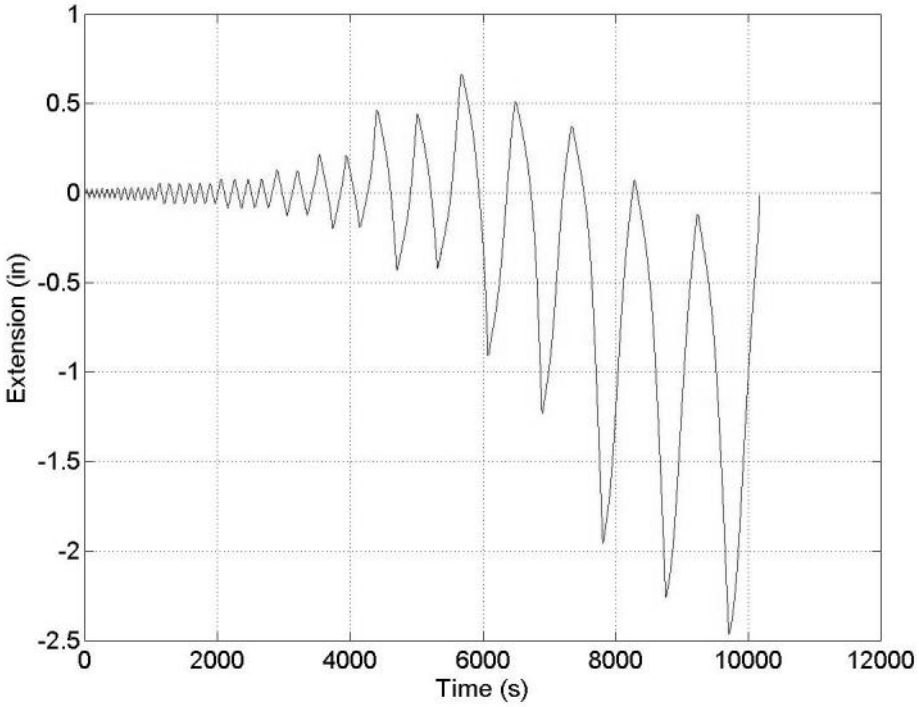

Figure 354: Specimen 12 (W36-PAF-array) – LVDT9

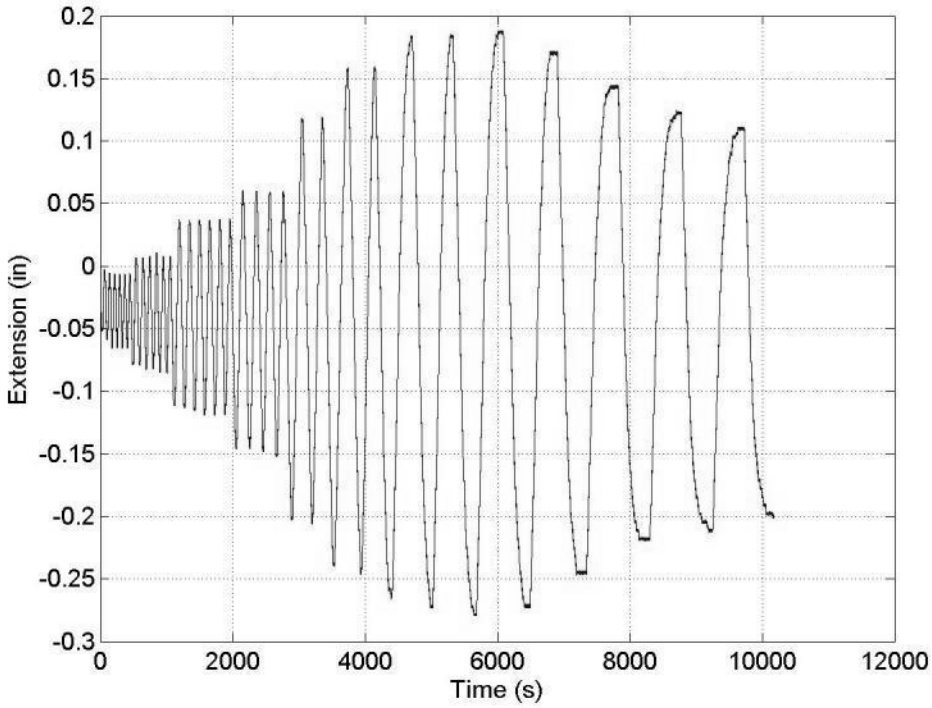

Figure 355: Specimen 12 (W36-PAF-array) - String Potentiometer 1 (column)

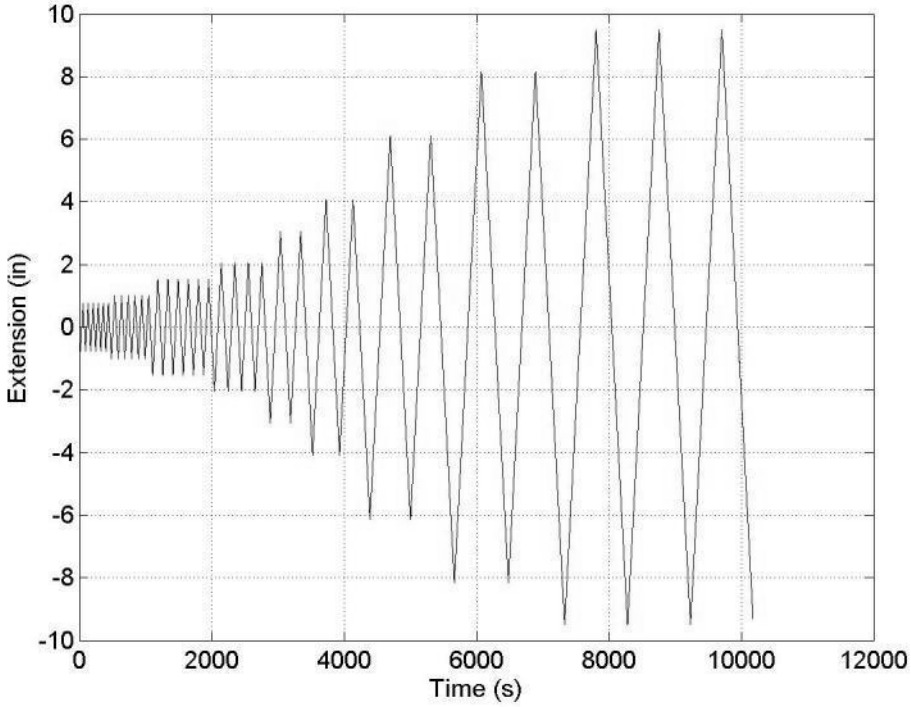

Figure 356: Specimen 12 (W36-PAF-array) - String Potentiometer 2 (actuator)

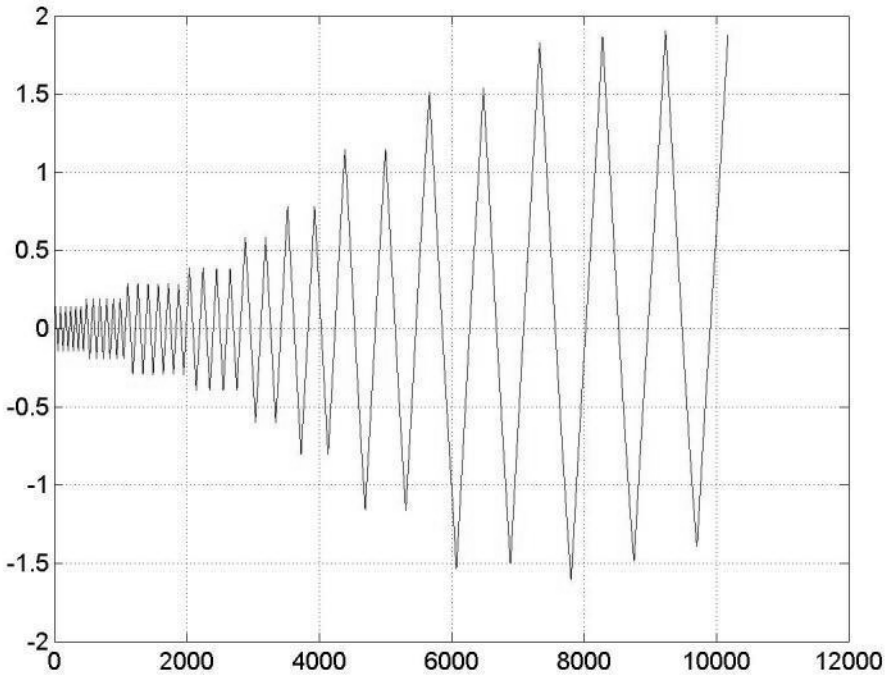

Figure 357: Specimen 12 (W36-PAF-array) - String Potentiometer 3 (beam)

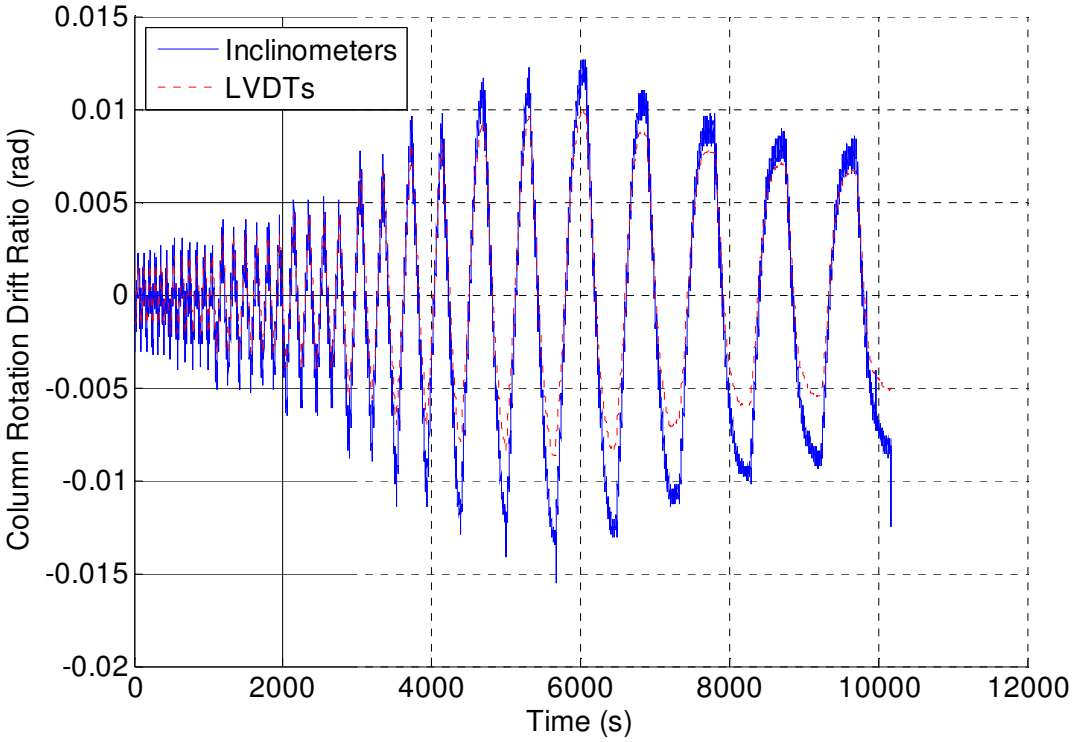

Figure 358: Specimen 12 (W36-PAF-array) - Column Rotation Comparison

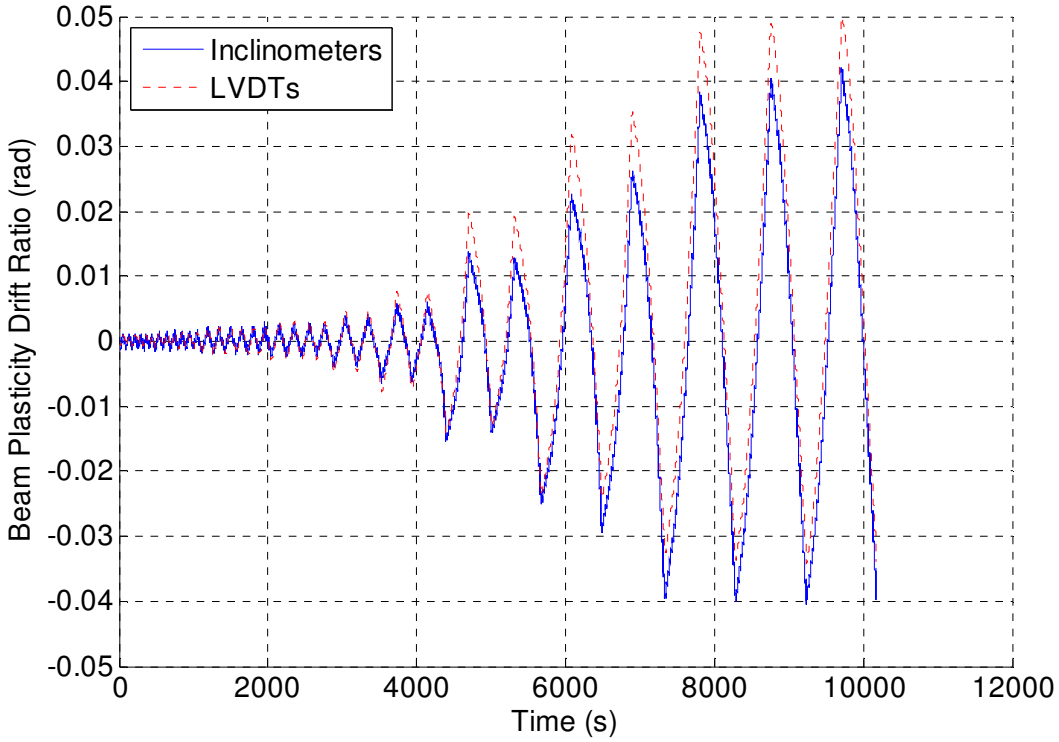

Figure 359: Specimen 12 (W36-PAF-array) - Beam Plasticity Comparison